JRC Scientific and Technical Reports

Proceedings
“Oceans From Space” Venice 2010

Extended Abstracts of the Contributions presented at the “Oceans form Space” Symposium
Scuola Grande di San Giovanni Evangelista, Venice (Italy), 26-30 April 2010

V. Barale, J.F.R. Gower, L. Alberotanza, ed.s

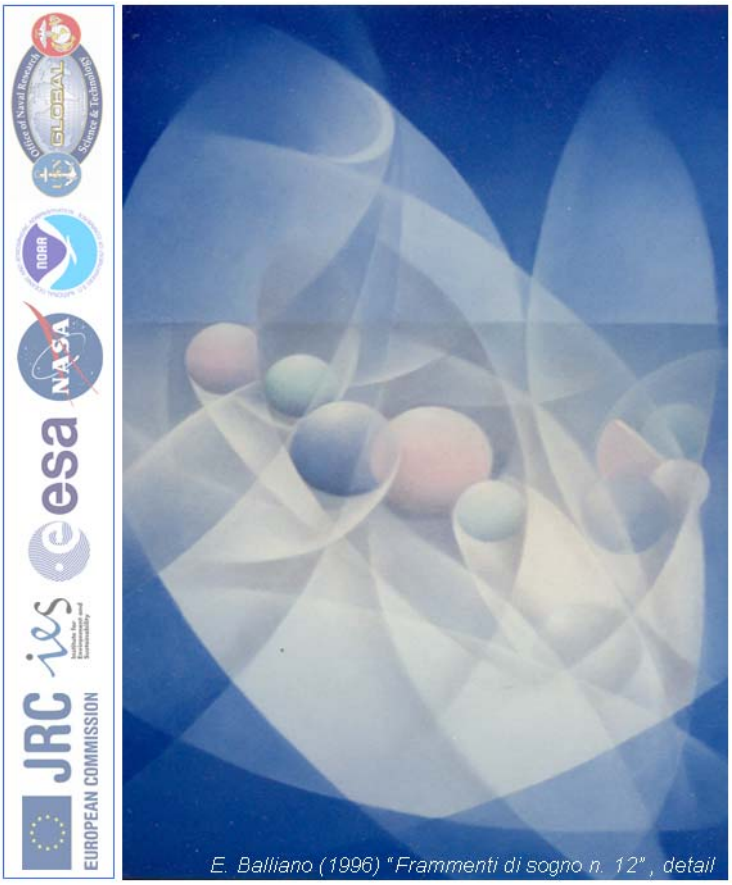

EUR 24324 EN - 2010

JRC
EUROPEAN COMMISSION
Institute for Environment and Sustainability

The mission of the JRC-IES is to provide scientific-technical support to the European Union's policies for the protection and sustainable development of the European and global environment.

European Commission
Joint Research Centre
Institute for Environment and Sustainability

Contact information
Address: V. Barale, IES JRC/EC (TP272)
Via E. Fermi 2749, I-21027 Ispra (VA), Italy
E-mail: vittorio.barale@jrc.ec.europa.eu
Tel.: +39 0332 789274
Fax: +39 0332 789034

http://ies.jrc.ec.europa.eu/
http://www.jrc.ec.europa.eu/

JRC 57986

EUR 24324 EN
ISBN 978-92-79-15577-2
ISSN 1018-5593
DOI 10.2788/8394

Luxembourg: Publications Office of the European Union

Printed in Italy

TITLE:

Proceedings
"Oceans from Space" Venice 2010

Extended Abstracts of the contributions presented at the "Oceans form Space" Symposium
Scuola Grande di San Giovanni Evangelista, Venice (Italy), 26-30 April 2010

EDITORS:

Vittorio Barale
European Commission, Joint Research Centre
TP 272, Via E. Fermi 2749, I-21027 Ispra (VA), Italy

e-mail:	tel	fax
vittorio.barale@jrc.ec.europa.eu	+39 0332 789274	+39 0332 789034

Jim F.R. Gower
Institute of Ocean Sciences, Fisheries and Oceans Canada
9860 West Saanich Road, Sidney, B.C. Canada V8L 4B2

e-mail:	tel	fax
Jim.Gower@dfo-mpo.gc.ca	+1 250 363 6558	+1 250 363 6746

Luigi Alberotanza
Istituzione Centro Previsioni e Segnalazioni Maree
Palazzo Cavalli, San Marco 4090, I-30124 Venezia, Italy

e-mail:	tel	fax
luigi.alberotanza@ismar.cnr.it	+39 041 2748787	+39 041 5210378

ABSTRACT:

The Extended Abstracts of the poster presentations delivered at the 4th "Oceans from Space" Symposium – held in Venice, Italy, on 26-30 April 2010 – address every facet of space sciences and technologies applied to marine and maritime issues. Missions, satellites, sensors, passive and active techniques, calibration and validation schemes, algorithms and models are covered. Applications range from the study of physical dynamical processes to that of biological and ecological status, from local to global scales. The results already achieved, or soon to come, demonstrate the potential of oceanographic remote sensing to explore the dynamical and bio-geo-chemical features of the World's Oceans.

ACKNOWLEDGEMENTS:

The 4th "Oceans from Space" Venice 2010 Symposium was made possible by grants provided for this purpose by the European Commission, Joint Research Centre (EC JRC); European Space Agency (ESA); National Aeronautics and Space Administration (NASA), USA; National Oceanic and Atmospheric Administration (NOAA), USA; Office of Naval Research, Global (ONRG), USA.

In particular, this work relates to Department of the Navy Grant N62909-10-1-1025 issued by Office of Naval Research Global. The US Government has a royalty-free license throughout the world in all copyrightable material contained herein.

REFERENCE:

V. Barale, J.F.R. Gower and L. Alberotanza, ed.s (2010). Proceedings "Oceans from Space" Venice 2010. European Commission, EUR 24324 EN, pp. 266.

Preface

The “Oceans from Space” Symposium series aims to provide, every ten years, a thorough state-of-the-art outline, a forum to debate topical issues and an overview of ongoing research, in the field of Satellite Oceanography. The present Proceedings refer to the 4th “Oceans from Space” edition – held once again in Venice, Italy, on 26-30 April 2010 – that followed the three previous events held in 1980, 1990 and 2000. During the Symposium, a number of invited speakers delivered key-note lectures on major historical achievements; selected subjects were dealt with in thematic seminars and panel discussions; current scientific work was presented in a sequence of poster sessions.

The present volume collects the Extended Abstracts of all submitted contributions that were delivered in the poster sessions. The papers address virtually every facet of oceanographic remote sensing, including missions, satellites, sensors, passive and active techniques, calibration and validation schemes, algorithms and models. The applications presented range from the assessment of physical parameters and dynamical processes to that of bio-geo-chemical cycles and ecological status, from local to global scales. However, the individual sessions did not focus on either single techniques or environmental aspects, but rather maintained a substantial interdisciplinary character. For this reason, the Extended Abstracts are not grouped according to thematic criteria, but are simply listed according to the alphabetical order of the first Authors’ names.

Thanks are due to all Contributors who provided the following wealth of scientific material, as well as to the sponsoring Agencies and International Organizations that made “Oceans from Space” possible:

- European Commission, Joint Research Centre (EC JRC),
- European Space Agency (ESA),
- National Aeronautics and Space Administration (NASA), USA,
- National Oceanic and Atmospheric Administration (NOAA), USA,
- Office of Naval Research, Global (ONRG), USA.

Venice, April 2010 Vittorio Barale

Observation Platform in Long Island Sound for Calibration/validation of Multi-and Hyperspectral Ocean Color Satellite Sensing of Coastal Waters

S. A. Ahmed [a], R.A. Arnone [b], A. Gilerson [a], S. Hlaing [a], A.Weidemann [b]

[a] Optical Remote Sensing Laboratory, City College, New York, NY, United States – ahmed@ccny.cuny.edu
[b] Naval Research Laboraory, Stennis Space Center – bob.arnone@nrlssc.navy.mil

Abstract – Improving satellite retrievals of inherent optical properties (IOPs) is increasingly focused on coastal waters because of adjacent population concentrations and susceptibility to anthropogenic impacts. However, their complexity has presented more retrieval challenges than open ocean waters. To address these concerns, and support multi snd hyper-spectral cal/val, and development of new retrieval techniques and algorithms for coastal waters, we have established a new scientifically comprehensive offshore platform, the Long Island Sound Coastal Observatory (LISCO). Its measurement suite combines multi-(SeaPRISM) and hyperspectral HyperSAS measurements for calibration/validations of current and future Ocean Color satellite as well as for hyperspectral sensors. Recent results from LISCO, which combine multi- and hyperspectral radiometer data radiometers are presented and compared with MODIS satellite data.

Key words: coastal water, platform, validation.

1. INTRODUCTION

Advances in oceanic bio-optical processes are expected to be more heavily focused on improving satellite retrieval products of inherent optical properties (IOP) of coastal waters, which, because of their complexity, offer more challenges than open ocean waters, where satellite observations and retrieval algorithms are already reasonably effective. Thus, the validation of the current and future Ocean Color satellite data is important for characterizing the optical environment connected with coastal waters, which are of importance because of population concentrations along them and their susceptibility to anthropogenic impacts. To address these concerns, and support present and future multi- and hyper-spectral calibration/validation activities, as well as the development of new measurement and retrieval techniques and algorithms for coastal waters, City College (CCNY) along with Naval Research Laboratory at Stennis Space Center, has established a new, scientifically comprehensive, off-shore platform, the Long Island Sound Coastal Observatory (LISCO), to serve as a venue and framework for combining multi- and hyperspectral radiometer emasurements with satellite and in-situ measurements and radiative transfer simulations of coastal waters, helping to and provide more effective closure for the whole measurement validation/simulation loop. Measurements from the platform are utilized for multi-spectral calibration/validation of current Ocean Color satellites (MODIS, MERIS, SeaWIFS) in coastal waters, and for evaluating future satellites missions (OCM2, Sentinel 2, NPOESS) with extension to cal/val of hyperspectral sensors (Hyperspectral Imager for Coastal Ocean, HICO), as well as for improvements in coastal IOP retrieval and atmospheric correction algorithms.

The platform combines an AERONET SeaPRISM radiometer (CIMEL ELECTRONIQUE, France) as a part of AERONET Ocean Color Network **(**Zibordi *et al*., 2009**),** with a co-located HyperSAS (Satlantic, Canada) set of radiometers capable of hyperspectral measurements of water leaving radiance, sky radiance and down welling irradiance. Both instruments were installed on the Long Island Sound Coastal Observatory (LISCO) in October 2009 and since then have been providing data. SeaPRISM data are transferred by the satellite link to NASA, processed by the NASA AERONET group and posted on the NASA AERONET website. HyperSAS data are transmitted by broadband cellular service to the CCNY server. The LISCO site is located ~2 miles from the shore on the oil offloading platform which belongs to the power generation company, National Grid. The coordinates of the site are N 40º57'16", W73º20'30" with an elevation of 12m. The instruments are positioned on a retractable tower on the platform. This is shown below in Fig. 1.

Figure 1. Retractable tower with SeaPRISM and HyperSAS instruments on the LISCO platform.

2. WATER PARAMETERS IN THE AREA NEAR THE PLATFORM

Analysis of area water characteristics were done from MODIS – Aqua satellite data, processed using SeaDAS software v. 5.0.3 with the standard atmospheric correction. Average chlorophyll concentration [Chl] values in the pixels in the immediate vicinity of the platform were found to be: 3-8 mg/l. Backscattering coefficients are in the range 0.01-0.02 m^{-1} , which assuming a backscattering ratio of 1% corresponds to about 1-2 mg/l of Total Suspended Solids. Non algal absorption, mostly due to CDOM for these TSS values, ranges from 0.1 to 0.3m^{-1}, where, according to NOAA HF Radar data, surface currents in the area are 0.2-0.4 m/s. These values are typical of moderate coastal waters. Time series of water parameters in the platform vicinity

show these to be typical for coastal water conditions, and the moderate variability observed, Fig 2, can be expected to help establish robust relationships between reflectance values and water parameters, facilitating application to satellite retrieval algorithms.

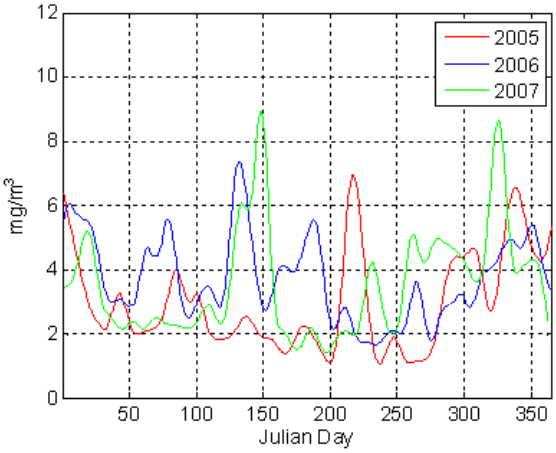

Figure 2. Chlorophyll Concentration (2005 – 2010)

The observed values and variability of parameters will also allow validation over a reasonable range of radiances. Additional study of MODIS satellite imagery also typically showed small spatial variability of parameters in the pixels near the platform, Fig 3. This permits SeaPRISM and HyperSAS measurements to be compared with satellite data averaged over neighboring (300-1000m) pixels.

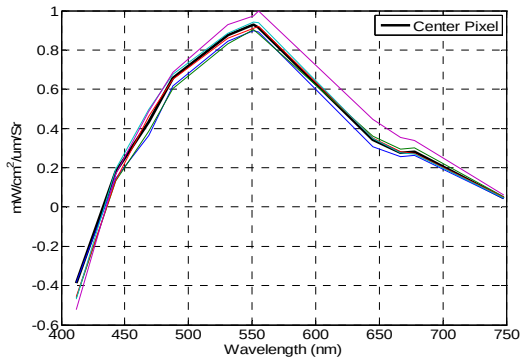

Figure 3. MODIS Normalized Water Leaving Radiances of platform and adjacent pixels (Jan 18 2010 18:15 UTC)

3. COMPARING SEAPRISM, HYPERSAS, MODIS

Fig 4, shows an excellent match for total water leaving radiances as measured by SeaPRISM, at specific discrete wavelengths, and HyperSAS, continuosly over the same wavelength range. Fig 5 shows a match for normalized water leaving radiances as obtained from MODIS and SeaPRISM, standard MODIS and Aeronet Protocols. The results shown use the NIR atmospheric correction. Furthermore, given the excellent match between the water leaving radiances of SeaPRISM and HyperSAS shown above in Fig 4, the expected HyperSAS response is also added in Fig 5 by fitting it to the SeaPRISM response at the latter's wavelengths. Direct independent derivation of HyperSAS response for the same scene is being investigated using its own atmospheric transmission measurements to independently validate SeaPRISM response and match-up with MODIS.

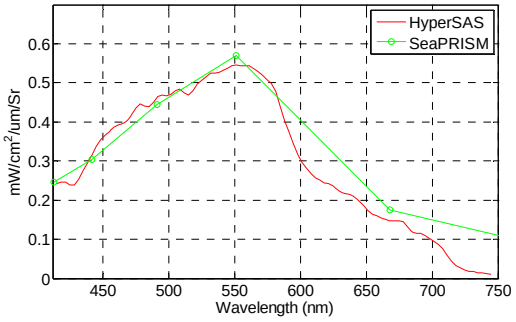

Figure 4. Comparison of total radiances (Jan 18 2010)

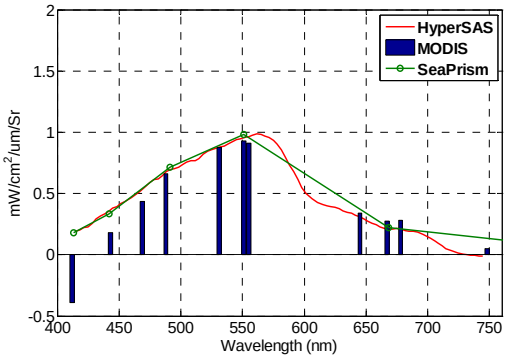

Figure 5. Comparison of Normalized Water Leaving Radiances (MODIS and LISCO Data)

4. CONCLUSION

It is expected that with the further development of measurement, processing and match up procedures currently underway, LISCO will fully prove its utility for calibration/validation of current Ocean Color satellites, for evaluating future satellites missions and hyperspectral sensors (HICO), as well as for improvements in coastal IOP retrievals and atmospheric correction algorithms.

ACKNOWLEDGEMENT

This work was partially supported by grants from the Office of Naval Research and the National Oceanographic and Atmospheric Administration.

REFERENCE

Giuseppe Zibordi, Frédéric Mélin, Stanford B. Hooker, Davide D'Alimonte, and Brent Holben (2004). "An Autonomous Above-Water System for the Validation of Ocean Color Radiance Data". IEEE Transactions on Geoscience and Remote Sensing, vol. 42, no. 2.

CDOM Assessment for Albanian and Montenegrin Coastal Areas

L. Alberotanza [a], C. Bassani [b*], F. Braga [a], R.M. Cavalli [b], S. Pignatti [c], F. Santini [b], A. Campanelli [d]

[a] Istituto di Scienze Marine, Consiglio Nazionale delle Ricerche, Venice, Italy – (l.alberotanza;federica.braga)@ismar.cnr.it
[b] Istituto per l'Inquinamento Atmosferico, Consiglio Nazionale delle Ricerche, Rome, Italy – (bassani;cavalli;santini)@lara.rm.cnr.it
[c] Istituto di Metodologie per l'Analisi Ambientale, Consiglio Nazionale delle Ricerche, Potenza, Italy – pignatti@imaa.cnr.it
[d] Istituto di Scienze Marine, Consiglio Nazionale delle Ricerche, Ancona, Italy – a.campanelli@an.ismar.cnr.it

Abstract – The spatial and temporal variability of within water body properties can be studied using airborne hyperspectral imagery so as to develop improved fine-scale water body mapping procedures. In order to perform these studies, in the eastern Adriatic coast running along Montenegro and Albania, three oceanographic cruise were carried out to evaluate and validate the hyperspectral approach by using *in situ* measurements. Several measurement stations have been situated along transects showing an high water parameter gradients. In each station radiative measurements were collected by means of the SpectraScan spectroradiometer following the SeaWiFS protocol in order to obtain the Rrs (Remote sensing signal) and water samples were collected for CDOM concentrations retrieval. The goal of the mission was to exploit the relationship between Rrs and the CDOM concentrations. A good correlation between CDOM and some Rrs band ratios was observed, thus encouraging the development of an empirical algorithm for CDOM concentration retrieve by remotely optical data.

Keywords: CDOM, coastal areas, hyperspectral.

1. INTRODUCTION

The CDOM (Coloured Dissolved Organic Matter), consisting of humic and fulvic acids, is produced by local organic particles degradation or originated from distant sources. In the last case, high concentrations can be find in the coastal areas, where the rivers allow high amounts of CDOM accumulated along their flow path. The methods exploited to retrieve CDOM by remote sensing ocean data, are based on empirical algorithms or complex physical models (Lee *et. al.*, 2002; Cavalli *et. al.*, 2009; Santini *et al.*, 2009). In Del Vecchio and Blough (2004), the empirical approach is shown like the most appropriate approach to investigate the CDOM spatial and seasonal variability for coastal waters. The present paper aims to validate a CDOM empirical algorithm retrieval in optically complex waters (case2 waters) of the Albanian and Montenegrin coast. At this purpose, various literature relationships have been applied to *in situ* collected data (Volpe *et al.*, 2007; Mannino *et al.*, 2008). The data were collected during three oceanographic cruise carried out in the eastern Adriatic coast running along Montenegro and Albania. In each station, spectral data were collected by means of the SpectraScan spectroradiometer following the SeaWiFS (Muller *et al.*, 2003) protocol in order to obtain the Rrs (Remote sensing signal). In addition water samples were collected for CDOM concentrations retrieve. The results show a clear relation between CDOM values obtained by the algorithm and the ones related to laboratory analysis.

2. DATA & METHODS

2.1 Study area

The study area is located on the eastern continental margin of the southern Adriatic sea (Figure 1). This area is interested in large biomass growth and high chlorophyll values. These characteristics are the crucial point for the validation of the empirical approach.

2.2 Field Measurements

The collected data were obtained from R/V G. Dallaporta (ISMAR-CNR, I) during three oceanographic cruise carried out in May 9-21 and June 24-29, 2008 and June 12-14, 2009. During the cruises, field measurements were collected along some transects (Figure 1) to investigate the spatial variability of physical, chemical and biological parameters.

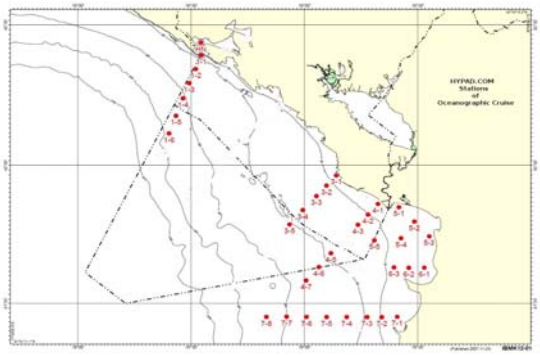

Figure 1. Study area.

The CDOM water samples were filtered through 0.2 μm Nucleopore membrane filters, then stored in the dark under refrigeration (4° to 8° C) and analysed on board within 24 hours using a Perkin Elmer spectrophotometer 550A model (10 cm pathlenght cuvette). Absorbance data were converted to absorption coefficient (a_{CDOM}), used as reference for the CDOM concentration, according to Mitchell *et al.* (2003):

$$a\,CDOM(\lambda) = (2.303/l)\,(AB_s(\lambda)) - (AB_{bs}(\lambda)) - (AB_{null}(\lambda)) \quad (1)$$

* Corresponding author. cristiana.bassani@lara.rm.cnr.it, tel. +39 06 49934686 & fax +39 06 49934211

where l is the cuvette pathlength, $AB_S(\lambda)$ is the optical density of the filtrate sample relative to purified water, $AB_{bS}(\lambda)$ is the optical density of a purified water blank treated like a sample relative to purified water, and $AB_{null}(\lambda)$ is the apparent residual optical density at visible or near infrared wavelength, where absorption by dissolved material is assumed to be zero.

2.3 Optical Measurements

The optical measurement above water were devoted to the R_{rs} (Remote sensing reflectance) retrieve, defined as:

$$Rrs = \frac{L_u(0_{up})}{E_d}$$
$$L_u(0_{down}) = L_u(0_{up}) + a\,L_{sky} \quad (2)$$

Where $L_u(0_{up})$ is the upwelling signal coming from just below the water surface (also known as the in-water radiance); E_d is the irradiance incident (downwelling) on the water surface; $L_u(0_{down})$ the signal above the water surface; L_{sky} is the sky radiance and *a* is a coefficient depending on the acquisition geometry. The R_{rs} is calculated by the SeaWifs protocol, see Mueller *et al.* (2003) for more details procedural steps. The R_{rs} is independent from the illumination condition and is, therefore, functional to characterize water target. In this way, the retrieved water surface reflectance is ready to determine and validate the empirical algorithm devoted to retrieve the CDOM directly from hyperspectral remote sensing data in the study area.

2.3 Results

The aim of this work was to find empirical relationships between the R_{rs} and the concentrations of the CDOM. Using the R_{rs} signal acquired in each station of the oceanographic cruises contextually to the compound concentrations obtained by laboratory analysis, various couples of bands and different literature analytical relationships were tested in regression procedures. The best relationship was found for CDOM by applying least square approach to field observations for evaluating the exponential decay function reported on Equation 3:

$$Log(Rrs(510)/Rrs(555)) = 3.462\,aCDOM \quad (3)$$

We found that the better band ratio was R_{rs} 510/ R_{rs} 555, which also gave the best correlation value (R=0.54) within the concentration range observed in situ (Figure 2).

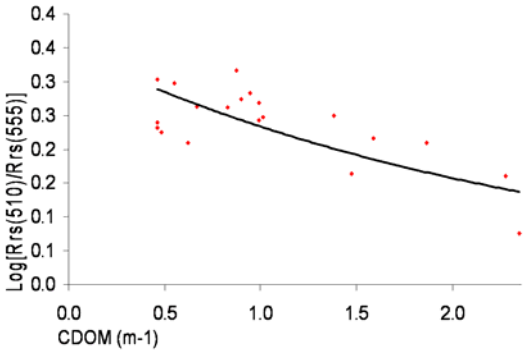

Figure 2. Regression between the logarithm of the band ratio and the CDOM concentrations, measured as the absorption coefficient at 440nm on in situ water samples.

3. CONCLUSIONS

An empirical algorithm has been determined for CDOM retrieve from hyperspectral remote sensing data. The results with a low correlation index (R=0.54) suggest to increase the dataset in order to improve the accuracy of the empirical approach applied to the hyperspectral data. The low correlation index was also expected for the high variability of the water body in the coastal area. Further oceanographic cruises are required to perform a robust statistical analysis in order to evaluate the robustness of the relation between the CDOM values and the R_{rs} (i.e., high correlation index). The capability to quantify the CDOM could lead to improve also the hyperspectral retrieval of other parameters, such as the Chorophyll-a. The empirical law obtained from at-ground optical measurements will be extended to the remote sensing data, such as the airborne Multispectral Infrared and Visible Imaging Spectrometer (MIVIS).

REFERENCES

Lee Z., K.L. Carder, and R.A. Arnone (2002). "Deriving inherent optical properties from water color: a multiband quasi-analytical algorithm for optically deep waters", Applied Optics, vol. 41, pp. 5755-5772.

Cavalli, R.M., G. Laneve, L. Fusilli, S. Pignatti and F. Santini (2008). "Remote sensing water observation for supporting lake victoria weed management", Journal of Environmental Management. In Press.

Del Vecchio, R., and N.V. Blough (2004). "Spatial and seasonal distribution of chromophoric dissolved organic matter and dissolved organic carbon in the Middle Atlantic Bight", Marine Chemistry, vol. 89, pp. 169-187.

Volpe, G., R. Santoleri, V. Vellucci, M. Ribera d'Alcalà, S. Marullo, F. D'Ortenzio (2007). "The colour of the Mediterrean Sea: Global versus regional bio-optical algorithms evaluation and implication for satellite chlorophyll estimates", Rem Sens Environ, vol. 107, pp. 625-638.

Mannino A., M.E. Russ, and B. Hooker (2008). "Algorithm development for satellite-derived distributions of DOC and CDOM in the U.S. Middle Atlantic Bight", J Geophys Res, vol 113, doi: 10.1029/2007/JC004493.

Muller, J.L., C. Davis, R. Arnone, R. Frouin, K. Carder, Z.P. Lee, R.G. Steward, S. Hooker, C.D. Mobley, S. and McLean (2003). "Above-water radiance and remote sensing reflectance measurement and analysis protocols". In: J.L. Mueller, G.S. Fargion, and C.R. McClain (Ed.), Ocean Optics Protocols for Satellite Ocean-Color Sensor Validation, Revision 4, Vol. III: Radiometric Measurements and Data Analysis Protocols (pp. 21–31). NASA Tech. Memo. 2003–211621/Rev4-Vol. III. NASA GSFC, Greenbelt, MD.

Mitchell, B.G., M. Kahru, J. Wieland, and M. Stramska (2003),. "Determination of spectral absorption coefficient of particles, dissolved material and phytoplankton for discrete water samples, in Ocean Optics Protocols for Satellite Ocean Color Sensor Validation", edited by G. S. Fargion, J. L. Mueller and C. R. McClain, pp. 39-64, NASA/TM-2003-211621/Rev4-Vol.IV NASA GSFC., Greenbelt, MD.

F. Santini, L. Alberotanza, R.M. Cavalli, S. Pignatti (2010). "A two-step optimization procedure for assessing water constituent concentrations by hyperspectral remote sensing techniques: An application to the highly turbid Venice lagoon waters". Remote Sensing of Environment vol. 114, pp. 887–898.

Integration of Water Colour and Sea Surface Temperature for coastal discharges: preliminary results

L. Alberotanza [a,*], C. Bassani [b], F. Braga [a], R.M. Cavalli [b], A. Palombo [c], S. Pignatti [c], F. Santini [b], R. Solorza [d]

[a] Istituto di Scienze Marine, Consiglio Nazionale delle Ricerche, Venice, Italy – luigi.alberotanza@ismar.cnr.it
[b] Istituto per l'Inquinamento Atmosferico, Consiglio Nazionale delle Ricerche, Rome, Italy – cavalli@lara.rm.cnr.it
[c] Istituto di Metodologie per l'Analisi Ambientale, Consiglio Nazionale delle Ricerche, Potenza, Italy – pignatti@imaa.cnr.it
[d] Del Comahue University, Neuquèn, Argentina

Abstract – Complex relations between human activities and natural environments and pronounced pressures on natural resources affect the Southeastern Adriatic coastal areas. This is an area with attractive yet fragile ecosystems, impacted by pressures from urbanization and tourism expansion. Indeed it is influenced by the inflow of rivers runoff and agricultural discharges. This research proposes a new approach for identifying and quantifying different kinds of discharge on coastal waters, integrating Sea Surface Temperature and Water Colour. Such parameters are obtained from Visible and Thermal remote sensing data acquired simultaneously with high spatial and spectral resolution. The results have been correlated with land use characteristics in order to understand if alterations are related to natural or human causes. This approach quickly highlights the possible alteration connected to the discharge that could be a potential risk for population and ecosystem located in coastal areas.

Keywords: SST and Water Colour anomalies, Adriatic Sea, coastal discharge.

1. INTRODUCTION

The coastal zone is an extremely dynamic system. Variations in concentration of its major constituents occur rapidly over space and time. Coastal areas are very sensitive to the impact of human activities and land use in watersheds, along the coast and further inland, of river basin discharges, and of marine processes. Recently, the development of new techniques, including remote sensing, may successfully provide systematic approaches for investigation in coastal regions. The study area includes part of the coastal zone of the Albania and Montenegro: the Montenegrin coast is mainly rocky with well formed cliffs, while on the South part, it is low, partly lagoon type and under the greater influence of freshwaters from the mainland. The Albanian coastal area is characterized by river mouths and lagoons system, sandy beaches with vegetative dunes. The southeastern Adriatic Sea has great international importance for its biodiversity and productivity, but the developing touristic and economic activities can impact on natural resources. A strategic management and monitoring plan is of crucial importance to ensure sustainable economic development in the long-term.
In the framework of HYPerspectral for ADriatic COastal Monitoring (HYPAD.COM) international project, the integration of the Earth Observation hyperspectral data (airborne and ground-based) has been performed to characterize the Albania and Montenegro coastal area and the surrounding lands. This research proposes a new approach for retrieving and characterizing discharges by a specific methodology integrating SST and Water Colour in order to identify the water anomalies associated to thermal anomalies related to different kinds of discharges. Such methodology allows us to identify all coastal discharges, to classify into three kinds of source (rivers, urban and agricultural runoff and karst springs) and to recognize if there is a correlation between the identified SST anomalies with the Water Colour. It is important that the Visible and Thermal images are been acquired simultaneously with a high spatial resolution for identifying and monitoring coastal water discharges. For this aim, the water characteristics (SST and Water Colour) have been retrieved from the hyperspectral remote sensing airborne data acquired by the Multispectral Infrared Visible Imaging Spectrometer (MIVIS). The results can quickly highlight the possible alteration and contamination related to the discharge that could be damaging for the ecosystem health.

2. MATERIALS AND METHODS

All the data have been acquired during the hyperspectral campaign carried out in the framework of the HYPAD.COM project. The campaign has been performed with airborne and ground-based instruments to collect and integrate information of the natural local balance of the Montenegrin and Albanian coastal ecosystem. The high suitability of airborne data are providing useful information to the local authorities concerning the environmental monitoring and managing, allowing the development of effective intervention policies and monitoring programs (Bassani *et al*., 2009; Santini *et al*., 2009).

2.1 Field Surveys and Remote Sensing Data

The in-situ data were collected during two oceanographic campaigns carried out on 2008: at the 32 georeferenced stations located along 6 transects perpendicular to coastline, radiometric measurements of surface radiance, water samples and CTD probe profiles are carried out. Sampling stations were chosen according to the coastal features, bathymetry, river inputs and general circulation of Adriatic.
The ground-based radiometric acquisitions have been performed by means of a portable spectroradiometer. The procedure for hyperspectral sea surface reflectance measurement is based on the acquisition of the upwelling and downwelling radiance according to SeaWifs Protocol (Fargion & Mueller, 2003). The water samples collected at surface and -10 m were analyzed in laboratory to retrieve

* Corresponding author. ISMAR-CNR, Castello 1364a, 30122 Venice, Italy. Tel. +39 041 2404700, Fax. +39 041 5204126.

absorption coefficient of CDOM, concentration of Chl-a and TSM. Hyperspectral imagery data have been acquired by MIVIS sensor: such data is characterized by high spatial resolution, high radiometric resolution and high spectral resolution having 102 channels distributed in the range of visible, near, medium and thermal infrared (0.4 - 12.7 nm).

2.2 Data Analysis

After the pre-processing steps, which included geometric correction using an own code and atmospheric correction according to the algorithm in Bassani et al (2006), the data was processed in order to retrieve SST and ocean colour and to classify the background and land use. The connection between Water Colour anomalies related to thermal anomalies is established when the water discharge alters or contaminates the ecosystem. The a priori condition is the water body homogeneity, including the invariance of water properties (coast or open sea) and bottom type, thus the presence of anomalies depends only on the discharge. The homogeneous water body was delimited with a buffer areas of 50 pixels from the coastal line to open sea and the SAM algorithm was applied to classify high depth bottom. Using the Rrs signal resampled to the MIVIS spectral resolution and the compounds concentration obtained by the laboratory analysis, various couples of bands ratios have been tested in linear regression procedures, in order to identify those which better represent the variations of the optical parameters. The analysis of the thermal data for the SST determination was based on a multichannel algorithm taking into account brightness temperature as result of emitted radiance, according to Ulivieri, C. (1994). In order to identify and recognize the discharges source and the possible alteration and contamination causes, the coastal area was classified in natural, urban and agricultural area.

An evaluation criteria was selected in order to recognize the possible correlation between anomalies of SST and Water Colour behavior, taking into account the advantages of high spatial and spectral resolution of hyperspectral data. The Separability Index (SI) according to Cavalli *et al*, (2007) was applied to identify the masks which delimit anomalies in the coastal thermal range and quantify the difference of water colour inside and outside the masks performed in the selected sites.

3. RESULTS

The Mean SST was defined as 26º C and a temperature range [21-29°C] were defined. In all the available images, 55 cold (<21°C) and 18 hot (> 29°C) anomalies were identified. The thermal anomalies were divided into three kinds of discharge according to thermal and land cover characteristics.

- Karst Springs characterized with cold water, situated essentially in high bottom;
- Urban discharge characterized with hot water, situated in different kinds of bottom;
- River runoff characterized with cold water, situated essentially in low bottom.

In order to integrate characteristics observed in Visible and Thermal spectral domain, a relation was established to characterize each kind of discharge with identified band ratio. In all available image, 38 Karst Springs were identified: the analysis of the SI for these discharges shows that thermal anomalies don't determine any Water Colour anomalies. The Urban discharges were found at 21 sites: the results of SI method show low values, i.e. there are not Water Colour anomalies related to these discharges. Such results could be wrong because they are usually a source of pollution and alteration of the water quality and coastal ecosystem. The low bottom and the presence of vegetation require an improvement of the algorithm that is not sensitive enough to discriminate the anomaly of Water Colour with these environmental conditions. The discharge of River runoff showed 6 sites. These discharges are characterized by cold temperature and low SI values. The SI values highlight that there are not Water Colour anomalies related to River runoff, while the expected results should be a high concentration of suspended sediments. This difference could be addressed to the low river flood. Besides, the area related to the River runoffs, from the coastal line, is much more extensive than the chosen buffer (50 pixels). The pixel amount of the buffer in the algorithm needs to be revised in function of the analysis of the area covered by a River runoff.

4. CONCLUSIONS

In conclusion, a methodology to identify thermal anomalies related to rivers runoff, urban and agricultural discharges and karst springs is presented. These kinds of discharges are a primary source of alteration and contamination which could be damaging for the ecosystem health. This research proposes a new approach for identifying and analyzing discharges coastal areas to recognize the Water Colour anomalies associated to thermal anomalies related to these three kinds of discharges. As future implementations, this research has the needles of improving the classification of the bottom to better identify the homogeneous background, and the identification of areas of buffer/background to point out the anomalies related to the river discharges.

REFERENCES

Bassani C., R.M. Cavalli, A. Palombo, S. Pignatti and F. Madonna (2006). "Laboratory activity for a new procedure of MIVIS calibration and relative validation with test data". Annals of Geophysics, Vol. 49, no. 1, pp. 45-56.

Bassani C., C. Cattaneo, R.M. Cavalli, L. Fusilli, S. Pascucci and S. Pignatti (2009). "The HYPerspectral for Adriatic Coastal Monitoring (HYPAD.COM) project". ISRSE 33rd Int. Symp. on Remote Sensing of Environment, Stresa (Italy), 4-8 May 2009.

Cavalli R.M., F. Colosi, A. Palombo, S. Pignatti and M. Poscolieri (2007). "Remote hyperspectral imagery as a support to archaeological prospection. Journal of Cultural Heritage". Vol. 8, pp. 272-283.

Fargion G.S. and J.L. Mueller (2003). "Ocean optics protocols for satellite ocean color sensor validation: Revision 2". NASA Tech. Memo.

Santini F., C. Bassani, A. Campanelli, R.M. Cavalli, M. Marini and S. Pignatti (2009). "Empirical algorithm for CDOM Assessment: Preliminary results of the Albanian and Montenegrin coastal areas". ISRSE 33rd Int. Symp. on Remote Sensing of Environment. Stresa (I), 4-8 May 2009.

Ulivieri C., M.M. Castronuovo, R. Francioni and A. Cardi (1994). "A split window algorithm for estimating land surface temperature from satellite"s. Advanced Space Research, Vol. 14, no. 3, pp. 59-65.

Complex Analysis of Sea Ice SAR Images

V. Alexandrov [a,b,*], O.M. Johannessen [b], S. Sandven [b], L. Bobylev [a,b], A. Yarigina [a], V. Volkov [a], N. Zakhvatkina [a,c].

[a] Nansen International Environmental and Remote Sensing Centre, St.Petersburg, Russia – vitali.alexandrov@niersc.spb.ru
[b] Nansen Environmental and Remote Sensing Centre, Bergen, Norway – stein.sandven@nersc.no
[c] Arctic and Antarctic Research Institute, St.Petersburg, Russia – natalia.piotrovskaya@niersc.spb.ru

Abstract – SAR images were used successfully for supporting navigation in the Northern Sea Route and conducting studies of sea ice conditions. Technique of their interpretation has been developed based on subsatellite observations, and signatures of major sea ice types and features were derived. Use of co- and cross-polarization ratios allows detecting ice forms, ice floes, leads and icebergs. A methodology of automatic interpretation of sea ice SAR images is under development. Ice type classification technique is based on neural network and Bayesian approaches. The algorithms of ice drift retrieval are based on cross-correlation and wavelet analysis. The results of analysis and processing of ENVISAT ASAR sea ice images are presented.

Keywords: sea ice, SAR, image classification, image analysis.

1. INTRODUCTION

Sea ice and iceberg monitoring is one of the most important objectives for satellite SAR missions. After the launching of ERS-1 satellite in 1991 Nansen Environmental and Remote Sensing Centre in Bergen and Nansen International Environmental and Remote Sensing Center in St.Petersburg in cooperation with the European Space Agency and Murmansk Shipping Company conducted a series of projects to demonstrate the possibilities of SAR data for sea ice monitoring and supporting navigation in the Northern Sea Route (Johannessen *et al*., 2007). The specification of SAR signatures for various sea ice types and features has been made based on subsatellite observations onboard nuclear icebreakers. Visual analysis of satellite images by an expert remains a major technique in their interpretation and is widely used. However, the role of automatic and semi-automatic techniques in interpretation of remote sensing data is constantly increasing. In this study techniques of automatic ice classification and ice drift retrieval have been developed. The main objective of this paper is to elaborate complex methods of interpretation and processing of SAR images of the sea ice.

2. INTERPRETATION OF SAR IMAGES

2.1 Retrieval of sea ice parameters from SAR images

The specification of SAR signatures for various sea ice types and features has been made during a series of sub-satellite experiments, and SAR images from ERS, Radarsat and Envisat satellites have been compared with observed sea ice conditions. Ice type, thickness, deformation rate, concentration and several other parameters have been visually estimated from icebreakers, video- and photo-survey data. Based on sub-satellite data analysis, the possibility of deriving the most important sea ice parameters from SAR images has been assessed.

During winter, several stages of ice development can be derived from SAR images, including new, young, first-year and old ice. Separate ice floes are detected when their size significantly exceeds the spatial resolution of radar, typically 150 m for ENVISAT ASAR. The deformation of first-year ice can be estimated and level, slightly deformed ice, moderately deformed and heavily deformed ice are distinguished. Shore and flaw polynyas are identified, and their width and area can be measured. The possibility to detect leads in drifting sea ice depends on their width and also the type of ice contained in them. Leads that are 100 m wide or more are detected in 100-m resolution SAR images. In most cases the fast ice and its boundary, as well as multiyear ice boundary are detected in SAR images. Ice displacement can be derived from successive SAR images, which allows calculating drift vectors and composing detailed charts of ice drift (Alexandrov *et al*., 2005). The following sea-ice parameters: ice edge location, sea-ice concentration, large ice floes, stripes of ice in water, ice drift vectors, and areas of convergence/divergence can all be derived from SAR in summer period (Sandven *et al.*, 2001).

Resemblance of SAR signatures for some sea-ice types and features could cause ambiguities in image interpretation. Thus it is difficult to distinguish between thin, medium, and thick first-year ice, and between second-year and multi-year ice. Detection of dry snow on sea ice is impossible, since it does not significantly influence backscatter in the C-band.

2.2 Analysis of co- and cross-polarization ENVISAT ASAR APM images

A series of calibrated Envisat ASAR APM images at HH- and HV-, VV- and VH-, HH- and VV-polarizations, acquired over various areas of the Arctic sea ice was analyzed. Conducted analysis showed that detection of new and young ice types is improved at co- and cross-polarizations. It was found that use of cross-polarization ratio allows identifying leads in multiyear ice, covered with young ice, which could not be recognized from single-polarization data. From cross-polarizations images it possible to distinguish icebergs in wind-roughened open water, which have similar backscatter at co-polarization.

3. AUTOMATED RETRIEVAL OF SEA ICE PARAMETERS

3.1 Ice type classification

The objective of sea ice classification is to categorize SAR image pixels into several ice categories, which are defined as a compromise between practical usability of classification results and information capability of SAR data to derive characteristics of sea ice, as defined by WMO.

The image processing chain includes pre-processing and classification. The backscatter coefficients for the major sea ice types at HH–polarization and 23° incidence angle, as well as angular dependencies of the backscatter for young, first-year and multiyear ice types are derived from calibrated ENVISAT ASAR Wide Swath Mode (WSM) images. Elaborated methodology of SAR image pre-processing includes the backscatter recalculation to the predetermined incidence angle, which allows obtaining range independent contrast for the same ice types.

A multilayer feed forward Neural Network (NN) algorithm is developed for the Arctic sea ice classification during the winter period. The structure of the NN is optimized for the sea ice classification in the Central Arctic. The input features for classification are texture of ASAR images and backscatter values. The number of neurons in the input layer corresponds to the number of textural image characteristics, which are obtained from the computation of the Grey Level Co-occurrence Matrix (GLCM). Parameters of texture features calculation (sliding window size and co-occurrence distance) from ASAR HH-polarization WSM images are estimated. Passing through the network the input vector is reorganized into the resulting vector in the NN output. The number of neurons at the output layer corresponds to the number of the classified sea ice types. Based on the visual interpretation of ASAR images, a neural network is trained for the classification of the first year level and rough ice and multiyear ice. The algorithm validation is done using Arctic and Antarctic Research Institution (AARI) ice charts and ice expert visual analysis. Preliminary neural network classification errors are 15% for level first year ice, 17% for deformed first year ice and 20% for multiyear ice.

The Bayesian algorithm, which makes a decision for the ice type with a maximum a posteriori probability, has been developed for classification of sea ice types in the Central Arctic. Conditional probabilities of the backscatter coefficients for multiyear, level first-year ice and rough first-year ice were calculated from calibrated ENVISAT ASAR images. The a priori probabilities for multiyear, level first-year ice and rough first-year ice in the Central Arctic amount to 0.9, 0.05, and 0.05, respectively. The results of automatic classification visually correspond to expert interpretation with the distinction that a number of small-scale features, which are usually omitted or generalized into larger regions in expert classification, are identified using this approach.

3.2 Ice drift retrieval

SAR images of sea ice captures two important characteristics of ice floe advection and differential non-rigid motion. Under these conditions retrieval of sea ice motion can be split on two stages:

- estimation of large-scale rigid motion and, specifically in this case, the overall translation or/and rotation of features between SAR image pairs;
- estimation of local translational component of the piece-wise continuous movement of granules or plates and affine motion includes the linear, non-translational components of motion.

The cross- correlation based approach is used for estimation of first type of motion, since this technique is capable of measuring very large shifts of many tens of pixels (Johannessen et al., 2007). Initial version of cross-correlation algorithm uses the binary search procedure in order to minimize computation time. Using this procedure assumes that the cross-correlation coefficient between two blocks in successive satellite images monotonically decreases with increasing distance in some area near the selected object. Conducted analysis showed that obtained scatterplots have several peaks in spatial distribution of cross-correlation coefficient, and the binary search procedure for finding maximum cross-correlation coefficient is not appropriate for SAR images. Due to this we limited search area as a maximum ice displacement for the period between image acquisitions taking into consideration maximum possible ice drift velocity. The updated algorithm has been validated by comparing the derived vectors with those, obtained by visual analysis. A comparison shows reasonable agreement between them and it is necessary to validate the algorithm in many more cases to assess the performance under different ice conditions.

4. CONCLUSION

The methodology of the complex interpretation and analysis of satellite SAR images of the sea ice has been developed based on a series of sub-satellite experiments, conducted in the Arctic in various seasons. It was found that the most important sea ice parameters can be derived from SAR images in winter and summer. Some ambiguities in SAR images interpretation are caused by the similarities of signatures for different sea-ice types and features. Analysis of data at co- and cross-polarizations allows detecting several sea ice parameters more reliably. Elaborated techniques allow automatic classification of sea ice types in the Central Arctic and ice drift retrieval from calibrated SAR images.

ACKNOWLEDGEMENTS

The authors acknowledge financial support of the EU projects “Ice Routes”, “Monitoring the marine environment in Russia, Ukraine and Kazakhstan using Synthetic Aperture Radar (MONRUK)”, ESA GMES project “SAR sea ice monitoring for climate Research – ICEMON”.

REFERENCES

Alexandrov, V.Y., S. Sandeven, K. Kloster, L.P. Bobylev, and L.V. Zaitsev (2005). “Comparison of sea ice signatures in OKEAN and RADARSAT radar images for the northeastern Barents Sea”. Canadian Journal of Remote Sensing, vol. 30, no. 6, pp. 882-892.

Johannessen, O.M., V.Y. Alexandrov, I.Y. Frolov, S. Sandven, L.H. Pettersson, L.P. Bobylev, K. Kloster, V.G. Smirnov, Y.U. Mironov, and N.G. Babich (2007). “Remote Sensing of Sea Ice in the Northern Sea Route: Studies and Applications”. Springer-Praxis, Chicheser, UK, 472 p.

Sandven, S., O. Dalen, M. Lundhaug, K. Kloster, V.Y. Alexandrov, and L.V. Zaitsev (2001). ”Sea Ice investigations in the Laptev Sea in Late Summer Using SAR Data”. Canadian Journal of Remote Sensing, vol. 27, no. 5, pp. 502-516.

The PRISMA mission

Cristina Ananasso [a,]*, and PRISMA Project Team

[a] Italian Space Agency, Rome, Italy – cristina.ananasso@asi.it

Abstract – In 2007, the Italian Space Agency (ASI) signed a contract for the design, development and deployment of the PRISMA mission. PRISMA stands for "PRecursore IperSpettrale della Missione Operativa" and is the follow-on of previous programs, either national (HypSeo) or international (JHM phase A, in cooperation with Canada), devoted to establish requirements, technologies and conceptual design of such a mission. The program is starting the C/D phase and has been completely funded by ASI, up to the system on-orbit commissioning. The launch is planned for the second half of 2011.

Keywords: Earth Observations, hyperspectral, environmental monitoring.

1. PROGRAM HIGHLIGHTS

1.1 Context

The Italian Space Agency has identified the "hyperspectral niche" as one of the fields of interest since about one decade. A dedicated roadmap is being established encompassing:

- definition of user needs, in cooperation with operational and scientific community;
- development and qualification of "critical technologies";
- system architecture and preliminary design;
- system deployment and exploitation

Specific programs (hyperspectral) undertaken so far are:

- Hypseo A/B phase (2002), National context;
- JHM A phase (2006-2007), cooperation between Italy and Canada;
- PRISMA B2/C/D/E1 phase (2008-2011), National context.

The prime contractor for the PRISMA mission is an industrial consortium formed by Carlo Gavazzi Space (CGS), Selex Galileo (GA) and Rheinmetall Italia (RHI), that form the industrial core team that coordinates the participation of other major Italian space companies, as subcontractors, such as Thales Alenia Space, responsible for the PDHT, and Telespazio, responsible for the overall Ground Segment.

1.2 Planning and status

The program has been completely funded by ASI up to the system on-orbit commissioning. The Kick Off meeting has taken place in January 2008 and the program is now starting the C/D phase; the launch is planned for the second half of 2011. After the launch, a 3 month in orbit commissioning phase is foreseen. At completion of the commissioning phase, the system will be delivered to ASI.

2. MISSION OVERVIEW

2.1 Mission Objectives

PRISMA is a National Program with the following objectives:

- implementation of an Earth Observation pre-operative mission;
- in orbit demonstration and qualification of an Italian state-of-the-art hyperspectral / panchromatic technology;
- validation of end-to-end data processing able to develop new applications based on high spectral resolution images;
- capitalization of ASI heritage, considering the Hypseo mission, the Italian-Canadian Joint Hyperspectral Mission (JHM) study.

2.2 Applications

The domain of hyperspectral applications is the following:

- detailed mapping of land cover and agricultural landscapes;
- risk Management Support & Hazard monitoring;
- (fires, landslides, volcanic and seismic risk);
- quality of inland waters;
- coastal zones and Mediterranean sea;
- Carbon cycle monitoring;
- urban functional areas mapping and monitoring;
- atmospheric turbidity: optical & spectral characterization;
- land surface hydrology and water management;
- security
- desertification.

2.3 Standard Products

The PRISMA Ground Segment will be located at the Geodesy Center in Matera (Italy) and it will include all the facilities (processors, help desk, catalogue, archive, user interface) to support the end users in ordering Standard Products intended to be the systematic basis for the generation of higher level applications products. The processing is performed starting from raw data and applying the following processing steps.

Level 0: Discriminates image, housekeeping and calibration data and provides formatted data product with appended metadata, including ancillary data and file formatting information.

* Corresponding author.

Level 1: Transforms Level 0 data into radiometrically corrected and calibrated radiance data in physical units. This product provides:

- top-of-atmosphere spectral radiance;
- cloud mask;
- sun-glint Mask;
- calibration and characterization data used;
- classification Mask.

Level 2: Transform Top-of-Atmosphere spectral radiance measurements into geophysical parameters.

2.4 Value Added Products / Applications

Standard Products will be the basis products for the generation of higher level applications products. A Value Added Application Segment (VAS) will be developed to provide level 3 and level 4 products.

Level 3 products are obtained by processing the system products together with the relevant auxiliary input data (e.g spectral libraries) and by using specific algorithms to provide biophysical, biochemical, geophysical, geochemical and environmental products derived from level 2c or level 2d data (classification products, features, concentrations, etc). Level 4: products are obtained by further elaboration of Level 3 products (e.g. statistical analysis, temporal trends, etc.).

3. SYSTEM OVERVIEW

3.1 System Architecture

The PRISMA satellite, placed in a sun synchronous orbit, will focus primarily on the European area of interest, enabling the download of the data on two ground stations located in Italy. Once the panchromatic/hyperspectral images are downloaded on ground, they are archived and processed up to level 2.

The PRISMA System is composed of the following integrated segments:

- A Space Segment, consisting in a single satellite placed in suitable LEO SSO orbit with an operational lifetime of at least 3+2 years. The satellite is made up of:
  - a Platform, based on the Italian small satellites standard platform already used on MITA and AGILE missions
  - a Payload, consisting in a Hyperspectral instrument and PAN camera
  - a Payload Data Handling & Transmission recurrent from COSMO-SkyMed
- A Ground Segment, comprising various centres located in Italy and including:
  - A Mission Control Centre, in charge of mission planning and management
  - A Satellite Control Centre, in charge of satellite command and control
  - An Instrument Data Handling System (IDHS), in charge P/L data reception, archiving, processing and interface with users

The selected orbit for the area of interest in the baseline configuration is sun synchronous with repeat cycle of 29 days (430 orbits).

- Orbit altitude : 614.8 km
- Inclination : 97.85°
- Local Time of Descending Node: 10.30.

3.2 Payload

The PRISMA Payload is composed of an imaging spectrometer (or hyperspectral imager), able to take images in a continuum of spectral bands ranging from 400 to 2500 nm, and a panchromatic camera. The Hyperspectral Instrument is based on a prismatic spectrometer concept.

4. CONCLUSION

The Italian Space Agency is founding a new hyperspectral mission that will be operative starting from 2012. PRISMA is conceived as a “public good” pre-operational and technology demonstrator mission, focused on the development and delivery of panchromatic/hyperspectral products and the qualification of the panchromatic/hyperspectral payload in space.

APPENDIX

PRISMA Project Team:

Quirino Rioli	Program Manager
Giancarlo Varacalli	System Engineer
Francesco Longo	Mission Engineer
Vittorio De Cosmo	Payload Engineer
Luciano Garramone	Mission Ground Segment Engineer
Ettore Lopinto	User Ground Segment Engineer
Rosa Loizzo	Products and Application Responsible
Rita Carpentiero	Product Assurance Manager
Cristina Ananasso	Liaison with the scientific community
Donatella Frangipane	Contract Officer

The Global Mean Sea Surface height from retracked satellite altimetry – Prospects for the Arctic Ocean.

O. B. Andersen[a], P. A. M. Berry[b], P. Knudsen[a], and T. Bondo[a]

[a]DTU Space, Juliane Maries Vej 30, DK2100 Copenhagen O, Denmark {oa,pk,tb}@space.dtu.dk
[b]EAPRS Laboratory, De Montfort University, The Gateway, Leicester LE1 9BH, UK

Abstract – The DNSC08MSS mean Sea Surface (MSS) is a new enhanced mapping of the mean sea surface height of the worlds oceans, derived from a combination of 12 years of satellite altimetry from a total of 8 different satellites covering the period 1993-2004. It is the first global MSS without a polar gap including all of the Arctic Ocean by including laser altimetry from the ICESat mission and auxiliary data close to the North Pole.

Keywords: sea surface height, double re-tracking, altimetry, Arctic Ocean.

1. INTRODUCTION

The mean sea surface (MSS) is a fundamental parameter in geodesy and physical oceanography. It is the time-averaged physical height of the oceans surface. In principle, a complete separation of the oceans mean and variable part requires un-interrupted infinite sampling in both time and space. The challenge in MSS mapping is to achieve the most accurate filtering of the temporal sea surface variability with a limited time span and simultaneously obtaining the highest spatial resolution. This is normally achieved by combining data from the highly accurate exact repeat mission (ERM), with data from the older non-repeating geodetic mission (GM) like ERS-1 and GEOSAT. In principle MSS mapping is relatively straight forward at low to medium latitudes. The problematic part is coastal and polar regions where the altimetric observations degrade due to the presence of land or sea ice. Consequently these regions are the focus regions for future improvements of both Mean Sea Surface as well as Mean Dynamic Topography models (see Figure 1 and Figure 2).

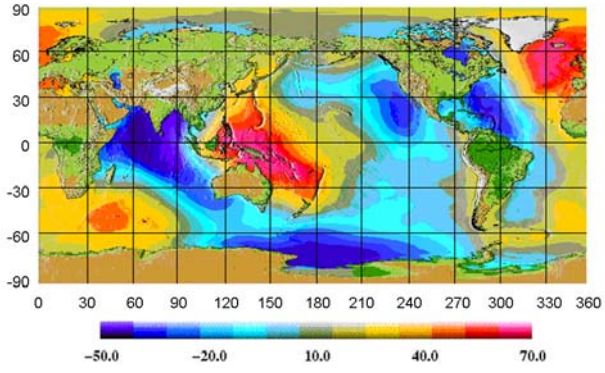

Figure 1. The DNSC08 Mean Sea Surface. Color scale in meters.

The Mean Dynamic Topography (MDT) is the quantity that bridges the geoid and the mean sea surface and the important parameter constraining large scale ocean circulation. By removing the EGM2008 geoid model (Pavlis et al., 2008) and slightly smoothing the residuals, the DNSC08MDT Mean Dynamic Topography is obtained solely from geodetic data and satellite altimetry. Hence it provides independent means of evaluating oceanographic derived MDT models.

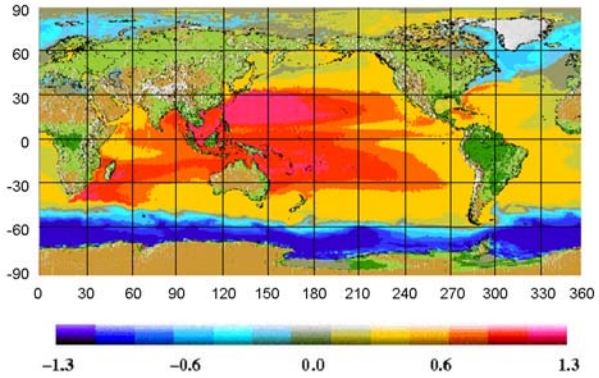

Figure 2. The DNSC08 Mean Dynamic Topography. Color scale in meters.

2. ARCTIC OCEAN

High latitude regions provide special problems for determining MSS and MDT models. This is because sea ice causes the radar return to be distorted. Laser altimetry from ICESat data were used to augment radar altimetry in the partly ice-covered parts of the Arctic Ocean (between 70°N - 86°N, 100°E - 270°E) and at latitudes above 80°N in all of the Arctic Ocean in order to extend the MSS towards the North Pole.

The ICESat data were only used in partly ice-covered regions due to the short averaging period. Lowest level filtered data were seen to map the sea surface in moderate to light ice covered regions where the narrow footprint of the laser frequently ranges to open leads between the ice-floats.

An example of the MDT in the Arctic Ocean is shown in Figure 3 where it has been derived from the difference between ICESat altimetry heights (mission 2B) and the EGM2008 geoid model. Clear thickening of the ice towards the coast of Greenland indicate that the laser most likely ranges from the top of the ice in this region.

3. IMPROVING THE MEAN SEA SURFACE.

The determination of the DNSC08 Mean Sea surface will be updated for this presentation with respect to increase the time span from 12 years to a total of 17 years spanning the Exact Repeat Missions of the TOPEX, JASON, ERS and ENVISAT satellites.

Editing of spurious SSH measurements close to sea ice also degrades the quality of SSH determination and seasonal coverage of data hampers the use of these for climate studies. Altimetry range and geophysical correction errors impacts sea level estimation as for instance errors in the oceanic tidal correction, drift in pressure models (in high latitudes), spurious measurements of wet troposphere correction (close to sea ice). A closer inspection of the various steps as well as ways to account for seasonal ice cover and consequently seasonal data coverage for computing MSS will be investigated.

Finally, retracked altimetry from the ERS and ENVISAT satellites will be included in the updated MSS.

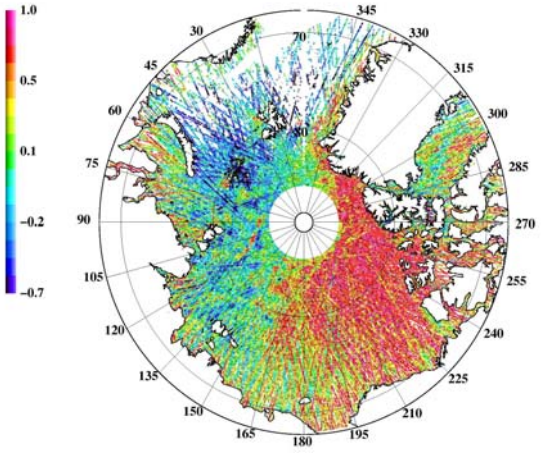

Figure 3. The Arctic Mean Dynamic Topography from Icesat and the EGM2008 geoid model.

4. RETRACKING SATELLITE ALTIMETRY IN THE ARCTIC OCEAN.

The original altimetric suffer from degradation in quality and coverage close to the coast and in Polar Regions as well as the occasionally wrongly retracking of these, even in the open ocean. In order to improve the quality of the exact repeat mission a double retracking technique for analyzing the waveform data has been developed.

Multiple retracking allows the system to retrack more data to increase the spatial coverage of the data. However, although altimetric waveforms are complex and are rapidly changing, with the presence of sea ice, the waveforms can be successfully retracked. New result from retracking the ERS1, ERS-2 and ENVISAT mission in

5. CONCLUSIONS

The DNSC08 Mean Sea surface and associated Mean Dynamic Topography will be presented along with new results on how these models are currently upgraded to represent longer timeseries spanning all current Exact Repeat Missions of the TOPEX, JASON, ERS and ENVISAT satellites. Furthermore the use of retracked altimetry from the ERS and ENVISAT satellites will be included in the updated MSS.

ACKNOWLEDGEMENTS

The authors would like to thank and acknowledge the space Agencies for making satellite altimetry data available. Many scientists have contributed to ensuring the high quality and add on information to these data.

REFERENCES

Andersen, O. B., and P. Knudsen (2009) DNSC08 mean sea surface and mean dynamic topography models. J. Geophys. Res., 114, C11, doi:10.1029/2008JC005179, 2009

Pavlis N. K, S. Holmes, S. Kenyon and J. K. Factor (2008), An Earth Gravitational model to degree 2160, Geophys. Res. Abs.,Vol. 10, SRef-ID: 1607-7962/gra/EGU2008-A-01891 EGU General Assembly

Appendix

The entire suite of DNSC08 fields (MSS, MDT, gravity, bathymetry and interpolation error) can be downloaded from space.dtu.dk or mailed on DVD by request to the authors (oa@space.dtu.dk).

Environmental Monitoring of an Offshore Power Plant in the North Adriatic Sea by Means Of Passive Remote Sensors

A. Annunziatellis, M. Manca Zeichen, M. G. Finoia, C. Virno Lamberti

ISPRA, via Casalotti, 300, 00166 Rome, Italy – aldo.annunziatellis@isprambiente.it, marta.mancazeichen@isprambiente.it

Abstract. Coastal marine environment is a complex system and its management requires adequate information. The area of Po river delta (North Adriatic Sea) has a relevant environmental importance in particular for its coast, lagoon and marine ecosystem and also for its economical value linked to fishing activity. The building up of an offshore power plant has suggested the use of satellite sensors as innovative technique in order to monitor the two different stages i.e. blank phase and construction phase including the pipeline offshore the Po delta and the offshore power plant. Satellite data coming from ocean colour and thermal sensors supplied a finer insight to the physical and biological phenomena occurring in the study area.

Keywords: passive remote sensing, monitoring, Adriatic Sea.

1. INTRODUCTION

The present study aims at exploiting remote sensing techniques in order to enhance the monitoring of a high value coastal marine area possibly affected by the construction of an offshore power plant and a pipeline in the Northern Adriatic Sea (Figure 1).

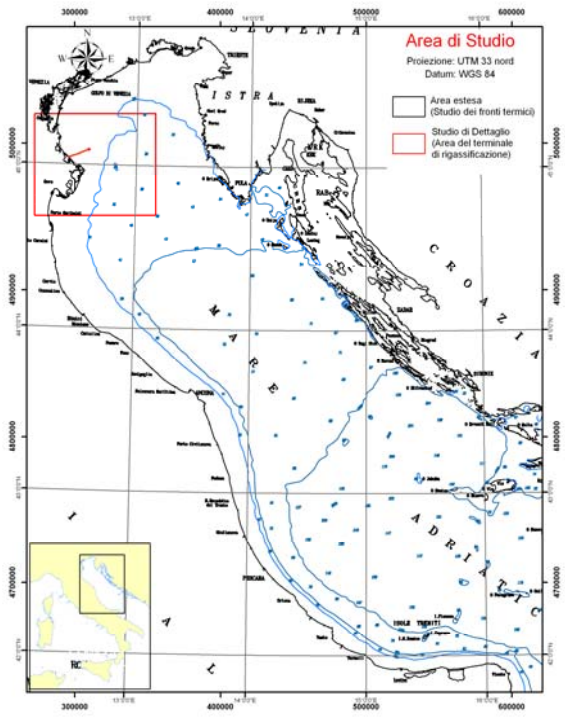

Figure 1. The study area (red square) in the Northern Adriatic Sea.

Satellite data are particularly suitable for this purpose because of the synopticity and high spatial temporal resolution. In order to monitor the area encompassing the pipeline and the offshore power plant thermal and ocean colour observations were collected. Thermal sensor observations supplied the sea surface temperature (SST skin). Ocean colour daily maps supplied the concentration of chlorophyll-like pigments (*chl*), coloured dissolved organic matter (CDOM) and total suspended sediment (TSS) at medium spatial resolution and particularly within the power plant area. Po delta lye in the North Adriatic Sea. Adriatic Sea is one of the most productive areas of the Mediterranean basin showing, as evidenced from ocean colour satellite data, the highest phytoplankton biomass and primary production (Böhm *et al*., 2003). Barale *et al*. (1986) showed direct relationship between the winter-spring phytoplankton distribution and the fresh water Po river run off. The heterogeneity of the phytoplankton pigment e.g. *chl* seems to be ruled by the fluctuation of the fresh water flow. The circulation of the Adriatic Sea is mostly cyclonic with three gyres (Artegiani *et al*., 1997a, b). At the river delta a plume is evident on the ocean colour images moving predominantly towards the south-east.

2. MATERIALS AND METHODS

Advanced Very High Resolution Radiometer (AVHRR) data were collected and supplied by the *Deutsche Zentrum fur Lüft und Raumfahrt* (DLR). Images were acquired as Multichannel Sea Surface Temperature Maps (MCSST) (McClain *et al*., 1985). Monthly means thematic maps, resulting from night-time observations, at spatial resolution of 1.1 km were downloaded for the period May 2005 to December 2008. *Medium Resolution Imaging Spectrometer* (MERIS), supplied by the *European Space Agency* (ESA) were processed and analysed in order to examine spatial and temporal variability of *chl*, CDOM and TSS. MERIS full resolution data (MER_FR) were acquired at processing level 2 performed by means of the algal_1 and algal_2 algorithms (Morel and Antoine, 2000; Doerffer and Schiller, 2007) at a spatial resolution of 300 m. Daily *chl*, CDOM and TSS maps were analysed for the period October 2005-May 2008.

3. RESULTS

The analysis of the monthly means SST skin maps in the study area (see Figure 2) showed lower temperature of about 1-2°C during May, June and August 2006 than on the same months of 2005. Figure 3 shows the whole set of *chl* maps calculated by means of algal_1 algorithm. The highest *chl* concentrations are located in the Po delta region and coincide with the Po plume which usually follows the cyclonic coastal current. The phytoplankton bloom peaks occurred in October 2005, April 2006 and October-November 2006. Figure 4 shows the CDOM maps calculated by means of algal_2 algorithm. The highest

CDOM concentrations were recorded in December 2005 and October 2006. Figure 5 shows the TSS maps calculated by means of algal_2 algorithm. The highest coastal concentrations were recorded in March 2006. However also during December 2005 and 2006 high concentrations of sediments were registered along the coast and offshore.

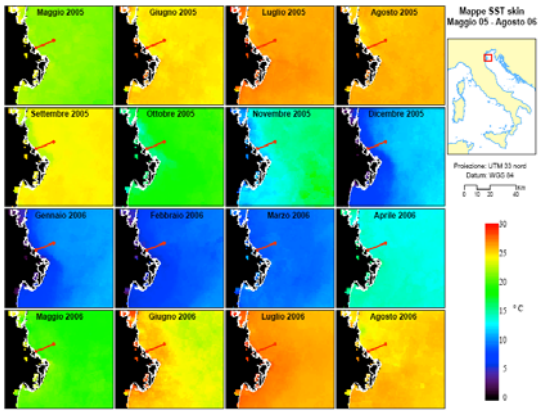

Figure 2. Monthly means AVHRR SST skin maps showing Po delta from May 2005 to August 2006 (blank phase). In red is shown the pipeline track.

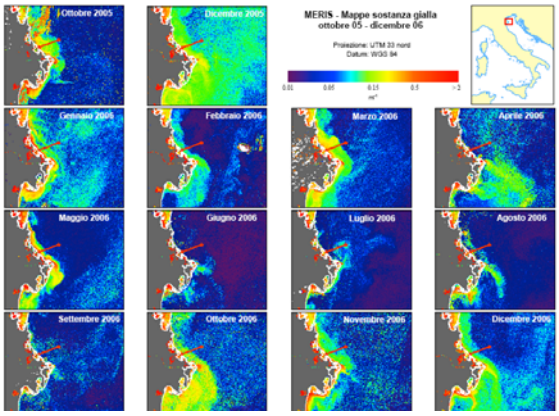

Figure 3. MERIS_FR daily *chl* maps showing Po delta from October 2005 to December 2006 (blank phase).

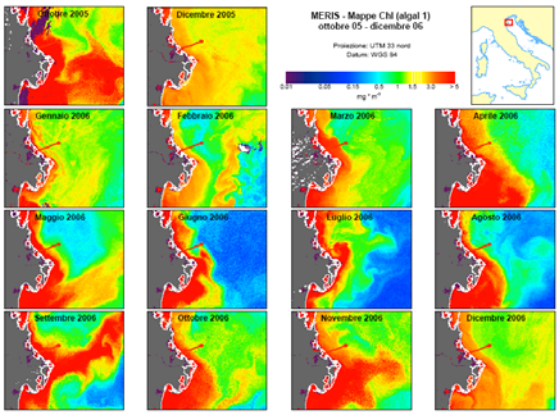

Figure 4. MERIS_FR daily CDOM maps showing Po river delta from May 2005 to August 2006 (blank phase).

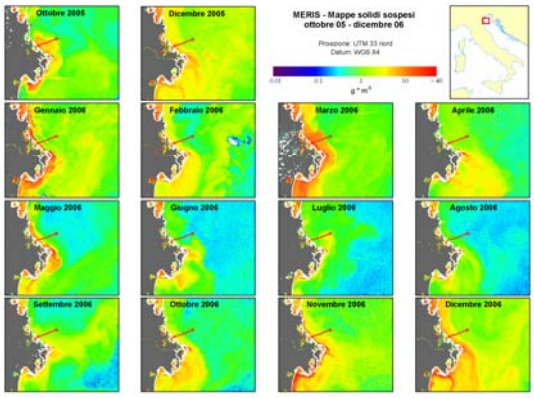

Figure 5. MERIS_FR daily TSS maps showing Po river delta from May 2005 to August 2006 (blank phase).

4. DISCUSSION

The SST skin maps evidenced two water masses showing a remarkable SST difference which were flowing along the coast and offshore according to the cyclonic costal current. The *chl* maps showed that during autumnal months the area of the pipeline and the power plant was hit by the Po plume whereas during the remaining months high *chl* values are due mostly to the cyclonic coastal current. Both CDOM and TSS maps showed peaks during autumnal and winter months probably linked to the increased Po river outflow.

5. CONCLUSIONS

The analyses performed shows that the satellite observations, and in particular the MERIS data, are particularly appropriate for the monitoring of those geophysical parameters that may be affected by anthropogenic activities.

ACKNOWLEDGEMENTS

The authors wish to thank ESA and DLR for providing the images used in the present work.

REFERENCES

Artegiani, A., Bregant, D., Paschini, E., Pinardi, N., Raicich F., and Russo, A., 1997a. “The Adriatic Sea general circulation : Part I: Air-Sea Interactions and water mass structure”. J. Physical Oceanography, 27: 1492-1514.

Barale, V., McClain, .R., and Malanotte-Rizzoli, P. (1986). “Space and time variability of the surface colour field in the Northern Adriatic Sea”. J. Geophys. Res.,91: 12957-12974.

Böhm, E., Banzon, V., D'Acunzo, E., D'Ortenzio, F., Santoleri, R. (2003). “Adriatic Sea surface temperature and ocean color variability during the MFSPP”. Annales Geophysicae, 137-149, 2003.

Doerffer, R. and Schiller, H. (2007). “The MERIS Case 2 water algorithm”. Int. J. Rem. Sen. 28 (3 & 4), 517–535.

Morel, A. and Antoine, D., (2000). “Pigment Index Retrieval in Case I Waters”. ESA Document PO-TN-MEL-GS-0005, 1-26.

McClain, E.P., Pichel, W.G. and Walton, C.C. (1985). “Comparative performance of AVHRR-based multichannel Sea Surface Temperatures”. J. Geophys. Res., 90, 11 587-11 601.

Ten-year achievements of the *BOUSSOLE* bio-optics time series project

D. Antoine[a,*], F. D'Ortenzio[a], P. Gernez[a,b], S.B. Hooker[c],
V. Vellucci[a], E. Diamond[a], B. Gentili[a], F. Louis[a], J. Ras[a]

[a] Laboratoire d'Océanographie de Villefranche (LOV), CNRS & Univ. Pierre et Marie Curie Paris 6, Villefranche sur Mer, France – antoine@obs-vlfr.fr
[b] Now at Marine Physical Laboratory, Scripps Institution of Oceanography, UC San Diego, La Jolla, CA 92093, USA
[c] NASA/Goddard Space Flight Centre/Code 614.8, Greenbelt, MD 20771, USA - stanford.b.hooker@nasa.gov

Abstract – The *BOUSSOLE* project (a French acronym that literally translates as "buoy for the acquisition of a long term optical time series") was initiated 10 years ago. The goal is to establish a long-term bio-optical time series in support to calibration of observations by ocean color remote sensing satellites, validation of the geophysical products derived from these observations, and fundamental research in bio-optics. This paper summarizes the achievements of the project in 10 years of operations, and our strategy for the next decade.

Keywords: bio-optics, ocean color, calibration/validation

1. INTRODUCTION

The era of ocean color remote sensing started about 20 years ago with the launch of the US National Aeronautics and Space Administration (NASA) Coastal Zone Color Scanner (CZCS) instrument, and entered in a more operational phase with the launch of the NASA Sea-viewing Wide Field-of-view Sensor (SeaWiFS) in September 1997. It rapidly became obvious that building global long-term time series of such observations require a high degree of accuracy, which is only achievable by combining the satellite observations with in situ observations. The goal of the BOUSSOLE project is precisely to establish a long-term time series of in situ measurements including radiometry, optical properties and the biogeochemical parameters needed for their interpretation (chlorophyll concentration).

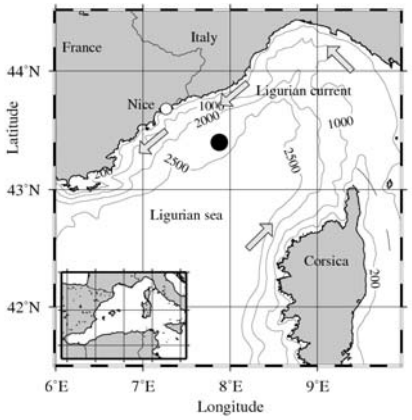

Figure1. NW Mediterranean Sea area, showing the southern coast of France and the island of Corsica plus the work area in the Ligurian Sea (black circle) for the BOUSSOLE activities. Grey arrows symbolize main current branches.

The project combines a fixed optical mooring of a new type, deployed 60 km off Nice over deep (2440 m) oceanic Case 1 waters in the northwestern Mediterranean Sea (Fig. 1), a program of monthly servicing cruises to the mooring site (complementary measurements), and a AErosol RObotic NETwork (AERONET) station on the coast.

2. ACHIEVEMENTS

2.1. Technological development

From the acknowledgement that buoys usually deployed for oceanographic work are not adapted to radiometry measurements, a new platform was conceived, built, tested and qualified, and finally operationally deployed since September of 2003 (Antoine et al., 2008a). It allows minimizing shading of radiometers and maximizing their stability so that cosine collectors remain as close as possible to horizontal. Briefly speaking, the principle is that of a "reversed pendulum", with Archimedes thrust replacing gravity. The system consists of a large sphere (Ø 1.8 m), stabilized at 18 m (i.e., out of the effect of most swells), and generating the main buoyancy of the system. Above it, a rigid, tubular, structure is fixed, which hosts the instrumentation onto horizontal arms (at 4 and 9 m). An ~3 tons thrust, mostly due to the sphere, ensures the stability of the complete system, which is subject to very limited forces from the superstructure of the buoy, which is referred to as a "transparent-to-swell" structure. With such a design, there is no large body at the surface generating shade. One-minute data acquisition sequences are performed every 15 minutes, with all instruments working simultaneously. Satlantic 200-series radiometers are used, measuring downward and upward plane irradiances (Ed and Eu), and upwelling nadir radiance (Lu) at two depths (nominally 4 and 9 m) and at the following 7 discrete wavelengths: 412, 443, 490, 510, 560, 670 and 681 nm. A Satlantic Multichannel Visible Detector System (MVDS) 200-series radiometer measures the downward plane irradiance Es at 4.5m above the water surface and at the same 7 wavelengths. Other instrumentation (see in Antoine et al., 2006) include a two-axis tilt and compass sensor at 9m, a Sea-Bird Electronics (Bellevue,Washington) 37-SI CTD measuring conductivity, temperature, and pressure at 9m, two Western Environment Laboratories (WETlabs) C-star transmissometers measuring the beam attenuation coefficient at 660 nm at 4 and 9 m, two WETlabs ECOFLNTU chlorophyll fluorometers at 4 and 9 m, and a Hydro-Optics, Biology, and Instrumentation Laboratories Inc. (HOBI Labs) Hydroscat-IV backscattering meter at 9m measuring a proxy to the backscattering coefficient at 4 wavelengths (443, 488, 560 and 620 nm).

* Corresponding author. CNRS/LOV, Quai de la Darse, BP8, 06238 Villefranche/mer, France. +33 4 93 76 37 23

2.2. Calibration / validation operations

Data provided by the BOUSSOLE project are now used for the calibration / validation ("cal/val") operations of the European Space Agency (ESA) Medium Resolution Imaging Spectrometer (MERIS), the NASA SeaWiFS and Moderate Resolution Imaging Spectroradiometer (MODIS) instruments. A comparison of the validation results for these three sensors was presented in Antoine et al. (2008b). Regular updates of the BOUSSOLE data are sent to space Agencies for incorporation into their cal/val data bases. A comparison of SeaWiFS vicarious calibration gains obtained with BOUSSOLE data and two other data bases was also performed (Bailey et al., 2008).

2.3. Scientific work

Various studies using BOUSSOLE data have been carried out up to now, including an analysis of high-frequency fluctuations of the underwater light field (Gernez and Antoine, 2009), a detailed validation of the bidirectional effect in various Case 1 waters (Voss et al., 2007), a study of the natural variability of bio-optical properties in Case 1 waters (Morel et al., 2007), the development and test of a method to determine the aerosol scale height (Dubuisson et al., 2009), the validation of atmospheric corrections in presence of desert dust (Banzon et al., 2009). Current studies deal with the diurnal variability of optical properties and their relation to primary production, and with the backscattering by marine particles.

3. FUTURE DIRECTIONS

Evolution of the instrument suite is underway, including now hyperpsectral sensors allowing a better match to the variety of spectral bands now present on the international fleet of ocean color sensors, and a more detailed study of the relationship between the composition of the ecosystem and optical properties. Additional instrumentation will be deployed at the occasion of campaigns of finite duration (e.g., 1 or 2 years), such as pCO2 sensors. Our strategy for the next decade is to maintain and even reinforce the close coupling between the role of long-term observation of BOUSSOLE and its scientific part.

4. CONCLUSION

The BOUSSOLE project is now established as one of the most comprehensive time series of bio-optics and radiometry measurements in the open ocean. Operations should continue over the next decade, providing data for fundamental research in marine optics and bio-optics, and for cal / val of future ocean color sensors such as the Ocean and Land Color Imager (OLCI) on the ESA Sentinel-3A and 3B satellites and the United State National Oceanic and Atmospheric Administration (NOAA) Visible and Infrared Imaging Radiometer Suite (VIIRS) on the National Polar-orbiting Operational Environmental Satellite System (NPOESS). Continuity in such time series is a key element towards the generation of multi-decadal and multi-sensor climate quality data records, which are mandatory to study long-term changes of the oceanic ecosystems in response to climate-driven changes in the physical environment.

ACKNOWLEDGEMENTS

The BOUSSOLE project was set up thanks to support and funding of several agencies, academic and governmental institutions, i.e. the Centre National de la Recherche Scientifique (CNRS), the Institut National des Sciences de l'Univers (INSU), and the Observatoire Océanologique de Villefranche (OOV). Financial support of the project comes from the French space agency (CNES), from the European Space Agency (ESA), through the European Space Research and Technology Center (ESTEC) contract 14393/00/NL/DC and ESRIN contracts 17286/03/I-OL and 21770/08/I-OL, and from NASA through a Letter of Agreement with the Université Pierre et Marie Curie (UPMC). The captains and crews of the Castor-02 vessel (Foselev Marine Company; mooring operations) and of the INSU R/V Tethys-II (monthly cruises) are also thanked for their help at sea.

REFERENCES

Antoine, D. M. Chami, H. Claustre, F. D'Ortenzio, A. Morel, G. Bécu, B. Gentili, F. Louis, J. Ras, E. Roussier, A.J. Scott, D. Tailliez, S. B. Hooker, P. Guevel, J.-F. Desté, C. Dempsey and D. Adams (2006). "BOUSSOLE : a joint CNRS-INSU, ESA, CNES and NASA Ocean Color Calibration And Validation Activity". NASA Technical memorandum N° 2006–214147, NASA/GSFC, Greenbelt, MD, 61 pp.

Antoine, D., P. Guevel, J.-F. Desté, G. Bécu, F. Louis, A.J. Scott and P. Bardey (2008a). "The « BOUSSOLE » buoy – A new transparent-to-swell taut mooring dedicated to marine optics : design, tests and performance at sea". Journal of Atmospheric and Oceanic Technology, vol. 25, pp. 968-989.

Antoine, D., F. D'Ortenzio, S.B. Hooker, G. Bécu, B. Gentili, D. Tailliez and A. Scott (2008b). "Assessment of uncertainty in the ocean reflectance determined by three satellite ocean color sensors (MERIS, SeaWiFS, MODIS) at an offshore site in the Mediterranean Sea (BOUSSOLE project)". Journal of Geophysical Research, vol. 113, C07013, doi:10.1029/2007JC004472.

Bailey S., S.B. Hooker, D. Antoine, B. Franz and P.J. Werdell (2008). "Sources and assumptions for the vicarious calibration of ocean color satellite observations". Applied Optics, vol. 47, no. 12, pp. 2035-2045.

Banzon V., H.R. Gordon, C. Kuchinke, D. Antoine, K. Voss, and R.H. Evans (2009). "Validation of a SeaWiFS dust-correction methodology in the Mediterranean Sea: Identification of an algorithm-switching criterion". Remote sensing of environment, vol. 113, pp. 2689–2700.

Dubuisson P., R. Frouin, L. Dufôret, D. Dessailly, K. Voss & D. Antoine (2009). "Estimating aerosol altitude from reflectance measurements in the O2 A-band, Remote Sensing of Environment", vol. 113, pp. 1899–1911

Gernez P and D. Antoine (2009). "Field characterization of wave-induced underwater light field fluctuations", Journal of Geophysical Research, vol. 114, C06025, doi:10.1029/2008JC005059

Morel, A., Claustre, H., Antoine, D. and B. Gentili (2007). "Natural variability of bio-optical properties in Case 1 waters: attenuation and reflectance within the visible and near-UV spectral domains, as observed in South Pacific and Mediterranean waters". Biogeosciences, vol. 4, pp. 913-925.

Voss, K., Morel, A. and D. Antoine (2007). "Detailed validation of the bidirectional effect in various Case 1 waters for application to Ocean Color imagery". Biogeosciences, vol. 4, pp. 781-789.

Remote sensing of episodic rainfall events impacting coastal areas in Puerto Rico

R.A. Armstrong *, Y. Detrés

Department of Marine Sciences, University of Puerto Rico, Mayaguez, PR 00708 –
roy.armstrong@upr.edu, yasmin.detres@upr.edu

Abstract – Runoff from intense precipitation associated to hurricanes and other tropical disturbances transports large volumes of sediment rich waters to the coast and insular shelf of Puerto Rico. Increasing turbidity reduces the incident light available for photosynthesis by corals which can adversely affect their growth rates and survival. Rain runoff also brings high nutrient loads which results in phytoplankton blooms that further decrease the amount of light reaching benthic communities. We used data from SeaWiFS and MODIS ocean color sensors to document the effects of intense precipitation over short time periods, resulting in high runoff and river discharge to coastal areas in Puerto Rico. These episodic events were responsible for unprecedented increases in chlorophyll concentrations.

Keywords: episodic events, ocean color, turbidity.

1. INTRODUCTION

Episodic events account from 23% to 58% of the yearly total sediment transport to coastal waters in Puerto Rico with the largest events exceeding the long-term mean annual sediment transport (Larsen and Webb, 2009). As a consequence, sedimentation increases seawater turbidity and decreases the amount of light reaching coral reefs. Rainfall runoff also brings high nutrient loads which results in phytoplankton blooms that further decrease the amount of light reaching benthic communities. Suspended sediments and eutrophication are the main factors responsible for the higher turbidity observed in Puerto Rico's coastal waters (Acevedo and Morelock, 1989; Burke and Maidens, 2004). Increasing turbidity reduces the incident light available for photosynthesis by corals (Souter and Linden, 2000) which can adversely affect their growth rates and survival (Kinzie *et al*., 1984).

Remotely-sensed data provide unprecedented views into the impact of transient events such as storms in the coastal zone. Changes in chlorophyll concentrations in the surface layers of the sea following the passage of storms has been documented (e.g. Gilbes *et al*., 2001; Babin *et al.*, 2004; Davis and Yan, 2004; Son *et al.*, 2006). Gilbes *et al.*, (2001) estimated that the torrential rains and runoff associated with Hurricane Georges delivered one thousand metric tons of nitrate to the coastal waters of Puerto Rico during a five day period in September 1998. The impact of this hurricane on water quality around Puerto Rico was dramatic. The intense precipitation over a short time period resulted in high runoff and river discharge that was responsible for the unprecedented increase in chlorophyll concentrations as detected by SeaWiFS. This was the first time, to our knowledge, that ocean color data is used to assess hurricane impacts in this region.

During three days in November 2003, an episodic rainfall event dumped more than 50 cm of rain over the interior of Puerto Rico. The resulting runoff and river discharge for the month exceeded historical maxima for many stations on the island (Figueroa-Alamo *et al.*, 2006) and lead to phytoplankton blooms over extensive areas around the island. In La Parguera, southwestern Puerto Rico, Chlorophyll-a (Chl-a) concentrations persisted for approximately two weeks and extended beyond the insular shelf. MODIS data showed that Chl-a returned to background values after two and a half weeks. During September 21-23, 2008, heavy rains brought 34 cm of rain to La Parguera resulting in a bloom of the toxic dinoflagellate *Cochlodinium polykrikoides* in coastal waters.

2. METHODS

Daily (Level-2) SeaWiFS and MODIS data were processed using Seadas software to derive Chl-a and K490 products at 1 km resolution. Images from before the episodic events were processed to establish baseline conditions while post-event images were used to quantify the amount and residence time of these water quality parameters in southwestern Puerto Rico.

3. RESULTS AND DISCUSSION

3.1 Rainfall-runoff During Hurricane Georges

Hurricane Georges made landfall in Puerto Rico during September 21-22, 1998. During this period there was a five-fold increase in rainfall from normal amounts. The subsequent flooding and discharge of sediments and nutrients to the coastal waters of Puerto Rico undoubtedly had a significant but transitory effect on the water quality in the areas where coral reefs live. The magnitude and duration of the perturbation of coastal water quality was estimated using SeaWiFS chlorophyll derived products. Images with minimal cloud cover were acquired on September 19, 25, 28, 30, and October 15 of 1998. Chlorophyll concentrations were relatively low in waters around Puerto Rico several days before Hurricane Georges made landfall. However, three days after Georges crossed the island, on September 25, the Chl concentrations increased dramatically. Several weeks after Hurricane Georges passed over Puerto Rico the concentrations of Chl returned to more typical values.

3.2 November 2003 Rainfall Event

The November 2003 episodic rainfall event dumped more than 500 mm of rain over the interior of Puerto Rico. The resulting runoff and river discharge lead to increased

* Corresponding author. P.O. Box 3202, Lajas, Puerto Rico, 00667, tel. (787) 899-2048, x-249, fax (787) 899-5500.

turbidity and Chl-a concentrations over extensive areas around the island (Figure 1). The impacts on coastal water quality in La Parguera, southwestern Puerto Rico were ascertained using MODIS satellite data measurements. Background Chl-a concentrations were relatively low in coastal waters around Puerto Rico on October 25 (Julian 298) and November 1 (Julian 305), before the rainfall event (Figure 2). The extensive rain started on November 13 (Julian 317) and continued throughout the following two days. The first cloud-free image available for the study area was for November 19, six days after the rain started. High Chl-a concentrations in La Parguera persisted for approximately two weeks based on field observations. Chlorophyll and K490 returned to typical baseline values after about two and a half weeks, as documented in the image of November 29 (Julian 333).

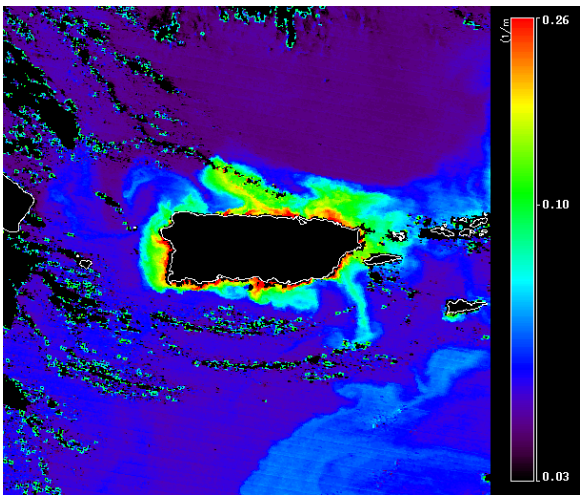

Figure 1. High runoff as depicted by K490 values around Puerto Rico during November 2003.

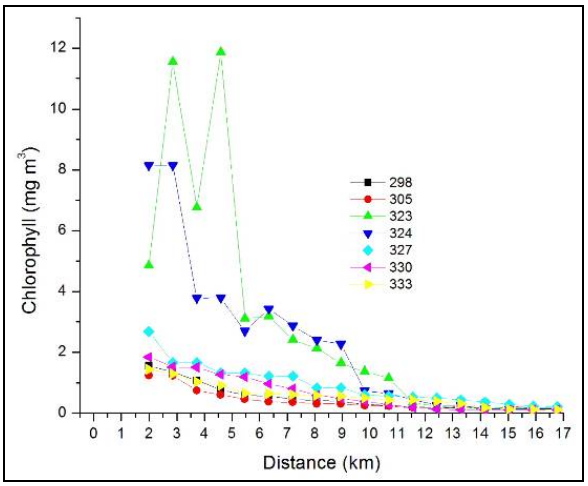

Figure 2. Time series of MODIS-derived chlorophyll along an inshore-offshore transect in southwestern Puerto Rico.

For both of these case studies, there is no information on the impact of these events on coral reef ecosystems due to the absence of field measurements, including benthic surveys. It is possible that significant quantities of the rain falling on the south coast drainage basin soaked into the ground to be discharged diffusely to coastal waters in the days and weeks following a rain storm (Gilbes *et al*., 2001). These studies, however, demonstrated the effectiveness of ocean color data to quantify the impact and evolution of episodic rainfall events in coastal water quality.

4. CONCLUSION

The impact of episodic rainfall events in water quality around Puerto Rico was determined using a time series of Chl and K490 derived products from SeaWiFS and MODIS satellite sensors. Up to three weeks after the events were required for these water quality parameters to reach baseline conditions. The residence time of elevated chlorophyll and suspended sediments can adversely affect coral reefs throughout the insular shelf resulting in bleaching and mortality. Field monitoring and benthic surveys will be required to quantify the biological impacts on benthic communities during future episodic rainfall events.

REFERENCES

Acevedo, R., J. Morelock and R. A. Olivieri. (1989). Modification of coral reef zonation by terrigenous sediment stress. Palaios. 4(1): 92-100.

Babin, S.M., Carton J.C., Dickey T.D., Wiggert, J.D. (2004). Satellite evidence of hurricane-induced phytoplankton blooms in an oceanic desert. J. Geophys. Res. 109: C03043.

Burke L. and J. Maidens (2004). Reefs at Risk in the Caribbean. World Resources Institute, Washington. 81 p.

Davis, A., Yan, X.H. (2004). Hurricane forcing on chlorophyll-a concentration off the northeast coast of the U.S. Geophys. Res. Lett. 31: L17304.

Figueroa-Alamo, C., Aquino, Z., Guzmán-Ríos, S., and Sánchez, A. (2006). Water Resources Data for Puerto Rico and the U.S. Virgin Islands: Water Year 2004.

Gilbes, F., R.A. Armstrong, R. Webb, and F. Muller-Karger. (2001). SeaWiFS Helps Assess Hurricane Impact in the Caribbean Sea. EOS, Transactions, American Geophysical Union, Vol. 82, No. 45, pp. 529 and 533.

Kinzie RA, PL Jokiel, and R York. (1984). Effects of light of altered spectral composition on coral zooxanthellae associations and on zooxanthellae in vitro. Mar Biol 78:239-248.

Larsen, M.C., and Webb, R.M.T. (2009). Potential Effects of Runoff, Fluvial Sediment, and Nutrient Discharges on the Coral Reefs of Puerto Rico: Journal of Coastal Research, 25(1), p. 189-208.

Son, S., Platt, T., Sathyendranath, S. and Lee, D. (2006). Satellite observation of biomass and nutrients increase induced by Typhoon Megi in the Japan / East Sea (JES). Geophys. Res. Lett. 33: L05607.

Souter, D and O. Linden. (2000). The health and future of coral reef systems. Ocean and Coastal Management 43:657-688.

Tropical Atlantic Dynamics
from the ARAMIS (Altimétrie sur un Rail Atlantique et Mesures In Situ) experiment

S. Arnault, Y. Tanguy

LOCEAN UMR CNRS/IRD/UPMC/MNHN, Paris, France –
sa@locean-ipsl.upmc.fr, ytlod@locean-ipsl.upmc.fr

Abstract - The Atlantic ocean is known to play a key role in the thermohaline circulation and climate. It is an interesting candidate for oceanic investigations in particular in the tropical domain. Thermohaline and circulation structures are thus investigated between 2002 and 2008 during the ARAMIS experiment using in situ data, Jason1 and Jason2 altimetry missions and numerical model results. The ARAMIS route which has been selected for the project crosses the major tropical Atlantic currents, the InterTropical Convergence Zone, the Salinity Maximum Water regions and it is overlaid by a satellite track.

Keywords: tropical ocean, altimetry.

1. INTRODUCTION

Tropical oceans, representing more than 70% of our planet, play a key role in climate investigations. Previous studies have evidenced the complexity of the tropical Atlantic Ocean variability, both in time and in space (Ruiz Barradas et al., 2000; Arnault and Kestenaere, 2003). Although a schematic diagram of average currents in the tropical Atlantic has been constructed, questions are still pending. For example, how does salinity and temperature variability affect the oceanic circulation? What are the pathways and mechanisms of the upper layer cross-gyre changes? Starting in 2002, the ARAMIS (Altimétrie sur un Rail Atlantique et Mesures In Situ) experiment aims to investigate these questions by combining in situ data sets, numerical models and satellites such as Jason1 and 2.

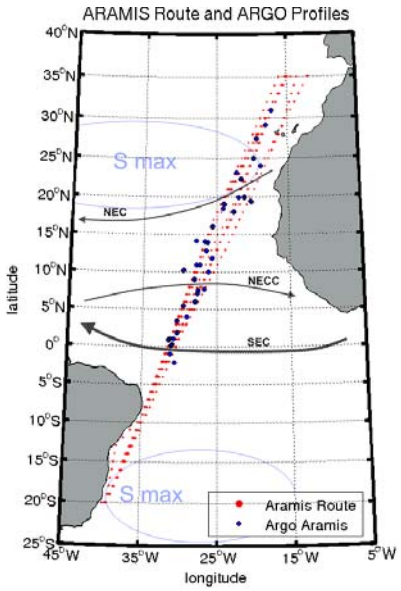

Figure 1. ARAMIS route.

2. THE ARAMIS EXPERIMENT

Twice a year, in spring then fall, when tropical Atlantic Ocean circulation reaches its minimum/maximum intensity in surface layers, temperature T and salinity S profiles have been collected along the ship route (Figure 1). Argo floats were also deployed during each voyage. Figure 2 gives an example of S transect obtained during ARAMIS 13 (October 2008) after processing. It shows a coherent picture, in agreement with seasonal heat flux variability, with equatorial dynamics such as upwelling and ITCZ migration, and with SMW formation (Gordon and Piola, 1983; Blanke et al., 2002). ARGO floats collected along the route during that period provides the same picture of S variability (Figure 3).

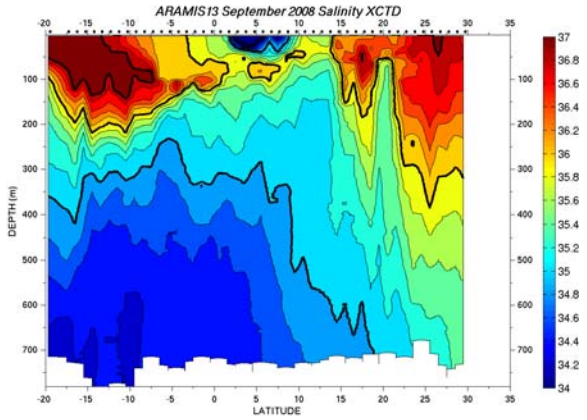

Figure 2. Salinity transect - ARAMIS 13

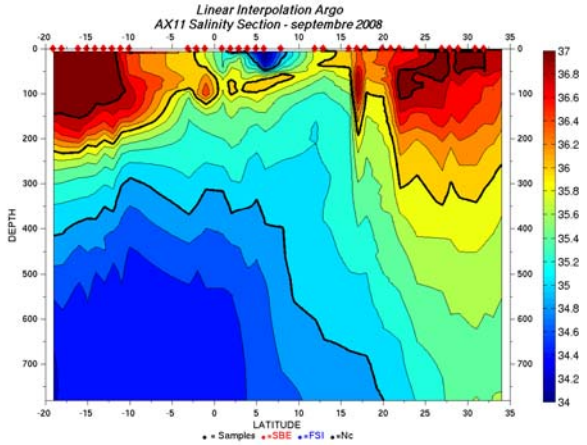

Figure 3. Salinity transect - ARGO floats

The comparison between these 2 different sets of in situ data is developed in Arnault and Tanguy (2010). Thanks to these data sets, tropical Atlantic barrier layer systems have

been identified and investigated (Tanguy et al., 2010).

3. COMPARISON WITH JASON1 AND JASON2

In situ ynamic heigths relative to 700 dbar obtained from T and S profiles have been compared to altimetric sea level. A first step of the study was to use "anomalies". But more interesting was a comparison in terms of "absolute values" thanks to the now available Mean Dynamic Topography (MDT, Rio05, http://www.aviso.oceanobs.com).

Figure 4 presents an example of such comparison. Both signals are in good agreement. In March 2003, the topographic signals just consist in a north-south slope. In July 2002, the contrast develops and shows a succession of highs and lows. Correlations are about 0,9.

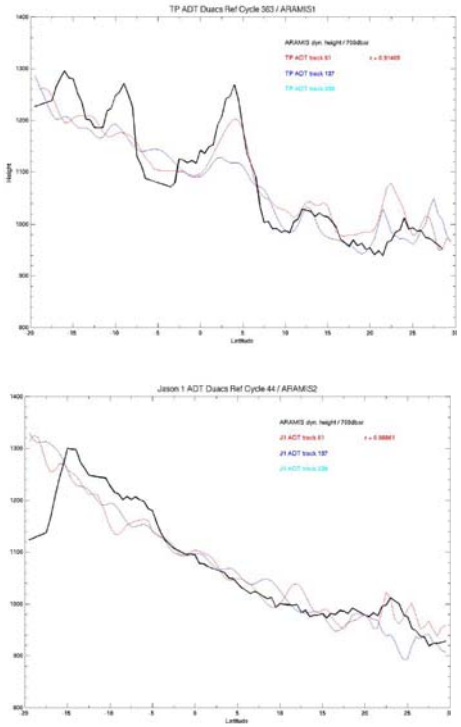

Figure 4. In situ and altimetric dynamic heigth signals for July 2002 and March 2003

The same kind of analysis was also done in terms of geostrophic currents, more sensitive to errors (Figure 5). They all give similar and impressive results.

A succession of alternatively westward or eastward currents can be observed especially between 5°S and 10°N. These currents are in agreement with the surface circulation characteristics in that period of the year: well developed westward SEC along the equator, eastward NECC north of it and westward NEC poleward.

4. CONCLUSION

The ARAMIS experiment was an excellent candidate to check in the tropical Atlantic the complementarity of various sources of data: in situ T and S profiles from expendable probes or ARGO floats and altimetric data. The results are promising either in terms of "absolute" or "anomaly", and either in terms of dynamic topography or geostrophic current. It offers opportunity for long term variability investigations thanks to the decades of altimetric missions.

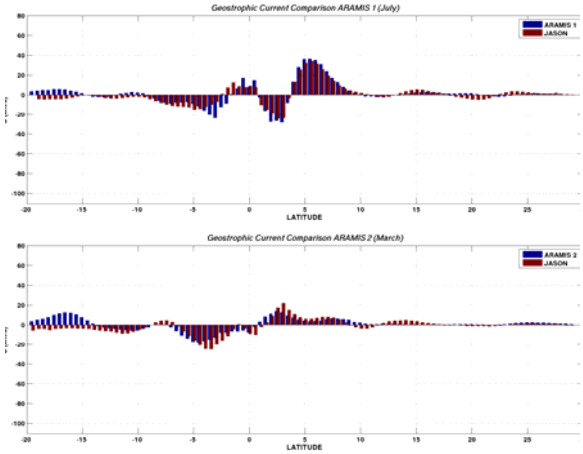

Figure 5. In situ and altimetric geostrophic currents in July 2002 and March 2003

ACKNOWLEDGEMENTS

We are grateful to the US IRD IMAGO, to the Hamburg Sud and to CGM/CMA crews for help during the ARAMIS campaigns. Special thanks to the Argo France and AVISO technical and scientific groups for free access to the databank and for advice on Argo and altimetric Ssalto/Duacs data. The ARAMIS program was founded by the French Centre National d'Etude Spatiales (CNES) and Institut de Recherche pour le Developpement (IRD) organizations. Support for this research was provided by IRD for S. Arnault and by the Ministere de l'Education Nationale, de l'Enseignement Superieur et de la Recherche for Y. Tanguy.

REFERENCES

Arnault S., E. Kestenaere (2004). Tropical Atlantic surface current variability from 10 years of TOPEX/Poséïdon altimetry. Geophys. Res. Lett., vol. 31, L03308, doi:1029/2003GL019210.

Arnault S., Y. Tanguy (2010). Can we use Argo floats in the Tropical Atlantic. En revision à J. Atm. Oceanogr. Techn.

Blanke, B., Arhan, M., Lazar, A., and G. Prevost (2002). A langrangian numerical investigation of the origines and fates of the salinity maximum water in the Atlantic. J. Geophys. Res. 107, 3163; doi:10.1029/2002JC001318.

Gordon, A.L., Piola, A.L. (1983). Atlantic Ocean upper layer salinity budget. J. Phys. Oceanogr. 13, 1293–1300.

Tanguy, Y., S. Arnault and P. Lattes (2010). Isothermal, mixed, and barrier layers in the subtropical and tropical Atlantic Ocean during the ARAMIS experiment. Deep-Sea Research I (2010), doi:10.1016/j.dsr.2009.12.012.

The Role of Satellite Data in Extended Reconstruction of Sea Surface Temperatures

V.F. Banzon [a,*], R.W. Reynolds [b], T.M. Smith [c]

[a] National Climatic Data Center (NOAA/NESDIS), Asheville, NC , USA – Viva.Banzon@noaa.gov
[b] Cooperative Institute for Climate and Satellites, Asheville, NC, USA – Richard.W.Reynolds@noaa.gov
[c] NOAA/STAR/SCSB, College Park, MD, USA – Tom.Smith@noaa.gov

Abstract – The Extended Reconstruction Sea Surface Temperature (ERSST) analysis, produced at the National Climatic Data Center (NOAA), was originally based on *in situ* observations. In the version 3 release, AVHRR data was added to the analysis from 1985 onwards. In this paper, we present ERSST version 3b (v3b) where the satellite data is removed from the monthly analysis due to a small but predominantly cold satellite bias over the recent period (~ 0.01 to 0.07 °C in terms of the global annual average). The bias caused a continuity problem in climate assessments that had been previously based on analyses using *in situ* data only. Nonetheless, satellite data still has an impact in the ERSST product in that the high frequency component is computed using modes derived from an analysis that includes AVHRR data.

Keywords: SST, AVHRR bias, climate assessment.

1. INTRODUCTION

The Extended Reconstruction Sea Surface Temperature (ERSST) is monthly 2°-gridded analysis product that was originally developed to analyze *in situ* data from 1856 to the present for global climate change studies (Smith and Reynolds, 2003). Since then, ERSST has been combined with land temperatures to make a merged global surface temperature product (Smith and Reynolds, 2005). The most recent modifications to ERSST and the merged processing were presented as version 3 (or v3) in Smith *et al*. (2008). The two main innovations were: 1) optimized settings for the merged analysis based on comparisons with simulation results, and 2) inclusion of satellite data to the ERSST analysis from 1985 onwards. For the latter, the Advanced Very High Resolution Radiometer (AVHRR) dataset was used because it represented the longest SST time series from a single sensor design.

In this article, we present version 3b (v3b, herein). This is a minor update to the ERSST processing that entails removal of the satellite data as an input to the analysis (and hence in the merged product as well). Smith *et al*. (2008) had discussed the impact of satellite data as an input in the ERSST analysis. In brief, spatial coverage was improved, sampling error was reduced, but a cold bias was introduced. The causes of the cold bias are discussed in detail in Smith *et al*. (2008). Here, the importance of satellite data to the ERSST analysis is re-examined in the context of the primary use: climate assessments. The intent is to highlight the continuing challenges in combining datasets with different bias characteristic in space and time. We focus on the period from 1985 onwards. However, for climate studies the ultimate goal is that ERSST should be consistent as possible with the pre-satellite era.

2. DATA AND METHODS

The input data and methodology for the v3 ERSST analysis are described in Smith *et a*l. (2008) and references therein, but a brief summary is provided here. The historic buoy and ship ocean temperature observations come from the International Comprehensive Ocean-Atmosphere Dataset (ICOADS), and monthly marine observations updates. For v3 only, AVHRR Pathfinder data were used from 1985-2005 and Operational U.S. Navy AVHRR were used from 2006 onwards. The SST observations are averaged onto a 2° grid, weighted by data type. The analysis is then performed on the anomalies that are computed with respect to a baseline (1971-2000). The low-frequency component is determined by averaging and filtering. Then, the high-frequency component is computed from the residuals using 130 Empirical Orthogonal Teleconnections (EOT) modes. The high- and low-frequency components are then summed to produce the final reconstructed value. The root mean square error is computed as the sum of sampling and analysis errors.

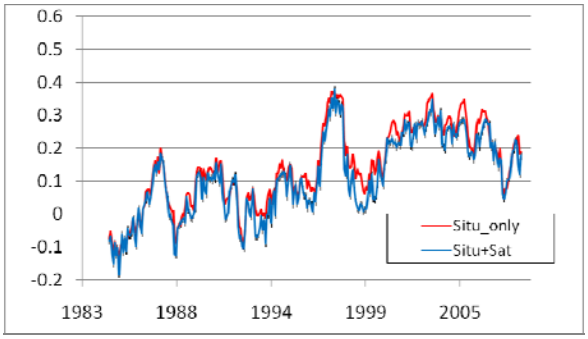

Figure 1. Monthly SST anomalies (°C) averaged from 60° S to 60° N produced by v3b (red) and v3 (blue) processing.

3. RESULTS AND DISCUSSION

The monthly ERSST anomalies are generally cooler for v3 than v3b, but the long term trend is similar (Figure 1). The slopes obtained by fitting a line to the each dataset provide similar rates of temperature increase of about 0.13 °C per decade. Since the two versions are very similar, one could state that the inclusion of satellite data do not appear critical in capturing the decadal scale SST change at global scales. This is because in situ data for this period are well-

* Corresponding author. National Climatic Data Center (NOAA/NESDIS), 151 Patton Ave., Asheville, NC 28802

distributed in space and time (Smith *et al.*, 2008). The satellite data also reduced the ERSST total error (Figure 2), especially south of 30° S. This reflects the improved spatial coverage when satellite data are used. But in general, even without the satellite data, the total error is generally small in most regions (<0.2). Before the 1900's the ERSST error is several times greater than that of the recent period (Smith and Reynolds, 2003; 2004).

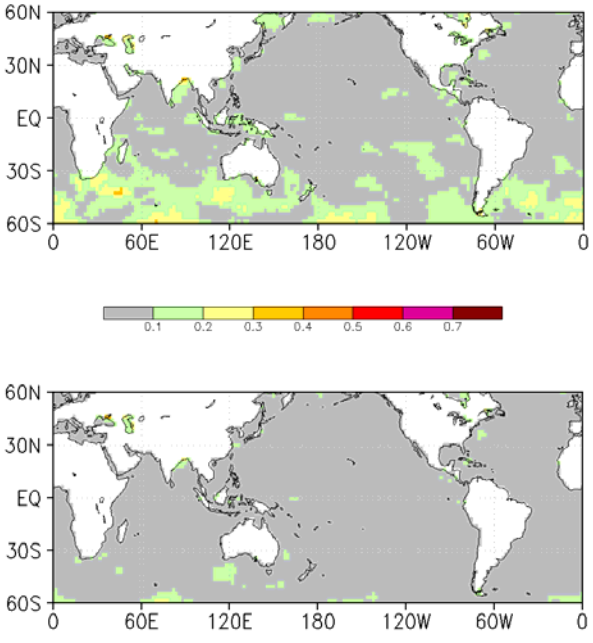

Figure 2. Total ERSST error averaged from 1985-2009 for (upper panel) v3 analysis; (lower panel) v3b analysis.

The annual global rankings are also affected by the satellite cold bias. For v3 and v3b, the five warmest years (from 1985 to 2007) are the same, but the sequence is different (Figure 3). While the standard deviations indicate that the differences among these five years are not significant, the change in the order created a problem for climate assessments because of inconsistencies with previous pronouncements that were based on in situ only analyses.

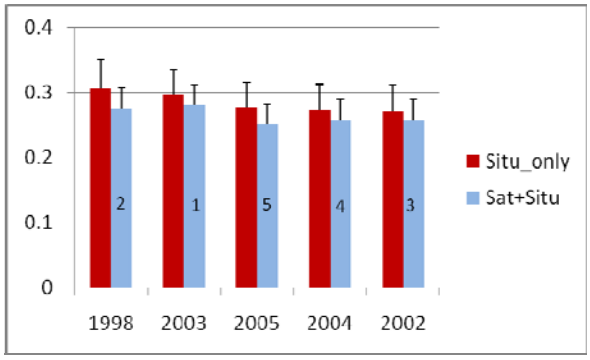

Figure 3. Annual average SST anomalies for the five warmest years (period from 1985 to 2007) for v3 (blue) and v3b (red). The sequence of years is from the warmest for v3b. The v3 rank is written on the bar. Error bars show standard deviation.

Since the world is >70% ocean, it is not surprising that these differences are also reflected in the global surface temperature rankings (Smith *et al.*, 2008). Note that other climate measures such as extreme values (minima and maxima per year) are also affected.

The other contribution of satellite data to ERSST is often overlooked. The high frequency component is computed using EOT modes from an analysis of *in situ* and AVHRR data for a fixed period (1985-2005). The EOT analysis is a separate one time effort and is not repeated at run time. One of the main causes of the difference between v3 and v3b is the lack of *in situ* data to support a mode that is detected in the satellite data. Smith *et al.* (2008) noted that this often occurred for the Southern ocean and adjacent areas. This situation can only be improved if the number of *in situ* observations were increased in the region.

4. CONCLUSION

Because the ERSST is intended primarily for use in climate assessments, it is reasonable to remove the satellite data from the analysis. The advantages of including satellite data, i.e., high-resolution spatial coverage and increased temporal sampling, are not highly valuable to a monthly analysis on a 2° grid. Satellite data still influences the ERSST product through the EOT modes used to estimate the high-frequency component. For the satellite era, a similar but higher resolution daily Optimally Interpolated SST product that uses *in situ* and satellite data is already available to users (Reynolds *et al.*, 2007). It would be better to focus efforts in examining the trends derived from the ERSST and OISST datasets and understanding the causes of the differences.

ACKNOWLEDGEMENTS

We would like to acknowledge Chunying Liu for running the OISST and ERSST operational codes.

REFERENCES

Reynolds, R.W., T.M. Smith, C. Liu, D. B. Chelton, K.S. Casey, and M.G. Schlax (2007). "Daily High-Resolution-Blended Analyses for Sea Surface Temperature". *Journal of Climate*, vol. 20, pp. 5473-5495.

Smith, T.M. and R.W. Reynolds (2005). A Global Merged Land, Air, and Sea Surface Temperature Reconstruction based on Historical Observations (1880-1997)". *Journal of Climate*, vol. 18, pp. 2021-2036.

Smith, T.M. and R.W. Reynolds (2003). "Extended Reconstruction of Global Sea Surface temperatures based on COADS Data (1854-1997)". *Journal of Climate*, vol. 16, pp. 1495-1510.

Smith, T.M. and R.W. Reynolds (2004). "Improved Extended Reconstruction of SST (1854-1997)". *Journal of Climate*, vol. 17, pp. 2466-2477.

Smith, T.M., R.W. Reynolds, T.C. Peterson and J. Lawrimore (2008). "Improvements to NOAA's Historical Merged land-Ocean Surface Temperature Analysis (1880-2006)". *Journal of Climate*, vol. 21, pp. 2283-2296.

Pigment, Temperature and Wind Patterns at two Mediterranean Sites

V. Barale *

Joint Research Centre, European Commission, Ispra , Italy – vittorio.barale@jrc.ec.europa.eu

Abstract – Satellite observations at two Mediterranean sites reveal the coupling of wind, temperature, pigments. The study, conducted at the monthly scale from 2000 to 2007, uses QuikScat wind speed to outline atmospheric forcing; AVHRR surface temperature to identify deep convection areas; and SeaWiFS pigment concentration to image the resulting algal blooms. At both sites, atmospheric forcing causes vertical mixing and nutrient upwelling from deep layers. As plankton growth in the otherwise oligotrophic basin is always nutrient-limited, the blooms triggered by these processes reflect the prevailing wind patterns (with variable time lags). The synergy between different sensors helps understanding cause-effect relationships in the marine environment.

Keywords: algal blooms, wind forcing, Mediterranean Sea.

1. INTRODUCTION

Satellite observations at two sites in the Mediterranean Sea reveal the coupling of wind, temperature and algal blooms. Monthly-mean, area-averaged values of satellite-derived parameters, from 2000 to 2007, were derived for the Gulf of Lion (3.5-7.5°E, 40.5-42.5°N), in the Ligurian-Provençal Sea, and for the Rhodes Gyre (26.0-31.0°E, 33.0-36.0°N), in the Levantine Basin (Figure 1). At both sites, atmospheric forcing is related to vertical mixing, nutrient upwelling from deeper layers, and consequent blooming that reflects the prevailing patterns of air-sea interaction (Barale et al. 2008).

2. SATELLITE DATA SOURCES

SeaWinds scatterometer (QuikScat) data were used to outline patterns of atmospheric forcing. Wind speed (WS) and direction at 10 meters over the surface were retrieved from measurement of backscattered power. The composite data used here are monthly means re-mapped onto a 0.25° grid. Sea surface temperature (SST) from the Advanced Very High Resolution Radiometer (AVHRR) was used to spot deep convection areas. The data originate from the NASA/NOAA Pathfinder Project, version 5.0, are processed to apply sensor calibration, correct atmospheric noise and derive SST, and re-mapped with a resolution of about 4 km. The composite data were obtained as a weighted mean of all valid pixels for each month and grid cell. Sea-viewing Wide Field-of-View Sensor (SeaWiFS) data were used to image the pigment field. The imagery was processed to correct top-of-the-atmosphere radiances for atmospheric noise, derive normalized water-leaving radiances, and compute chlorophyll-like pigment concentration (Chl). Each image was re-mapped with a resolution of about 2 km. Monthly composites were obtained from the re-mapped data, using all valid pixels for a given month and grid cell. A single WS, SST, Chl average value for the whole area was derived from each monthly mean (Figure 2).

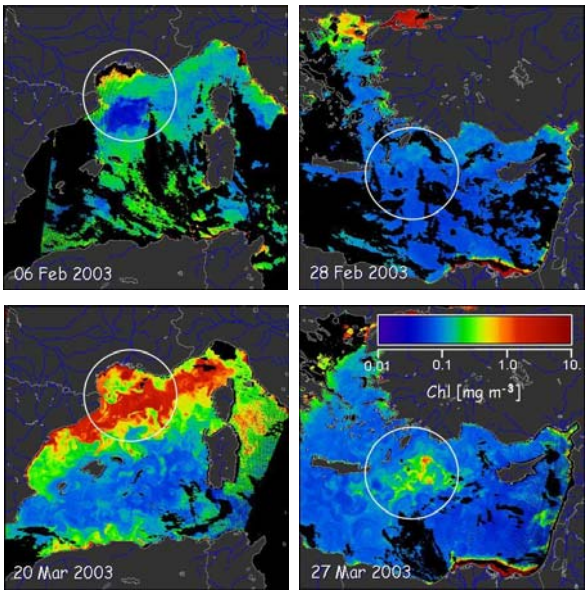

Figure 1. SeaWiFS-derived Chl in the Gulf of Lion (upper left: deep convection; lower left: blooming) and in the Rhodes Gyre (upper right: spin off; lower right: blooming).

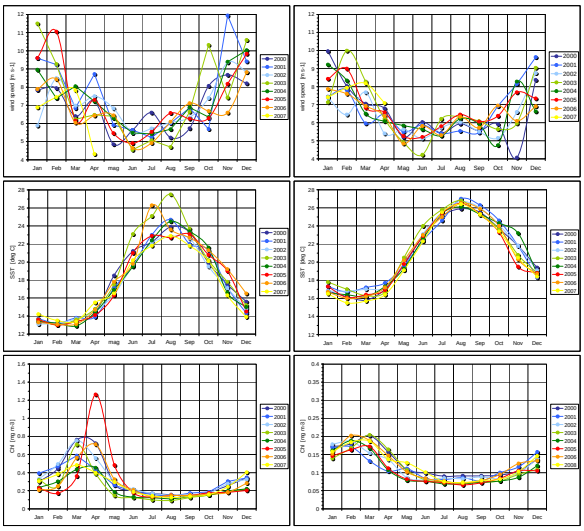

Figure 2. Monthly-mean, area-averaged WS (upper panels), SST (middle panels) and Chl (lower panels), for the Gulf of Lions (left side) and the Rhodes Gyre (right side).

3. WS, SST and Chl TIME SERIES

In the NW basin, northerly winds increase surface density through intense evaporation and cooling, and generate deep convection processes (Hermann et al. 2008). This leads to the overturning of the water column, which brings cold

* Corresponding author. TP272, Via E. Fermi 2749, 21027 Ispra (VA), Italia. Tel +39 0332 789274, Fax +39 0332 789034.

nutrient-rich waters to the surface, and favours the onset of algal blooms (as the water column warms up and stabilizes). Figure 3 (left panels) shows that higher WS corresponds to lower SST, and that higher Chl values occur at lower SST. An increasing WS generates higher Chl, but only up to a point, if the convection becomes so deep to prevent any blooming. In the SE basin, northerly winds blowing along the Aegean Sea funnel through the straits between Crete and Rhodes, generating a (quasi) permanent vortex pair (Millot and Taupier-Letage 2005). This consists of the cyclonic Rhodes Gyre (in which the divergence due to Ekman pumping is linked to the upwelling of cold, nutrient-rich waters) and the anti-cyclonic Ierapetra Gyre (in which the convergence is linked to the downwelling of warm, nutrient-poor waters). Figure 3 (right panels) shows that higher WS corresponds to lower SST and higher Chl. Increasing WS just brings higher Chl, as no deep convection is generated in this case. Note that the correlation is not highest when the Chl values are matched with the WS of the same month (Figure 4). In the Gulf of Lions, at 0 time lag, both linear fit and second order polynomial fit show essentially no correlation (R^2 = 0.1, 0.05), due to the occurrence of deep convection. As the time lag increases, so does the correlation. The maximum is reached after 2 months, *i.e.* when Chl values are matched with the WS of 2 months before (R^2 = 0.28 for both fits). At even greater time lags, the correlation decreases again to very low values (R^2 ~ 0 after 5 months). The rationale of this must take into account two factors: first, the biological response of the ecosystem cannot be instantaneous, after the set up of conditions favourable to algal growth (*i.e.* the increase in nutrient concentration due to vertical mixing); second, when the wind is strongest, the continuing deep convection can prevent the blooming, which starts only when the wind field relaxes again and stratified conditions prevail. In the Rhodes Gyre, both linear and polynomial fit show a positive correlation (R^2 = 0.42, 0.43) at 0 time lag. But the highest correlation is reached with a time lag of 1 month, *i.e.* when Chl values are matched to WS of the preceding month (R^2 = 0.63 for both linear and polynomial fit). At higher time lags, the correlation decreases quickly to very low values (R^2 ~ 0.4 at 2 months, R^2 = 0.07 at 3 months, and R^2 ~ 0 at 4 months). Again, this points to a delay of the biological response to the set up of conditions favourable to algal growth, but on a shorter time scale (as in this case the increase in nutrients is due to Ekman pumping within a cyclonic gyre, and not to sustained deep convection, continuing for long periods).

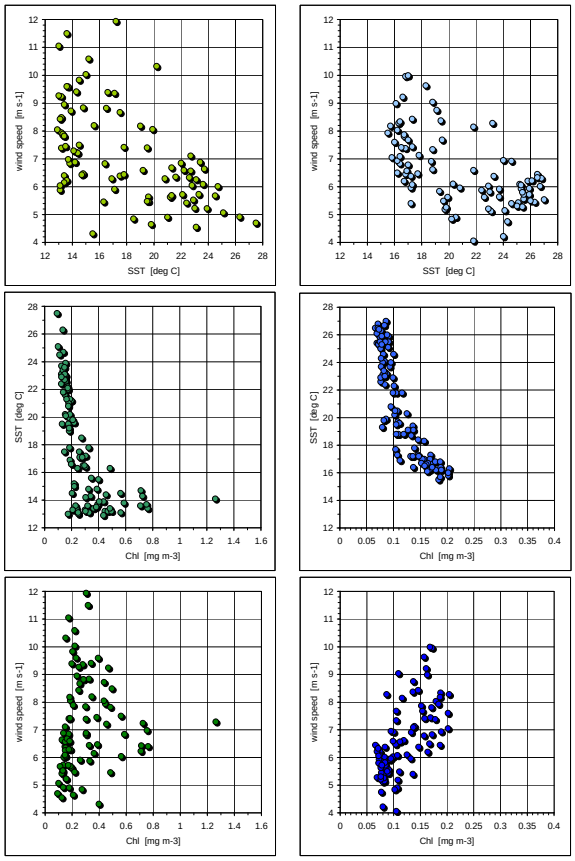

Figure 3. Scatter plots of 2000-2007 monthly-mean, area-averaged values of Chl and WS (upper panels), SST and WS (middle panels), Chl and SST (lower panels), for the Gulf of Lion (left side) and the Rhodes Gyre (right side).

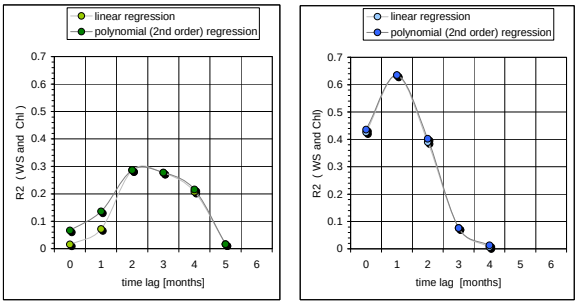

Figure 4. R^2 values, from linear and 2nd order polynomial regressions of Chl and WS, at successive time lags, for the Gulf of Lion (left panel) and the Rhodes Gyre (right panel).

4. CONCLUSION

The combined analysis of microwave, thermal infrared and optical data shows that the Ligurian-Provençal Sea and the Levantine Basin constitute notable exceptions to the typical oligotrophy of the Mediterranean Sea. At the NW site, winter winds lead to convective processes, which trigger vertical mixing and then sizeable spring blooms, once the wind regime relaxes and stratification sets in. In the SE site, upwelling due to Ekman pumping, within the cyclonic component of the wind-generated Rhodes-Irapetra vortex pair, also results in similar, if weaker, algal blooms.

ACKNOWLEDGEMENTS

QuikScat data are produced by Remote Sensing Systems and supported by the NASA (see http://www.remss.com/). SeaWiFS and AVHRR data are available from the JRC EC **E**nvironmental **M**arine **I**nformation **S**ystem (**EMIS**). For data and processing details see http://emis.jrc.ec.europa.eu/.

REFERENCES

V. Barale, J.M. Jaquet, and M. Ndiaye (2008) Algal blooming patterns and trends in the Mediterranean Sea as derived from the SeaWiFS data set (1998-2003). Remote Sensing of Environment, vol 112 (8), pp 3300-3313,

M. Hermann, S. Somot, F. Sevault, C. Estournel, and M. Déqué (2008) Modeling the deep convection in the northwestern Mediterranean Sea using an eddy-permitting and an eddy-resolving model: case study of winter 1986-87. Journal of Geophysical Research, vol 113, pp xxx-xxx.

C. Millot and I. Taupier-Letage (2005) Circulation in the Mediterranean Sea. In: A. Saliot ed., The Mediterranean Sea, The Handbook of Environmental Chemistry, Vol 5, Springer-Verlag Berlin, Heidelberg, pp 31-66.

Robustness of global mean sea-level from satellite altimetry data

S. M. Barbosa [a,*], J. A. O. Matos [b]

[a] University of Lisbon, IDL, Lisboa, Portugal – sabarbosa@fc.ul.pt
[b] University of Porto, FEP and CMUP – jamatos@fep.up.pt

Abstract – This work examines the robustness of global mean sea-level derived from satellite altimetry data. The influence of local oceanographic phenomena on global sea-level variability is assessed by computing a global mean sea-level curve from the observations in the central part of the data distribution. The results show that the global mean sea-level curve derived from satellite altimetry observations is robust, since the influence of ENSO and ocean circulation phenomena on global sea-level variability is negligible, contributing to increase global sea-level rise by only 0.16 mm/year.

Keywords: sea-level; satellite altimetry; ENSO

1. INTRODUCTION

Satellite altimetry has become in the last 15 years a mature technique, successfully applied in several Earth observation contexts (e.g. Fu and Cazenave, 2001). It is a key component of ocean monitoring from space in general and global sea-level observation in particular. Sea-level is a fundamental geophysical parameter. The height of the sea surface responds to mass and density changes in the ocean as well as changes in the atmosphere above it, providing comprehensive information on oceanographic and atmospheric phenomena. Global sea-level change is an important climate change indicator, yielding a record of climate changes in the Earth's system. It is also a potential hazard, since coastal populations can be directly and indirectly affected by global sea-level rise with consequent social and economic impacts. Satellite altimetry has allowed to study in a unprecedented way the variability of sea-level at the global scale. By providing high-quality observations of the height of the sea-surface on a nearly global and spatially uniform scale, satellite altimetry has given a detailed picture of global sea-level change and shown that it exhibits considerable spatial variability, with positive and negative trends up to several times the global mean (e.g. Cazenave and Nerem, 2004). Global sea-level change is often summarised by the global mean, resulting from a spatial weighted average over the whole globe of the satellite altimetry measurements obtained within each cycle of the satellite (e.g. 10 days). However, this representation does not take into account the spatial variability within each cycle. This work examines the robustness of the global sea-level curve derived from satellite altimetry observations

2. DATA

Satellite altimetry data from Topex/Poseidon and Jason-1 missions are obtained from the RADS database (Scharroo, 2009) The data are Sea Level Anomalies (SLA), derived from the difference of the altimeter range and the DNSC08 mean sea surface (Andersen and Knudsen, 2009). The altimeter range is corrected of all standard instrumental and geophysical effects, including the inverse barometer effect (MOG2D model). Data are taken from January 1993 to December 2008, corresponding to Topex/Poseidon cycles 11 to 360 and Jason-1 cycles 18 to 254.

3. RESULTS

The global mean sea-level curve derived by spatially averaging the altimetry observations for each cycle is shown in Figure 1. The spatial averaging is performed by weighting the satellite observations by the cosine of the corresponding latitude and by equi-area weighting (e.g. Nerem, 1995). The results are very similar for the two weighting schemes.

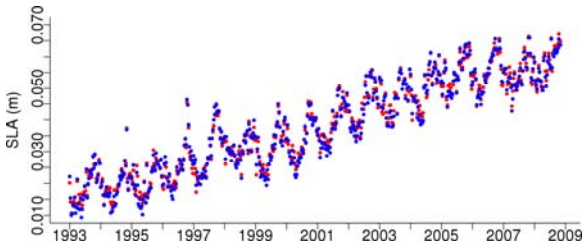

Figure 1. Time series of global mean sea-level derived from cosine (red) and equi-area (blue) spatial weighting.

As an example of the spatial distribution of SLA, Figure 2 shows the values for cycle 190 (November 1997). Clearly visible are the sea-level signature of the El Niño – Southern Oscillation (ENSO) phenomenon, and the high variability areas associated with major current systems (e.g. Gulf Stream, Agullas, Kuroshio). These correspond mainly to local, oceanographic-driven sea-level changes; therefore should not be representative of global sea-level variability. Figure 3 shows the same data but with the SLA values outside the 1st and 3rd quantiles set as missing. Figure 4 shows the global mean sea-level curve obtained by spatially averaging the SLA for each cycle with weighting by the cosine of latitude but considering only the SLA values within the 1st and 3rd quantiles (corresponding to 25% and 75% of the observations, respectively). This conservative estimate of global mean sea-level variability using only the observations between the 1st and 3rd quantiles is not very different from the global mean sea-level curve shown in Figure 1. However, the difference between the two estimates of global sea-level variability (Figure 5) yields a non-random pattern, indicating that the conservative

* Corresponding author. Faculdade de Ciências, Universidade de Lisboa, Campo Grande, Edifício C8, 1749-016 Lisboa.

estimate is characterised by higher SLA for the 1996-1998 period encompassing the strong 1997-1998 ENSO event and lower SLA around 1991-2002 and 2007-2009.

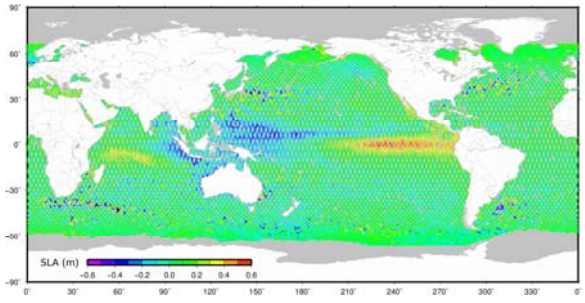

Figure 2. Sea level anomalies for Topex cycle 190.

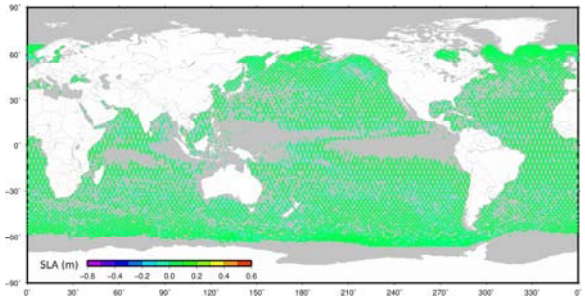

Figure 3. Sea level anomalies for Topex cycle 190 within the 1st and 3rd quantiles

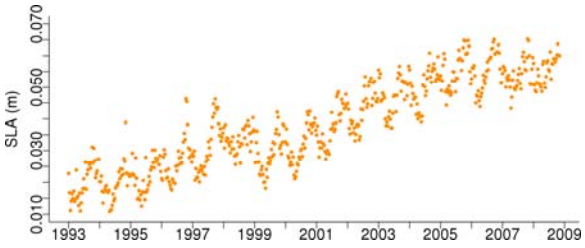

Figure 4. Time series of global mean sea-level derived by spatially averaging the SLA within the 1st and 3rd quantiles.

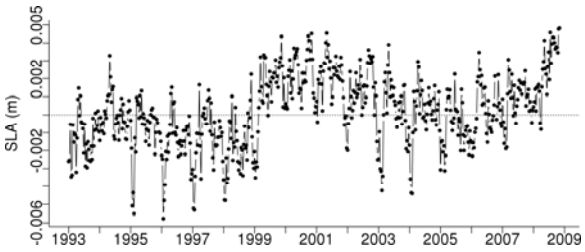

Figure 5. Difference between global mean sea-level curves in Fig. 1 and Fig. 4 (total – quantiles mean)

In terms of linear trends, the global mean sea-level curve derived by considering all the observations yields a statistically significant slope of 2.92 (+- 0.05) mm/year (without any temporal filtering and including seasonality). The global sea-level curve considering only the observations within the 1st and 3rd quantiles yields a statistically significant slope of 2.76 (+- 0.054) mm/year. The difference between the two curves corresponds to a statistically significant trend of 0.16 (+- 0.017) mm/year.

4. CONCLUSION

The robustness of the global mean sea-level curve derived from satellite altimetry data has been examined in this work. In order to assess the influence of local oceanographic phenomena on global sea-level variability, the global mean sea-level curve obtained by spatially averaging all the observations is compared with a conservative estimate based only on the observations within the 1st and 3rd quantiles. The results show that the effect of local oceanographic phenomena on global sea-level variability, as assessed by removing the 25% lowest and highest observations, is to increase global sea-level rise by 0.16 mm/year. Although this value is statistically significant when considering formal errors, it is within the more realistic error of ~0.4 mm/year (Leuliette et al, 2004). Therefore the global mean sea-level curve is robust, and the influence of ENSO and ocean circulation phenomena on global sea-level rise seems to be negligible. Nevertheless, the influence could be more dramatic in the case of shorter records (e.g. if considering only the Topex/Poseidon mission), emphasising the importance of present and future satellite altimetry missions for achieving a long and continuous record of global sea-level variability.

ACKNOWLEDGEMENTS

FCT supported this work through the Compromisso para a Ciência Programme Ciência 2008. Satellite altimetry data were obtained from the RADS database. Thanks are also due to the R development core team for the R software and to P. Wessel and W.H.F. Smith for GMT.

REFERENCES

Andersen, O.B., and P. Knudsen (2009). “DNSC08 mean sea surface and mean dynamic topography models”, Journal of Geophysical Research 114, pp C11001.

Fu, L., and A. Cazenave (2001). “Satellite Altimetry and Earth Sciences”, Academic press

Cazenave, A., and R.S. Nerem (2004). “Present-day sea level change: observations and causes”, Reviews of Geophysics 42. pp RG3001.

Leuliette, E.W., R.S. Nerem and G.T. Mitchum (2004). “Results of TOPEX/Poseidon and Jason-1 calibration to construct a continuous record of mean sea level”, Marine Geodesy 27, pp 79-94.

Nerem, R.S. (1995). “Measuring global mean sea level variations using Topex/Poseidon altimeter data”, Journal of Geophysical Research 100, pp 25135-25152.

Scharroo, R. (2009). “RADS User Manual and Format Specification”, version 3.0.

Quality Control and Validation of MERIS Coastal Products

K. Barker[a, *], G. Moore[b], C. Kent[a], J-P Huot[c], S. Lavender[a]

[a] ARGANS Ltd, Plymouth, UK – kbarker@argans.co.uk
[b] Bio-Optika, Gunnislake, UK – geraldfmoore@googlemail.com
[c] ESA ESTEC , Noordwijk , The Netherlands – Jean-Paul.Huot@esa.int

Abstract – Marine coastal regions are highly dynamic areas with significant environmental, recreational, commercial and industrial importance. Long term monitoring of these areas can be provided through radiometric measurements from (amongst others) ESA's MERIS instrument. The nature of these optically complex areas is such that the methods and algorithms applied to open ocean waters do not always meet accuracy requirements needed for useful coastal zone monitoring. In this paper we describe ongoing activities including the Bright Pixel Atmospheric Correction (BPAC), laboratory experiments, in-situ data collection and protocol documentation.

Keywords: MERIS, coastal, BPAC, NIR, MERMAID.

1. INTRODUCTION

The MEdium Resolution Imaging Spectrometer (MERIS) instrument, onboard ESA's ENVISAT satellite, has been providing global coverage of ocean colour - through the use of 5 cameras and 15 programmable spectral bands covering the visible and near-infrared (NIR) - since 2002. The primary mission of MERIS is to provide accurate measurements over coastal regions; highly dynamical areas of high environmental, recreational, commercial and industrial importance. Coastal waters create a particular challenge for satellite remote sensing because the colour is influenced by a complex mixture of substances dissolved and suspended within it. ARGANS and Bio-Optika (both UK-based) are working with ESA, the MERIS Quality Working Group (QWG) and MERIS Validation Team (MVT), to improve accuracy and general product quality in these regions. The ESA project ('Technical Assistance for the Quality Control and Validation of MERIS Coastal Marine Products', hereafter known as 'MERIS Coastal') began in July 2008 within the framework of MERIS calibration and validation activities, the forthcoming third MERIS reprocessing and to provide a continuation of research and support from MERIS through to the Sentinel-3 Ocean and Land Colour Instrument (OLCI). Here we present some of the work undertaken through a variety of activities such as laboratory experiments, in-situ data collection, collaboration with scientific institutions, algorithm research and validation, data mining and literature and code reviews.

1.1 Bright Pixel Atmospheric Correction for the third MERIS reprocessing

In the open ocean, around 90% of the signal reaching the satellite sensor in the visible range of the spectrum comes from the atmosphere. In the NIR wavelengths however, nearly the entire signal originates in the atmosphere, therefore enabling these bands to be used to determine atmospheric conditions, and extrapolate them to the visible wavelengths. However over bright coastal waters, this so called 'black pixel' assumption does not apply because the suspended material backscatters in the NIR wavelengths, adding to the measured signal and causing overestimation of the atmospheric contribution. Therefore a 'bright pixel' atmospheric correction (BPAC) is needed. Moore *et al.,* (1999) developed the original MERIS BPAC, and within this new project further developments have been undertaken. The BPAC algorithm was modified to use backscatter, b_b, as an IOP rather than suspended matter that was essentially a proxy for b_b. New f/Q factors (which relate the water-leaving radiance to irradiance) have been modelled using Hydrolight; due to the range of water that the BPAC algorithm needs to cover, approximately 10,000 runs of Hydrolight were needed per band in order to have a good density of points for curve fitting. Previous f/Q versions (Morel and Gentili, 1993) fail in high turbidities ($\omega \rightarrow 1.0$) and led to a new method whereby f/Q is a function of absorption (a) and backscatter, specifically $a/(b_b+a)$, and thus applicable to waters with $\omega=1.0$. This has the advantage of enabling the temperature and smile effects to be included in future MERIS reprocessings. The generated tables allow an estimate of sediment absorption to be calculated, and have been calculated for all wavelengths, for both OCLI and MERIS, so that they can be used for developing f/Q relationships for the normalisation of in-situ reflectance. The tables have been implemented in a test version of the new MERIS processor, developed at ACRI-ST in France. The updated BPAC was validated using simulated data and extracted data from specific scenes, in collaboration with Suzanne Kratzer (University of Stockholm). An interesting side outcome of the BPAC is that it will also retrieve chlorophyll concentration as well as concentrations for suspended sediment and Coloured Dissolved Organic Material (CDOM).

1.2 Experimental determination of water properties in the NIR

This aspect of the project aims to experimentally determine water properties in the NIR wavelengths (>700nm), for various validation activities, through a series of precise measurements of water reflectances. Using previously published literature (Bale et al. 1994, Pope and Fry, 1997, Mantovani and Cabral, 1992) and water absorption values from the MERIS Reference Model Document (RMD) from the MERIS Third Reprocessing, a set of tests were run on HYDROLIGHT to quantify the influence of a specially-designed black butyl-lined measurement tank on the

* Corresponding author. ARGANS Ltd, Unit 3 Drake Building, Tamar Science Park, Plymouth, UK.

radiometric properties with the explicit purpose of determining the properties of water in the NIR with respect to changes in salinity, temperature and total suspended matter (TSM). Initial testing of the tank has been completed with investigations currently focused on the radiometric calibration and characterisation of the radiometers to be used; this is proceeding with the use of a specially designed bench calibration unit. The outcome of these experiments will allow validation of the current water reflectance ($\rho_w(\lambda)$) model and forms an important part of deriving water properties in coastal waters where sediment type and concentration, and salinity can be highly variable.

1.3 Improved methodology for in-situ radiometric measurements

In-situ data collection of the radiometric properties of water are important for the validation of satellite-borne optical sensors and the algorithms used to derive geophysical parameters. As well as working closely with field scientists already making in-situ measurements, Bio-Optika and ARGANS have developed and built a floatation rig specifically designed to deploy a RAMSES TriOS radiometer for radiometric measurements in the visible and NIR wavelengths, but without incurring the effects of tilt. Measurement protocol examination, in collaboration with the MERIS QWG, has recently highlighted the significant extent to which tilt can affect measurements of direct solar irradiance (Es), which propagates the error through to $\rho_w(\lambda)$. The new floating rig will allow subsurface measurements to be made at a distance far enough away from the operator to reduce bias and inaccuracies, and is designed to counteract the motion of waves and ensure the sensors remain vertical; this development represents a significant advancement in the design of small-scale measurement devices which are not intended to be fixed and therefore stabilised (such as the BOUSSOLE buoy in the Mediterranean, or the MOBY buoy at Lanai, Hawaii). The floatation rig is currently undergoing sea trials in Sagres, Portugal, and once operational, the data collected will be submitted to the MERis MAtchup In-situ Database (MERMAID) for continuing validation of MERIS products.

2. MERIS OPTICAL MEASUREMENT PROTOCOLS

In the framework of MERIS QWG activities, MERMAID (http://hermes.acri.fr/mermaid/home/home.php) aims at making available an easy-to-use centralised database of merged in-situ optical measurements with concurrent MERIS acquisitions. Through collaboration with field scientists for in-situ measurements and ACRI-ST for MERIS matchups, MERMAID is now much expanded since its inception, and includes a number of datasets from coastal sites such as the AERONET-OC (Zibordi *et al.,* 2009), Gustav-Dahlen Tower and Helsinki Lighthouse sites, as well as data submitted from individual investigators (and members of the MERIS Validation Team, the MVT) located in, e.g. the Irish Sea (D. McKee, University of Strathclyde), the NW Baltic Sea (S. Kratzer, University of Stockholm) and Sagres (Algarve; J. Icely). Under this contract, and with the assistance of the MERIS QWG and the field researchers, ARGANS has collated and synthesised into one document the MERIS Optical Measurement Protocols that describe the methodologies used for the in-situ radiometric measurements in MERMAID and cover a large variety of different instruments including profilers, fixed buoys and above water sensors. The document is currently under review by the MERIS QWG and will shortly be made available on the MERMAID website.

3. CONCLUSIONS

Remote sensing of coastal waters forms a highly critical part of the monitoring these dynamic and environmentally important regions. MERIS was designed with coastal monitoring as a primary goal, and through this project we have made significant advancements to product improvement and at the least, to coastal product validation. Further work planned for the project (laboratory measurements, in-situ measurements and algorithm validation) aims to further evolve of ideas for the understanding of these optically complex waters.

ACKNOWLEDGEMENTS

The authors would like to acknowledge the following: ACRI-ST (MERIS processing, processing updates and coordination, MERIS to in-situ matchups), ESA (contract no. 21652/08/I-OL), the MERIS QWG, and the MVT contributing valuable in-situ data to MERMAID.

REFERENCES

Bale *et al*., 1994. Laboratory measurements of the spectral properties of estuarine suspended particles, *Journal of Aquatic Ecology*, 28(3-4), pp237-244.

Barker *et al*. (2008). "The MERis MAtchup In-situ Database (MERMAID)". Proceedings of the 2nd (A)ATSR and ENVISAT Symposium, Frascati, Italy, Spetember 2008.

Mantovani, J.E. and Cabral, A.P. 1992. Tank depth determination for water radiometric measurements, *IJRS,* 13:14, pp2727-2733,

MERIS Reference Model Document (RMD): Third Reprocessing. ESA, 2010. http://earth.esa.int/pub/ESA DOC/ENVISAT/MERIS/reference model i4r1.pdf.

Moore, G. Aiken, J. and Lavender, S. 1999. The atmospheric correction of water colour and the quantitative retrieval of suspended particulate matter in Case II waters: application to MERIS. IJRS, vol. 20, no. 9,

Morel, A. and Gentili, B. 1993. Diffuse reflectance of oceanic waters Vol 2 Bidirectional aspects. Applied Optics. Vol. 32, No. 33.

Pope, R.M. and Fry, E.S. 1997. Absorption spectrum (380-700nm) of pure water. II. Integrating cavity measurements. *Applied Optics*. Vol. 36, Iss 33, pp8710-8723

Zibordi, G. et al., 2009. AERONET-OC: A Network for the Validation of Ocean Color Primary Products Journal of Atmospheric and Oceanic Technology. Volume 26, Issue 8

The Winter Migration of Whale Sharks to the Northern Arabian Sea: A Study Using Satellite Remote Sensing

Beena Kumari

Marine and Earth Sciences group, Space Applications Centre (ISRO), Gujarat, India – beena@sac.isro.gov.in

Abstract – This study suggest that whale shark migration to the northern Arabian sea during winter months is probably for the purpose of feeding. Satellite data (chlorophyll-a from SeaWiFS and sea surface temperature from NOAA-AVHRR) allowed to identify the chlorophyll rich grounds in this part of the world ocean compared to the southern region. This understanding was facilitated due to their synoptic coverage. Whale sharks, which travel to almost every ocean, contribute to the idea that the combined use of ocean colour and thermal infrared images are an appropriate tool to identify potential areas of Whale Shark aggregation for sightings. This study improves our understanding of the whale shark occurrence and aggregation during winter monsoon in northern regions of Arabian Sea. While availability of food is a function of physical process in the region, the linear relationship between whale shark catches and phytoplankton biomass provides evidence that whale sharks adapt their movements directly to food availability and their migration within a region may be precisely timed to coincide with seasonal productivity events.

Keywords: whale shark, SST, chl-*a*, monsoon, Arabian Sea.

1. INTRODUCTION

The Whale shark (*Rhincodon typus*) is the world's largest fish. Whale sharks are widely distributed in the warm tropical waters (excluding the Mediterranean) worldwide, usually between latitudes 30° N and 35° S in tropical and warm temperate seas, both oceanic and coastal. Like any other gentle giant these animals are also facing extinction and need scientific attention. Whale sharks are currently protected in Australia, Maldives, Philippines, USA, Gulf of Mexico and the Atlantic coast.

In India, whale sharks were caught opportunistically for decades, because of high export value for their skin, meat and fins. Records on whale shark capture and incidental landings (Traffic-India) show the occurrence of whale sharks on the west coast of India, with report of very few catches from the east coast. The shelf - coastal waters of Gujarat in the northeastern Arabian Sea is reported to be one of the favorite visiting spots for the whale shark during winter monsoon period and they have been visiting the shores of Gujarat for hundreds of year.

The Arabian Sea experiences unique oceanographic features and events compared to other world oceans, The semi-annual reversal of monsoon winds are divided into southwest (June-September) and northeast (December-February) monsoon phases with two transition periods, spring inter monsoon (March-April-May) and fall inter monsoon (October-November). Southwest (SW) monsoon winds cause vigorous and deep anti- cyclonic surface circulation in the Arabian Sea, inducing both coastal and open ocean upwelling (Shetye, et al. 1994). During northeast (NE) monsoon, cold dry northeast winds blow over the Arabian Sea causing cyclonic circulation. Accordingly, waters north of 15°N experiences densification and sinking of surface waters leading to convective mixing and deepening of the mixed layer (Prasanna and Prasad, 1996). Surface currents dissipate and hydrographic conditions in the Arabian Sea approach those of a well-stratified and unperturbed tropical ocean during the transition period between the two monsoon phases.

The SW and NE monsoon periods drive the biological production in the Arabian Sea. During SW monsoon intense upwelling both in the coastal waters off Somalia, Arabia and in the adjacent open ocean waters causes deepening of mixed layer and injection of nutrients from thermocline. This process results in very high levels of biological production in the western Arabian Sea (Brock *et al.* 1991). Similarly wind driven upwelling and consequently high production is observed during the SW monsoon in the southeastern part of the Arabian Sea. However during rest of the season, this region is almost oligotrophic. In the NE monsoon phase, surface cooling and densification leads to sinking and convective mixing triggering intense biological production in the northern Arabian Sea (Prasanna and Prasad, 1996).

2. METHODS

A study has been carried out using satellite-derived chlorophyll-*a* (chl-*a*) an index of phytoplankton biomass, sea surface temperature and the whale shark sighting and landing data. The analysis was carried out for three years (1998-2000). Monthly images of chlorophyll-*a* (chl-*a*) concentration, and sea surface temperature (SST) were derived for eastern Arabian Sea from *Sea-viewing Wide Field-of-View S*ensor (SeaWiFS) and *National Oceanographic and Atmospheric Administration-Advanced Very High Resolution Radiometer* (NOAA-AVHRR) respectively. Whale sharks (*Rhincodon typus*) landing data was obtained from a survey conducted by Traffic-India, (*Trade Records Analysis of Flora & Fauna In commerce*) of *World Wide Fund* (WWF)-India and *Central Institute of Fisheries Technology* (CIFT), India. Mean chl-*a* concentration in the study area (between 20º-22° N and 69°-70° E) covering continental shelf and adjoining offshore region of coast (depth > 25m) was observed to be significantly higher (4.23 mg m^{-3} in February and 3.88 mg m^{-3} in March) compared to regions seaward of study area (Mean=1.51 mg m^{-3} for February and 1.16 mg m^{-3} for March) and in southern latitudes of eastern Arabian Sea (Mean= 0.27 mg m^{-3} for February and 0.23 mg m^{-3} for March). SST in the study area ranged from 23º-26ºC for February and March whereas SST in the southern latitudes

ranged from 27º-29ºC. SST in regions outside the study area was marginally warmer by 0.5ºC. A significant relationship between whale shark landings off Gujarat, chl-*a* concentration and SST was observed.

3. RESULTS

The results indicates a significant relationship between whale shark catches and chl-*a*. Whale shark aggregation and abundance could be a result of availability of high primary biomass. This is evident when chl-*a*, (an index of phytoplankton biomass) distribution pattern is examined from south to north, which reveals an increasing trend in phytoplankton biomass from southern to northern latitudes. The increase in primary biomass in northern latitudes of Arabian Sea has been well documented by Banse and McClain, 1986; Prasanna and Prasad, 1996; Bhattathiri et al., 1996. This period corresponds to the winter monsoon (December-March) in northern Indian Ocean characterized by cold dry northeasterly winds leading to enhanced evaporation and lowering of sea-surface temperature. Accordingly, surface waters experience densification and sinking, leading to convective mixing and injection of nutrients into upper mixed-layer, triggering primary production and increase in phytoplankton biomass. Strong correlation between low SST and whale shark catches is implicit in the inverse relationship between SST and chl-*a*, indicating the influence of physical process in growth of phytoplankton biomass.

A probable explanation for the occurrence of large number of whale sharks in regions of high phytoplankton concentration lies in their physiology and feeding strategy. Being a very large animal the whale shark may require daily a large quantity of forage to sustain an optimum physiological demand. Whale shark feeds on planktonic organisms and is a suction filter feeder. Due to its specific feeding behaviour, they are probably dependent on dense aggregations of prey organisms. Last and Stevens, 1994 have reported that whale sharks move their heads from side to side, vacuuming in seawater rich in plankton, or aggressively cut swathes through schools of prey. The frequent turns may keep the whale sharks in the denser parts of the plankton patches. The large number of whale shark catches in the study area, where phytoplankton biomass was very high seems to support this view.

4. CONCLUSION

The rsults presented in this study suggest that whale shark migration to the northern Arabian sea during winter months is probably for the purpose of feeding. The satellite data for the period considered clearly indicates the chlorophyll rich grounds in this part of the world ocean compared to the southern region. This understanding was facilitated due to the synoptic coverage of satellite data. Whale sharks, which travel to almost every ocean, contribute to the idea that the combined use of ocean colour and SST images are an appropriate tool to identify potential areas of Whale Shark aggregation for sightings.

This study improves our understanding of the whale shark occurrence and aggregation during winter monsoon in northern regions of Arabian Sea. While availability of food is a function of physical process in the region, the linear relationship between whale shark catches and phytoplankton biomass provides evidence that whale sharks adapt their movements directly to food availability and their migration within a region may be precisely timed to coincide with seasonal productivity events.

REFERENCES

Banse, K. and McClain, C.R., 1986, Winter blooms of phytoplankton in the Arabian Sea as observed by the Coastal Zone Color Scanner. *Mar Ecol Prog Ser*, 34, 201-211.

Brock, J.C., Mcclain, C.R., Luther M.E, Hay W.W., 1991 The phytoplankton bloom in the northwestern Arabian Sea during the southwest monsoon of 1979. *J Geophys Res*, 96, 20623-20642.

Prasanna Kumar, S. and Prasad, T.G., 1996, Winter cooling in the northern Arabian Sea. *Current Science*, 71, 834-841.

Shetye, S. R., Gouveia, A. D. and Shenoi, S. S. C., 1994, Circulation and water masses of the Arabian Sea. *In Proc. Indian Acad. Sci. (Earth Planet. Sci.)* 107-123.

Calibration and Validation of AVHRR Sea Surface Temperatures using Observations from Ships of Opportunity

H. Beggs [a,*], R. Verein [b], G. Paltoglou [c]

[a] Centre for Australian Weather and Climate Research (CAWCR), Bureau of Meteorology, Melbourne, Australia – h.beggs@bom.gov.au
[b] CAWCR, Bureau of Meteorology, Melbourne, Australia – r.verein@bom.gov.au
[c] CAWCR, Bureau of Meteorology, Melbourne, Australia – g.paltoglou@bom.gov.au

Abstract – As part of the Integrated Marine Observing System (IMOS), hull-contact temperature sensors have been installed on four ships of the Australian Volunteer Observing Fleet in order to improve the accuracy of satellite SST measurements over the Australian region. These data, along with SST observations from thermistors installed in water intakes on three research vessels and two tourist ferries, are uploaded to the Global Telecommunications System within 24 hours of observation. Comparisons between SST observations from seven of these vessels, Advanced Along-Track Scanning Radiometer (AATSR), Advanced Very High Resolution Radiometer (AVHRR) and buoys indicate that IMOS ships produce SST data with comparable errors to those available from drifting buoys. Including the IMOS ship SST data in combination with drifting buoy observations will therefore benefit the calibration, validation and bias-correction of AVHRR SST over regions lacking in buoy observations such as coastal regions and the Southern Ocean.

Keywords: SST, AATSR, AVHRR, hull-contact sensors.

1. INTRODUCTION

Remotely sensed sea surface temperature (SST) data are important inputs to ocean, numerical weather prediction, seasonal and climate models. In order to improve calibration and validation of satellite SST in the Australian region, there is a need for high quality in situ SST observations with greater timeliness, spatial and temporal coverage than is currently available. Regions particularly lacking in moored or drifting buoy observations are the Indonesian seas, close to the Australian coast (including Bass Strait) and the Southern Ocean (Zhang et al., 2009). Typically, SST observations from the ships of opportunity program (SOOP) in the Australian region are either of uncertain accuracy or difficult to access in a timely manner, and have therefore not been used for calibration or near real-time validation of satellite SST observations. From 2008, the Integrated Marine Observing System (IMOS: http://www.imos.org.au) Project has enabled accurate, quality controlled, SST data to be supplied in near real-time (within 24 hours) from SOOPs and research vessels in the Australian region.

2. SHIP SST DATA

As part of IMOS, the Bureau of Meteorology (Bureau) is instrumenting seven vessels of the Australian Volunteer Observing Fleet with hull-mounted temperature sensors (Sea Bird SBE 48), supplying high-quality bulk SST observations every hour. There are also two passenger ferries reporting one minute averaged SST measurements for CSIRO Marine and Atmospheric Research (Rottnest Island ferry) and the Australian Institute of Marine Science (Whitsunday Island to Hook Reef ferry). In addition, there are real-time SST data streams available from two Australian research vessels (RV Southern Surveyor and SRV Aurora Australis). In total, eleven vessels by the end of 2010 will contribute near real-time data to IMOS (Table A). For further details see Beggs et al. (2009a).

Table A. Details of IMOS Ship SST Data Available Via the GTS and IMOS Ocean Portal

Vessel	Callsign	Data Start	SST Sensor
RV Southern Surveyor	VLHJ	4 Feb 2008	SBE 3
PV SeaFlyte (Rottnest Is Ferry)	VHW5167	30 Apr 2008	SBE 38
RV L'Astrolabe	FHZI	30 Dec 2008	SBE 38
RSV Aurora Australis	VNAA	12 Oct 2008	SBE 38
PV Spirit of Tasmania II (Bass Strait Ferry)	VNSZ	10 Dec 2008	SBE 48
PV Fantasea One (Whitsunday Ferry)	VJQ7467	5 Nov 2008	AD590
MV Portland	VNAH	20 Jun 2009	SBE 48
MV Stadacona	C6FS9	10 Aug 2009	SBE 48
MV Highland Chief	VROB	30 Sep 2009	SBE 48
MV Iron Yandi	VNVR	-	SBE 48
PV Pacific Sun	MNPJ3	-	SBE 48

All SST data are quality assured (Beggs et al., 2009a) and placed in real-time on the Global Telecommunications System (GTS). The QC'd SST data are also available in netCDF format with QC flags and metadata via the IMOS ocean data portal (http://bluenetdev.its.utas.edu.au). Figure 1 shows the tracks of ships providing IMOS SST data from 4 Feb 2008 to 10 November 2009 to the IMOS data portal and the GTS. Table B gives the mean and standard deviation of 10 arcmin averaged, Meteo Product AATSR

* Corresponding Author. Bureau of Meteorology, GPO Box 1289 Melbourne Vic 3001 Australia.

SST from EnviSat (converted to foundation SST following Beggs et al., 2009a) minus the various ship SST data streams over the region 60°E – 190°E, 20°N – 70°S, during 1 December 2008 to 31 October 2009. The data are considered matched if within the same UTC day and ± 1/12° in latitude and longitude to the AATSR observation. For comparison, we include matchups between SST observations from AATSR and non-IMOS ships and drifting and moored buoys in the same region.

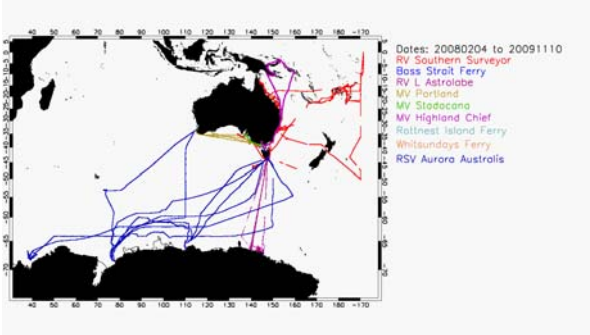

Figure 1. Locations of IMOS ship SST observations from 4 February 2008 to 10 November 2009 from the first nine vessels listed in Table A.

Table B. Mean and Standard Deviation of AATSR foundation SST minus In Situ SST.

In Situ Data Stream	Number of Matchups	Mean (K)	Standard Deviation (K)
RV Southern Surveyor	7410	0.05	0.46
RV L'Astrolabe	3146	-0.04	0.30
RSV Aurora Australis	2322	-0.12	0.27
PV Spirit of Tasmania II	256	-0.14	0.29
PV Fantasea One	1089	-0.38	0.38
MV Portland	76	0.03	0.40
MV Highland Chief	36	-0.30	0.42
Non-IMOS Ships	2817	-0.07	1.71
Drifting and Moored Buoys	9646	-0.04	0.34

3. AVHRR SST DATA

The Bureau, in conjunction with a number of consortia, receives High Resolution Picture Transmission (HRPT) Advanced Very High Resolution Radiometer (AVHRR) data generated from NOAA-17, 18 and 19 satellites from six ground stations located around Australia (Melbourne, Perth, Darwin, Townsville, Alice Springs and Hobart) and two in Antarctica (Casey and Davis stations). As part of IMOS the Bureau has recently upgraded its SST processing system to use improved processing methods (Beggs et al., 2009b) and comply with the Group for High Resolution SST (GHRSST – http://www.ghrsst.org) file formats. Regression coefficients for the day/night SST algorithms used in the processing (Beggs et al., 2009b) were calculated using drifting buoy SST data covering the region 70°E to 190°E, 20°N to 70°S, available from the GTS.

Table C gives the mean and standard deviation of IMOS nighttime, 1 km resolution, NOAA-18 AVHRR SST minus SST data from two IMOS ships (traversing regions with sparse or no buoy deployments) and drifting buoys over the region 70°E to 190°E, 20°N to 70°S, during 1 December 2008 to 31 October 2009. The data are considered matched if within ± 2 hours and collocated within the pixel.

Table C. Mean and Standard Deviation of Nighttime AVHRR SST from NOAA-18 minus In Situ SST.

In Situ Data Stream	Number of Matchups	Mean (K)	Standard Deviation (K)
RSV Aurora Australis	69	0.02	0.15
PV Spirit of Tasmania II	116	-0.03	0.21
Drifting Buoys	1065	0.00	0.24

4. CONCLUSION

Initial comparisons between AATSR, AVHRR, buoy and IMOS ship SST observations indicate that the IMOS ship data have comparable errors to those obtained from drifting buoys. In waters with little or no coverage by buoys, AVHRR SST calibration, validation and bias-correction will be improved by using IMOS ship SST observations in addition to available drifting buoy SST data.

ACKNOWLEDGEMENTS

The European Space Agency supplied the AATSR Meteo Product (ATS_MET_2P) files used in this study. The work was supported by the Integrated Marine Observing System (IMOS) – an initiative of the Australian Government being conducted as part of the National Collaborative Research Infrastructure Strategy.

REFERENCES

References from Journals:

Zhang, H.-M., R.W. Reynolds, R. Lumpkin, R. Molinari, K. Arzayus, M. Johnson and T.M. Smith (2009). "An integrated global observing system for sea surface temperature using satellites and in situ data – Research to Operations", Bull. Am. Met. Soc., Jan 2009, pp. 31-38.

References from Websites:

Beggs, H., R. Verein, H. Kippo, M. Underwood, I. Barton, C. Steinberg, E. Schulz, R. Hibbins, A. Thomas and G. Ball (2009a). "Enhancing Ship of Opportunity Sea Surface Temperature Observations in the Australian Region", GHRSST 2009 International Users Symposium Conference Proceedings, Santa Rosa, USA, pp. 147-150. http://www.ghrsst.org/modules/documents/documents/IGUS_Extended_Abstracts.pdf

Beggs, H., L. Majewski and G. Paltoglou (2009b). "New Australian High Resolution AVHRR SST Products from the Integrated Marine Observing System", GHRSST 2009 International Users Symposium Conference Proceedings, Santa Rosa, USA, 29-30 May 2009, pp. 29-32. http://www.ghrsst.org/modules/documents/documents/IGUS_Extended_Abstracts.pdf

EUMETSAT in Operational Space Oceanography: Ensuring the quality, enhancing the services.

H. Bonekamp [a], A. O Carroll[a], C. Anderson[a], J. Figa[a], F. Parisot[a]

[a] EUMETSAT, Darmstadt , Germany – Hans.Bonekamp@eumetsat.int

Abstract – The European Organisation for the Exploitation of Meteorological Satellites (EUMETSAT) delivers a growing set of operational, satellite-based ocean data products and services which are of fundamental importance to operational oceanography and monitoring the ocean component of the climate system. This contribution highlights several EUMETSAT activities and investigations targeted to ensure and to enhance the quality of the data streams and the associated services.

Keywords: METOP**,** ASCAT, JASON-2, operational oceanography.

1. INTRODUCTION

EUMETSAT's infrastructure, services and expertise are key ingredients for the establishment and sustainment of operational oceanography as for example currently developed in the framework of the Global Monitoring for Environment and Security" (GMES) and its Marine Core services' (MCS), see e.g., Drinkwater et al (2010). To mention for example - in terms of already operational products - are sea surface temperatures from AVHRR and SEVIRI, ocean vector winds from ASCAT and near real time sea surface heights and significant wave heights from JASON-2. Customers include the National Meteorological Services of EUMETSAT's Member and Cooperating States, government agencies, numerical weather prediction, marine meteorological and climate centers, ocean modeling centers, polar research centers, fishing and offshore industries and coastal engineers. In this endeavor, EUMETSAT closely cooperates with other space agencies and institutes.

The first objective is to ensure reliable timely data streams of satellite based observations in a fully operational manner. Lower level processing is dominantly done in the central ground segment in Darmstadt. For ocean applications, the ground segment is extended by the Ocean and Sea Ice (OSI) Satellite Application Facility (SAF) to do e.g. higher level product generation. The OSI SAF is established in April 1997 under the leadership of Météo-France in cooperation with its counterparts in Norway, Denmark, Sweden and the Netherlands. Other EUMETSAT objectives are training and research, to respectively widen the use of the available data products and to ensure that quality of the observations is known and commeasures the state of the art.

In this paper we do not want to list the various products available. Up-to-date overviews can be obtained on internet the EUMETSAT's Product Navigator and the OSI SAF Web sites, see www.eumetsat.int and www.osi-saf.org. Instead we bring the attention to three different investigations targeted to ensure and to enhance the quality of the various data streams and the associated services.

2. ASCAT TRANSPONDER CALIBRATION

ASCAT on METOP-A measures wind speed and direction over the global oceans. The wind product are available via the OSI SAF. In addition, operational products for surface soil moisture and sea ice drift are also produced. The underlying basic measurement provided by the ASCAT is the normalized radar backscatter. ASCAT backscatter calibration is performed using three active calibration point targets (transponders) which have very accurately known point target cross-sections. The calibration strategy and results are described in Wilson et al. (2010).
Figure 1 shows the applied gain pattern model overplayed with transponder measurements as obtained in the winter 2008 Cal/Val external calibration campaign to illustrate that a close agreement can be achieved. ASCAT radiometric accuracy is estimated to be approximately 0.3 dB or better.

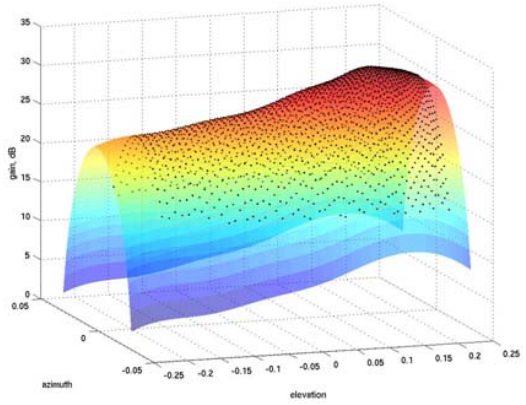

Figure 1. The gain pattern model in antenna coordinates overlaid with corresponding transponder measurements fro the ASCAT transponder campaign winter 2007/2008.

3. IASI SST

Surface skin temperature over land and sea from the IASI Infrared Atmospheric Sounding Interferometer (IASI) are operationally produced since April 2008, see August et al. (2008). The resolution varies from 12km at nadir to 40km at the swath-edge. Validation studies against AATSR data have shown the IASI SSTs to have a bias of around 0.3K with standard deviations below 0.3K. Work has been on-going to produce the IASI SST data in the Global High Resolution Sea Surface Temperature project (GHRSST) L2P format. An important part of the L2P specification is the provision of Single Sensor Error Statistics (SSES). These are defined for IASI using satellite zenith angle and fractional cloud information which are provided within the Level 2 processing facility and combined enable quality levels from 0 to 5 to be assigned to the pixel-level data. The

SSES bias and standard deviations for each quality level are determined from analysing a database containing the IASI SSTs collocated with the OSI-SAF Metop/AVHRR *in situ* matchup database (MDB), referred to as the IMDB (IASI MDB).

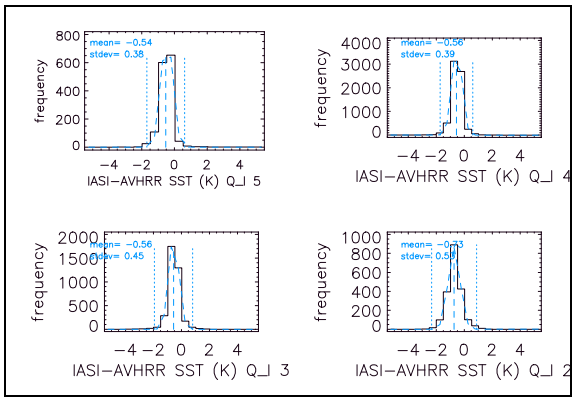

Figure 2. IASI-AVHRR SST differences in different L2P quality levels.

Figure 2. shows the application of the SSES where differences between IASI L2 PPF and AVHRR L3 SSTs are displayed for 5th March 2008 (night-time only). Separate histograms are shown for each quality level where 5 are the best quality data. The standard deviations of the differences are shown to decrease with increasing quality level. Ongoing investigations include: cloud detection and masking issues, sea-ice zone, and retrievals affected by aerosol.

4. FUTURE JASON ORBITS

In the context of Post-EPS - the METOP follow-on program - studies have been conducted to propose new orbits for the reference mission with lower altitudes and with similar or even better performances than the current Jason orbit at the height of 1336 km. The orbit geometry determines among others the temporal and spatial sampling, tidal aliasing properties, aspects of Precise Orbit Determination and expected mission life time The studies undertaken have been inclusive to weight the different aspects, different applications in a context of a constellation of planned and proposed altimeter missions. First conclusions do indicate that there exists suitable orbit canditates with lower altitudes and with similar or even better performances than the actual Jason's orbit, see Carrère et al (2009). These candidates will be discussed in the context of the Jason-3 follow-on preparation activities.

4. CONCLUSION

EUMETSAT conducts and supports a variety of investigations targeted to ensure and to enhance the quality of the operational satellite ocean data streams and the associated services. Key investigations are highlighted.

REFERENCES

August T, P. Schlüssel, X. Calbet, A. Arriaga, O. Oduleye and T. Hultberg *First validations of the operational IASI L2 surface temperature,* in Proceeding of the 2008 EUMETSAT user conference, Darmstadt 2008.

Carrère L., F. Lefêvre, J. Dorandeu, G Dibarboure P. Schluessel, H . Bonekamp. *Post EPS altimeter mission orbit determination : test of potential orbits* , OST ST meeting Seattle 2009 (poster presentation). www.aviso.oceanobs.com/fileadmin/documents/OSTST/2009/poster/Carrere2.pdf

Drinkwater M., H. Bonekamp, B. Chapron, C. Donlon, J-L Fellous, P. DiGiacomo, E. Harrison, P-Y. Le Traon, E. Lindstrom, S. Wilson, *Status and outlook for the Space component of an Integrated Ocean Observing System* to appear in Proceedings of the "OceanObs'09: Sustained Ocean Observations and Information for Society" Conference (Vol. 1), Venice, Italy, 21-25 September 2009, Hall, J., Harrison D.E. and Stammer, D., Eds., ESA Publication WPP-306, 2010.

Wilson J.J.W., C. Anderson, M. A. Baker, H. Bonekamp, J. Figa Saldaña(1), R. G. Dyer, J. A. Lerch, G. Kayal, R. V. Gelsthorpe, M. A. Brown, E. Schied, S. Schutz-Munz, F. Rostan, E. W. Pritchard, N. G. Wright, D. King and Ü. Önel(6) *Radiometric Calibration of the Advanced Wind Scatterometer Radar ASCAT carried on-board the METOP-A Satellite.* Accepted for publication in TGRS, 2010.

A 10 year long time series of SeaWiFS data shows spatial and temporal variability of phytoplankton blooms in the Scotia Sea region

I. Borrione *, R. Schlitzer

Alfred Wegener Institute for Polar and Marine Research, Bremerhaven, Germany
Ines.Borrione@awi.de, Reiner.Schlitzer@awi.de

Abstract – Monthly averaged satellite imagery of chlorophyll *a* in the south-western Atlantic Ocean shows intense and recurrent blooms around the Antarctic Peninsula, the Island of South Georgia and the South Sandwich Islands. Analysis of a 10 year long time series of SeaWiFS ocean color images allows studying seasonal trends and inter-annual variability. Although specific areas show a regular pattern of low or high productivity, certain years appear to be strikingly productive or well below the climatological average. Circulation patterns, continental shelves as well as Antarctic Circumpolar Front are shown to be the major factors controlling extension of highly productive patches.

Keywords: Scotia Sea, SeaWiFS, primary productivity.

1. INTRODUCTION

The Scotia Sea area, included between the North and South Scotia Ridge (SSR), and between the Drake Passage and the South Sandwich Islands (SSI), has always been recognized as a High Nutrient Low Chlorophyll (HNLC) region which experiences intense summer phytoplankton blooms; it is characterized by an average depth greater than 2000m, where ridges, trenches, plateaus and islands complicate its bathymetry. The main water masses are those included in the Antarctic Circumpolar Current (ACC) which carries a uniquely high nutrient content. While the current flows next to continental shelves waters are naturally fertilized with iron, enhancing primary productivity. Ecosystems around the Antarctic Peninsula and the South Sandwich Islands result more complex by the advance and retreat of sea-ice.

Bands of enhanced chlorophyll *a* concentration (Chl-a) are strongly localized around island ecosystems and shallower topographic features (i.e. the Antarctic Peninsula continental shelf, the SSR and offshore the island of South Georgia, hereafter SG). Previous works indicate that in this domain in-situ Chl-a may reach values higher than 10 mg/m^3 (Korb *et al.*, 2004; Holm-Hansen *et al.*, 2004). The iron deficiency hypothesis (Blain *et al.*, 2001) together with sea-ice melting (Smith *et al.*, 2008), ocean circulation patterns (i.e. eddies), and the "island mass effect" (Blain *et al.*, 2001) may jointly explain such striking events for a HNLC region. A synoptic study of such a vast region is possible only via satellite imagery, although winter darkness does not allow measurements between April and July; nevertheless, remote sensing remains for this region the key observational tool where weather and sea-state conditions strongly limit high resolution in-situ measurements.

2. RESOLVING TEMPORAL AND SPATIAL DYNAMICS

2.1 SeaWiFS data

SeaWiFS derived estimates of surface Chl-a were obtained from the Goddard Distributed Active Center. Level-3, monthly composites at 9 km resolution were retrieved for the period between January 1998 and December 2007. As winter conditions limited ocean color coverage of the domain, analysis was restricted to the spring and summer seasons. Each monthly Chl-a image was combined into a climatological average. The Chl-a relative error was calculated as the ratio between the standard deviation and the climatological average and was used to infer its variability. Single monthly images were finally observed to pin-point years which appear to be exceptionally productive or well below average.

2.2 Seasonal trends

Although data is limited to latitudes greater than 60S, due mostly to sea-ice extent, data coverage is sufficient to show August as the month where Chl-a starts increasing. Most of the domain has concentration values close to zero, except along shallower bathymetries (SSR and north of the South Georgia basin) where they are included between 0.2 and 0.5 mg/m^3. Absolute Chl-a values progressively increase till December when they go beyond 3 mg/m^3. In this month surface areas with Chl-a concentrations greater than 0.5 mg/m^3 reach their maximum extension. After January productivity starts decreasing. In March, concentrations remain below 1 mg/m^3. Fig. 1 shows three snapshots (September, December and March) of the recurrent bloom north of SG, as an example of the above described seasonal trend.

2.3 Inter-annual variability

The climatological average of the most productive months (December and January) shows high Chl-a above the Argentine Shelf, and along a band running from the Antarctic Peninsula continental shelf, above the SSR, up to the SSI. A high productive plume is found also north of SG, spreading eastward. Nevertheless, this pattern is not fully representative: certain years, in fact, may show a significantly lower or higher productivity. In December 2000, for example, the bloom north of SG is strongly reduced, and limited to a narrow band of high productivity extending east of the island, following a meandering path. Regions of greater inter-annual variability appear to be the surroundings of island ecosystems, such as the western Antarctic Peninsula, and the SSI.

* Corresponding author. Am Alten Haven 26, D-27658 Bremerhaven, Germany.

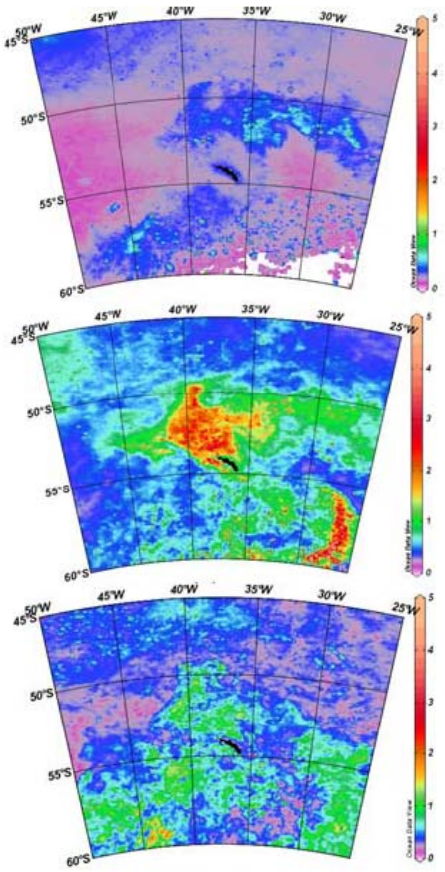

Figure 1. Climatological average of SeaWiFS-derived estimates of surface Chl-a, for September (top), December (middle) and March (bottom) of the region surrounding South Georgia island. The sequence shows the development of the recurrent summer bloom north of the island.

2.4 The Shackelton Fracture Zone – an example of permanent low productivity

Similarly to the area upstream the Drake Passage, where Chl-a remains below 0.2 mg/m^3 throughout most of austral summer, also the region adjacent the Shackelton Fracture Zone shows constant low productivity values (Fig. 3-left, violet region delimited by the 0.2 Chl-a contour). The ridge extends across Drake Passage acting as a barrier to the ACC, deflecting the Southern ACC Front westward. The relative error map for the same region (Fig. 2 - right), confirms that this low productivity region shows no variability (relative error<0.5).

2.5 Factors confining phytoplankton blooms

Spatial development of patches with high Chl-a appears to be mostly controlled by circulation patterns, extension of continental shelves and position of the ACC fronts. The highly productive regions of the Argentine Shelf and the western Antarctic Peninsula fall in the first case: the greatest Chl-a gradient, coincides with the 500m depth bathymetry contour. Circulation patterns, as inferred from surface drifter trajectories seem to control the shape of the western border of the bloom north of SG bloom. Finally, the borders north and south of the plume extending east of SG, coincide approximately with the Polar Front and the Southern Antarctic Circumpolar Current Front, respectively. Another factor, localized in the northwestern Weddell Sea, may be the melting of sea-ice which may stabilize surface waters and release trapped particles, possibly rich in bio-available Iron. This effect could occur at the eastern tip of the Antarctic Peninsula: Fig. 2 (left).

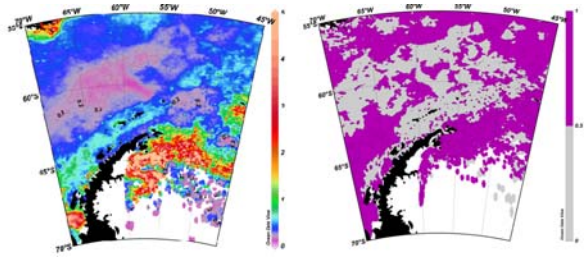

Figure 2. Climatological average of SeaWiFS-derived estimates of Chl-a for Dec (left); and of the relative error (RE) of the measurement calculated as the ratio between the standard deviation and the climatological average of Dec (right). The map focuses on the region around Shackelton Ridge. The results show this region to be consistently low in productivity (RE <0.5 grey, RE>0.5 magenta).

3. CONCLUSION

A decade of SeaWiFS ocean color images has allowed studying the development and distribution of primary productivity in the Scotia Sea and along the Antarctic Peninsula. Results show seasonal enhanced productivity along shelf areas and the main island ecosystems. Although certain blooms occur regularly every year, their extension and maximum Chl-a concentration can be very variable. Circulation patterns, bathymetry and ACC front are responsible for their location and extension.

ACKNOWLEDGEMENTS

This work was funded by the ESSReS (Earth System Science Research School) scholarship.

REFERENCES

Blain S., T.Tréguer, S. Belviso, E. Bucciarelli, M. Denis, S. Desabre, M. Fiala, V.M. Jézéquel, J. Le Fèvre, P. Mayzaud, J.-C. Marty and S. Razouls (2001). "A biogeochemical study of the island mass effect in the context of the iron hypothesis: Kerguelen Islands, Southern Ocean". Deep-Sea Research Part I, vol. 48, pp. 163-187.

Holm-Hansen O., M. Kahru, C.D. Hewes, S. Kawaguchi, T. Kameda, V.A. Sushin, I. Krasovski, J. Priddle, R. Korb, R.P. Hewitt, B.G. Mitchell (2004). "Temporal and spatial distribution of chlorophyll-a in surface waters of the Scotia Sea as determined by noth shipboard measurements and satellite data". Deep-Sea Research Part II vol. 51, pp.1323-1331.

Korb R.E. and M. Whitehouse (2004). "Contrasting primary production regimes around South Georgia, Southern Ocean: large blooms versus high nutrient, low chlorophyll waters". Deep-Sea Research Part I, vol. 51, pp. 721-738.

Smith R.C., D.G. Martinson, S.E. Stammerjohn, R.A. Iannuzzi and K. Ireson (2008). "Bellingshausen and western Antarctic Peninsula region: Pigment biomass and sea-ice spatial/temporal distributions and interannual variability". Deep-Sea Research Part II, vol. 55, pp. 1949-1963.

Satellite-derived chlorophyll predicts breeding success of seabirds at a NE Pacific seabird colony

Gary Borstad[a,*], William Crawford[b], J. Mark Hipfner[c,] Richard Thomson[b]

[a] ASL Borstad Remote Sensing Inc., Sidney, BC, Canada, gborstad@aslenv.com
[b] Institute of Ocean Sciences, Fisheries and Oceans Canada, Sidney, BC Canada, william.crawford@dfo-mpo.gc.ca,richard.thomson@dfo-mpo.gc.ca
[c] Environment Canada, RR#1 5421 Robertson Road, Delta, BC Canada, mark.hipfner@ec.gc.ca

Abstract – At the largest seabird colony on the Pacific coast of Canada, the breeding success of the rhinoceros auklet (*Cerorhinca monocerata*) varies dramatically among years and is generally correlated to SST. We show that the reproductive success of these piscivorous auklets is more dependably related to the spring phytoplankton bloom, as derived from satellite water colour measurements, than to SST as has been reported previously. High correlation obtained between the spring chlorophyll, upwelling favourable winds, and fledgling production suggest bottom-up control of the birds' reproduction via phytoplankton, zooplankton and the forage fish on which the birds feed.

Keywords: seabirds, chlorophyll.

1. INTRODUCTION

Marine birds are often used as indicators of food supply in the coastal ocean because they are highly mobile animals with high metabolic requirements that must feed frequently in prey rich areas (e.g. Abraham and Sydeman, 2004). At the largest seabird colony on the west coast of Canada (Triangle Island (50°52' N, 129°05' W), the timing and success of breeding in several seabird species has been studied intermittently since 1976 (Figure 1). Bertram et al (2001) reported a negative relationship between breeding success of rhinoceros auklets (*Cerorhinca monocerata*) at Triangle Island and April sea surface temperature (SST) at the nearby Pine Island light station, attributing the relationship to impacts on prey availability. Sea surface temperature (SST) is widely used in marine studies (esp. seabirds) as a general proxy for ocean productivity, and is *in general* a good predictor of seabird success in California Current system (Abraham and Sydeman, 2004). However, the correlation between auklet success and SST grossly over-estimated fledgling production at Triangle Island in both 1976 and 2007, when there was an almost complete breeding failure (Fig. 1). The rhinoceros auklet is a highly colonial marine bird that lays eggs in early May. Eggs hatch beginning in mid June, and chicks are fed small forage fish typically derived from the top 20 m of the water column until they leave the nest in mid August. Breeding success is maximal in years in which the population as a whole lays early and nestling diets are rich in juvenile age 0 sandlance *Ammodytes hexapterus*, a small herring-like forage fish (Bertram et al, 2001). Waters surrounding Triangle Island lie in the transition zone between the California and Alaska Currents. Strong winds from the southeast during winter push northward-flowing coastal currents along the Pacific coast. Coriolis force pushes these flows against the coast and eastward toward the mainland. Sometime after late March, the winds weaken and reverse direction. By summer the prevailing winds are from the northwest. This results in a westward flow past the colony of cooler surface waters generated by upwelling along the mainland coast and tidal mixing over shallow banks near the colony (Crawford et al. 1985). We examined the correlation of breeding success of rhinoceros auklets at Triangle Island with local and regional ocean conditions as mapped by satellite imagery in an attempt to find a better environmental correlate for auklet breeding success than sea surface temperature at Pine Island, ~100 km away from the colony.

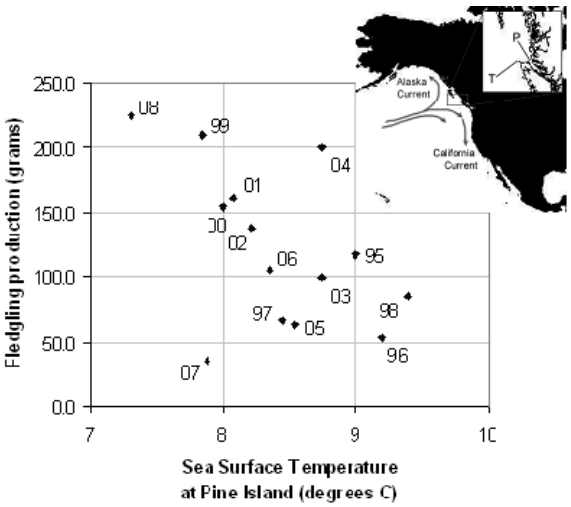

Figure 1. The relationship between SST and rhinoceros auklet production failed in 2007. T marks the Triangle Island colony. P marks Pine Island light station.

1.1 Data and methods

We examined correlations between fledgling production (the average mass (g) of fledged chick produced per egg laid) and near-surface ocean chlorophyll concentration derived from Level 3 SeaWiFS monthly composites. We first mapped the chlorophyll pixels most highly correlated with auklet production (Figure 2) by regressing each pixel of the April chlorophyll image time series (Figure 3) against auklet production. We then defined a Region of Interest (ROI) containing those pixels showing squared correlations with probability greater than 95%, and averaged the chlorophyll concentration in the ROI by month. Finally, these averages were regressed as a separate time series to produce the plot in Figure 4. We also examined the

* Corresponding author. 1986 Mills Road, Sidney, BC Canada V8L5Y3.

relationship between auklet production and near-surface winds measured at a near-by meteorological buoy in Queen Charlotte Sound. With gap filling and averaging, we computed southeast and northwest components of winds to examine alongshore and cross-shore components. We further averaged the SE component winds for years categorized as *good* and *poor* for fledgling production (above and below the average for the 1998 – 2008 period) as in Figure 5.

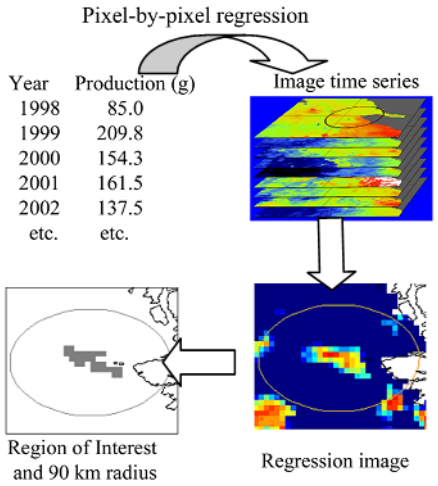

Figure 2. Calculation of an 'image regression' to map the area exhibiting the highest correlation between April chlorophyll and auklet production.

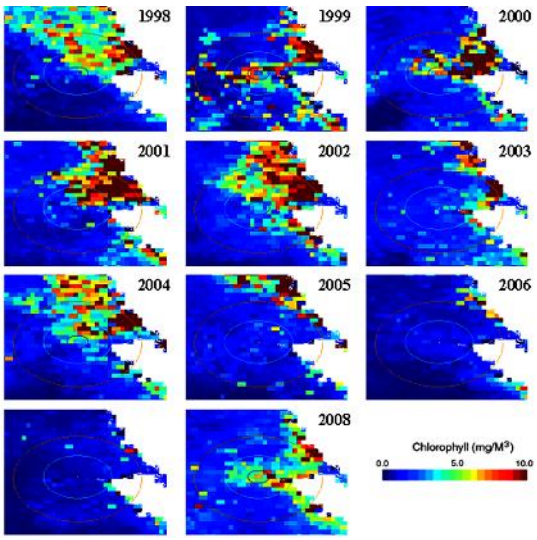

Figure 3. Average chlorophyll concentration for the month of April in the period 1998 – 2008.

1.2 Results and discussion

The Triangle Island seabird colony, at the center of the 90km radius ellipse shown in Fig. 2, experiences a large variation in chlorophyll concentrations during April. Fig. 4 shows that auklet production is closely related to April chlorophyll concentrations. The time series of the SE component of the near-surface winds at a nearby meteorological buoy (Figure 5) shows that rhinoceros auklet are more likely to breed successfully in years with significantly weaker average winds from the southeast in April, reinforcing the choice of this month as most critical for auklet chicks.

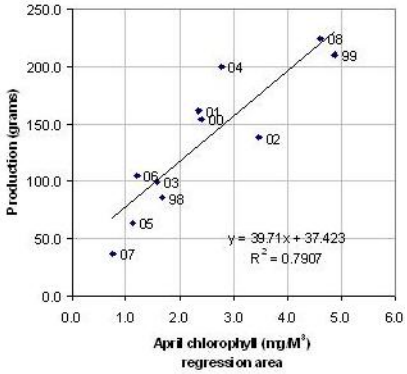

Figure 4. Rhinoceros auklet production is closely related to the average monthly chlorophyll concentration in the waters immediately surrounding the colony (Region of Interest mapped in gray in the lower left panel in Fig. 2).

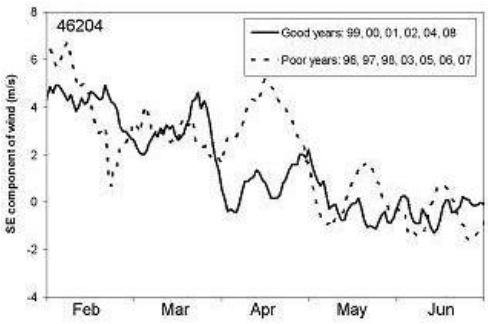

Figure 5. Rhinoceros auklets breed more successfully when the SE component of the winds in April is lower (allowing upwelling and westward flow past the island).

4. CONCLUSION

Although the known foraging range for rhinoceros auklets is up to 90 km (ellipse in Fig. 2), the most highly correlated chlorophyll pixels are tightly clustered over shallow water surrounding the colony (Region of Interest in Figure 2). These are piscivorous birds, and we interpret this correlation as indicating bottom-up control over the seabird breeding, mediated through the survival and energetic content of juvenile sandlance that they feed their chicks, and the herbivorous zooplankton that juvenile sandlance feed on.

ACKNOWLEDGEMENTS

This work was funded by the Canadian Space Agency via the Government Related Initiatives Program (GRIP). Peter Willis, Mar Martinez and Leslie Brown provided assistance.

REFERENCES

Abraham, C. L., and W. J. Sydeman, 2004. Ocean climate, euphausiids and auklet nesting: inter-annual trends and variation in phenology, diet and growth of a planktivorous seabird *Ptychoramphus aleuticus*. Mar. Ecol. Prog. Ser. 274:235-250.

Bertram, D.F., D. Mackas and S. McKinnell, 2001. The seasonal cycle revisited: interannual variation and ecosystem consequences. *Prog. Oceanogr*. 49, 283-307.

Crawford, W. R., W. S. Huggett, M. J. Woodward and P. Daniel, 1985. Summer circulation of the waters of Queen Charlotte Sound. *Atmosphere-Ocean* 23, 393-413.

Interannual variability of the Mediterranean oligotrophy area, as derived from 11 years of SeaWiFS observations

E. Bosc

Marine Environment Laboratories (MEL-IAEA) 4, Quai Antoine 1er MC-98000 Monaco – e.bosc@iaea.org

Abstract – Size variations of oligotrophic areas are good indicators of change in ocean biology. An 11-years time series of monthly SeaWiFS ocean color data was used to analyze spatial and interannual variations of the Mediterranean Sea Oligotrophy. Despite strong seasonal and interannual variations, Mediterranean Sea oligotrophy shows a stable trend over years. This result differs from other study on oligotrophic provinces around the world ocean which tend to recently extend at an accelerating rate. World and basin scale climate oscillations seem to have low influence on the decadal trend of the Mediterranean oligotrophic area size. The reasons for these specific interannual variations remain questionable.

Keywords: Mediterranean Sea, SeaWiFS, oligotrophy.

1. INTRODUCTION

The Mediterranean Basin is a semi-enclosed sea which has been extensively studied over the last decades, both because of local interest from surrounding countries, and because it is often considered to be "a model of the world ocean itself". The Mediterranean Sea is declared to be the most vulnerable region in the world regarding to man-made climate change and its impacts (IPCC 2007). Recent studies show a global extension of the world ocean oligotrophic area (Polovina et al., 2008, Irvin and Oliver 2009). This expansion of low chlorophyll waters has been related to the mechanism of stratification but its causes remain controversy.

The aim of this paper is to analyze the spatial and interannual variations of Mediterranean's oligotrophic surface water over more than 11 years time-series, and to evaluate if trend follows current observations of the world ocean desert evolution.

2. DATA AND METHODS

To investigate how the Mediterranean oligotrophic province is varying in size, we computed an annual average of each monthly fraction of the entire Mediterranean Sea surface chlorophyll concentration bounded by 0.10 mg.m^{-3}. This computation is based on surface chlorophyll concentration estimated from data collected by the SeaWiFS ocean color satellite sensor from Sep. 1997 to April 2009. Monthly mapped composites are provided by the Ocean Biology Processing Group (http://oceancolor.gsfc.nasa.gov) under the reference Reprocessing 5.1.

By choosing relatively low chlorophyll concentration limits, we excluded influence of coastal processes that can act at different time and space scales than climatic oscillations. This also allows to not taking into account controversial high algal biomass estimation from satellite data in turbid areas (Sathyendranath, 2000).

To better investigate the interannual variations of the oligotrophic province size, we de-seasoned the time-series of monthly chlorophyll concentrations by dividing each monthly data by the corresponding monthly value from the 11 years climatology (figure 1).

3. RESULTS AND DISCUSSION

Over the studied period, the Mediterranean Oligotrophic Area (hereafter 'MedOA') was shown to highly expand and contract seasonally (Figure 1). This extension can be represented as the percentage of MedOA over the whole Mediterranean surface. This percentage was shown to be low in winter, from November to February (less than 20 % of the total Mediterranean surface for most of the studied years) and high in summer (up to 85% of the total Mediterranean surface). The highest chlorophyll concentration take place during the bloom in spring, mainly in the north occidental basin (Bosc et al., 2002), even though smaller MedOA percentage are surprisingly observed in winter. This can be due to spring bloom and oligotrophic self-regulating processes.

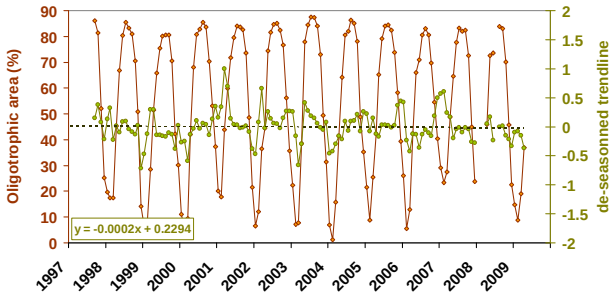

Figure 1. Variation of the MedOA over the time-series (1997-2009): Left axis, percentage of the whole Mediterranean Sea surface that is oligotroph (defined by surface chlorophyll concentration less than 0.10 mg.m^{-3}). Right axis, same numbers as in left axis but de-seasoned considering the 11-years MedOA climatology: trend line (green) and regression line (dash).

The main spatial feature is the general gradient from north to south and from west to east of the Mediterranean Sea oligotrophy (figure 2). Except for the Adriatic Sea, the whole Eastern basin is oligotrophic at least half of the year. The de-seasoned trend line shown in figure 1 (right axis), confirms that even in oligotrophic province, often expected to be the most stable area of the Mediterranean Sea, the interannual variations are surprisingly high. Oligotrophic area is 25% bigger in winter 2007 than in winter 2004.

The Mediterranean Sea is subject to climatic forcing and oligotrophic extension may be related to episodic climate events. For example, summer 2003 European heat wave and its consequences on the Sea Surface Temperature (Feudal and Shuka, 2007) may explain the largest MedOA of the time series (up to 87% of the whole Mediterranean surface in July - August 2003) and also, March-April 2001 anomalous blooming described by Barale et al., (2008) is probably the cause of atypically high MedOA observed (52 % for that year and on average 30% ± 7 % for the other years).

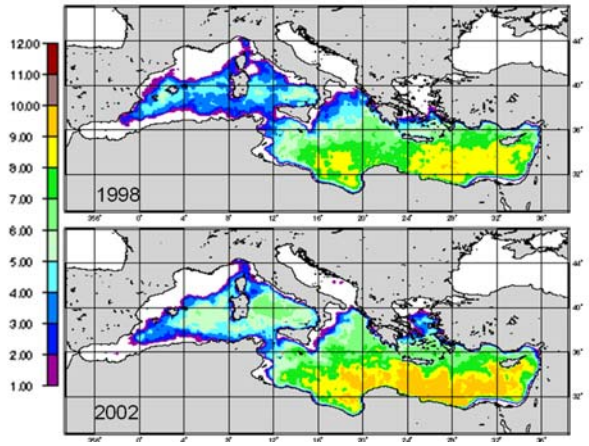

Figure 2. Spatial variation of the Monthly Mediterranean oligotrophy for 1998 and 2002. Colors correspond to the monthly occurrence of oligotrophy per 12 months (scale 1 to 12).

Despite those examples of episodic event consequences on the Mediterranean Sea Oligotrophy, it is important to note that over the whole period, the monthly MedOA shows no statistically significant trend (figure 1, dashed line). This is not comparable with observations derived from SeaWiFS data in oligotrophic sub-tropical gyres, where authors report that surface increase up to 4% per year (McClain et al., 2004; Polovina et al., 2008; Irwin and Oliver 2009).

Although the SeaWiFS mission is probably not long enough to certainly confirm a strong link between oligotrophic variations and climate oscillations, Irwin and Oliver (2009) have shown a correlation between Pacific Decadal Oscillation (PDO) index and surface of three majors' ocean world oligotrophic provinces. Such results were also reported in McClain et al., (2004). In both papers, no evidence of link between oligotrophy and PDO index was claimed and questions still remain. In our study, no such correlation between Mediterranean oligotrophy and PDO index has been observed. No description of teleconnection between Mediterranean Sea oligotrophy and Pacific basin-scale trends was found in the literature.

In Polovina et al. (2008), authors argue that expansion of the low chlorophyll waters is mainly based on increased vertical stratification and then could be a consequence of global warming. The Mediterranean Sea is also subject to global warming influence (IPCC 2007) but our oligotrophic index, actually based on only one decade surface chlorophyll estimations, does not reflect any climate change evolution.

4. CONCLUSION

Our results indicate that despite strong seasonal and interannual variations, Mediterranean Sea oligotrophic area is stable compared to other oligotrophic provinces around the world which tend to extend at an accelerating rate. Climate variation is not necessarily a result of directional climate change. More extreme meteorological events in Europe may episodically alter the biogeochemical and physical properties of sea water without any consequences on decadal trend of the size of Mediterranean Sea oligotrophy area.

ACKNOWLEDGEMENTS

Satellite data provided by the ocean colour processing team (oceancolor.gsfc.nasa.gov)

REFERENCES

Barale, V., Jaquet, J., & Ndiaye, M. (2008). Algal blooming patterns and anomalies in the Mediterranean Sea as derived from the SeaWiFS data set (1998–2003). Remote Sensing of Environment, 112(8), 3300-3313.

Bosc, E., Bricaud, A., and Antoine, D. (2004) Seasonal and interannual variability in algal biomass and primary production in the Mediterranean Sea, as derived from 4 years of SeaWiFS observations, Global Biogeochem. Cycles, 18, GB1005, doi:10.1029/2003GB002034.

Feudale, L., and J. Shukla (2007), Role of Mediterranean SST in enhancing the European heat wave of summer 2003, Geophys. Res. Lett., 34, L03811

IPCC (2007) Climate Change 2007: The Physical Science Basis. Contribution of Working Group I to the Fourth Assessment. Report of the Intergovernmental Panel on Climate Change., Vol. Cambridge University Press, Cambridge, United Kingdom and New York, NY, USA

Irwin, A. J., and M. J. Oliver (2009), Are ocean deserts getting larger?, Geophys. Res. Lett., 36, L18609, doi:10.1029/2009GL039883.

McClain, C. R., S. R. Signorini, and J. R. Christian (2004), Subtropical gyre variability observed by ocean-color satellites, Deep Sea Res., Part II, 51, 281–301.

Polovina, J. J., E. A. Howell, and M. Abecassis (2008). Ocean's least productive waters are expanding, Geophys. Res. Lett., 35, L03618, doi:10.1029/2007GL031745.

Sathyendranath, S. (Ed.) (200), Remote sensing of ocean colour in coastal, and other optically-complex, waters. IOCCG Report, vol. 3. Dartmouth, Nova Scotia: IOCCG Project Office.

Advantages and Consequences of Satellite Wind Instruments Responding to Stress Rather Than Wind

Mark A. Bourassa *

Center for Ocean-Atmospheric Prediction Studies and Deptartment Of Meteorology,
Florida State University, Tallahassee, FL, USA – bourassa@coaps.fsu.edu

Abstract – Satellite wind sensors are more directly sensitive to stress than to wind. This finding has several advantages: more accurate stress upper ocean and deep ocean process studies, more accurate drag for the atmosphere, and more accurate estimates of surface turbulent heat fluxes. However, there are also negative consequences, such as less accurate surface wind convergence for atmospheric lifting and precipitation. One big problem for climate studies is that satellite observations are assimilated like buoy and ship winds, in a manner that does not account for the physical differences in satellite winds. The biases due to this assimilation are large than long term trends.

Keywords: stress, wind, bias, forcing, climate.

1. INTRODUCTION

It has been shown that scatterometer winds respond more directly to surface vector stress than to surface vector wind. This finding has been backed up with observations of a systematic error in satellite winds associated in proportion to the square root of air density (F. Wentz, personal communication, 2008; Bourassa et al. 2010), and with sea state dependencies (Bourassa 2006) as seen in ECMWF assimilations (Hans Hersbach, personal communication 2009), as well as long observed and well modeled dependencies on boundary-layer stratification (Ross et al. 1985). This paper addresses several ways to make use of this knowledge.

2. APPLICATIONS

Data assimilation and the construction of data sets both benefit from data without regional and temporal biases. Simply considering the air density in the estimation of satellite winds removes large scale seasonal and regional biases. These biases are typically less than 10% (within mission specifications); however the consequences on heat fluxes and ocean mixing are likely to be considerable for climate scale application and for deriving near surface convergence around atmospheric fronts. An example of air density related errors (Figure 1) shows over estimates of wind speed associated with cold air.

2.1 Stress Applications

Stress is a key player for drag at the bottom of the atmosphere, and for dynamical forcing of the ocean. For ocean applications, it is the curl of the stress that is needed.

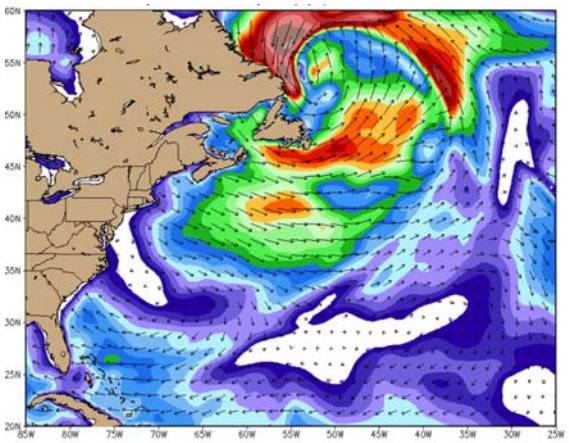

Figure 1. Example errors in 10m wind speed associated with a cold air trailing a strong North Atlantic storm. The example is based on NCEP's GFS analysis at 0.5 grid spacing, with every 9th vector shown.

However, stress is non-linearly related to wind speed; therefore, winds with no biases and random errors have biases in the stress and the curl of the stress. There is also non-negligible error in the conversion of wind to stress (1):

$$\tau = \rho C_D u^2 \quad (1)$$

where τ = scalar stress
ρ = air density
C_D = drag coefficient
u = wind speed

In this form, the drag coefficient is a function of the wind speed, boundary-layer stratification, currents, and sea state. Without sufficient knowledge of these other variables, there can be considerable bias and random error in the stress estimates. Direction measurement of the stress removes all these problems, provided that the stress retrievals are sufficiently accurate. However, this also implies related errors in the calculation of winds.

2.2 Estimates of Surface Turbulent Fluxes

Surface fluxes of evaporation (2), latent heat (3), and sensible heat (4) are also dependent on stress-related considerations mentioned above.

$$E = \rho C_p C_E (q_{air} - q_{sfc}) u, \quad (2)$$
$$Q = L_v E, \quad (3)$$

* Corresponding author. Center for Ocean Atmospheric Prediction Studies, Florida State University, 2035 E. Dirac Dr./Suite-200 Johnson Bldg, Tallahassee, FL 32310 USA. Tel +1 850 6446923; Fax +1 850 644 5092.

$$H = \rho C_p C_H (\theta_{air} - \theta_{sfc}) u, \quad (4)$$

where E = evaporative flux density
Q = latent heat flux density
H = sensible heat flux density
C_p = heat capacity of air
L_v = latent heat of vaporization
C_E = moisture transfer coefficient
C_H = heat transfer coefficient
q = specific humidity
θ = potential temperature

The two transfer coefficients (C_E and C_H) are both proportional to the square root of the drag coefficient. With less commonly used equations, it can be shown that these fluxes are proportional to the square root of the kinematic stress (the stress divided by air density). In other words, the variability in the square root of kinematic stress that is not explained by the wind speed term in (2-4) is contained in C_E and C_H.

A great advantage of direct observation of stress is that all these dependencies are captured in the stress. Therefore, biases associated with erroneous sea state assumptions and incorrect currents are removed from the calculation of the surface turbulent heat and moisture fluxes. For example Fig. 2 shows regional biases in monthly heat fluxes due to ignoring sea state. These biases can largely be avoided through observations of stress.

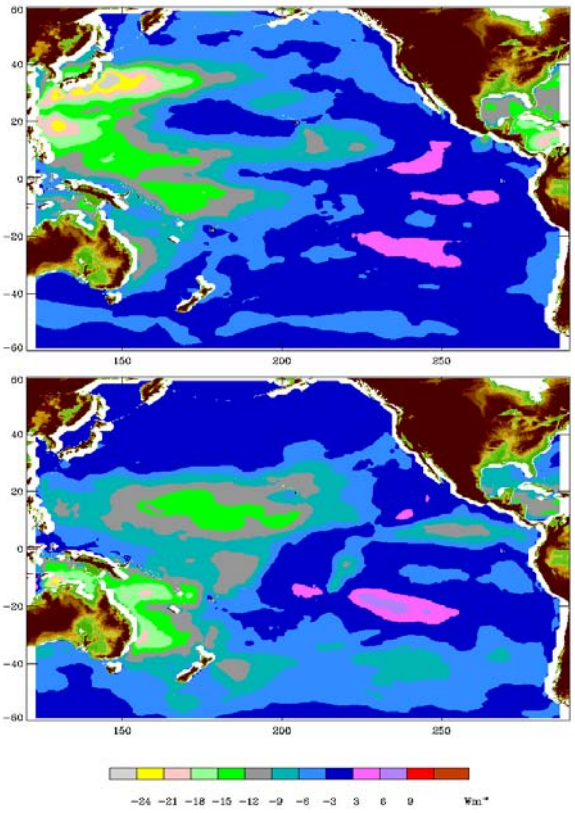

Figure 2. Monthly biases in latent heat flux for (top) January 1999 and (bottom) June 1999 due to ignoring dependence on surface water waves.

2.3 Complications in the Climate Record

The historical climate record treats satellite winds as physically identical to ship and buoy winds. For example, reanlyses assimilate satellite winds in this fashion. A test with the ECMWF assimilation of satellite winds (H. Hersbach, personal communication, 2009) revealed that treating winds as stresses removed considerable differences between the satellite winds and the model winds.

Open ocean portions of reanalyses are based on ship and buoy data in the pre-satellite period, and largely based on satellite data in the satellite period. If the satellite data are not properly adjusted (from stress to wind), there will be regional and temporal biases during the satellite period. If there is no adjustment, the worst case change will be similar to the biases seen in Fig. 2. Consequently, the change in the observing system, and the oversimplification of the satellite data, results in a spurious trend in winds and heat fluxes. This trend is likely to be large compared to the roughly $3Wm^{-2}$ regional change over 50 years or the $1Wm^{-2}$ global change over 50 years.

3. CONCLUSION

There are substantial benefits to better understanding what satellite data accurately represents. The direct observations will lead to considerably more accurate surfaces fluxes of momentum (stress), moisture, and heat. Proper treatment of satellite observations in reanalyses should remove a spurious trend that is likely to be substantial in comparison to natural variability on multi-decadal scales. Both of these considerations will aid in our understanding of climate on a wide range of spatial/temporal scales.

ACKNOWLEDGEMENTS

This work was supported by NASA's physical oceanography program and NASA NEWS, as well as NOAA OCO. I thank Ryan Maue for generating Fig. 1.

REFERENCES

Bourassa, M. A., (2006). "Satellite-based observations of surface turbulent stress during severe weather". Atmosphere - Ocean Interactions, Vol. 2., ed., W. Perrie, Southampton, UK, Wessex Institute of Technology Press, 35 – 52 pp.

Bourassa, M. A., E. Rodriguez, and R. Gaston (2010). "Summary of the 2008 and 2009 NASA Ocean Vector Winds Science Team Meeting". *Bull. Amer. Meteor. Soc.*, (in press).

Ross, D. B., V. J. Cardone, J. Overland, R. D. McPherson, W. J. Pierson Jr., and T. Yu, (1985): "Oceanic surface winds". *Adv. Geophys.*, **27**, pp. 101-138.

SCIAMACHY PhytoDOAS global data set of different phytoplankton groups: retrieval, validation and first application

A. Bracher [a], T. Dinter[a], A. Sadeghi[a], B. Schmitt[a], I. Peeken[b], Y. Ye [c], M. Vountas[d], J.P Burrows[d], R. Röttgers [e]

[a] Helmholtz University Young Investigators Group PHYTOOPTICS, Alfred-Wegener-Institute (AWI), Bremerhaven and Institute of Environmental Physics, University of Bremen, Germany – bracher@uni-bremen.de; tilman.dinter@awi.de; alireza.sadeghi@iup.physik.uni-bremen.de; bettina.schmitt@awi.de

[b]Polar Biological Oceanography, AWI, Bremerhaven, and MARUM (Center for Marine Environmental Sciences), Bremen, Germany – ilka.peeken@awi.de

[c]Biogeociences, AWI, Bremerhaven, Germany – ying.ye@awi.de

[d] Institute of Environmental Physics, University of Bremen, Germany – marco.vountas@iup.physik.uni-bremen.de; burrows@iup.physik.uni-bremen.de

[e] Institute for Coastal Research, GKSS, Geesthacht Research Center, Geesthacht, Germany – ruediger.roettgers@gkss.de

Abstract – Global information on the quantitative distribution of major functional phytoplankton types (PFTs) of the world ocean is important for understanding the marine phytoplankton's role in the global marine ecosystem. In this study global biomass distributions of different dominant PFTs from 2008 were derived from data of the ENVISAT satellite sensor SCIAMACHY analysed with PhytoDOAS, a method of Differential Optical Absorption Spectroscopy (DOAS) currently specialized for diatoms and cyanobacteria (Bracher et al. 2009). These global maps of phytoplankton distribution were validated with collocated in-situ PFT data. The global PFT satellite data sets are used as input data for a biogeochemical model. First applications are presented.

Keywords: phytoplankton groups, retrieval, validation

1. INTRODUCTION

To understand the marine phytoplankton's role in the global marine ecosystem and biogeochemical cycles it is necessary to derive global information on the distribution of its biomass and primary production, in particular the distribution of major functional phytoplankton types (PFT) in the world oceans. Using common ocean color sensors like SeaWiFS or MERIS, only the overall phytoplankton biomass or the dominant phytoplankton group can be derived (e.g. Alvain et al. 2008). In order to get a global quantitative estimate of different PFT in the oceans, the Differential Optical Absorption Spectroscopy (DOAS), a technique established for extraction of atmospheric components from high spectrally resolved UV-VIS data, was adapted to the retrieval of the absorption and biomass of two major phytoplankton groups (PhytoDOAS) from data of the Scanning Imaging Absorption Spectrometer for Atmospheric Chartography (SCIAMACHY) satellite sensor (Bracher *et al.* 2009). Within this method, hyperspectral information of SCIAMACHY is used to obtain the distinctive absorption characteristics from the different phytoplankton groups. In the presented study the method has been extended to another wavelengths range in order to differentiate within the prokaryotic algae between phycoerythrine containing cyanobacteria and other procaryotic phytoplankton (mainly Prochlorococcus-type). We have extracted the quantitative phytoplankton group information for one year from SCIAMACHY. The data set was validated against in-situ data and used for first applications in a biogeochemical model study.

2. DATA AND METHODS

Within this study the PhytoDOAS method was applied to SCIAMACHY data to extract information on different phytoplankton groups. SCIAMACHY measures back scattered solar radiation in the UV-Vis-NIR spectral region with a high spectral resolution (0.2 to 1.5 nm). In order to identify these characteristic absorption spectra in SCIAMACHY data in the range of 430 to 500 nm we used in-situ measured phytoplankton absorption spectra from two different RV Polarstern expeditions where different phytoplankton groups (diatoms and cyanobacteria) were representing or dominating the phytoplankton composition. In addition, SCIAMACHY data in the range of 530 to 590 nm were analysed with PhytoDOAS to identify absorption of the photosynthetic pigment phycoerythrin.

3. RESULTS

Results from PhytoDOAS clearly show the absorption inprints from different phytoplankton groups in the SCIAMACHY data (see Fig.1; and see also Figure 3 in Bracher *et al.*, 2009).

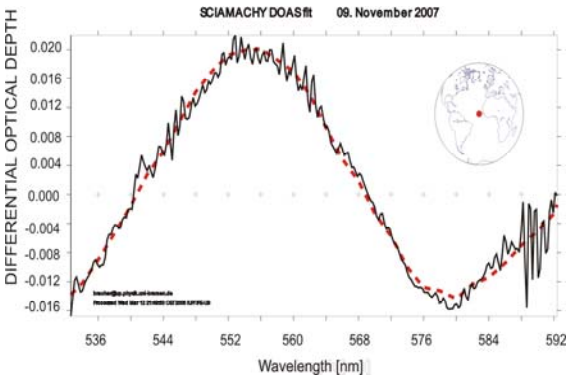

Figure 1. Differential Optical Depth of a spectral PhytoDOAS fit with SCIAMACHY data (black) from 9 Nov 2007 at 11°N and 23°W for phycoerythrine containing phytoplankton. Phytoplankton group specific differential absorption cross section of a pure cyanobacteria natural sample was used (taken from Atlantic cruise ANTXXIII-1 at 23°N and 22°W on 29 Oct 2005). The scaled in-situ phytoplankton differential absorption of this phytoplankton group is shown in red.

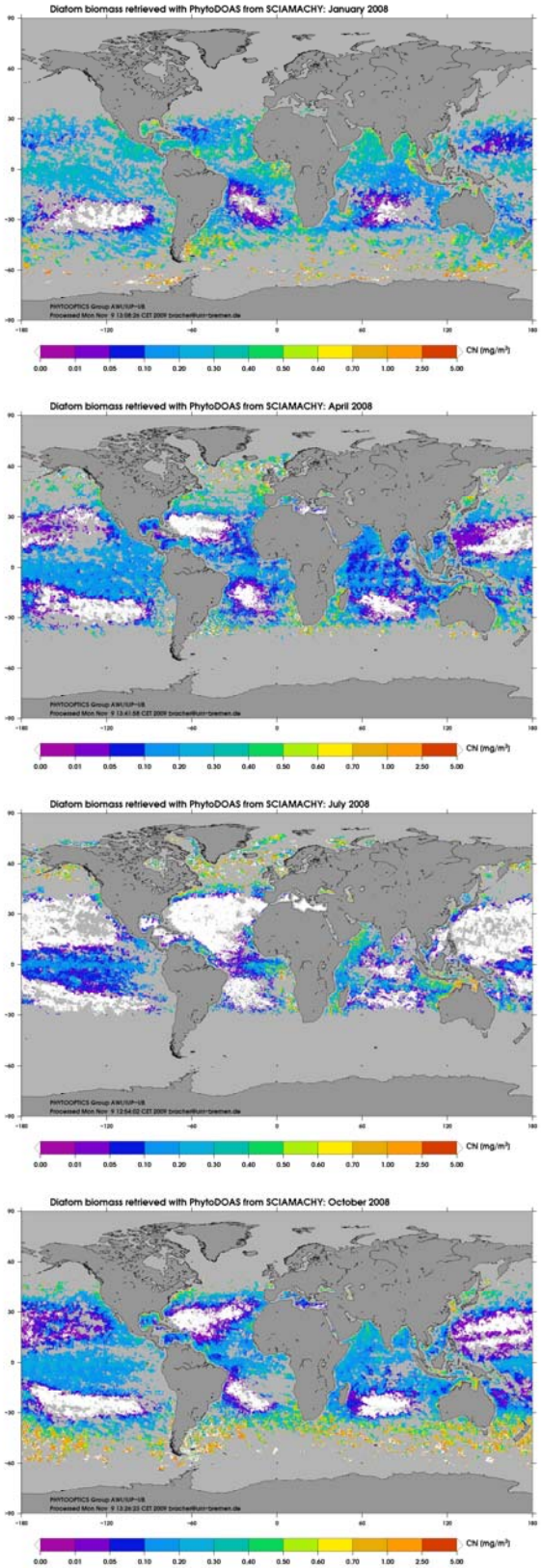

Figure 2. Monthly averages of global diatom biomass (chl-a) determined by using PhytoDOAS with SCIAMACHY data: Jan, April, Jul and Oct of 2008. At grey areas no SCIAMACHY data were available, white areas no diatom absorption has been detected.

The conversion of these differential absorptions by including the information of the light penetration depth, according to Vountas *et al.* (2007), leads to globally distributed biomass concentrations for these characteristic phytoplankton groups (corresponding to chl a). Monthly averages for the global biomass concentrations of the three phytoplankton groups for the year 2008 have been retrieved. These global maps of phytoplankton distribution were validated with collocated in-situ data from various Atlantic cruises in 2008 determined via HPLC pigment analysis and applying the CHEMTAX program (Mackey *et al.*, 1996). Fig. 2 shows the global diatom biomass distributions for monthly means (Jan, Apr, Jul, Oct) of 2008 retrieved with PhytoDOAS from SCIAMACHY data. Yearly data sets of Globcolour data (merged SeaWiFS /MODIS/MERIS chl-a product) and PhytoDOAS phyco-erythrine-containing phytoplankton biomass distributions have been used as initial conditions to constrain a 1-dim model of Fe speciation and biogeochemistry, coupled with the General Ocean Turbulence Model (GOTM) and a NPZD-type ecosystem model which has been applied for the Tropical Eastern North Atlantic Time-Series Observatory (TENATSO; model details in Ye *et al.*, 2009).

4. CONCLUSION

The PhytoDOAS method applied to SCIAMACHY satellite measurements enables for the first time to establish a global data set on quantitative distribution of different phytoplankton groups. As first applications has shown this data base can be used by a wider community for the purposes of optical and ecosystem modeling.

AKNOWLEDGEMENTS

The authors thank the crew, principal investigators and other scientists on board the various cruises with RVs Polarstern, D'Atalante and MSM Merian for their support. We thank DLR and ESA for SCIAMACHY level-1 data. Funding has been supplied by the European Union via the project "SHIVA" , the Helmholtz Impuls and Network Fond, and the Alfred-Wegener-Institute.

REFERENCES

Alvain, S., Moulin, C., Danndonneau, Y., and Loisel, H. (2008) "Seasonal distribution and succession of dominant phytoplankton groups in the global ocean: A satellite view" Global Biogeochem. Cycles, vol. 22, GB3001.

Bracher, A., Vountas, M., Dinter, T., Burrows, J.P., Röttgers, R., Peeken, I. (2009) "Quantitative observation of cyanobacteria and diatoms from space using PhytoDOAS on SCIAMACHY data." Biogeosci., vol. 6, pp. 751-764.

Vountas, M., Dinter, T., Bracher, A., et al. (2007) "Spectral Studies of Ocean Water with Space-borne Sensor SCIAMACHY using Differential Optical Absorption Spectroscopy (DOAS), Ocean Sci., vol. 3, pp. 429–440.

Y. Ye, Völker, C., and Wolf-Gladrow, D. A. (2009) "A model of Fe speciation and biogeochemistry at the Tropical Eastern North Atlantic Time-Series Observatory site." Biogeosciences, vol. 6, pp. 2041-2061.

The Coastcolour Project

C. Brockmann [a,*], R. Doerffer[b], S. Sathyendranath [c], S.B. Groom [c], K. Ruddick [d], R. Santer[e], V. Brotas [f], S. Pinnock [g]

[a] Brockmann Consult, Geesthacht , Germany – carsten.brockmann@brockmann-consult.de
[b] GKSS Forschungszentrum, Geesthacht, Germany – roland.doerffer@gkss.de
[c] Plymouth Marine Laboratory, Plymouth, United Kingdom – SBG@pml.ac.uk
[d] MUMM, Brussels, Belgium - K.Ruddick@mumm.ac.be
[e] LISE Adrinord , Wimereux, France - richard.santer@univ-littoral.fr
[f] Centro de Oceanografia, Faculty of Sciences, University of Lisbon, Lisbon, Portugal - vbrotas@fc.ul.pt
[g] ESA ESRIN, Frascati, Italy - simon.pinnock@esa.int

Abstract – After more than 7 years in space the ESA MERIS instrument has delivered a unique dataset of ocean colour measurements of the coastal zone, at 300m resolution and with a unique spectral band set. The ESA DUE coastcolour project aims at finding best fitting algorithms for different coastal zones globally distributed. Internationally discussed protocols and Case 2 algorithms, data processing, validation, a round robin exercise and stimulation of data exploitation will be the main elements of the project. The results will include a coherent processed large data set covering the whole MERIS mission, internationally discussed protocols, and a near real time service for coastal MERIS Full Resolution products.

Keywords: Coastcolour, MERIS-FR, Case-2 waters

1. INTRODUCTION

The importance of the coastal zone for economic activities, and the anthropogenic stresses on the ecosystem, have been described and discussed widely throughout the past 20 years. Responding to this, ESA designed the MERIS instrument specifically to provide measurements most suitable for coastal zone management and research. In space for 7 years, MERIS has delivered a unique global dataset of coastal zones at 300m spatial resolution, which deserves dedicated processing with internationally agreed algorithms, and provision of products targeted to specific user needs, properly documented and easily accessible. Beyond this immediate goal this dataset will become an important contribution to further understanding of the coastal zone in climate change, its importance in the global carbon cycle, the generation of biogenically-active gases and its sensitivity and response to changes in temperature, sea level and water mass distribution.

The ESA project CoastColour, funded under the DUE programme, will work towards these objectives by developing, demonstrating, validating and inter-comparing different Case 2 algorithms over a global range of coastal water types, identifying best practices, and promoting discussion of the results in an open, public form.

2. USER DRIVEN APPROACH

32 globally distributed research and operational groups concerned with ocean colour remote sensing and coastal zone management have been identified as champion users for coastcolour. 12 coastal areas have been defined where coastcolour will generate its products responding to the needs of these users.

It is a goal of the project to broaden this user community and to welcome additional users. Users are encouraged to formulate their requirements for their coastal site, and to contribute to the project with in-situ data and review of products and project results.

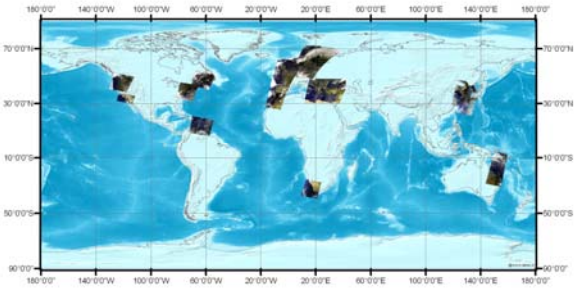

Figure 1. 12 main test sites of the coastcolour project

2. PROJECT ACTIVITIES

The project work will be performed in 5 activities:

Activity 1: Algorithm definition and development
Through discussion with the users, within the team and with the science team, all user requirements and algorithm requirements have been reviewed with the goal to identify in detail how the final CoastColour (CC) algorithms will look like and which data are required to calibrate and validate them. The algorithms will be implemented as BEAM processors.

Activity 2: Production
Within a processing system an advanced Level 1 product (L1P) will be processed including advanced geolocation,

* Brockmann Consult, Max-Planck-Str. 2, D-21502 Geesthacht, carsten.brockmann@brockmann-consult.de

correction for adjacency effect, glint correction, correction of the smile effect, cloud screening and a land/water screening. Two Case-2 waters algorithms will be applied to the data set. The processing system will be based on the BEAM processing technology.

Activity 3: Validation
The validation starts with a review of existing protocols and the release of a CoastColour Protocol, in agreement with the international community and specifically compliant with the QA4EO guidelines.

Activity 4: Round Robin for intercomparison of water processing algorithms
A Round Robin intercomparison of Case2 algorithms will involve the international user community on a voluntary basis. A protocol for the performance of the Round Robin will be established. A dataset comprised of L1P as well as L2R water leaving reflectances will be distributed to the users which will run their water retrieval algorithms.

Activity 5: Communication and interaction with international groups and users
Case2 waters are of high interest to the international user community as expressed by the impressive number of participants of the CoastColour user consultation meeting and subsequently the commitment the users gave by proposing their sites to ESA. 12 sites have been defined to be champion user sites. The users defined site specific requirements on primary and derived products.
A close contact with the users and international bodies through the user consultation workshops and direct consultation will be held.

A first user consultation meeting is scheduled for the second half of November 2010 in ESRIN, Frascati (Rome, Italy).

4. COASTCOLOUR PRODUCTS

Coastcolour will process all available MERIS Full Resolution (300m) of the champion user test sites (and possibly more). The coastcolour products will include a set of basic quantities which will be generated over all sites:

- TOA radiances
- Remote sensing reflectances
- Identification of Case-1 vs Case-2 waters
- IOPs
- Chl, SPM, CDOM
- Water clarity (euphotic zone depth, Secchi disk depth)
- Turbidity
- PAR
- Aerosol optical depth
- Chlorophyll-a fluorescence line height
- Errors, error statistics

An attempt will be made to generate additional experimental, site specific products, including (list under consolidation):

- Primary productivity
- Phytoplankton biomass
- phytoplankton functional types, abundance and particle size distribution
- biomass of cyanobacterial blooms
- new products derived from MERIS fluorescence band; algal bloom monitoring using fluorescence band

4. MAIN RESULTS

The aim of the coastcolour project is to enlarge the usage of the MERIS FR products and achieve accepted water quality products for the coastal zone. The results coming out of the project will be:

- Internationally discussed protocols for Case2 waters processing including algorithm performance assessment;

- A global set of MERIS FR data of coastal zones at a regional scale, processed with best possible algorithms for Level 1, with best possible regional algorithms for water leaving reflectances and IOPs, and demonstrating processing of regional higher level specific products; all products including per pixel error/uncertainty estimates;

- An international comparison of Case 2 algorithms, involving all relevant stakeholders and open to the scientific community;

- Actively demonstrating and promoting MERIS capabilities for Case 2 water processing to the international ocean colour radiometry community, and increase of usage of MERIS within and outside Europe;

- Preparation of the future exploitation of MERIS and Sentinel 3 products for operational Case 2 product applications and for climate change studies.

ACKNOWLEDGEMENTS

The project funded under the ESA DUE programme, contract No.22807/09/I-AM

The project is supported by a team of consultants, including Prof. Yu-Hwan Ahn (KORI, East Asian Waters processing), Dr. Jim Gower (DFO, Fluorescence Line Height), Dr. Mark Dowell (JRC, classification of marine waters), Dr. Stewart Bernard (CSIR, Regional IOPs and HABs), Prof. Zhongping Lee (U. Mississippi, Analytical Case2 Algorithm), Dr. Bryan Franz (NASA, Ocean Colour Biology from SeaWiFS and MODIS) and Dr. Thomas Schröder/Dr. Arnold Dekker (CSIRO, inversion algorithms and regional IOPs).

On the use of MODIS data to detect oil spills: the Lebanon case

B. Bulgarelli [a,*], S. Djavidnia[b]

[a] Joint Research Centre, European Commission, Ispra , Italy – barbara.bulgarelli@jrc.ec.europa.eu
[b] European Maritime Safety Agency, Lisboa, Portugal – samuel.djavidnia@emsa.europa.eu

Abstract – With its higher resolution bands, its two daily acquisitions, and the possibility to obtain near real-time data free of charge, the NASA MODIS optical sensor shows interesting potential as a cost-effective tool for oil spill monitoring in the marine environment. All available MODIS images acquired during the Lebanon crisis in summer 2006 are hereby analyzed to study under which conditions MODIS is able to detect oil features on the sea surface and which kind of information can be retrieved.

Keywords: optical remote sensing, oil spill.

1. INTRODUCTION

The Lebanon oil pollution in the summer of 2006 was due to the leakage from a ground-based source. On July 13 and 15, 2006, in the course of the conflict in the Middle East, the oil-fuelled power plant of Jieh, located directly on the Lebanon coastline, approximately 30 km south of Beirut, was hit by bombs. Part of the power plant storage tanks caught fire and were burning for several days. A large part of the fuel was spilled into the Mediterranean Sea as a result of the blast. The Lebanese ministry of environment estimated that approximately 30,000 tons of heavy fuel oil was emitted into the sea. Due to the strong coastal ocean current and winds from south westerly directions, in addition to the war situation that prevented the implementation of measures and actions to contain the disaster, the oil spill moved along the Lebanese coast northward and contaminated large part of the coast, reaching Syrian waters. The pollution resulting from this spill is one of the largest natural disasters which has occurred in the Mediterranean Sea. Synthetic aperture radar (SAR) is still the most efficient and superior satellite technology for operational oil spill detection, due to its wide area coverage and day and night all-weather capabilities. Nevertheless, it is the synergetic use of sensors working in different parts of the electromagnetic spectrum, which can achieve the most promising results. With its higher resolution bands, its two daily acquisitions, and the possibility to obtain near real-time data free of charge, the NASA MODIS optical sensor shows interesting potential as an additional, complementary and cost-effective tool for oil spill monitoring in the marine environment. Preliminary match-ups performed during the Lebanon crisis between MODIS and the SAR data have already showed MODIS capability to detect oil features (Bulgarelli and Tarchi, 2006). The Lebanon case represents a unique situation of an oil slick of large extension that, due to long-time source leakage, persisted for a considerable time in a region and in a period of the year with favourable climate conditions. All these circumstances allowed the creation of an large data set of MODIS images where the same oil slick was observed under a wide variety of geometrical and meteorological conditions. Using available SAR data as reference, such data set has been extensively analyzed to study under which conditions MODIS is able to detect oil features on the sea surface and which kind of information can be retrieved. The SeaDAS atmospheric correction code was used to process MODIS images from Level 0 to Level 2.

2. THE LEBANON DATA SET

For the time period extending from 13.07.2006, when the first bomb hit the Jieh platform, to 31.08.2006 (when the MIC bulletin stated that aerial surveillance didn't detect any collectable oil floating on the surface - MIC 2006) and for the region of interest (the Lebanon coast from Jieh northward and the southern Syrian coast), all available MODIS Terra and Aqua L0 images have been downloaded from the "*Level 1 and Level 2 Browser*" of the *NASA Ocean Color Web*. This amounts to a total of 45 MODIS Aqua and 47 MODIS Terra L0 images. All images were further processed, displayed and visually analyzed using the SeaDAS code (http://oceancolor.gsfc.nasa.gov/seadas/). Out of the sample, about 20% of the images were discarded because of complete cloud coverage of the area of interest. Each MODIS image at L1B was visually analyzed in order to identify suspected features. True reference was considered the temporally closer available SAR image (Tarchi et al., 2006). The visual analysis was done at all resolutions and wavelengths. A *suspected feature visibility (SFV) code* ranging between 0 (nothing detected) and 3 (very well visible suspected feature) was associated to each resolution of each visualized image. Suspected features were detected in at least one band in more than 40% of the cases. The highest number of detections occurred at 500m resolution bands, but of course the visibility of the detected features was always better, i.e. sharper, at 250m resolution. For the whole sample, suspected feature visibility was analyzed in detail in terms of i) meteorological conditions (i.e., wind speed and atmospheric turbidity), ii) observation geometry, and; iii) illumination geometry.

3. RESULTS

3.1 Meteorological conditions

Suspected feature visibility was not influenced by wind speed and aerosol optical thickness in their observed range of variation (wind speed ranging between 1.3 to 7.7 m/sec

* Barbara Bulgarelli, JRC-EC, TP670, via Fermi 1, I-21020 Ispra. Tel.: ++39-0332-785778

and aerosol optical thickness at 555nm ranging between 0.1 and 0.6) Most likely the result would have been different fo a wider range of variation in meteorological conditions.

3.2 Observation geometry

The zenith angle of observation θ_v represents a key factor in oil feature visibility, since slanted observations of the target pixels are associated with decreased pixel ground resolution and increased atmospheric contamination. Histogram 1 shows the θ_v distribution for the whole MODIS sample. For the analyzed Lebanon data set, it was always possible to detect suspected features in at least one band for θ_v<40deg . On the contrary, it was never possible to detect suspected features for θ_v>50deg,(condition which occurred in 27% of cloud-free images).

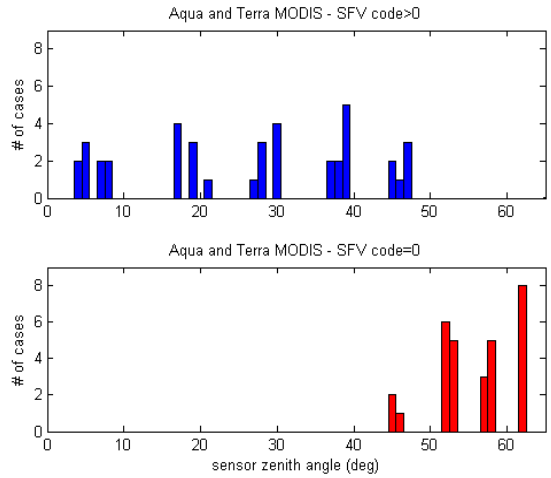

Fig. 1 Histogram distribution of the sensor zenith angle θ_v for all MODIS data: above, in blue, test cases which evidenced suspected features in at least one band; below, in red test cases with no suspected features detected.

3.3 Illumination conditions

The combined sun-sensor geometry has great influence on suspected feature visibility, since it may give raise to sun glint contamination. Sun glint contamination occurs when direct solar radiance hitting the sea surface is directly reflected into the sensor field of view. For perfectly flat surfaces this would occur only when the sensor is in specular position with respect to the Sun. The water surface is indeed never flat and hence a large number of pixels are affected by sun glint contamination. Suspected feature visibility is remarkably different for areas contaminated or not contaminated by sun glint, since different is the mechanism behind oil feature detection.

Sun glint contamination

In presence of sun glint contamination, features detection was possible at any sensor optical band, but was at its best at high resolution band 859nm. The sign of the contrast ranged from negative to positive (depending on the sun-sensor geometry), but maintained the same sign throughout sensor bands. Features detection in presence of glint contamination depends (as for SAR) on the different surface physical properties of oil and water: oil dampens the surface roughness, affecting in this way the sun reflected light pattern. The sunlight reflected by the surface is so much greater than the sunlight reflected from below the surface, that the retrieval of information about in-water constituents is severely compromised. Indeed an analysis of the retrieved products showed that features tend to be misinterpreted as atmospheric phenomena. No spectral properties of the observed feature could hence be retrieved.

Absence of Sun glint contamination

Oil detection in absence of sun glint contamination is not possible at low sensitivity Near Infrared (NIR) high resolution bands, but suspected features were visible at medium/low resolution bands. Best feature visibility occurred in the blue bands, where oil absorption is at a maximum. The potential retrieval of spectral information requires a careful application of the SeaDAS atmospheric correction code, since it does not account for possible oil features, and hence easily misinterprets sea surface features as atmospheric ones. The retrieved spectral information are additionally extremely difficult to interpret in absence of *in situ* validation. Moreover, features are located in a coastal region characterized by optically complex waters and where adjacency effects from nearby mainland are important.

4. CONCLUSION

The detailed statistical analysis of the Lebanon MODIS data set pointed out that, for a viewing angle lower than 40 degrees, MODIS was always able to detect oil spill features. In presence of sun glint contamination, MODIS high resolution bands can be effectively used to locate oil features. No spectral properties can be reasonably retrieved. Reflected sunlight contamination severely compromises the retrieval of information about in-water constituents. Despite this, MODIS images acquired in glint conditions may be used in conjunction with SAR images to follow the evolution of the potential slicks. Indeed, since MODIS does not tilt to avoid looking into the sun glint field, its glint affected areas tend to be considerably larger than for those sensors which do tilt, such as SeaWiFS. In this case, slightly more than 40% of the retained data set was acquired in sun glint conditions. For what concerns oil detectability in absence of sun glint contamination, no detection is possible at low sensitivity NIR high resolution bands. Suspected features were only visible at medium/low resolution bands, particularly in the blue where highest oil absorption occurs. Spectral information can be retrieved by carefully applying ad hoc atmospheric correction. Results are nevertheless difficult to interpret in absence of in situ measurements.

ACKNOWLEDGEMENTS

This work was funded within the scope of the EMSA – EC JRC collaboration for the development and support of satellite monitoring techniques for oil spill detection.

REFERENCES

Bulgarelli B. and D. Tarchi (2006), “Exploratory use of MODIS in oil-spill monitoring”, in “Workshop on monitoring activities related to oil pollution in Lebanon” EUR 22531 EN

Tarchi D., J. Fortuny, G. Ferraro, S. Meyer-Roux, O. Muellenhoff, K. Topouzelis and A.J. Sieber (2006) “The use of satellite imagery during the pollution crisis in Lebanon”, in “Workshop on monitoring activities related to oil pollution in Lebanon” EUR 22531 EN

MIC Message n. 16, “Lebanon: marine and coastal pollution”, EC, Civil Protection Co-Operation Mechanism, 31/08/2006

Modeling the Adjacency Effect in Coastal Waters: the North Adriatic Sea

B. Bulgarelli [a,*], V. Kisselev [b], G. Zibordi [c]

[a] IPSC, Joint Research Centre, European Commission, Ispra , Italy – barbara.bulgarelli@jrc.ec.europa.eu
[b] EOMAP GmbH & Co.KG, Gilching, Germany – kiselev@eomap.com
[c] IES, Joint Research Centre, European Commission, Ispra , Italy – giuseppe.zibordi@jrc.ec.europa.eu

Abstract – A methodology to quantify the adjacency effects in remotely sensed data from coastal waters is presented. Specifically, the dependence of the adjacency effects due to changes in the land-ocean reflectance is decoupled from the dependencies of satellite data on measurement geometry and atmosphere. A set of realistic test cases for typical SeaWiFS observation conditions is proposed to simulate the adjacency effects along a transect in the North Adriatic Sea embracing the Aqua Alta Oceanographic Tower, (AAOT, 45.31N, 12.51E), used for satellite ocean color calibration and validation activities. A 3D backward MonteCarlo code and the Finite Elements Method (FEM) plane-parallel highly accurate radiative transfer code are used.

Keywords: adjacency effect, optical remote sensing, radiative transfer.

1. INTRODUCTION

The adjacency effect originates from the presence of a scattering atmosphere over a nonuniform reflecting surface, which causes the radiance from high reflectivity areas to spill over the adjoining low reflectivity observed regions, increasing their apparent brightness (Santer and Schmechtig, 2000). The present paper proposes an accurate modeling of the adjacency contribution in a specific area of the Northern Adriatic Sea characterized by complicated coastal pattern originated by the Venice Lagoon. Specifically, the method aims at modeling the adjacency effect for a set of realistic geometric, atmospheric, water and land parameters encountered in typical SeaWiFS observation conditions along a transect including the Aqua Alta Oceanographic Tower (AAOT, 45.31N, 12.51E), used as a platform for marine and atmospheric time series measurements utilized for satellite ocean color calibration/validation activities (Zibordi et al. 2009). The adjacency radiance is parameterized to decouple the dependence on land and water reflectances from the geometric and atmospheric dependencies. A 3D backward MonteCarlo (MC) code (Roberti, 1997), modified to simulate a plane-parallel atmosphere bounded by inhomogeneous bottom reflecting surface is applied. The highly accurate plane-parallel Finite Element Method (FEM) numerical algorithm (Bulgarelli et al., 1999), based on the finite element method, is also used as a reference.

2. THE ADJACENCY RADIANCE

In general terms, an image of an object is the combination of the original signal *f(x,y)*, convolved with the entire system point spread function (PSF) *h(x,y)*, adding noise *n(x,y)* as:

$$g(x,y) = n(x,y) + f(x,y) \otimes h(x,y) \tag{1}$$

In agreement with this formulation, any adjacency contribution L_{adj} received by a space-sensor observing the water surface at (x_0,y_0) and due to the spatial proximity of the coast can be modeled as:

$$\begin{aligned} L_{adj}(x_0,y_0) = &\left\{E_d(x,y)\cdot\rho(x,y)/\pi\cdot M(x,y)\right\}\otimes h(x,y;x_0,y_0) - \\ &-\left\{L_w(x,y)\cdot M(x,y)\right\}\otimes h(x,y;x_0,y_0) - \\ &-\left\{L_{surf}(x,y)\cdot M(x,y)\right\}\otimes h_{spec}(x,y;x_0,y_0) \end{aligned} \tag{2}$$

where the dependency on θ, θ_0, ϕ, ϕ_0, τ, ω_0 and λ_i is omitted for simplicity.

M(x,y) indicates the land-mask matrix defined as:

$$M(x,y) = \begin{cases} 1 & \text{for land pixels} \\ 0 & \text{otherwise} \end{cases} \tag{3}$$

$h(x,y;x_0,y_0)$ is the atmospheric point spread function (APSF) and $h_{spec}(x,y;x_0,y_0)$ is the analogous for an underlying specularly reflecting surface. $E_d(x,y)$ is the total downgoing irradiance, and $\rho(x,y)$ the Lambertian albedo assumed for land regions. L_w is the radiance leaving the water surface from the water bulk: the so-called water leaving radiance, and L_{surf} is the radiance reflected by the water surface.

By assuming an average refectance ρ_b for the land regions, and negligible adjacency contribution from surrounding water areas, i.e.,

$$R_{rs}(x,y) = L_w(x,y)/E_d(x,y) \approx R_{rs}(x_0,y_0),$$

equation (2) can be written as:

$$\begin{aligned} L_{adj}(x_0,y_0) = &\left[\rho_b/\pi - R_{rs}(x_0,y_0)\right]\cdot\left\{M(x,y)\cdot E_d(x,y)\right\}\otimes h(x,y;x_0,y_0) - \\ &-L_{surf}(x,y)\cdot M(x,y)\otimes h_{spec}(x,y;x_0,y_0) \end{aligned} \tag{4}$$

By introducing the following notations:

$$\begin{aligned} C(x_0,y_0) &= M(x,y)\cdot E_d(x,y)\otimes h(x,y;x_0,y_0) \\ W(x_0,y_0) &= L_{surf}(x_0,y_0)\cdot M(x,y)\otimes h_{spec}(x,y;x_0,y_0) \end{aligned} \tag{5}$$

where C and W are functions of x, y, x_0, y_0, μ, μ_0, ϕ, ϕ_0, ω_0, τ and λ_i, ,

equation (4) becomes:

* Corresponding Author. IPSC, JRC-EC, TP670, via Fermi 2749, I-21027 Ispra (VA), Italy. Tel +39-0332-785778.

$$L_{adj}(x_0, y_0) = [\rho_b / \pi - R_{rs}(x_0, y_0)] \cdot C(x_0, y_0) - W(x_o, y_o) \quad (6)$$

This expression allows for decoupling the dependence of land and water reflectances from the geometric and atmospheric dependencies. The terms $C(x_0,y_0)$ and $W(x_0,y_0)$ can be simulated for a set of representative geometric and atmospheric cases using the 3D MC code.

3. GEOMETRIC AND ATMOSPHERIC CASE STUDIES

Simulations of the functions C and W is proposed at the SeaWiFS center wavelengths for a coupled atmosphere-ocean system with a flat sea surface and in the absence of whitecaps. The atmosphere is divided into 14 layers to resolve the aerosol and molecules vertical distribution (Bulgarelli and Zibordi, 2003). Several combinations of geometric and atmospheric parameters are chosen (see Table 1) as representative of typical SeaWiFS observational conditions for the analyzed regions (Berthon et al. 2002).

Table 1: Geometric, atmospheric parameters used in the simulation of the adjacency effect. The parameters defining the standard case are in bold, while those defining the other cases are given in brackets.

θ_0	**45**^{o} (25 ^{o} -65 ^{o})
φ_0	**270** ^{o}
θ_v	**20** ^{o} , **50** ^{o}
$\Delta\varphi$	± **70** ^{o}
v	**1.7** (1.4, 1.9)
α	**0.05** (0.02, 0.08)
ω_{0a}	**Maritime**, Continental (1)

(1) acording to WMO (IAMAPRC, 1984)

The inhomogeneous reflecting surface is divided in 51x51 squared pixels centered at the AAOT site (Figure 1). The grid discriminating between land and water pixels is extracted from the operational land/water mask used in the REMBRANDT code (Bulgarelli, 2000) to process SeaWiFS data form the Northern Mediterranean Sea. Such grid covers an area spanning between 44.85N and 45.75N and between 11.96E and 13.10E. The surface cells are assumed squared with 2x2 km size. A representative transect is selected (Fig. 1) starting from the coast, crossing the Venice Lagoon and hence embracing the AAOT site.

4. CONCLUSION

A specific methodology has been proposed to evaluate the adjacency contribution in a specific area of the Northern Adriatic Sea characterized by the complicated coastal pattern characterizing the Venice Lagoon. A parameterization of the adjacency effects, relying on the separation of land and water effects from geometric and atmospheric dependencies, has been illustrated. A set of realistic geometric and atmospheric parameters encountered in typical SeaWiFS observation conditions in the area has been selected to realistically simulate the adjacency contribution along a transect including the Aqua Alta Oceanographic Tower (AAOT, 45.31N, 12.51E), used as site for the production of marine and atmospheric measurements for calibration/validation of satellite ocean color data. Both 3D and plane-parallel radiative transfer algorithms have been applied.

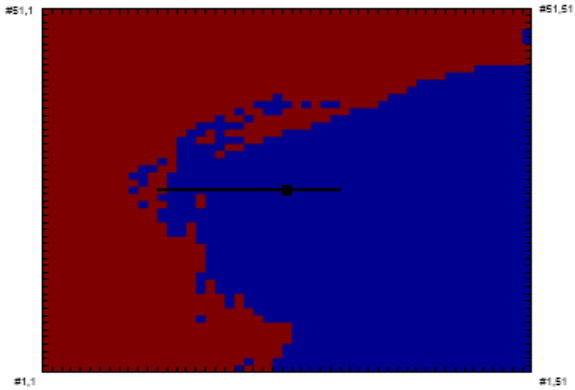

Figure 1: SeaWiFS mask (51x51 pixels) for the North Adriatic Sea for latitude 11.96E to 13.10E and longitude 44.85N to 45.75N. The black line represents the transect, extending from (45.31N, E) to (45.31N,E). The black square locates the AAOT position (45.31N, 12.51E)

REFERENCES

Santer, R., & Schmechtig, C. (2000). Adjacency effects on water surfaces: Primary scattering approximation and sensitivity study. Applied Optics, 39, 361−375.

Zibordi G., J-F. Berthon, F. Melin, D. D'Alimonte, S. Kaitala, (2009) Validation of satellite ocean color primary products at optically complex coastal sites: Northern Ariatic Sea, Northern Baltic Proper and Gulf of Finland", Remote Sens. Of Env. 113, 2574-2591

Roberti, L. (1997), "Monte Carlo radiative transfer in microwave and in the visible: biasing techniques", Appl. Opt. 36, 7929-7938

Bulgarelli B., V. Kisselev and L. Roberti (1999), "Radiative transfer in the atmopshere-ocean system: the finite-element method", Appl. Opt. 38, 9, 1530-1542

Bulgarelli, B., & Zibordi, G. (2003). Remote sensing of ocean color: Accuracy assessment of an approximate atmospheric correction method. International Journal of Remote Sensing, 24, 491−509.

Bulgarelli B. and Melin F. (2000), "SeaWiFS data processing code REMBRANDT version 1.0", EUR 19154 EN

Berthon, J. F., Zibordi, G., Doyle, J. P., Grossi, S., van der Linde, D., & Targa, C. (2002). Coastal Atmosphere and Sea Time Series (CoASTS), part 2: Data analysis. In S. B. Hooker & E.R. Firestone (Eds.), NASA Tech. Memo. TM-2002-206892, v. 20 Greenbelt, MD: NASA Goddard Space Flight Center (25 pp.)

IAMAPRC (1984), "A preliminary cloudless standard atmosphere for radiation computation', World Climate Programme, WCP-112, WMO/TD-No. 24, Boulder Colorado (USA)

Bio-optical characteristics of the Black Sea from satellite data

V. Burenkov, O. Kopelevich, S. Sheberstov, S. Vazyulya

Shirshov Institute of Oceanology, Russian Academy of Sciences, Moscow, Russia – oleg@ocean.ru

Abstract – Some problems of application of satellite ocean color data and interesting phenomena revealed in the Black Sea are discussed. The most interesting feature of the Black Sea observed from satellite data is that the basin grows turbid in each June from year to year, and intensity of that phenomenon can be linked to the winter sea surface temperature.

Keywords: ocean color, Black Sea.

`1. INTRODUCTION

The Black Sea is a striking example of the basin with Case 2 waters where, by definition, variability of seawater optical properties are influenced not just by phytoplankton and by the material associated with it, as in Case 1 waters, but also by other substances independent of phytoplankton. In the Black Sea such substances are the particulate and dissolved matter brought in the most part by river run-off. With the advent of satellite ocean color scanners the study of seasonal and inter-annual changeability of different large-scale processes in the Black Sea has become possible thanks to unique capability of satellite observations to provide long-term quasi-continuous series of data for the whole basin. In this presentation some problems of application of satellite ocean color data and interesting phenomena revealed in the Black Sea are discussed.

2. PROBLEMS OF APPLICATION OF SATELLITE OCEAN COLOR DATA IN THE BLACK SEA

The first problem arises from that the Black Sea is the Case 2 waters. The standard algorithms for processing of satellite ocean color data, derived mainly from Case 1 waters, break down in such kind of waters. In the Black Sea the standard algorithm can overestimate chlorophyll concentration (*Chl)* more than twice (Kopelevich et al., 2004, 2008). One of reasons of such overestimation is that the standard algorithm is based on a regression equation meaning a definite relationship between the chlorophyll and yellow substance absorption coefficients. If seawater absorption increases due to enhanced content of yellow substance brought by rivers, the algorithm attributes that additional absorption to increasing chlorophyll concentration and overestimates the latter.

The regional processing algorithms for the Black Sea were developed on the basis of data from field measurements, and a few CD-ROMs were issued with the bio-optical characteristics of the Black Sea derived by using these regional algorithms (Kopelevich et al., 2004, 2008, 2009). They include various bio-optical parameters such as chlorophyll concentration, the particle backscattering and yellow substance absorption coefficients which manifest spatial and temporal variability of three important seawater constituents – photosynthetic phytoplankton, particulate and colored organic matter. The last CD-ROM, accessible from Website (Kopelevich et al., 2009), comprises the data from 1998 to 2008. In 2008 a difficulty with SeaWiFS data, used before for construction of the long-term series since 1998, has arisen (SeaWiFS instrument was powered off several times due to the loss of GPS and attitude data in the space telemetry). MODIS-Aqua data were used for continuation of the series, and a procedure of joining SeaWiFS to MODIS-Aqua has been developed (Kopelevich et al., 2009).

3. THE BLACK SEA GROWS TURBID IN JUNE

One of the most interesting phenomena revealed from satellite ocean color data is that the Black Sea grows turbid in each June. That is clearly displayed by the enhanced values of the particle backscattering coefficient b_{bp} observed in the whole basin in June (Burenkov et al., 2005, 2007; Kopelevich et al., 2004, 2008).

There were two hypotheses suggested to explain the enhanced values of b_{bp} in June: (i) the particulate matter from the river run-off spreading to the whole basin across the boundary Rim Current by mesoscale eddies and via turbulent exchange; (ii) coccolithophore bloom covering the whole basin (Cokacar et al. 2001, 2004). Since 2004, in parallel with satellite observations, field measurements were carried out in the eastern part of the Black Sea each June; they included both optical measurements and determination of chlorophyll-a, total suspended matter and coccolithophoride concentrations. The results obtained allowed us make several conclusions.

In 2004 a significant correlation was found between the coccolithophore concentration and the particle backscattering coefficient b_{bp} as well as between the coccolith concentration and b_{bp} . The effect of the river run-off on the b_{bp} values was also found - the changes of surface salinity, *S*, and of the particle backscattering coefficient, b_{bp}, along the ship track were in contrary directions. It was hard to separate out the effects of the coccolithophore bloom and the river run-off because the latter also affected the coccolithophore bloom.

Pronounced discrepancies in the appearance and spatial distribution of the enhanced values of b_{bp} were found in the subsequent years. In 2004, 2005, 2007 and 2009 the area of the enhanced values of b_{bp} was mainly observed in the coastal zone; it is believed that can be caused by both the coccolithophore bloom and the river run-off. In 2006 and 2008 that covered the essential part of the eastern open sea and was separated off the coastal zone; no doubt that was caused by the coccolithophore bloom. In 2008 the highest values of b_{bp} were observed in the latter half of June whereas in 2009 they occurred in the end of May.

Joint analysis of satellite data on the particle backscattering coefficient b_{bp} and the sea surface temperature *SST* has revealed very close connection in the eastern open part between the highest values of b_{bp} in June and the monthly mean of *SST* in February (the coldest month in winter season). As seen from Figure 1, their changes are in antiphase, and the highest values of b_{bp} are observed after a cold winter.

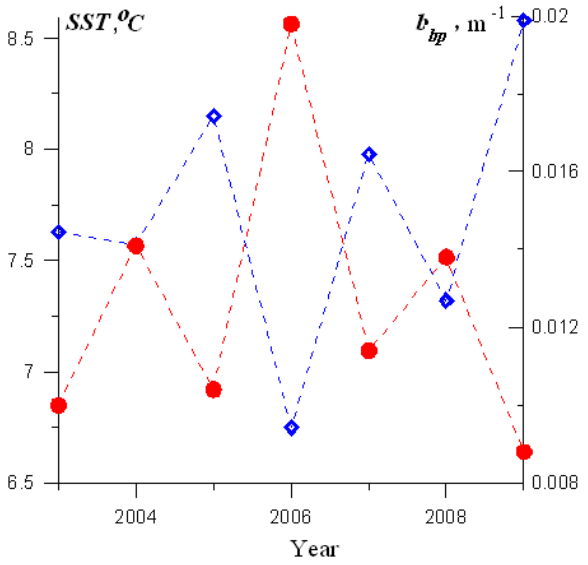

Figure 1. Interannual changes of the monthly means of the sea surface temperature (blue) and of the particle backscattering coefficient (red) in the eastern open part of the Black Sea in June.

Figure 2 shows spatial distributions of the b_{bp} values in June in 2006 and 2009. As seen, the distributions are quite different, and in 2006 the b_{bp} values were much higher than in 2009. This discrepancy may be linked to a noticeable difference in the winter *SST*: the monthly mean in February was 6.75°C in 2006 and 8.58°C in 2009.

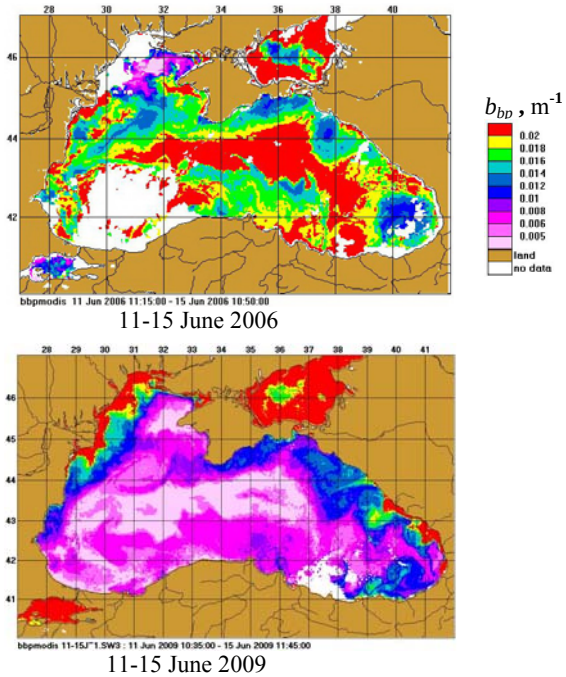

11-15 June 2006

11-15 June 2009

Figure 2. Spatial distributions of the particle backscattering coefficient in the Black Sea averaged over 11-15 June 2006 (top) and 11-15 June 2009 (bottom).

A possible explanation of the observed phenomenon is the more intensive vertical convection after cold winter promoting the biogen inflow to the near-surface layer.

4. CONCLUSION

The most interesting feature of the Black Sea observed from satellite data is that the basin grows turbid in each June from year to year, and intensity of that phenomenon can be linked to the winter sea surface temperature.

ACKNOWLEDGEMENTS

SeaWiFS and MODIS data used were obtained from the Goddard Distributed Active Archive Center under the auspices of the National Aeronautics and Space Administration.

REFERENCES

References from Journals:

Burenkov, V., O. Kopelevich, L. Pautova et al. (2005). "Possible causes of the increased content of suspended particles in the northeastern part of the Black Sea in June", Oceanology, vol. 45, Suppl. 1, pp.39-50.

Burenkov, V., O. Kopelevich, S. Sheberstov et al. (2007). "The June maxima of the particle backscatter in the Black Sea: results of three years satellite and field studies". Proceedings of IV International Conference "Current Problems in Optics of Natural Waters (ONW'2007)". Nizhny Novgorod. pp. 157-160.

Cokacar, T., N. Kubilay, T. Oguz (2001). "Structure of E. huxleyi blooms in the Black Sea surface waters as detected by SeaWiFS imagery". Geophys. Res. Lett.. vol. 28, pp. 4607-4610.

Cokacar, T., T. Oguz, N. Kubilay (2004). "Interannual variability of the early summer coccolithophore blooms in the Black Sea: impacts of anthropogenic and climatic factors". Deep Sea Research, vol. 51, Part 1: Oceanographic Research Papers, pp. 1017-1031.

Kopelevich, O., V. Burenkov, S. Ershova et al. (2004). "Application of SeaWiFS data for studying variability of bio-optical characteristics in the Barents, Black and Caspian Seas". Deep-Sea Research II, vol. 51, pp. 1063-1091.

Kopelevich, O., V. Burenkov, S. Sheberstov (2008). "Case Studies of Optical Remote Sensing in the Barents Sea, Black Sea, and Caspian Sea". Remote Sensing of the European Seas, Vittorio Barale, Martin Gade, (Eds.). Springer, pp. 53-66.

Kopelevich, O., V. Burenkov, S. Sheberstov, S. Vazyulya, E. Bayanova (2009). "Monthly distributions of bio-optical characteristics in the Russian Seas from satellite ocean color data in the period 1998-2008". Proceedings of the Y International Conference Current problems in Optics of Natural Waters (ONW 2009), St. Petersburg, pp. 115-120.

References from Websites:

Kopelevich, O., V. Burenkov, S. Sheberstov, S. Vazyulya, E. Bayanova, E. Lukyanova (2009). Bio-optical characteristics of the Barents, White, Black, and Caspian Seas from data of satellite ocean color scanners. Moscow, Russia. http://optics.ocean.ru.

Long-term (2002-2006) accuracy assessment of a new multi-algorithm method for detecting harmful algal blooms of *Karenia brevis* along the central west Florida shelf

Gustavo A. Carvalho [a,b], Peter J. Minnett [a,b], Lora E. Fleming [b,c], Viva F. Banzon [a,d], Warner Baringer [a], Mariana Framinan [a], Cynthia A. Heil [e]

[a] University of Miami - Rosenstiel School of Marine and Atmospheric Science, Meteorology and Physical Oceanography - gcarvalho@rsmas.miami.edu
[b] NSF NIEHS Oceans and Human Health Center, University of Miami
[c] University of Miami - Miller School of Medicine, Department of Epidemiology and Public Health, Miami, FL.
[d] Now at Remote Sensing & Applications Division, National Climatic Data Center (NOAA-NESDIS), Asheville, NC, USA
[e] Florida Fish and Wildlife Conservation Commission, Fish and Wildlife Research Institute, St. Petersburg, FL.

Abstract: A yearly basis analysis verifies the robustness of a new multi-algorithm method for detecting harmful algal blooms of *Karenia brevis* along the central west Florida shelf. The detection results are satisfactory if the entire dataset is analyzed together.

Keywords: MODIS, harmful algal bloom, Florida coast.

1. INTRODUCTION

Harmful algal blooms (HABs) of the toxic marine dinoflagellate *Karenia brevis* are commonly observed along the west coast of Florida. Besides causing recurring negative economic and ecological consequences, the so-called Florida Red Tide is a major causative factor of human health problems. Water quality monitoring for the occurrence of *K. brevis* blooms is essential, and thereby a fundamental requirement for mitigation efforts and sustainable resource management. Carvalho et al. (2010c) have tested the performance of a new multi-algorithm method that uses satellite measurements for the remote identification of *K. brevis* blooms along the central west Florida shelf (CWFS) during the boreal Summer-Fall period (i.e. July to December). Details of this Hybrid Scheme at: http://etd.library.miami.edu/theses/available/etd-04162008-210856/. A brief overview is given in the following.

1.1. The Hybrid Scheme

The Hybrid Scheme uses two different algorithms: the Bio-optical Technique, described in Canizzaro (2004), and the Empirical Approach, introduced in Carvalho (2008). These two algorithms have successfully, and similarly, mapped the location of a field-verified *K. brevis* bloom at the end of August 2001 in SeaWiFS and MODIS-Terra imagery (Carvalho et al., 2010a). Within geographical (CWFS) and seasonal (July-December) constrains, optimized versions of the Bio-optical and Empirical algorithms have shown similar success in automatically identifying the Florida Red Tide in a long time-series of MODIS-Aqua data from July, 2002 to October, 2006 (Carvalho et al., 2010b). Since the classification of each pixel into the presence or absence of the Florida Red Tide by each algorithms is not necessarily the same, their combined use provides a mechanism for better synoptic mapping of *K. brevis* blooms, and a measure of the confidence of the identification (Carvalho et al., 2010c).

1.2. Bio-optical Technique

This technique suggests that HAB-positive pixels should be identified with a classification scheme based on two criteria: satellite measured particulate backscatter (b_{bp}(550nm)) lower than the value calculated with Morel (1988) model, simultaneously occurring with high chlorophyll (Chl>1.5mg/m^3). Meanwhile, cases not meeting these two criteria are classified as HAB-negative.

1.3. Empirical Approach

This approach is very similar to the Bio-optical Technique but identifies pixels to be HAB-positive based on the value of a precursor to $b_{bp}(\lambda)$ in the ocean color processing chain, i.e. water-leaving radiance (L_w(550nm)), that must be lower than the magnitude of total scatter (b(550nm)) calculated with Morel (1988) model, as a function of Chl. HAB-negative cases are those not meeting this condition.

1.4. Objective

The main goal of this study proposes to verify the performance of the Hybrid Scheme with a yearly basis analysis for verifying the annual robustness of the method for strengthening possible operational applications.

2. METHOD

The methodology of current investigation follows the steps of Carvalho et al. (2009b). Figure 2 in Carvalho et al. (2010c) shows a flowchart summarizing the processing steps used to determine the long-term capabilities of the Empirical Approach and the Bio-optical Technique.

2.1. Data

Data from the the MODIS sensor onboard the Aqua satellite (see http://oceancolor.gsfc.nasa.gov/cgi/browse.pl?sen=am) were processed with the SeaDAS software package, version 5.0.3 (http://oceancolor.gsfc.nasa.gov/seadas), and all level-1A files were radiometrically calibrated and geometrically corrected to produce independent level 2 (L2) data products using MSL12,4 version 5.2.3. The *in situ* validation occurred with a comprehensive *in situ* database of the abundances of *K. brevis* (cells l^{-1}), provided by the Florida Fish and Wildlife Conservation Commission's Fish and Wildlife Research Institute. These match-up pairs are used to determine the individual accuracy of the Bio-optical and Empirical algorithms and to assess the robustness of the Hybrid Scheme.

2.2. Accuracy assessment

The assessment of the accuracy of the algorithms in discriminating between HAB (containing 1.5x10^4 cells l^{-1}) from non-blooming conditions (containing < 1.5x10^4 cells l^{-1}) is evaluated with basic statistical metrics: specificity, false negatives, sensitivity and false positives are invoked along with the positive and negative predictive values (and

its inserses). The overall accuracy is also computed. These statistics are strongly influenced by the prevalence of red tide, i.e. the observed frequency of red tide expressed as the ratio between the red tide samples and the total population. In a flawless algorithm, all *a priori* known red tide samples would be correctly flagged as HAB-positive at the same time as all existing non-boom cases are expected to be classified as HAB-negative.

3. RESULTS

The overall accuracy of the Hybrid Scheme is good (Table A), ranging from 68% (in 2006) to 83% (in 2002 and 2005). Conversely, a more detailed examination of the basic statistical metrics revels that the sole use of this measure misleads the user. Table B depicts the sensitivity and specificity values – the percentages of false negatives and false positives, respectively, can be found by subtracting these values from 100. Table C shows the positive and negative predictive values (their inverse can also be calculated in the same manner as the false conditions). It can be seeing that the low value of the prevalence of red tide (Table D) has a strong influence over the basic statistical metrics, especially in the first 3 years where the weak positive predictive values are observed.

4. CONCLUSIONS

The performance of the Hybrid Scheme is good if taking into account measurements of overall accuracy (Table A). However, the analysis accounting for each years separately demonstrates that the small incidence of valid red tide match-ups (i.e. low prevalence of red tide; Table D) has an influence on the final accuracy of the Hybrid Scheme. This is particularly noted in the first three years on the in relation to the positive predictive value. On the whole, the robustness of this new multi-algorithm method is also satisfactory if the entire dataset is analyzed together (Tables B and C).

Table A. Overall Accuracy of the Hybrid Scheme

Years	Overall accuracy
2002	(3+46)/(5+54) = 83%
2003	(5+35)/(8+46) = 74%
2004	(5+39)/(5+54) = 75%
2005	(79+27)/(89+39) = 83%
2006	(24+30)/(38+33) = 76%
All	**(116+177)/(145+226) = 79%**

Table B. Specificity and sensitivity of the Hybrid Scheme

Years	Sensitivity	Specificity
2002	3/5 (60%)	46/54 (85%)
2003	5/8 (63%)	23/46 (76%)
2004	5/5 (100%)	39/54 (72%)
2005	79/89 (89%)	27/39 (69%)
2006	24/38 (63%)	30/33 (90%)
All	**116/145 (80%)**	**177/226 (78%)**

Table C. Predictive values of the Hybrid Scheme

Years	Positive predictive value	Negative predictive value
2002	3/11 (27%)	46/48 (96%)
2003	5/17 (27%)	23/38 (92%)
2004	5/20 (25%)	39/39 (100%)
2005	79/91 (87%)	27/37 (73%)
2006	24/27 (88%)	30/44 (68%)
All	**116/165 (70%)**	**177/206 (86%)**

Table D. Prevalence of red tide of the Hybrid Scheme

Years	Prevalence of red tide
2002	(5/59) = 9%
2003	(8/55) = 15%
2004	(5/59) = 9%
2005	(89/128) = 70%
2006	(38/71) = 54%
All	**(145/371) = 39%**

REFERENCES

Cannizzaro, J.P., 2004. Detection and quantification of *Karenia brevis* blooms on the West Florida Shelf from remotely sensed ocean color imagery. M.S. Thesis, 71pp., University of South Florida at St. Petersburg, FL.

Carvalho, G.A., 2008. The use of satellite-based ocean color measurements for detecting the Florida Red Tide (*Karenia brevis*), M.S. Thesis, 174pp., University of Miami RSMAS-MPO at Miami, FL, 11 April. Available at: http://etd.library.miami.edu/theses/available/etd-04162008-210856

Carvalho, G.A., Minnett, J.P., Banzon V.F., Baringer W., 2010a. Locating the Florida Red Tide (*Karenia brevis*) using SeaWiFS and MODIS data, Remote Sens Environ. (submitted)

Carvalho, G.A., Minnett, J.P., Banzon V.F., Baringer W., Heil C.A., 2010b. Long-term evaluation of three satellite ocean color algorithms for identifying harmful algal blooms (*Karenia brevis*) along the west coast of Florida, Remote Sens Environ. (submitted)

Carvalho, G.A., Minnett, J.P., Fleming, L.E., Banzon V.F., Baringer W., 2010c. Satellite remote sensing of harmful algal blooms: A new multi-algorithm method for detecting the Florida Red Tide (*Karenia brevis*), Harmful Algae. (accepted)

Morel, A., 1988. Optical modeling of the upper ocean in relation to its biogenous matter content (case I waters). J. Geophys. Res. 93, 10,749-10,768

Arctic marine primary production in respect to changes in sea ice cover.

A. Cherkasheva [a,*], A. Bracher [b], C. Melsheimer [c]

[a] Helmholtz Graduate School for Polar and Marine research POLMAR, Institute of Environmental Physics, University of Bremen, Germany – acherkasheva@uni-bremen.de
[b] Helmholtz University Young Investigators Group PHYTOOPTICS, AWI, Bremerhaven and Institute of Environmental Physics, University of Bremen, Germany – astrid.bracher@awi.de
[c] Institute of Environmental Physics, University of Bremen, Germany – melsheimer@uni-bremen.de

Abstract – This study provides up-to-date information on the primary production (PPR) changes in the Arctic. PPR values retrieved from different sensors data (MERIS, MODIS, SeaWiFS) are taken into account. The impact of factors, driving primary production change in the Arctic is estimated by comparing PPR values to sea ice, wind speed, sea surface temperature (SST), chlorophyll-a (CHL) and Photosynthetically Active Radiation (PAR) satellite data. Results will be validated by Polarstern Cruise ARK XXV (June-July 2010), as well as by AWI, PANGAEA, NASA SeaBASS in-situ data.

Keywords: primary production modeling, validation.

1. INTRODUCTION

The influence of the rapid changes in sea ice coverage on Arctic marine primary production has not been studied so far due to the lack of sufficient in-situ measurements and gaps in satellite data in high latitudes.

To study this in more detail we want to investigate the interaction between the changing sea ice coverage, other physical parameters (*e.g.* sea surface temperature, wind field/ocean currents) and phytoplankton biomass and primary production in the Arctic Ocean by using in-situ, remote sensing and modeling techniques.

2. DATA AND METHODS

Primary production (PPR) maps, representing PPR averaged for every month of the years 2002-2007, were obtained using the Vertically Generalized Primary production Model by Behrenfeld and Falkowski (1997) (VGPM). The standard VGPM primary production dataset of Oregon State University is based on MODIS CHL, MODIS SST and SeaWiFS PAR data. It does not fully cover the years after 2007 due to the problems with SeaWiFS data delivery. For this reason it was supplemented by the dataset from the sensor MERIS on ENVISAT.

Additional CHL and PPR data was taken from GlobColour web-site, the European service for ocean color data. GlobColour primary production, as compared to the standard VGPM PPR dataset, should give more reliable results since it is based on the 3-sensor merged MERIS-MODIS-SeaWiFS chlorophyll-a data. Unfortunately Glob-Colour PPR is a demonstration product available for just one particular year (2003) and therefore was taken only for a comparison. The differences between standard VGPM PPR (Figure 1) and GlobColour PPR (Figure 2) in July 2003 can be seen in the figures.

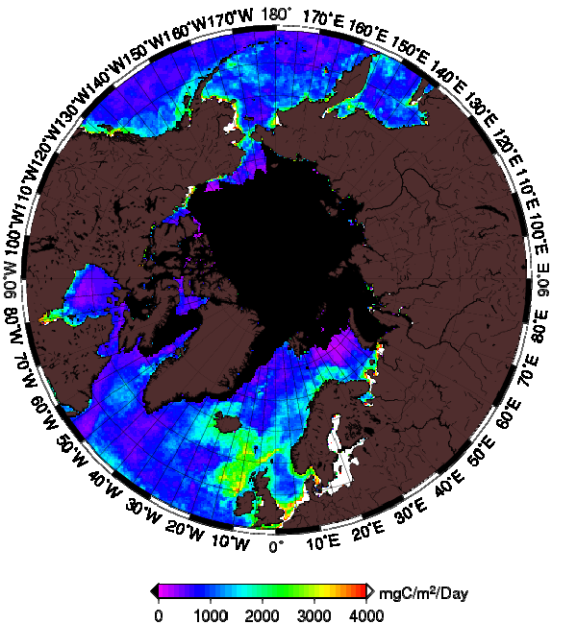

Figure 1. July 2003 primary production, grid spacing 1/6°, VGPM with SeaWiFS PAR, MODIS SST and CHL as input parameters.

To investigate the various factors influencing primary production variability in the Arctic, data of sea surface temperature (MODIS), wind speed (ECMWF reanalysis data), sea ice cover (PHAROS group, University of Bremen), chlorophyll-a (merged GlobColour MERIS-MODIS-SeaWiFS) and PAR (SeaWiFS) were used to produce maps with the same time averaging as PPR maps and then analyzed in respect to primary production variability.

Our results were compared to the studies of Arrigo *et al.* (2008) and Pabi *et al.* (2008). Arrigo *et al.* (2008) and Pabi

* Corresponding Author: IUP, University of Bremen, POBox 330440, 28334 Bremen, Germany. Tel: +49-421-218-62182; fax: +49-421-218-4555

et al. (2008) also studied the PPR variability in the Arctic, but with different input data and a different primary production model.

VGPM is a global model and therefore may have errors in output for not taking into account regional features of the Arctic waters. The next step of our work is to obtain the parameters that depend on the vertical structure of the waters and strongly vary regionally (such as z_{eu} – depth of the euphotic layer) not from the satellite (which is the standard approach), but from *in situ* measurements.

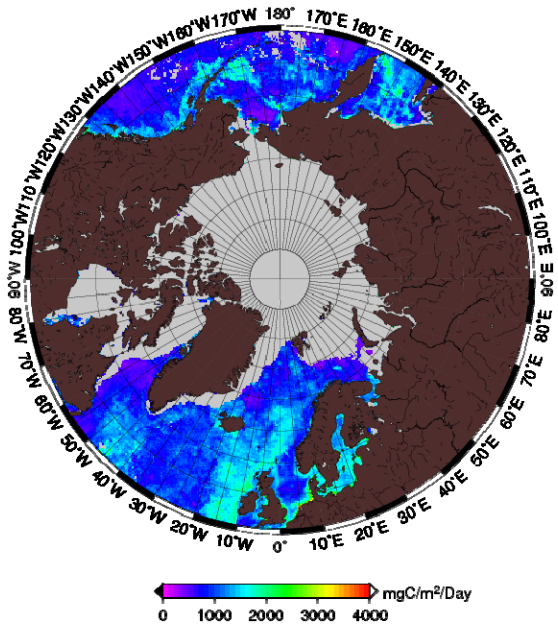

Figure 2. July 2003 primary production, grid spacing 1/12°, GlobColour product with MERIS PAR and merged MERIS-MODIS-SeaWiFS CHL as input parameters.

Chlorophyll-a and primary production values are then planned to be compared to those obtained from the coupled ocean-ice-ecosystem model by Losch *et al.* (2008) to give suggestions for improving this model for the application to the Arctic Ocean. Results of the comparison shall determine whether the model spatial resolution is sufficient to capture the variability observed by satellite (*i.e.* the most comprehensive validation data currently available). Spatial patchiness in the satellite data will be assessed and compared with the range in model data at all available resolutions.

3. VALIDATION OF RESULTS

The available *in situ* primary production data from the Arctic are not enough for judging the quality of our PPR estimates. Therefore, results will be validated by the primary production modeled from available bio-optical and oceanographic in-situ data.

For this purpose we plan to use the same model as in the case of satellite data (VGPM) and input *in situ* data from AWI, PANGAEA and NASA SeaBASS archives. However, it is a challenge to find all of the parameters required to construct PPR using VGPM (CHL, PAR, SST and z_{eu} parameters) taken at the same time and place. This motivated us to additionally collect all data needed during the ARK XXV Polarstern cruise (June-July 2010).

4. CONCLUSION.

In our study we have analyzed both standard (Oregon State University VGPM) and present-day (GlobColour merged MERIS-MODIS-SeaWiFS) primary production datasets. The influence of oceanographic and bio-optical factors on primary production variability was studied by comparing PPR datasets to the ones of sea surface temperature (MODIS), wind speed (ECMWF reanalysis data), sea ice cover (PHAROS group of University of Bremen), chlorophyll-a (merged GlobColour MERIS-MODIS-SeaWiFS) and PAR (SeaWiFS). Results were compared to Arrigo *et al.* (2008) and Pabi *et al.* (2008) which refer to similar subject.

Our future plans are to use in-situ datasets in order to not only validate PPR estimates, but as well account for regional Arctic features in the global VGPM model. The final results will be used to improve the coupled ocean-ice-ecosystem model by Losch et al.

ACKNOWLEDGEMENTS

The study is being carried out with the financial support of POLMAR Helmholtz Graduate School for Polar and Marine research. Funding has been supplied to one of us (A. Bracher) by the Helmholtz Impuls and Network Fond and the Alfred-Wegener-Institute (Project: PHYTOOPTCS). The authors are thankful to ESA, NASA, GlobColour and Robert O'Malley (Oregon State University, USA) for data delivery and M. Huntemann and T. Dinter (University of Bremen, Germany) for the help in data processing.

REFERENCES

Arrigo, K. R., G. van Dijken, and S. Pabi (2008). “Impact of a shrinking Arctic ice cover on marine primary production”. Geophysical Research Letters, vol. 35, L19603, doi:10.1029/2008GL035028.

Behrenfeld, MJ, PG Falkowski (1997). “Photosynthetic rates derived from satellite-based chlorophyll concentration”. Limnology and Oceanography, vol. 42, 1-20.

Losch, M., M. Schröter, S. Hohn, & C. Völker (2008). “High-resolution modelling of phytoplankton distribution and adaptation”. NIC Symposium 20-21 February 2008, Forschungszentrum Jülich; proceedings (NIC series 39)/ organized by John von Neumann Institute for Computing. Ed. by Gernot Münster, Forschungszentrum Jülich, 289-296.

Pabi, S., G. L. van Dijken, and K. R. Arrigo (2008). “Primary production in the Arctic Ocean, 1998–2006”. J. Geophys. Res., 113, C08005, doi:10.1029/2007JC004578

Assimilation of MODIS chlorophyll data with a physical-ecosystem model of the Western English Channel

S. Ciavatta [*], R. Torres, T. Smyth

Plymouth Marine Laboratory, Plymouth, United Kingdom – s.ciavatta@pml.ac.uk, rito@pml.ac.uk, TJSM@pml.ac.uk

Abstract – Ocean colour data collected by MODIS in 2006 were assimilated in a coupled 3D hydrodynamic-ecosystem model (POLCOMS-ERSEM) of the Western English Channel (WEC, UK) by means of the localized Ensemble Kalman Filter (EnKF). The WEC encompasses coastal, shelf waters and open ocean inputs. Five day composites of surface chlorophyll-a were used and the assimilation results were compared with in-situ observations collected at one monitoring station. The observations include nutrients, chlorophyll-a and phytoplankton biomass of several functional groups in coastal regime (station L4, weekly data). The results show that the assimilation of satellite products lead to the improvement in the model performance with respect to the "free simulation". These results indicate that the assimilation of remote sensed data is a feasible and promising approach for improving our understanding of carbon dynamics in shelf seas.

Keywords: data assimilation, carbon cycle, shelf seas.

1. INTRODUCTION

Assimilation of satellite ocean colour data with coupled physical-ecosystem models have been proved to be a useful approach to hindcast the evolution of biogeochemical variables in ocean systems, e.g. Gregg (2008). Nevertheless, few applications dealt with shelf-seas systems, because, on one hand, the complexity of the hydrodinamic-biogeochemical processes to be modeled, and, on the other, the uncertainty of ocean colour data in areas influenced by land inputs of coloured dissolved organic matter (CDOM) and suspended solids (Fontana *et al.*, 2009).

The aim of the present work is to investigate the improvements of chlorophyll and nutrient hindcasts in the Western English Channel lead by the application of a data assimilation system for ocean colour data based on the Ensemble Kalman Filter (Evensen, 2004) and the European Regional Seas Ecosystem model (ERSEM-2004, Blackford *et al.*, 2004)

2. METHODS

2.1 The study area and the data

The Western English Channel (WEC) is a shallow channel (<100m) that separates the south of the UK from mainland Europe. The WEC is in a boundary region between oceanic and neritic waters, with a wide range of shelf environments ranging from tidally mixed waters to seasonally stratified areas and frontal regions.

Surface chlorophyll values measured by MODIS in 2006 have been used. The individual images were processed by the NERC Earth Observation Data Acquisition and Analysis Service (NEODAAS) at the Plymouth Marine Laboratory. The original 1km pixel images were filtered with a 7km median filter to make the data equivalent to the 7km by 7km domain resolution of the model. The data was later combined into 5 day composites using a median function.

2.2 The physical-ecosystem model

The Western English Channel model (Lewis and Allen, 2009) couples a 3D finite difference hydrodynamic model (POLCOMS), a vertical turbulence model (GOTM) and the European Regional Seas Ecosystem model (ERSEM-2004, Blackford *et al.*, 2004). ERSEM is a Functional Group model that divides the ecosystem into aggregated groups representing basic functional roles (production, consumption and decomposition) for both the pelagic and benthic systems. These are subdivided into size classes to create a food-web with five phytoplankton groups, three zooplankton and one bacteria group including a dissolved and particulate detritus pool (Blackford *et al.*, 2004). Physiological processes and population dynamics are described by de-coupled fluxes of carbon and nutrients between functional groups.

2.3 The data-assimilation system

The data assimilation system here applied is based on the localized Ensemble Kalman Filter (EnKF) proposed by Evensen (2004). In the EnKF scheme, Gaussian errors are assigned to the model initial conditions and to model dynamics, generating an ensemble of model states, which are integrated forward in time. When observations are available, an analysis scheme is used to update the ensemble members. and the mean of the ensemble is taken as final solution. In the application here presented, the EnKF was run as a "local analysis". This means that each water column in the model is assimilated independently so that only the covariances that exist within each water column are taken into consideration. This has the benefits of spatial differences in ecosystem functioning/status (i.e. coastal waters – stratified – mixed shelf waters) being accounted for. The pixels used in the assimilation on each water column are selected within a radius of 25km or 49 pixels which ever is larger in waters deeper than 40m. In shallower depths, the search radius is limited to 7km and 9 pixels to account for the larger physical and biological heterogeneity of coastal waters

3. RESULTS AND DISCUSSION

The localized EnKF was applied to the weekly assimilation of the chlorophyll composites relative to the period January-

[*]Corresponding author. Prospect Place, Plymouth PL1 3DH, United Kingdom, Tel.:+44 (0)1752 633429..

April 2006, when phytoplankton blooms were observed in the Western English Channel. Figure 1 exemplifies the outcome of an assimilation step, on 28 January 2006, showing the chlorophyll satellite data, the model forecast, and the chlorophyll distribution estimated by using the EnKF.

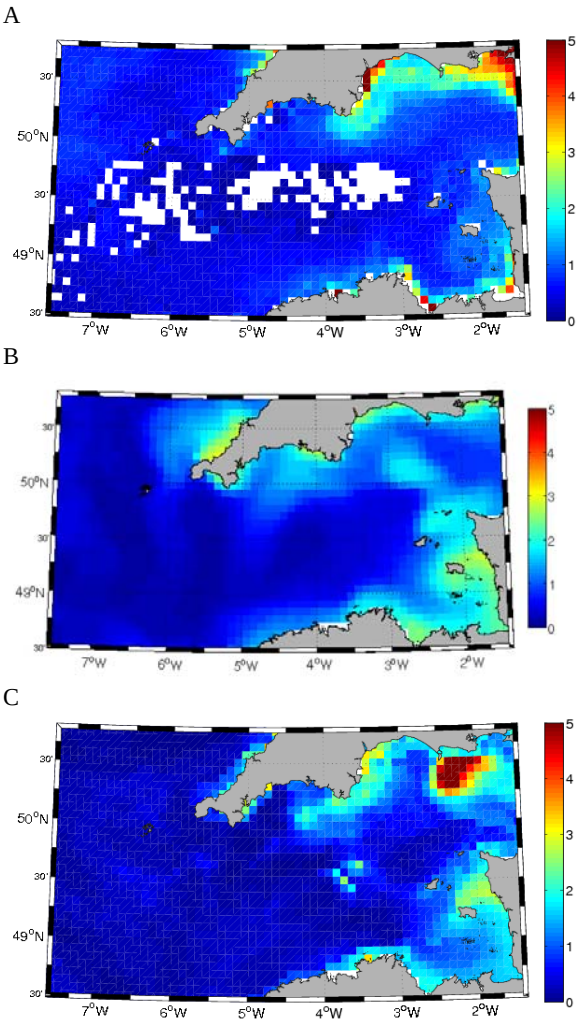

Figure 1. Surface distribution of chlorophyll a data (mg m-3) on 28 January 2006 from satellite data (A), model prediction (B), and EnKF correction (C)

As one can see in the figure A, the satellite estimates of the chlorophyll distribution were effected by the cloud coverage, leading to areas of missing data in the central part of the channel. The model overestimated the chlorophyll concentrations on the north coast of Cornwall (B), but the EnKF was capable to partly reconcile the model and satellite estimations (C). Nevertheless, Figure 1c shows also that the assimilation scheme can lead in some cases to spurious chlorophyll values (exemplified by the relatively high values on the up right corner). Such spurious values indicated that thinner localizations in the assimilation scheme should be adopted in the areas adjacent the coast, in order to contain the effect of high satellite values possibly due to riverine inputs of CDOM.

An example of the hindcast of nutrient concentrations provided by the assimilation scheme is shown in Figure 2. In the graph, the climatological evolution of nitrate observations at the sampling station L4, 7 miles South of Plymouth, is compared with the ensemble values forecasted by the model and with the ensemble values corrected by the EnKF. As one can see, the assimilation scheme reduced, in most of the cases, the ensemble variance and aligned the ensemble mean values closer to the data.

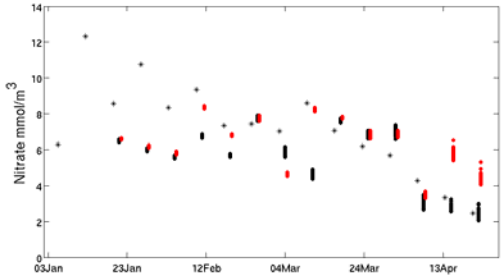

Figure 2. Climatological values of nitrate at station L4 (stars) compared with the ensemble model forecasts (black dots) and with the values corrected by the EnKF (red dots).

4. CONCLUSION

Data assimilation of ocean colour data is a useful approach for improving the hindcast of biogeochemical variables in shelf-seas. In particular, the adoption of an adequate localized assimilation scheme is relevant for dealing with anomalous observations related to external inputs of CDOM into the coastal areas.

ACKNOWLEDGEMENTS

This work was supported by the EU project ECOOP, NERC founding for Oceans2025 and the National Centre for Earth Observation (NCEO). The authors thank NEODASS for satellite data provision.

REFERENCES

Blackford, J.C., J.I. Allen and F.J. Gilbert (2004). “Ecosystem dynamics at six contrasting sites: a generic modelling study”. Journal of Marine Systems, vol. 52, pp. 191-215.

Evensen, G. (2004). “Sampling strategies and square root analysis scheme for the EnKF”. Ocean Dynamics, vol. 54, pp. 539-560.

Fontana, C., C. Grenz, C. Pinazo, P. Marsaleix and F. Diaz (2009). “Assimilation of SeaWiFS chlorophyll data into a 3D-coupled physical-biogeochemical model applied to a freshwater-influenced coastal zone”. Continental Shelf Research, vol. 29, pp. 1397-1409.

Gregg, W.W. (2008). “Assimilation of SeaWiFS ocean chlorophyll data into a three-dimensional global ocean model”. Journal of Marine Systems, vol. 69, pp. 205-225.

Lewis, K. and J.I. Allen (2009). “Validation of a hydrodynamic-ecosystem model simulation with time series data collected in the western English Channel”. Journal of Marine Systems, vol. 77, pp. 296-311.

Lidar identification of oil spills during the PRIMI cruise

F. Colao, R. Fantoni, L. Fiorani*, I. Menicucci, M. Nuvoli, A. Palucci, G. Terranova

Laser Applications Section, Italian National Agency for New Technologies, Energy and Sustainable Economic Development (ENEA), Frascati, Italy – luca.fiorani@enea.it

Abstract – The lidar fluorosensor POLI, developed by the Laser Applications Section of ENEA, participated to the PRIMI cruise. Thanks to optical filtering and electronic gating, POLI remotely sensed sea water also in daylight and was thus able to carry out H24 real-time oil spill identification. These measurements are good candidates for the cal/val of oil spill detection by radar and optical satellite sensors.

Keywords: POLI, lidar fluorosensor, oil spill.

1. INTRODUCTION

Illegal discharges and navigation accidents can produce oil spills that are a major threat for the marine ecosystems of the Mediterranean Sea. In this field, the Satellite Oceanography Group of CNR-ISAC (Italian National Research Council-Institute of Atmospheric Sciences and Climate) organized the first cruise to validate the Italian seas oil spill detection and forecast system developed within the ASI (Italian Space Agency) funded program PRIMI (pilot project on hydrocarbon marine pollution). The PRIMI system consists of four components: two oil slick detection subsystems by multi-platform SAR (synthetic aperture radar) and satellite optical imagery, an oil spill displacement forecast subsystem – based on numerical circulation models – and a central archive that provides a web-GIS (geographic information system) service to users (http://vlbiop.mt.asi.it). The system releases also meteorological, oceanographic and in situ information.

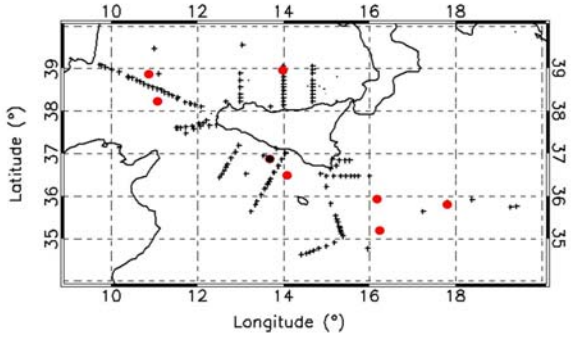

Figure 1. PRIMI cruise. Crosses and dots indicate hydrographic stations and oil spills, respectively.

In the framework of a validation cruise, the Laser Applications Section of ENEA (Italian National Agency for New Technologies, Energy and Sustainable Economic Development) deployed its LIF (laser-induced fluorescence) sensor POLI (POrtable LIdar fluorosensor) on-board the CNR R/V (research vessel) Urania. The validation cruise took place from August 6 to September 7, 2009, in the Sicily Strait, an area affected by intense oil tanker traffic (Fig. 1). During the cruise, POLI remotely sounded the water surface by operating H24, thus providing a real-time spatio-temporal picture of oil spills in a wide sea region. This information can be used for the cal/val of oil spill detection by satellite SARs (ASAR, ERS-2 and COSMO-SkyMed) and satellite multispectral optical sensors (MERIS, MODIS).

2. INSTRUMENTS AND METHODS

The main parts of a lidar fluorosensor are a frequency tripled Nd:YAG and a telescope detecting Raman scattering by water, LIF by CDOM (chromophoric dissolved organic matter) and algal pigments (chlorophyll-a, phycoerythrin and phycocyanin). The lidar fluorosensors developed at ENEA (Barbini *et al.*, 2001) are technological products of PNRA (Italian Antarctic research program) and participated to oceanographic campaigns in the Mediterranean Sea and Indian, Pacific and Southern Oceans. Thanks to narrowband filtering and electronic gating, LIF signals do not need corrections for radiometric and spectral characteristics of solar irradiance and surface reflectance. Furthermore, due to the short distance from the target, atmospheric effects are negligible. This explains why their data can be regarded as sea truth and have been provided to WOOD (Worldwide Ocean Optics Database) of ONR (Office of Naval Research) and SeaBASS (SeaWiFS Bio-optical Archive and Storage System) of NASA (National Aeronautics and Space Administration). Moreover, they have been used for the calibration of the bio-optical algorithms (Barbini *et al.*, 2003) of the ocean colour satellite radiometers MERIS, MODIS and SeaWiFS.

Figure 2. POLI installed on the R/V Urania's mezzanine deck.

* Corresponding author. ENEA, Via Enrico Fermi 45, 00044 Frascati, Italy, tel.: +39-06-94005861, fax: +39-06-94005312.

All the POLI subsystems, i.e. laser source, collecting telescope, detection optics and acquisition electronics are completely new and allowed the miniaturization of the apparatus now contained in a fly case of 0.7×0.7×0.8 m^3 (Fig. 2), according to the guidelines of the MIUR FIRB Italian project MIAO (microsystems for hostile environments). The more important upgrades are the following: the laser source is now a diode-pumped frequency-tripled Nd:YAG with a repetition rate of 1 kHz, developed for POLI under our specifications; the collecting telescope is a variable focal Cassegrain telescope designed and realized in our laboratory; the detection optics is based in high reflectance dichroic mirrors and high transmission interference filters; the acquisition electronic has been modified in order to elaborate the larger number of lidar returns and integrates a noise subtracting module (patented). After the extreme cold of Arctic campaigns, the very high temperature of PRIMI cruise was a severe test bench for POLI.

3. RESULTS AND DISCUSSION

Oil spills can be identified by observing changes in signal amplitude on a spectral band peaked at the Raman emission, called here RSC (Raman spectral channel). Nevertheless, it has to be noted that, although a decrease in RSC is expected in most cases of deep UV (ultraviolet) laser excitation, it might be possible for near UV – like the 355 nm wavelength transmitted by POLI – that the RSC signal amplitude in presence of oil spills could increase because of the simultaneous presence of the total fluorescence acquired at the nominal position of the Raman emission. To overcome this problem, the BOF (background oil fluorescence) has been evaluated by a signal interpolation providing the baseline amplitude at the RSC. Eventually, RI (Raman intensity), a variable free from interference, has been obtained – subtracting BOF from RSC – and effectively correlated with oil type and thickness.

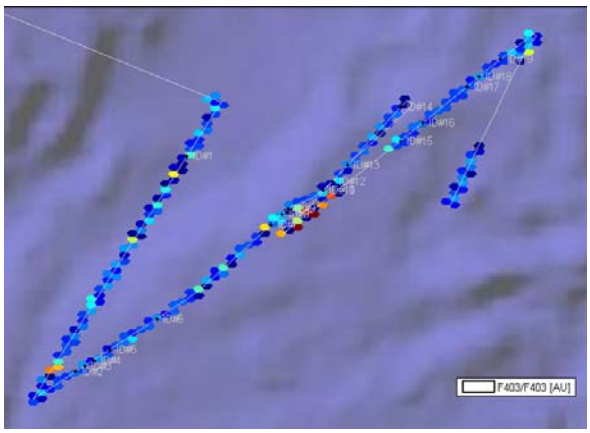

Figure 3. Oil slick detection by lidar. Measurement carried out on August 12, 2009, in the OS2 station. Dark blue colours correspond to RI below the threshold, orange/red/brown to high RI – identifying the oil slick – and intermediate colours to transition regions.

An example of oil slick detection is given in Fig. 3.

The ratio of RI measured inside and outside the oil spill is a function of thickness and attenuation coefficient of the oil film. The attenuation coefficient depends on the oil type and its value can be found in the literature. According to Hoge and Swift (1980) the following relation holds:

$$d = -(k_e - k_r)^{-1} \ln(R^*/R) \quad (1)$$

where d = oil spill thickness in m
k_e = oil attenuation coefficient at the excitation wavelength in m^{-1}
k_e = oil attenuation coefficient at the Raman wavelength in m^{-1}
R* = RI inside the oil slick
R = RI outside the oil slick

Although lidar is a fast tool for the identification of oil spills, it has to be noted that, according to Brown and Fingas (2003), it can not measure oil thickness larger than 10-20 µm, simply because the excitation UV laser light is completely absorbed by oil and does not reach the underlying water.

4. CONCLUSIONS

The lidar fluorosensor POLI has been successfully operated during the PRIMI cruise and provided oil spill identification. Although POLI could fail in case of very thick hydrocarbon slicks, this study shows that it is a useful tool for the fast identification of oil spills. This capability allows to discern between actual hydrocarbon slicks and false positives/negatives and thus to validate satellite oil spill detection.

ACKNOWLEDGEMENTS

The authors thank PRIMI for allowing the participation to the cruise, the chief scientists (Dr. F. Bignami and Dr. E. Böhm), the campaign participants and the R/V Urania's crew and technicians for their help on board. This work has been supported by CNR-funded R/V Urania's ship time.

REFERENCES

Barbini, R., F. Colao, R. Fantoni, L. Fiorani and A. Palucci (2001). "Remote sensing of the Southern Ocean: techniques and results". Journal of Optoelectronics and Advanced Materials, vol. 3, no. 4, pp. 817-830.

Barbini, R., F. Colao, R. Fantoni, L. Fiorani and A. Palucci (2003). "Lidar fluorosensor calibration of the SeaWiFS chlorophyll algorithm in the Ross Sea". International Journal of Remote Sensing, vol. 24, no. 16, pp. 3205-3218.

Brown, C.E. and M.F. Fingas (2003). "Review of the development of laser fluorosensors for oil spill application". Marine Pollution Bulletin, vol. 47, no. 9-12, pp. 477-484.

Hoge, F.E. and R.N. Swift (1980). "Oil film thickness measurement using airborne laser-induced water Raman backscatter". Applied Optics, vol. 19, no. 19, pp. 3269-3281.

Laser-induced fluorescence measurement of sea water bio-optical parameters during the SESAME campaign

F. Colao, R. Fantoni, L. Fiorani*, A. Palucci, M. Sighicelli

Laser Applications Section, Italian National Agency for New Technologies, Energy and Sustainable Economic Development (ENEA), Frascati, Italy – luca.fiorani@enea.it

Abstract – The laser spectrofluorometer CASPER and the lidar fluorosensor ELF, developed by the Laser Applications Section of ENEA, participated to the SESAME campaign. These sensors are based on laser-induced fluorescence and measure organic matter and algal pigments in sea water. Their data can be used to describe the environment monitored and for the cal/val of ocean colour satellite radiometers.

Keywords: laser-induced fluorescence, DOM, chlorophyll.

1. INTRODUCTION

Marine phytoplankton plays a major role in climate regulation. This explains the international efforts in the accurate monitoring of bio-optical parameters that provide useful information on algal biomass and its life cycle. An example of such studies is the oceanographic campaign organized by CNR-IBF (Italian National Research Council-Institute of Biophysics) in the frame of the integrated project SESAME (Southern European Seas: Assessing And Modelling Ecosystem changes) supported by the EC.

In the framework of the SESAME campaign, the Laser Applications Section of ENEA (Italian National Agency for New Technologies, Energy and Sustainable Economic Development) deployed its LIF (laser-induced fluorescence) sensors CASPER (Compact and Advanced laser SPEctrometer for Riade) and ELF (Enea Lidar Fluorosensor) on-board the CNR R/V (research vessel) Urania. The data acquisition took place from March 26 to April 6, 2008, in the Western part of Mediterranean Sea.

2. INSTRUMENTS AND METHODS

CASPER (Caputo-Rapti *et al.*, 2008) is a laser spectrofluorometer realized for the Italian project RIADE (integrated research for applying new technologies and processes for combating desertification) and is based on double filtration (30 μm and 0.22 μm) and double excitation (frequency quadrupled Nd:YAG laser emitting at 266 nm and diode laser emitting at 405 nm) in order to detect both dissolved and particulate components of natural waters coming from aquifers, rivers, lakes and seas. After the first filtration (30 μm), that eliminates unwanted materials, the sample contains both dissolved and particulate components and it is introduced in the first cuvette, where it can be irradiated by both wavelengths separately. The second filtration (0.22 μm) allows only the dissolved matter to pass into the second cuvette that, once more, can be crossed by a beam either at 266 nm or 405 nm. The double excitation extends the range of detectable components: the fluorescence yield of oils, polycyclic aromatic hydrocarbons, and proteins is higher if excited at 266 nm, while that of CDOM (chromophoric dissolved organic matter), chl-a (chlorophyll-a) and other algal pigments is higher if excited at 405 nm. Eventually, the emission spectra give information on the chemical composition of the samples: e.g. chl-a, if excited at 405 nm, will emit at about 680 nm. Once calibrated with known samples, CASPER reaches in absolute concentrations: e.g. 0.1 μg/l for chl-a and 0.1 mg/l for dissolved organic matter. CASPER is a good candidate for field campaign because it is battery operated, fully controlled by a portable computer and one measurement takes less than one minute, without further sample preparation.

ELF is one of the lidar fluorosensors developed by the Laser Applications Section of ENEA, already used for the cal/val of ocean colour satellite radiometers (Barbini et al., 2003). ELF is based on a Nd:YAG laser (transmitter) and a Cassegrain telescope (receiver). Thanks to optical filtering and electronic gating, it remotely senses weak optical signals also in daylight.

3. RESULTS AND DISCUSSION

The area of Northwestern Mediterranean shelf ecosystem, including the Lion Gulf, the Baleari Islands down to the Eastern costs of Sicily (Fig. 1), has been selected in order to investigate the human impact through the coastal ecosystem functioning. Moreover, this area is important also for the basic coastal ecosystem structure, involving the cycling and export of carbon, the energy budgets and the impact of river inputs on the behaviour of the pelagic and benthic coastal overall systems. Station 8, in the middle of this area, represents the starting point for a SW transect to Gibraltar, for a NW transect to the Lion Gulf and a link for the connection to Sicily.

During the SESAME campaign, ELF sounded remotely the surface layer operating H24 while CASPER analyzed water samples collected at the scheduled stations with Niskin bottles at different depths: in some sense, they are complementary instruments and can provide a spatio-temporal picture of CDOM and algal pigments in a wide marine region.

The thematic map of chl-a retrieved from ELF data during the SESAME campaign is given in Fig. 2. Large algal blooms have been identified in the Lion Gulf, with a spatial extent ranging from 50 to 200 km, and in the Spain and Sardinia costs. This feature reveals the capability of ELF to real-time address the scientific guidelines of the campaign.

* Corresponding author. ENEA, Via Enrico Fermi 45, 00044 Frascati, Italy, tel.: +39-06-94005861, fax: +39-06-94005312.

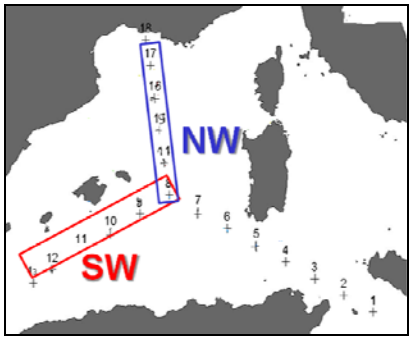

Figure 1. Transects and stations performed during the spring 2008 SESAME oceanographic campaign.

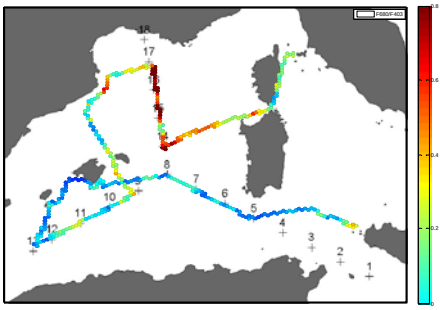

Figure 2. Thematic map of chl-a (Raman units) retrieved by ELF along the SESAME cruise.

During SESAME, a pore size of 0.8 μm was selected for the second filtration of CASPER, in order to discriminate the presence of nano-plankton in the marine samples.

The two CDOM fluorescence depth profiles, measured at 450 nm after the second filtration, along the SW and NW transects, are compared in Fig. 3. The presence of water masses containing CDOM is more evident in the SW transect – from the central station (8) to the last one (13), close to the Gibraltar Strait – with respect to the NW deep waters.

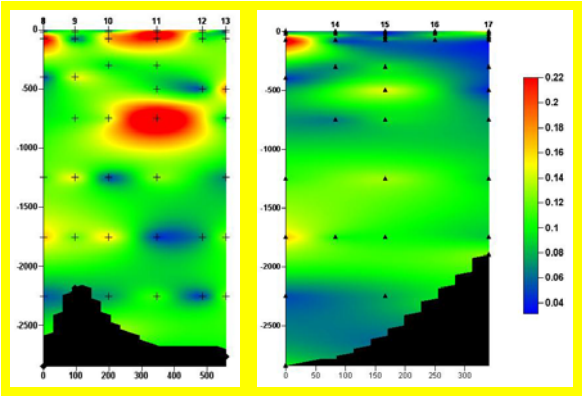

Figure 3. CDOM fluorescence depth profiles (Raman units) measured by CASPER along the SW (left) and NW (right) transects. The samples are indicated by the black symbols.

The ultraviolet fluorescence component, measured at 320 nm after the second filtration, has been ascribed to the emission of protein-like components. Its depth profiles along the SW and NW are shown in Fig. 4. In this case, it is more evident the difference in water masses between the two transects. In particular, it is noticeable the presence of two water stratification in the SW transect.

CASPER released also superficial Chl-a and CDOM distributions as well as depth distributions of Chl-a (after first and second filtration, in order to discriminated between micro-/nano- and pico-plankton), phycocyanin, CDOM and protein-like components (tyrosine and tryptophan).

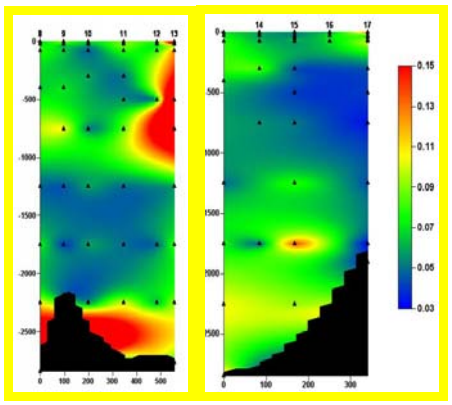

Figure 4. Protein-like fluorescence depth profiles (Raman units) measured by CASPER along the SW (left) and NW (right) transects. The samples are indicated by the black symbols.

4. CONCLUSIONS

The laser spectrofluorometer CASPER and the lidar fluorosensor ELF have been successfully operated during the SESAME campaign. They provided measurement of organic matter and algal pigments in a large area of the western part of Mediterranean Sea. From one hand, superficial data can be used for cal/val activities, from the other one, thematic maps and depth profiles give a picture of the spatio-temporal distribution of sea water bio-optical parameters, thus providing information on the biogeochemical cycles of the Mediterranean Sea.

ACKNOWLEDGEMENTS

The authors thank SESAME for allowing the participation to the campaign, Dr. C. Santinelli (chief scientist) and Prof. A. Seritti, the cruise participants and the R/V Urania's crew and technicians for their help on board.

REFERENCES

Barbini, R., F. Colao, R. Fantoni, L. Fiorani and A. Palucci (2003). "Lidar fluorosensor calibration of the SeaWiFS chlorophyll algorithm in the Ross Sea". International Journal of Remote Sensing, vol. 24, no. 16, pp. 3205-3218.

Caputo-Rapti, D., L. Fiorani and A. Palucci (2008). "Compact laser spectrofluorometer for water monitoring campaigns of Southern Italian regions affected by salinization and desertification processes". Journal of Optoelectronics and Advanced Materials, vol. 10, no. 2, pp. 461-469.

The Hyperspectral Imager for the Coastal Ocean (HICO) on the International Space Station

M.R. Corson [a,*], R.L. Lucke [a], O. Davis [b], A. Snyder [a], R. Korwan [a], R. Mcglothlin [c], D. Butcher [c], L. Wood [c]

[a] U.S. Naval Research Laboratory, Washington, DC, USA – mike.corson@nrl.navy.mil, robert.lucke@nrl.navy.mil, william.snyder@nrl.navy.mil, daniel.korwan@nrl.navy.mil,
[b] Oregon State University, Corvallis, OR, USA - cdavis@coas.oregonstate.edu
[c] Praxis, Inc., Alexandria, VA, USA – norm.mcglothlin.ctr@nrl.navy.mil, steven.butcher.ctr@nrl.navy.mil, dan.wood.ctr@nrl.navy.mil

Abstract – The Hyperspectral Imager for the Coastal Ocean, launched to the International Space Station in September 2009, is the first spaceborne hyperspectral imager optimized for environmental characterization of the coastal zone. From the Space Station orbit HICO provides access to a variety of coastal types worldwide for scientific study and environmental product algorithm development, and HICO imagery is used to produce maps including coastal bathymetry, organic and inorganic matter in the water, bottom characteristics, and water optical properties. This article will discuss the performance requirements of the spaceborne imager, the design of the flight hardware, and show examples of the environmental products retrieved from HICO imagery.

Keywords: hyperspectral, coastal remote sensing, space station

1. INTRODUCTION

Environmental characterization of the coastal ocean is a vital part of planning and executing naval operations in the coastal zone. The rapid and safe execution of operations ranging from military to humanitarian relief depends on accurate maps of bathymetry, water clarity, harmful blooms, and bottom characteristics. However, the coastal ocean is complicated, containing suspended and dissolved organic matter, suspended and dissolved inorganic matter, with a wide range of bottom types and depths, all of which can vary over tens to hundreds of meters. Spaceborne multispectral imagers such as MODIS and MERIS, which are successful at characterizing the relatively simple open ocean, generally do not provide sufficient information to characterize the complicated coastal environment.

Hyperspectral imaging has developed into a powerful tool for environmental characterization of the coastal ocean using remotely-sensed imagery. In contrast to multispectral imagers, a hyperspectral imager records a contiguous spectrum of the light received from each pixel in the scene. This extra spectral information can be exploited to produce the desired maps of environmental properties (Davis *et al.*, 2006). More than two decades of research at the U.S. Naval esearch Laboratory (NRL) and other laboratories has produced imaging system requirements and product algorithms to retrieve environmental information from hyperspectral imagers on aircraft platforms. A natural next step, building on this aircraft experience, is spaceborne hyperspectral imaging offering repeat access to the variety of coastal types distributed worldwide.

2. HICO DESIGN AND PERFORMANCE

2.1 HICO Design and Performance

The Hyperspectral Imager for the Coastal Ocean (HICO), sponsored by the U.S. Office of Naval Research (ONR) as a component of ONR's Innovative Naval Prototype (INP) program, is the first spaceborne hyperspectral imager optimized for the coastal ocean. As an INP, HICO must satisfy two goals: demonstrate a new ability to satisfy unmet naval needs for coastal characterization and demonstrate ways to dramatically reduce cost and time to produce space instruments. HICO achieves the first goal by producing maps of coastal bathymetry, water content and optical properties, and bottom type, which are currently unavailable from spaceborne instruments.

HICO's performance requirements are tailored for coastal environmental imaging, based on the heritage of decades of airborne experience and product validation. A primary performance requirement is high signal-to-noise ratio when imaging coastal scenes from space. Water scenes have low albedo, and are imaged through the Earth's atmosphere which is significantly brighter than the underlying water scene due to scattered sunlight. This atmospherically-scattered light must be removed because it contains no information about the water scene. However, removing the atmospherically-scattered light inevitably degrades the signal-to-noise ratio of the water scene after removal, leading to the initial high signal-to-noise ration requirement. HICO is designed and tested to have a signal-to-noise ratio greater than 200 to 1 for water-penetrating wavelengths when imaging a 5% albedo scene. HICO images over all water-penetrating wavelengths, with spectral binning of 5.7 nm which is sufficient to capture the shape of coastal ocean spectral features. HICO's ground sample distance, which is the footprint of a single image pixel on the water surface, is approximately 90 m, providing sufficient spatial resolution for this proof-of-concept demonstration. HICO's primary performance requirements, derived from airborne coastal hyperspectral experience at NRL and other laboratories, are shown in Table A.

* Corresponding author. Remote Sensing Division, U.S. Naval Research Laboratory, 4555 Overlook Ave. SW, Washington, DC 20375 USA. Telephone: (202) 404-2475. Fax: (202) 404-5689.

Table A. HICO Performance Parameters

Parameter	HICO Performance
Signal-to-noise ratio	> 200 to 1 for water-penetrating wavelengths
Wavelength range	400 to 900 nm
Spectral bin width	5.7 nm
Ground sample distance	90 m
Image scene width	42 km at nadir
Image scene length	190 km
Cross-track pointing	45 deg left to 30 deg right
Scenes per orbit	1 maximum

2.2 HICO Imager Fabrication and Launch

The second HICO goal as an Innovative Naval Prototype is to demonstrate innovative ways to reduce the cost and time required to build a space payload. HICO satisfied this goal by using Commercial-Off-The-Shelf components wherever possible. The spectrometer, CCD camera and computer are COTS items. Because the camera and computer are not designed to operate in vacuum they are housed in hermetic enclosures filled with nitrogen gas. A particularly interesting use of COTS hardware is the rotary mechanism used to point the HICO line of sight to maximize imaging opportunities. The mechanism is a commercial motorized rotary stage intended for use in a laboratory vacuum system. The HICO flight imager is shown in Fig. 1.

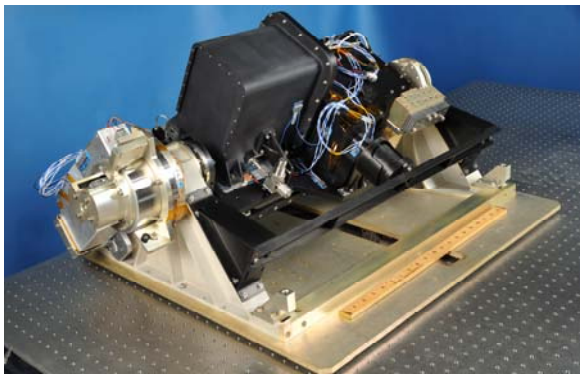

Figure 1. HICO flight imager. The ruler in this picture is 0.5 m long. (NRL photograph).

HICO was launched from the Japanese Aerospace Exploration Agency's Tanegashima Space Center on September 10, 2009. On September 24, 2009 the payload module containing HICO and a second NRL instrument, the Remote Atmospheric and Ionospheric Detection System (RAIDS), was docked to the Exposed Facility of the Japanese Kibo module on the International Space Station.

3. HICO ENVIRONMENTAL PRODUCTS

A preliminary example HICO product is the relative bathymetry map of an area of the Yellow Sea off the coast of South Korea (Fig. 2) The left panel shows a conventional color image made using 3 color bands (red, green, blue) from a HICO image of the scene. This picture shows extensive shallowly-submerged mud flats and channels formed by the tides. These mud flats and channels are dynamic, and safe navigation requires accurate bathymetry.

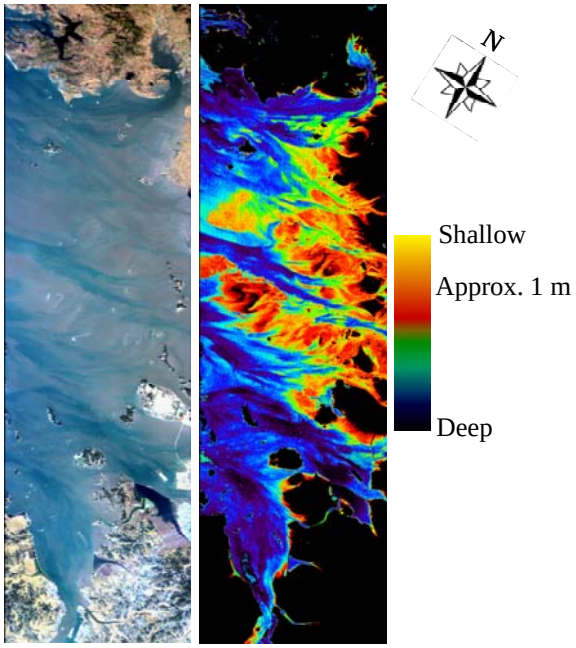

.

Figure 2. Left: Color picture of an area of the Yellow Sea off the coast of South Korea constructed using three HICO color bands. The scene is approximately 42 x 190 km. Right: False-color relative bathymetry map retrieved from HICO image data.

The right panel is a false-color relative bathymetry map produced using two selected HICO spectral bands. While this bathymetry map is qualitative and has not been validated, it does correspond well to the visible mud flats and channels in the picture on the left, indicating the potential of spaceborne hyperspectral imaging for environmental characterization of the coastal ocean.

4. CONCLUSION

The Hyperspectral Imager for the Coastal Ocean demonstrates the ability to produce coastal environmental products from spaceborne imagery. HICO and its products are pathfinders for future operational systems.

ACKNOWLEDGEMENTS

The relative bathymetry map in Fig. 2 was provided by C.M Bachmann at the Naval Research Laboratory, using the method of Bachmann (2008). HICO is launched and flown under the direction of the DoD Space Test Program.

REFERENCES

Bachmann, C.M., et al. (2008), "Very shallow water bathymetry retrieval from hyperspectral imagery at the Virginia Coast Reserve (VCR'07) multi-sensor campaign", Proceedings of the 2008 IEEE International Geoscience & Remote Sensing Symposium, Boston, MA, USA.

Davis C.O., K.L. Carder, B.-C. Gao, Z.P. Lee, and W.P. Bissett (2006), "The development of imaging spectrometry of the coastal ocean", IEEE Proceedings of the International Geoscience and Remote Sensing Symposium, 4, pp. 1982-1985.

Application of ocean color remote sensing in monitoring of the Southern Baltic Sea ecosystem

M. Darecki [a,*], P. Kowalczuk[a]

[a] Institute of Oceanology PAS, Sopot, Poland – darecki@iopan.gda.pl

Abstract – The optical properties of the Baltic waters, which represents an extreme example of optically-complex Case 2 waters, are mainly dominated by absorption by relatively high concentration of colored dissolved organic matter (CDOM). Optical signatures of Baltic Sea waters differ significantly from those of open oceans blue waters, so the remote sensing of the bio-optical characteristics of this ecosystem, has to be based on locally tuned or developed algorithms. The Remote Sensing Laboratory of the Institute of Oceanology PAS in Sopot have carried a research and development of remote sensing algorithms for the Baltic Sea for more than twenty years. The major achievements of the IOPAS in that field and ongoing activities will be presented.

Keywords: ocean color, case 2 waters, CDOM, Baltic Sea.

1. INTRODUCTION

The Baltic Sea is as an enclosed sea which is particularly vulnerable to the effects of economic development. Due to the social and economic importance of the Baltic Sea and high anthropogenic pressure on its ecosystem this area requires a regular monitoring of environmental processes. The effective Baltic Sea monitoring program need to incorporate field measurements, development of ecological and hydrodynamical models and implementation of remote sensing technology. The Baltic Sea has unique optical properties because of its semi-enclosed character, very high outflow of fresh water from the drainage area and limited water exchange with the North Sea. The Baltic Sea, located in the temperate climatic zone, undergoes a well established seasonal hydrological cycle, which shapes the inherent optical properties. Seasonal changes in the inherent optical properties have an impact on apparent optical properties, including changes of their spectral signature (Darecki et al., 2003; Kowalczuk et al., 2005). The optical properties of the Baltic waters differ significantly from those of open oceans, so the application of ocean color remote sensing for monitoring of the bio-optical characteristics of its ecosystem, has to be based on different algorithms. Development and validation of locally tuned empirical algorithms for retrieval of optically active water constituents, which were based on previously recognized seasonal dynamics of IOP's and AOP's, was main activity of the IOPAS's Remote Sensing Laboratory for over the last two decades.

2. *IN SITU* DATA AND METHODS

2.1 The study area and field observations program

The systematic long-term bio-optical observation program in the Baltic Sea carried out by the IOPAS has started in late 1980'ties and is continued by these days. The field measurements were conducted on more than 100 cruises in the southern Baltic Proper (Fig. 1) covering the months from February to May and September to November. The geographical coverage of the samples includes the Gulf of Gdansk, the Pomeranian Bay, Polish and German coastal waters and open sea (Baltic Proper). The observation program included *in situ* measurement of IOP's and AOP's and as well the water sampling for laboratory measurements of the sea water constituents. (see Olszewski et al. 1992, Darecki et al., 1995, Kowalczuk 1999)

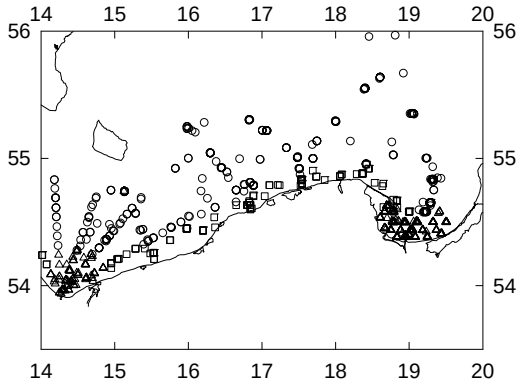

Figure 1. Location of the sampling stations. Most of the points represents over 20-50 samplings during the period 1990-2009

2.2 Radiometric measurements

The systematic measurements of the radiometric profiles of incident solar irradiance and upwelling radiance in the function of depth has started in 1993 with the use of variety of commercially available and developed at IOPAS radiometers systems, e.g.: Biospherical MER2040 and recently C-OPS , Satlantic OCP-100, and hyperspectral TRIOS Ramses sensors. This field measurement, conducted according to rigorous data acquisition protocols enabled to construct empirical algorithm for retrieval of the chlorophyll *a* concentration and CDOM absorption, that were applicable to local conditions in the Baltic Sea.

* Corresponding author. Institute of Oceanology, Polish Academy of Sciences, ul.Powstańców Warszawy 55, PL-81-712, Sopot, Poland, phone: +48 58 7311818, fax +48 58 551 2130

3. REMOTE SENSING ALGORITHMS FOR THE RETRIEVAL OF OPTICALLY ACTIVE SEA WATER CONSTITUENTS IN THE SOUTHERN BALTIC

3.1 Chlorophyll *a* concentration

Darecki et al. (2003) found a strong influence of CDOM absorption on the quantitative and qualitative features of spectral reflectance of two different water bodies with similar chlorophyll content. Therefore application of global algorithms for retrieval of chlorophyll *a* concentration e.g. OC4v4, in the Baltic Sea would lead to severe overestimation of this parameters (Darecki and Stramski, 2004). The empirical algorithm for estimation of chlorophyll a concentration have been proposed by Darecki et al., (2005) that has the following form:

$$Chla(Baltic4) = 10^{(-0.028-3.901R)} \quad (1)$$

where R=log (max(Rrs(443),Rrs(490),Rrs(510))/Rrs(*555*)). The accuracy of this algorithm in the Baltic Sea have been assessed for 26%.

3.2 CDOM absorption

The empirical algorithm for estimation of CDOM absorption in the southern Baltic Sea have been based on the nearly 600 radiometric measurements and simultaneous water sampling for spectrophotometric measurements of CDOM absorption performed between 1993 and 2001. The algorithm have been optimized for potential application of SeaWiFS and MODIS wavebands and optimized for local conditions (Kowalczuk et al., 2005). The empirical relationships between log-transformed spectral reflectance ratios and CDOM absorption coefficient at □ = 400 nm have a form of the second order polynomial:

$$a_{CDOM}(400) = 10^{(-0.29-0.708\cdot X+1.12\cdot X^2)} \quad (2)$$

where: X=log10(Rrs(490)/Rrs(555)). The performance of this algorithm have been assessed with use of the independent *in situ* data set of radiometric measurements and CDOM absorption coefficient product from SeWiFS and MODIS imagery. The locally tuned empirical algorithm showed the best performance when applied to SeaWiFS or MODIS satellite data, and CDOM absorption coefficient could be retrieved with an averaged accuracy of 25% (Kowalczuk et al. 2010)

3.3 Other bio-optical parameters

Responding to demand for remotely estimation various marine biooptical parameters, development of the new algorithms has been carried out at the IOPAS. Among many others, the algorithm for estimation of the euphotic zone depth (Ze) was recently developed:

$$Ze = 2.125+5.701*X-0.310*X^2 \quad (3)$$

where X=Rrs(490)/Rrs(665)
The RMS error when this algorithm is applied to the in situ data from the all seasons, is less then 20%

4. SYSTEMATIC SOLUTIONS FOR MONITORING OF THE BALTIC ECOSYSTEMS

Presented above the ocean color algorithms for estimation of bio-optical parameters in the Baltic Sea have been implemented in the monitoring scheme that utilized available information from satellite based Earth observing platforms into a system for monitoring the environmental state of the Baltic Sea. Recently developed system called DESAMBEM is a set of diagnostic models that assimilates the incident solar radiation, sea surface temperature and concentration of chlorophyll a data from various satellite sensors for estimation of primary production in the water column in the Baltic Sea (Woźniak et al., 2008, Darecki et al., 2008). The passive remote sensing methods can provide information over selected area only for cloud free, or partly cloudy conditions. Those conditions are very hard to achieve in high latitudes. Therefore it is essential to link the remote sensing with existing ecological and hydrodynamical models. Need for short range (of order of 2-5 day) ecological prognostic models capable to assimilate the information from satellite remote sensing platforms is the primary driver or research and development in the costal oceanography for next decade. The IOPAS have been recently awarded a major project funded through the European Commission Structural Funds to built an operational system for monitoring the Baltic Sea ecosystem that would link the ecological and hydrodynamical models with existing bio-optical models and satellite remote sensing observations. The project called SatBałtyk is in the start up phase and will be continued for the next 5 years.

ACKNOWLEDGEMENTS

This presentation was supported by the project SatBałtyk (WND-POIG.01.01.02-22-011 /09)

REFERENCES

Darecki M., A. Weeks, S. Sagan, P. Kowalczuk and S. Kaczmarek, 2003. Optical characteristics of two contrasting case 2 waters and their influence on remote sensing algorithms. Continental Shelf Research, 23(3-4), 237-250.

Darecki M. and Stramski D., (2004) Remote Sensing of Environment, 89/3, 326-350.

Darecki M., S. Kaczmarek and J. Olszewski, 2005. SeaWiFS ocean colour chlorophyll algorithms for the southern Baltic Sea. International Journal of Remote Sensing, 26(2), 247–260.

Darecki M., and Others, 2008. Algorithms for the remote sensing of the Baltic ecosystem (DESAMBEM). Part 2: Empirical validation: Oceanologia, 50(4), pp. 509-538.

Kowalczuk P., 1999. Seasonal variability of yellow substance absorption in the surface layer of the Baltic Sea. Journal of Geophysical Research, 104(C12), p. 30047-30058.

Kowalczuk P., J. Olszewski, M. Darecki and S. Kaczmarek, 2005. Empirical relationships between Coloured Dissolved Organic Matter (CDOM) absorption and apparent optical properties in Baltic Sea waters. International Journal of Remote Sensing, 26(2), 345-370.

Kowalczuk P., M. Darecki, M. Zabłocka and I. Górecka, 2010. Validation of empirical and semi-analytical remote sensing algorithms for estimating absorption by Colored Dissolved Organic Matter in the Baltic Sea from SeaWiFS and MODIS imagery. Oceanologia in press.

Olszewski, J., Sagan, S., Darecki, M., 1992. Spatial and temporal changes in some optical parameters in the southern Baltic. Oceanologia, 33, 87– 103.

Woźniak and Others, 2008a. Algorithm for the remote sensing of the Baltic ecosystem (DESAMBEM). Part 1: Mathematical apparatus: Oceanologia, 50(4), pp. 451-508

Data Processing and First Products from the Hyperspectral Imager for the Coastal Ocean (HICO) on the International Space Station

C.O. Davis [a *], R. A. Arnone [b], R. Gould [b], M.R. Corson [c], and M. Montes [c]

[a] Oregon State University, Corvallis, OR, USA - cdavis@coas.oregonstate.edu
[b] U.S. Naval Research Laboratory, Oceanography Division, Stennis Space Center, MS - arnone@nrlssc.navy.mil, gould@nrlssc.navy.mil
[c] U.S. Naval Research Laboratory, Washington, DC, USA – mike.corson@nrl.navy.mil, marcos.montes@nrl.navy.mil

Abstract – The Hyperspectral Imager for the Coastal Ocean (HICO) was installed on the International Space Station on September 24, 2009. HICO is the first spaceborne hyperspectral imager optimized for environmental characterization of the coastal zone. HICO data are collected and processed to produce maps including coastal bathymetry, bottom characteristics, and water column optical properties. Here we describe the HICO data processing system and give examples of HICO products.

Keywords: hyperspectral, coastal remote sensing, space station.

1. INTRODUCTION

The coastal ocean is a very complicated environment containing high levels of phytoplankton, suspended and dissolved organic matter, suspended sediments with various bottom types and depths, all of which can vary significantly on scales of tens to hundreds of meters. While multispectral ocean color imagers with 1 - 4 kilometer spatial resolution are excellent for imaging the open ocean the coastal ocean requires higher spatial sampling and multispectral data generally does not contain sufficient information to quantify and characterize the coastal environment (Davis et al. 2007). Over the past two decades, hyperspectral imaging from aircraft platforms has developed as a powerful method of characterizing the coastal environment. A hyperspectral imager records a contiguous spectrum of the light received from each pixel in the scene, and this extra spectral information is exploited to produce the desired maps of bathymetry, water constituents, and other coastal properties (Goetz, et al. 1985; Davis et al. 2006).

The Hyperspectral Imager for the Coastal Ocean (HICO) (Corson, et al. 2005) is the first spaceborne imaging spectrometer designed specifically to sample the coastal ocean. HICO will sample selected coastal regions at approximately 90 m with full spectral coverage (400 to 900 nm sampled at 5.7 nm) and a high signal-to-noise ratio to resolve the complexity of the coastal ocean. HICO is sponsored by the Office of Naval Research as an Innovative Naval Prototype (INP), and will demonstrate coastal products including water optical properties (absorption and scattering coefficients), bottom types, and bathymetry and on-shore vegetation maps. As an INP, HICO also demonstrates innovative ways to reduce the cost and schedule of this space mission including using Commercial Off-The-Shelf (COTS) components where possible. HICO was built in 16 months by the Naval Research Laboratory and was completed in July 2008 and integrated into the HICO and RAIDS Experimental Payload (HREP) in August 2008. HICO was integrated, launched and flown with support from and under the direction of the DoD Space Test Program. HREP was launched on the Japanese H-2 Transfer Vehicle (HTV) September 10, 2009. The HTV rendezvoused with the ISS on September 17, 2009. HREP was installed on September, 24, 2009 and the first HICO imagery was collected on September 25, 2009. HICO is operating normally and Image quality is excellent. A companion paper in this volume by Corson et al. discusses the HICO imager and its performance. Here we give an overview of the data handling and processing and we present results for coastal regions and river mouth areas.

2. HICO DATA PROCESSING SYSTEM

HICO is a demonstration sensor and data is collected for particular study areas, from a target list compiled by NRL personnel with input from Navy, university, and international partners. The standard HICO scene is 42 x 192 km and a maximum of one scene is collected on each 90 minute orbit. Data requests are compiled by NRL and sent to the ISS by NASA for execution. Data is transmitted from the ISS to NASA Marshall Space Flight Center and then transferred to NRL in Washington DC (NRL-DC) for processing. The initial processing from level 0 (raw data) to level 1b (calibrated radiances with geolocation information) includes dark current subtraction, CCD smear correction, 2nd order correction, spectral calibration and radiance calibration (Fig. 1).

The calibrated data are then sent to NRL Stennis Space Center (NRL-SSC) for further processing using the NRL SSC Automated Processing System (APS). APS was developed for processing SeaWiFS, MODIS and other multispectral ocean color data. It ingests level 1b data and produces a wide range of standard products. APS was modified in two fundamental ways to process HICO data: the capability to ingest full hyperspectral data cubes was added, along with the capability to apply hyperspectral algorithms to make a variety of products from that data. Thus, APS HICO has two processing lines: one for making standard APS products from HICO data convolved to multispectral bands and one for exploiting the full hyperspectral data. Using the multispectral line HICO data is binned spectrally to simulate MODIS data and then processed to produce all the standard MODIS products but at 90 m ground sample distance (GSD) instead of the MODIS 1 km GSD. This is important in coastal areas were the tides, diurnal winds, river outflow and bottom features create complex patterns in the coastal ocean (Fig. 2).

The Hyperspectral processing is more experimental. As HICO is the first ocean color hyperspectral sensor in space we have not previously developed automated processing for

hyperspectral ocean color data. The hyperspectral processing branch includes several options for atmospheric correction and product production. Additionally, the calibrated hyperspectral image cube is available and that data is being used at NRL, OSU and other universities and laboratories for developing new hyperspectral algorithms.

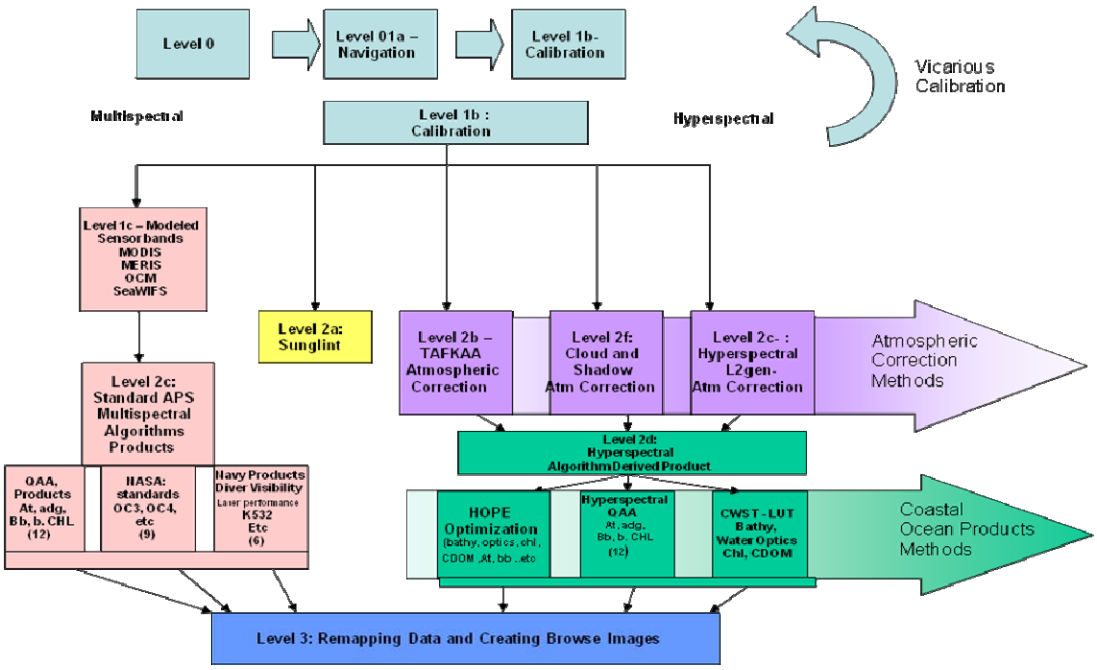

Figure 1. Flow diagram for the HICO data processing system. The initial processing from Level 0 to 1b (blue boxes) is done at NRL-DC. The remaining processing is done in APS at NRL-SSC. The multispectral processing line (pink boxes) is used to produce MODIS like products at 90 m GSD. The Hyperspectral processing line (purple and green boxes) uses multiple approaches for atmospheric correction and product production to test and evaluate new approaches to take advantage of the full spectral data. Level three and higher processing (geolocation, binning, remapping, etc.) is then done to both data types.

3. EXAMPLE HICO PRODUCTS

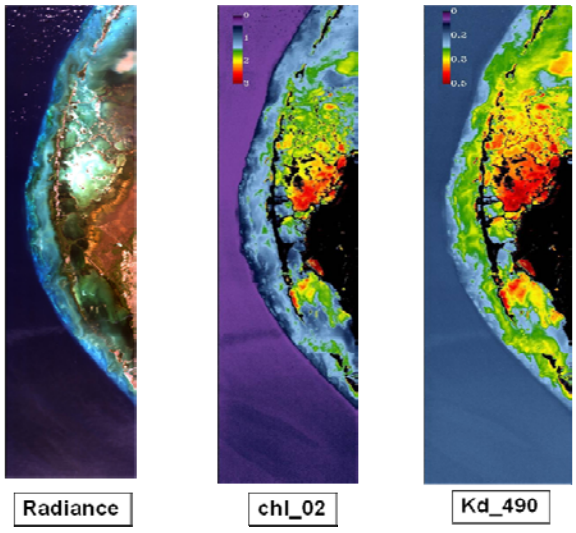

Figure 2. Example APS products from a HICO image of the Florida Keys near Key Largo. Orientation is from southwest at the top to northeast at the bottom.

Figure 2 is an image of the Florida Keys near Key Largo showing data products produced with the multispectral HICO processing in APS. We continue to test and validate new products from HICO, in particular for the full hyperspectral data.

4. CONCLUSION

The Hyperspectral Imager for the Coastal Ocean (HICO) demonstrates the ability to produce coastal environ-mental products from spaceborne imagery. HICO and its products are pathfinders for future operational systems.

REFERENCES

Davis C.O., K.L. Carder, B.-C. Gao, Z.P. Lee, and W.P. Bissett (2006). "The development of imaging spectrometry of the coastal ocean". IEEE Proceedings of the International Geoscience and Remote Sensing Symposium, 4, pp. 1982-1985.

Davis, C. O., M. Kavanaugh, R. Letelier, W. P. Bissett, and D. Kohler, (2007). "Spatial and spectral resolution considerations for imaging coastal waters". Coastal Ocean Remote Sensing, edited by R. J. Frouin and Z. P. Lee, Proc. of. SPIE vol. 6680, 66800P, pp. 1-12.

Goetz, A. F. H., Vane G., Solomon J., and Rock B. N., (1985). "Imaging spectrometry for Earth remote sensing". Science, vol. 228, pp. 1147−1153.

Corson, M. R., D. R. Korwan, R. L. Lucke, W. A. Snyder and C. O. Davis (2008). "The Hyperspectral Imager For The Coastal Ocean (HICO) On The International Space Station". IEEE Proceedings of the International Geoscience and Remote Sensing Symposium, 978-1-4244-2808-3/08.

Observation of phytoplankton size classes in the NW Atlantic Ocean from space

E. Devred [a], S. Sathyendranath [b], V. Stuart [a], T. Platt [b]

[a] Bedford Institute of Oceanography, DFO, Dartmouth, N.S., Canada – devrede@mar.dfo-mpo.gc.ca, vstuart@ioccg.org
[b] Plymouth Marine Laboratory, Plymouth, United Kingdom – ssat@pml.ac.uk, tplatt@dal.ca

Abstract – Phytoplankton cell size plays a major role in the study of biogeochemical cycles. Here, we propose a method to derive the fractional contributions of micro-, nano- and picoplankton to total chlorophyll-a using phytoplankton absorption and chlorophyll-a concentration. The method is successfully tested against *in situ* data collected in the Northwest Atlantic. The method is applied to phytoplankton absorption retrieved from ocean-colour data measured by the SeaWiFS sensor over two selected areas: the Scotian Shelf and the Gulf Stream. Analysis of eight-day time series of phytoplankton size class in the two selected areas during the year 2007 gave detailed information about the biological activity in two different ecosystems.

Keywords: phytoplankton size, absorption, Atlantic Ocean

1. INTRODUCTION

Phytoplankton size distribution provides key information when studying biogeochemical cycles in marine ecosystems. Various methods, including microscopy, genetic analysis, flow cytometry and pigment composition have been developed to infer phytoplankton groups and/or species or size distribution from samples collected at sea. However, these methods are costly and do not allow large spatial and temporal sampling of the ocean. On the other hand, satellite observations provide an ideal spatio-temporal coverage to study biological activity in the ocean. Only a few attempts have been made at identifying phytoplankton groups or size classes using ocean-colour data (e.g., Sathyendranath et al., 2004; Alvain et al., 2005). Here we propose an alternative method that quantifies the contributions to chlorophyll-a from three size classes. Phytoplankton absorption is closely related to phytoplankton size (Duysens, 1956). We used changes in the specific absorption of phytoplankton due to packaging effect and pigment composition as cell size increases (absorption normalized to chlorophyll-a concentration), to derive the fractional contributions of micro-, nano- and picophytoplankton to total chlorophyll-a concentration. Comparisons with phytoplankton size class derived from pigment composition showed good agreement. Application of our algorithm to eight-day composite images from SeaWiFS provides insight on the succession of phytoplankton during the Spring and Autumn blooms in the Northwest Atlantic.

2. DATA AND METHOD

2.1 Data

Chlorophyll-a concentration (Chl-a), pigment composition measured by High Performance Liquid Chromatography (HPLC) and phytoplankton absorption at 443, 490, 510, 555 and 670 nm collected in the Northwest Atlantic between 1996 and 2003 were used to develop and validate our method (N = 733, Figure 1). Details about protocols and processing of the data can be found in Stuart et al. (2000). Seven diagnostic pigments were used to derive phytoplankton cell size from HPLC measurements according to Uitz et al. (2006). The pigments were fucoxanthin and peridinin as markers of microphytoplankton; butanoloxyfucoxanthin-19, hexanoloxyfucoxanthin-19 and alloxanthin as markers of nanophytoplankton; and, chlorophyll-b and zeaxanthin as markers of picophytoplankton. Uitz et al. (2006) method was modified to account for the presence of fucoxanthin in nanophytoplankton (Devred et al., submitted).

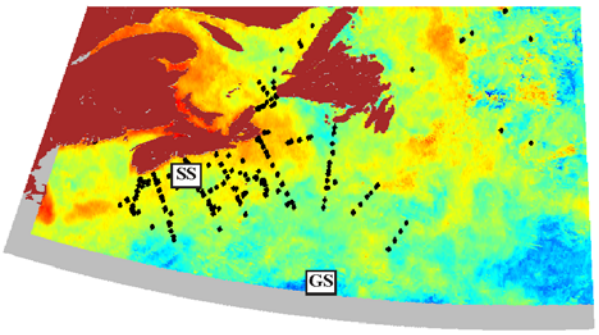

Figure 1. Location of sampling (black dots). The boxes marked SS and GS correspond respectively to the eight-day time series of phytoplankton size classes on the Scotian Shelf and in the Gulf Stream

Satellite data consisted of daily remote sensing reflectances for the year 2007 from SeaWiFS, which were converted into phytoplankton absorption at 443, 490, 510, 555 and 670 nm according to Devred et al. (2006). Daily images were composited over an eight-day period to reduce the number of missing pixels due to cloud coverage. The fraction of each phytoplankton size class was inferred from satellite-derived phytoplankton absorption and Chl-a in two 30x60 km^2 boxes, which were representative of two different types of ecosystem (Figure 1): one on the Scotian Shelf (coastal) and one in the Gulf Stream (oligotrophic).

2.2 Method

The additive property of phytoplankton was used to express the total phytoplankton specific absorption as the sum of the contribution of each phytoplankton size class:

$$a_C^* = F_m a_m^* + F_n a_n^* + F_p a_p^*, \qquad (1)$$

where a^* stands for the specific absorption of phytoplankton, F represents fractional contributions and the subscripts m, n and p indicate micro-, nano and picophytoplankton respectively. Provided that the specific absorption of each size class (Devred et al., submitted) and

total chlorophyll-*a* concentration are known, the fractional contributions (F_i, $i = p,n,m$) can be found by solving the following system of equations:

$$\begin{bmatrix} a_m^*(\lambda_1) & a_n^*(\lambda_1) & a_p^*(\lambda_1) \\ \vdots & \vdots & \vdots \\ a_m^*(\lambda_i) & a_m^*(\lambda_i) & a_m^*(\lambda_i) \end{bmatrix} \begin{bmatrix} F_m & F_m & F_m \end{bmatrix} = \begin{bmatrix} a_C^*(\lambda_1) \\ \vdots \\ a_C^*(\lambda_i) \end{bmatrix}, \quad (2)$$

where $\lambda_{1...i}$ are the wavelengths of interest, under the condition that each of the F_i remain positive and that their sum be equal to one. In theory, three equations are sufficient to solve the problem. However, the use of additional wavelengths strengthens the statistical significance of the results when using noisy data. We found that the use of five wavelengths improved the agreement with *in situ* measurements. Here we have used the SeaWiFS wavebands: 443, 490, 510, 555 and 670 nm. The 412 nm band was not used to avoid possible effects of phaeopigments and potentially high errors from atmospheric correction.

3. RESULTS AND DISCUSSIONS

Absorption-retrieved phytoplankton size class showed a good agreement when compared to HPLC-retrieved data. In fact, 80% (N = 733) of the retrieved size classes agreed within 20% of the observations, which is very promising considering the different methods used in the comparison. In the absence of a more reliable method, such as cell count or flow cytometry, it is difficult to speculate on the sources of the residual discrepancies.

Time series of the fractions of phytoplankton size classes on the Scotian Shelf (Figure 2) and the Gulf Stream (Figure 3) reveal the dynamics of phytoplankton blooms in the Spring and Fall of 2007, as well as the interannual variation of the phytoplankton community structure.

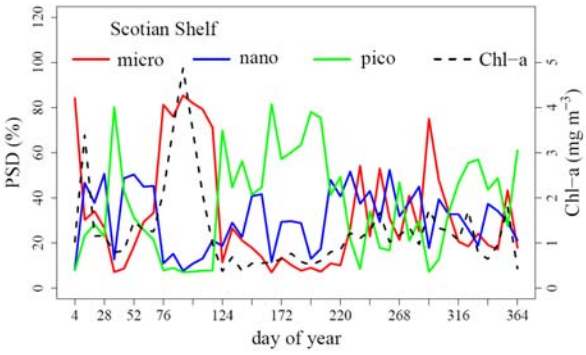

Figure 2. Time series of micro-, nano-, picophytoplankton and Chl-a in a 30x60 km^2 box located on the Scotian Shelf.

Both the Scotian Shelf and the Gulf Stream areas show a strong Spring bloom with respective maximum Chl-a of 5 and 2.7 mg m^{-3}. Whereas microphytoplankton is the dominant decaying. Again, microphytoplankton become dominant on the Scotian Shelf in the Autumn when the water column is mixed by atmospheric events bringing nutrients to the photic zone. In the Gulf Stream, nanophytoplankton represent the dominant size class during the Autumn bloom. In Summer when the stratification is at the maximum and in Winter when light is a limiting factor, picophytoplankton represent more than 80% of the total biomass.size class on the Scotian Shelf, its signal is less pronounced in the Gulf Stream where nanophytoplankton reaches values as high as 60% when the bloom starts

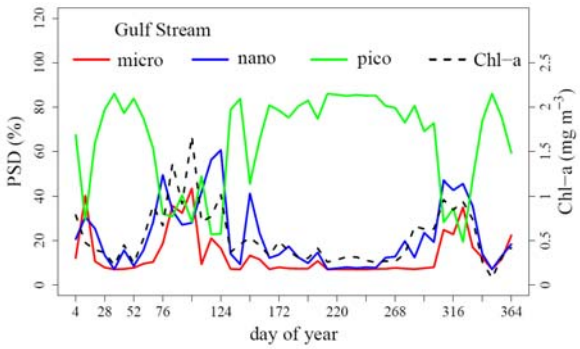

Figure 3. Time series of micro-, nano-, picophytoplankton and Chl-a in a 30x60 km^2 box located in the Gulf Stream.

ACKNOWLEDGEMENTS

We thank the NASA SeaWiFS project and GeoEye Inc. for making SeaWiFS data available. This work was funded by the Canadian Space Agency under the GRIP program. This work is also a contribution to the Oceans2025 and NCEO programmes of NERC (UK).

REFERENCES

Alvain, S., C. Moulin, Y. Dandonneau, and F. M. Bréon (2005) "Remote sensing of phytoplankton groups in case 1 waters from global seawifs imagery". Deep-Sea Res., vol. 52, pp.1989–2004.

Devred, E., S. Sathyendranath, and T. Platt, Inversion based on semi-analytical reflectance model, in Remote sensing of inherent optical properties: Fundamentals, tests of algorithms, and applications, edited by L. Z. (ed), Reports of the International Oean-Colour Coordinating Group, No. 5, IOCCG, Dartmouth, Canada, 2006

Duysens, L. M. N. (1956) "The flattening of absorption spectrum of suspensions, as compared to that of solutions". Biochim. Byophys. Acta., vol. 19, 1–12, 1956.

Sathyendranath, S., L. Watts, E. Devred, T. Platt, C. Caverhill, and H. Maass (2004) "Discrimination of diatoms from other phytoplankton using ocean-colour data". Mar. Ecol. Prog. Ser., vol. 272, pp. 59–68.

Stuart, V., S. Sathyendranath, E. J. H. Head, T. Platt, B. D. Irwin, and H. Maas, (2000) "Biooptical characteristics of diatom and prymnesiophyte populations in the Labrador Sea". Mar. Ecol. Prog. Ser., vol. 201, pp. 91–106.

Uitz, J., H. Claustre, A. Morel, and S. B. Hooker (2006) "Vertical distribution of phytoplankton communities in open ocean: An assessment based on surface chlorophyll". J. Geophys .Res., 111, doi: 10.1029/2005jc003207.

Atmospheric correction of sun glint contaminated ocean colour data of MERIS

Roland Doerffer [a], Helmut Schiller [a], Marco Peters [b]

[a] GKSS Research Center, Institute for Coastal Research, Germany - roland.doerffer@gkss.de
[b] Brockmann Consult, Germany - marco.peters@brockmann-consult.de

Abstract - a procedure has been developed for data of the Medium Resolution Imaging Spectrometer MERIS, which is used to determines water leaving radiance reflectances from top of atmosphere (toa) reflectances even in the presence of high sun glint. The procedure is an artificial neural network (NN), which was trained with a large set of simulated toa reflectances for 12 of the 15 MERIS bands. Simulations include in-water optical properties as well as different aerosols, thin cirrus clouds and a wind dependent rough sea surface. Input to the NN are the toa reflectances and the sun and viewing angles.

Keywords: atmospheric correction, sun glint, MERIS.

1. INTRODUCTION

Direct sun light, which is specularly reflected at the sea surface (sun glint), may contaminate more than half of an ocean colour scene. Depending on latitude, observation geometry and wind speed the sun glint may surpass the path radiance at 865 nm outside glint by a factor of 10. In particular the spectral bands in the near infrared, which are used for atmospheric correction of case 1 waters, are contaminated significantly.

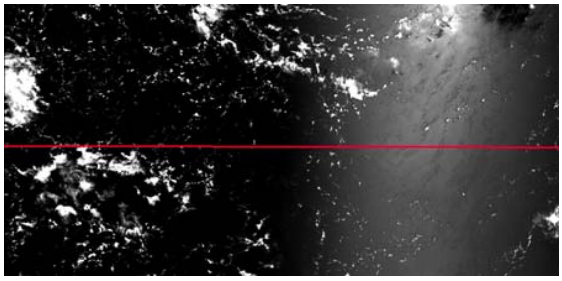

Figure 1: MERIS toa radiance band 9, 708 nm, Hawaii 20030705.

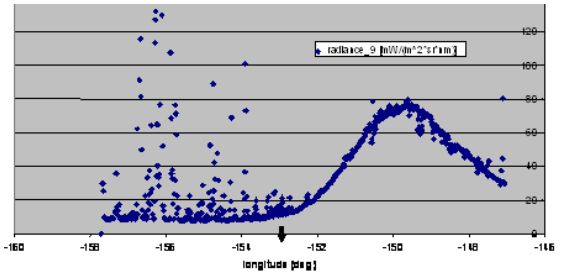

Figure 2. Radiance of band 9 along transect of Fig. 1

In principle sun glint can be calculated from the solar zenith angle, die viewing direction and the slope distribution of the surface waves (Kay et al., 2009). However, the wave slope distribution for a pixel at the exact time of overflight is not known, due to fast variations of wind, slicks and interfering wave systems. In most cases areas with high sun glint are masked and excluded from further processing. In many cases half of the image is masked out. Thus the only chance to determine glint is by its reflectance spectrum.

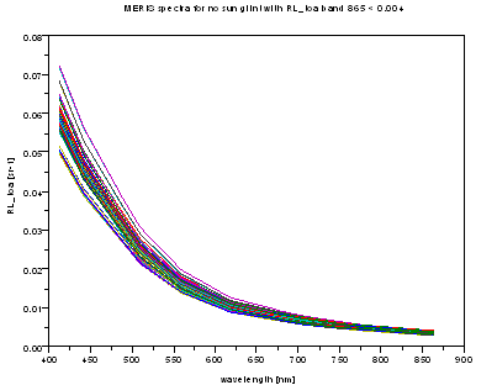

Figure 2: Toa radiance reflectance spectra, Hawaii, outside glint

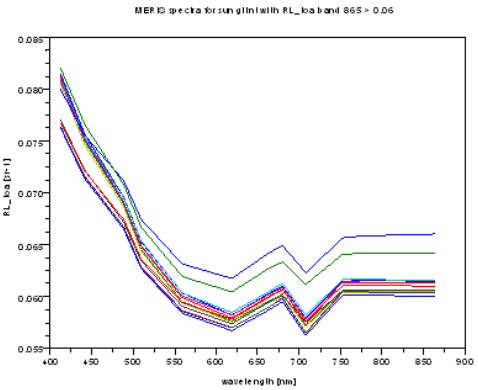

Figure 4. Toa radiance reflectance spectra, in max. glint

2. PROCEDURE

For the analysis of the problem we have set up a special version of a Monte Carlo Photon Tracing (MCPT) code, which allows us to label and count glint photons separately from the others. This MCPT code was then used to simulate bi-directional toa reflectances over different types of waters for various aerosol optical properties and glint effects. Altogether a set of about 1 Mio cases was simulated. It covers an aerosol optical thickness at 550 nm of 0-0.6 and an Angstrom coefficient in the range 0.1 - 2.2. Input to the NN are the bi-directional top of standard atmosphere reflectances at 12 MERIS bands, the solar zenith angle and the viewing direction in x,y,z-coordinates. Outputs, among other variables, are the water leaving radiance reflectances, the path radiance reflectances and the transmittances in the 12 bands. The RLws are used as input to a further NN for retrieving water optical variables. The procedure has

been implemented in the case 2 regional plugin processor (C2R), which is part of the BEAM distribution (envisat.esa.int/beam), and which is open to the public.

3. PERFORMANCE

The performance was tested with various images of case 1 and case 2 waters from different latitudes. Images were included with large slick patterns to test the performance for these conditions, as demonstrated in Fig. 5-7.

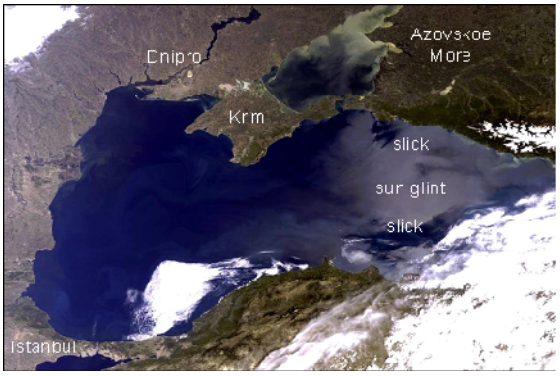

Figure 5. MERIS L1 RGB image Black Sea, 20070512.

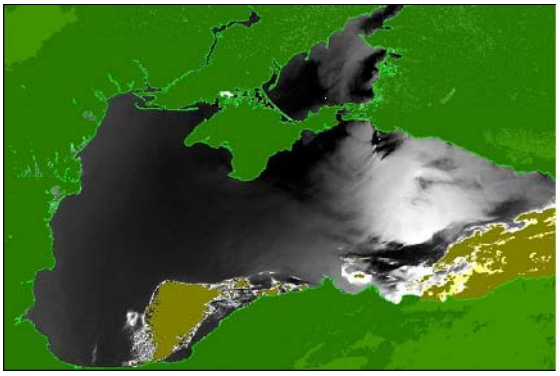

Figure 6. Output of the NN: path radiance with glint.

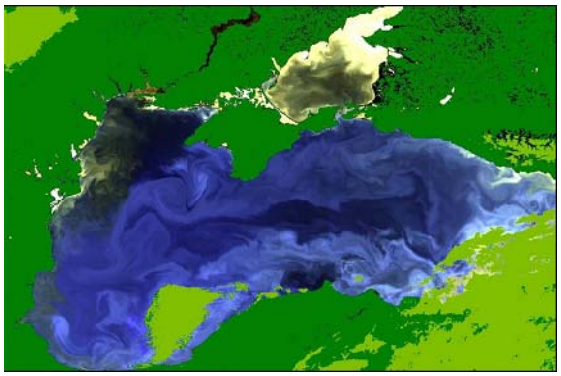

Figure 7. Output of the NN: water leaving radiance reflectance, as RGB image.

4. VALIDATION

The validation was performed using the MERMAID data set, which is complied by ESA from various data sets and mainly used to validate the atmospheric correction and calibration of MERIS. Her we show only the results when compared to the MOBY optical buoy, which is moored close to Hawaii (courtesy of Michael Ondrusek, NOAA). Fig. 8 shows the scatter plot with the 1by1 line for only pixels with no sun glint (from the left side of the image). The different colours indicate the spectral bands 1-9. Fig. 9 demonstrates the performance for only high glint cases. Obvious is the similar performance for both data sets, with slightly more scatter in the glint data.

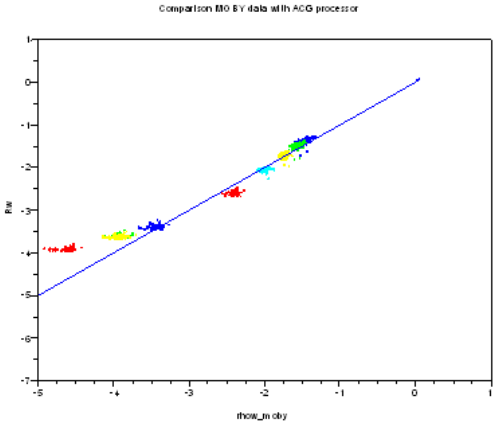

Figure 8. Scatter plot comparison RLw MERIS derived using NN with MOBY, no glint, log10 scale.

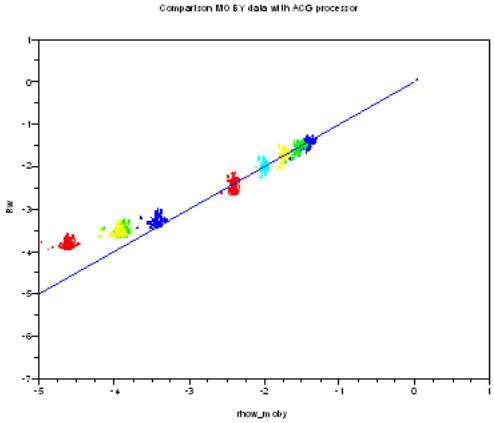

Figure 9. As Figure 8, but for high glint cases.

5. CONCLUSIONS

It has been demonstrated that the water leaving radiance reflectances can be determined from toa reflectances with nearly the same quality for sun glint contaminated areas - even for a glint ratio of 10 - as for the non sun glint part of an image. A separation between sun glint and path radiance caused by aerosol scattering is not possible with the band set of MERIS. Thus, the glint correction has to be embedded into the atmospheric correction procedure.

ACKNOWLEDGEMENTS

This research work was supported by the European Space Agency ESA under Contract 20598/07/I-OL.

REFERENCES

Kay, Susan, John D. Hedley, Samantha Lavender (2009): Sun Glint Correction of High and Low Spatial Resolution Images of Aquatic Scenes: a Review of Methods for Visible and Near-Infrared Wavelengths, Remote Sens. 1, 697-730

The Global Monitoring for Environment and Security (GMES) Sentinel-3 Mission

C. Donlon*, B. Berruti, , J. Frerick, U. Klein, C. Mavrocordatos, J. Nieke, B. Seitz, J. Stroede, H. Rebhan and M.R. Drinkwater

European Space Agency-ESTEC, Noordwijk, The Netherlands – craig.donlon@esa.int

Abstract – In the frame of the Global Monitoring for Environment and Security (GMES) initiative, jointly conceived by the European Space Agency (ESA) and the European Commission, ESA is developing the Sentinel-3 system to respond to the requirements for operational global scale, near-real-time ocean, ice and land monitoring. The system will provide a fast revisit rate and at medium resolution (300 – 1000m). In order to meet the needs of the operational oceanography user community, the Sentinel-3 satellite data will support the operational generation of a generalised suite of high-level geophysical products, including as priority: sea-surface topography, sea-surface temperature, and ocean colour data. The system has been designed to ensure continuity to existing ENVISAT radar altimetry and multi-spectral Visible and Infrared ocean and land-surface radiance observations of ERS and ENVISAT instrumentation, and includes small enhancements to meet the operational revisit requirements and to facilitate new products and future evolution of services. Sentinel-3 is planned for launch in the 2013 timeframe.

Keywords: Sentinel-3, SST, ocean colour, altimetry, GMES.

1. INTRODUCTION

The Global Monitoring for Environment and Security (GMES) is a initiative for the implementation of a European capacity to provide independent and permanent access to reliable Earth observation data (http://ec.europa.eu/gmes). GMES has been established to fulfill the growing need amongst European policy makers to access accurate and timely information services to better manage the environment, understand and mitigate the effects of climate change and ensure civil security. A complete description of GMES services can be found at the above link, and at http://boss4gmes.customers.arjuna.eu.

In the framework of GMES, ESA is developing the Sentinel-3 system to respond to the requirements for operational global scale, near-real-time ocean, ice and land monitoring with fast revisit rate and at medium resolution (300 – 1000m). In order to meet the needs of the operational oceanography user community, the Sentinel-3 satellite data will support the operational generation of high-level geophysical products, including as priority: sea-surface topography, sea-surface temperature, and ocean colour data. The system has been designed to ensure continuity to existing ENVISAT radar altimetry and multi-spectral Visible and Infrared ocean and land-surface radiance observations of ERS and ENVISAT instrumentation, and includes small enhancements to meet the operational revisit requirements and to facilitate new products and future evolution of services.

2. SENTINEL-3 USERS

Sentinel-3 addresses core user community requirements in the following domains.

Numerical Weather/Ocean Prediction: Satellite ocean observation data will improve existing predictive capability by providing a better understanding of global ocean processes that govern ocean and weather patterns. This is particularly important as coupled ocean-atmosphere model systems are now being developed and implemented. A network of global ocean (satellite and in-situ) observations is required to provide the data input for boundary condition specifications in advanced numerical weather prediction models. Operational availability of ocean observations (radiance/reflectance data and derived geophysical parameters together with uncertainty estimates) is a prerequisite to data assimilation and ultimately consistent, improved predictions of atmospheric and oceanic conditions.

Coastal Zone Monitoring: Demands for information on the health and state of coastal waters are growing in response to population pressure. Thus, there is a requirement for environmental monitoring of water quality and phenomena such as harmful algal blooms (HAB) and habitat assessment in addition to weather and ocean nowcasting and forecasting. The characteristics of the coastal phenomena and the importance of the area for aquaculture, sea-defences, and tourism each justify the observation of coast related parameters with enhanced accuracy, uncertainty estimation and resolution.

Open Ocean and Ice Monitoring: The health and state of the oceans can only be assessed with the aid of globally comprehensive, integrated observations. Satellite measurements from polar orbiting platforms such as Sentinel-3 provide a core component of an integrated observing system as they provide consistent, synoptic coverage of the global ocean on a daily basis. With such data, together with measurement uncertainty estimates, working in synergy in the framework of ocean modeling systems and data assimilation, it will be possible to increase the predictability of characteristics such as sea-state, ice formation, ocean circulation, and the impact of physical conditions on ocean biogeochemistry. The open ocean also provides important boundary conditions for coastal regions.

* Corresponding author.

Global Land Monitoring Applications: Sentinel-3 will provide daily coverage of the Earth, facilitating global fast revisit observation of the land surface. These data will allow the study of parameters such as regional and continental-scale land cover, vegetation state or vegetation productivity, and fire location, intensity and effects (such as burnt scar area). Sentinel-3 shall compliment other missions that provide higher resolution but longer revisit times, with a suite of channels that include infrared bands for land surface temperature and fire observation.

Environmental Policy and Law: Through international negotiations, governments have agreed to numerous conventions which, although not in all cases explicitly stated, embody the requirements for measuring various ocean parameters globally in a concerted, systematic way.

Maritime Safety and Security: At National and EU level, recognition of the importance of solving problems associated with the pollution consequences of shipping accidents, passenger vessel safety, and, more recently, with potential terrorist actions, has led to the formation of institutions responsible for coordinating legislation.

Global and Climatic Change: Many of the products requested by the communities indicated above will be of interest to the scientists studying global and climatic change. Monitoring climate using GCOS Essential Climate Variables (ECV) and according to GCOS climate monitoring principles is prerequisite to formulating strategies to adapt to and mitigate climate change impacts. Operational missions are the only way to provide a long term, consistent quality data-base required to monitor and study the regulating effect which ocean processes exert on climate.

3. SENTINEL-3 PAYLOAD

The Sentinel-3 space segment consists of two satellites, Sentinel 3 A and B platforms, which both carry the following instruments:

- An Ocean and Land Colour Instrument (OLCI), a spectrometer imaging in pushbroom mode with an across-track electronic scan, strongly inherited from the MERIS of Envisat, with same class of performance in the visible bands, associated with a larger coverage accounting for Sun glint.
- A Sea and Land Surface Temperature Radiometer (SLSTR), a conical imaging radiometer with a dual view (near-nadir and inclined) capability, presenting design heritage from the AATSR of Envisat with same class of performance, associated with a larger coverage. Unlike AATSR, SLSTR implements a double scanning mechanism for a much larger swath, and allowing for the synergetic use of both OLCI and SLSTR instruments over the broad region of swath overlap
- A SAR Radar ALtimeter (SRAL) instrument, a dual-frequency altimeter, derived from the Alcatel Alenia Space line of products such as SIRAL of CryoSat, and Poseidon-3 of Jason-2, providing low resolution sea surface measurements to ensure continuity of the RA-2 ones of Envisat, and high along-track resolution sea-ice monitoring in nadir SAR mode.
- A Microwave Radiometer (MWR), which supports the SRAL to achieve the overall altimeter mission performance by providing the wet atmosphere delay correction to SRAL data.
- A GNSS Assembly, suitable for the Precise Orbit Determination (POD) processed on ground to achieve the overall altimeter mission performance. Real time navigation and dating information from this equipment will provide spacecraft navigation and dating functions as well as the control of the Radar Altimeter open-loop tracking function.
- A DORIS Assembly as a Customer Furnished Item, which constitutes a complementary POD data provider for the Ground Segment as well as a potential (TBC) backup to the GNSS Assembly for the specific commanding of the SRAL Open Loop tracking mode.
- A passive Laser retro-reflector (LRR).

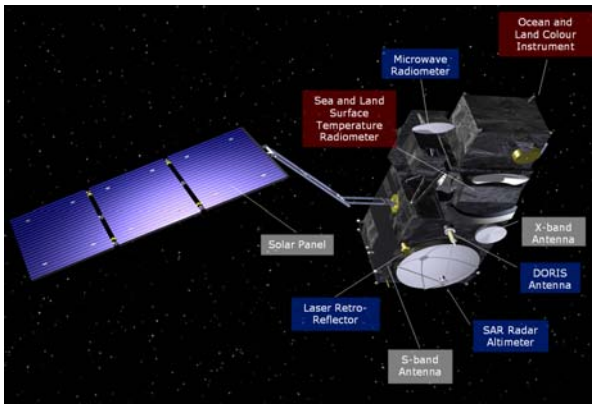

Figure 1. Artists impression of the Sentinel-3 satellite.

The Sentinel-3 surface topography mission responds to the primary objective of providing accurate, high density altimetry measurements from a high-inclination orbit with long exact repeat cycle, to complement the JASON ocean altimeter series. A reference sun-synchronous orbit at 814 km altitude is presently selected for Sentinel-3 (14+7/27 revolutions per day) with a local equatorial crossing time of 10:00 a.m., as a compromise between optical instrument and altimetry needs. In this orbit configuration two simultaneously-orbiting satellites are required to support full imaging of the oceans in less that 2 days after taking sun-glint contamination into account, whilst delivering global land coverage in just over 1 day at the equator. The orbit also maximises complementarily with the NPOESS satellite series.

4. CONCLUSION

Sentinel-3 is a European polar orbit satellite system for the provision of operational marine and land services within the European Global Monitoring for Environment and Security (GMES). Sentinel-3 will ensure continuity to existing ENVISAT radar altimetry and multi-spectral Visible and Infrared ocean and land-surface radiance observations of ERS and ENVISAT instrumentation, and includes small enhancements to meet the operational revisit requirements and to facilitate new products and future evolution of services. The Sentinel-3 system is characterised by two satellites on-orbit that will provide continuous systematic acquisitions, facilitating routine operations. The data is processed, calibrated and the resulting products routinely distributed for assembly and assimilation into operational ocean models.

Operational Remote Sensing Services for Environmental Monitoring of German Coastal Waters
- The GMES Research Project DeMarine-Environment -

S. Dorendorf [a,*], A. Neumann [b], B. Baschek [c], K. Stelzer [d], J. Schröter [e]

[a] Federal Maritime and Hydrographic Agency (BSH), Hamburg, Germany – sonja.dorendorf@bsh.de
[b] German Aerospace Center (DLR), Berlin, Germany – andreas.neumann@dlr.de
[c] Federal Institute of Hydrology (BfG), Koblenz, Germany – baschek@bafg.de
[d] Brockmann Consult (BC), Geesthacht, Germany – kerstin.stelzer@brockmann-consult.de
[e] Alfred-Wegener-Institute for Polar and Marine Research (AWI), Bremerhaven, Germany – jens.schroeter@awi.de

Abstract – Within the framework of GMES, the German research project DeMarine-Environment develops and improves user specific remote sensing services for environmental monitoring. The following fields are served: coastal water quality monitoring, oil spill drift forecast, monitoring of intertidal flats and improvement of numerical model forecast by data assimilation. All services are provided at a pre-operational level.

Keywords: GMES, operational service, coastal waters, environmental monitoring

1. INTRODUCTION

The German research project DeMarine-Environment focuses on the development and improvement of remote sensing services for national marine environmental monitoring responsibilities. As a national GMES project, it serves as an interface between German users, mostly local or regional authorities, and European GMES institutions and activities. Marine environmental protection in the EU is regulated by international regional conventions, like OSPAR for the North-East Atlantic and HELCOM for the Baltic, as well as European directives, especially the Marine Strategy Framework Directive and the Water Framework Directive. To achieve a good environmental status of the EU waters by 2020, the two latter request from the member states a detailed assessment of the state of the environment, a definition of "good environmental status" at regional level, and the establishment of clear environmental targets and monitoring programs. This comprehensive approach necessitates new assessment tools. Because of the area-wide data acquisition, earth observation via satellites could be an important addition to traditional marine environmental monitoring practices. GMES - Global Monitoring for Environment and Security - is a joint initiative of the European Commission (EC) and the European Space Agency (ESA) with the goal to provide Europe with an independent and secure access to global Earth observation information. New tools combining information and data from space-borne, air-borne and in-situ observation systems as well as numerical models are to be developed to provide decision support in questions on Land, Sea and Atmosphere, Climate Change, Emergency Response and Security. For each of the sectors, so called Core Services (CS) will provide standardized multi-purpose information on a European level, whereas Downstream Services (DSS) will serve specific regional or local information needs. To be accepted by the end-users, services have to match their very specific application needs. Hence, users should be closely integrated in the development of DSS. In 2008, the German government set up the national marine GMES project DeMarine-Environment. It aims at the development of user-specific DSS in water quality and wadden sea monitoring, oil spill detection and forecast, as well as assimilation of satellite data into a numerical ocean model. The services shall be provided on an operational basis for the German coastal waters of North and Baltic Sea.

2. TOPICS AND FIRST RESULTS

The goal of DeMarine-Environment is to ensure the usage of GMES infrastructure by German marine end-users, and to communicate their needs to the European GMES level. Four subprojects develop and improve GMES services in the following fields:

2.1 Water Quality in Coastal Waters

The partners DLR, BC and GKSS have been involved in many projects on the development of services for the monitoring of water quality and algal blooms in North and Baltic Sea. Since MarCoast, services based on MERIS data in reduced resolution (RR) data are provided operationally by DLR and BC. Remote sensing of coastal zones is challenging because of high sediment load, shallow regions, narrow straits and irradiations from land. Furthermore, the characteristics (e.g. high concentration of SPM, strong gradients, patchiness, spatial and temporal heterogeneity) require an especially high spatial and temporal resolution. Hence, the subproject aims at a regionalization of MarCoast products and a utilization of MERIS full resolution (FR) data, i.e. 300m instead of 1200m. Moreover, water quality indicators with respect to Water Framework Directive and Marine Strategy are to be developed. A harmonization of the processors used by DLR and BC and porting of modules to the software package BEAM have been realized. MERIS-FR processing chains have been implemented both for North Sea and Baltic Sea. So prototype FR products for water constituents and algal blooms are available, as seen in Fig. 1, SPM in the Baltic Sea. As a specific method for the spectral detection of algal blooms, an automatic novelty-finder is run as prototype. The preprocessing with the MERIS Case-2-Regional algorithm has been improved for

* Corresponding author. Bernhard-Nocht-Str. 78, 20359 Hamburg, phone/fax 0049-40-3190-3181/-5000

atmospheric correction, glint correction and polarization of atmosphere, leading to an improvement in all secondary parameters.

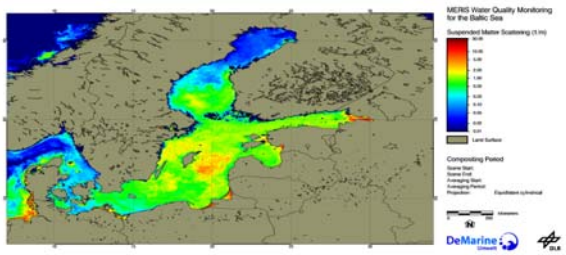

Figure 1. Prototype MERIS-FR Water Quality Product: SPM in the Baltic Sea

2.2 Oil Spill Drift Forecast

In Germany, for oil spill monitoring and combat, a combined system of remote sensing techniques, drift models and combat tools is applied. Satellite data (ENVISAT-ASAR, RADARSAT-1 and -2) is received via the EMSA CleanSeaNet service. Whereas aerial surveillance is done by two national aircraft, equipped with multiple oil specific sensors and coordinated by the Central Command for Maritime Emergencies (CCME). In case of a major oil detection, the CCME informs BSH to run a drift simulation. The goal of the subproject is to improve the German oil spill monitoring and combat by combining oil detection and drift modeling into one system. More specific, BfG and BSH aim at a partly automated integration of RS data from CleanSeaNet and aircraft into the BSH drift model. So far, an offline version of the interface has been realized at BfG. As input to the model, it provides not only the satellite derived centroid but also the distribution of the oil. Test cases are run with aircraft confirmed satellite detections. It is planned to implement the interface at BSH, so that the operational drift simulations can utilize the improved input information based on remote sensing data. Further, a web-based version connecting to the SeaTrackWeb system is aimed at.

2.3 Integration of Optical and SAR Earth Observation Data for the Monitoring of Intertidal Flats

For the German Wadden Sea, optical RS sensors are being used for sediment classification and habitat mapping. Because useful data - acquired at low tide during daylight and good cloud conditions – are rare for the German North Sea coast, and optical and SAR data provide supplement information of the intertidal flat surfaces, a combination of both can be utilized for an improved habitat mapping. Therefore, the subproject aims at the development of a synergistic classification system based on in-situ, optical and radar observations for the monitoring of intertidal flats. The method used for the classification of optical remote sensing data is based on a linear spectral unmixing and feature extraction from the spectral reflectances (Brockmann and Stelzer 2008). For an improved validation, a biotop knowledgebase has been set up. The university of Hamburg conducted a multi-frequential analysis of L-, C,- and X-band radar (from ALOS PALSAR, ERS SAR and ENVISAT ASAR, and TerraSAR-X, respectively) for sediment classification.

2.4 Development and Implementation of a Data Assimilation Scheme for an Operational Model of North and Baltic Sea

The numerical circulation model of BSH – BSHcmod – is used operationally for the analysis and forecast of water levels, currents, salinity and temperature, as well as drift of objects in the North and Baltic Sea. A direct linkage between observations and model simulations via data assimilation forms a promising opportunity to improve the model forecasts. In this subproject, a scheme for assimilation of satellite SST data into BSHcmod is to be developed and implemented to improve the forecast, especially for SST and ice. A sequential data assimilation is performed. The AWI implemented and tested three different Kalman filters for assimilation of NOAA – AVHRR SST into BSHcmod: Fixed Error Covariance Reduced Rank, Global SEIK and Local SEIK (Nerger *et al.*, 2006). For a three months forecast run with eight ensembles assimilating SST every 12 hours, the Local SEIK shows best results compared to independent SST data. Further tests and adjustments have to be performed to make sure the forecast of the other model parameters is not degraded. The implementation in the operational model system of BSH is planned.

3. CONCLUSION

DeMarine-Environment contributes to improved environmental monitoring services for German coastal waters by closely integrating the end-users into the development process. In all subprojects, the first results are promising, leading to services at an operational or pre-operational level by the end of the project.

ACKNOWLEDGEMENTS

The authors are grateful to all colleagues participating in DeMarine-Environment. The project receives funding from the German Ministry of Economy (BMWi).

REFERENCES

Brockmann, C., and K. Stelzer (2008). "Optical Remote Sensing of Intertidal Flats", in "Remote Sensing of the European Seas", V. Barale and M. Gade (Eds.), Springer, Heidelberg, pp. 117-128.

Gade, M. and K. Stelzer (2009). "On the Joint Use of Microwave and Optical Remote Sensing Sensors for the Observation of Dry-Fallen Intertidal Flats in the German Bight". 33rd Intern. Symposium on RS of Environment.

Kübert, C. and B. Baschek (2009). "Geoinformationen aus Fernerkundungsdaten zum Initialisieren eines Öldriftmodells". INTERGEO 2009, poster.

Nerger L., Danilov, S., Hiller, W. and J. Schröter (2006). "Using sea-level data to constrain a finite-element primitive-equation ocean model with a local SEIK filter". Ocean Dynamics, vol. 56, no. 5-6, pp. 634-649.

New satellite altimetry products to study regional and coastal seas

C. Dufau * and the PISTACH Team

Collecte Localisation Satellite CLS, Ramonville Saint-Agne , France – cdufau@cls.fr

Abstract – Crucial needs are expressed for satellite altimetry near the coastlines where human activities are concentrated. In these peculiar oceanic regions, satellite altimeter techniques are unfortunately limited by the emerged lands. To fulfil these needs, the French space agency, CNES, funded the development of the PISTACH prototype dedicated to Jason-2 altimeter processing in coastal ocean. The new PISTACH products provide new retracking solutions, several state-of-the-art or with higher resolution corrections in addition to standard fields.

Keywords: coastal altimetry, re-tracking, wet tropospheric correction

1. INTRODUCTION

Since the launch of Topex-Poseidon in 1992, satellite altimetry has become one of the most essential elements of the Earth's observing system. Its global view of the ocean state has permitted numerous improvements in the environment understanding, particularly in the global monitoring of climate changes and ocean circulation.

Near the coastlines where human activities have a major impact on the ocean, satellite altimeter techniques are unfortunately limited by a growth of their error budget. This loss of quality is due to land contamination in the altimetric and radiometric footprints but also to inaccurate geophysical corrections (tides, high-frequency processes linked to atmospheric forcing).
Despite instruments are perturbed by emerged lands until 10 km (altimeter) and 50 km (radiometer) off the coasts, measurements are present and may contain useful information for coastal studies.

In order to recover more qualified data closer to the coast, the French Spatial Agency (CNES) has decided to enhance the data processing on those areas. For this purpose, within the PISTACH project, CLS has developed a coastal-dedicated treatment applied to the new satellite mission Jason-2. This paper presents and illustrates this new set of satellite data available since November 2008 over coastal oceans.

2. WHAT'S NEW WITH PISTACH?

2.1 New retracking solutions

Altimeter echoes (waveforms) are highly perturbed by emerged lands wrt. open ocean returns (fig. 1) and thus require a dedicated retracking strategy.

Within PISTACH, the retracking is organized around three steps: classification of the waveforms, filtering of the waveforms (only before MLE4 retracking) and application of four different retrackings:

- Ice1: position of the center of gravity of the echo
- Ice3: ~Ice1 but restricted to a portion of the echo indicated by the classification
- Oce3: MLE4 retracking after filtering of the waveforms
- Red3: MLE3 retracking restricted to a portion of the echo indicated by the classification

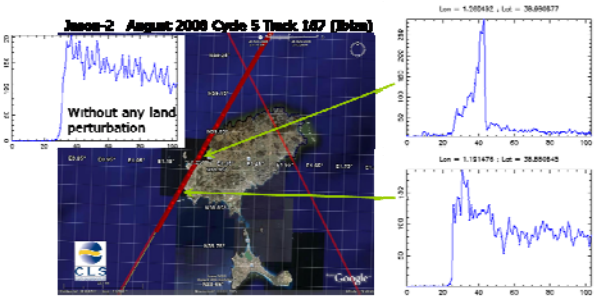

Figure 1. Perturbed altimeter echoes approaching the coast

2.2 Improvements in the wet tropospheric correction

Two different wet tropospheric corrections are implemented in the PISTACH prototype:

- The composite correction: a model correction (ECMWF) replaces the radiometer near the coasts (<50 km). For the transition, the model correction is generally shifted at the nearest valid radiometer correction. For more complicated cases, an interpolation and a detrending of the model correction are additionally done.

- The land decontamination correction: The radiometer measures the Brightness Temperature TB(f) which is contaminated by land. A correction is computed : TBcorr(f)=TB(f)-corr(p,f) with corr (p , f) = [TBland(f) – TBsea (f)] × $\boldsymbol{p}$ (f) and p= land proportion in the pixel (fig. 2)

2.3 Local high-resolution geophysical corrections

The PISTACH products include several state of the art geophysical corrections as well as higher resolution local models, in addition to the content of standard Jason2 S-IGDR:

* Corresponding author. CLS, 8-10 rue Hermes, 31520 RamonvilleSt Agne, France,+33561393916 & +33561393782

- Tides: GOT 4.7 (Ray) and T-UGO regional models from LEGOS (soon)
- MSS: GOCINA over the North Atlantic, DNSC08 (global), CLS01(global) + Error fields on all MSS
- Bathy: MGG/ETOPO2V2 (US coasts), ETOPO2V2 (Black and Baltic seas), WebTide (NW Atlantic, Hudson Bay)
- DAC: HR Global solution and T-UGO regional models from LEGOS (TBC)
- Mean Dynamic Topography: Rio 2007 (Mediterranean Sea)
- Distance to shoreline

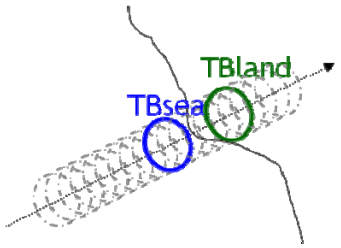

Figure 2: Use of the last TB measured over the sea and the first over the land for computing a new wet tropospheric correction near the coasts.

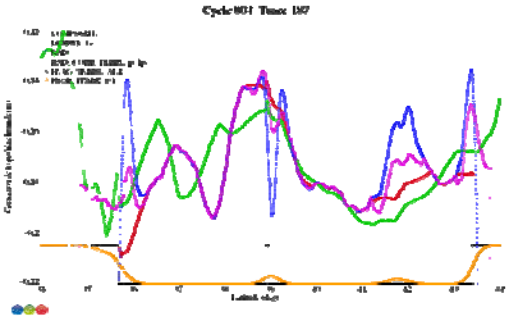

Figure 3: Comparison of several wet tropospheric corrections. Track 187 (cycle 4- Jason 2) – Med. Sea

3. THE PISTACH PRODUCTS

3.1 Format and contents

The PISTACH products use a NetCDF format very similar to Jason-2 GDR format with same variable names and around 80 additional new fields like all the retracking outputs (class, ranges, sigma0, SWH, …). A description of each variable is given in the header.

These products are high-resolution along-track data at both 1hz (6km) and 20 Hz (300m) sampling rate. They cover the whole ocean plus a 25 km fringe over lands. For one cycle and uncompressed, they weigh around 7 Go. They can be freely download since November 2008 on AVISO website: http://www.aviso.oceanobs.com/ (data / products / SSH/ global/ coastal..).

3.1 Coastal applications

A Sea Surface Height is obtained by combining the following PISTACH fields: SSH= satellite altitude – Range (from one retracking) –Sea Surface Bias – Atmospheric corrections (iono, wet , dry) – tides (pole, land and ocean) – HF dynamics

Several combinations of retracking, tidal models, wet tropospheric corrections,… are then available. For obtaining a SL Anomaly, a Mean SSH has to be removed: Three MSSH are provided in PISTACH products: Global CLS01V1 (on 1993-1999, 1/30°), Global DNSC08 (on 1993-2004, 1/60°) and the local GOCINA (North Atlantic)

Compared to the classical products (Jason2 – 1hz – with editing), there is an actual benefit for the coastal oceanography to process the current PISTACH products (fig. 4) : Where the standard Jason-2 GDR stops at ~10 km from the coast, the PISTACH processing allows recovery of reliable measurements up to 5 km from the shoreline.

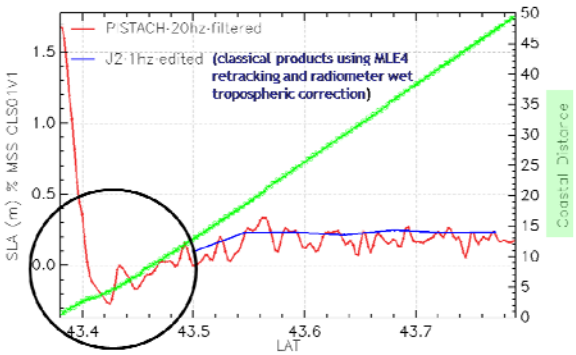

Figure 4: Comparison of PISTACH (red)along-track high-resolution altimeter products (SLA) – track 248 in the Bay of Biscay with standard along-track altimeter products (blue) during Jason-2 cycle 24. The green curve indicates the distance to the coast in kilometers.

4. CONCLUSION

The new coastal altimetric PISTACH products include new retracking solutions, new wet tropospheric corrections, several state-of-the-art geophysical solutions as well as higher resolution global/local models in addition to the content of standard Jason-2 products. The prototype has been commissioned and products are accessible to scientific users. They presently need to be analyzed deeper to determine adequate filtering and editing strategies and to be assessed with independent data.

Trichodesmium blooms in the South Western Tropical Pacific (SWTP) Ocean: 30 years of observations from CZCS, POLDER, SeaWiFS and MODIS

C. Dupouy [a,*], D. Benielli [b], Y. Dandonneau [c], and T.K. Westberry [d]

[a] LOPB, Centre IRD de Nouméa, Nouvelle Calédonie – cecile.dupouy@ird.fr
[b] UMR6110, Laboratoire d'Astrophysique de Marseille, France –, dominique.benielli@oamp.fr
[c] LOCEAN-IRD, Univ. Pierre et Marie Curie, France – yd@lodyc.jussieu.fr
[d] Oregon State University, Corvallis, USA – toby.westberry@science.oregonstate.edu

Abstract – *Trichodesmium*, a major colonial cyanobacterial nitrogen fixer often associated with picoplanktonic cells, forms large blooms in tropical oligotrophic oceans and enhances CO_2 sequestration by the ocean due to its ability to fix dissolved dinitrogen. Its large chlorophyll blooms with a regular pattern in the SWTP have been detected with all ocean colour sensors (CZCS, POLDER, SeaWiFS and MODIS). Here, an algorithm has been developed for discriminating radiance anomalies observed in SeaWiFS imagery over the summertime in the SWTP and is validated with in situ observations of *Trichodesmium* accumulations for the period 1997-2004. The fraction of pixels identified as *Trichodesmium* in the region 5°S-25°S 160°E-190°E is low (between 0.1 and 0.5%) but is about 100 times higher than previous algorithms indicate. A monthly climatology of the distribution of *Trichodesmium* blooms in the SWTP is presented.

Keywords: *Trichodesmium*, New Caledonia, N_2 fixation.

1. INTRODUCTION

Oceanic N_2 fixation has been postulated to regulate atmospheric CO_2 over geological time via the enhancement of biological sequestration of CO_2 in the ocean and this mechanism is especially important in oligotrophic tropical oceans, where N_2 fixation is the major source of «new N» (Capone et al., 2007; Deutsch et al., 2007; Bonnet et al., 2009). In the South Western Tropical Pacific (SWTP), the Coastal Zone Color Scanner has detected large summer surface blooms (Dupouy et al., 1988) where 20% of the total biomass was caused by *Trichodesmium* (Dupouy et al., 2000; Neveux et al., 2006). These blooms were less reflective than coccolithophorid blooms (Grepma et al., 1988) but more reflective than *Gyrodinium* spp. blooms in the English Channel (Dupouy, 1982; Holligan et al., 1983) detected by CZCS. Dupouy et al. (2008) characterized optical properties of *Trichodesmium* colonies around New Caledonia. Nitrogen fixation estimates from nine cruises in the SWTP by both *Trichodesmium* and picoplanktonic forms in the SWTP was high compared with global estimates (Moutin et al., 2005; Garcia et al., 2007).
Classical remote sensing algorithms for *Trichodesmium* bloom detection fail in showing the seasonality of *Trichodesmium* blooms in the South Western Tropical Pacific (Westberry et al., 2006). Here we present a new algorithm for SeaWiFS which allows the detection of *Trichodesmium* surface blooms in the SWTP. This algorithm is based on the Physat classification method which has prooved promising in discriminating several dominant phytoplankton groups from their radiance anomalies (Alvain et al., 2005).

2. MATERIALS AND METHODS

The classification method, "Physat", (Alvain et al., 2005) was initially developed for the discrimination of major phytoplankton groups at global scale in Case 1 waters. Waters dominated by diatoms, *Prochlorococcus*, *Synechococcus*-like cyanobacteria or nanoeukaryotes could thus be discrimnated according to their radiance anomaly spectra

$$nL^*w\ (\lambda) = nLw(\lambda) / <nLw(\lambda)>. \quad (1)$$

where $<nLw(\lambda)>$ is the likelihood of nLw at a given chlorophyll concentration, computed as the average of a large global SeaWiFS dataset, and nL*w is the radiance anomaly relative to this average. The main advantage of Physat is to remove the first order variability in ocean color caused by chlorophyll concentration while preserving the variability that may be specifically caused by individual phytoplankton species or other optically active components, thus greatly reducing the signal to noise ratio. The methodological advantage of Physat is that it provides objective and quantitative criteria allowing characterization of radiance anomaly spectra at each pixel. Here, the ratios of SeaWiFS normalized water leaving radiance are then used to build a look up table analogous to the Physat one, but based on K_{490} instead of chlorophyll. Then, we obtain a "radiance anomaly spectrum" (RAS)

$$nL^*w_{K490}\ (\lambda) = nLw\ (\lambda) / < nLw\ (\lambda)_{K490} >. \quad (2)$$

All SeaWiFS daily Level 2 GAC orbits from 1998-2004 and covering the Western Pacific Ocean (160°E-160°W/25°N-25°S area) were used to compute the look up table, in order to avoid biases due to space and time averaging in Level 3 data. The latter products were provided by NASA/GSFC (reprocessing 5.2) and included water leaving radiance (nLw (λ)) at 6 channels (442, 490, 510, 550, and 670 nm) as well as chlorophyll concentration and the SeaWiFS "K490" product, at a spatial resolution of 4 km x 4 km (28 pixels for one degree). Therefore, the algorithm described herein is restricted to this spatial and temporal resolution.

* Corresponding Author. LOPB, IRD Nouméa; tel 687 26 07 29, fax 687 26 43 26.

The definition of the RAS of *Trichodesmium* in the SeaWiFS satellite imagery was made both empirically and statistically. Ten austral summertime scenes from 2003 and 2004 were sufficient to define the spectral shape of anomalies corresponding to the presence of high concentration of *Trichodesmium* as observed in January 2003 (near the peak abundance obtained during the Diapalis 7 cruise, 6000 trichomes per Liter (Neveux et al., 2006) and in January 2004 (maximum abundance of 6500 trichomes per Liter East of New Caledonia during the Motevas cruise transect. The majority of pixels for the region around New Caledonia in summer 2003 and 2004, present a characteristic "shape" i.e. either 1) always a "bump" at 412 nm (positive $nL^*w_{K490}(412)$), 2) never a "bump" at 555 nm (nul or negative nL*w 555), 3) always troughs at 443, 490 and 510 nm (negative $nL^*w_{K490}(443)$, $nL^*w_{K490}(490)$ and $nL^*w_{K490}(510)$), and 4) never a trough at 670 nm (rather neutral $nL^*w_{K490}(670)$. A weighting of these criteria (a weight of 2 for the first and last criteria (numbers 1 and 4) and weights lower than 1.5 for other criteria) allows the selection of pixels which approach an ideal curve.

3. RESULTS

The algorithm was tested on all Level-2 GAC water leaving radiance and chlorophyll surrounding New Caledonia, Vanuatu and Fiji Islands. Note that this corresponds to an extremely large number of pixels (in total: between 5 10^4 and 1 10^6 pixels) with a similar number of non-cloudy pixels screened for each year and season.

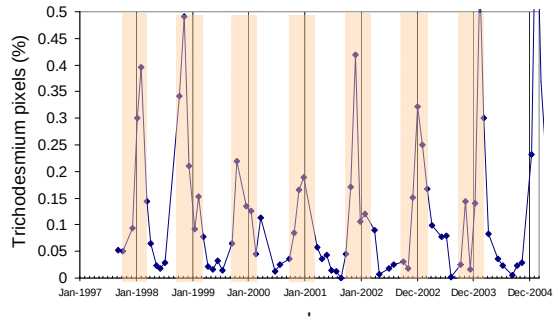

Figure 1 *Trichodesmium* blooms by SeaWiFS in the SWTP.

Maximum percent cover of *Trichodesmium* blooms retrieved by the algorithm appears in January, which is also the period of maximum sea surface temperature and the period of high abundance of *Trichodesmium* near the islands. Indeed, winter transects were characterized by low abundance or a total absence of *Trichodesmium* filaments at the surface. More importantly, the percentage of retrieved *Trichodesmium* pixels varies among years, with maximal values in 1998, 1999 and 2003 and 2004 as seen in the time series of *Trichodesmium*-flagged pixels (Figure 1).

4. CONCLUSION

The percentage of *Trichodesmium*-flagged pixels is low (maximum 0.5% of the non-cloudy pixels) but is still higher than the number of pixels retrieved in the area by the algorithm of Westberry et al (2006). The algorithm was tested in the SWTP and must still be used in other *Trichodesmium* rich areas in the oligotrophic tropical ocean.

ACKNOWLEDGEMENTS

IRD and CNRS (PROOF) supported the Diapazon program and the nine Diapalis cruises in the SWTP. The French Navy is thanked for its support. This work is a continuation of bloom detection activities initiated by Michel Viollier at the Laboratoire d'Optique Atmospherique, University of Lille, France.

REFERENCES

Alvain S., C. Moulin, Y. Dandonneau and F.M. Breon (2005). "Remote sensing of phytoplankton group in case 1 waters from global SeaWiFS imagery". Deep Sea Res. I, vol. 52, pp. 1989-2004.

Bonnet, S., I. Biegala, P. Dutrieux, L. O. Slemons and D. Capone (2009). "Nitrogen fixation in the Western equatorial Pacific: Rates, diazotrophic cyanobacterial size class diversity and biogeochemical significance". Global Biogeochem. Cycles, vol. 23, doi:10.1029/2008GB003439.

Capone D.G., and A.N. Knapp (2007). "Oceanography: A marine nitrogen cycle fix ?". Nature, vol. 445, pp. 159-160.

Deutsch C., J. L. Sarmiento; D. M. Sigman, N. Gruber and J. P. Dunne (2007). "Spatial coupling of nitrogen inputs and losses in the ocean". Nature, vol. 445, doi:10.1038/nature05392.

Dupouy, C., M. Petit and Y. Dandonneau (1988). "Satellite detected cyanobacterial bloom in the southwestern tropical Pacific: Implication for oceanic nitrogen fixation". Int. J. Remote Sensing, vol. 9, pp. 389-396.

Dupouy C., J. Neveux, A. Subramaniam, M. Mulholland, J. Campbell, J. Montoya, E. Carpenter and D. Capone (2000). "Satellite captures *Trichodesmium* blooms in the Southwestern Tropical Pacific". EOS Transactions AGU, 81, pp. 13, 14-16.

Dupouy, C., J. Neveux, G. Dirberg, R. Röttgers, M. Tenório and S. Ouillon (2008). "Bio-optical properties of the marine cyanobacteria *Trichodesmium* spp.", Journal of Applied Remote Sensing, vol. 2, pp. 1-17.

Garcia, N., P. Raimbault, and V. Sandroni (2007). "Seasonal nitrogen fixation and primary production in the Southwest Pacific: nanoplankton diazotrophy and transfer of nitrogen to picoplankton organisms". Mar. Ecol. Prog. Ser., vol. 343, pp. 25–33.

GREPMA (Viollier, M., Sournia, A., Birrien, M.-J., Chretiennot-Dinet, P., Le Borgne, P., Le Corre, P., Morin, P., and Olry, J. P.), 1988. "Satellite (AVHRR:NOAA-9) and ship studies of a coccolithophorid bloom in the western English Channel". Marine Nature, 1 (1), 1–14.

Holligan, P.M., M. Viollier, C. Dupouy, and J. Aiken (1983). "Satellite studies on the distribution of chlorophyll and dinoflagellate blooms in the Western English Channel". Cont. Shelf Res., vol. 2, pp. 81-96.

Moutin T., N. Van Den Broek, B. Beker, C. Dupouy, P. Rimmelin, and A. Le Bouteiller (2005). «Phosphate availability controls *Trichodesmium* spp. biomass in the SW Pacific Ocean". Mar. Ecol. Prog. Ser., vol. 297, pp. 15–21.

Neveux, J., M. Tenorio, C. Dupouy and T. Villareal (2006). "Spectral diversity of phycoerythrins and diazotrophs abundance in tropical South Pacific". Limnol. Oceanography, vol. 51, no 4, pp. 1689-1698.

Westberry, T. K., and D. Siegel (2006). "Spatial and temporal distribution of *Trichodesmium* blooms in the world's oceans". Global Biogeochemical Cycles, vol. 20, 4016, doi10.1029/2005BG002673002517.

2010: MOBY begins a third decade of service

M.E. Feinholz, M.A. Yarbrough, S.J. Flora, T. Houlihan, D. Peters [a], B.C. Johnson, S.W. Brown [b], K. Voss [c], D.K. Clark [d], M. Ondrusek [e], Y.S. Kim [f], A.C. Parr [g]

[a] Moss Landing Marine Laboratory, 8272 Moss Landing Road, Moss Landing, CA 95039, USA
[b] National Institute of Standards and Technology, 100 Bureau Drive Stop MS 8441, Gaithersburg, MD 20899, USA
[c] University of Miami Physics Department, 1320 Camposano Dr, Coral Gables, FL 33124, USA
[d] Marine Optical Consulting, 842 Mill Creek Rd, Arnold, MD 21012, USA
[e] DOC/NOAA/NESDIS/STAR, 5200 Auth Road, Camp Springs, MD 20746, USA
[f] Perot Systems Corporation, 5200 Auth Road, Camp Springs, MD 20746, USA
[g] Space Dynamics Laboratory, Utah State University, 1695 North Research Park Way, North Logan, UT 84341, USA

Abstract – Since Oceans From Space Venice 2000 the Marine Optical BuoY team has been busy: 1.) continuing a decade-long climate quality water-leaving radiance record, 2.) detailing and reducing the radiometric uncertainty budget, and 3.) preparing for the next-generation of MOBY.

Keywords: MOBY, vicarious calibration, ocean color.

1. INTRODUCTION

Since 1996 the Marine Optical BuoY (MOBY) has made *in situ* measurements at the Hawaii mooring site, providing Lwn timeseries for vicarious calibration of satellite ocean color sensors, including SeaWiFS, OCTS, POLDER, IRSI-MOS, and MODIS (Franz *et al.*, 2007).

The current best estimate of the uncertainty budget of the MOBY Lu values of less than 5% (Brown *et al.*, 2007) has been achieved by: a platform designed to minimize shadowing affects and depth fluctuations, instrument characterizations for radiometric sensitivity to ambient temperature and stray light effects in the single grating spectrographs, extensive pre and post-deployment calibration via NIST-calibrated radiometric standards with NIST on-site monitoring, during-deployment internal reference sources, diver calibrations and cleanings, and biologic anti-fouling techniques.

Throughout, the MOBY team has actively collaborated on intercalibration projects such as SIRREX (Johnson *et al.*, 1995), SIMBIOS (Meister *et al.*, 2003), AERONET (Holben *et al.*, 2001), and SORTIE (Voss *et al.*, 2009) – see appendix below for definition of abbreviations.

2. METHODS, QUALITY-CONTROL, ANALYSIS

MOBY measures Ed and Lu at 3 depths, plus Es via collectors fiber-optically connected to two single-grating spectrographs with 1024 channels total, between 350 and 950 nm, resulting in a spectral sampling of less than 1 nm. This high spectral resolution allows computing band-averaged Lwn values that are weighted for a variety of satellite ocean-color sensors' spectral bands.

Ancillary measurements include internal and external instrument temperatures, depth, X/Y tilt, and compass direction. Two MOBYs have been rotated through 3-4 month deployments continuously since February 1994 at a deep-water mooring West of Lanai, Hawaii.

Deployment cruises are often combined with other bio-optical experiments (ex: MOCE, SORITE), and small-boat SCUBA diver maintenance cruises are launched from Maui approximately monthly. MOBYs are refurbished and recalibrated between deployments at the University of Hawaii Marine Center on Oahu.

MOBY radiation measurements sample underwater Ed and Lu sequentially, with Es references interspersed - an optical "profile" requires 30 min to 1 hour to complete. Diffuse attenuation coefficients, KE and KL, with Es ratios are used to compute water-leaving radiance, Lw, which is solar-normalized to yield Lwn (Clark *et al.*, 2003).

Extensive efforts to characterize and correct for spectral stray light in all MOBY systems resulted in correction factors to Lw between -4.0% to +9.6% for MODIS bands 8-13 (Feinholz *et al.*, 2009). We continue to investigate the effect of, and plan to apply a correction for instrument self-shading in MOBY Lu measurements (Mueller, 2007). We also continue a rigorous calibration schedule - NIST calibrated radiometric standards and monitors, routine inter-comparison with NIST-traceable radiometers and sources - and are prepared to re-analyze the extensive MOBY time-series data set.

3. FUTURE DIRECTIONS

Development progresses with next-generation MOBY-C (Yarbrough *et al.*, 2007). Simultaneous acquisition of multiple fiber-optic collectors are estimated to reduce measurement uncertainty between 20% to 60%, relative to the sequentially sampled MOBY spectrographs. Characterization to-date of 2 new prism-grating-prism in-line spectrographs (Resonon, Inc.) with 14-fiber bundles includes: CCD camera noise, wavelength calibration, spectral stray light, imaging behavior, and system response.

4. CONCLUSION

With support from NOAA and NIST, the MOBY project will continue to provide high-quality vicarious calibration data to the international ocean color community.

ACKNOWLEDGEMENTS

This work is funded by NOAA grant NA08NES4400014 to MLML, supported by the NIST / NOAA MOU: "Calibration Services for the Marine Optical Buoy (MOBY) Operations" between NOAA/NESDIS and NIST/PL, and the NIST Co-operative agreement 70NANB8H8113 to MLML "Fiber Optic Ocean Color Sensor Development".

REFERENCES

Brown, S.W., S.J. Flora, M.E. Feinholz, *et al.*, (2007). "The Marine Optical BuoY (MOBY) radiometric calibration and uncertainty budget for ocean color satellite sensor vicarious calibration". Proc. SPIE, vol. 6744, 67441M.

Clark, D.K., M.A. Yarbrough, M. Feinholz *et al.*, (2003). "MOBY, A Radiometric Buoy for Performance Monitoring and Vicarious Calibration of Satellite Ocean Color Sensors: Measurement and Data Analysis". NASA Tech. Memo., 2003-211621, Rev 4, vol. VI, pp. 3-34.

Feinholz, M.E., S.J. Flora, M.A. Yarbrough, *et al.*, (2009). "Stray Light Correction of the Marine Optical System". J. Atmos. Oceanic Technol., vol. 26, pp. 57-73.

Franz, B.A., S.W. Bailey, P.J. Werdell, and C.R. McClain (2007). "Sensor-independent approach to the vicarious calibration of satellite ocean color radiometry". Appl. Opt., vol. 46, pp. 5068-5082.

Holben, B.N., D. Tanré, A. Smirnov, *et al.*, (2001). "An emerging ground-based aerosol climatology: Aerosol optical depth from AERONET". J. Geophys. Res., vol. 106(D11), pp. 12067-12097.

Johnson, B.C., S.S. Bruce, E.A. Early, *et al.*, (1995). "The Fourth SeaWiFS Intercalibration Round-Robin Experiment (SIRREX-4), May 1995". NASA Tech. Memo. 104566, vol. 37, pp. 65.

Meister G., P. Abel, K. Carder, *et al.*, (2003). "The Second SIMBIOS Radiometric Intercomparison (SIMRIC-2), March-November 2002". NASA Tech. Memo. 2003-01930, pp. 65.

Mueller, J. (2007). "Self-Shading Corrections for MOBY Upwelling Radiance Measurements". http://moby.mlml.calstate.edu/sites/default/files/2007_NOAA_Self-Shading%20Corrections%20for%20MOBY.pdf

Voss K.J., S. McLean, M. Lewis, *et al.*, (2009). "An example crossover experiment for testing new vicarious calibration techniques for satellite ocean color radiometry". Submitted to J. Atmos. Oceanic Technol.

Yarbrough, M., S.J. Flora, M.E. Feinholz, *et al.*, (2007). "Simultaneous measurement of up-welling spectral radiance using a fiber-coupled CCD spectrograph". Proc. SPIE, vol. 6680, 66800J

APPENDIX

Abbreviations used above: Lwn, normalized water-leaving radiance; Lu, upwelling radiance; Ed, downwelling irradiance; Es, surface-incident irradiance; MOBY, Marine Optical BuoY; SeaWiFS, Sea-viewing Wide Field-of-view Sensor; OCTS, Ocean Color and Temperature Sensor; POLDER, Polarization Detection Environmental Radiometer; IRSI-MOS, Modular Optoelectronic Scanner on the Indian Research Satellite; MODIS, Moderate Resolution Imaging Spectrometer; MOCE, Marine Optical Characterization Experiment; SIMBIOS, Sensor Intercomparison for Marine Biology and Interdisciplinary Oceanic Studies; AERONET, Aerosol Robotic Network; SIRREX, SeaWiFS Intercalibration Round-Robin Experiment; SORTIE, Spectral Ocean Radiance Transfer Investigation and Experiment.

The First Attempt to Test Correlation between MODIS Chlorophyll-a Concentrations and In Situ Measurments in The Southern Caspian Sea

F. Fendereski [a] *, A. Salman Mahiny [a], S. A. Hosseini [a], H. Fazli [b]

[a] Gorgan University of Agricultural Sciences and Natural Resources, Gorgan, Iran – fendereski_f@yahoo.com, a_mahini@yahoo.com, hoseini_abbas@yahoo.com
[b] Assistant Professor, Caspian Sea Ecology Research Centre (EACS), Sari, Iran – hn_fazli@yahoo.com

Abstract – The MODIS chlorophyll-a data set compared with in situ chlorophyll data from the southern Caspian Sea. The analysis revealed an overestimation of chlorophyll-a concentration by MODIS in the area. The results also indicated a root mean square (RMS) log error of 39.4%, using 53 data points where in situ and satellite data were coincident and collocated. The artificial Neural Network (ANN) was also applied using in situ measurements and satellite imagery. The evaluation of predictive capability of ANN approach was satisfying (RMS log error 18.9%). The results show that retrieving chlorophyll-a concentration in the southern Caspian Sea from satellite is possible and will be improved using ANN along with correlated environmental parameters.

Keywords: MODIS, chlorophyll-a, Caspian Sea.

1. INTRODUCTION

The Caspian Sea is the world's largest inland water body with no outlet to the ocean. Its surface area and volume are about 4×10^5 km^2 and 7.8×10^4 km^3. The Caspian Sea is divided into the northern, middle, and southern parts (Sur *et al.*, 2000). The Southern Caspian has the largest volume - some 64 % of the total volume, and its area amounts to 35 % of the total area of the sea (Aladin and Plotnikov, 2004).
Phytoplankters are the dominant primary producers in aquatic environments. In open oceanic waters, they are the sole source of energy transfer that control life in higher trophic levels. Apart from playing this significant role, primary production and phytoplankton biomass provide input into local, regional and global models of biogeochemical cycles, which in turn are applied in developing multidisciplinary models for climate change (Kyewalyanga et al., 2007). Chlorophyll-a (chl-a) concentration has also an important economic effect in coastal and marine environments on fisheries resources and marine aquaculture development (Radiarta and Saitoh, 2008). In such cases, it is required to characterize and quantify large-scale temporal and spatial variability in phytoplankton biomass and primary production (Kyewalyanga et al., 2007). Satellite estimates have been found to be useful to study spatial and temporal variability of chl-a. They provide synoptic views of spatial distribution unachievable by other means, and are ideally suited to cover the broad range of space and time scales associated with coastal and marine applications (Radiarta and Saitoh, 2008). Despite the necessity of understanding dynamics of chl-a and its fluctuations in marine ecosystems and also the undeniable importance of remote sensing in achieving this aim, to date no officially reported research has been conducted on this subject for the southern Caspian Sea.
Artificial neural network (ANN) approach provides the means to flexibly model nonlinear relationships. It has great capacity in predictive modeling, i.e. all the characters describing the unknown situation must be presented to the trained ANN, and the identification (prediction) is then given (Lek and Gue'gan, 1999). Due to these characteristics, this approach was used in this study, deploying satellite imagery and some in situ measurements, to investigate possibility of gaining better results in chlorophyll estimation from satellite imagery in the area.

2. MATERIAL AND METHODS

2.1 Study Area

The study area is located between 36.33º to 47.07º N and 45.43º to 54.20º E. Sampling took place aboard the R/V Gilan from the 14th to the 27th October, 2008, covering a total of 60 stations distributed along 11 transects as shown in Fig. 1. Bottom depth ranged from 16 to 840 m.

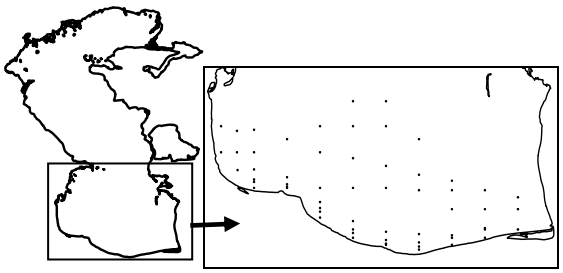

Figure 1. Map showing the Caspian Sea and the transects for CTD stations

2.2 Methods

At each station, CTD profiles were conducted for temperature, pH, dissolved oxygen, conductivity, salinity, turbidity and chlorophyll a concentration. To compare chl-a concentration from ocean-color sensor with that measured in the field, chlorophyll images were downloaded (Level-2 Aqua MODIS, 1 km resolution). In situ data were coincident (occurring within the same time) and collocated (occurring within a single pixel). Because of poor visibility due to clouds, 7 out of 60 stations were eliminated. Comparison was made by computation of RMS log error as:

$$\mathrm{RMS} = \sqrt{\frac{\sum\left[\log(S)-\log(I)\right]^2}{n}}\times 100 \qquad (1)$$

* Corresponding Author. Gorgan University of Agricultural Sciences and Natural Resources, Gorgan, Iran.

where S = Satellite chlorophyll
I = in situ chlorophyll
n = number of samples

We also divided the stations into those occurring in coastal areas (defined as bottom depth>100 m) and offshore areas, and performed RMS log error analysis for the two. In addition, we applied ANN with satellite chlorophyll, temperature, dissolved oxygen, pH and turbidity as inputs and measured chlorophyll as output target of the model. Table A shows environmental variables used as input to the ANN model. The reliability of the model estimations was examined using RMS log error of observed chlorophyll concentrations and model predictions.

3. RESULTS AND DISCUSSION

Field measurements of chl-a concentration varied from 0.65 to 2.17 (mg/m^3) compared to satellite chlorophyll data (1.4 to 4.86 (mg/m^3)). Comparison of in situ and MODIS chlorophyll values along all 11 transects showed MODIS to be overestimating chlorophyll in the area. As can be seen in Table B, RMS log error for this comparison was 39.4% and average error was 1.59. We also tried to separate coastal stations to see if the observed bias would be reduced using only offshore ones. Results showed RMS log error of 38.9% for offshore stations (a total of 31 stations) compared to that 39.4% RMS log error observed for all stations, indicating no significant difference between the two in this study. Furthermore, we used artificial neural networks in this study. ANNs have recently become the focus of much attention, largely because of their wide range of applicability and the power with which they can treat complicated problems. ANNs can identify and learn correlated patterns between input data sets and corresponding target values. After training, ANNs can be used to predict the output of new independent input data (Lek and Gue'gan, 1999). We also used some parameters as inputs to this model (Table A). These variables were shown to be ecologically related to phytoplankton biomass. We also utilized satellite chlorophyll data as the other input to the model. Our objective was to investigate whether the bias observed in the previous results would be reduced using this approach. Table B shows the RMS log error and average error, after applying the ANNs to the test data (18.9% and 0.47, respectively). A brief comparative look at the results in Table B shows that using the ANN model along with environmental variables gives a good prediction of chlorophyll concentration from satellite imagery. The large size of the Caspian Sea requires space borne sensors to monitor phytoplankton pigment concentration at adequate time and space scales (Sur et al., 2000). In this study, we used Aqua MODIS chlorophyll data. Further studies need to be done using other sensors' data. Like many other marine ecosystems in the world, proposing a local algorithm for the southern Caspian Sea is also recommended. In addition, in this study, we used some in situ measured parameters as input variables to the model, but if we want to use this approach for retrieving chlorophyll concentration from satellite data, we require more accurate environmental data. For this purpose, applicability of satellite derived environmental data (e.g., SST) and some stable parameters (e.g., bathymetry) need to be examined.

Table A. Environmental Variables Used in the ANN Model

Variable	Ave.	SD
Temperature (Cº)	22.45	1.25
DO (ppm)	7.72	0.36
pH	8.24	0.1
Turbidity (FTU)	2.97	2.46
Satellite chl-a (mg/m^3)	2.78	0.89
Chl-a (mg/m^3)	1.21	0.33

Table B. RMS Log Error and Bias between In Situ Data and the Aqua MODIS and ANN Prediction Chlorophyll Data

	RMS Log Error %	Mean In Situ chl-a ± Bias
In Situ vs. Satellite Chl-a Data	39.4%	1.21±1.59
In Situ vs. Predicted Chl-a Using ANN	18.9%	1.07±0.47

4. CONCLUSION

Moderate agreement between MODIS and in situ chlorophyll data, together with satisfying results from ANN model wherein ecologically important parameters were also included, reveals the necessity of further studies on extracting chlorophyll-a from satellite in the area using simultaneous sea sampling and application of modern techniques like ANN. We also should not neglect the unavoidable requirement of developing a local algorithm for this purpose in the area.

ACKNOWLEDGEMENTS

We would like to thank the Captain and crew members of the R/V Gilan and the Caspian Sea Ecological Research Centre. We are also very grateful to Vittorio Barale and Kwang-Seuk Jeong for their help in applying the methods and interpreting the results.

REFERENCES

Nicolai Aladin and Igor Plotnikov (2004). The Caspian Sea. Lake Basin Management Initiative, Thematic Paper, 29 P.

Kyewalyanga, M. S., Naik, R., Hegde, S, Raman, M., Barlow, R. and M. Roberts (2007). "Phytoplankton biomass and primary production in Delagoa Bight Mozambique: Application of remote sensing". Journal of Estuarine, Coastal and Shelf Science, vol. 74, pp. 429–436.

Lek, S. and J.F. Gue'gan (1999). "Artificial neural networks as a tool in ecological modelling, an introduction". Journal of Ecological Modelling, vol. 120, pp. 65-73.

Radiarta, I. N. and S. Saitoh (2008). "Satellite-derived measurements of spatial and temporal chlorophyll-a variability in Funka Bay, southwestern Hokkaido, Japan". Journal of Estuarine, Coastal and Shelf Science, vol. 79, pp. 400-408.

Sur, H. I., Ozsoy, E. and R. Ibrayev (2000). "Satellite-derived flow characteristics of the Caspian Sea". In *Satellites, Oceanography and Society* (ed. D. Halpern), pp. 289-296. Elsevier Oceanography Series.

Global and Regional Study of MODIS SST Accuracy

M. Framiñan *, P.J. Minnettt, R.H. Evans

University of Miami, RSMAS/MPO, Miami, U.S.A.– mframinan@rsmas.miami.edu, pminnett@rsmas.miami.edu, revans@rsmas.miami.edu

Abstract – Improving the accuracy of satellite derived products is a constantly evolving effort. Thousands of new in-situ measurements of sea-surface temperature are available every month, increasing our capabilities to evaluate the uncertainties in the satellite retrievals and their characteristics. The variability in the accuracy is studied here using data from the MODIS SST Matchup Data Base (MMDB) of co-located in-situ and satellite measurements. Monthly, seasonal and inter-annual statistics and spatial distribution are analyzed to investigate the residual error variability during the period 2000-2007 and 2002-2007 for MODIS-TERRA and MODIS-AQUA, respectively. The differences between day and night retrievals, as well as TERRA and AQUA SST retrievals are evaluated. Results allow the identification of regions where errors are larger than the global estimates and quantify their differences.

Keywords: MODIS, SST, validation.

1. INTRODUCTION

Current uncertainties in the sea-surface temperature (SST) retrievals (bias errors of <0.2 K with a scatter of 0.3-0.5 K) approach those that are required for climate research. However, these estimates of accuracy are specified on a global basis and result from the application of globally optimized atmospheric correction algorithms. More detailed analysis of the differences between the satellite and in situ measurements reveals patterns of larger, systematic discrepancies that are clearly related to the atmosphere and ocean variability.

The residual errors in the atmospheric correction are significant contributions to the satellite SST retrieval uncertainties, and these are most pronounced where the atmospheric conditions depart significantly from the ensemble of conditions used to derive the calibration coefficients. The effect of the atmosphere on the upward propagating emission from the sea surface is dependent on the air-sea temperature difference, ΔT. The relative uniformity of ΔT, globally, aids in the accurate measurement of SST by spaceborne infrared radiometers, but when anomalous ΔTs exist, larger systematic errors in the SST retrievals can be expected. There is evidence that the accuracy of the retrievals could be markedly improved by developing algorithms with regional and temporal optimization, especially in situations which are known to introduce larger errors into the current retrievals. Such situations are characterized by atmospheric conditions that deviate from the climatological mean, and include: 1) Very moist (dry) atmospheres, such as those present at low (high) latitudes. 2) Areas with presence of aerosols in the atmosphere. 3) Areas with an anomalous atmospheric water vapor distribution, such as dry layers. 4) Regions with anomalously large air-sea temperature differences, such as those observed in equatorial or coastal upwelling areas.

In this study, the spatial and temporal variability in the accuracy of MODIS SST is evaluated on global and regional scales. Monthly, seasonal and inter-annual statistics and spatial distribution are analyzed to investigate the residual error variability during the period 2000-2007 and 2002-2007 for MODIS-TERRA and MODIS-AQUA, respectively. Results allow the identification of regions where errors are larger than the global estimates and their quantification. An analysis using environmental parameters provides insight on the factors affecting the retrievals in each region, contributing to a better understanding of the error budget associated with the SST measurements.

2. DATA AND METHODOLOGY

The residual errors, the differences between satellite-derived and the in situ measurements, are studied here using the long-wave sea SSTs derived from MODIS thermal infrared bands 31 and 32 at 11 μm and 12 μm wavelengths. The data correspond to the MODIS SST Matchup Data Base (Evans et al., 2006) of co-located in-situ and satellite data within 30 minutes of overpass and $\pm$ 0.1^{o} of latitude and longitude. In-situ observations include buoys and data from the ship-based Marine-Atmospheric Emitted Radiance Interferometers (M-AERI). The M-AERI is a Fourier- Transform infrared interferometer with very stable internal blackbody calibration targets that provides spectra of the oceanic and atmospheric emission in the wavelength range from ~3 to ~18 μm (Minnett, et al., 2001).

The residual errors were interpolated to a grid 0.25x0.25 degree in latitude and longitude. Global maps and statistics of were obtained for the TERRA and AQUA retrievals. Distributions for day/night dataset, quality levels (0, 1, 2), annual, seasonal and monthly were analyzed.

A total of 3,095,044 in-situ observations were available in the match up-database for MODIS/*Aqua* retrievals for the period 2002–2007, and 3,096,973 for MODIS/*Terra* for 2000-2007.

3. RESULTS

The best quality level, qsst=0, has 289,913 and 299,803 points for *Aqua and Terra*, with bias of -0.180±0.428 K and -0.149 ±0.453 K, respectively, corresponding to the skin effect.

* Corresponding Author: 4600 Rickenbacker Cswy. Miami, FL, 33149, USA. Tel (1-305) 421-4837, Fax (1-305) 421-4696.

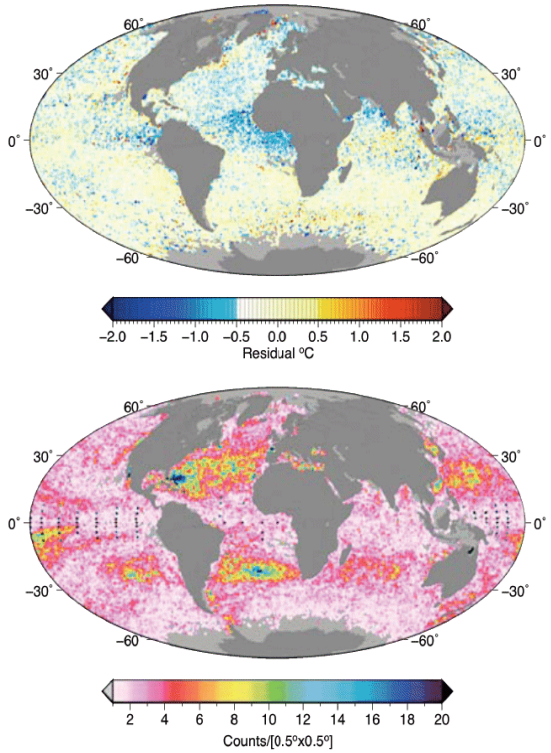

Figure 1. MODIS AQUA SST Residuals and counts in each 0.5°x0.5° degree box.

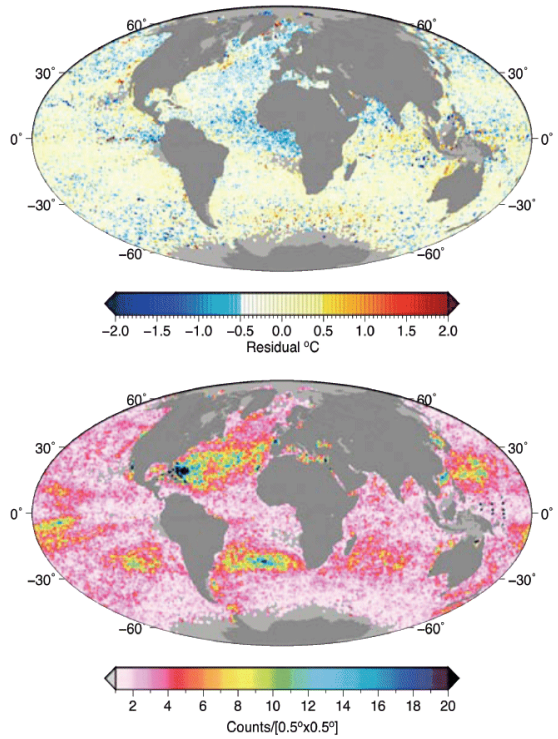

Figure 2. MODIS TERRA SST Residuals and counts in each 0.5°x0.5° degree box.

The global distribution of residual error is presented in Figure 1 and Figure 2 for AQUA and TERRA, respectively. Characteristics of the residuals are shown in Table A. Results for monthly, seasonal and annual distributions are presented.

Table A. MODIS SST residual error.

		N	Mean	Bias
AQUA	All	289913	−0.180	0.428
	Day	180192	−0.158	0.444
	Night	109714	−0.218	0.397
TERRA	All	299803	−0.149	0.453
	Day	176125	−0.118	0.470
	Night	123667	−0.194	0.423

4. SUMMARY AND CONCLUSION

The match-up database provides global coverage and allows the identification of areas were the uncertainties are larger than the global estimates. Although the analyses are being conducted using MODIS data from the two NASA EOS satellites *Terra* and *Aqua*, the results are likely to be applicable to other infrared radiometers The global distribution show regions with significant temporal variability, as well as areas with poor coverage or no data points (light grey in Figure 1 and 2). This is the case in most shallow coastal regions and polar latitudes. Further efforts are needed to better represent the variability in these areas through rigorous ship-based measurements of the ocean surface and geophysical variables, to provide the basis for enhanced algorithms that compensate for the effects of the sources of these additional uncertainties.

ACKNOWLEDGEMENTS

We are grateful to Ms. Kay Kilpatrick and Ms. Elizabeth Williams for their work in maintaining the MMDB. This work is funded by the NASA Physical Oceanography Program, Dr Eric Lindstrom, though grants NNX07AF83G and NNX08AE58G.

REFERENCES

Evans, R. H., K.Kilpatrick, P. J. Minnett, S. Walsh, V. Haliwell, and W. Baringer, 2006: Error Hypercube - a Novel Method to Characterize Bias and Uncertainty for Satellite Infrared Measurements of Sea Surface Temperature.13th Ocean Sciences Meeting, Honolulu, HI, 20- 24 February 2006.

Minnett, P. J., R. O. Knuteson, F. A. Best, B. J. Osborne, J. A. Hanafin, and O. B. Brown, (2001), "The Marine-Atmospheric Emitted Radiance Interferometer (M-AERI), a high-accuracy, seagoing infrared spectroradiometer". Journal of Atmospheric and Oceanic Technology, vol.18, pp. 994-1013.

Deriving Mesoscale Surface Current Fields from Multi-Sensor Satellite Data

M. Gade [a], B. Seppke [b], L. Dreschler-Fischer [b]

[a] Universität Hamburg, Institut für Meereskunde, Germany – martin.gade@zmaw.de
[b] Universität Hamburg, Fachbereich Informatik, Germany – [seppke ; dreschler]@informatik.uni-hamburg.de

Abstract – Sequential multi-sensor satellite images from Envisat ASAR and WiFS are used for the computation of mesoscale surface currents in the southestern Baltic Sea (Southern Baltic Proper). Marine surface films of different origin and accumulated algae at the water surface are imaged by the sensors working in the optical, infrared, and microwave part of the electromagnetic spectrum and can thus be used as tracers for the local motion of the sea surface. Taking advantage of the sufficiently short time lags between the multiple image acquisitions (from less than one hour to one day) and of the high spatial coverage we calculated surface motion fields by enhancing and combining image-processing techniques. Our computed two-dimensional surface current fields are compared with, and they complement, existing data from numerical models.

Keywords: multi-sensor, surface currents, optical flow.

1. INTRODUCTION

Remote sensing data from satellite-borne sensors working at the same or different electromagnetic frequencies can be used to derive ocean current fields, if the same features are visible in the different data sets and if the data were acquired within a certain time period, which depends on the lifetime of the observed features, on the current speed, and on the sensors' spatial resolution. These features may be driven by the local surface motion, and the correlation of the two-dimensional data sets may therefore allow for the calculation of mesoscale ocean current fields. While several studies have been performed on the use of single sensor types (i.e. either optical or radar) for the calculation of surface motion, the combined use of those sensors for sea surface current estimates has not sufficiently been demonstrated so far. Marine surface films are well suited for such kind of data analyses, because they may change both the sea surface roughness and its emissivity of electromagnetic waves (Gade *et al.* 2003, and literature cited therein), and may thus be visible on both optical and radar imagery.

Operational current models such as those run at the Swedish Meteorological and Hydrographical Institute (SMHI) or at the German Federal Maritime and Hydrographic Agency (BSH) provide mean currents in the uppermost meters, but not the motion of the very sea surface. This information may be gained from remote sensors. Depending on the observed features, the sensors' imaging characteristics and of the amount of available data we have applied different methods: a fast normalized cross-correlation analysis was performed with single-channel (synthetic aperture radar) data. A differential method based on the Gradient (or Optical Flow) Constraint Equation (Horn and Schunck, 1981) was used for series of multi-channel data acquired at the same electromagnetic bands and within a short period of time. We present examples for each of the methods.

2. RESULTS

Series of satellite images showing imprints of singular sea surface features may be used to derive local surface currents through a maximum cross correlation (MCC) analysis. We have used a pair of ENVISAT ASAR Wide Swath-Mode images acquired on May 15, 2005 over the south-eastern Baltic Sea (Fig. 1) at 09:00 UTC and 20:25 UTC. The white rectangle inserted into Fig. 1 denotes the 82.5 km × 60 km area, where two oil spills have been detected in both images as dark irregular patches.

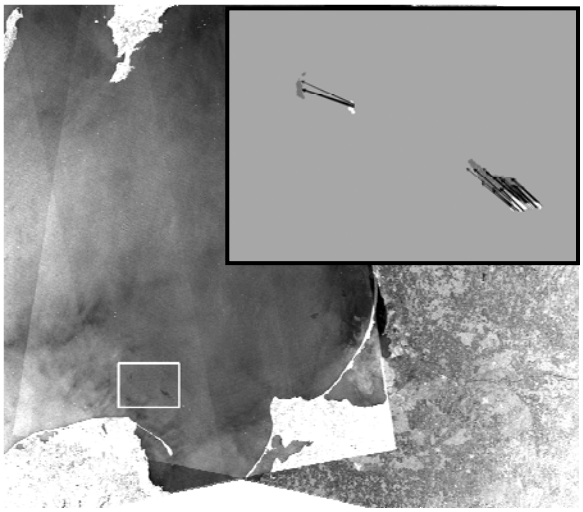

Figure 1. Composite of two ASAR images of the southeastern Baltic Sea acquired on May 15, 2005. The white square north of the Bay of Gdansk denotes the (82.5 km × 60 km) part of the images used for the correlation analysis, whose results are inserted on the upper right.

After the feature detection in the first SAR image we calculated the two-dimensional cross-correlation of the surrounding 50 pixels × 50 pixels area of each detected feature point and the corresponding, but larger (230 pixels × 230 pixels) part of the second SAR image. The local maximum of this correlation was used to determine the surface motion vectors. Our results are inserted in Fig. 1. The white patches in the background origin from the ASAR image acquired at 09:00 UTC, whereas the dark grey patches origin from ASAR image acquired at 20:25 UTC. The arrows are mostly parallel and denote a mean surface speed between 17 cm/s and 28 cm/s.

Our results are in good agreement with modeled currents obtained with the HIROMB model run at SMHI (Fig. 2). In both cases a drift towards north-west was derived. Moreover, according to HIROMB the drift of the north-western spill should be (slightly) larger, which was confirmed by our analysis.

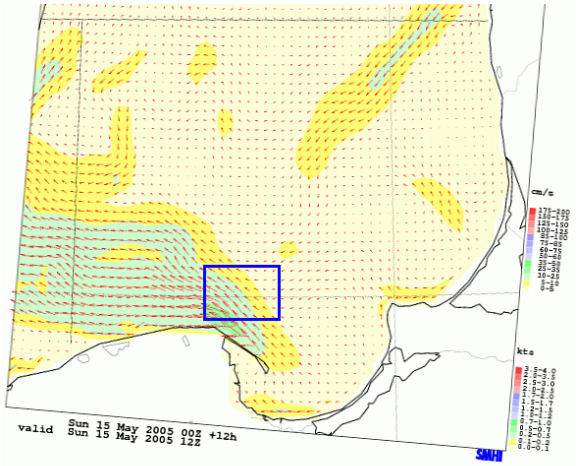

Figure 2. Modeled sea surface currents on May 15, 2005, in the Southern Baltic Proper. Results were obtained with the HIROMB model run at SMHI. The blue square denotes the areas, in which the oil spills were detected (Fig. 1).

The composite of the two WiFS images acquired on July 30, 1999, at 10:03 UTC and 10:39 UTC, and showing imprints of cyanobacteria surface accumulations, is shown in Fig. 3. From both acquisitions band 1 was used for our analyses, whose results are inserted on the upper right of Fig. 3. In the shaded areas (where the algae caused pronounced signatures) we calculated realistic surface currents of about 25 cm/s - 35 cm/s.

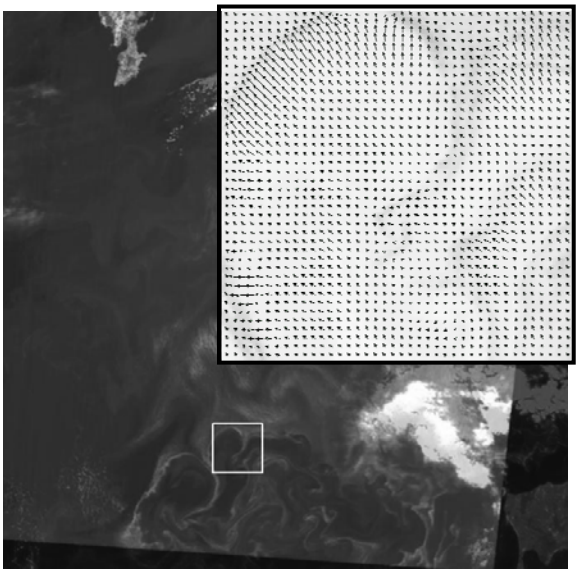

Figure 3. Composite of two WiFS images of the Southern Baltic Proper from July 30, 1999. Gotland's southern tip is visible in the upper left part. The white square denotes the (22.5 km × 22.5 km) subsection used for the differential analysis, whose results are inserted on the upper right.

The corresponding model results from the BSHcmod are shown in Fig. 4. Whereas our results show a general surface motion towards north (note that Fig. 3 is not georeferenced), the BSHcmod predicted a mean current of the uppermost 8 m layer towards south-east. At the time of image acquisitions a moderate wind of 5 m/s from the south was measured on Hel Peninsula (Poland), which apparently forced a northbound surface motion in the area of interest. Apparently this motion can be detected using sequential satellite imagery, whereas it may not be strong enough to influence the mean current in the uppermost sea layer.

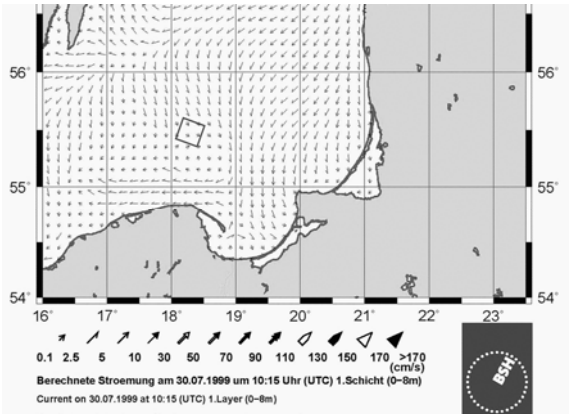

Figure 4. Modeled sea surface currents on July 30, 1999, in the Southern Baltic Proper. Results were obtained with the BSH current model. The inserted square denotes the location of the area, for which surface motions were calculated from satellite images (Fig. 3).

3. CONCLUSIONS

We have demonstrated that multi-sensor satellite data can be used to compute small-scale pixel motions, if accumulated algae or oil spills are present on the water surface. The two methods applied for this study are a cross-correlation analysis and a differential method based on the Optical Flow algorithm of Horn and Schunck (1981). Because of the different imaging characteristics, the first method was applied using SAR imagery (at 150 m pixel size), whereas the latter was applied using optical and NIR imagery (at 188 m pixel size). Both methods, however, are not restricted to certain pixel sizes.

Resulting surface current fields, like those presented in this paper, may complement model results provided by local hydrographic agencies, particularly since their results were calculated for a mean water depth of some meters and on a much coarser grid (e.g., 4 m depth and a 5' × 6' grid, respectively, see the available data from the SMHI). The use of satellite data, as shown herein, may therefore be a valuable addition to the existing model data.

ACKNOWLEDGEMENTS

Thanks are due to Stephan Dick of BSH and to Anette Jönsson of SMHI for providing the model data, and to Olga Lavrova of IKI, Moscow, for her help identifying the ASAR images showing oil spills.

REFERENCES

Gade, M., G. Fiedler, and L. Dreschler-Fischer (2003). "Two-dimensional Sea Surface Current Fields Derived From Multi-sensor Satellite Data", Proceed. IGARSS'03, IEEE, Piscataway, NJ, USA, pp. 3540-3542.

Horn, B.K.P., and Schunck, B.G. (1981). "Determining Optical Flow". Art. Intell., 17, pp. 185-189.

Multi-Sensor Remote Sensing of the Wadden Sea Ecosystem on the German North Sea Coast

M. Gade [a], K. Stelzer [b]

[a] Universität Hamburg, Institut für Meereskunde, Germany – martin.gade@zmaw.de
[b] Brockmann Consult, Germany – kerstin.stelzer@brockmann-consult.de

Abstract – High-resolution multispectral remote sensing data from satellite-borne optical sensors have already been used for the classification of sediments, macrophytes, and mussels in the German Wadden Sea. Since the use of those sensors in northern latitudes is strongly limited by clouds and haze, we included synthetic aperture radar (SAR) data, allowing earth observation that is independent of cloud coverage and daytime. The data acquired at different radar bands (L, C, and X band, from ALOS PALSAR, ERS SAR and ENVISAT ASAR, and TerraSAR-X, respectively) have been used to analyse their potential for crude sediment classification on dry-fallen intertidal flats and for detecting benthic fauna such as blue mussel or oyster beds. The information gained from optical and SAR sensors, together with in-situ observations, will yield an improved classification of different sediment types, together with mussel beds and sea grass.

Keywords: multi-sensor, Wadden Sea, sediment classification, benthic fauna.

1. INTRODUCTION

The increasing requirements of coastal monitoring, to some extend, can be met deploying remote sensing techniques that allow for relatively cheap surveillance of large coastal areas. Optical sensors are already being used for sediment classification on intertidal flats, and promising results have been achieved through the classification of different sediment types, vegetation, and mussel beds (see Fig. 1). However, because of the strong dependence on daylight and cloud conditions, useful optical data (acquired at low tide) from the German North Sea coast are rare. A classification system based on spaceborne remote sensing data would therefore strongly benefit from the utilization of synthetic aperture radar (SAR) data.

Gade *et al.* (2008) suggested to use multi-frequency SAR data for a sediment classification on exposed intertidal flats. However, current spaceborne SAR sensors operate at single frequencies, and as a consequence, SAR data from different satellites have to be used for multi-frequency SAR classification purposes. Because they are usually acquired with a considerable time lag in between, a profound knowledge of the radar backscatter properties of the sediment types, and their dependence on weather conditions, tidal cycle, and imaging geometry is needed, which can only be gained from a joint analysis of multi-satellite SAR data and optical remote sensing data, together with a-priori knowledge gained during in-situ campaigns. The sub-project 4 of the German national project DeMarine-Environment (DMU) is particularly devoted to this synergistic approach.

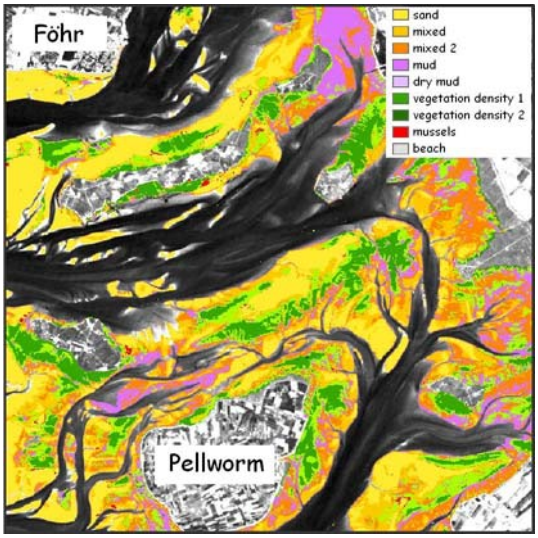

Figure 1. Sediment classification for the North Frisian DMU testsite "Halligenwatt", as generated from Landsat TM data from July 2, 2007 (original data © eurimage 2007)

2. RESULTS

The method used for the classification of optical remote sensing data is based on a linear spectral unmixing and feature extraction from the spectral reflectances (Brockmann and Stelzer 2008). All extracted information from the optical data is combined in a decision tree, which is used to relate each pixel to a class representing different surface types, i.e., five sediment types, two vegetation density classes, one mussel class and a dry and bright sands class. The water coverage, having a strong influence on the spectral reflectance and on the radar backscattering, is considered within the endmember selection for the linear spectral unmixing. Fig. 1 shows the result of a classification applied to a Landsat-5 TM scene from July 2, 2007.

The spatial variations of different sediment types, along with the occurrence of mussel beds, see grass, and macro algae, is typical for the test site "Halligenwatt" in Schleswig-Holstein. Fig. 2 shows two SAR images of the test site that were acquired from different satellites on the same day, during, or shortly after, low tide. The ENVISAT ASAR image in the upper panel was acquired on October 18, 2007, at 09:55 UTC (at low tide), and the ALOS PALSAR image in the lower panel was acquired on the same day, at 10:23 UTC (28 minutes after low tide). Note the different radar contrast of the exposed intertidal flats, which cannot be attributed to the different acquisition time (water level). In general, the radar backscattering from the exposed tidal flats is much lower than that from the surrounding wind-roughened sea surface, because of a strong north-westerly wind (12-13 m/s).

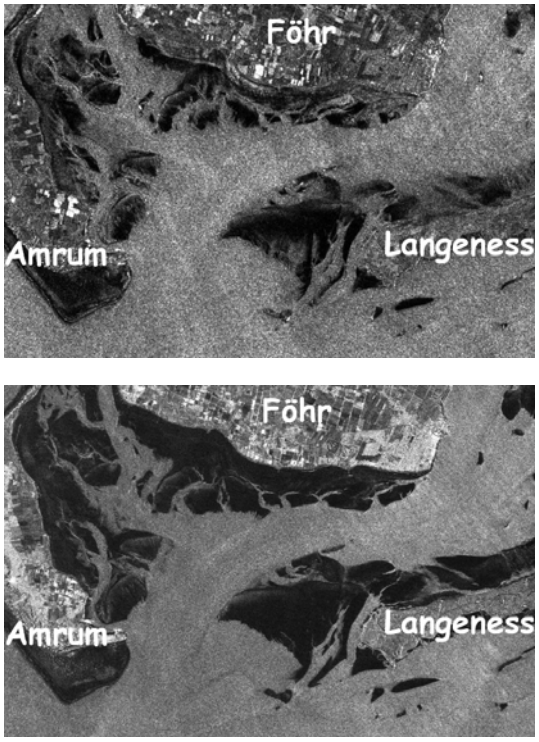

Figure 2. Two SAR images (37.5 km × 25.0 km) of the test site "Halligenwatt", acquired at, or shortly after, low tide. Top: ENVISAT ASAR image (© ESA 2007); bottom: ALOS PALSAR image (© JAXA 2007).

The southern test site "Lütetsburger Plate" in Lower Saxony is dominated by a strong spatial variation of different sediment types, along with a high coverage by mussels. During summer season, some regions are covered by sea grass and green algae. Thus, a simple classification method that assumes bare sediments cannot be applied in this area. Fig. 3 demonstrates how the test site is imaged by SAR sensors working at different radar bands: the upper panel shows an ALOS PALSAR (L-band) image acquired on April 12, 2008, at 21:43 UTC, 23 minutes after low tide, and the lower panel shows a TerraSAR-X (X-band) image acquired on August 30, 2008, at 17:10 UTC, 34 minutes after low tide. The location of the tidal creeks can be identified through enhanced radar backscattering from the sediment on their edges. This local enhancement of the radar backscatter was already found by Gade *et al.* (2008) who attributed it to an enhanced current-induced surface roughness of the sediments (i.e. sand ripple height). However, some irregular bright patches in the left part of both SAR images are not due to sand ripples, but due to mussel beds. That is, for the first time, benthic fauna on exposed intertidal flats has been imaged by multi-frequency (L, C, and X band) SAR sensors.

3. CONCLUSIONS

Within subproject 4 of the national German project DeMarine-Environment (DMU) data from optical sensors and multi-satellite SAR images of exposed intertidal flats are analyzed to improve existing classification systems by including SAR data. For the first time, extensive mussel beds (composed of a mixture of Pacific oysters and blue mussels) have been observed in multi-frequency SAR imagery. However, the strength of their signatures, and thus the capability of SAR sensors to detect and to classify them, may depend on the seasonal change in coverage by brown algae.

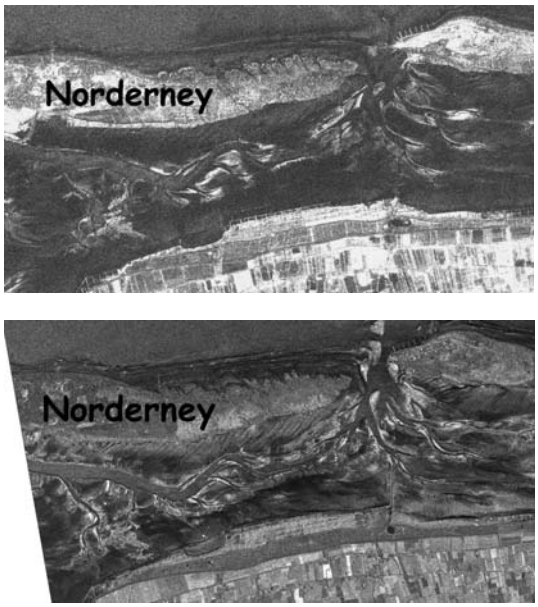

Figure 3. Two SAR images (25.7 km × 13.4 km) of the test site "Lütetsburger Plate", acquired shortly after low tide. Top: ALOS PALSAR image (© JAXA 2008); bottom: TerraSAR-X image (© DLR 2008).

During later stages of the project, results from in-situ campaigns will be included, along with further classification results derived using optical remote sensing data. Of particular interest will be to investigate how the observed SAR signatures depend not only on radar frequency and polarization, but also on the season, on weather conditions, and on the tidal phase. A profound knowledge of all main factors contributing to the observed SAR signatures is essential for any improvement of existing classification systems, and our preliminary results show evidence that multi-satellite SAR data can be used for an improved sediment classification on exposed intertidal flats.

ACKNOWLEDGEMENTS

The authors are grateful to the colleagues participating in DeMarine-U's sub-project 4, who contributed to the results presented herein. DMU receives funding from the German Ministry of Economy (BMWi) under contract 50 EE 0817.

REFERENCES

Brockmann, C., and K. Stelzer (2008). "Optical Remote Sensing of Intertidal Flats", in "Remote Sensing of the European Seas", V. Barale and M. Gade (Eds.), Springer, Heidelberg, pp. 117-128.

Gade, M., W. Alpers, C. Melsheimer, and G. Tanck (2008). "Classification of sediments on exposed tidal flats in the German Bight using multi-frequency radar data", Remote Sens. Environ., vol. 112, pp. 1603-1613.

Comparison Between Seabed Geoforms Identified From Satellite Data and Tide Current Properties Estimated by Numerical Models

Domingo A. Gagliardini [a,b], Mariano Tonini [c], Elbio D. Palma [d]

[a] Centro Nacional Patagónico, Boulevard Brown s/n, (9120) Pto. Madryn, Argentina – agaglia@iafe.uba.ar
[b] Instituto de Astronomía y Física del Espacio, Ciudad Universitaria, (1428) Buenos Aires, Argentina
[c] Instituto Argentino de Oceanografía, Camino de La Carrindanga, (8000) Bahía Blanca, Argentina – mtonini@criba.edu.ar
[d] Dto. de Física, Universidad Nacional de Sur, Avenida Alem 1253, (8000) Bahía Blanca, Argentina – uspalma@criba.edu.ar

Abstract - ERS-SAR and LANDSAT-TM/ETM systems have demonstrated to be an efficient tool for providing a systematic and synoptic view of the sea bottom topography in coastal zones. Dynamical models are able to describe ocean circulation and estimate tidal currents and energy dissipation. Both procedures have been used to monitor the Argentinean Patagonian coast. This paper compares the seabed geoforms identified by these satellites over this region with tide current properties estimated by a high resolution three dimensional numerical model. It is shown that both types of methods present coherent results. Bigger geoforms are found in zones where tidal currents and dissipated energy values calculated by the model are higher.

Keywords: geoforms, tide current, numerical model.

1. INTRODUCTION

As seen in Fig. 1, the San Matias (SMG) and San Jorge (SJG) gulfs are located on the Atlantic coast of South America between 40 º 47 'S and 47 º 06 'S.

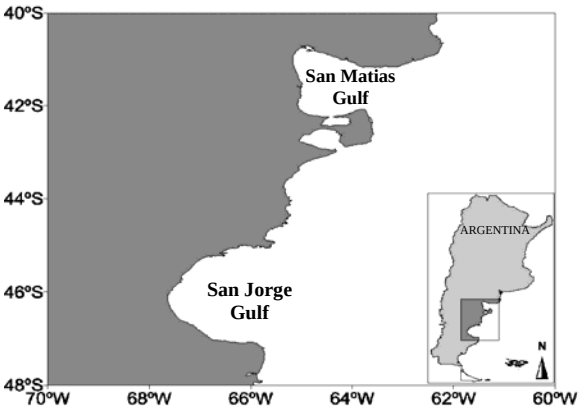

Figure 1. San Matias and Jorge gulfs.

This area is characterized by strong tidal currents with a high rate of heat dissipation and several fronts, representing one of the most important oceanographic regions of the Argentinean Continental Shelf (Acha *et al*, 2004). This paper compares the data obtained in both gulfs entries using information provided by ERS-SAR and LANDSAT-TM/ETM with those achieved using the Princeton Ocean Model (POM; Tonini *et al*., 2006). This comparison showed a strong coincidence between the observed bottom irregularities and places where tidal currents and dissipated energy are highest according to the POM.

2. SATELLITE DATA AND NUMERICAL MODEL

Satellite data used were obtained by ERS-SAR systems and LANDSAT-TM/ETM+ and registered by the receiving station of the Argentine Agency for Space Activities. The numerical model selected (POM-Blumberg and Mellor, 1987), which has been extensively tested and validated in coastal applications, has a mean resolution of 3km and is forced with the M2 tidal component along its open boundary.

3. RESULTS

The entrance of the SMG is an open basin about 60 meters deep. At the north, where tidal currents reach values up to 2 m s^{-1}, LANDSAT-TM/ETM and ERS-SAR images show sand waves with average heights of 4 m (7 m in some cases) and lengths of 80 to 240 m. While in the south, where currents take values around 2 m s^{-1} sand waves are larger with an average height of 10 m (reaching 17 meters in some cases) and a length of 680 m (Gagliardini *et al*., 2004 and 2005). These larger and higher dunes appear in all images while the small waves do not. Both types of dunes are shown in Fig. 2.

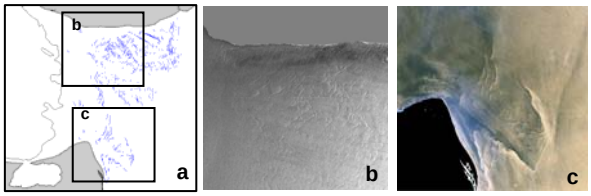

Figure 2. Bedforms identified at the entrance of the San Matias gulf: a) map of bathymetric features identified with ERS-SAR and LANDSAT-TM/ETM data; b) SAR images of the north area, indicated with a square in a, covered by small sand dunes; c) optical images of the south area, indicated with a square in a, with large sand dunes.

In the region of the Patagonian Gulfs, semidiurnal tides are one of the main stressors of the ocean. Particularly the M2 component, as measured by POM, explains over 80% of the variance in the kinetic energy of currents in the internal platform. Quasi-rectilinear flows can be seen south of GSJ and near the entrance of SMG, as seen in Fig. 3a and b respectively, where currents are more intense (~ 2 m s^{-1}). The pattern of the tidal ellipses in the deep areas inside the gulfs is more circular. The velocity vectors rotate counterclockwisely in most of the region, with the exception of NE Valdes Peninsula and southern SJG where

currents are more intense. The tidal ellipses of the bottom flux have patterns similar to those shown in Fig. 3a and d, only the magnitude is higher due to the absence of bottom friction. The tidal residual current, defined here as the Eulerian mean of the instantaneous currents, is primarily generated by the nonlinear interaction between the oscillatory flow and the irregular bottom topography, coastal geometry and bottom friction. Fig. 3b and e show the Eulerian residual currents and the associated current function calculated by the model, forced with the M2 component averaged over a 15 day period. Both gulfs show counterclockwise gyres that dominate the residual circulation. Residual currents show values of about 2 cm s^{-1} and 30 cm s^{-1} in the coastal region of SJG and SMG respectively.

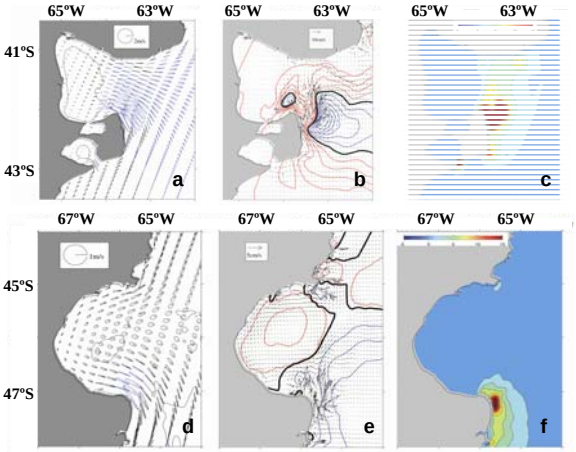

Figure 3. POM ouputs in GSM and GSJ: a) and d) bottom flow ellipses; b) and e) residual tidal currents; c and f, dissipated energy.

As seen in Fig. 3a, b and c, satellite results show the presence of sand waves in the SMG in the areas where tidal ellipses, residual currents and energy dissipation values calculated with the POM are highest. So, using satellite data, those areas of GSJ where POM showed similar results were investigated. This led to the observation, for the first time, of bottom irregularities in the SJG, shown in Fig. 4.

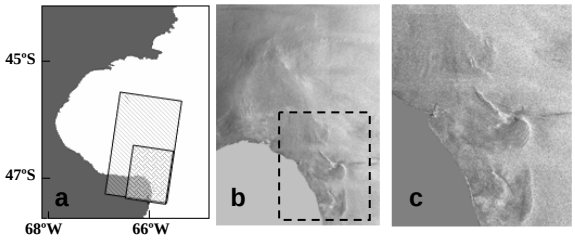

Figure 4. Bathymetric features at the entrance of San Jorge Gulf: a) map with the areas covered in figures b and c; b) microwave image of an elevation of 40 m above the sea floor; c) microwave image of located at the edges of the elevation (c, zoom of the area indicated in b).

4. DISCUSION

Ocean sand waves are transverse bedforms developed in response to tidal currents. Tides with moderate intensity form minor sea bed forms denominated ripples; larger sand waves are generated as tide intensity rises. Therefore, in the north of SMG, where tidal current measurements reach values up to 1 m s^{-1} sand waves are much smaller than in the south where currents take values around 2 m s^{-1}. These results coincide with the POM outputs regarding bottom flow ellipses and residual tidal currents as seen in Fig. 3a and b, as well as with the Simpson-Hunter index for maximum values of dissipated energy, as shown in Fig. 3c.

As seen en Fig 3d, e and f, similar results obtained for SJG suggested the presence of bottom irregularities near the south part of the gulf, which were found using satellite data, as shown in Fig. 4.

5. CONCLUSION

Seabed geoforms identification from satellite data and tide currents properties estimated by numerical models show coherent results. Bigger geoforms are found in zones where tidal current and dissipated energy values calculated by the POM are higher. This demonstrates that model results can be also useful in the identification of new bottom irregularities.

ACKNOWLEDGEMENTS

The authors thank the Argentine Comisión Nacional de Actividades Espaciales (CONAE) and European Space Agency (ESA) for providing the images used in this paper.

REFERENCES

Acha, E.M., H. W. Mianzan, R. Guerrero, M. Favero, and J. Bava (2004). “Marine Fronts at the continental shelves of austral South America Physical and ecological processes”. Journal of marine Sciences, vol 44, pp. 83-105.

Blumberg, A. F. and G. L. Mellor. “A description of a three-dimensional coastal ocean circulation model”. Three-Dimensional Coastal ocean Models, edited by N. Heaps, 208 pp., American Geophysical Union, 1987.

Gagliardini, D.A., A. Dogliotti, H. Karszenbaum y F. Grings (2004). “Comparison of bathymetric features detected by ERS-SAR and LANDSAT-TM data over San Matias gulf, Argentina”. International Journal of Biodiversity, Oceanology and Conservation, vol. 68, no. 2, pp. 201-208.

Gagliardini D. A., S. Aliotta, A. I. Dogliotti y P. Clemente Colón (2005). “Identification of bed forms through ERS SAR images in San Matias gulf, Argentina”. J.A.G. Cooper & D.W.T. Jackson, Journal of Coastal Research, vol. 21, no. 1, pp. 193-201.

Tonini, M., E.D. Palma, A.L. Rivas (2006). “Modelo de alta resolución de los golfos patagónicos”. Mecánica Computacional, vol. XXV, pp. 1441-1460.

Video-camera monitoring of hydrosedimentary processes and coastal works impacts in Valras (Herault, France)

Pierre Gaufrès [a,*], Bruno Andres [a], Didier Rihouey[b], Jérémy Dugor [b]

[a] CETMEF (Institute for Maritime and Inland Waterways), Aix-en-Provence, France
Pierre.Gaufres@developpement-durable.gouv.fr
[b] CASAGEC – University of Pau and Pays de l'Adour, Anglet, France

Abstract – Shoreline stability is an important issue along most Mediterranean coasts. European project *Meddoc Interreg Beachmed-e* focused on the strategic management of beach protections along the Mediterranean coastal zone. In the framework of this project, a video monitoring system has been settled in Valras, Gulf of Lions (France). Important beach retreat has been observed for decades on this shoreline and 12 breakwaters have been built until 2007. From January to May 2008 similar protections, submerged breakwaters and 95 000 m^3 sandbeach nourishment have been added. This paper presents the use of video monitoring technique to estimate the impact of engineering works.

Keywords: video quantification, erosion, coast protections.

1. INTRODUCTION

The management of coastal erosion requires to grasp all spatial-time scales of morpho-sedimentary evolution. For a few years, the use of digital video system in order to quantify these evolutions has been an autonomous and cheap alternative to traditional monitoring devices (Holman & Stanley, 2007). CETMEF associated with University of Pau and Pays de l'Adour (CASAGEC) have installed in September 2007 a real time digital video quantification system in Valras-Plage, France (34). The project is financed within the framework of Beachmed-e (Interreg-III C) driven by the Conseil Général of Hérault. This article shows applications of video monitoring in order to assess the impacts of defensive works carried out on Valras beaches. The video system is presented associated with hydro-sedimentary features of the site and defensive works. Results of weekly video monitoring of the shoreline during maritime works are analysed and finally, limits and development projects are debated.

2. HELPFUL HINTS

2.1 Pictures acquisition system

A lot of coastal processes have a surface water visual signature. Recently, several video techniques have been applied to monitor coastal systems. Kosta System, developed by CASAGEC and AZTI Tecnalia is a video monitoring device which allows to capture synchronized data with variable frequency (up to 2 Hz). A Kosta System station contains several video cameras installed close to the shoreline at the highest point, overlooking the beach. Two types of type of pictures can be obtained :

1. Snapshot
2. Timex pictures (10 minutes time exposure)

To calibrate external parameters on raw pictures, several and clearly visible ground control plots (GCP) are recorded with a centimeter DGPS. Next, the points are converted by photogrammetry from 2D picture coordinates into 2D true coordinates.

2.2 Photogrammetry technique

Video quantification applied to coastal environments monitoring is based on photogrammetry technique (Trucco & Verri, 1998). It allows to turn an "oblique raw picture" (Fig 1.a.) into "metric plan picture" (Fig 1.b.). This previous processing of pictures is based on a connection between the picture coordinates (u,v) and corresponding position in the true world.

Figure 1. Oblique raw picture (a) and metric plan picture (b) in Valras-Plage

3. OTHER RECOMMENDATIONS

3.1 Geographic situation and context

Located at the extreme south-west of the Hérault region, Valras-Plage is a sandy coast exposed to erosion since the sixties due to a harbour dyke influence at Orb river mouth across longshore drift (Fig.2). Successive longshore and crosshore protections (dykes, break-waters) have locally reduced erosion. Moreover, the urbanization has spread out on the dune ridge depriving it from natural protection against storm events.

Figure 2. Valras-Plage localization

* Corresponding author. CETMEF - 2, Boulevard Kennedy, CS 90385, 13097 Aix-en-Provence Cedex 02, France.

3.2 Hydrodynamics conditions

The Gulf of Lions has semi-diurnal with diurnal disparity tidal range (0,4 m maximum) : one of the two daily tides is always weaker than the other one. So, the roughness is controlled by sea states from south-south-west and north-east (Certain, 1999). The important fetch of this part of the Mediterranean sea allows the development of a powerful swell which can exceed 4 m of significant high.

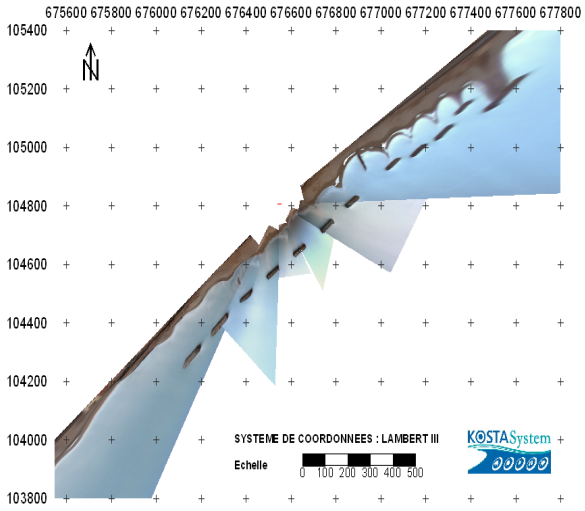

Figure 3. SIG integration of plan metric panoramic picture from 6 video cameras of Valras-Plage.

3.3 Description of video stations

The number of cameras, their height and lenses focal distance conditionned the area and the accuracy of the videos pictures. The video station (Fig.2) has been installed at the top of a forty seven meter high building located next to the beach and provides real time shoreline monitoring. The CCD video cameras are 0,8 Mega pixels. The system is covering 4 km of the coast (Fig. 3) with a sub-metric transverse resolution at the shoreline level (Fig.4.a) and with a metric longitudinal resolution 300 m away from the station and about 20 m per pixels 1,5 km away from the station (Fig.4.b).

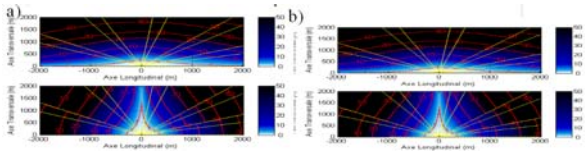

Figure 4. Transverse (a) and longitudinal (b) resolution map of Valras-Plage video station.

4. RESULTS

4.1 Shoreline monitoring

In this study, “shoreline” defines instantaneous position of water/earth interface. Shoreline is therefore depending on tide level, atmospheric pressure, wind and storm conditions. Tide data of nearest tide gauge (Sète) is analysed for video pictures exploitation.

4.2 Errors valuation / Beach areas calculation

As we detect the shoreline, the error led by sea level variation is growing up as the slope is getting weaker. Weakest beach slopes are generally located in tombolos axis (Fig.5.a). So as to estimate the error led by sea level variations, two beach profiles from a bathymetry realized after defence works in may 2008 (Fig.5.b) are compared below.

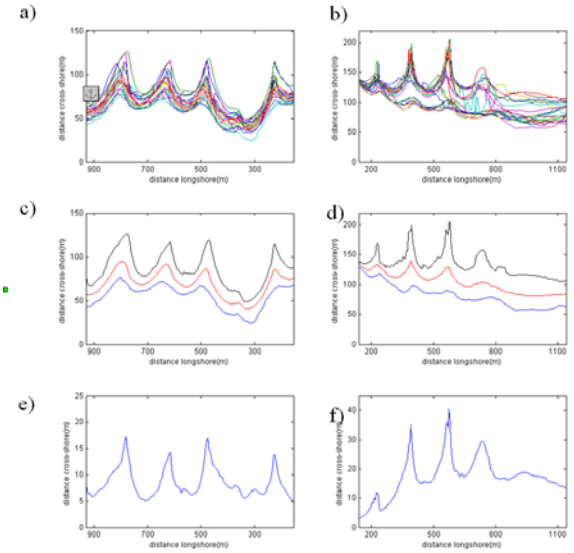

Figure 5. Shoreline monitoring. Temporal series of shoreline to the East Valras-Plage (a) and West Valras-Plage (b). Maximum, mean and minimum location of shoreline East (c) and West (d). Standard variation of temporal series of shoreline East (e) and West (f).

5. CONCLUSION

A digital video quantification system for coast erosion monitoring has been setted up in September 2007 at Valras-Plage, France (34) where many defensive coastalworks were builded in 2008. A weekly detection of shoreline position has been brought into operation for the work period. The estimation of errors led by sea level variations on the areas calculation allowed to underline trends of “natural” evolution and impact of beach nourishment. The video monitoring as been particularly usefull in order to quantify long term redistribution of beachnourishment and shoreline evolution in the shadow area of breakwaters and downstream the drift where the coast, more vulnerable, is protected by submerged works.

ACKNOWLEDGEMENTS

Valras-Plage City, Bel-Horizon property manager, Météo France (wind data), Service Hydrographique et Océanographique de la Marine and Direction Régionale de l'Equipement du Languedoc-Roussillon (tide data).

REFERENCES

Certain R. (2002), “Morphodynamique d'une côte sableuse macrotidale à barres : le Golfe du Lion (Languedoc-Roussillon)". Thèse de doctorat, Université de Perpignan.

Holman R.A, Stanley J. (2007), “The history and technical capabilities of Argus”. Coastal Engineering, Vol 54, pp 477-492.

Trucco E., Verri A. (1998),“Introductory Techniques for 3-D Computer Vision”. Prentice Hall, Inc.

Experience of oil pollution operational monitoring with a web-geoinformation approach

O. Gershenzon [a], A. Kucheiko [a], V. Zatyagalova [a], N. Filimonova [a,*], V. Stanovoy [b]

[a] RDC ScanEx, Moscow, Russia – olga@scanex.ru, kucheiko@scanex.ru, vzatyagalova@scanex.ru, anataly@scanex.ru
[b] AARI, St-Petersburg, Russia – Stanovoy@lens.spb.ru

Abstract – The engineering-technological Center ScanEx (www.scanex.ru) has developed and implemented a technology of operational satellite monitoring for the purpose of supervising the ecological conditions of water areas. The technology is constructed on gathering, operative processing and analysing of the data, received with optical and radar satellites on a network of own universal ground stations "UniScan". The complex analysis of optical and radar imageries will allow compensating constraints related to each information type. Also ScanEx Center use the model of oil spill drift and transformation in the Arctic seas – the OilMARS (Oil Spill Model for the Arctic Seas), developed in AARI. A geoinformation approach was developed and introduced for fully-fledged and comprehensive analysis of satellite images and objective evaluation of information on pollution sources. The approach is based on combined remote GIS- and WEB-technologies for collecting dissociated data in common information space for the purpose of conducting an express analysis of the environmental situation in the offshore area. The web-mapping service, was developed on the basis of ScanEx' Web GeoMixer geoportal technologies. The user receive geoinformation complex products and can make operative decisions for planning of operations on liquidation of pollution of water area.

Keywords: operational monitoring, oil pollution, geoportal.

1. INTRODUCTION

The engineering-technological Center ScanEx (see details at www.scanex.ru) has developed and implemented a technology of operational satellite monitoring for the purpose of supervisingm the ecological conditions of water areas. The technology is constructed on gathering, operative processing and analysing of the data, received with optical and radar satellites on a network of own universal small-sized ground stations "UniScan".

The main specifics of the projects are:

- high frequency of imaging to ensure detection of oil pollutions of water surfaces (average revisit period constituted 1-2 days);
- integrated analysis of radar and multispectral optical images, operatively received by ScanEx RDC ground stations;
- combination of remote data, GIS-, WEB-technologies, oil pollution modeling systems, AIS data and attributive data in common geospatial environment;
- real-time representation of satellite images and analysis results through web-mapping services.

The monitoring process utilizes a multi-satellite monitoring technique thus allowing high monitoring frequency (average revisit period constituted 1-2 days), which no individual satellite (RADARSAT-1 and -2, ENVISAT, Landsat 5, EROS-A/B, MODIS) would be capable to support.

2. SATELLITE MONITORING

Space radar sensors and in particular synthesized aperture radars (SAR) were selected for this application since in unfavorable weather conditions they represent the only appropriate method of obtaining information on large offshore areas. SAR enables detection of any type of oil and petroleum products films owing to its high sensitivity to changes of sea surface roughness occurring due to the action of film surface tension. However, a number of natural factors and oil slick look-alikes (biogenic films, wind shadows, rain cells, manifestations of subsurface waves, etc) that could appear in radar images considerably complicate the imagery interpretation process. Combined application of radar and multispectral optical images of medium resolution from the Landsat 5 satellite help to identify the nature of certain slicks origin and in turn confirm presence of oil slicks in subsequent radar imageries. Also, the complex analysis of optical and radar imageries will allow compensating constraints related to each information type. For instance, in lower clouds conditions radar imagery is indispensable while in lower wind conditions optical imagery is applicable.

Another important factor in origin identification of detected slicks in satellite imagery is realized through the analysis of multi-temporal images and juxtaposition of data with the results of prediction calculations. In the projects the ScanEx Center use the model of oil spill drift and transformation in the Arctic seas – the OilMARS (Oil Spill Model for the Arctic Seas), developed in AARI. The OilMARS takes into account drift and transformation of oil pollution on the sea surface occurred through emergency oil spills from fixed and moving sources. If a slick-alike film is detected in radar data the OilMARS model shows a shift between estimated and actual slick position in subsequent imagery.

Lastly, a geo-information approach was developed and introduced for fully-fledged and comprehensive analysis of satellite images and objective evaluation of information on pollution sources. The approach is based on combined remote GIS- and WEB-technologies for collecting dissociated data in common information space for the

* Corresponding author. 22/5 L'va Tolstogo str., Moscow, Russia.

purpose of conducting an express analysis of the environmental situation in the offshore area. Available information was used in GIS, which greatly aided the expert in the process of identification and classification of pollution: sea basin properties, navigational data, elements of geologic and geophysical bottom structure, oil and gas bearing capacity of the offshore area and fuel and energy complex infrastructure, data of automatic ship identification system (AIS). The AIS system ensures possibility of near-real time identification of ships for determination of their potential involvement in oil spills. The web-mapping service, which provides fast browsing of large data volumes using the Internet and high performance of the system through the method of their preliminary preparation, was developed on the basis of ScanEx' Web GeoMixer geoportal technologies. The web interface provides closed multi-user access.

The approach allows implementation in the common information web-space the near real-time visualization of satellite data and their processing results, assessment of multi-temporal data, collection and integration of dissociated information in the common interface including remote users' data (for instance, field measurements materials) and other on-line sources; it allows data exchange and cataloging as well as information analysis. As a result an expert receives comprehensive information on the current situation in the area under control, which is used as basis for conducting an analysis and making decision on a pollution source. As a result the radar image and digital maps of distribution of oil pollution or geoinformation complex products (vector maps of oil pollution, ship-navigation conditions with indication of vessels' coordinates, maps of parameters of bioefficiency of a sea surface) is given to the user. The user, on the basis of the timely notification, can make operative decisions for planning of operations on liquidation of pollution of water area for the purpose of prevention of their further distribution.

3. CONCLUSION

The monitoring results show that space radar imagery is a valuable information source in supporting activities of the oil and gas complex. High frequency of satellite imagery ensures reliable control with high probability of detecting pollution and capability to track dynamics of slick distribution. The used system complex in combination with the web-geoinformation approach enables reliable identification of nature and source of pollution and assessment of impacted area. Positive experience of application of the given approach is received at different projects. It is shown that cartographical web service is the ideal solution for research of space time distribution of oil pollution in the sea and can be considered as the basic part of operative system of monitoring of oil pollution.

Correlating SST Satellite Data to the Spatial Distribution of Spawning Aggregations of Argentine Hake (Merluccius hubbsi) in San Matías Gulf, Patagonia, Argentina

R. González [a,*], M. Ocampo-Reinaldo [a, c], C. Schneider [e], M. A. Romero [a, c], M. Maggioni [a], G. Williams [b, c], G. Cabrera [f], M. Narvarte [a, c], A. Gagliardini [b, d]

[a] Instituto de Biología Marina y Pesquera Alte. Storni, Univ. Nac. del Comahue, San Antonio Oeste (RN), Argentina – racg05@gmail.com
[b] Centro Nacional Patagónico (CENPAT), Puerto Madryn (Ch), Argentina
[c] Consejo Nacional de Investigaciones Científicas y Técnicas (CONICET)
[d] Instituto de Astronomía y Física del Espacio (IAFE), Ciudad Autónoma de Buenos Aires, Argentina
[e] Asociación para la Conservación y el Estudio de la Naturaleza (ACEN), Córdoba, Argentina
[f] INVAP SE, San Carlos de Bariloche (RN), Argentina

Abstract – The relationship between SST satellite data and the distribution pattern of Argentine hake during spawning season in the San Matías Gulf was analyzed. Data of hake abundance and temperature in the water column were obtained during a research survey with bottom trawl net. SST data obtained from MODIS sensor were validated with *in situ* observations and correlated with hake abundance indexes. Hake abundance showed positive correlation with SST and higher hake densities were observed in areas with high stratification in the water column. The spatial pattern of hake distribution during the reproductive season appears strongly related to a cyclonic gyre which would produce favorable conditions for the spawning process and the development of hake early stages.

Keywords: hake, spawning, SST, Patagonia.

1. INTRODUCTION

SST data provided by satellites have been used to study distribution patterns of fishing resources (Laurs *et al*., 1984; Yáñez *et al*., 1996). Although direct relationships between SST and spatial distribution of fishes were found mainly for pelagic resources, this topic appears scarcely studied for demersal and benthic species. The Argentine hake *Merluccius hubbsi*, the most important fishing resource in the Argentine Sea, is a demersal-pelagic species distributed along the Southwest Atlantic Ocean. Recent studies (Williams *et al*., in press) carried out in San Matías Gulf (SMG), northern Patagonia, demonstrated the existence of relationships between a seasonal frontal system inferred by satellite data and the distribution of hake during summer months. It has been also hypothesized that spatial pattern of hake during the peak of the reproductive activity (spring), could be influenced by other oceanographic phenomenon (i.e.: a cyclonic gyre). The aim of this study is to analyze the distribution pattern of hake during the spawning season and its potential relationships with the main oceanographic features of SMG.

2. MATERIAL AND METHODS

Data of hake abundance (catch per unit of effort –CPUE-, expressed in kg/hour) for 41 sampling sites (fishing hauls) in SMG (Fig 1.) were obtained during a research cruise carried out from November 2 to 9, 2009.

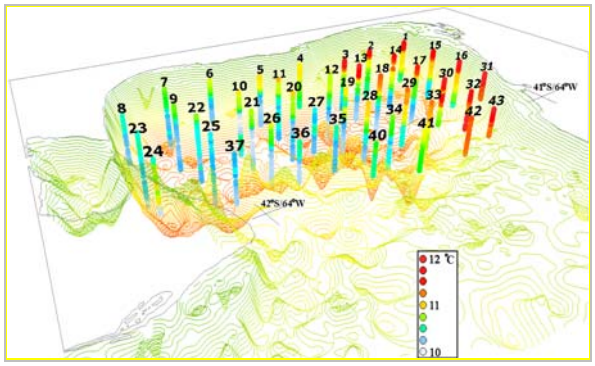

Figure 1. Location of hauls in SMG (numbers). Vertical bars indicate temperature in the water column.

A survey was performed with the FV "Viernes Santo" (29.4 m length; 800 HP), a vessel equipped with a 110' bottom trawl net. Water temperature and depth were recorded continuously in each haul with a CTD probe mounted on the buoy-rope of the net. SST data from CTD were previously calibrated and validated with two multiparameter probes YSI® Mod6600 and Mod556. Daily level-3 Local Area Coverage (LAC) MODIS SST data were acquired from Red Antares for the survey dates. SST product was mapped to a Geographic (Lat-Lon)/WGS84 projection at 0.01x0.01º resolution. Temperature and depth data from CTD were used to calculate the vertical variation of temperature (ΔT, in °C/10m) for each haul location. Potential relationship between ΔT, SST and spatial distribution of hake inferred from the CPUE were explored using linear regression. To improve the fitting of models only CPUE data into the bathymetric range of Argentine (90-130 m) were used.

3. RESULTS

SST data provided by MODIS sensor showed an acceptable correlation with calibrated CTD records (Fig. 2). Hake CPUE showed positive correlation with ΔT data (Fig. 3), indicating that more abundant hake schools were associated to locations with stratification (thermocline) in the water column. Fishing hauls with higher hake catches (CPUE >

*Corresponding author. Güemes 1030 (8520) San Antonio Oeste (RN), Argentina. TE/Fax: +54 2934 430764.

1000 kg/h) and ΔT values over 0.08 °C/10m (hauls 1, 2, 3, 15, 16, 30, 32 and 33) were located in the northern area of SMG. This positive correlation was also observed for SST data obtained from CTD records (Fig. 4) and MODIS observations (Fig. 5).

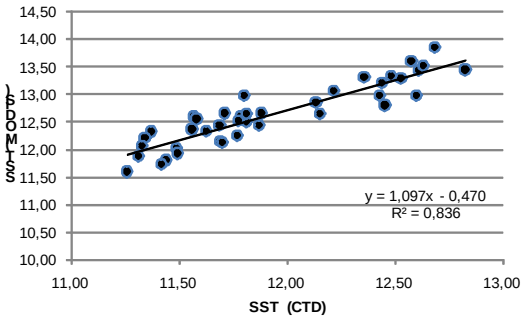

Figure 2. Relationship between SST data obtained from the CTD and MODIS sensor.

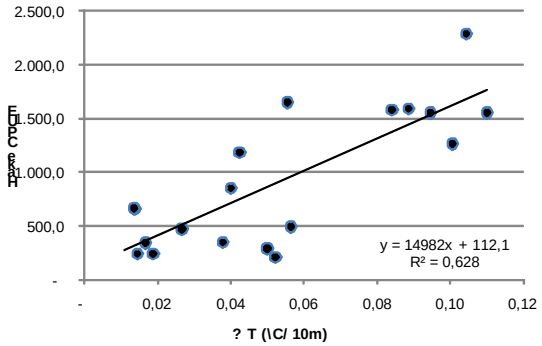

Figure 3. Relationship between ΔT and hake abundance.

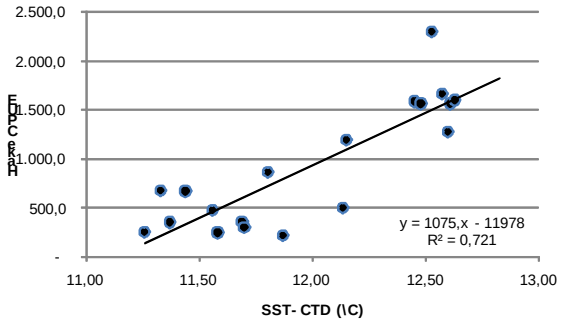

Figure 4. Relationship between SST data obtained from CTD and hake abundance.

3. DISCUSION

This study revealed that hake distribution during the peak of the reproductive season is strongly associated to high stratified water masses located in the northern area of SMG. Scasso and Piola (1988) described a cyclonic gyre around 70 Km diameter centered in the 41°15'S in this area during spring-summer months. Gagliardini and Rivas (2004) reported that this area is characterized by the development of a seasonal thermocline whose depth is determined by the balance between the surface flux and the combined mixing action of wind and tide. CTD records during this study showed locations with the presence of the thermocline between 20 and 80 m depth. On the southwestern boundary of the gyre, a tidal frontal system is established in the same seasons, producing the separation of the northern warmer waters from the relatively colder ones of the southern sector.

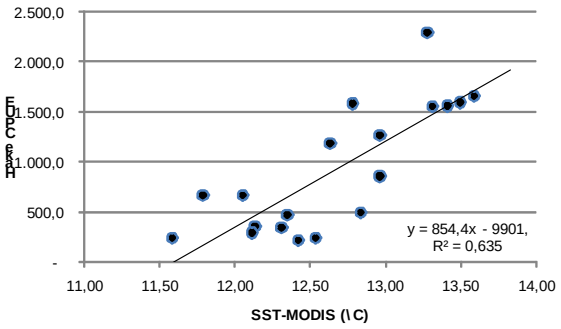

Figure 5. Relationship between SST data obtained from MODIS sensor and hake abundance.

It is known that thermoclines create positive conditions to concentrate food, serving as favorable first-feeding sites for fish larvae (Bakun, 1996). Thermocline and environmental conditions generated by the cyclonic gyre in northern SMG would contribute to the success of reproductive process of Argentine hake. Future research should be addressed to elucidate the ecological role of both the cyclonic gyre and the frontal system in the context of the pattern of annual migration of the SMG hake stock.

ACKNOWLEDGEMENTS

The authors would like to thank Red Antares for the production and distribution of the used data (http://www.antares.ws). This study was supported by the Ministry of Production of Río Negro Province and the Argentine Agencia Nacional de Promoción de Promoción Científica y Tecnológica (Projects PID371and PICT1575/FONCyT).

REFERENCES

Bakun A. (1996). Patterns in the ocean. Ocean processes and marine population dynamics. Univ. of California Sea Grant, California, USA, 323 pp.

Gagliardini D. and A. Rivas (2004). "Environmental characteristics of San Matías Gulf obtained from Landsat-TM and ETM+ data". Gayana 68 (2) Supl. TI. Proc., pp. 186-193.

Laurs R. M., P. Fiedler and D. Montgomery (1984). "Albacore tuna catch distributions relative to environmental features observed from satellite". Deep-Sea Res. 31 (9), pp. 1085-1099.

Piola, A.R. and L. M. Scasso (1988). "Circulación en el Golfo San Matías". Geoacta, 15, pp. 33-51.

Williams, G., M. Ocampo Reinaldo, M. Narvarte, R. González, J. Esteves, and D. Gagliardini (In press). "TM/ETM, AVHRR and SeaWiFs sensor studies in San Matías Gulf (Argentina): relation with fishing and oceanographic surveys data". International Journal of Remote Sensing.

Yañez E., V. Catasti, M. A. Barbieri and G. Böhm (1996). "Relaciones entre la distribución de recursos pelágicos pequeños y la temperatura superficial del mar registrada con satélites NOAA en la zona central de Chile". Investigaciones Marinas, N° 24, pp. 107-122.

Satellite Optical Water Mass Classification to Map Coastal Hypoxia

R.W. Gould [a,*], M.D. Lewis [b], R.D. Smith [c], and D.S. Ko [d]

[a] Naval Research Laboratory, Stennis Space Center, Mississippi, USA – Richard.Gould@nrlssc.navy.mil
[b] Naval Research Laboratory, Stennis Space Center, Mississippi, USA – David.Lewis.CTR@nrlssc.navy.mil
[c] OTI, Stennis Space Center, Mississippi, USA – Regina.Smith@nrlssc.navy.mil
[d] Naval Research Laboratory, Stennis Space Center, Mississippi, USA – Dong.Ko@nrlssc.navy.mil

Abstract – We applied an optical water mass classification technique to estimate the areal extent of coastal hypoxia in the northern Gulf of Mexico. Partitioned absorption coefficients (phytoplankton, sediment/detrital, and CDOM) derived from satellite ocean color imagery are coupled with a stratification index (surface-to-bottom temperature difference) derived from a circulation model. Optical properties (relative and absolute absorption coefficients) were extracted from a 10-year climatology of monthly satellite composites to define expected optical conditions of hypoxic waters, which were delineated by mid-summer ship surveys (LUMCON, 2009). Then, for a given year, the satellite-derived optical properties are compared to the expected conditions and coupled with the model-derived water column stratification index, to provide a real-time spatial estimate of hypoxia.

Keywords: water mass, optical classification, hypoxia.

1. INTRODUCTION

The frequency, extent, and severity of coastal hypoxic events are increasing worldwide due to increasing eutrophication (Larsen, 2004). Hypoxia occurs when water column oxygen levels drop below 2 mg/l, and these low oxygen levels can potentially impact local fisheries and benthic organisms, with important ecological and economic consequences. This "dead zone" off the coast of Louisiana forms every summer and is the second largest hypoxic zone in the world. It is thought that agricultural fertilization upstream leads to the increased nutrient loading on the continental shelf, stimulating a phytoplankton bloom. As the bloom stimulated by this nutrient-rich discharge of the Mississippi and Atchafalaya Rivers sinks to the bottom and decays, oxygen levels are depleted in the process. In addition to the bloom decay, water column stratification is also a required condition for hypoxia development, to prevent mixing with surrounding oxygen-replete waters.

Typically, ship-based survey cruises are conducted to map the extent of bottom hypoxic waters. Each summer since 1985, monitoring cruises have been conducted by the Louisiana Universities Marine Consortium (LUMCON) to map the spatial extent of the Louisiana hypoxic zone. This measurement represents the officially-reported size of the hypoxic zone, which has varied from about 4,000 – 22,000 km^2, with the maximum size reported in 2002 (LUMCON, 2009). There is currently a national mandate to decrease the size of the hypoxic zone to 5,000 km^2 by 2015, mostly by a proposed 40% reduction in annual nitrogen discharge into the Gulf of Mexico. A monitoring program is required to assess whether these goals are being met. However, ship sampling is expensive and is not spatially or temporally synoptic. So, the question is, can surface satellite imagery be used to map the spatial extent of bottom-water hypoxia?

2. METHODS

To estimate areas of possible hypoxia, we couple satellite ocean color imagery with a stratification index derived from a circulation model, in a three-tiered testing approach. The premise is that by comparing current optical properties to properties observed in past hypoxic events, we can "predict" where hypoxia is likely to occur in the current image. We first compare the relative optical composition, then we examine the absolute optical properties, and finally we assess the water-column stratification.

2.1 Satellite Imagery/Processing

NRL has collected, processed, and archived a 10-year time series of SeaWiFS ocean color imagery covering the northern Gulf of Mexico from 1998-2007. All imagery was processed using the NRL automated satellite processing system (Martinolich and Scardino, 2009). A near-infrared atmospheric correction tuned for coastal waters was applied.

2.2 Circulation Modeling

A real-time ocean nowcast/forecast system (ONFS) has been developed at the Naval Research Laboratory (NRL). The NRL ONFS is provides short-term forecasts of ocean current, temperature, salinity, and sea level variation including tides. It is based on the NCOM hydrodynamic model, but has additional components such as data assimilation and improved forcing. A nested model with 2-km horizontal resolution and 40 vertical layers has been implemented in the northern Gulf of Mexico. The surface-to-bottom (or surface to 100 m in deeper waters) vertical temperature gradient from this model is used as our stratification index.

2.3 Mapping Hypoxia

First, we apply an optical water mass classification (OWMC) system developed at NRL to the imagery (Gould and Arnone, 2003). The OWMC can help identify and track oceanographic features, similar to the approach employed by physical oceanographers using temperature/salinity diagrams. The total absorption coefficient is partitioned into individual absorption components, due to phytoplankton at 443 nm ($a_\varphi 443$), sediment/detritus at 443 nm ($a_d 443$), and CDOM at 443 nm ($a_{CDOM} 443$). We then

* Corresponding author. NRL Code 7331, SSC, MS 39529, USA. Tel (228) 688-5587, Fax (228) 688-4149.

calculate the percent of the total absorption coefficient due to each of the three components, and produce pseudo-color RGB images of the optical patterns, by loading % a_d into the red channel, % a_φ into the green channel, and % a_g into the blue channel. Thus, areas dominated by relatively high detrital loads appear red in the image, areas of high phytoplankton absorption appear green, and areas of higher CDOM absorption appear blue.

For each year from 1998-2007, we created monthly composite OWMC image covering coastal Louisiana for June and July. Also for each year, we digitized the hypoxia map produced by the LUMCON group. Figure 1 shows an example OWMC image for July 2007, a year with one of the largest measured hypoxic zones (20,500 km^2). The cruise-mapped hypoxic area is indicated in red. Using the digitized hypoxia map, we then extracted the absorption percentages for all of the image pixels falling in the "hypoxic zone" from the OWMC composite image, and plotted these on a ternary diagram. This procedure was repeated for all 10 years, and a frequency ternary plot was generated (Figure 2).

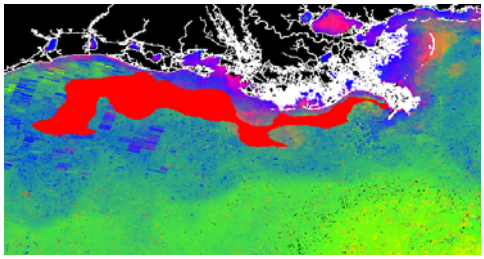

Figure 1. OWMC image for July 2007 (SeaWiFS). Pixel colors indicate relative optical characteristics, as described in the text. Area delineated by red pixels indicates the hypoxic region for summer 2007 as determined from the LUMCON regional survey cruise.

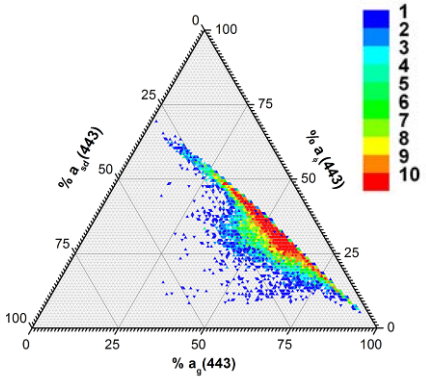

Figure 2. Frequency ternary diagram showing the optical characteristics of hypoxia pixels. Axes are the partitioned absorption percentages. The colors represent frequency (the number of years at least one hypoxia pixel exhibited the specific optical characteristics indicated).

In addition to the frequency plots based on the number of years, similar plots were created based on total number of pixels. This approach only represents changes in the relative optical composition across an image; to more completely characterize the water masses, similar analyses were performed using the absolute magnitudes of the partitioned absorption coefficients, and frequency ternary plots (based on years and total pixels) were generated from these results as well.

3. RESULTS

To test the approach, we estimated hypoxic pixels in the July 2007 OWMC image, and compared these to the actual hypoxia distribution as determined by the cruise sampling. A three-tiered test was applied: first, pixels were marked as possibly hypoxic if their relative optical properties matched the historical properties in at least 9 years and occurred at least 500 times (i.e., in at least 500 pixels over the 10 years); next, if their absolute optical properties matched the historical properties in at least 9 years and 500 times; and finally, if the surface-to-bottom temperature gradient from the model was positive (temperature increased with depth). The intersection of these three regions determined the final prediction (Figure 3). Note the close correspondence with the actual hypoxic region in Figure 1. We calculate areas of estimated hypoxia and comparison statistics for all 10 years.

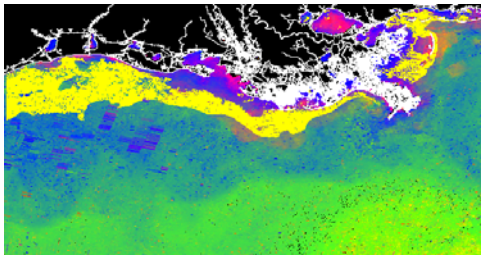

Figure 3. Predicted hypoxic region for July 2007 (yellow).

4. CONCLUSION

Satellite ocean color imagery can be used to augment ship surveys and delineate areas of expected hypoxic conditions in near-real time, providing coastal managers with a new monitoring tool.

ACKNOWLEDGEMENTS

This work was supported by US Environmental Protection Agency funding to NRL through an Advanced Monitoring Initiative and by NRL Program Element PE0601153N. We are grateful to Dr. Nancy Rabalais and LUMCON personnel for collection and distribution of ship-based hypoxia maps.

REFERENCES

Gould, R.W., Jr. and R. A. Arnone (2003). "Optical Water Mass Classification for Ocean Color Imagery," in *Proceedings: Second International Conference, Current Problems in Optics Of Natural Waters*, I. Levin and G. Gilbert, eds., St. Petersburg, Russia.

Larsen, J. (2004). "Dead zones increasing in the world's coastal waters", http://www.earth-policy.org/index.php?/plan_b_updates/2004/update41

Louisiana Universities Marine Consortium (2009). "Hypoxia in the northern Gulf of Mexico", http://www.gulfhypoxia.net

Martinolich, P. and T. Scardino (2009). "Automated Processing System User's Guide Version 3.8", NRL. Washington, D. C. http://www7333.nrlssc.navy.mil/docs/aps_v3.8/html/user/aps/aps.html

Satellite remote sensing of the spring bloom in the coastal waters of British Columbia using FLH

J. Gower [a], S. King [a], S. Statham [b], R. Fox [c], T. Van Manen [d]

[a] Institute of Ocean Sciences, Sidney, BC, Canada – jim.gower@dfo-mpo.gc.ca
[b] Department of Geography, University of Victoria, Victoria, BC, Canada
[c] School of Earth and Ocean Sciences, University of Victoria, Victoria, BC, Canada
[d] Department of Physics and Astronomy, University of Victoria, Victoria, BC, Canada

Abstract – We present evidence for seeding of the spring bloom in a major coastal inlet (Strait of Georgia, BC, Canada) from narrow, glacial inlets feeding into the Strait. The blooms were mapped using the FLH signal from satellite colour sensors, which gave better results than the more standard algorithms based on green-to-blue ratios. Detection of the blooms in the narrow inlets required the Full Resolution data from MERIS. The blooms entering the Strait often take a characteristic shape, which we call the Malaspina Dragon. Their presence is confirmed by a variety of in-situ sensors.

Keywords: chlorophyll, FLH, spring bloom, coastal.

1. INTRODUCTION

MERIS and MODIS imagery in February and March of the years 2001 to 2009 show a recurring pattern which suggests seeding of the early spring bloom in the Strait of Georgia from deep, glacial inlets to the north. High chlorophyll values are first observed in Jervis and Sechelt inlets in mid-February, and are later observed in Malaspina Strait, an arm of the Strait of Georgia, before spreading across the main body of the Strait in late February and early March.

We call the pattern the "Malaspina Dragon" after its shape in satellite imagery in 2005, 2008 and 2009 shortly after it enters the Strait. It appears that the main spring bloom in the Strait of Georgia occurs earlier in years when the Dragon is active, suggesting that seeding from inlets should be added to the list of factors controlling timing. In 2009, the presence and evolution of the bloom was confirmed using an ocean glider, deployed in the Strait from February 18 to March 10. Also, ship samples showed that the bloom forming the dragon pattern consisted of diatoms (*Thalassiosira* spp.). In January 2010 we installed a recording fluorometer in surface water on a marina float in Egmont, near the junction of Sechelt and Jervis Inlets. We plan also to repeat the glider mission in the Strait.

2. SATELLITE DATA

The satellite image data that we use consist of the fluorescence signal (FLH, for Fluorescence Line Height) computed to show the added radiance at 685 nm due to chlorophyll fluorescence. Figure 1 shows the Dragon bloom pattern on February 18, 2009. Here, the remains of a bloom are observed throughout Sechelt and Jervis Inlets, while the strong bloom in Malaspina Strait and the Strait of Georgia, takes the form of the Dragon. Similar images for February 9, 11, 15 and 20, 2009 show the progress of the blooms in the two inlets.

Also shown in Figure 1 are spectra derived from top of atmosphere radiances in the 15 bands of MERIS. The radiances are plotted on the left axes for a pixel in the bloom (red line) and for a pixel in adjacent clear water (green line). The heavy blue line shows the difference between these two spectra on an expanded scale (right axes). The enhanced radiance at 681 nm due to solar-stimulated chlorophyll fluorescence, can be clearly seen. The difference spectrum also shows the absorption of blue light (radiance step between 510 and 560 nm) that also indicates the presence of chlorophyll in the surface water.

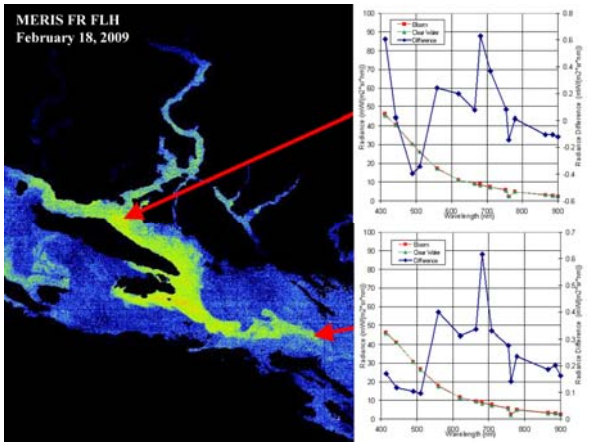

Figure 1. MERIS full resolution (300 m) image for 18 February 2009 showing spectra derived from level 1 (top of atmosphere) radiances. The Malaspina Dragon pattern is visible in the FLH image. Spectra show the radiance peaks due to chlorophyll fluorescence.

The satellite images we have collected give the first observations of "seeding from inlets" into the Strait of Georgia. This "seeding" has been suggested in the past as a mechanism for triggering the main spring bloom in the Strait, but has not been previously observed. These results suggest a need for improved monitoring of the timing and spatial pattern of phytoplankton growth in February and March of each year, in Sechelt and Jervis Inlets as well as in the main body of the Strait.

Figure 2 shows true colour images (left of each pair, showing snow over high land, cloud cover and a digital coastline) compared with FLH imagery (right in each pair) showing surface chlorophyll. A single, relatively cloud-free day in late February is shown for each year. The "Malaspina Dragon pattern is seen in 2005, 2008 and 2009. Blooms in

narrow inlets to the north (Jervis and Sechelt Inlets) are seen in all years back to 2002 except 2003 and 2006.

3. CONCLUSIONS

MODIS and MERIS satellite FLH (1 km resolution) images are essential for monitoring timing and pattern of the spring bloom in the Strait. We find FLH performs better in these coastal waters than the standard chlorophyll algorithms based on blue-to-green radiance ratios. Higher resolution (300m) images from the MERIS satellite are needed for detecting the early blooms in Jervis and Sechelt Inlets.

We are grateful to NASA and ESA for providing the satellite data, and to CSA, the Canadian Space Agency, for providing improved access to the higher resolution MERIS images by upgrading Canadian ground stations. Satellite data should continue to be available in future years, but at present, *in-situ* surface data are rare and intermittent.

ACKNOWLEDGEMENTS

Funding for this work was provided by the Canadian Space Agency under the GRIP program and by the Canadian Department of Fisheries and Oceans.

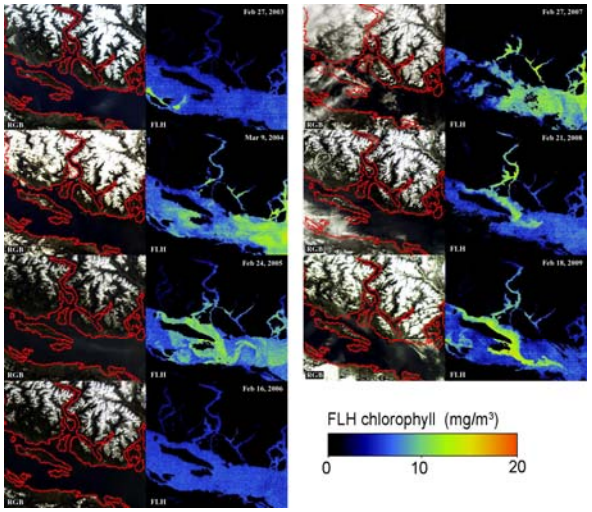

Figure 2. MERIS full resolution (300 m) images for each year, 2003 to 2009, true colour (left) and FLH (right). The Malaspina Dragon pattern is visible in FLH images for 2005, 2008 and 2009. Blooms are visible in Jervis or Sechelt Inlets or both, in all years except 2003 and 2006. A scale at lower right relates FLH to mg.m^{-3} of chlorophyll.

Validation of Salinity from Space: a Canadian Contribution

J. Gower [a], S. King [a], R. Fox [b], I. Yashayaev [c]

[a] Institute of Ocean Sciences, Sidney, BC, Canada – jim.gower@dfo-mpo.gc.ca
[b] School of Earth and Ocean Sciences, University of Victoria, Victoria, BC, Canada
[c] Bedford Institute of Oceanography, Dartmouth, NS, Canada

Abstract – Three satellites to measure sea surface salinity (SSS), soil moisture and ice cover are planned for operation in the near future: The European Space Agency's Soil Moisture and Ocean Salinity (SMOS), NASA's Aquarius satellite and the Soil Moisture Active Passive (SMAP) mission, also operated by NASA. Salinity measurements need to be made close to the sea surface to duplicate the satellite's lack of penetration below a few centimeters into the water. In this poster we demonstrate Canada's contribution to monitoring ocean salinity and discuss methods for satellite salinity validation. We hope to see the first sea surface salinity data from SMOS in time for the Venice Oceans from Space meeting.

Keywords: salinity, SMOS, Aquarius, SMAP.

1. INTRODUCTION

Three satellites to measure sea surface salinity (SSS), soil moisture and ice cover are planned for operation in the near future. The European Space Agency's Soil Moisture and Ocean Salinity (SMOS) Satellite was launched in November 2009 and is now in its commissioning phase. NASA's Aquarius satellite, whose primary goal is to measure SSS, is slated for launch in late 2010. The Soil Moisture Active Passive (SMAP) mission, also operated by NASA, is being developed for launch in the 2012 to 2013 timeframe. SMOS is the first satellite designed to measure SSS and consequently the need for validation is high. Salinity measurements need to be made close below the sea surface to duplicate the satellite's lack of penetration below a few centimeters into the water. In this poster we demonstrate Canada's contribution to monitoring ocean salinity and discuss methods for satellite salinity validation. Autonomous gliders and special Argo floats are being investigated as possible data sources. We hope to see the first sea surface salinity data from SMOS in time for the Venice Oceans from Space meeting.

2. SATELLITE SALINITY MISSIONS

SMOS

SMOS, successfully launched on November 2 2009, aims to provide data at 35Km spatial resolution with a revisit time of 3 days at the equator. The sensor, MIRAS, the Microwave Imaging Radiometer using Aperture Synthesis, will use 69 L-band antennae on a Y shaped structure. It will cross-correlate microwave signals with all combinations of antennae out to a maximum antenna separation of 7.5 m, duplicating the spatial resolution of an antenna of this diameter. This allows it to form an image every 1.2 seconds, of an area about 1000Km across. Accuracy goal is 0.2 PSU.

Aquarius

The Aquarius mission is a joint project between NASA (United States) and CONAE (Argentina). Scheduled for launch in May 2010, the instrument will have a 100km spatial resolution and an accuracy goal of 0.1-0.2 PSU for weekly to monthly averages. The Aquarius instrument uses an integrated radiometer and scatterometer, both sharing a 2.5-m diameter dish antenna. The integrated L-band (1.26GHz) scatterometer will correct errors due to surface roughness. Aquarius was featured in the *Oceanography* Special Issue on Salinity, (Vol. 21, No. 1, March 2008), which contains a number of articles on salinity, as well as a paper written by the Aquarius team.

SMAP

The Soil Moisture Active Passive (SMAP) is a proposed NASA mission with potential for measuring SSS. The launch time frame is 2012 – 2013. The radiometry techniques used by Aquarius and SMAP are the same, and the instruments are very similar, but SMAP has a 6m parabolic antenna, hence giving three times the spatial resolution. The key improvement that would enable SMAP to measure ocean salinity would be thermal stabilization on the radiometer and radar. As SMAP's spatial resolution is higher than that of SMOS of Aquarius, SMAP may be good option to measure coastal salinity.

3. CANADIAN RESEARCH VESSEL TIME SERIES

Canada has maintained time series of ocean properties off the Atlantic coast since about 1920 and off the Pacific coast since 1956. The Atlantic data collection included weather station Bravo at 56.5N, 50.5W, which was occupied continuously from 1968 to 1975. Measurements are now continued much more rarely in this area, and more regularly in other areas under the Atlantic Zone Monitoring Program. Pacific data collection is mainly along line P out to station Papa at 50N, 145W. The station was occupied continuously from 1956 to 1982 and has been visited regularly since, three to four times per year. Up to 16 stations of ocean data are collected along Line P, between Papa and the mouth of Juan de Fuca Strait on the coast. These collection programs provide time series of data against which we will initially judge the quality of satellite salinity data. We will have to allow for the fact that satellites will measure the top few cm of the water column. Measurements from ships typically result in mixing (by the ship) of the top 5 m of the water column, with the shallowest data being collected at about this depth.

4. GLIDER DATA

Ocean gliders are one potential data source for validating sea surface salinity measurements from space. We are using the Slocum Glider made by Webb Research to analyze salinity structure at the sea surface. A Glider moves through the water column in a saw-tooth pattern, propelled forward by attached wings and changes in its buoyancy. It gives salinity measurements with minimal disturbance to the water column, which is a common problem with shipboard measurements. We estimate it can make accurate measurements of salinity within about 10 cm of the surface. A glider can travel large distances for several weeks without surface support. We have had 5 glider missions in coastal waters around Vancouver Island and are planning to measure SSS in the open ocean on a mission to the Bowie Seamount, 180 Km off the Queen Charlotte Islands. Figure 1 shows the near surface salinity measurements from a mission in the Strait of Georgia in western Canada in 2008.

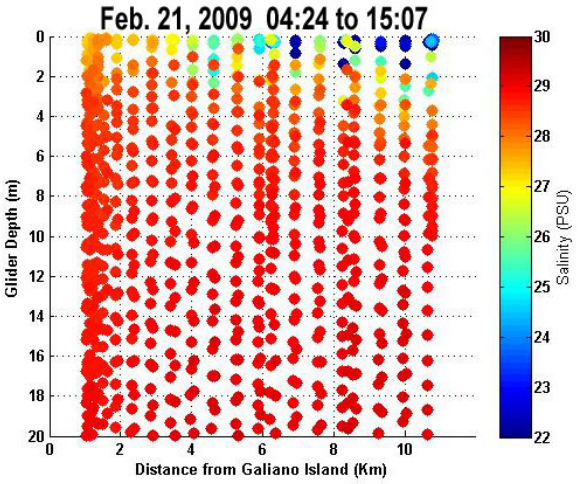

Figure 1. Near surface salinity measurements from an ocean glider in the Strait of Georgia on February 21 2009. Distance from Galiano Island represented on the x-axis is to the southwest into the Strait into the area influenced by the Fraser River plume.

5. ARGO IN THE LABRADOR SEA

The series of near surface salinity measured by the Argo floats in the central region of the Labrador Sea (over its deep basin) in figure 2 reveals a moderate seasonal cycle which accounts only for about half the observed variance. For comparison, the temperature record shows a much higher contribution of the seasonal cycle to the total variance (93%). Compared to temperature, the sea surface salinity of the Labrador Sea is more affected by irregular influences relevant to climate change and large scale oceanic and atmospheric processes. In particular, we observe a strong surface freshening that started in the second half of 2008 which is probably associated with an anomalous influx of fresh water from the Arctic (via Davis or Denmark straits). This recently started and still ongoing phenomenon calls for further investigation, for which satellite salinity observations may become an important asset.

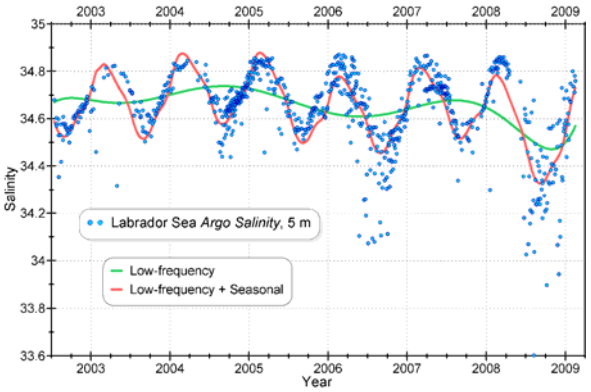

Figure 2. The seasonal signal of near surface salinity measured by Argo in the Labrador Sea.

6. CONCLUSIONS

The salinity satellites will provide a new and comprehensive view of the sea surface, giving information on oceanic fresh water fluxes, precipitation, evaporation, and other parts of the hydrologic cycle which have previously been difficult to measure. Canada has several datasets with strong potential for validation and calibration of the satellite salinity data. Measuring close enough to the surface to compare with the satellite will be difficult in some cases. We are evaluating ocean gliders for measuring near the surface. Argo floats give good coverage and typically measure at about 5 m and deeper. Some are being modified to give data closer to the surface, for comparison with satellite measurements.

ACKNOWLEDGEMENTS

Funding for this work was provided by the Canadian Space Agency under the GRIP program and by the Canadian Department of Fisheries and Oceans. The glider was used under contract with the Canadian Center for Ocean Gliders.

A global survey of intense surface plankton blooms and floating vegetation using MERIS MCI

J. Gower, S. King

Institute of Ocean Sciences, Sidney, BC, Canada – jim.gower@dfo-mpo.gc.ca

Abstract – The MERIS imager on the European Envisat satellite has spectral bands which give a new capability for detection of intense surface plankton blooms. We use MERIS data to compute MCI (Maximum Chlorophyll Index), which measures the radiance peak at 709 nm in water-leaving radiance, indicating the presence of a high surface concentration of chlorophyll a against a scattering background. The index is high in "red tide" conditions (intense, visible, surface, plankton blooms). A bloom search based on MCI has resulted in detection of a variety of events in marine waters and lakes round the world. Global MCI composite images are produced daily from all MERIS (daylight) passes of Reduced Resolution (RR) data, starting soon after MERIS launch, in June 2002. This paper gives examples of plankton bloom events and derived statistics of bloom occurrence.

Keywords: phytoplankton blooms, MERIS, ocean colour.

1. INTRODUCTION

The MEdium Resolution Imaging Spectrometer (MERIS) was launched on the European Envisat satellite in June 2002. We use MERIS to compute the MCI (Maximum Chlorophyll Index). This shows the amplitude of a peak near 709 nm in the radiance spectrum of light reflected from the earth's surface, which several authors have associated with high levels of chlorophyll a in ocean, coastal and lake water targets, such as plankton blooms and floating or benthic plants.

The index is unique to MERIS among satellites for monitoring large ocean and coastal areas, in that a band near 709 nm is not present on either MODIS or SeaWiFS. We have demonstrated use of the MCI to detect plankton blooms (Gower et al., 2008), floating *Sargassum* (Gower et al., 2006) and "superblooms" of Antarctic diatoms associated with platelet ice (Gower and King, 2007).

2. SATELLITE DATA

The MCI is computed as radiance at 709 nm above a linear baseline defined by radiances at 681 and 753 nm. In our global search, this is calculated only for pixels for which radiance at 865 nm is less than 15 mW m^{-2} sr^{-1} nm^{-1} to eliminate land pixels and areas of strong sun glint, haze or cloud. MCI values are computed from level 1 spectral radiance data before atmospheric correction, since the events we are studying typically give radiances too high to be handled by atmospheric-correction algorithms.

Global MCI composite images derived from all MERIS RR data are produced using GRID computing capabilities at ESRIN, according to specifications based on detection of bloom and vegetation events in a number of locations round the world, including the coasts of Canada, the USA, India, Chile and Antarctica (Gower et al., 2008).

After inspecting nearly 8 years of MERIS global MCI data, we have found several areas in which blooms are regularly made visible by MCI. The satellite data show bloom intensity, area and date. For species identifications we rely on local observers.

3. YELLOW SEA EXAMPLE

Figure 1 shows a bloom indicated by an extended bright patch of high MCI water off the coast of China immediately seaward of the high-sediment plume of the Chiang-Jiang river on 12 September 2008. This is the highest MCI signal detected by MERIS in this area in the nearly seven years of observation so far.

The spectra show a significant increase in back-scattered radiance from 500 to 800 nm. The strong MCI signal is apparently due to absorption at 665 and 681 nm, presumably by chlorophyll a, which also absorbs strongly at wavelengths shorter than 520 nm. We interpret the spectrum as indicating high chlorophyll concentrations in surface water with significant sediment load.

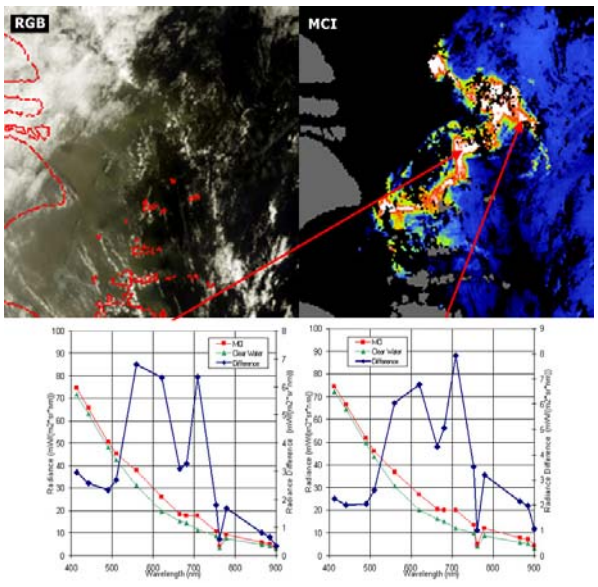

Figure 1. MERIS RR image of a high-MCI bloom near the edge of the Chiang Jiang River plume on 12 September 2008. The area of high MCI signal is just outside the edge of the sediment plume shown in the true colour (RGB) image. Spectra below show that the MCI signal is due to absorption by chlorophyll a.

4. ANTARCTICA EXAMPLE

Figure 2 shows the monthly MCI composite computed for Antarctica for February 2007. An area in the south-west Weddell Sea shows high MCI signal (Gower and King, 2007). This is where a superbloom event was reported in February/March 1968, and near where events were reported

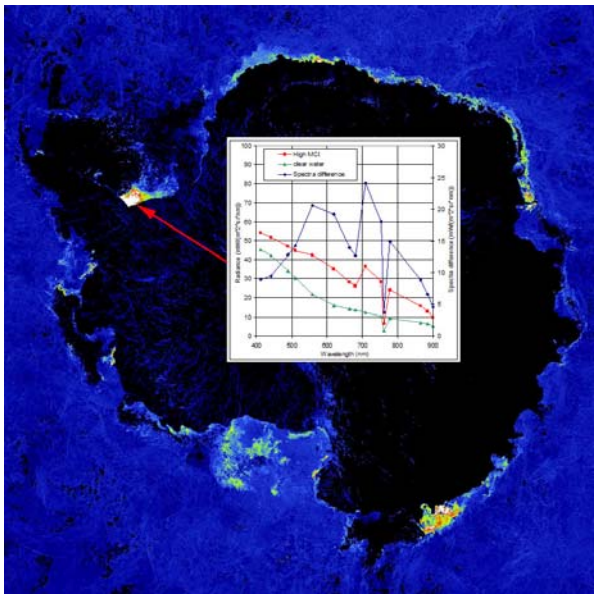

Figure 2. An area of high MCI index (upper left), indicating a high levels of chlorophyll a among ice in the Weddell Sea. The image is a monthly composite of daily global MCI composites for February 2007. The inset shows spectra in the high-MCI area (red) compared to a nearby open-water area (green). The difference (blue) is plotted using the right-hand axis. Other areas off Wilkes Land (bottom right) and along the ice edge off Queen Maud Land (top) also show high values of the index.

in other coastal areas of the Weddell Sea in October/November 1986 and Febrary/March 1983 (Smetacek et al., 1992). The spectrum in Fig 2 shows that the high MCI signal is due to a strong radiance peak at 709 nm with an associated dip at 665 and 681 nm, similar to the spectra in Figure 1. This dip can be interpreted as a reduction in the radiance back-scattered by ice, due to absorption by chlorophyll a near 670 nm. The time series of total MCI signal summed over all longitudes south of 60S latitude (Figure 3) shows an apparent increase in this type of bloom in Antarctic waters between 2003 and 2009.

4. CONCLUSIONS

The ability of the MCI index derived from MERIS data to detect and map the variety of events shown here, indicates the importance of the spectral band at 709 nm. Although the MCI will not detect all of the harmful algal blooms (HABs) that are causing increasing damage to aquaculture, tourism and coastal water quality, it clearly has a role in detecting and monitoring some surface, high-chlorophyll events, occurring under clear-sky conditions. It also has a role in mapping blooms in ice and turbid water and in mapping floating vegetation. The present nearly seven years of data shows blooms over an increasing range of areas and gives improving statistics on seasonal and interannual variability. The data record is not yet long enough to show climate-related or other longer-term trends.

Future observations based on MCI depend on maintaining the capability provided by MERIS. The present US sensors SeaWiFS and MODIS and the planned future sensor VIIRS lack the band at 709 nm. The major limitation of MERIS, especially when compared to MODIS, is in its relatively narrow swath width, which at 1150 km is about half that of MODIS. This is not wide enough to allow daily coverage of all areas. Also, there are at present two MODIS instruments in orbit, on the Terra and Aqua satellites, again increasing coverage. Ideally, future versions of the MERIS sensor would image over an increased swath width, and would also have two sensors in orbit at all times.

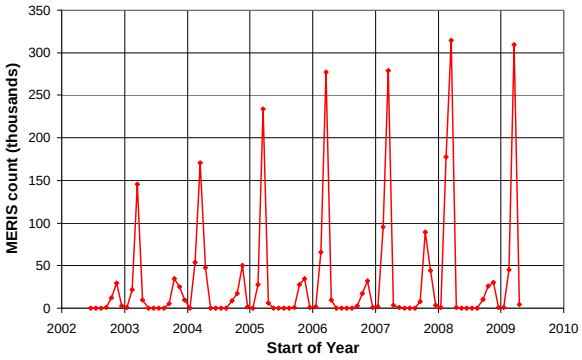

Figure 3. The time series of total bloom intensity south of 60S summed over all longitudes. Data show an apparent increase in total occurrence of this type of bloom in March of the years 2003 to 2009. MCI also indicates a smaller (spring) peak in October/November of each year.

ACKNOWLEDGEMENTS

Funding for this work was provided by the Canadian Space Agency under the GRIP program and by the Canadian Department of Fisheries and Oceans.

REFERENCES

Gower, J. F. R., Hu, C., Borstad, G.A. and King, S., 2006, Ocean color satellites show extensive lines of floating *Sargassum* in the Gulf of Mexico. *IEEE* Transactions on Geoscience and Remote Sensing, 44, pp. 3619-3625.

Gower, J.F.R and S. King, 2007, "An Antarctic ice-related "superbloom" observed with the MERIS satellite imager" Geophysical Research Letters, 34, doi: 10.1029/2007GL029638, 2007.

Gower, J.F.R., S.A. King and P. Goncalves, 2008, Global monitoring of plankton blooms using MERIS MCI, International Journal of Remote Sensing, 29, 6209-6216.

Smetacek, V., R. Scharek, L.I. Gordon, H. Eicken, E. Fahrbach, G. Rohardt and S. Moore, 1992, Early Spring phytoplankton blooms in ice platelet layers of the southern Weddell Sea, Antarctica, Deep-Sea Research, I 39, 153-168.

Observations of floating *Sargassum* vegetation in the Gulf of Mexico and North Atlantic using MERIS

J. Gower, S. King

Institute of Ocean Sciences, Sidney, BC; Canada – jim.gower@dfo-mpo.gc.ca

Abstract – We use satellite imagery from the European Space Agency (ESA) Medium Resolution Imaging Spectrometer (MERIS) optical sensor to make the first mapping of the full distribution and movement of the population of *Sargassum* in the Gulf of Mexico and western Atlantic. For most of the years for which we have data (2002 to 2008), the results show a seasonal pattern in which *Sargassum* originates in the northwest Gulf of Mexico in the spring of each year, and is then advected into the Atlantic. The *Sargassum* appears east of Cape Hatteras as a "*Sargassum* jet" in July and ends northeast of the Bahamas in February of the following year. This pattern is consistent with historical surveys from ships. MERIS provides a spectral band which greatly improves discrimination of floating vegetation from confusing signals such as cloud and sun-glint.

Keywords: Sargassum, MERIS, ocean colour.

1. INTRODUCTION

The MERIS Imager on the Envisat satellite showed extensive areas containing long, narrow, meandering slicks in the north-western Gulf of Mexico in the early summer of 2005 (Gower et al., 2006). The same features are detectable in MODIS and SeaWiFS imagery. Gower et al. (2006) used the wider spatial coverage provided by MODIS to follow the seasonal pattern of *Sargassum* in the Gulf of Mexico between September 2004 and October 2005. In several cases the *Sargassum* affects sun-glint patterns by reducing surface roughness, showing that it should also be visible in SAR (Synthetic Aperture Radar) images. However, in none of these cases do the satellite data provide the more definitive spectral signature provided by MERIS.

We have since extended our previous survey (Gower et al., 2006) using the global MERIS data set provided by ESA's G-POD (Grid Processing On Demand) system for the time period June 2002 to December 2009. Results show an annual cycle of *Sargassum* distribution in the Gulf of Mexico and North Atlantic, with considerable interannual variability.

2. SATELLITE DATA

We make use of an index, the MCI (Maximum Chlorophyll Index) available from MERIS, but not from MODIS or SeaWiFS, which provides good discrimination of floating and coastal vegetation, as well as intense surface plankton blooms (Gower et al., 2008). The index measures the local peak in water-leaving radiance near 705 nm, which has been identified as a measure of high concentrations of surface chlorophyll *a* and is also shown to be a sensitive detector of the "shifted red-edge" characteristic of marine and floating vegetation.

MCI is computed from the above-atmosphere spectral radiances (Level-1 data) measured for each pixel of the satellite image data to show excess radiance at 709 nm, above a baseline defined by linear interpolation between the neighboring spectral bands at 681 and 754 nm. Figure 1 shows an example of detection of Sargassum off the east coast of the US. The floating weed is spread into long lines by surface shear in the Gulf Stream. Spectra show the characteristic red-edge of vegetation.

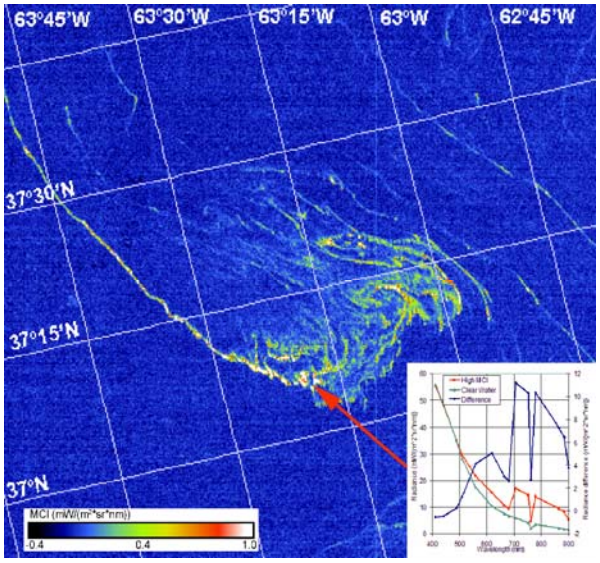

Figure 1. Floating *Sargassum* in the Gulf Stream near 63W, 37N imaged as MCI on October 22, 2007 by ESA's ocean sensor, MERIS at its full spatial resolution of 300 m. Colours indicate MCI value as shown by the colour bar. Inset shows top-of-atmosphere radiance spectra for a pixel containing high *Sargassum* concentration (red, and red arrow) and for nearby clear water (green). The difference spectrum (blue, right axis) shows the "red-edge" of land vegetation.

3. DISTRIBUTION ANALYSIS

To derive monthly distributions of *Sargassum*, composites of MCI signal at 5 km spatial resolution are analyzed by computing the frequency distribution (histogram) of MCI values in each one-degree square. We assume that all MCI values exceeding the mean ocean background value in that one-degree square by a threshold amount, indicate presence of *Sargassum*. Squares that include coastlines and other fixed areas where MCI is observed to be high, such as coral reefs and areas with frequent coastal plankton blooms, are masked in all months. We name the sum of the number of MCI values above threshold, multiplied by the amount by which MCI exceeds its background value (in mW m^{-2} nm^{-1}

sr^{-1}) as "MERIS count." We take this count as being proportional to the total amount of *Sargassum* in each one-degree square.

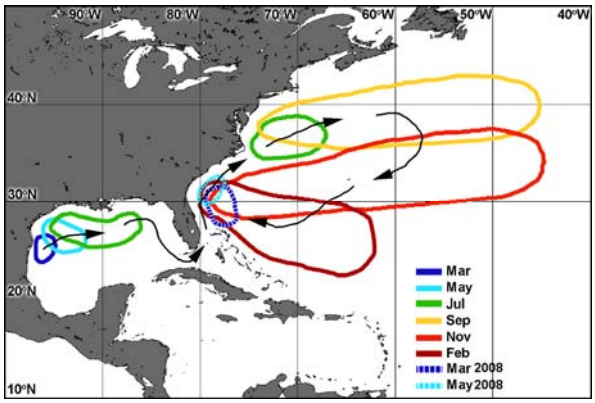

Figure 2. Simplified outline diagram showing the average extent of *Sargassum* in March, May, July, September, November and February, based on MERIS count distributions by month as shown in Figure 2. Only in 2008 does MERIS detect significant *Sargassum* in the Atlantic between March and June (dashed outlines).

4. CONCLUSIONS

Our observations for the period 2003 to 2008 show growth of *Sargassum* in the northwest Gulf of Mexico between March and June each year, with *Sargassum* appearing in the Atlantic, north and east of Cape Hatteras, starting in about July (Figure 2). In all years except 2008, we observe low total *Sargassum* amounts in the Atlantic before this annual injection from the Gulf of Mexico. Observations for 2003 to 2007 suggest that most *Sargassum* has a life-time of one year or less, with the major "nursery area" being in the northwest Gulf of Mexico. If *Sargassum* were longer-lived, we would expect to observe more evidence of *Sargassum* in the Atlantic northeast of the Bahamas, in February to May in these years. Only in 2008 do observations show significant concentrations in this area, with circulation back into the Gulf Stream. This circulation would be consistent with the traditional picture of the Sargasso Sea as being the main repository of *Sargassum* biomass.

MERIS shows large amounts of *Sargassum* in the Gulf of Mexico in the years 2003 to 2005, compared to the Atlantic, but smaller amounts in 2006 to 2008. The average of all years suggests that the Gulf of Mexico is the dominant *Sargassum* "nursery area," but clearly a longer time-series is required to better determine its relative importance. The observation of a significant average flow of about one million tonnes of *Sargassum* out of the Gulf of Mexico in most years implies a carbon flux which needs to be accounted for in productivity and carbon models.

The motion of the *Sargassum* in the Atlantic follows a consistent pattern from year to year. The observed distributions are consistent with earlier ship observations, and explain many of the apparent discrepancies found in them.

We have used the satellite data to search for similar evidence of long-lived pelagic *Sargassum* in other oceans of the world, and find a smaller amount near Madagascar, but nothing in other areas.

Satellite images based on appropriate spectral bands are clearly a valuable source of data for surveys of *Sargassum*, but with limitations due to spatial resolution, cloud cover and sun-glint. We note that the satellite may miss significant quantities of *Sargassum* if it is too evenly distributed or mixed beneath the surface by wind. We plan to expand our study to include correlation with observed wind speed. In the future, satellite observations can continue to provide a lengthening time series of data of the type we present here. Satellites can also play an important role in selecting the sampling pattern for any future ship survey.

Future observations of *Sargassum* depend on maintaining the capability provided by MERIS. The present US sensors SeaWiFS and MODIS and the planned future sensor VIIRS lack the band at 709 nm which make possible the computation of MCI, used here for detection of *Sargassum*. The major limitation of MERIS, especially when compared to MODIS, is in its relatively narrow swath width, which at 1150 km is about half that of MODIS. This is not wide enough to allow daily coverage of all areas. Also, there are at present two MODIS instruments in orbit, on the Terra and Aqua satellites, again increasing coverage. Ideally, future versions of the MERIS sensor would image over an increased swath width, and would also have two sensors in orbit at all times.

ACKNOWLEDGEMENTS

Funding for this work was provided by the Canadian Space Agency under the GRIP program and by the Canadian Department of Fisheries and Oceans.

REFERENCES

Gower, J. F. R., Hu, C., Borstad, G.A. and King, S., 2006, Ocean color satellites show extensive lines of floating *Sargassum* in the Gulf of Mexico. *IEEE* Transactions on Geoscience and Remote Sensing, 44, pp. 3619-3625.

Gower, J.F.R., S.A. King and P. Goncalves, 2008, Global monitoring of plankton blooms using MERIS MCI, International Journal of Remote Sensing, 29, 6209-6216.

Ice Dynamics in Lincoln Sea and Nares Strait

P. Gudmandsen [a], S. Hanson [b], J. Wilkinson [c], L. Toudal Pedersen [b]

[a] National Space Institute, Technical University of Denmark, Lyngby, Denmark – prebeng@space.dtu.dk
[b] Danish Meteorological Institute, Copenhagen, Denmark – sha@dmi.dk - ltp@dmi.dk
[c] Scottish Association for Marine Science, Oban, Scotland, UK – jpw28@sams.ac.uk

Abstract – Freshwater variability, i.e. low-salinity water and sea ice, is the subject of current studies of indications of Arctic climate change. The region of the Lincoln Sea and the Nares Strait is an important contributor to the outflow of ice from the Arctic Ocean and therefore is subject to monitoring of sea ice flux. This paper presents examples of high-resolution ice dynamics in the region using data from satellite radar data and drifting buoys. Such complementary large-scale/small scale studies are necessary because the region is subject to large tidal forcing and strong wind events.

Keywords: sea ice, tides, Lincoln Sea, Nares Strait.

1. INTRODUCTION

Since Kozo (1991) first described the 'gulf-club' shape feature of openings of the sea ice canopy in the southern Lincoln Sea this important 'polynya like' feature has been subject to a series studies. His observations were based on NOAA data but later, data from passive and active microwave satellite data including SSM/I, ERS-1 and Radarsat-1 were applied to determine the area flux of sea ice into the Nares Strait southwards (Agnew (1998), Gudmandsen (2000), Kwok (2005)). An overview of the fluxes from the Arctic Ocean crossing the Canadian polar shelf is presented by Melling et al. (2006). 13 years of observations with Radarsat-1 and Envisat data show annual variations of the area flux into the Nares Strait with the last four years presenting a distinct feature that might reflect large-scale variations in the Arctic Ocean (Kwok et al., 2010).

Studies of the small-scale variations of sea ice drift has been carried out by deployment of a number of buoys in the Lincoln Sea and the Nares Strait in May 2006, 2007 and 2008 complementing the large-scale drift obtained with remote sensing data acquired by satellites at irregular intervals and variable repetition time. This paper presents examples obtained from the campaign in 2008 when eight buoys were deployed in the Lincoln Sea and the Nares Strait.

2. REGION OF INTEREST

The region of interest is composed from north to south by the Lincoln Sea bordering the Arctic Ocean to the north, and the Nares Strait with Robeson Channel, Hall Basin, Kennedy Channel, Kane Basin and Smith Sound opening into the North Water and Baffin Bay further south. Hans Island is a 2.3 km^2 island in the centre of the Strait. The 500-km long Nares Strait is bordered by high mountains, attaining to 1500 m in Ellesmere Island and 500 m on the Greenland side, controlling the wind that essentially has two major components oriented along the Strait forcing the ice drift (Samelson et al. 2006).

3. METHODS

The eight buoys deployed in the region were developed by the Scottish Association for Marine Science (SAMS), in Oban, Scotland. They consist essentially of three parts: a GPS receiver, a communication unit and a control unit encased in a small box with a battery. Communications is established by way of the Iridium communications system that relays position data every 20 minutes to SAMS. The lifetime is determined by the state of the host floe with the buoys ceasing operation by the mechanical destruction of the floe or by the melt of the floe or when the battery is discharged.

Large-scale ice observations are based on data from the Advanced Synthetic Aperture Radar (ASAR) on the European satellite Envisat operated in its 400-km Wide Swath Mode. It is reprocessed to a spatial resolution of 150 m that in general permits identification of ice features applied in a computer-controlled interactive process for determining the movement of floes from two consecutive radar scenes.

The analyses are supported by half-hourly mean winds obtained from the automatic weather station installed on Hans Island on 4 May 2008 (Wilkinson et al., 2009) and hourly data from a fine-mesh meteorological model (Samelson and Barbour, 2008).

4. OBSERVATIONS

4.1 Prelude

The Lincoln Sea - Nares Strait is a coupled system of ocean current and ice flux controlled by wind but also by ice barriers that form at the entrance to Nares Strait and/or at places in the Strait. These barriers may last for weeks or months causing a complete stop of the ice transport through the Strait (Kwok et al, 2010). Thus, an ice barrier was present in central, western Kane Basin from early April 2008 to early June where the southwards ice transport was gradually resumed. This had a marked influence on the conditions in Lincoln Sea and in the northern part of the Strait with opposite-directed ice movements through the gate of Robeson Channel caused by changing winds.

4.2 Buoy tracks

Five buoys were placed in Lincoln Sea along the 65° Meridian at intervals ranging from 28 to 193 km, the southern most at a distance from the shore of Ellesmere

Island of 33 km. This line of deployment corresponds largely to that exploited by the Switchyard project operated in the 2003-07 period. Three other buoys were placed on floes near he entrance to the Robeson Channel and in the Kennedy Channel, one of them few kilometres north of Hans Island.

Figure 1 shows tracks of two of the buoys from their deployment to the end of their operation (18 May – 10 August) showing almost 'parallel' tracks in the period 18 May to 26 June (including a period with no data available). Although placed at a distance of only 47 km they experienced very different tracks partly due to a strong south-eastern wind out of the coast of Ellesmere Island influencing one of the buoys and not the other. The 54-km northeast helix movements of the one buoy demonstrate tidal movements in the ice canopy at small ice concentration. Similar but much smaller movements are observed with the other buoy situated in an ice canopy of a large ice concentration. Figure 2 shows the 20-minute clockwise velocity during one tidal period of about 24 hours in the form of a tidal ellipse modified by the 10-km north-eastern drift of the floe.

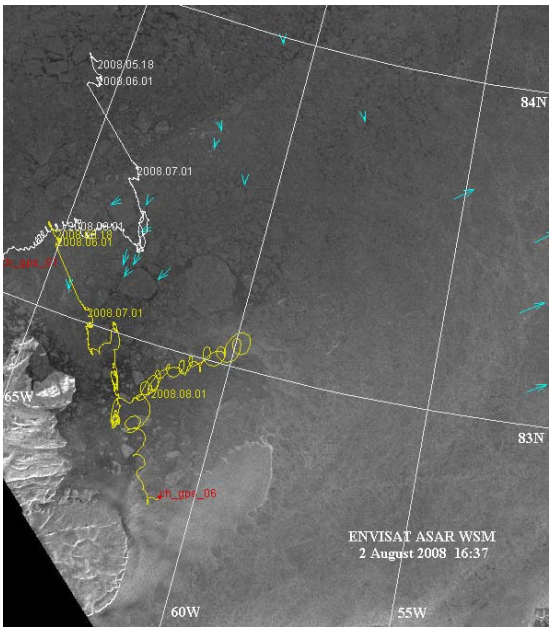

Figure 1. Tracks of two buoys (buoy 01 in white and buoy 06 in yellow) in Lincoln Sea plotted on an ASAR scene of 2 August 2008 acquired at 16:37. The vectors in the eastern part of the scene indicate ice movements in the 18.4-hour period between two ASAR acquisitions ranging from 5 to 9 km (7.5 to 14 cm/s). The pattern of a south-eastern wind is seen as reflections from ripples on open water and melt-water ponds.

5. CONCLUSIONS & ACKNOWLEDGEMENTS

The presentation is extracted from a report describing the three buoy campaigns 2006, 2007 and 2008 carried out under different ice conditions. The studies are carried out under the auspices of the IPY with support by the Commission of Scientific Research in Greenland, the Danish National Space Institute, the US National Science Foundation, UK Natural Environmental Research Council, International Space Science Institute, the European Space Agency and the PolarView programme.

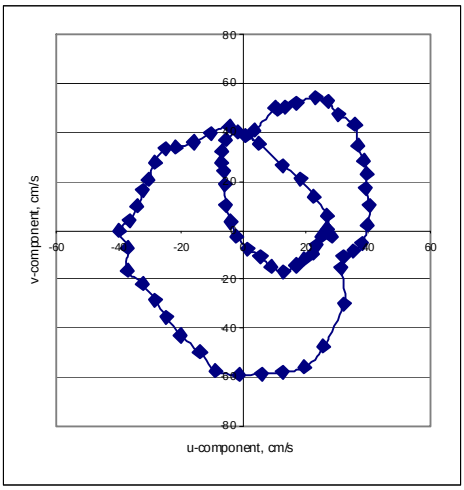

Figure 2. Tidal ellipse for 2 August 2008, 11:20 – 10:40. Each point is the end point of a velocity vector in a 20-minute period. The largest vector of 59 cm/s corresponds to a movement of 709 meter.

REFERENCES

Agnew, T.A. (1998). Drainage of multi-year sea ice from the Lincoln Sea. *Can. Met. Oceanogr. Soc. Bulletin* 26(4): 101-103.

Gudmandsen, P. (2000). A remote sensing study of Lincoln Sea. *Proc. ESA ERS-ENVISAT Symposium*, Gothenburg, Sweden, 16-20 October 2000, Paper No: 402, 7 pp.

Kozo, T.L. (1991). The hybrid polynya at northern end of Nares Strait. *Geophys. Res Lett.* 16 *2059-2062*

Kwok, R. (2005). Variability of the Nares Strait ice flux. *Geophys. Res. Lett.* 32, L24502, doi: 101029/2005GL024768.

Kwok, R., L. Toudal Pedersen, P. Gudmandsen and S.S. Pang (2010). Large sea ice outflow into the Nares Strait in 2007. *Geophys. Res. Lett.*, 37, L03502,doi:10.1029/2009GL041872,2010.

Melling, H. and 9 co-authors (2008). Freshwater fluxes via Pacific and Arctic outflows across the Canadian polar shelf. Chapter 9 of *Arctic-Subarctic Ocean Fluxes: Defining the Role of the Northern Seas in Climate*, R. Dickson, J. Meincke and P. Rhines, eds., Springer, 193-247.

Samelson, R.M., T. Agnew, H. Melling and A. Muenchow (2006). Evidence for atmospheric control of sea-ice motion through Nares Strait. *Geophys. Res. Lett.* 33, L02506, doi:10.1029/2005GL025016.

Samelsom, R.M., P.L. Barbour (2008). Low-level winds, orographic channeling and extreme events in Nares Strait: a model-based mesoscale climatology. *Monthly Weather Review*, 136, 4746-4759.

Wilkinson, J., P. Gudmandsen, S. Hanson, R. Saldo and R.M. Samelson (2009). Hans Island: Meteorological Data from an International Borderline. EOS Trans. Amer. Geophys. Soc., 90, pp.190-191.

Review of Chinese Spaceborne Ocean Observing Systems Onboard Sensors and Data Products (1988-2025)

Ming-Xia He *, Shuangyan He, Yunfei Wang

Ocean Remote Sensing Institute, Ocean University of China, Qingdao, China – mxhe@ouc.edu.cn

Abstract – Information on the Chinese spaceborne earth observing satellite (and spacecraft) missions between 1988 and 2025 are comprehensively collected, including historical, in-orbit and planned (or future) satellites. A detailed introduction of seven satellite (and spacecraft) series including FY-n, HY-n, ZY-n, HJ-n, SZ-n, CRS-n and DMC/BJ-1 is given. Furthermore, the satellite (and spacecraft) observing systems for ocean color, sea surface temperature, sea surface height, sea surface vector winds and SAR are listed respectively according to onboard sensors.

Keywords: ocean observing system.

Table 1 shows Chinese spaceborne earth observing satellite missions by launch date, including historical, on-orbit and planned (or future) satellites. There are 7 satellite series in all FengYun satellites (FY-n), ocean satellites (HY-n), resource satellites (CBERS, ZY-n) and environment satellites (HJ-n) are jointly implemented by China National Space Administration (CNSA) and related application sectors, which are China Meteorological Administration (CMA), State Oceanic Administration (SOA), Ministry of Land and Resources (MLR) and Ministry of Civil Affairs (MCA) / Ministry of Environmental Protection (MEP) respectively.

Shenzhou spacecrafts (SZ-n) and Chinese Remote Sensing satellites (CRS-n or YG-n) are implemented by CNSA. Disaster Monitoring Constellation / BeiJing-1 micro-satellite (DMC / BJ-1 micro-satellite) are implemented by Ministry of Science and Technology of China (MOST)..

Table 1

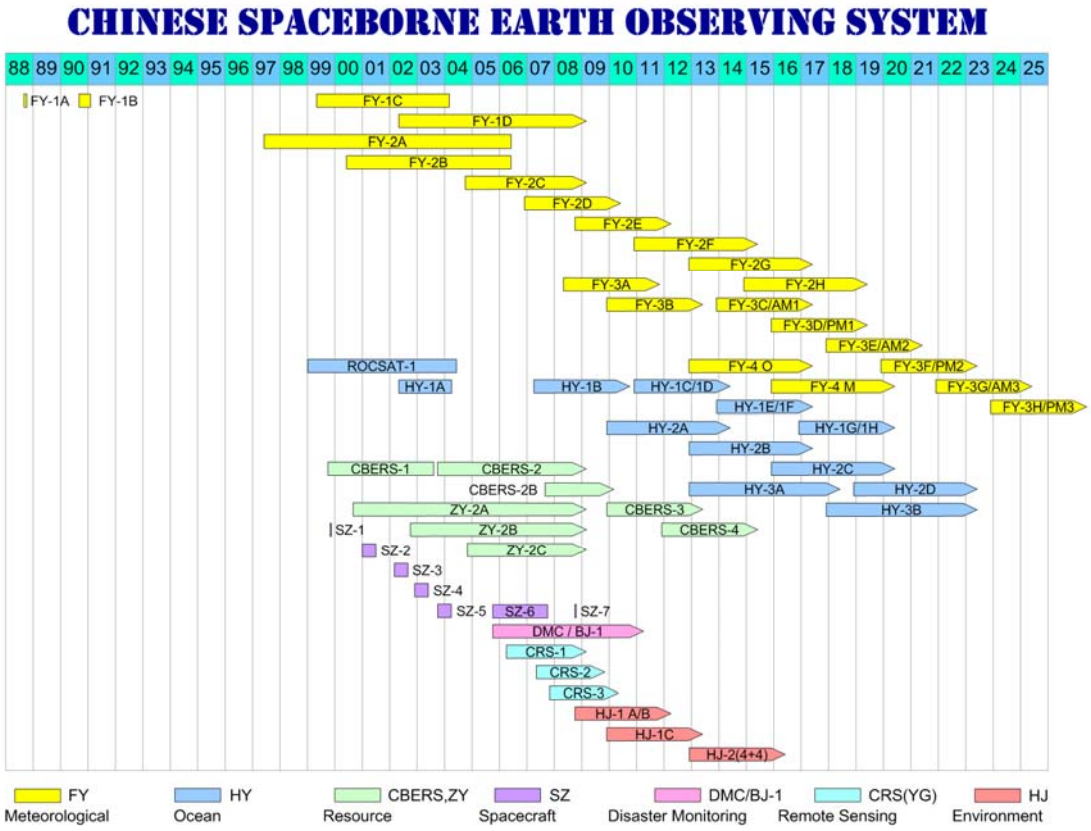

* Corresponding author.

All above satellite and spacecraft series are capable of ocean observation, and therefore comprise the Chinese spaceborne ocean observing system. Tables 2 to 7 list the missions carrying ocean color sensors, infrared and microwave radiometers, altimeters, microwave scatterometers, SARs and high spatial resolution optical sensors respectively.

Table 2

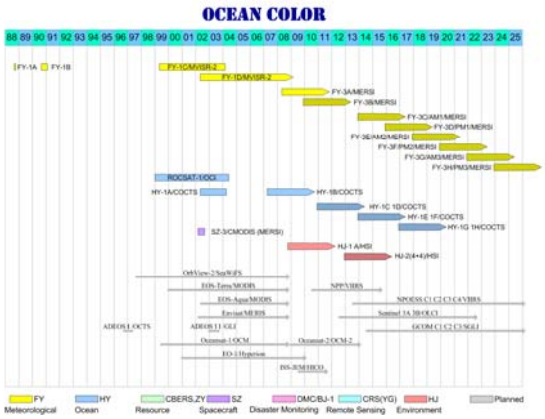

Table 3

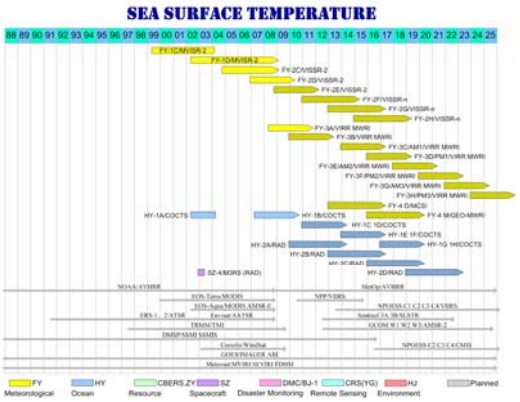

Table 4

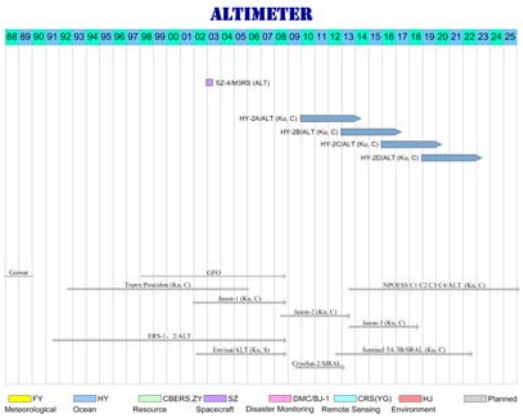

The performance of sensors onboard the Chinese and other similar ocean observing satellites is compared and discussed and the gap is pointed out. The 21 sensors in-orbit onboard Chinese ocean observing systems and other similar satellite sensors are listed. A summary of 21 sensors used for ocean observation is presented.

Table 5

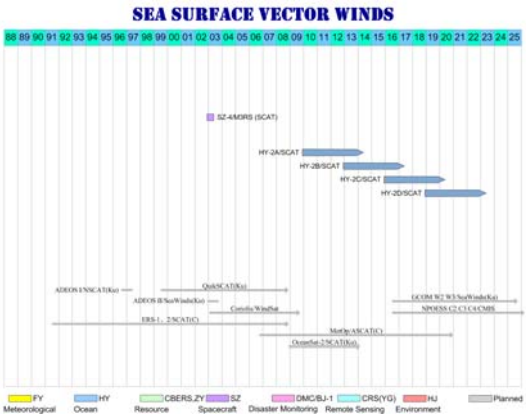

Table 6

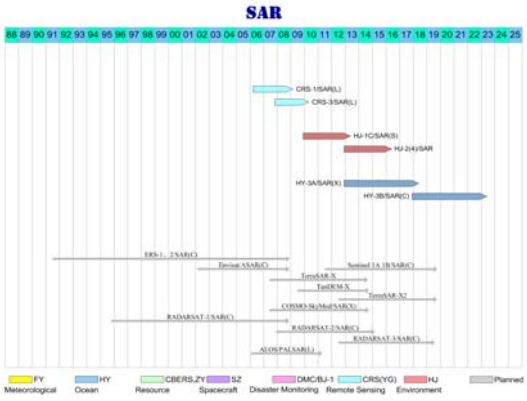

Table 7

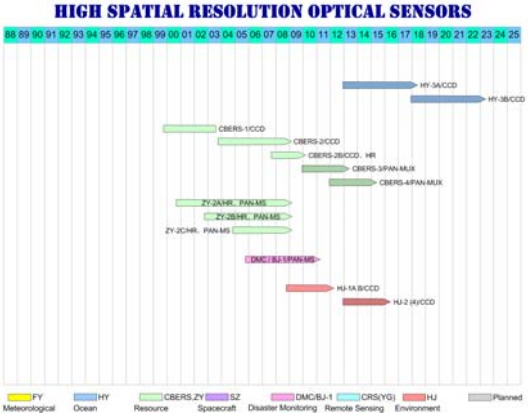

Ten sensors can be used for quantitative retrieval of ocean environmental parameters. The other sensors can be applied to coastal zone observation. The technological specifications and data products of FY-3A / MERSI, FY-3A / MWRI, HY-1B / COCTS, HJ-1A / HIS and several infra-red sensors are introduced respectively. Only the services of ocean satellite data products of sea surface temperature (SST) and ocean color parameters are available in present.

Further, there are merely L1 data product provided for hyper-spectral sensors and microwave sensors.

ACKNOWLEDGEMENTS

This study is supported by EC FP-6 DRAGONESS Project.

Mapping of Oil Films in the Context of Global Change

A.Yu. Ivanov *

P.P. Shirshov Institute of Oceanology, Russian Academy of Sciences – ivanoff@ocean.ru

Abstract – This paper reviews and discusses the problem of the remote sensing of oil films in the context of global change. Sea surface oil films play a significant role in globally important processes such as exchange of momentum, heat and gas between the ocean and the atmosphere. Among remote sensing techniques, spaceborne SAR is considered to be a primary sensor for oil spill surveillance. Recent studies on oil pollution demonstrated high potential of the SAR-equipped satellites. The European and Asian seas have been chosen as test basins to work out an oil spill mapping technology using SAR image sets and geographic information systems. Wide use of GIS or GIS-approach offers a method for accounting of global impact of oil films, both natural and man-made, that can lead to improvement of air-sea interactions in climate models.

Keywords: global change, ocean-atmosphere interactions, oil film / slick / spill, SAR, GIS.

1. INTRODUCTION

In the first half of the XX century, crude oil took over as a source of energy, and the problem of oil spills in the sea became of public concern. The interaction of spilled oil with the marine environment damages the marine ecosystems and influences ocean-atmosphere interactions. The impact of accidental spills is not only catastrophic for nearby coastal zones, but have far-reaching consequences, as previously was not thought. Natural oil slicks and oil spills floating on the sea surface are detectable by synthetic aperture radars (SAR), because they damp the short surface waves that are responsible for the radar backscattering (Alpers and Espedal 2004). The European and Asian seas have been chosen as test basins to work out an oil spill mapping technology using data sets of the ERS-1/ERS-2, Radarsat-1 and Envisat SAR images, and recent studies on oil pollution demonstrated high potential of SAR-equipped satellites (see, e.g., Gade and Alpers (1999)). An approach and methodology for oil spill mapping, considering a GIS as a framework for analysis, have been developed (Ivanov and Zatyagalova 2008). However, currently there is no an estimating method for determination how fully and how frequently an ocean region is covered by oil films, if even slick signatures are presented in the SAR imagery. Oil spill distribution maps can be valuable source of information about oil spill distribution, statistics and sources. They allow scientists identification of most polluted waters and vulnerable areas that is an important step in developing of the monitoring scenario. Further, spatial distribution and extent of surface films based on satellite remote sensing can be provided. Sea surface films play a significant role in global exchange processes between the ocean and the atmosphere, and GIS-approach offers a method for the accounting of global impact of oil films, which could lead to an improvement of air-sea interactions in climate models.

2. MARINE OIL FILMS AND THEIR ROLE IN OCEAN-ATMOSPHERE INTERACTION

Natural and man-made oil films affecting the physical properties of the air-sea interface, and, in turn, have impact on a number of important processes determining the ocean-atmosphere interaction, among them are: energy transfer from wind to waves, retardation of evaporation and convective exchange, sea surface temperature variability, gas exchange, formation of skin-layer and foam on the sea surface and others (Kraus 1972, Monin and Krasitskii 1985, Toba 2003). Existing knowledge about effects of oil films on marine environment, ocean-atmosphere interaction and global warming, in the current situation of global changes, are insufficient (Toba 2003). These effects are studied only partially and locally. Their global impact and a role in global changes are poor understood. Their regional and global estimates are very approximately, because real extent and distribution of oil slicks as well oil spills in the world ocean is indeed unknown.

3. REMOTE SENSING OF OIL SPILLS

Optical, infrared (IR) and ultraviolet (UV) sensors, microwave radiometers and radars (SLAR and SAR) onboard aircrafts or spacecrafts are the tools for remote sensing of marine oil spills (Fingas and Brown 2000). Spaceborne systems used visible bands are susceptible to false detections of oil due to sun elevation, clouds, viewing geometry, etc. Traditional satellite optical sensors (e.g., MODIS) have not been of much use for oil spill detection due to spatial resolution of ~1 km. Middle and high resolution optical sensors (e.g., ETM/Landsat, HRV/Spot, Aster/Terra) don't provide operational daily observations, and their data are of limited spatial coverage. Airborne remote sensing sensors, such as IR/UV systems, microwave radiometers and fluorometric lasers have low spatial resolution and operational applicability. Among remote sensing techniques, spaceborne SAR is considered to be a primary sensor for global oil slick/spill surveillance. It was shown many times that SAR allows detection, localization and furnishing with information on the dimensions and extent of oil spills (Gade and Alpers 1999).

4. MAPPING OF OIL SPILLS IN MARINE ENVIRONMENT

GIS-approach developed worldwide and summarized by Ivanov and Zatyagalova (2008) uses a wide set of detailed geographic (coastline, bottom topography, currents, etc.)

* Corresponding author. Nakhimovsky prospect, 36, Moscow, 117997, Russian Federation; tel: +7 (495) 129-2781.

and industrial information (onshore and off shore oil & gas infrastructure, ship lanes, etc.) about a marine basin. All this information can be arranged in a GIS allowing manipulating all kind of spatial data including remote sensing data and images. Why a GIS-approach is important for this task?

First, GIS approach is a tool for improving oil spill identification and classification in SAR imagery. A number of limitations of SAR for oil spill detection is being recognized. Operational service based on SAR images still depends on an operator's experience, and analysis of large volumes of additional information. It is proposed, therefore, that GIS-approach and use of geographic, remote sensing, contextual and other ancillary information can make an important aid to correctly interpret the dark signatures, providing a tool for analysis (Ivanov and Zatyagalova 2008). Second, GIS-approach allows scientists to calculated spatial distribution (extent) and total area of detected oil spills that, under certain assumptions about a thickness of oil films, can give information about total volume of spilled oil. Further monthly/annually trends in oil pollution can be analyzed. Finally, knowledge obtained in long-term monitoring based on GIS-approach can be used as one of parameters in climatic models enabling us to see an impact of oil films on trends in climate changes. A GIS and its databases for the marine basins can be compiled from data of several sources, e.g., geographic maps, nautical charts, global/regional models, regional archives, corporative databases, satellite images, other data and information. All datasets and geographic information have to be compiled together in a GIS envelope. Thus, GIS providing an efficient storage, retrieval, analysis and visualization of geographic, environmental and industrial information is considered to support oil spill mapping and identification. Example of GIS-based oil spill distribution map for the East China Sea is shown on Fig. 1. In order to validate a methodological approach on regional scales, a number of mapping projects have been carried out (Ivanov and Zatyagalova 2008, Shi *et al.* 2008).

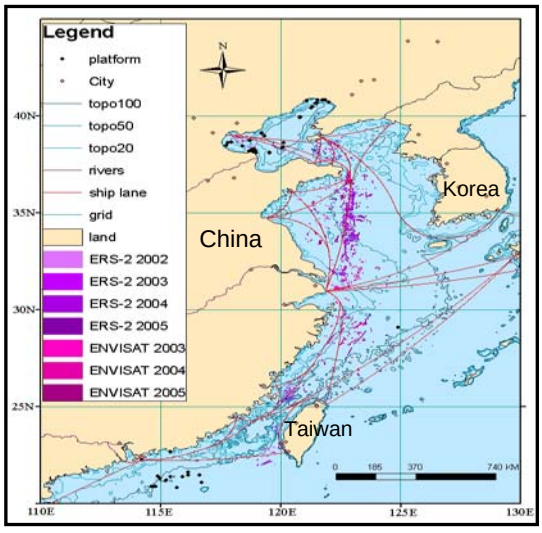

Figure 1. GIS-made oil spill distribution map for the East China Sea (Shi *et al.* 2008)

5. CONCLUSION

Significant advances have been made over the last decades in estimating air-sea fluxes over the ocean (Toba 2003). Oil films from time to time covering the ocean surface can now be resolved with at sufficient temporal and spatial resolution by using remote sensing techniques. The use of satellite derived oil spill products that have the appropriate resolution instead assimilation products can give a great opportunity to investigators. Natural and man-made oil slicks affecting the physical properties of the air-sea interface, and, in turn, have impact on a number of important processes determining the ocean-atmosphere interaction. Existing knowledge about their effects on a marine environment, ocean-atmosphere interaction and global changes, in the situation of global changes, is insufficient. Although conventional technologies can provide more of the required data, the remote sensing can do more wide spatial and temporal coverage, providing new information products and effective solutions. Through multi-temporal imaging, SAR techniques and GIS-approach can provide information on oil slick location and extent. It seems in context of global changes a set of oil spill distribution maps, which, when combined and generalized, are some kind of an answer to global challenges. Now remote sensing is a critical element of any ocean monitoring system and plays an increasingly important role in oil slick monitoring. In its present state, optical satellite imagery doesn't offer much potential for oil spill mapping. The imaging SAR has become an important tool in monitoring of marine oil spills due to its high resolution, all-weather and day-n-night capability. In the last decades SAR's potential for oil spill detection have been widely demonstrated in the coastal and open ocean. It is realistic to hope that modern SAR-equipped, multi-swath, multi-resolution and multi-polarization families of satellites, such as Radarsat, Cosmo-SkyMed, TerraSAR-X and future Sentinel, will play a significant role in providing real time data and information on oil slick distribution worldwide.

REFERENCES

Alpers, W. and H. Espedal (2004). "Oils and surfactants". In: "Synthetic Aperture Radar Marine User's Manual". Washington: US Department of Commerce, pp. 263-276.

Fingas, M. and C. Brown (2000). "Oil-spill remote sensing - An update", Sea Technology, vol. 41, pp. 21-26.

Gade, M. and W. Alpers (1999). "Using ERS-2 SAR images for routine observation of marine pollution in European coastal waters". In: The Science of the Total Environment 237/238. London: Elsevier Science B.V., pp. 441-448.

Ivanov, A.Yu. and V.V. Zatyagalova (2008). "A GIS approach to mapping of oil spills in a marine environment", International Journal of Remote Sensing, vol. 29, no. 21, pp. 6297-6313.

Kraus, E.B. (1972). "Atmosphere-ocean interaction". London: Oxford University Press.

Monin, A.S. and V.P. Krasitskii (1985). "Phenomena on the ocean surface". Leningrad: Gidrometeoizdat (in Russian).

Toba, Y. (Ed.) (2003). "Atmosphere-ocean interactions" Kluwer Academic Publishers.

Shi, L., A.Yu. Ivanov, M.-X. He and C. Zhao (2008). "Oil spill mapping in the western part of the East China Sea using synthetic aperture radar imagery", International Journal of Remote Sensing, vol. 29, no. 21, pp. 6315-6329.

Quality Control Operations for Space-Borne Optical Sensors

J. Jackson [a,*], C. Kent [a], A. Borg [a], D. Sautreau [a], S. Lavender [a], L. Bourg [b], S. Saunier [c], P. Goryl [d]

[a] ARGANS Ltd, Plymouth , United Kingdom – jjackson@argans.co.uk
[b] ACRI-ST, Sophia-Antipolis, France
[c] Gael Consultant, Champs-sur-Marne, France
[d] ESA, ESRIN, Frascati, Italy

Space-borne optical sensors often provide global coverage of a variety of surface parameters that are utilised by a large scientific community. There is a consistent high demand for products – especially Near-Real-Time (NRT), and this need has resulted in a stable and integrated approach to Quality Control (QC) throughout a mission's lifetime. A general overview and description of the protocols and procedures carried out by the MERIS, MODIS, SeaWiFS and Landsat Sensor Performance Product and Algorithms (SPPA) Teams is provided in order to encourage QC knowledge transfer for space-borne sensors.

Keywords: quality control, Landsat, MERIS, MODIS, SeaWiFS.

1. INTRODUCTION

Many space-borne optical sensors provide global coverage of a variety of parameters such as Ocean Colour (above surface reflectance of visible light), Sea Surface Temperature and Land usage. QC and support for the optical sensors MERIS, MODIS, SeaWiFS and Landsat (5 and 7) is provided through SPPA Teams based at ARGANS - with expert support from ACRI-ST and Gael Consultant - under the Vega-lead IDEAS consortium. Several systematic and manual activities are performed and utilised by the SPPA Teams in order to provide consistent QC and support to the global remote sensing community. In addition to providing specific QC activities and reporting for the individual sensors, the SPPA Teams located at ARGANS form part of the wider IDEAS Optical Group - which also includes the AATSR, ALOS/AVNIR-2, ALOS-PRISM, and JERS-1 instruments, and provides monthly reporting on all activities to ESA.

2. MERIS SPPA

The MERIS (MEdium Resolution Imaging Spectrometer) instrument onboard ESA's ENVISAT satellite has been providing optical measurements in the solar reflective range (visible to near-infra-red) since 2002. The daily coverage of the MERIS instrument is 15 orbits; resulting in a large number of specific products generated in NRT and downstream (Consolidated) processing, and in both Full (300m) and Reduced (1200m) Resolutions.

2.1 Product Quality Control

Daily MERIS production is monitored through automatically generated reports that provide information on the duration of all products (across all product levels) for each orbit – and thereby ensures NRT monitoring of the operational state of the instrument. The Daily Report (DR) can also be used to highlight any delays in dissemination to the ESA Ground Stations and their Rolling Archives (RA). The monitoring of product generation by filename and duration is supplemented by the use of Quicklooks generated for each product; allowing a rapid, accessible check of product quality. Any anomalous product generation found in the DR are investigated by the SPPA Team and advice is issued to ESA.

AMALFI (ASAR MERIS AATSR Labelling Facility Inspection) is the offline Quality Control tool system used to perform operational QC on products as they are written onto media for delivery to Users. Any products that fail the AMALFI tool are subjected to an in-depth investigation by the MERIS SPPA Team using open source programs such as BEAM VISAT (Brockmann Consult, 2010) and bespoke code. Results of the investigation - indicating whether the product is suitable for distribution -are provided to the AMALFI operator, who then distributes the media with the AMALFI test results along with the results of the SPPA Team's investigation.

2.2 Service Requests and Processor Evolution

The MERIS SPPA Team provides support to ESA through the validation of new software and hardware updates. A generic MERIS test dataset (TDS) has been defined to allow validation of MERIS processing across a variety of situations such as clear (no cloud) ocean, clear land, cloud, and coastal zones, and deliberately includes known product anomalies such as missing frames and errors in consolidation. Validation of a newly-processed TDS utilises bespoke code developed at both ARGANS and ACRI-ST so as to allow direct comparison with previous validations, and highlights any issues with the software/hardware update. A recent validation included the transfer of MERIS L1 and L2 processing from the AIX platform to Linux, and the implementation of this change at all processing stations.

2.3 Scientific Community Support

The MERIS SPPA Team fully support the wide MERIS User community by constant communication with the MERIS Quality Working Group (QWG) and responding to external User requests via the ESA Earth Observation Helpdesk. This is supplemented by allowing the entire data QC procedures - including daily reporting and Long Loop

* Corresponding Author. ARGANS Ltd, Tamar Science Park, 15 Davy Road, Plymouth, PL6 8BY. +441752 764298

Sensor Analysis (LLSA) - to be fully transparent through a variety of media including: documentation, a newly formed User forum entitled ODESA (ESA, 2010a), and FAQs, with comments, feedback and questions actively encouraged to allow constant evolution of the mission's data quality.

3. LANDSAT SPPA

The Landsat SPPA Team provides support for European coverage of Landsat 5 and 7 products as an ESA Third Party Mission (TPM). Landsat 5, (launched in 1984), and Landsat 7,(launched in 1999), provide high resolution land coverage in the visible to thermal wavelengths of light through the Thematic Mapper (TM) and Enhanced Thematic Mapper (ETM+) respectively. European Landsat products in a variety of product formats - including RAW, FAST, GEOTIFF and CEOS – can be ordered through the ESA EOLI (ESA, 2010b) catalogue for either FTP or DVD delivery.

3.1 Product Quality Control

Systematic QC by the Landsat SPPA Team for Landsat 5 and Landsat 7 products differs from the methodology employed for the QC of MERIS, MODIS and SeaWiFS; products generated are not retrieved at ARGANS, but all processed products are analysed at the point of processing in the Station using the QUISS tool (soon to be AMALFI 2) developed by Gael Consultant. Any product failures raised as a result are subjected to a number of tests by the Landsat SPPA Team in order to determine whether they are "fit for purpose" and onward dissemination to the User community. In addition to the QUISS tests performed at the processing station, the Landsat SPPA Team retrieves a large number of Landsat 5 TM sys-corrected products for LLSA each day. Long Loop Sensor Analysis involves the comparison of radiometric values between multiple products located over specific areas such as the Libyan Desert and Lacrau (France), and provides a historical timeline of the radiometric accuracy of the instrument throughout the lifetime of the mission

4. MODIS SPPA

The MODIS (MODerate Imaging Spectrometer) instrument was launched onboard the NASA Terra and Aqua satellites in 1999 and 2002 respectively, acquiring measurements in 36 spectral bands (visible to thermal wavelengths). European coverage of MODIS data is now provided as an ESA TPM and is accessible (at level 1B) through the MERCI MODIS website (ESA, 2010c), developed by Brockmann Consult.

4.1 Product Quality Control

Daily reporting for MODIS (Aqua and Terra) is performed in a similar manner to MERIS. Daily Reports containing orbit information and quicklooks for rapid assessment of product quality, and any erroneous products found as a result are downloaded and assessed using bespoke code developed at ARGANS. The resulting anomaly reports provide detailed information with regard to the products processing parameters and overall data quality.

In addition to NRT QC of products from the MERCI MODIS online catalogue, the MODIS SPPA Team also provides NRT QC support under the GMES framework to the MyOcean MODIS Rolling Archive; this dataset contains European Coverage Level 1A (un-calibrated Top-of-Atmosphere) MODIS AQUA products. All products are automatically downloaded and interrogated using the open-source SeaDAS (NASA) program, and are subsequently further processed to Level 2 (derived surface parameters) and an image outputs generated.

New tools are currently under development at ARGANS to expand the scope of the service to ESA. Amongst these are scripts to predict product generation in order to ensure orbit acquisition consistency, and bespoke modification of erroneous products to allow nominal geolocation Auxiliary Data File (ADF) production in the event of missing frames within the product.

5. SEAWIFS SPPA

The SeaWiFS (Sea viewing Wide Field-of-view Sensor) instrument was launched onboard GeoEYE's OrbView-2 satellite in 1997, and acquires radiometric measurements of the Earth's surface in eight spectral bands (visible to NIR wavelengths). European coverage of SeaWiFS data is now provided as an ESA TPM and is accessible (at Level 0) through the MyOcean Rolling Archive under the GMES framework.

5.1 Product Quality Control

The SeaWiFS SPPA Team provides support to ESA through automated download and investigation of all products supplied on the MyOcean SeaWiFS Rolling Archive. As with the MyOcean MODIS products, processing up to Level 2 (surface derived parameters) using the open-source software SeaDAS (NASA) is carried out at ARGANS, with quicklooks generated at both Level 0 and Level 2, and thereby providing NRT monitoring of product quality

6. CONCLUSION

Satellite-borne optical sensors provide invaluable data regarding the changes and alteration in the atmospheric, oceanic and terrestrial environments to the global scientific community; resulting in a consistent requirement to ensure the generated products are of sufficient quality throughout the lifetime of the mission. The activities of the MERIS, MODIS, SeaWiFS and Landsat SPPA Teams at ARGANS benefit from the expert support of ACRI-ST and Gael Consultant, and as a result provide support to ESA in a variety of QC activities including automated analysis and checking of products, long loop sensor analysis, software and hardware update validations, general monitoring of product catalogues, and support to User forums and FAQs.

REFERENCES

Brockmann Consult. (2010). The BEAM Project. http://www.brockmann-consult.de/cms/web/beam.

ESA. (2010a). The ODESA Project. http://odesa-info.eu/.

ESA. (2010b). The ESA EOLI Catalogue. http://earth.esa.int/EOLi/EOLi.html.

ESA. (2010c). The MERCI MODIS Catalogue. http://merci-modis.eo.esa.int/merci/welcome.do.

Mapping of Ocean Bio-Geochemical Provinces Using Correlations between Satellite-Derived Winds and Chlorophyll

M. Kahru [a], S.T. Gille [a], R. Murtugudde [b], P. Strutton [c], B.G. Mitchell [a]

[a] Scripps Institution of Oceanography, University of California San Diego, La Jolla, California, USA – mkahru@ucsd.edu
[b] 2207 CSS Bldg/ESSIC, University of Maryland, College Park, MD 20742, USA
[c] College of Oceanic and Atmospheric Sciences, Oregon State University, Corvallis, Oregon, USA

Abstract – Global time series of satellite derived winds and surface chlorophyll concentration (*Chl-a*) show patterns of coherent areas with either positive or negative correlations. The correlation between Chl-a and wind speed is generally negative in areas with deep mixed layers and positive in areas with shallow mixed layers. These patterns are interpreted in terms of the main limiting factors that control phytoplankton growth, i.e. either nutrients or light, and are used in objective mapping of the biogeochemical provinces of the world ocean.

Keywords: ocean color, wind, phytoplankton.

1. INTRODUCTION

Phytoplankton production and biomass in the world ocean is limited by nutrient (N, P, Si, Fe) concentrations (Chisholm and Morel, 1991) and/or the mean light level due to vertical mixing and seasonal variability in daily insolation (Siegel *et al*., 2002). A number of authors (Platt and Sathyendranath, 1988; Longhurst *et al*., 1995) have proposed the definition and use of quasi-stable biogeochemical provinces as a means of assessing basin scale oceanic productivity and biogeochemical characteristics. We use the correlation between time series of satellite derived winds and surface chlorophyll-a concentration (*Chl-a*, mg m^{-3}) to objectively map the main biogeochemical provinces in the world ocean based on the dominant mechanisms responsible for the variability in phytoplankton biomass.

2. DATA

Satellite-derived Level-3 (i.e. binned and mapped) data sets of chlorophyll-a concentration (*Chl-a*, mg m-3) were obtained from NASA's Ocean Color website (http://oceancolor.gsfc.nasa.gov/) and the European Space Agency's GlobColour project (http://www.globcolour.info). *Chl-a* datasets using standard Case 1 water algorithms (O'Reilly *et al*., 1998; Morel and Maritorena, 2001) were obtained. Daily data from individual sensors (OCTS, Nov-1996 to Jun-1997; SeaWiFS, Sep-1997 to Apr-2002) and those merged from multiple sensors (SeaWiFS, MERIS, MODIS-Aqua) with weighted averaging by the GlobColour project were composited into 5-day and monthly time series from Nov-1996 to Dec-2009. Monthly and 5-day anomalies of *Chl-a* were created as the ratio of the value during the current period to the long-term mean of the respective time period and expressed as percentage anomaly, i.e. 100*(*Anomaly* – 1).

Cross-Calibrated Multi-Platform (CCMP) ocean surface wind data (Ardizzone *et al*., 2009; Atlas *et al*., 2008) derived through cross-calibration and assimilation of data from SSM/I, TMI, AMSR-E, SeaWinds on QuikSCAT, and SeaWinds on ADEOS-II were used. In this study, we used level 3.5 wind speed (*U*, m/s), wind speed squared, zonal and meridional components of wind speed (*u* and *v*, m/s) and pseudostress (*u*U and *v*U, m^2/s^2). Monthly and 5-day anomalies of the wind variables were constructed by subtracting the long-term mean value of the respective period from the value during each individual period. The CCMP wind data were available from Jul-1987 to Dec-2008 and the overlapping period during which both *Chl-a* and wind data were available extended from Nov-1996 to Dec-2008. Mixed layer depth climatology data were obtained from http://www.locean-ipsl.upmc.fr/~cdblod/mld.html (de Boyer Montégut *et al*., 2004) and monthly MLD data from http://www.science.oregonstate.edu/ocean.productivity/ (Behrenfeld *et al*., 2005).

3. RESULTS

The correlation between wind speed and Chl-a anomalies shows coherent and statistically significant patterns over the world ocean (Fig. 1). These patterns can be interpreted in terms of the main limiting factors that control phytoplankton growth, i.e. either nutrients or light. The strength of wind-induced upwelling and mixing is governed by the wind stress. We therefore also calculated the correlations between *Chl-a* anomalies and squared or cubed wind speed (not shown), both of which produced correlation patterns that were identical to those shown in Fig. 1. It is essential that the correlations be calculated for seasonally normalized values (anomalies), as otherwise the annual cycle would have the dominant influence, e.g. at mid-latitudes the typically strong winds and low Chl-a in the winter would produce a strong negative correlation. The correlations between wind speed and SST anomalies (not shown) have a much simpler pattern and are mostly negative, except in areas such as the eastern tropical Pacific and eastern tropical Atlantic where the interannual modes of variability dominate. The broad features of the correlation patterns between *Chl-a* and wind speed anomalies at mid-latitudes correspond well to the mean depth of the mixed layer in spring. Spring mixed layers are typically the deepest mixed layers observed during the year. The mixed layer shallows during the summer, and water that was contained within the mixed layer in spring becomes the water that can easily be entrained into the mixed layer through summer. Deep spring mixed layers imply that the water below the summer mixed layer has low stratification, and therefore that small increases in summer wind can easily remix the upper ocean and reestablish deep mixed layers. Both in the North Pacific and North Atlantic the correlations between *Chl-a* and wind speed anomalies change from negative to positive where the spring mixed layer becomes shallower. Also, in comparison with the North Pacific, the North Atlantic has deeper mixed layers and more negative correlation between *Chl-a* and

wind speed anomalies. In the Southern Ocean spring mixed layers are particularly deep in the regions of intermediate or mode water formation along the northern flank of the ACC in the Indian and Pacific Oceans. Within these regions, *Chl-a* is negatively correlated with wind speed, and to the north, where mixed layers are shallower, *Chl-a* is positively correlated with wind speed. A number of patches with positive wind speed/*Chl-a* correlations occur inside the Southern Ocean, e.g. the Scotia Sea, north-east from the Antarctic Peninsula, and these regions tend to have shallower spring mixed layers. Correlation patterns of *Chl-a* anomaly with the eastward and the northward wind pseudostress also show coherent and characteristic patterns (not shown) that are used in the classification of the ocean domains. K-means and hierarchical cluster analyses were applied to the global correlations between *Chl-a* anomaly and wind speed, wind speed anomaly, eastward and northward pseudostress and the correlation between SST anomaly and wind speed anomaly. The derived clusters are similar to the patterns shown in Fig.1but the exact number of clusters and other details depend on the details of the clustering method.

4. CONCLUSION

The large-scale correlation patterns between winds and surface *Chl-a* concentration are determined by the main controlling factors of phytoplankton growth (nutrient or light) and allow objective mapping of the main bio-geochemical regimes in the world ocean. Areas where phytoplankton growth and biomass are primarily controlled by the upward flux of nutrients from below the euphotic zone show positive correlation with wind speed and areas with a deep mixed layer show negative correlation between *Chl-a* and wind speed. More complicated patterns are evident in the equatorial zone.

ACKNOWLEDGEMENTS

We thank NASA Ocean Color Processing Group and ESA GlobColour group for satellite data, H. Wang and M. Manzano for help in preparing figures. Financial support was provided by the NASA Ocean Biology and Biogeochemistry Program and the National Science Foundation.

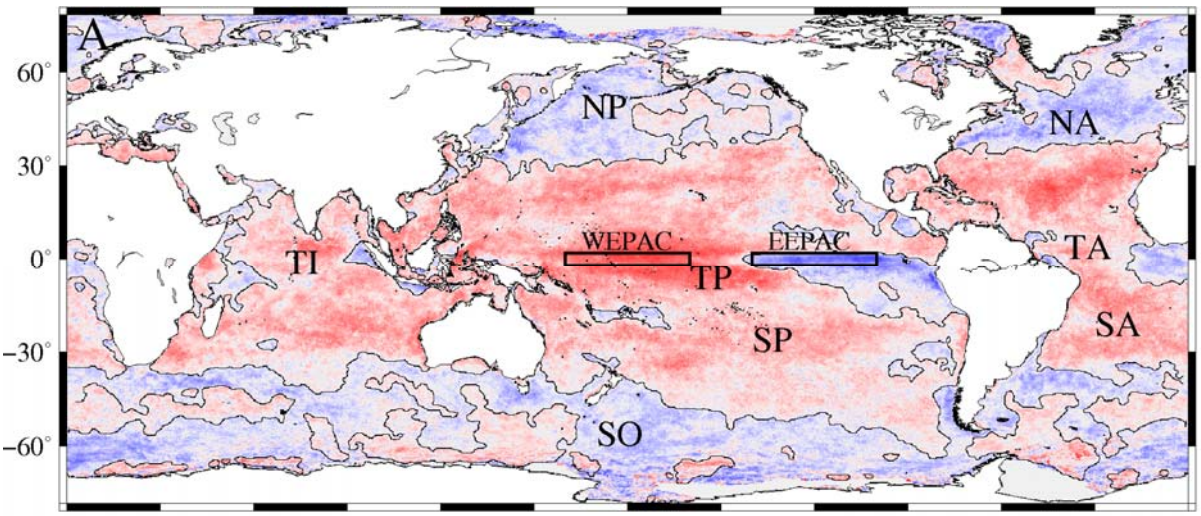

Figure 1. Correlation coefficient (*R*) between monthly wind speed anomaly and Chl-a anomalies. *N* = 144, the critical value, *Rcrit* (0.95) = 0.164, *Rcrit* (0.99) = 0.214, i.e. the correlation in most of the red and blue areas is statistically significant. Western Equatorial Pacific (WEPAC, 2ºN□2ºS, 160ºE□160ºW), Eastern Equatorial Pacific (EEPAC, 2ºN□2ºS, 140ºW□100ºW). The black curves are contour lines of *R* = 0 and separate regions with positive correlations (red) from those with negative correlations (blue). TI = Tropical Indian Ocean, NP = North Pacific, TP = Tropical Pacific, SO = Southern Ocean, SP = South Pacific, NA = North Atlantic, TA = Tropical Atlantic, SA = South Atlantic.

REFERENCES

Behrenfeld, M. J., E. Boss, D.A. Siegel and D.M. Shea (2005). "Carbon-based ocean productivity and phytoplankton physiology from space". *Global Biogeochem. Cycles*, 19, GB1006.

Ardizzone J., R. Atlas, and R.N. Hoffman (2009). "New multiplatform ocean surface wind product available". *Eos Trans. AGU*, vol. 90, p. 231.

Atlas R., J. Ardizzone, and R.N. Hoffman (2008). "Application of satellite surface wind data to ocean wind analysis", *Proc. SPIE*, 7087, 70870B.

Chisholm, S.W. and F.M.M. Morel (1991). "What controls phytoplankton production in nutrient-rich areas of the open sea?". *Limnol. Oceangr*., vol. 36, pp. 1507-1970.

de Boyer Montégut, C., G. Madec, A. S. Fischer, A. Lazar and D. Iudicone (2004). "Mixed layer depth over the global ocean: an examination of profile data and a profile-based climatology". *J. Geophys. Res*., vol. 109, C12003.

Siegel, D. A., S.C. Doney and J.A. Yoder (2002). "The North Atlantic spring phytoplankton bloom and Sverdrup's critical depth hypothesis". *Science*, vol. 296, pp. 730–733.

MOX: A high-performance Monte Carlo code for in-water radiative transfer modeling in a high-resolution two-dimensional domain

T. Kajiyama [a,*], D. D'Alimonte [b], G. Zibordi [c], J. C. Cunha [a]

[a] CITI, DI/FCT, Universidade Nova de Lisboa, Caparica, Portugal – {t.kajiyama, jcc}@di.fct.unl.pt
[b] CENTRIA, DI/FCT, Universidade Nova de Lisboa, Caparica, Portugal – davide.dalimonte@gmail.com
[c] Joint Research Centre, European Commission, Ispra, Italy – giuseppe.zibordi@jrc.ec.europa.eu

Abstract – This paper presents a new Monte Carlo (MC) code for modeling in-water radiative transfer processes within the framework of Ocean Color (OC) applications. The code numerically computes the up-welling radiance as well as upward and downward irradiance in a high-resolution two-dimensional (2D) grid space accounting for the effects of sea-surface waves. To overcome the computational load intrinsic to MC simulations, the code employs the state-of-the-art high-performance computing techniques, enabling large-scale MC simulations on modern supercomputers. This results in a fast and versatile software tool applicable in the context of optical oceanography to investigate various uncertainty budgets affecting *in situ* radiometric measurements.

Keywords: Monte Carlo, ocean color, radiative transfer.

1. INTRODUCTION

Quantitative analysis of uncertainties due to environmental effects and measurement protocols on *in situ* radiometric products derived from optical profiles performed in coastal waters is a key task for OC applications. In fact, accuracy estimates are fundamental for a better utilization of *in situ* radiometric measurements for the validation of OC remote sensing (RS) products and for the development of bio-optical algorithms for high-level OC RS products. Examples of space sensors for OC applications include ESA's MERIS on-board of the ENVISAT platform as well as NASA's SeaWiFS on-board of the OrbView-2 satellite and MODIS on-board of the AQUA platform. Among various sources of perturbations, the present study addresses the in-water light focusing effects induced by sea-surface waves (Zaneveld *et al*., 2001; Zibordi *et al*., 2004). Additional examples of uncertainties requiring accuracy assessments are those due to sensor tilt during the deployment of in-water profiling systems and those affecting above-water radiometric measurements. Theoretical investigations of the perturbations on *in situ* radiometric products are expected to make a substantial contribution to the accuracy assessments of field radiometric measurements and additionally provide valuable insights for improving measurement protocols. This study employs a statistical method based on MC simulations to quantify the effects of in-water light focusing on *in situ* radiometric products. A novel OC MC code, hereafter referred to as MOX, has been developed, and experimental results showed that the MOX code is capable of generating accurate high-resolution 2D representations of in-water radiometric fields including the up-welling radiance (L_u) as well as the upward and downward irradiance (E_u and E_d) in the presence of sea-surface waves (D'Alimonte *et al.,* 2010). MOX is based on high-performance computing (HPC) solutions to overcome the computational load intrinsic to MC simulations (Kajiyama *et al*., 2009). In the OC literature, MC methods have been widely employed (Leathers *et al*., 2004) to investigate the wave-induced light focusing effect (Zaneveld *et al*., 2001), the influence of near-surface bubble clouds on RS ocean reflectance (Piskozub *et al*., 2009), the propagation of a short light beam through turbulent oceanic flow (Bogucki *et al*., 2007), and to model various apparent optical properties (AOPs) in a three-dimensional setting (Gimond, 2004). However, the assumption of a flat sea surface, the lack of simulation results on E_u and L_u, or the coarse spatial resolution do not permit existing OC MC codes to thoroughly quantify the uncertainties induced by sea-surface focusing effects over optical profile data products.

2. METHODS

MOX data products are derived by (1) MC simulations of L_u, E_u and E_d radiometric fields; and (2) by linear regression of subsurface values and diffuse attenuation coefficients from log-transformed radiometric values collected through virtual optical profiling.

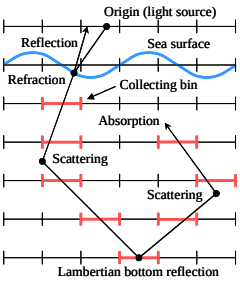

Figure 1. MOX ray-tracing scheme.

Each radiometric field is associated with a real matrix whose entries are computed by tracing a large number of photons and recording their trajectories into three matrices for L_u, E_u and E_d. Figure 1 shows a 2D grid space and a typical photon trajectory in MOX. The grid space is represented as layers of photon collecting bins. At the origin, photon weight w is defined by the sky-radiance distribution and the diffuse-to-total irradiance ratio. The photon weight and direction are updated across the air-sea interface on the basis of the Snell and Fresnel equations. Each time the photon intersects a collecting bin (as highlighted in Fig.1), w is added to the matrix element corresponding to that bin. In the water medium with attenuation c, absorption a, and volume scattering function $\beta(\theta)$, the optical distance l that the photon travels before

* Corresponding author. Quinta da Torre, 2829–516 Caparica, Portugal, Tel: +351–212–94–8536, Fax: +351–212–94–8541.

undergoing a scattering or absorption event follows the probability density function $p(l) = e^{-l}$, where $l = c \cdot r$ and r is the geometrical distance. Sample values of l are obtained by solving $P(l) = q$ for l, where P is the cumulative distribution function of l (i.e., the integral of p from 0 to l), and q is a random number uniformly distributed on the interval 0 to 1. The scattering coefficient b (i.e., the integral of β over all directions) and scattering phase function $\tilde{\beta} = \beta / b$ define the probability density function $p(\theta) = 2\pi\tilde{\beta}(\theta)\sin(\theta)$. Scattering angles θ are sampled by solving $P(\theta) = q$ for θ, where P is the cumulative distribution function of θ (i.e., the integral of p from 0 to θ). At the end of each sampled path l, w is scaled by the single scattering albedo $\varpi = (c - a) / c$. When w becomes smaller than threshold ζ_w, tracing of a new photon is started. Subsurface values $\Re(0^-)$ and diffuse attenuation coefficients $K_\Re$ are derived through virtual optical profiling, where $\Re$ denotes one of the three radiometric quantities. Specifically, samples of the radiometric quantities $\Re(z_i)$ at various depths z_i within a subsurface layer $[z_1, z_2]$ with homogeneous optical properties are taken from the elements of the radiometric matrices along the deployment path of a virtual free-fall optical profiling system. Since $\Re$ decreases approximately exponentially with depth (Mobley, 1994), the least squares regression of log-transformed $\Re(z_i)$ is then employed to yield the subsurface values $\Re(0^-)$ and diffuse attenuation coefficients $K_\Re$.

3. RESULTS

The agreement with Hydrolight (Mobley, 1994) simulations in the plane parallel case has demonstrated the MOX capability to model radiative transfer processes with uncertainties of a few percent. Analyzing simulations for sea-surface waves of 5 m width and 0.5 m height, it has been found that the number of photons required for a thorough investigation of sea-surface focusing effects on E_d, E_u and L_u are 10^6, 10^8 and 10^{10}, respectively. Coefficients of variation of subsurface radiometric values have been found varying between 0.5 and 2% for $E_d(0^-)$, below 0.45% for $E_u(0^-)$, and between 0.1 and 0.55% for $L_u(0^-)$, when considering a range of deployment speeds and sampling frequencies applicable to nowadays optical systems. Figure 2 illustrates simulated E_d, E_u and L_u radiometric fields accounting for two harmonic wave components (a wave of 5 m width and 0.5 m height, and another of 0.5 m width and 0.05 m height) at the spatial resolution of 1 cm. The number of traced photons is 10^9. The light focusing induced by the sea-surface waves significantly perturbs the E_d field. The E_u and L_u fields are less affected by the sea-surface focusing effects because E_u and L_u only depend on backscattered photons. Computing these radiometric fields took 2921.7 sec. using 64 AMD quad-core Opteron 2.3 GHz processors on TACC Ranger (University of Texas at Austin). In a separate test case with 10^8 photons traced, the serial execution time was 16973.1 sec., which reduced to 17.0 sec. (i.e., a ≈1000 times speedup) by a parallel execution using 512 processors. A significant variation has been observed in the execution time of the parallel MOX code with different simulation configurations, especially depending on various attenuation and absorption coefficients, volume scattering functions, sun positions, and wave settings.

4. CONCLUDING REMARKS

MOX enabled a comprehensive study of in-water light focusing and defocusing effects. It was applied to determine the statistical noise intrinsic to MC simulations allowing for the quantification of the focusing effects on *in situ* radiometric products. Computation time constraints were addressed by employing HPC techniques. Future work directions include: a) investigation of glint perturbations on above-water radiometric products; b) MOX performance optimization by means of GPU cards integrated into multi-core personal computers; and c) execution time prediction based on an analytical model of the MOX performance, to better utilize available computing resources.

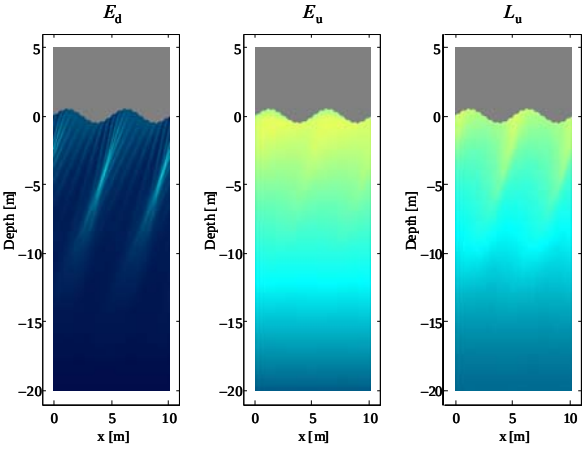

Figure 2. Examples of simulated light fields.

ACKNOWLEDGEMENTS

This research was supported by the Portuguese Foundation for Science and Technology (FCT/MCTES) through the Ciência 2007 Program, as well as by the European Space Agency (ESA) through the contract number C22576–00. We would like to thank Dr. Daniel Stanzione and the staff of the Texas Advanced Computing Center (TACC) for granting us access to the Ranger supercomputer through the UT Austin | Portugal Program funded by FCT/MCTES.

REFERENCES

Bogucki, D. J. *et al*. (2007). "Monte Carlo simulation of propagation of a short light beam through turbulent oceanic flow." Optics Express 15, 13988–13996.

D'Alimonte, D. *et al*. (2010). "A Monte Carlo code for high spatial resolution ocean color simulations." Applied Optics (submitted).

Gimond, M. (2004). "Description and verification of an aquatic optics Monte Carlo model." Environmental Modelling and Software 19, 1065–1076.

Kajiyama, T. *et al*. (2009). "High-performance ocean color Monte Carlo simulation in the Geo-Info project." Proc. PPAM 2009, LNCS, Springer (to appear).

Mobley, C. D. (1994). "Light and water: Radiative transfer in natural waters." Academic Press.

Leathers, R. A. *et al*. (2004). "Monte Carlo radiative transfer simulations for ocean optics: A practical guide." Naval Research Laboratory.

Piskozub, J. *et al*. (2009). "Small-scale effects of underwater bubble clouds on ocean reflectance: 3-D modeling results." Optics Express 17, 11747–11752.

Zaneveld, J. R. *et al*. (2001). "Influence of surface waves on measured and modeled irradiance profiles." Applied Optics 40, 1442–1449.

Zibordi, G. *et al*. (2004). "An evaluation of depth resolution requirements for optical profiling in coastal waters." Journal of Atmospheric and Oceanic Technology 21, 1059–1073.

Advanced Acoustical Wave Gauge for Verification of Retrieval Algorithms for Remote Sensing of the Ocean from Space

V. Karaev*, M. Kanevsky, Eu. Meshkov

Institute of Applied Physics RAS, Nizhny Novgorod, Russia – volodye@hydro.appl.sci-nnov.ru

Abstract – An advanced underwater acoustical wave gauge is developed. An advantage of the new wave gauge in comparison with conventional sea buoy is its ability to measure just characteristics of sea gravity waves which influence backscattering of electromagnetic waves by sea surface. The new wave gauge is capable of measuring all 2nd statistical moments of sea waves and this information can be used for developing advanced radar systems for remote sensing of the ocean. Scheme of observation and retrieval algorithms are discussed.

Keywords: acoustical wave gauge, retrieval algorithm.

1. INTRODUCTION

Modern spaceborne radars enable one to obtain global information about near-surface wind and significant wave height by applying special retrieval algorithms. The precision of a retrieval algorithm is verified by comparing the retrieved parameters with the data of in-situ measurements of these parameters. The main source of field data is a set of sea buoys. The main problem of buoy data deals with limitation of the measurable wavelength of sea waves, for example, some buoys can measure waves only longer than 10 m. This limitation does not influence measurements of significant wave height. However, it is not possible to measure variance of slopes by sea buoys, because short gravity waves make the main contribution to variance of slopes. Hence the existing buoy cannot be used for validation of the slope retrieval algorithm of the advanced radar. For example, the effective variance of slopes can be retrieved now by Precipitation Radar data but the precision of the new retrieval algorithm cannot be checked by means of buoy data and hence these data cannot be used in the wave model (WAM). Information about variance of slopes is very important for improvement of numerical wave models, for example, the ECMWF wave prediction system. In this paper, we consider a new underwater acoustical wave gauge capable of retrieving variance of slopes. Data of the new wave gauge will be used for validation of the slope retrieval algorithm.

2. ACOUSTICAL WAVE GAUGE

2.1 Theoretical background

To describe backscattering of centimeter acoustical waves at small incidence angles, the Kirchhoff method is used (Isakovich, 1973). In this method, it is assumed that scattering takes place in the parts of the large-scale wave profile oriented perpendicularly to incident radiation. Small ripple on a large-scale wave induces diffusion scattering and decreases backscattering power in comparison with that on smooth surface. In our previous papers we had considered the retrieval of variance of slope for microwave radar at nadir probing. The theoretical analysis and field experiments have confirmed the efficiency of developed retrieval algorithms. The measurements were carried out from helicopter helicopter (Karaev *et al.*, 2008a; Karaev *et al*., 2008b). It is not possible to use such expensive method for validation of retrieval algorithms in the global scale. Therefore, we suggest employing an underwater Doppler acoustical system with a knife-like antenna beam for measurements of sea wave parameters.

2.2 Scheme of observation

We can, evidently, consider two variants of installation of the new acoustical wave gauge. The first variant is to install the underwater wave gauge at the sea bottom or stable platform and to connect it by a cable with a small surface buoy. This buoy measures wind speed and is the source of electricity and the transmitter of data. The second variant is an underwater acoustical block connected with conventional sea buoy. The scheme of observation is shown in fig. 1.

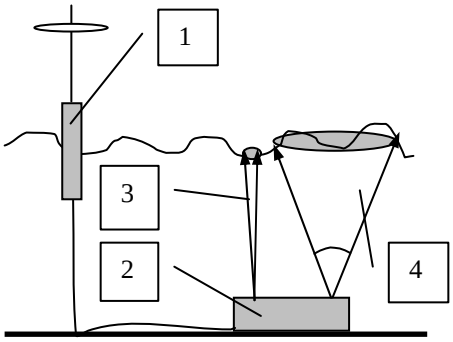

Fig. 1. Scheme of underwater Doppler acoustical system: 1 – buoy with transmitter, power source, and wind gauge, 2 – acoustical block, 3 – vertical narrow acoustic beam, 4 – knife-like acoustic beam.

To retrieve the wave parameters it is necessary to use two knife-like beam antennas ($\delta_x >> \delta_y$) oriented perpendicularly in the horizontal plane and a narrow beam (δ_y). The antenna beam is assumed to be Gaussian, where

* Corresponding author. 46 Uljanov str., 603950 Nizhny Novgorod, Russia. Tel +7 (831) 416-49-28, Fax +7 (831) 436-59-76.

δ_x , δ_y is the antenna beam pattern at the half-power level along the ***X*** and ***Y*** axes, respectively.

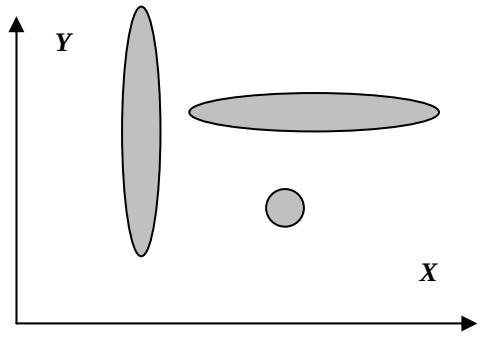

Fig. 2. Scheme of antenna footprints

The scheme of antenna footprints is shown in Fig. 2. Let us suppose that first footprint is oriented along the ***Y*** axis, the second footprint is oriented along the ***X*** axis, and hence $\delta_x(1) = \delta_y(2)$ and $\delta_y(1) = \delta_x(2)$. The last beam is symmetrical and $\delta_y(1) = \delta_y(3) = \delta_x(3)$.

2.3 Basic formulas of retrieval algorithm

As a result of measurements, we have three widths of the Doppler spectrum Δf_{10} ($\Delta f_{10}(1), \Delta f_{10}(2), \Delta f_{10}(3)$) and three normalized radar cross sections ($\sigma_0(1), \sigma_0(2), \sigma_0(3)$). This is enough for retrieval of all 2nd statistical moments of sea waves. The 2nd moments can be calculated by the following formulas:

$$s_{xx}^2 = \frac{\sigma_0^2(2)\delta_x^2 - \sigma_0^2(3)\delta_y^2}{5.52\left(\sigma_0^2(3) - \sigma_0^2(2)\right)}, \quad (1)$$

$$s_{yy}^2 = \frac{\sigma_0^2(3)\delta_y^2 - \sigma_0^2(1)\delta_x^2}{5.52\left(\sigma_0^2(1) - \sigma_0^2(3)\right)}, \quad (2)$$

$$K_{yt}^2 = \left[\left(\frac{\Delta f_{10}(1)\cdot\lambda}{4\sqrt{2\ln(10)}}\right)^2 - \left(\frac{\Delta f_{10}(3)\cdot\lambda}{4\sqrt{2\ln(10)}}\right)^2\right] \times \left[\frac{5.52\left(s_{yy}^2 + \delta_y^2/5.52\right)\left(s_{yy}^2 + \delta_x^2/5.52\right)}{\delta_x^2 - \delta_y^2}\right], \quad (3)$$

$$K_{xt}^2 = \left[\left(\frac{\Delta f_{10}(2)\cdot\lambda}{4\sqrt{2\ln(10)}}\right)^2 - \left(\frac{\Delta f_{10}(3)\cdot\lambda}{4\sqrt{2\ln(10)}}\right)^2\right] \times \left[\frac{5.52\left(s_{xx}^2 + \delta_y^2/5.52\right)\left(s_{xx}^2 + \delta_x^2/5.52\right)}{\delta_x^2 - \delta_y^2}\right], \quad (4)$$

$$s_{tt}^2 = \left(\frac{\Delta f_{10}(3)\lambda}{4\sqrt{2\ln(10)}}\right)^2 + \frac{K_{xt}^2}{s_{xx}^2 + \delta_y^2/5.52} + \frac{K_{yt}^2}{s_{yy}^2 + \delta_x^2/5.52}. \quad (5)$$

where s_{xx}^2 and s_{yy}^2 are the slope variances along the ***X*** and ***Y*** axes, and s_{tt}^2 is the variance of the vertical component of the orbital velocity. The correlation coefficients of slopes and the vertical component of the orbital velocities $K_{xt(\tau)}$ and $K_{yt(\tau)}$ at the time τ = 0 are used. The correlation coefficients are calculated by the formula:

$$K_{\alpha\beta} = 0.5\frac{\partial K(\vec{\rho},\tau)}{\partial\alpha\partial\beta}\bigg|_{\vec{\rho},\tau=0}, \quad (6)$$

where $K(\vec{\rho},\tau)$ is the correlation function of sea wave heights. Application of the acoustical system with three antenna beams enables us to retrieve all statistical 2nd moments of sea waves and validate the new retrieval algorithms for spaceborne radar.

3. CONCLUSION

Advanced radar systems cannot develop without an improvement of contact measurements of sea wave parameters. Only the procedure of retrieval algorithm validation offers an opportunity of using retrieved data in numerical wave models. Conventional buoys are unable to measure variance of slopes and thus they cannot be used for validation of new retrieval algorithms. We developed an advanced underwater acoustical buoy for measurements of the 2nd moments of sea waves. The retrieval algorithms are based on the algorithms developed for radar with a knife-like beam and hence they measure just sea wave parameters as radar does. The new wave gauge can stimulate further development of spaceborne radars for remote sensing of the ocean.

ACKNOWLEDGEMENTS

The work is supported by the Russian Fund of Fundamental Research (projects N 09-05-97016 and 10-05-00181) and by the Scientific School-1244.208.2.

REFERENCES

Isakovich, M.A., (1973), General acoustics, (in Russian), Moscow, Nauka, 1973, 495 p.

Karaev, V., Kanevsky, M., Meshkov, E. (2008a), Retrieval of sea waves parameters on radar data (in Russian), Issledovanie Zemli iz Kosmosa, N 1, 44-55

Karaev, V., Kanevsky, M., Meshkov, E. (2008b), Measurement of variance of water surface slopes by a radar: verification of algorithms, Radiophysics and Quantum Electronics, 51, N 5

Optical Remote Sensing Technique of the Gulf of Gabès: Relation between Turbidity, Secchi Depth and Total Suspended Matter

R. Katlane Essersi [a], B. Nechad [b], K. Ruddick [b], F. Zargouni [a]

[a] Faculty of Mathematical, Physical and Natural Sciences of Tunisia – Katlanerim@yahoo.fr, fouadzargouni@yahoo.fr
[b] Management Unit of the North Sea Mathematical Models (MUMM), Royal Belgian Institute for Natural Sciences – K.Ruddick@mumm.ac.be, b.nechad@mumm.ac.be

Abstract – Optical remote sensing is used in the gulf of Gabès to provide scientific information to support environmental management for this area. The gulf of Gabès is located in the southern east coast of Tunisia. It is a shallow continental shelf with semi-diurnal tides. Industrial activities in this area have contributed to the degradation of the biodiversity of the ecosystem with eutrophication problems. To assess the long-term effect of anthropic and natural discharges on the Gulf of Gabès, water quality and light penetration in the coastal waters are estimated from relationship derived from in situ measurements of total suspended matter, secchy depth and turbidity. Semi empirical algorithms are used to retrieve turbidity and total suspended matter product from MODIS imagery. A preliminary validation of these products is presented, based on in situ measurements and MODIS matchups.

Keywords: turbidity, Secchi depth, TSM, Gulf of Gabès.

1. INTRODUCTION

The objective of this study is to use the optical remote sensing technique to estimate water quality in the gulf of Gabès and impact of industrial discharge. The industrial zone is located in the central gulf of Gabès in the port of Gannouche (Fig.1). In this area, little is known about the distribution of the total suspended matter concentrations (TSM), which are a good indicator of water quality.

Recent seaborne measurements campaigns of turbidity (TUR) were carried out in the gulf of Gabès. In this study, in situ measurements of TUR and MODIS-derived TSM and TUR are compared and correlated, to adapt a semi-empirical model established for the turbid waters, to the Gulf of Gabès. The performance of these models is assessed and satellite maps of TSM in this region are presented.

1.1 Regional Situation

The gulf of Gabès is located in the southern of oriental Tunisia in the East Coast (Figure 1), between the Tunisian shelf and Djeffara coast; there are two basins with bathymetric threshold to join Kneiss and Jerba islands. The gulf of Gabès has a typical morphology, with monotonous continental shelf of low depth with very soft slope at 250 Km of the coast, with the presence of some channel of tide roaming the plateau.

Generally the climate of the region of Gabès is influenced by the tempered, humid and hot Mediterranean air coming from the East, but also by the subtropical, dry and hot saharian aspect coming from the South-west with the sandy wind.

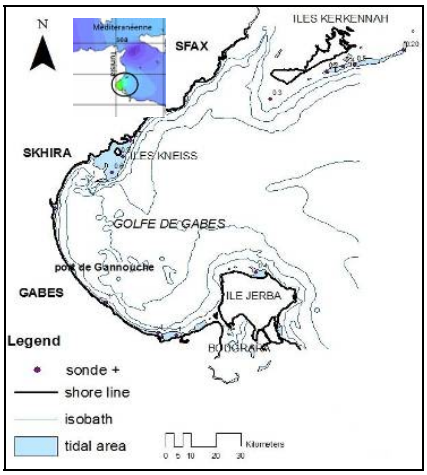

Figure 1. Geographic location and morphology under sea.

2. MAIN BODY

2.1 Data

In situ data were collected from 5th to 7th July 2009 and on the 6th and 8th of October 2009, concurrently with the satellite overpass. These seaborne measurements consist of TUR (NTU), water transparency (m), TSM (mg/l), chlorophyll *a* (µg/l) (in Table A) and temperature (°C). The MODIS Level 2 products are provided by the NASA OBPG (http://oceancolor.gsfc.nasa.gov/).

Table A.
Summary of measurement ranges (see locations in Fig.1).

Locations	TUR (NTU) min, max	TSM (mg/l) min, max	CHL (µg/l) min, max
P. Gannouch	1.88, 3.88	2.2, 5	0.5, 1
Jerba	0.5, 2.12	1.4, 2.8	<0.5, 1.6
Kneiss	0.2, 5.5	0.7, 6.1	<0.5, 4.7
Sfax-Kerkennah	1, 3.1	1.6, 3.9	<0.5, 1.3
L. Bougrara	-, 9.9	-, 30	-, 14

2.2 Methodology

TSM concentration and TUR maps were derived using respectively the algorithms [2] and [3], applied to MODIS remote sensing reflectance at band 667nm (Rrs^{667}). These bio optical algorithms perform well in the Belgian coastal waters, charaterised by high turbidity. Here, they are tested over the gulf of Gabès.

2.3 Results

In situ TSM and TUR show a strong correlation R^2=0.879, with the linear relationship: $TSM = 0.94\,TUR - 0.64$. Inverse proportionality between the Secchi depth and *in situ*

TUR or TSM was observed in all the sites. However, anomalies were found between the secchi values and TSM derived from MODIS at the region of Gannouche, where high turbidity is mainly due to industrial waste. The recent phosphogypsum waste makes an opaque film on the water's surface, causing such a strong turbidity that, after a certain time, it undergoes either decantation or dissolution [5]. This anomaly is also found at the regions of Kneiss, Skhira and Sfax due to the large tidal range in these shallow water areas, which causes an abrupt variation of the secchy: the largest depth is 6.2 m but lowest value is 1.5m with a visible sea bottom due to the sudden change in bathymetry from 7m to 1.5m. This can also distort the relationship between the *in situ* data and the MODIS satellite data which provides spatial resolution images of 1km. In the area surrounding the Kerkennah and Kneiss islands, there is a large benthic population mostly made up of posidonia and cymodocea [1]. Thus, the low bathymetry, water transparency and amount of benthic algae explain the high values of TSM as shown in the MODIS. TSM and TUR data satellite record high value for the particular regions of Sfax Kerkennah, Kneiss, jerba north and the lagoon of Bougrara. These locations with low water column, present more benthic algae and are subject to important change in water levels due to tides.

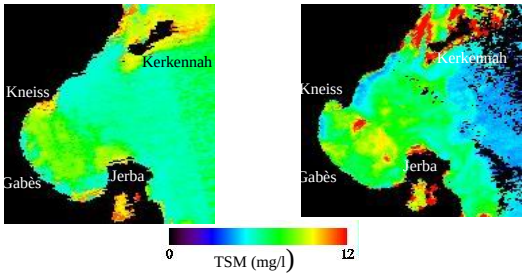

Figure.3 TSM(mg/l) distribution in the Gulf of Gabès, derived from MODIS image taken on October 8th 2009 on the right. MODIS image taken on July 5th 2009 on the left

Figure 4 shows huge differences between in situ and satellite derived TSM measurements. Unfortunately, most high turbidity data were masked out in MODIS products, so only clearer waters data could be used as matchups. For that reprocessing of L2 images is necessary, using an atmospheric correction more adapted to these highly turbid waters. After that, the semi empirical model may be adapted for each region in the gulf of Gabès, especially for the Kneiss, lagoon of Bougrara and Sfax-Kerkennah.

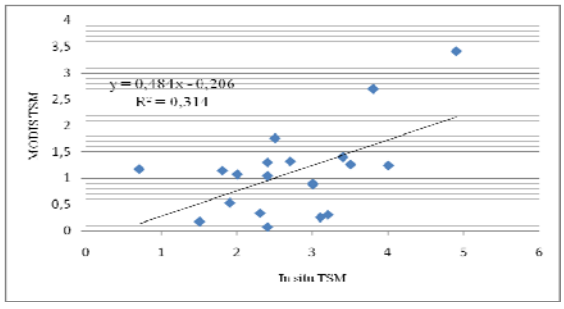

Figure 4. Scatter plot of MODIS-derived TSM(mg/l) versus *in situ* TSM(mg/l), with linear regression curve

The linear regression between *in situ* and satellite measurement shows a very low correlation $TSM^{MODIS} = 0.484\,TSM^{in\,situ} - 0.206$ with a very low regression coefficient $R^2 = 0.314$. The reflectance data extracted from MODIS imagery over the matchup stations shows very low reflectance values, sometimes even negative, for certain stations at 412µm and 443µm. This could be due to poor atmospheric correction in these clear waters, but also due to the non adaptability of this TSM algorithm for clear waters.

3. CONCLUSION

In order to map TSM distribution in the gulf of Gabès, a effort was made to tune a TSM algorithm for this region, MODIS derived TSM and in situ matchups taken in July and October 2009 were collected and compared. Unfortunately, these data do not cover the full range of TSM values (<5mg/l), especially the high values encountered near the coast. They showed little correlation with MODIS derived TSM. In order to estimate TSM concentrations in the turbid areas of the gulf of Gabès, a larger amount of *in situ* data from different locations and dates would be needed. This will allow the calibration of a locals TSM algorithms for mapping of TSM from MODIS imagery.

ACKNOWLEDGEMENTS

This study was funded by Unit of Structure and Modéle Geologic of Faculty of Sciences of Tunisia. The remote sensing team of MUMM are thanked for the help provided with the processing of MODIS imagery. I thank the GCT for their assistance on in situ measurement in the Gulf of Gabès. The NASA ocean color data distribution team at GSFC is acknowledged for the distribution of MODIS data.

REFERENCES

[1] Ben Mustafa K., Hattour, A., Mehetli, M., El abed, A. and Tritar, B. (1993)- State of the bionomics benthic infra and circalittoral to the Gulf of Gabes National Institute for the sciences and Technology of the sea Salammbô, Vol.26

[2] Nechad, B., de cauwer V., Park Y., ET Ruddick K. (2003)-Suspended Particulate Matter (SPM) mapping from MERIS imagery. Calibration of a regional algorithm for the Belgian coastal waters. MERIS user workshop, 10-13th November 2003. (Frascati). A SP-549.

[3] Nechad B., K.G. Ruddick and G. Neukermans, 2009.Calibration and validation of a generic multisensor algorithm for mapping of turbidity in coastal waters. Proceedings of SPIE "Remote Sensing of the Ocean, Sea Ice, and Large Water Regions" Conference held in Berlin (Germany), 31 August 2009. Proc. of SPIE Vol. 7473, 74730H. doi: 10.1117/12.830700

[4] Bjaoui B., Rais S., et Koutitonsky V. (2004), Modelisation of the phosphogypsum spreading in the gulf of GabesBull. National Institute for the sciences and Technology of the sea. Salambô.vol.31,2004

Modeling the transfer of light at the ocean surface: an approach based on high-resolution surface wave models

S. Kay [a,*], J. Hedley [b], S. Lavender [c], W.A.M. Nimmo-Smith [d]

[a] Marine Spatial Ecology Lab, University of Exeter, UK – sk284@exeter.ac.uk
[b] Marine Spatial Ecology Lab, University of Exeter, UK – J.D.Hedley@exeter.ac.uk
[c] ARGANS Ltd, Plymouth, UK – samantha.lavender@argans.co.uk
[d] Marine Institute, University of Plymouth, UK – alex.nimmo.smith@plymouth.ac.uk

Abstract – Marine remote sensing relies on optical models of the air-water interface, which are accurate for slope statistics but not elevation variance. These models preclude studies of processes such as wave shadowing and spatial reflectance patterns. Here Monte Carlo techniques are used for high resolution surface models incorporating slope & elevation features on scales from mm to tens of m. Sample surfaces were constructed using the unified Elfouhaily *et al.* (1997) spectrum and the Heron *et al.* (2006) spreading function. They validated well against a Cox and Munk slope statistics model, but displayed differences at non-orthogonal reflectance directions. The model framework is efficient enough to enable routine investigations into the spatial optics of the air-water interface.

Keywords: modeling, radiative transfer, wave spectrum.

1. INTRODUCTION

Optical and infrared marine remote sensing applications require a detailed understanding of the behavior of light at the air-water interface. Existing hydrological radiative transfer models incorporate air-water interface treatments based on the statistics of observed sea surface slopes established by Cox and Munk (1954). Due to high computational demand these models do not attempt to accurately describe the distribution of sea surface elevations, so phenomena such as multiple reflections between wave sides, the shadowing effect of large waves and spatial variation in reflectance cannot be captured. The aim of this work was to evaluate the feasibility of constructing and optically characterizing 3-dimensional representations of the sea surface that capture surface features and spatial variation over several orders of magnitude. An additional aim was to update current results by utilizing recently published wave spectra and directional spreading functions. An efficient Monte Carlo ray-tracing algorithm was used to evaluate bidirectional transmission and reflectance distribution functions (BRDFs) in a form suitable for incorporation into radiative transfer models used for remote sensing.

2. CREATING SEA SURFACE REALIZATIONS

2.1 Method

Sea surface realizations of 16384 × 16384 vertices were constructed from the 2-dimensional elevation variance spectrum, using the linear assumption that the elevation can be expressed as a harmonic series of wavenumber components (Thorsos 1988). Here the aim was to encompass as much as possible of the 10^{-2} to 10^{3} rad m^{-1} wavenumber range of the omnidirectional spectrum of Elfouhaily *et al.* (1997). The spreading function suggested by Elfouhaily *et al.* does not include the bimodal directional distribution observed in more recent work, so here a slightly modified version of the spreading function proposed by Heron *et al.* (2006) was used. Integration of the hybrid Elhouhaily-Heron spectrum shows that it gives a better fit to the crosswind to upwind ratio of Cox and Munk than using the original spreading function of Elfouhaily *et al.* (1997), except at very low wind speeds (Fig 1).

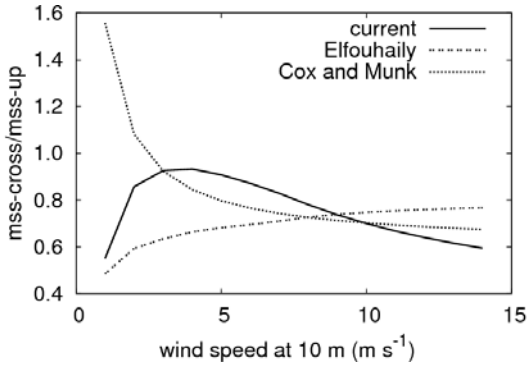

Fig 1. Ratio of mean square slopes in the crosswind and upwind directions as calculated using the Cox and Munk formulae, the spectrum used in the current work and the directional spectrum of Elfouhaily *et al.* (1997).

2.2 Evaluating surface realizations

Current memory limits still require a compromise to be made in the selection of a usable wavenumber range from the elevation variance spectrum. In the implementation developed here a grid of 16384 × 16384 vertices for the spectral and spatial domains was found to be the upper limit on an 8 GB machine. Using a high wavenumber range of 0 - 2000 rad m^{-1}, with discrete increment Δk = 0.13 rad m^{-1}, gives accurate mean square slope but underestimates the elevation variance (Fig 2, left panels, high-Δk). Conversely a lower wavenumber range of 0 - 400 rad m^{-1}, with Δk = 0.025 rad m^{-1}, captures elevation variance more accurately at the expense of mean square slope (Fig. 2, right panels, low-Δk). Using the high wave-number range, features as small as a few mm can be modeled (Fig. 3).

* Corresponding author. Marine Spatial Ecology Lab, Hatherly Laboratory, University of Exeter, Prince of Wales Road, Exeter EX4 4PS. Tel: +44 (0)1392 723757, Fax: +44 (0)1392 723700

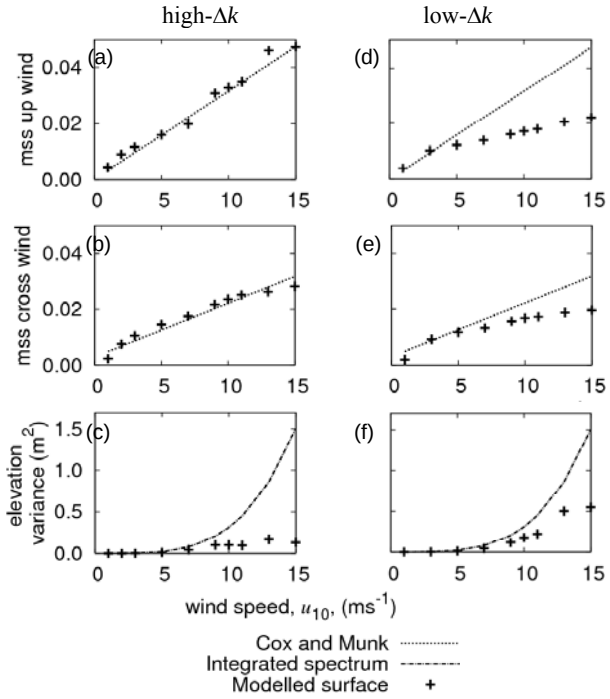

Figure 2. Upwind (a,d) and crosswind (b,e) mean square slope for a modeled surface compared to the Cox and Munk model. (c,f) Elevation variance of the modeled surface compared to the integrated spectrum. The left panels show the high-Δ*k* range and the right panels low-Δ*k*.

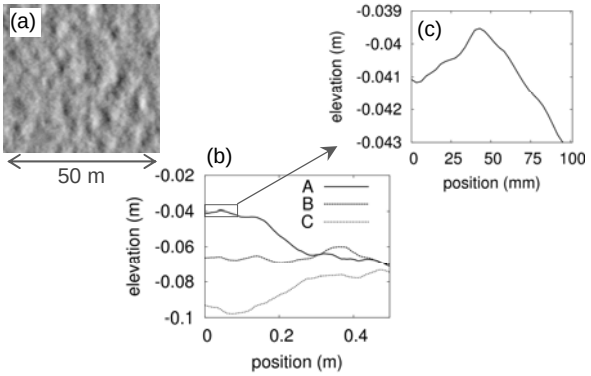

Figure 3. (a) Visualization of a sea surface created using the high-Δ*k* range, with a wind of 3 m s^{-1} from the left. Image width is 50 metres. Grey levels show elevation: white = +0.25 m, black = -0.25 m. (b) Elevation against position for three arbitrary 0.5 m lines on the surface. (c) The first 0.1 m of line A enlarged.

3. DIRECTIONAL REFLECTANCE FUNCTIONS

The Monte Carlo optical model was applied to surfaces constructed according to the two different schemes of Fig. 2, high-Δ*k* and low-Δ*k*, and a Cox and Munk slope-statistics surface (CM), constructed using the method of Mobley (1994). Model predictions show close agreement (Fig. 4), though the reflectance of the low-Δ*k* surface differs more from that of the CM surface: this is as expected since its mean square slopes are systematically lower (Fig. 2). The high-Δ*k* surface gave close agreement with CM in the solar plane, but showed increased forward reflectance at 45º to the solar plane (Fig. 4b). The Heron *et al.* (2006) spreading function improves on the Cox and Munk formulae by providing values at non orthogonal directions, and this difference in reflectance indicates the possibility of improving on existing sea surface optical models.

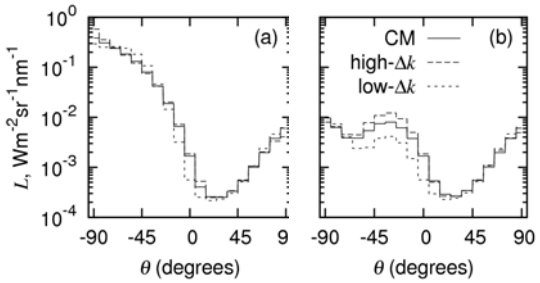

Figure 4. Modeled reflected radiance (a) in the solar plane and (b) at 45°, for clear sky conditions with a solar zenith angle of 45° and a wind speed of 10 ms^{-1}. CM: model based on Cox and Munk slope statistics; high-Δ*k* and low-Δ*k:* surfaces constructed from two wavenumber ranges (Fig. 2).

4. CONCLUSION AND FUTURE WORK

Processing time for surface construction and ray-tracing was about 3 hours, so high resolution modeling of sea surfaces is feasible on a standard workstation. Our results indicate that recent developments in spreading function models may have optical consequences of relevance, at least to off-nadir viewing sensors. Adaptive local subdivision of the surface grid may be one approach to achieve sea surface modeling across the full wavenumber range provided by published wave spectra. Future work will also incorporate polarization and assess spatial variation in the reflectance function. The model has the potential to improve radiative transfer modeling for ocean color imaging and other aquatic remote sensing applications, and could inform improved techniques for atmospheric correction and sun glint removal.

ACKNOWLEDGEMENTS

This work was supported by ARGANS Ltd and Great Western Research. J. Hedley is funded by the NERC.

REFERENCES

Cox, C, and W Munk (1954). "Measurement of the roughness of the sea surface from photographs of the suns glitter". Journal of the Optical Society of America, vol. 44, no. 11, pp. 838-850.

Elfouhaily, T., B. Chapron, K. Katsaros, and D. Vandemark (1997). "A unified directional spectrum for long and short wind-driven waves". Journal of Geophysical Research-Oceans, vol. 102, no. C7 pp. 15781-15796.

Heron, M.L., W.J. Skirving, and K.J. Michael (2006). "Short-wave ocean wave slope models for use in remote sensing data analysis". IEEE Transactions on Geoscience and Remote Sensing, vol. 44, no. 7, pp. 1962-1973.

Mobley, C.D. (1994). "Light and Water: Radiative Transfer in Natural Waters". San Diego, Calif.: Academic Press.

Thorsos, E.I. (1988). "The validity of the Kirchhoff approximation for rough-surface scattering using a Gaussian roughness spectrum". Journal of the Acoustical Society of America, vol. 83, no. 1, pp. 78-92.

Satellite imagery (2005-2007) and hydrological measurements of observed upwelling and distribution of transformed Amur river waters along the northern coast of Sakhalin Island

F.F. Khrapchenkov

V.I. Il'ichev Pacific OceanologicalInstitute FEB RAS, Vladivostok, Russia – fedi@poi.dvo.ru

Abstract – The features of the distribution of the transformed waters along the northern coast Sakhalin Island are analyzed on the basis of the remote measurements data from satellites of series NOAA and hydrological measurements in 2005-2007. The runoff lens and upwelling is well traced on IR-images from July to September. On the edge of the lens along the coast it is formed the runoff front with temperature of water 9.5 ^{o}C and salinity 28.5 psu, and under the lens it is formed sharp layer of discontinuity of salinity (up to 1 psu/m), temperatures (up to 2 ^{o}C /m).

Keywords: upwelling, transformed waters, Sakhalin.

1. INTRODUCTION

The continental shelf has a large extent in the north and north-west parts of Okhotsk Sea, but the oceanic circulation is not researched well with instrumental measurement and there is only schematic description based on water mass, ice and boat drift distribution analysis and only some short-term measurement. The current measurement with different current meters and drifters in 1996-2000 showed that East-Sakhalin current was south directed and had considerable seasonal variation (Mizuta, et al., 2001). However, summertime south winds domination leads to the almost complete absence of East-Sakhalin current from June till September (current velocity in the area of shelf boundary is about 5-10 cm/s). The upwelling effect is discovered in the north-east shelf area of Sakhalin Island with instrumental measurement and satellite imaging data in the 90-s of last century (Krasavtsev, et. al., 2000).

2. THE RUNOFF LENS OF THE AMUR RIVER

Numerous occurrences of upwelling along the coast in July-September 2005-2007 were discovered by satellite imaging analysis (NOAA-12-18, Satellite Imaging Center IACP FEB RAS). Upwelling became apparent 5-6 and 19-21 of August in 2005. The cold water field was to the south of Piltun bay during the first period and to the north of Piltun bay reaching the north end of Sakhalin Island (fig. 2) during the second period. Hydrological measurement data during that period shows that the width of cold water field with temperature less than 6º C on the surface variated from 5 to 10miles (Fig.2). There were periodic appearances of upwelling effect in the north-east shelf area of the Sakhalin Island in 2006: 16-17 of July, at the end of July and early August, 19-23 of August and the first half of September. Hydrological measurement data during that period shows that the sea surface temperature was lower than during short-term upwelling in August 2005 (Fig. 3). In 2007 satellite imaging data shows appearance of upwelling effect at the middle of July, early August, 16-17 of August, 23 of August and early September.

Figure 1. Sakhalin Island and Area of Observing.

Appearances of upwelling effect were also registered to the north of Levenshtern cape reaching Severniy bay: 19 of August 2005, 26 of July and 7 of September 2006, 16-17 and 23 of August 2007. There was also upwelling effect appeared in the Sakhalinskiy Bay on 23 of August 2007 after several days of storm weather and north-east winds. According to the hydrological measurement the sea surface temperature decrease to 0º C in the area of Severniy Bay and 2º C behind the leeward coast in the east part of Sakhalinskiy Bay. So the data shows appearance of upwelling effect in summer in the area around the north end of Sakhalin Island when dominating wind direction is from south-east to north-east. This phenomena is appeared in the north-east shelf area with south wind dominating. Though the upwelling effect appearing and warm water setting-down from the coast to the sea does not depend on the tide phase. The dimensions of upwelling effect area are variated from several tens to 120 miles along the coast and 5-30 miles away from the coast. The position of the runoff lens of the Amur River and its area essentially changes depending on the features of atmospheric circulation and intensity of the tidal phenomena in this region. On the borders of the lens of freshening waters significant gradients of temperature and salinity and quick change of water color from brownish to deep-blue are observed. Freshening of the surface layer in the lens is traced up to depth of 20 m, thus the most fresh water borrows a surface layer about 5 m thick. The runoff lens is well traced on IR-images from July to September. There is specific broad sand bar in this part of the shelf and reverse tidal currents are dominating on it along the coast (current velocity exceed 1m/s, estimated as the boat drift during calm and measured in July-September 2007). Contrasts of color and temperature on the borders of Amur stock lenses make it easy to identify its spatial dimensions and help in the research patterns of their distribution.

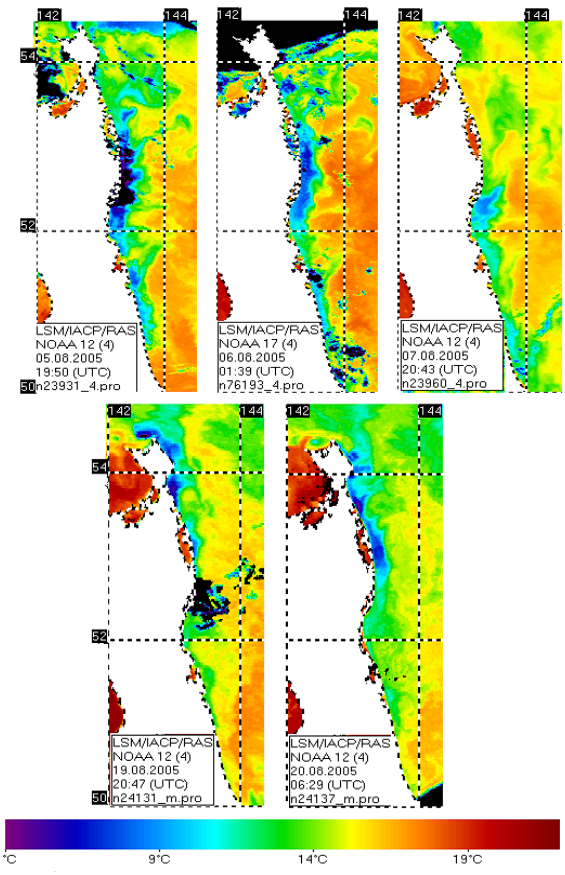

Figure 2. Sea surface temperature distribution, satellite imaging data, August 2005.

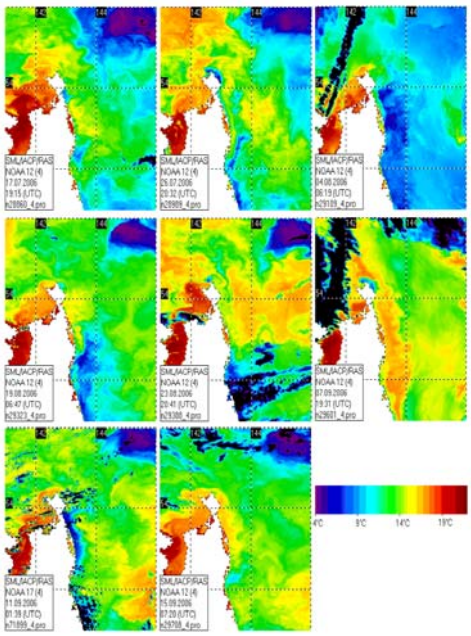

Figure 3.The surface temperature of water off the coast of Sakhalin in 2006.

The satellite images 2006 and 2007 (Fig. 3) in light tones can be seen that at the exit of the main channel stream flow first moves in a northwesterly direction and then deflected to the right to form anticyclonic meander in the eastern part of Sakhalin Bay. The jet is coming to the coast of the peninsula Schmidt (northern part of Sakhalin Island), and then forks (mushroom structure in the photo). Some water remains in the range of stock lenses, and another part goes towards the northern tip of Sakhalin Island. The runoff lens is clearly seen in the IR - images in summer (Fig. 3). The pictures show that the inner heated region surrounding the lens of water with lower temperature, modified at the boundary of the lens due to the vertical and horizontal mixing with surrounding waters. Along the coast on the edge of the lens is formed runoff front separating the water with a temperature of 14 to 9.5^{0}C and salinity from 26 to 28.5 psu. Under the lens there is a sharp jump in the layer salinity (up to 1 psu / m), temperature (up to 2^{0}C / m) and density (Fig.4). The Amur transformed waters extend along east coast down to gulf of Nabeel to the middle of September where there are at this time fronts of temperature and salinity.

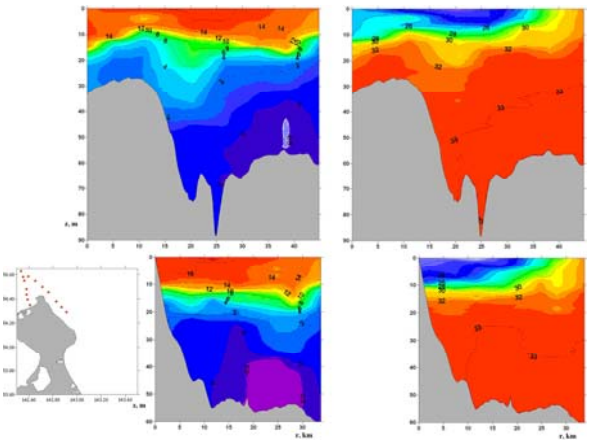

Figure 4. Distribution of temperature and salinity in a Gulf of Northern, august 21, 2007.

3. CONCLUSION

Thus, in the summer in the coastal area from the Gulf of Chayvo to the Gulf of Odoptu place short-term (within hours) changes in temperature and salinity of surface water associated with the action of tidal currents, and long-term (several days), the evolving phenomena of upwelling. These changes lead to the fact that in the coastal region that alternately come Amur, the Okhotsk Sea near-bottom water rich in nutrients. Such a regime creates favorable conditions for the development of the benthos.

REFERENCES

Krasavtsev V.B., Puzankov K.L., Shevchenko G.V. (2000). Wind-induced upwelling in the area of the northeastern Sakhalin shelf. FERHRI Special Issue no. 3, Vladivostok: Dalnauka, p. 106-120.

Mizuta, G., Y. Fukamachi, K.I., Ohshima and M. Wakatsuchi (2001). Southward current off the east coast of Sakhalin in the Sea of Okhotsk observed from 1998 to 2000. The 16th International Symposium on Okhotsk Sea and Sea Ice, p. 198-205.

Rutenko A.N., Sosnin V.A., Khrapchenkov F.F. (2009). Coastal upwelling on the Shelf of Sakhalin. Meteorology and Hidrology, no. 2, p. 44-53.

Suspended Particulate Matter Concentration and Composition in the Surface Layers of the Atlantic Ocean derived from Data of Ocean Color Scanner MODIS

A.A. Klyuvitkin*, V.I. Burenkov, S.V. Sheberstov

P.P.Shirshov Institute of Oceanology of the Russian Academy of Sciences, Moscow, Russia – klyuvitkin@ocean.ru

Abstract – New data about suspended particulate matter (SPM) and its biogenic component (BM) spatial distribution in the surface layer of the Atlantic Ocean are presented. The study is based on data of ocean scanner MODIS-Aqua recalculated using field data collected during eight transoceanic cruises in the Atlantic Ocean.

Keywords: suspended matter, Atlantic Ocean.

1. INTRODUCTION

The distribution and redistribution of marine SPM are of great importance in interpreting the biological, chemical and geological processes acting in the deep sea. Particulate matter from the productive surface layer descends through the water column slowly by individual particle settling and rapidly by fecal pellet or marine snow transport, providing organic-rich food to the benthic communities. Ultimately, the material in flux to the seafloor may become part of the sedimentary record (Listzin, 1996; Richardson, 1987).

Presently, a primary source of particulate matter to the deep ocean is the surface waters. Rivers and, in arid regions, atmospheric input, and, in cold climates, glaciers, deliver high suspended loads of terrigenous material. Primary production of organic matter is the main internal source of oceanic SPM. Phytoplankton and zooplankton detritus and pellets sink, comprising a large fraction of the material in transit through the water column.

In turn the SPM concentration and composition can be determined from data of ocean color scanners. This leads to possibility of global monitoring of SPM distributions from satellites. The simplified algorithm for determination of the particle backscattering coefficient b_{bp} from satellite data was developed in (Burenkov *et al*., 2001). It was used for construction of satellite imageries of SPM in the Barents Sea. For some other regions (White Sea, Black Sea, Caspian Sea) appropriate algorithm were obtained in (Kopelevich *et al*., 2007). The first attempt to calculate this algorithm for the Atlantic Ocean was made in (Burenkov *et al*., 2007). New data on remote (satellite) SPM studies in the Atlantic Ocean are presented below.

2. METHODS

2.1 Field studies

During 2001–2005 eight transatlantic cruises aboard RV *Akademik Fedorov*, RV *Akademik Ioffe*, RV *Akademik Mstislav Keldysh* and RV *Akademik Sergey Vavilov* were carried out. Surface water samples for SPM determination were collected mainly during the ship movement several times in a day. Sea water was filtered with an in-line vacuum filtration system through a preweighed 47 mm diameter nuclepore filter with 0.4 μm pores and glass microfibre filter Whatman GF/F. Sample collecting were carried out from North to South Atlantic in different climatic zones including coastal regions. Main components of SPM composition were obtained in our coastal laboratories: terrigenous lithogenic matter=10*Al (Kuss and Kremling, 1999), POM=2*POC (Krishnaswami and Sarin, 1976), $CaCO_3$ and Opal, as biogenic SiO_2. This data permit us to divide SPM on two main parts – lithogenic and biogenic (POM+$CaCO_3$+Opal). Values of "calculated" SPM concentration (the sum of lithogenic and biogenic SPM) closely replicate original SPM concentrations.

2.2 Satellite data

For each water sample point data of ocean scanner MODIS-Aqua were received from NASA/Goddard Space Flight Center (http://oceancolor.gsfc.nasa.gov/) and they were used to derive particle backscattering coefficient b_{bp} by algorithm described in (Burenkov *et al*., 2001, 2007). Data on chlorophyll distribution were obtained too.

3. RESULTS AND DISCUSSION

Following relationships connecting b_{bp} and SPM (1) and also between chlorophyll and biogenic SPM (2) were received (fig. 1 and 2 show these relationships):

$$SPM = 95 * b_{bp}^{0.99} \quad (1)$$

$$BM = 197.1 * \ln(Chl) + 644.8 \quad (2)$$

where BM = biogenic SPM concentration
Chl = chlorophyll concentration

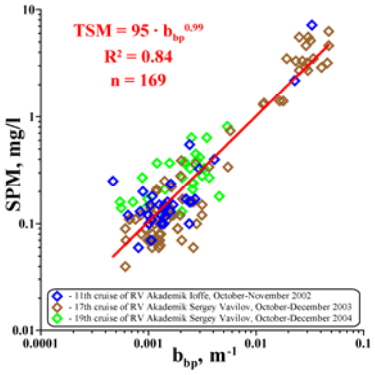

Figure 1. Correlation between SPM (determined from the water samples) and b_{bp} (derived from MODIS-Aqua data).

* Corresponding author. 36, Nahimovski prospect, Moscow, Russia, 117997; tel/fax: +7 (499) 1247737.

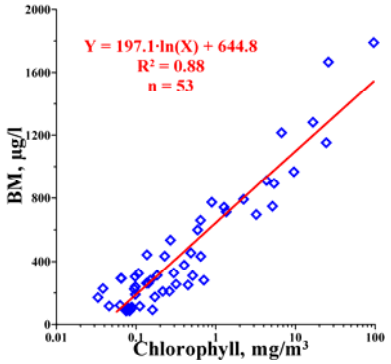

Figure 2. Correlation between BM (determined from the water samples) and chlorophyll (MODIS-Aqua data).

These relationships were used for estimation of SPM and BM concentration in the Atlantic Ocean. The examples of their spatial distribution in the surface layers of the Atlantic Ocean obtained from satellite data are given in Fig. 3.

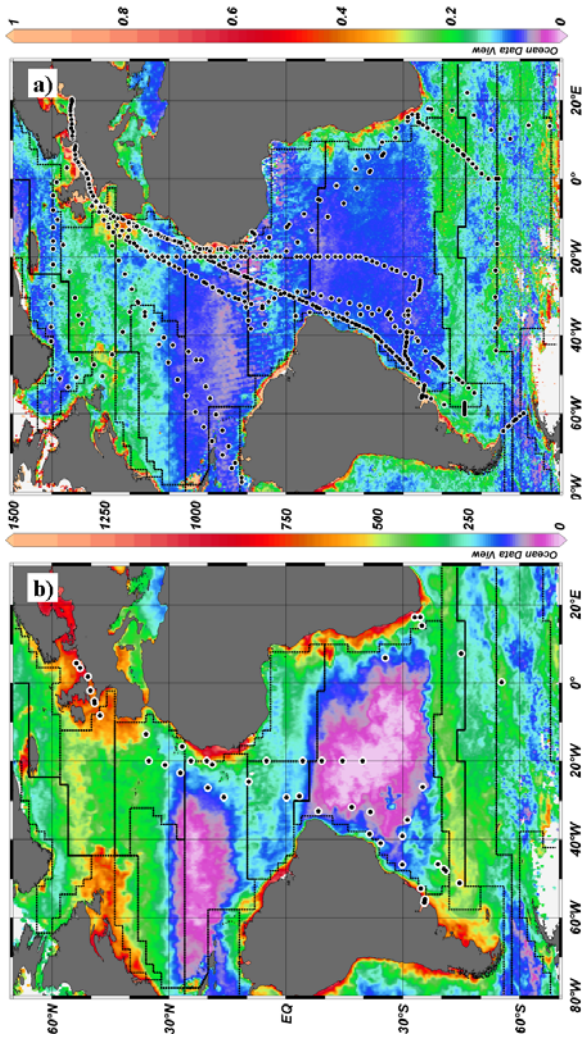

Figure 3. Spatial distribution of (a) SPM, mg/l, and (b) BM, µg/l, in the Atlantic Ocean recalculated from data of ocean color scanner MODIS-Aqua using field data. Monthly climatology for October 2002–2005. Dots are points of samples used for calculation.

First of all, two main types of natural zonality are well seen: both latitudinal climatic and circumcontinental. In whole the highest concentrations for all over the ocean are observed in coastal provinces. The most significant are the zones of the marginal filters in the river mouths. The second productive group of coastal provinces includes upwellings – Canary (North-West African) and Benguala. In open ocean the belts of both SPM and BM maximum coincide with Eutrophic and Mesotrophic waters of the Northern and Southern humid temperate zones and also humid Equatorial zone. Close similarity of SPM and BM distribution suggest us about prevailing role of biogenic material in pelagic SPM formation. This correlation is broken only in Saharan dust affected zone and in coastal provinces of the Atlantic Ocean.

ACKNOWLEDGEMENTS

MODIS-Aqua data used in this study were produced by the SeaWiFS Project at Goddard Space Flight Center and obtained from the Goddard Distributed Active Archive Center. This work was financially supported by the program of the Earth Sciences Department of the Russian Academy of Science “Nanoparticles in the Earth spheres…”, the grant of support of Leading Scientific Schools NSh-3714.2010.5. and the grant of support of Young Scientists MK-734.2010.5.

REFERENCES

Burenkov, V.I., S.V. Ershova, O.V. Kopelevich, S.V. Sheberstov and V.P. Shevchenko (2001). “Estimation of spatial distribution of suspended matter in the Barents Sea derived from data of ocean color scanner SeaWiFS”. Oceanology. vol. 41, no. 5, pp. 622-628.

Burenkov, V.I., A.A. Klyuvitkin and S.V. Sheberstov (2007). “Suspended matter concentration in surface layers of the Atlantic Ocean derived from data of ocean color scanner MODIS”. Proc. IV Iternational Conference “Current problems in optics of natural waters” (Nizhny Novgorod, Russia, September 2007), pp. 154-156.

Kopelevich, O.V., V.I. Burenkov, S.V. Sheberstov, O.V Prokhorenko and S.V. Vazyulya (2007). “Continuation of the long-term series of data in the bio-optical characteristics of the Russian Seas from satellite ocean color data”. Proc. IV Iternational Conference “Current problems in optics of natural waters” (Nizhny Novgorod, Russia, September 2007), pp. 75-78.

Krishnaswami, S. and M.M. Sarin (1976). “Atlantic surface particulates: composition, settling rates and dissolution in the deep sea”. Earth and Planetary Science Letters, vol. 32, pp. 430-440.

Kuss, J. and K. Kremling (1999). “Spatial variability of particle assotiated trace elements in near-surface waters of the North Atlantic (30°N/60°W to 60°N/2°W), derived by large volume sampling”. Marine Chemistry, vol. 68, pp. 71-86.

Lisitzin, A.P. (1996). “Oceanic sedimentation: Lithology and geochemistry”. Wash. (D.C.): Amer. Geophys. Union, 400 p.

Richardson, M.J. (1987). “Particle size, light scattering and composition of suspended particulate matter in the North Atlantic”. Deep-Sea Research, vol. 34, no. 8, pp. 1301-1329.

SeaWiFS Project, NASA/Goddard Space Flight Center and ORBIMAGE. http://oceancolor.gsfc.nasa.gov.

The GOCE User Toolbox – GUT
An ESA effort to facilitate the use of GOCE Level-2 products

P. Knudsen [a], J. Benveniste [b]

[a] DTU Space, Juliane Maries Vej 30, DK2100 Copenhagen, Denmark – pk@space.dtu.dk
[b] ESA/ESRIN, Earth Observation Science and Applications Department, Frascati, Italy

Abstract. The GOCE User Toolbox (GUT) is a compilation of tools for the utilisation and analysis of GOCE Level 2 products. GUT supports applications in Geodesy, Oceanography and Solid Earth Physics. The GUT Tutorial provides information and guidance on how to use the toolbox for a variety of applications. GUT consists of a series of advanced routines that carry out the required computations. It may be used on Windows PCs, UNIX/Linux Workstations, and Mac. The toolbox is supported by The GUT Algorithm Description and User Guide and The GUT Install Guide. A set of a-priori data and models are made available as well.

Keywords: GOCE gravity, altimetry, ocean circulation.

1. BACKGROUND

The Gravity and Ocean Circulation Experiment - GOCE satellite mission is a new type of Earth observation satellite that will measure the Earth gravity and geoid with unprecedented accuracy. Combining GOCE geoid models with satellite altimetric observations of the sea surface height substantial improvements in the modelling of the ocean circulation and transport are foreseen. No ocean circulation products are planned to be delivered as level-2 products as part of the GOCE project so that a strong need exists, for oceanographers, to further process the GOCE level-2 geoid and merge it with Radar Altimetry. The primary requirement of oceanographers is to have access to a geoid and its error covariance at the highest spatial resolution and accuracy possible, although required resolution depends on application. For effective use of the geoid data, knowledge of the error covariance is mandatory.

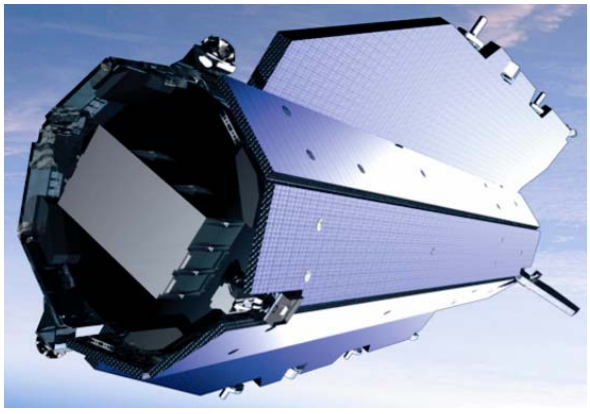

Figure 1. The GOCE satellite.

Within the ESA supported GUT Specifications project, the user requirements for GUT associated with geodetic, oceanographic and solid earth applications were consolidated.

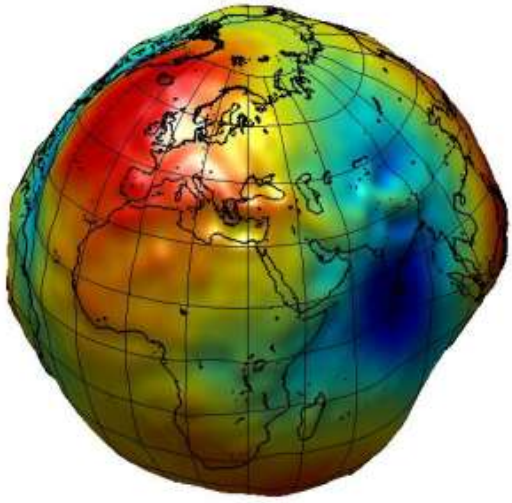

Figure 2. GOCE aims at improving geodetic applications such as computation of the gravity field and the geoid.

For all applications the absolute minimal requirement of the toolbox includes the computation of geoid heights from the set of spherical harmonic coefficients at a given user-specified harmonic degree and order. For oceanographic applications the key quantity to be computed is the mean dynamic topography which basically is the height of the mean sea surface relative to the geoid. For this application GUT provide the tools for converting the mean sea surface and the geoid into the same geodetic system and for carrying out the needed filtering to compensate for the different resolution capabilities of the two surfaces. Furthermore, a-priori mean dynamic topography models derived from e.g. ocean circulation models, may be used.

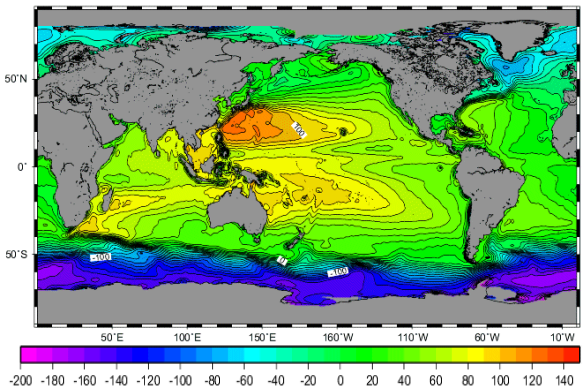

Figure 3. For oceanographic applications of GOCE its main goal is to enhance the mean dynamic topography (prepared by M-H Rio, CLS).

2. THE GOCE USER TOOLBOX

The GOCE User Toolbox GUT is a compilation of tools for the utilization and analysis of GOCE Level 2 products. GUT support applications in Geodesy, Oceanography and Solid Earth Physics. The GUT Tutorial provides information and guidance in how to use the toolbox for a variety of applications. GUT consists of a series of advanced computer routines that carry out the required computations. It may be used on Windows PCs, UNIX/Linux Workstations, and Mac. The toolbox is supported by The GUT Algorithm Description and User Guide and The GUT Install Guide. A set of a-priori data and models are made available as well.

Hence, the GUT package includes

- The source package for building on UNIX/Linux/Mac
- Binary packages for Linux and Windows that include BratDisplay (v2.0.0b)
- The GUT Algorithm Description and User Guide (v1.2)
- The GUT Tutorial (Beta version)
- The GUT Install Guide (applicable to ALL packages).

The a-priori data package gut-apriori.zip is available as well.

GUT use GOCE data associated with the following GOCE-L2 products:

- EGM_GCF_2: Spherical harmonic series in ICGEM format
- EGM_GEO_2: Grid with geoid heights in Grid format
- EGM_GAN_2: Grid with gravity anomalies in Grid format
- EGM_GVE_2: Grid with east-west vertical deflections in Grid format
- EGM_GVN_2: Grid with north-south vertical deflections in Grid format
- EGM_GVC_2: Variance-covariance matrix file of the spherical harmonics coefficients

These products will be stored in XML format, except for the Variance-Covariance Matrix (Internal HPF VCM format).

In addition GUT uses auxiliary data such as MSS and errors, MDT, DEM in NetCDF format (COARDS/CF standard).

GUT is a command line processor. Its output may be exported and visualised using the ESA Basic Radar Altimetry Toolbox BRAT (http://earth.esa.int/brat).

Applications of the Variance-covariance Matrix require additional software not included in GUT. The software has been developed by Georges Balmino and made available to the community. Those applications require heavy computational resources. In the current version of GUT documentation and tutorial they are not supported.

3. FUTURE WORK

The GUT will be further developed through a collaborative effort where the scientific communities participate. Originally, the idea about the scope of a GOCE toolbox exists came from the scientific users, especially from experience gained through GRACE data processing. Any new effort should build directly on this insight and should expand on user needs in a flexible way. The EU supported GOCINA and GOCINO projects are another source of valuable information about needs and solutions that will be consulted while developing GOCE user needs and toolbox functionalities.

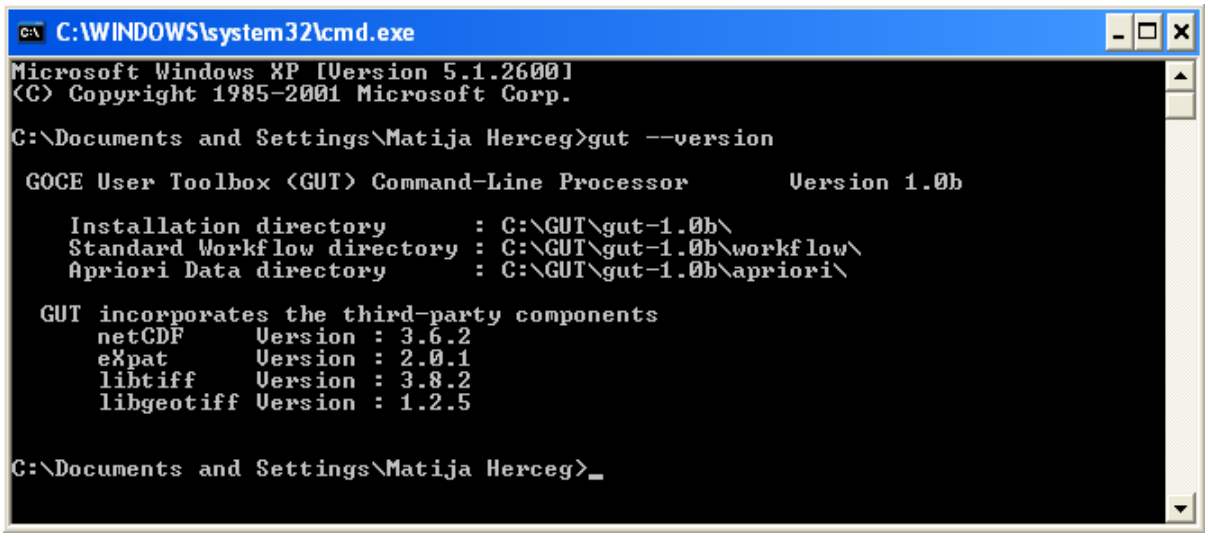

Figure 4. GUT is a command line processor.

A Spaceborne View at Archeological Sites on Intertidal Flats on the German North Sea Coast

J. Kohlus [a], M. Gade [b]

[a] Office for Coastal Protection, National Park and Marine Protection Tönning, Germany – joern.kohlus@lkln.landsh.de
[b] Universität Hamburg, Institut für Meereskunde, Germany – martin.gade@zmaw.de

Abstract – More than 375 years ago, a big storm surge in the German Bight of the North Sea destroyed farmland, farms, and villages, and killed a great number of both cattle and men. The big (second) "Mandränke" of 1634 is still one of the most famous storm surges in the area of the North Frisian Wadden Sea. We present first results of our analyses of spaceborne SAR data, which show imprints of former settlements in the area, which was destroyed by the "Mandränke". For the first time, data from the high-resolution TerraSAR-X are used to demonstrate that residuals of former agricultural areas can still be detected from space. The data are complemented by aerial photographs and in-situ data.

Keywords: SAR, Wadden Sea, fossil landscapes, storm surges, TerraSAR-X.

1. INTRODUCTION

In the Middle Ages, farmsteads and villages were built along the German North Sea coast, surrounded by farmland and also floodplain forests. The houses were mostly built on dwelling mounds, protected by small dikes, and ditches were built to take out the water of the farmlands. In the mid 14th century, a period of bad harvests due to cold summers, corresponding hunger, and the Black Death in 1350, the population in that area was reduced by about 75%. As a result, the small dykes had been in a bad condition. On January 16, 1362, after more than 24 hours of severe storm, the small dykes broke and a great number of both cattle and men died. During that storm surge, large land areas used as farmland were lost to the sea, and they haven't been diked ever since. After this biggest catastrophe of the late Middle Ages in northern Europe it took a long time until new dikes were built to protect the marsh land. The new farmland was structured by a wide-meshed system of ditches. Dykes enclosed larger polders than in the centuries before, and farmhouses on terps were connected by narrow lanes. Still there was ongoing land destruction by the extraction of salt; however, the marsh land had also become an important region for farming.

Another major storm surge occurred on October 11, 1634, again destroying farmland, farms, and whole villages, and killing cattle and men. The big (second) "Manndränke" is still the most known storm surge in history in the area of the North Frisian Wadden Sea. Major parts of the populated area were destroyed and the swampy land changed its face and became the Wadden Sea as it is known in modern times. Over the years, great parts of this former agricultural area have been buried by muddy and sandy sediments, which nowadays form the German Wadden Sea, and which fall dry once during each tidal cycle. Under the permanent action of the tidal forces, morphodynamics take place, the muddy and sandy marine sediments are partly driven away, and traces of former peat digging, farmland, and settlements appear again on the bottom of the Wadden Sea. These sedimental structures show distinct biological effects and are often marked by benthic organisms. Since those areas are difficult to reach and, thus, to observe from the ground, spaceborne sensors have proven to be advantageous for a systematic observation of the residuals of those historical places.

2. RESULTS

When today erosion moves away the muddy and sandy marine sediments on intertidal flats, banks of peat, old clay, and structures of farmland and settlements appear again on the dry-fallen surface. Fig. 1 shows an aerial photograph taken in July 2009 from dry-fallen intertidal flats north-east of the German island of Pellworm. Clearly visible are linear structures that witness the historical land use, before the great "Mandränke". Also visible is the sandy sediment, by which those structures were buried, and which was driven apart by the action of currents and waves.

Figure 1. Aerial photograph taken on July 29, 2009, at low tide and showing residuals of former settlements in the German Wadden Sea, close to a tidal creek (upper left). Image courtesy of Kai Eskildsen, LKN.

Fig. 2 shows a reconstruction of a historical lane, with ditches on either side, which can be found on the intertidal flats north of Pellworm and which caused structures like those shown in Fig. 1. Fossil farmland structures, mostly ditches, but also lanes or dykes, cannot be observed through their relief of less than 10 cm. Rather it is the sediments on the lost pastures that are different from those in the linear structures of ditches. Typical wadden sediments on the flat sand banks consist of marine fine sand, which had been the basic compound of the old marsh land and which is still a major part of the marine environment. The surface of the fossil ditches is different. In the center there are pillowy sediments while the ditch edges are often stabilized by fossil

roots and other plant material connected with the sediment. This causes narrow ridges with thicknesses of only 10 cm to 20 cm, which can still be observed.

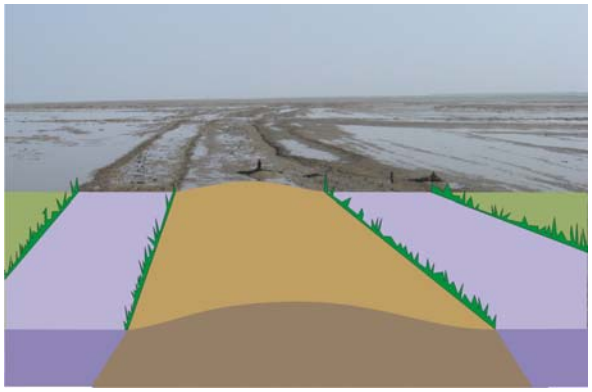

Figure 2. Reconstruction of a medieval lane (Kohlus 2008) crossed by a ditch in the background.

Such linear structures have been observed during field campaigns north off Pellworm. Fig. 3 shows an aerial photograph of the island's north coast, with the locations of residuals of historical land use superimposed.

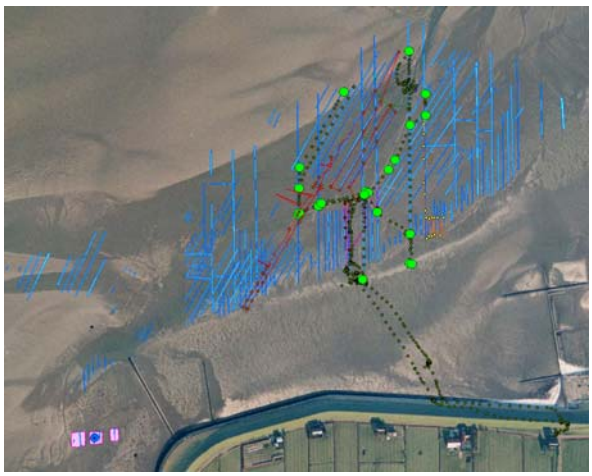

Figure 3. Aerial photograph of dry-fallen intertidal flats north off Pellworm. Superimposed are locations of ditches and lanes (green and brown) and of fossil terps and field structures provided by the State Archeological Department of Schleswig-Holstein (purple and blue).

The high-resolution X-Band synthetic aperture radar (SAR) aboard the German TerraSAR-X allows for mapping the Wadden Sea surface from space, and SAR images with a pixel spacing of less than 1 m can be used to detect small-scale surface structures if they are linked with a variation of the surface roughness of the Wadden Sea sediments. As an example, Fig. 4 shows a small (1900 m × 2000 m) section of a TerraSAR-X image acquired on August 3, 2009, over the same area as shown in Fig. 3. The residuals of the historical structures can clearly be delineated as linear bright and dark signatures. For the first time, thus, residuals of historical land use in the North Frisian Wadden Sea are detected by a spaceborne SAR sensor. Moreover, a direct comparison of the SAR image and the available data from aerial survey and field campaigns (Fig. 4 and Fig. 3, respectively) demonstrates that formerly unknown structures have been identified by TerraSAR-X (cf. the upper image center in both figures).

Results from our field campaigns prove that it is the former system of ditches that causes the distinct signatures on the SAR imagery. The change in surface roughness, together with the high-resolution capability of TerraSAR-X

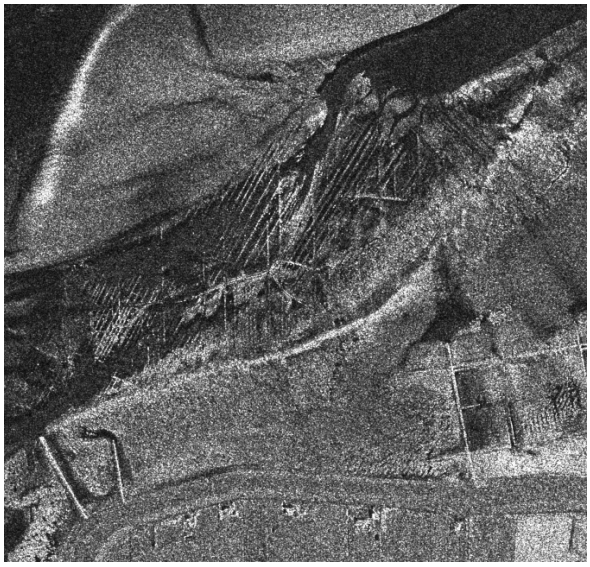

Figure 4. Section (1900 m × 2000 m) of a TerraSAR-X image of dry-fallen intertidal flats north off Pellworm. Residuals of historical land use can be delineated through linear bright and dark structures. © DLR 2009.

3. CONCLUSIONS

High-resolution TerraSAR-X images can be used to complement archeological surveys on intertidal flats on the German North Sea coast. The radar images the former systems of ditches, dating back to the 14th century and to the 16th/17th century. The observed signatures are due to different sediment types, which in turn are due to the very ditch morphology. Moreover, different sediments cause different biological effects and are also often marked by benthic organisms. Thus, the ditch structures containing more biogenic material may be a preferred habitat of certain mussels while sand worms (*Arenicola marina*) are usually found on sandy sediments. Those benthic organisms may cause different surface roughness patterns that can be sensed by the high-resolution X-Band SAR.

ACKNOWLEDGEMENTS

The authors are grateful to Kai Eskildsen for providing the aerial photograph and to Katharina Prenzel for processing the TerraSAR-X image. This work was partly funded by the German Ministry of Economy (BMWi) under contract 50 EE 0817 (DeMarine-U).

REFERENCES

Bantelmann, A., Kuschert, R., Panten, A. and T. Steensen (1995): "Geschichte Nordfrieslands", Boyens, Heid, 472p..

Indian Ocean tropical cyclone investigations using satellite remote sensing

Y. Kuleshov [a, *], K. Zhang [b], Y-A. Liou [c], A. G. Pavelyev [d], F. Chane-Ming [e], F. Roux [f]

[a] National Climate Centre, Bureau of Meteorology, Melbourne, Australia – y.kuleshov@bom.gov.au
[b] School of Mathematical and Geospatial Sciences, RMIT University, Melbourne, Australia – k.zhang@rmit.edu.au
[c] Center for Space and Remote Sensing Research (CSRSR), National Central University, Taiwan – yueian@csrsr.ncu.edu.tw
[d] Institute of Radio Engineering and Electronics of Russian Academy of Sciences, Russia – pvlv@ms.ire.rssi.ru
[e] Laboratoire de l'Atmosphére et des Cyclones, UMR CNRS-Météo-France-Université de la Réunion, France – fchane@univ-reunion.fr
[f] Laboratoire d'Aérologie, Université Paul Sabatier, CNRS, UMR 5560, Toulouse, France – frank.roux@aero.obs-mip.fr

Abstract – Tropical cyclones, the most destructive climatological hazards, are temperature-sensitive weather phenomena and a possible increase in their activity as the response to a warmer climate is debated. An international experiment on investigating the characteristics of the Indian Ocean tropical cyclones – SWICE (South-West Indian ocean tropical Cyclone Experiment) - is tentatively planned for January and February 2011. It is expected that satellite remote sensing and conventional observations will provide an unprecedented data set of atmospheric and oceanic characteristics – a scientific task of high importance for the tropical cyclone research over the Indian Ocean basin where only a few *in situ* measurements exist. Detailed plans for the investigation of the Indian Ocean tropical cyclone characteristics during SWICE using satellite remote sensing techniques are presented and potential outcomes are outlined.

Keywords: tropical cyclones, Indian Ocean.

1. INTRODUCTION

Tropical cyclones are the most dangerous and damaging climatic hazards which regularly affect countries in the Indian, North Atlantic and Pacific Oceans. Intensity of tropical cyclones and severity of their impact may increase as a result of global warming. However, reliable predictions of tropical cyclone changes are difficult since they are highly variable and climatic mechanisms of this variability are not well understood. It is therefore important to improve the understanding of tropical cyclones and possible changes of their activity and intensity due to global warming. Research on the effects of climate change on tropical cyclone activity in the Atlantic and the Pacific Oceans has attracted considerable attention of the scientific community in the past few decades. However, climatic mechanisms responsible for tropical cyclone variability are still not well understood. Our research is focused on the investigation of tropical cyclones in the Indian Ocean which remains the least studied oceanic basin among all other oceans.

2. TROPICAL CYCLONE VARIABILITY

There is significant inter-annual and inter-decadal variability in tropical cyclone activity due to natural climate variability related to large-scale climatic driving forces such as for example El Niño-Southern Oscillation (ENSO) phenomenon. In addition, with climate changing rapidly on a global scale, it is important to understand the causes of changes in regional tropical cyclone frequencies, intensities and tracks. One of the major large-scale environmental contributors governing tropical cyclone genesis and development is ocean thermal energy. It is well documented that the sea surface temperatures (SSTs) over the major tropical cyclone basins have increased over recent decades (Knutson *et al*., 2006; IPCC, 2007). Physical mechanisms of cyclone formation and development suggest strong relationship between tropical cyclone activity and SSTs (Gray, 1968). Theoretical and modelling studies indicate that in response to increasing SSTs there should be a concomitant increase in the cyclone intensity (Emanuel, 1987; Holland, 1997). However, factors other than SSTs also play an important role in regulating cyclone characteristics, including vertical wind shear and mid-tropospheric moisture (Gray, 1979; Nolan and Rappin, 2008). Examining the number of tropical cyclones and cyclone days over the past 35 years, in an environment of increasing SSTs, a large increase in the number and proportion of tropical cyclones reaching categories 4 and 5 in the North Pacific, South-West Pacific and Indian Oceans was reported (Webster *et. al.,* 2005). However, positive trends in the numbers of the most intense cyclones in the South Indian Ocean appear to be influenced to some extent by changes in data quality (Kuleshov *et. al.,* 2010).

Attempts have been made to find explanations for tropical cyclone variability through analysis of the relationship between cyclone activity in the Indian and the Pacific Oceans and the ENSO (Kuleshov *et al.,* 2009). However, apart from the ENSO, other broad scale climate patterns such as the Indian Ocean Dipole, the Pacific Decadal Oscillations and others need to be studied in detail to fully understand tropical cyclone variability. To improve understanding of atmospheric and oceanic conditions favourable for tropical cyclone genesis and development, an international experiment on investigating the Indian Ocean tropical cyclone characteristics – SWICE (**S**outh-**W**est **I**ndian ocean tropical **C**yclone **E**xperiment) - is tentatively planned for January and February 2011. It is expected that satellite remote sensing and airborne (*in situ* and dropsonde) observations will provide an unprecedented data set of atmospheric and oceanic characteristics – a scientific task of importance for tropical cyclone research over the Indian Ocean basin where only a few *in situ* measurements exist.

* Corresponding author: GPO Box 1289, Melbourne, Victoria, Australia. Tel: +61 3 9669 4896. Fax: +61 3 9669 4760.

3. SATELLITE REMOTE SENSING FOR TROPICAL CYCLONE RESEARCH

To overcome deficiencies in the observing networks over the oceans, satellite remote sensing has been used extensively over decades. Observations from polar orbiting and geostationary satellites are vital in improving the understanding of the relationships between tropical cyclones and their atmospheric and oceanic environment. Physical methods have been used to estimate winds from visible and infrared observations from the Geostationary Meteorological Satellites and for determining temperature and moisture from NOAA and NASA's advanced infra-red and microwave sounding systems. Recently, new satellite-derived data obtained using GPS Radio Occultation (RO) technology became available. These satellite-derived data are of high accuracy and currently provide as many as 1,000-2,500 temperature and moisture profiles daily (Liou *et al*, 2008). In the context of this research, data from six FORMOSAT-3/COSMIC satellites will provide a large number of atmospheric profiles in or in the vicinity of the storms therefore offering more specific information on their interaction with the environment (Liou *et al*, 2008).

New methodologies of satellite remote sensing for tropical cyclone research based on FORMOSAT-3/COSMIC RO, visible, infrared and microwave space-based observations are applied in this research. In particular, novel GPS RO methodology (Pavelyev *et al.*, 2009) with emphasis on deriving 3-D structure of the atmosphere has been developed and it will be applied for tropical cyclone investigations. The instruments from MEGHA-TROPIQUES mission such as MADRAS (a microwave imager aimed at studying precipitation and cloud properties) and SAPHIR (a 6-channel microwave radiometer for the retrieval of water vapour vertical profiles and horizontal distribution) will be tested. The key physical parameters at different altitudes in the atmosphere and at the ocean surface will be measured, diagnostics of global and regional atmospheric and oceanic changes will be studied and physical mechanisms responsible for these changes will be investigated.

4. SOUTH-WEST INDIAN OCEAN EXPERIMENT

New satellite remote sensing methodologies will be verified during SWICE - an international experiment dedicated to comprehensive investigations of the Indian Ocean tropical cyclone characteristics. One of the goals of SWICE is to investigate potential contribution of new data from satellite and airborne observations to improve the understanding of relationship between tropical cyclones and their atmospheric and oceanic environment. Particularly important is to obtain simultaneous satellite remote sensing observations and *in situ* measurements of atmospheric and oceanic characteristics using radiosondes, dropsondes and moored buoys. These comprehensive *in situ* measurements will be used to validate and improve the accuracy of the satellite remote sensing data. In particular, data about temperature and moisture profiles derived from various sources (radiosondes, dropsondes, FORMOSAT-3/COSMIC RO and the instruments from MEGHA-TROPIQUES mission) will be used to cross-validate the observations as well as to deduce more reliable and precise methods of deriving 3-D fields of atmospheric characteristics.

5. CONCLUSION

An important scientific question will be addressed in this research – what are the key large-scale climatic forces responsible for changes in tropical cyclone activity in different regions of the Indian Ocean? Outcomes of this research will allow to significantly advance our knowledge about environment in which the Indian Ocean tropical cyclones form and intensify, to develop new satellite remote sensing methodologies for tropical cyclone investigations and to establish the key large-scale environmental factors responsible for cyclone variability and change. Our team has strong backgrounds in atmospheric studies and cordially invites potential international collaborators to contribute to oceanic component of this research.

REFERENCES

Emanuel, K. A. (1987). "The dependence of hurricane intensity on climate". Nature, vol. 326, pp. 483–485.

Gray, W. M. (1968). "Global view of the origin of tropical disturbances and storms". Mon. Weather Rev. vol. 96, pp. 669-700.

Gray, W.M. (1979). "Hurricanes: Their formation, structure and likely role in the tropical circulation". Meteorology over the Tropical Oceans, (ed. D.B. Shaw), Royal Meteorological Society, pp. 155-218.

Holland, G. J. (1997). "The maximum potential intensity of tropical cyclones". J. Atmos. Sci., vol. 54, pp. 2519-2541.

IPCC 2007: IPCC WG1 AR4 Report. http://ipcc-wg1.ucar.edu/wg1/wg1-report.html

Knutson, T. R., T. L. Delworth, K. W. Dixon, I. M. Held, J. Lu, V. Ramaswamy, M. D. Schwarzkopf, G. Stenchikov and R. J. Stouffer. (2006). "Assessment of twentieth-century regional surface temperature trends using the GFDL CM2 coupled model". J. Clim., vol. 19, pp. 1624-1651.

Kuleshov, Y., F. Chane Ming, L. Qi, I. Chouaibou, C. Hoareau and F. Roux. **(**2009). **"**Tropical cyclone genesis in the Southern Hemisphere and its relationship with the ENSO". Annales Geophysicae, vol 27, pp. 2523-2538.

Kuleshov, Y., R. Fawcett, L. Qi, B. Trewin, D. Jones, J. McBride and H. Ramsay. (2010). "Trends in tropical cyclones in the South Indian Ocean and the South Pacific Ocean". J. Geophys. Res., vol. 115, D01101, doi:10.1029/2009JD012372.

Liou, Y.-A., M. Hernandez-Pajares, V. Chandrasekar and E. R. Westwater. (2008). "Guest Editorial – Special Session on Meteorology, Climate, Ionosphere, Geodesy, and Reflections from the Ocean Surfaces: Studies by Radio Occultation Methods". IEEE Trans. Geosci. Remote Sensing, vol. 46, no. 11, doi:10.1109/TGRS.2008.2005049.

Nolan, D. S., and E. D. Rappin (2008). "Increased sensitivity of tropical cyclogenesis to wind shear in higher SST environments". Geophys. Res. Lett., vol. 35, L14805, doi:10.1029/2008GL034147.

Pavelyev, A. G., Y. A. Liou, J. Wickert, A. L. Gavrik and C. C. Lee. (2009). "Eikonal acceleration technique for studying of the Earth and planetary atmospheres by radio occultation method". Geophys. Res. Lett., vol. 36, L21807, doi:10.1029/2009GL040979.

Webster, P. J., G. J. Holland, J. A. Curry and H.-R. Chang. (2005). "Changes in tropical cyclone number, duration, and intensity in a warming environment". Science, vol. 309, no. 5742, pp. 1844 – 1846, doi: 10.1126/science.1116448.

MERIS Third Reprocessing: Calibration and Algorithm Changes and their Expected Impact on Derived Products

E.J. Kwiatkowska [a,*], L. Bourg [b] and the MERIS Quality Working Group

[a] European Space Agency, ESTEC, Noordwijk, The Netherlands – ewa.kwiatkowska@esa.int
[b] ACRI-ST, Sophia-Antipolis, France – ludovic.bourg@acri-st.fr

Abstract – MERIS is a Medium Resolution Imaging Spectrometer operating in the reflective solar spectral range from aboard the ENVISAT platform. MERIS has been on orbit since 2002 and it has been providing a continuous global record of ocean color as well as land and atmospheric observations. MERIS data are now undergoing their third major reprocessing. This paper describes the major changes in instrument calibration and algorithms and explains their impact on the stability and accuracy of MERIS time series.

Keywords: MERIS, reprocessing, calibration, validation.

1. INTRODUCTION

MERIS is a push-broom optical spectrometer aboard the European Space Agency's ENVISAT platform flown in sun-synchronous descending polar orbit with a 10am equator crossing time (MERIS PH, 2006). Five cameras acquire overlapping parts of the Earth's swath adding to its total width of 1150 km. The five cameras image each cross-track line in the spectral range from 390 to 1040 nm. MERIS 15 programmable bands are built by assembling relevant 1.25 nm micro-bands at each camera CCD. MERIS primary goal is monitoring global oceans to improve our understanding of the ocean biogeochemistry and productivity in the climate system. Ocean color is a difficult measurement because in the visible spectrum most of the signal upwelled from the ocean is an order of magnitude smaller than the signal obtained at the satellite, due to intense atmospheric scattering and strong water absorption (Antoine and Morel, 1999). Continuous efforts to characterize instrumental drifts when on-orbit are therefore critical to the detection of long-term biogeochemical change in the oceans and to the quantification of environmental impacts. Constant improvement of the algorithms increases the scientific output from the mission. As a culmination of these efforts, MERIS is currently undergoing its third major reprocessing. This paper describes only the major changes since the second reprocessing in 2006.

2. CALIBRATION AND CHARACTERIZATION

MERIS radiometric accuracy requirements call for less than 2% uncertainty in the reflectance of detected signal relative to the Sun and for 2% in inter-band accuracy. On-board radiometric calibrations use two white Spectralon solar diffusers. The diffusers are deployed every 15 days and every three months, respectively, where diffuser-2 is applied as a stability monitor for diffuser-1. The radiometric calibration is dependent on the precise knowledge of the instrument spectral response. Band center wavelengths for each pixel need to be within less than 1 nm uncertainty. The oxygen absorption band, 761.875 nm, has algorithmic constrains within 0.1 nm. Three methods are used for spectral calibration: on-board Spectralon solar diffuser doped with erbium, Fraunhofer lines and the O_2-A band. MERIS diffuser calibrations are performed at the orbital South Pole. MERIS polarization sensitivity is below 0.3%.

2.1 Spectral calibration

MERIS spectral model remains unchanged in the third reprocessing. The model describes spectral variations across the field of view (FOV) of the cameras, the smile effect, which have an almost linear cross-track dependence up to 1 nm (Delwart *et al.*, 2007). The discontinuities between the cameras are up to 1.5 nm. The model defines the spectral dispersion law of each CCD at the center of the camera FOV and represents it as a polynomial based on the detector row. The variation across the camera FOV is modeled as a polynomial of the CCD detector column. The wavelength dependence in the CCD detector band-widths is represented by a third polynomial. The model error is ±0.2 nm compared to measurements. Camera 4 does not exhibit the smile effect. Cross-track variations from the mean camera spectral response are stable. However, the mean responses in cameras 2 and 4 have been trending with time. The operational model is frozen at the mid-2003 point. At this time, both cameras had already rapidly drifted by 0.1 to 0.15 nm, respectively, since launch and became stabilizing. They are currently at 0.15 and 0.2 nm shift. No obvious temporal drifts are observed in cameras 1, 3 and 5.

2.2 Radiometric calibration

The third reprocessing improves MERIS radiometric degradation through additional calibrations acquired since 2004 and a new modeling approach (Bourg and Delwart, 2006). Updated diffuser aging is used. Diffuser-1 now has up to 1.4% mean drift in reflectance relative to diffuser-2. The highest degradation is in the blue bands and the trend is fairly linear with time. In pre-launch characterizations, both diffusers showed bidirectional reflectance distribution function (BRDF) within ±0.5%. The on-orbit BRDF model exhibits a residual dependence on the Sun azimuth angle which shows as a ±0.5% variation in radiometric gains. In order to eliminate the Sun azimuth cycles from the BRDF model, the previous calibration normalized the gains in all bands to the gain in the near-infrared (NIR) band at 900 nm, which appeared not to degrade. After eight years on orbit, the NIR degradation is not negligible and it varies between the cameras up to 0.5% in camera 5. The new radiometric calibration does not use the gain normalization and it centers on the solar diffuser measurements at the mean Sun

* Corresponding author. ESA-ESTEC, TEC-EEP, Keplerlaan 1, 2200 AG Noordwijk, The Netherlands, tel: +31715656771.

azimuth. Results show that MERIS radiometric sensitivity typically degrades the fastest in the blue. The degradation is currently up to 3.5% in camera 5 and it varies with camera.

2.3 Ocean color vicarious adjustment

A vicarious adjustment is now introduced in the level 2 ocean color processing in the NIR and visible bands. The correction largely follows the methodology implemented for other ocean color missions (Mazeran *et al*., 2008).

3. GEOPHYSICAL ALGORITHM CHANGES

The third reprocessing brings significant improvements in MERIS geophysical algorithms. The algorithms are described in detail in MERIS ATBDs (2010).

3.1 Initial pre-processing and meteorological products

An advanced pixel classification is implemented that is based on data from ESA AlbedoMap and GlobCover programs and on improved surface pressure. Tests are included for brightness and pressure over oceans and for pressure and ice/snow plausibility over land. Better cloud identification is expected, including cirrus. A threshold on elevation is introduced for inland water identification. Surface pressure is currently derived using a neural network of O_2 transmittance at the 761.865 nm band instead of a polynomial. The estimate of O_2 transmittance benefits from a better approximation of the absorption-free reference which is now interpolated between two bands at 753.75 and 778.75 nm. The smile effect is reduced through wavelength dependence. The neural-network cloud top pressure is modified and employs enhanced straylight handling. The total column water vapor algorithm is modified by applying a neural network instead of a polynomial. Over clouds, the water vapor product benefits from the new pressure and ESA AlbedoMap data. AlbedoMap is also used in cloud albedo, optical thickness and cloud type algorithms. A modified smile correction is applied over oceans. It separately accounts for Rayleigh reflectance and the rest of the total signal in the modeling of total reflectance in the nominal wavelengths. The modeling uses linear interpolation from the adjacent bands which is smoother for log-transformed Rayleigh. The total reflectance is corrected up front for stratospheric aerosols and gaseous absorption.

3.2 Algorithms over oceans

The standard set of 13 aerosol models is complemented by three non-absorbing "blue" models. The "blue" models combine micro-physical properties of small particles with the inherent optical properties (IOPs) derived from AERONET measurements. AERONET solar extinctions and sky radiances are used from coastal and island sites. New look-up-tables (LUTs) are generated for top-of-the-atmosphere Rayleigh reflectance, aerosols, $\rho_{Path}/\rho_{Rayleigh}$ versus total aerosol optical thickness (AOT), and total upward and downward transmittances including the coupling between the atmospheric scattering and the Fresnel reflection at the sea surface. Aerosol polarization is now included in addition to Rayleigh polarization. The bright-pixel atmospheric correction is significantly enhanced. The f'/Q LUTs are updated and now entirely parameterized in the IOPs of pure water and particulates per band, wind speed and geometry. Pure seawater and particulate NIR absorptions are upgraded. To support better discrimination between low (<10 $g.m^{-3}$) and high sediments either a low band set, 709, 779 and 865 nm, or a high band set, 779, 865 and 885 nm, is exploited. The final value of particulate backscattering is used for case-2 water flagging. Water-leaving reflectances at 779, 865 and 885 nm are reported in standard products. The algorithm is disabled in case-1 waters. OC4Me is a semi-analytical chlorophyll-*a* algorithm for case-1 waters. It is a fourth-degree polynomial of the maximum irradiance reflectance ratio among R_{560}^{443}, R_{560}^{490} and R_{560}^{510}. The algorithm is based on the new case-1 bio-optical model. OC4Me is more consistent with chlorophyll algorithms from other missions. The case-2 water neural network is updated to reflect improved radiative transfer modeling and changes in derived water-leaving reflectances and ancillary data. Flag PCD_1_13 indicates confidence in water-leaving reflectances and now allows for small negative values.

3.3 Algorithms over land

The aerosol correction applies a model of dark and stable surface reflectance that is extended to brighter targets and processed from AlbedoMap data. It uses two or three bands from the set of 413, 443, 490 and 665 nm to limit low surface reflectance in the red and overestimation of AOTs. There are no algorithmic changes in MERIS global vegetation index (GVI) and terrestrial chlorophyll index. However, GVI by-products, reflectances at 681 and 865 nm, are now corrected for bidirectionality and extended to non-vegetated bright land areas. Both indices benefit from improved instrument calibration and pixel classification.

4. CONCLUSIONS

The third reprocessing provides advances in MERIS radiometric stability, accuracy and derived products. The new calibration improves MERIS long-term stability, particularly in the blue and green bands. Vertical striping is expected to decrease. The vicarious calibration impacts the accuracy of MERIS ocean products and is anticipated to bring them in closer agreement with ground measurements from the MERis MAtchup In-situ Database (MERMAID) archive. Enhanced meteorological, ocean and land algorithms add to MERIS scientific contributions.

REFERENCES

Antoine, D. and A. Morel (1999). "A multi scattering algorithm for atmospheric correction of remotely sensed ocean colour (MERIS): principle and implementation for atmospheres carrying various aerosols including absorbing ones". Int. J. Remote Sensing, vol. 20, no. 9, pp. 1875-1916.

Bourg, L. and S. Delwart (2006). "MERIS instrument calibration". Proc. 2nd MAVT, ESRIN, Italy (ESA SP-615). http://envisat.esa.int/workshops/mavt_2006

Delwart S., R. Preusker, L. Bourg, R. Santer, D. Ramon and J. Fischer (2007). "MERIS in-flight spectral calibration". Int. J. Remote Sensing, vol. 28, no. 3, pp. 479-496.

Mazeran, C., K. Barker, S. Lavender, L. Bourg and D. Antoine(2008). "Vicarious adjustment of marine reflectance for MERIS". MERIS/(A)ATSR User Workshop, ESRIN, Italy. http://earth.esa.int/cgi-bin/confm8.pl?abstract=238

MERIS Algorithm Theoretical Basis Documents (2010). ESA. http://envisat.esa.int/instruments/meris/atbd/

MERIS Product Handbook (2006). ESA. http://envisat.esa.int/handbooks/meris/

Observations of the Chlorophyll-a Concentrations, Estimates from the Blue-Green ratio and the Fluorescence Signal Using MERIS Measurements on the East and West Coast of Canada

F. Labonté*, J. Fischer

Institute for Space Sciences, Freie Universität Berlin, Berlin, Germany –
francoise.labonte@wew-fu-berlin.de, juergen.fischer@wew-fu-berlin.de

Abstract – We present results from a preliminary study comparing the estimates of two MERIS chlorophyll-a retrieval algorithms, the blue-green band-ratio MERIS C and MERIS Fluorescence Line Height (FLH), applied to case II waters on the East and West Coast of Canada using image analysis. Furthermore, radiative transfer simulations are used to investigate the impact of ocean properties on the chlorophyll-a retrieval, based on the blue-green ratio and the fluorescence.

Keywords: chlorophyll-a, fluorescence, MERIS.

1. INTRODUCTION

To preserve the biosphere and to use it efficiently, it is necessary to gain a deep insight into the dynamics of the primary production process on our planet. Variability of chlorophyll-a (C_a) concentration in the ocean, for example, is one of the most important components of this process and can be readily observed from satellites. Most C_a space-borne retrieval algorithms are based on blue-green band-ratio but in coastal waters (case II waters) fail due to the simultaneous presence of phytoplankton, suspended matter and yellow substance. In recent years, more sophisticated multispectral techniques have been used to monitor the optical relevant properties of coastal waters using sensors such as the MEdium Resolution Imaging Spectrometer (MERIS) instrument on Envisat, but uncertainties remain due to variability of interfering substances. Here, we present results from a preliminary study comparing results of two MERIS C_a retrieval algorithms, the MERIS C (Morel and Antoine, 2000) and MERIS Fluorescence Line Height (FLH) (Gower *et al.,* 1999) in sediment-free regions on the East and West Coast of Canada using image analysis. In addition, radiative transfer simulations investigating the impact of the ocean properties, such as the concentration and the vertical profile of C_a variability, on the blue-green ratio and the sun-stimulated C_a fluorescence (Fischer and Schlüssel, 1990) using the Matrix Operator Model (MOMO) (Fell and Fischer, 2001) are going to be presented.

2. METHODS

2.1 Images Analyses

Image analyses using the BEAM 4.6.1 software are performed for the MERIS C and FLH algorithms for ocean C_a using MERIS Version 1.9.1a Level 2 Reduced Resolution (RR) data at 1.2 km.

2.2 Radiative Transfer Simulations

Radiative transfer (RT) calculations are simulated by means of MOMO to specifically study the impact of ocean properties on the C_a retrieval. MOMO resolves the ocean ratio into a number of ocean sub-layers which enables us to study the impact of the vertical stratification of phytoplankton and other ocean constituents. All MERIS channels will be simulated for different ocean and atmospheric conditions.

3. ALGORITHMS

3.1 MERIS C

The MERIS C algorithm uses three different polynomials in order to estimate the C_a concentration from the 443/560 or the 490/560 or the 510/560 band ratios. The switch from one band ratio to another one is based on the C_a concentration itself.

$$[C_a] = 10\text{^}(a_0 + a_1R + a_2R^2 + a_3R^3 + a_4R^4 + a_5R^5)$$

$$R = \log_{10} [R_{rs}(\lambda_0)/R_{rs}(560)] \quad (1)$$

$[C_a] < 1$ $\lambda_0 = 443$ a = [0.2115, − 1.844, 1.282, − 2.747, 2.865, − 1.204]

$1 < [C_a] < 10$ $\lambda_0 = 490$ a = [0.3866, − 2.626, 2.572, − 7.156, 10.15, − 6.895]

$[C_a] > 10$ $\lambda_0 = 510$ a = [0.3900, − 3.864, 3.168, − 20.33, 63.21, − 113.9]

where $[C_a]$ = chlorophyll-a concentration, mg/m^3
a = Absorption coefficient of water constituents, m^{-1}
R = Blue-green ratio, dimensionless
R_{rs} = Remote sensing reflectance, sr^{-1}

3.2 FLH

The FLH algorithm measures the height of the C_a fluorescence peak near 680nm above a linear baseline. It uses bands 7 (665nm), 8 (681nm) and 9 (709nm) of MERIS that have been specifically designed to detect the sun-stimulated C_a fluorescence.

$$L_F - L_R - (L_L - L_R)((\lambda_F - \lambda_R)/(\lambda_L - \lambda_R)) \quad (2)$$

where λ_F, λ_L, λ_R = respectively the center wavelengths of fluorescence band and two baseline bands
L_F, L_L, L_R = respectively the radiances of fluorescence band and two baseline bands

* Corresponding author. Institute for Space Sciences, FUB, Carl-Heinrich-Becker-Weg 6-10, 12165 Berlin, Germany.

It should be noted that the impact of water vapor on the 709nm channel is uncertain and the transmittance may have to be corrected.

4. PRELIMINARY RESULTS

Figure 1 shows the fluorescence (FLH) images for (a) the Vancouver Island for 22 September 2009 and (b) the East Coast of Canada for 11 September 2009. Values are increased (only partly due to fluorescence) in areas where other suspended matter load could influence the signal. The color scale and range of computed FLH values are shown by the color bar. The MERIS FLH images show artifacts (image stripping) in the channel observation geometry; this is evidence of continuing problems with instrument effects.

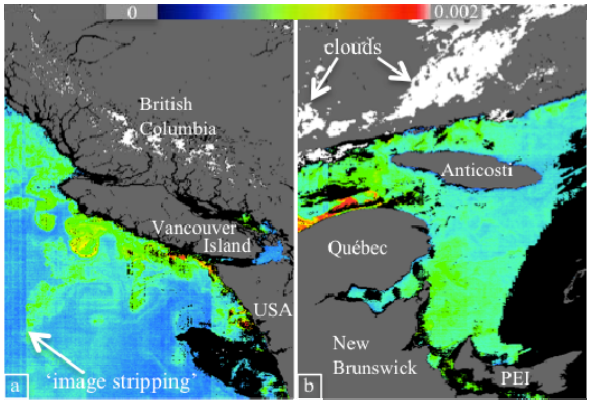

Figure 1. FLH signal computed with BEAM from bands 7, 8 and 9 of MERIS RR level 2 data for (a) Vancouver Island and (b) East Coast of Canada.

Figures 2 and 3 shows scatter plots for the two selected regions of Canada. MERIS fluorescence is compared with MERIS C_a. The two regions show similar relations for C_a values below about 2 mg/m^3, but diverge for higher values. The black curve is a best fit to these areas.

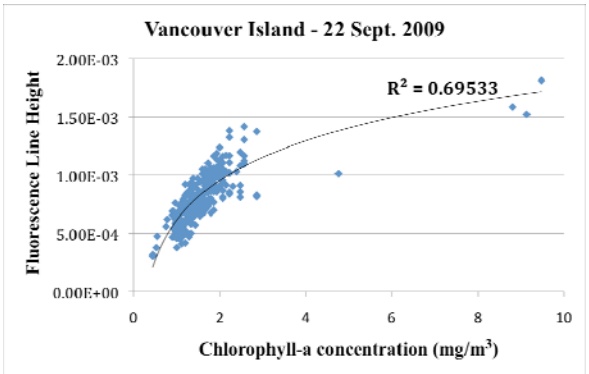

Figure 2. Scatter plot of data from Figure 1 (a). FLH signal computed from Level 2 RR data, against C_a concentrations from the Level 2 MERIS C data for the Vancouver Island on 22 Sept. 2009.

In Figure 3, it shows relatively low fluorescence at high C_a values, while Figure 2 shows higher values. Both Figure 2 and 3 shows point well above the model line. This divergence points to the possibility of locating and studying areas where the fluorescence signal appears higher or lower than expected which can be caused by yellow substance (DOC) or sediments.

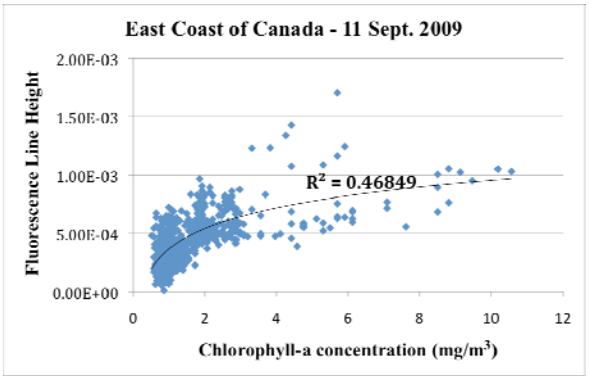

Figure 3. Scatter plot of data from Figure 1 (b). FLH signal computed from Level 2 RR data, against C_a concentrations from the Level 2 MERIS C data for the East Coast of Canada on 11 Sept. 2009.

5. DISCUSSION & NEXT STEPS

Several challenges deserve immediate attention to enable the operational application of MERIS FLH data in coastal oceanography. First, computing the difference between images for different coastal regions in Canada to assess anomalies can help attribute changes to specific C_a dynamics. Secondly, RT simulations of ocean properties using MOMO will help characterize the impact of ocean properties on the C_a and fluorescence retrievals and allow for preliminary algorithmic error estimation. The impact of atmospheric parameters will also be investigated.

ACKNOWLEDGEMENTS

This work is supported by the Institute for Space Sciences, Freie Universität Berlin, Germany.

REFERENCES

Fell, F. and J. Fischer (2001). "Numerical simulation of the light field in the atmosphere-ocean system using the matrix-operator method". Journal of Quantitative Spectroscopy and Radiative Transfer, vol. 69, pp. 351-388.

Fischer, J. and P. Schlüssel. "Sun-stimulated chlorophyll fluorescence 2: Impact of atmospheric properties". International Journal of Remote Sensing, vol. 1, no. 12, pp. 2149-2162.

Gower, J.F.R., R. Doerffer and G.A. Borstad (1999). "Interpretation of the 685nm peak in water-leaving radiance in terms of fluorescence, absorption and scattering, and its observation by MERIS". International Journal of Remote Sensing, vol. 20, no. 9, pp. 1771-1786.

Morel, A. and D. Antoine (2000). "Pigment index retrieval in case 1 waters, MERIS Algorithm Theoretical Basis Document". ATBD2-9, pp. 1-25.

The Use of Spectral Derivatives to Measure Suspended Matter Concentration in Estuarine and Coastal Waters from Multispectral Sensors

P. Larouche [a,*], B. Ricard [a], N. Martiny [b], J.-M. Froidefond [c]

[a] Institut Maurice-Lamontagne, Pêches et Océans Canada, Mont-Joli, Québec, Canada – Pierre.Larouche@dfo-mpo.gc.ca
[b] UMR 5210 CNRS, Université de Bourgogne, Dijon, France – nadege.martiny@u-bourgogne.fr
[c] UMR 5805 (DGO) CNRS / Université Bordeaux-1, Talence, France – jm.froidefond@epoc.u-bordeaux1.fr

Abstract – Total suspended matter is a basic parameter to measure in estuarine and coastal zones. A general algorithm to measure the concentration of suspended matter using a derivative approach and multispectral data is presented. This methodology has been adapted from previous work done with hyperspectral data that showed the great potential of the spectral derivative approach compared to normal band ratios. Tests made using a variety of in situ measurements showed that the new algorithm can provide measurements of suspended matter over a wide range of concentrations (0-400 mg l^{-1}) with typical accuracy of 35%. This algorithm will be particularly useful for applications to remote areas where local algorithms are not available.

Keywords: suspended matter, estuarine waters, coastal waters, multispectral.

1. INTRODUCTION

Estuaries and coastal zones are often turbid waters where the water transparency is reduced by the presence of suspended particulate matter. The pronounced color signatures from suspended matter suggest a potential remote sensing approach to evaluate water turbidity. Several models including the use of neural networks have been proposed to link total suspended matter (TSM) concentrations to the spectral signature of water surfaces. Some of them showed significant relationships and succeeded in quantifying TSM with acceptable uncertainty. However, in all these studies, the data used were specific to a particular environment characterized by a sediment type having its own spectral signature. The aim of the present study is thus to develop a more general approach to suspended matter concentration retrieval using optical multispectral measurements. For that purpose, we based our analysis on previous works (Chen et al., 1992; Goodin et al., 1993; Han and Rundquist, 1997; Fraser, 1998; Larouche et al., 2003), that showed that first spectral derivative variations were representative of TSM quantity.

2. MATERIAL AND METHODS

Water optical properties vary according to the constituents of the upper surface layer: suspended particulate matter (both organic and inorganic) and coloured dissolved organic matter (CDOM). For suspended particulate matter, the main factors are the concentration, the size and the refractive index of the material. To achieve the project's goal, it was necessary to build a data set covering a broad range of concentrations and representing distinct environments. Data was thus acquired in the St. Lawrence estuary, Hudson Bay, Beaufort sea and oued Sebou covering a wide range of suspended matter concentration (0-400 mg l^{-1}) and sediment types. SeaWiFS, MODIS, MERIS and Landsat-7 spectral bands were simulated using 145 hyperspectral measurements of water leaving radiances acquired with a portable spectroradiometer. Remote sensing reflectance was estimated using:

$$R_{RS}(\lambda) = L_w(\lambda) / [(\pi \times S_g(\lambda)) / R_g(\lambda)] \quad (1)$$

where L_w is the above water upwelling radiance measured by the sensor pointing towards water (W m^2 sr^{-1}); S_g is the radiance measured by the sensor pointing towards a near lambertian reflector (W m^2 sr^{-1}); R_g is the known reflectances of that reflector and π is theoretically the relationship between incidental radiances (E_s) and near-Lambertian surface radiances (S_g) and carries units of steradian from the integration over solid angle (Mobley, 1994). In parallel to the optical measurements, water samples were collected near the surface to measure TSM concentration for each station. Glass fibre filters having (0.7 µm) pores have been used everywhere except in the Beaufort sea where Anotop ® filters of pore 0.4 µm have been used. The TSM concentration uncertainty was estimated at 15% using available duplicates and triplicates samples. The derivative of the spectra was calculated from the simulated bands using:

$$\text{Derivative} = \Delta Rrs_{(band)} / \Delta\lambda_c \quad (2)$$

Where $Rrs_{(band)}$ is the mean Rrs over a specific spectral band and λ_c is its the central wavelength.

3. RESULTS

The analysis showed that better results were reached when algorithms were developped for TSM loads lower or higher than 10 mg l^{-1}. The spectral slope between 500 and 600 nm is used to decide which algorithm should be used with steeper slopes corresponding to higher TSM concentrations. Table 1 shows the results of the algorithm development for the four targetted satellite sensors. In general, the accuracy of the algorithm is around 30%. Comparison with other proposed algorithms is difficult as there is no standard way to report the accuracy of algorithms. Some authors use the RMS error (either % or concentration), some the r^2 correlation coefficient and others use bias (absolute or not). To further evaluate the performance of the method, we used 88 independent spectral measurements from the Adour

* Corresponding author. 850 route de la Mer, B.P. 1000, Mont-Joli, Québec, Canada G5H 3Z4.

(France) and Congo river plumes using a towed mini-catamaran (Froidefond and Ouillon, 2005). Results showed that the TSM concentration was estimated with a precision of 37,5%. This is only a slight reduction of performance considering the variety of optical and TSM measurement methodologies used during the various projects and the different nature of the drainage basins. The proposed derivative approach works well because phytoplankton dominates the spectral shape when concentrations are less than 10 mg l^{-1}. The blue to green slope is thus very effective to measure this type of particles. For higher TSM concentrations, the remote sensing reflectance around 650 nm is more sensitive to inorganic particles backscattering while the 550 nm reflectance is almost saturated leading to the use of the 550-650 band slope as an indicator of TSM.

4. CONCLUSION

The use of a spectral derivative approach showed that it was possible to build a general algorithm to estimate TSM over a wide range of concentrations. The algorithm can provide a satisfactory first order estimate of TSM for applications to estuaries and coastal regions independent from the suspended matter nature except maybe for very specific environments such as iron or chalk laden waters.

ACKNOWLEDGEMENTS

This work was made possible with the financial support of the Department of Fisheries and Oceans Canada. Support was also provided by the Agence Universitaire Francophone for the sampling in the Oued Sebou, by the National Science and Engineering Research Council of Canada for the sampling in the Beaufort Sea and Hudson Bay, by the Department of National Defence (Canada) for the sampling in the Vancouver island area, the CNES for the sampling in the Adour plume and the SHOM for the sampling in the Congo river plume. Support was also provided by the Université de Bordeaux-1.

REFERENCES

Chen, Z., P. J. Curran and J. D. Hansom (1992). Remote Sensing of Environment, vol. 40, no. 1, pp. 67-77.

Fraser, R. N. (1998). International Journal of Remote Sensing, vol. 19, no. 8, pp. 1579-1589.

Froidefond, J.-M. and S. Ouillon (2005). Optics Express, vol. 13, no. 3, pp. 926-936.

Goodin, D. G., L. Han, R. N. Fraser, D. C. Rundquist and W. A. Stebbins (1993). Photogrammetric Engineering and Remote Sensing, vol. 59, no. 4, pp. 505-510.

Han, L. and D. C. Rundquist (1997). Remote Sensing of Environment, vol. 62, no. 3, pp. 253-261.

Larouche, P., M. El-Mouttaki and A. Djouai (2003). Télédétection, vol. 3, no. 1, pp. 85-96.

Mobley, C. D. (1994). Light and Water - Radiative Transfer in Natural Waters. Academic Press, San Diego.

Table 1. TSM algorithms developped using multispectral sensors. Band refers to the sensor band number, λ is the band wavelength, P is the slope calculated using equation 2 and E is the mean absolute relative error.

Sensor		Band	λ (nm)	Equation	E (%)
SeaWiFS	Discrimination	4 5	500 - 520 545 - 565	If P(4,5) < 0,00013, TSM < 10 mg l^{-1} or If P(4,5) > 0,00013, TSM > 10 mg l^{-1}	29
	< 10 mg l^{-1}	4 5	500 - 520 545 - 565	$TSM = 1.0709e^{16453\,(P(4,5))}$	
	> 10 mg l^{-1}	5 6	545 - 565 660 - 668	$TSM = 143.65\ e^{11907\,(P(5,6))}$	
MODIS	Discrimination	11 12	526 – 536 546 - 556	If P(11,12) < 0,00013, TSM < 10 mg l^{-1} or If P(11,12) > 0,00013, TSM > 10 mg l^{-1}	28
	< 10 mg l^{-1}	11 12	526 – 536 546 - 556	$TSM = 1.0956e^{17226\,(P(11,12))}$	
	> 10 mg l^{-1}	12 13	546 – 556 662 - 672	$TSM = 133.84e^{12256\,(P(12,13))}$	
MERIS	Discrimination	4 5	505 – 515 555 - 565	If P(4,5) < 0,00013, TSM < 10 mg l^{-1} or If P(4,5) > 0,00013, TSM > 10 mg l^{-1}	30
	< 10 mg l^{-1}	4 5	505 – 515 555 - 565	$TSM = 1.0958e^{16812\,(P(4,5))}$	
	> 10 mg l^{-1}	5 6	555 – 565 615 - 625	$TSM = 124.5e^{11617\,(P(5,6))}$	
Landsat 7	Discrimination	1 2	450 – 515 525 – 605	If P(1,2) < 0,0001, TSM < 10 mg l^{-1} or If P(1,2) > 0,0001, TSM > 10 mg l^{-1}	31
	< 10 mg l^{-1}	1 2	450 – 515 525 – 605	$TSM = 1.2109e^{19205\,(P(1,2))}$	
	> 10 mg l^{-1}	2 3	525 – 605 630 - 690	$TSM = 135.89\ e^{12716\,(P(2,3))}$	

Complex Investigation of Meteorological, Hydrological and Hydrodynamic Regime of the Caspian Sea Based on Satellite Altimetry Data

S.A. Lebedev [a,*], A.G. Kostianoy [b]

[a] Geophysical Center, Russian Academy of Sciences, Moscow, Russian Federation – lebedev@wdcb.ru
[b] P.P. Shirshov Institute of Oceanology, Russian Academy of Sciences, Moscow, Russian Federation – kostianoy@ocean.ru

Abstract – The aim of this publication is to show the results of the application of satellite altimetry methods to the investigation of seasonal and interannual variability of the sea level, wind speed and wave height in different parts of the Caspian Sea and Kara-Bogaz-Gol Bay, and the Volga River level. The Caspian mean sea surface (MSS) was investigated basing on the space-time variability of equipotential sea surface or sea surface height, that gave an opportunity to analyse spatial variability of the Caspian Sea level change rate. This work is based on the 1992–2009 TOPEX/Poseidon (T/P) and Jason-1/2 (J1/2) datasets.

Keywords: mean sea level, altimetry, Caspian Sea.

1. INTRODUCTION

The Caspian Sea is the world's largest isolated water reservoir, with only isolation being its significant dissimilarity from the open seas. The isolation of the Caspian Sea from the ocean and its inland position make the significance of its outer thermohydrodynamic factors, specifically, heat and water fluxes through the sea surface, and river discharge on sea level variability, formation of its 3D thermohaline structure, and water circulation (Kosarev and Yablonskaya, 1994).

Over the past half-century, there was the Caspian Sea level regression until 1977 when the sea level lowered to -29 m (Fig. 1). It is obvious that man's impact led to a more than 2.5 m regression of the Caspian Sea level caused by the creation of cascade reservoirs in the Volga and Kama rivers.

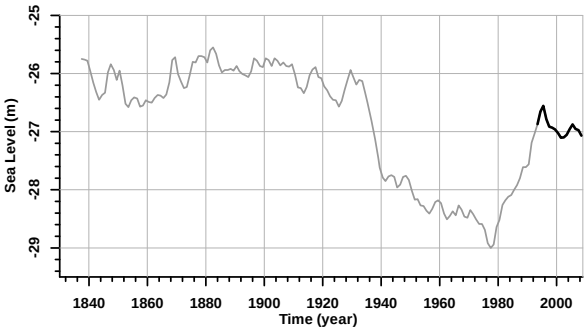

Fig. 1 Interannual variations of the Caspian Sea level measured by sea level gauges (gray line) and satellite altimetry (black line) from 1837 till 2009

This drop is considered to be the deepest for the last 400–500 years (Kostianoy and Kosarev, 2005). In 1978 the water level started to rise rapidly, and now it has stabilized at the -27 m level. There has been increasing concern over the Caspian Sea level fluctuations.

Satellite altimetry measures sea surface height (SSH) relative to a reference ellipsoid (or the gravity center) that allows elimination of vertical Earth's crust lift from interannual level variation. It was shown that spatial and temporal resolution of satellite altimetry data allows to investigate seasonal, interannual and space-time variability of the Caspian Sea level (Cazenave *et al.* 1997; Lebedev and Kostianoy, 2005, Crétaux and Birkett, 2006; Lebedev and Kostianoy, 2008; Kouraev *et al.*, 2010).

2. DATA AND METHODOLOGY

For this investigation altimetric measurements from both the T/P and J1/2 satellites were used for the following reasons. The position of T/P and J1/2 ground tracks (Kosarev and Kostianoy, 2005) is optimal for analysis of sea level variations in the Caspian Sea. The precision of SSH measurements by T/P and J1/2 to the relative reference ellipsoid is 1.7 cm, which is higher than other altimetry missions. At the same time, accuracy of sea level measurements is of ~4 cm that allows adequate accuracy for specific studies to be conducted. The orbital repeat period (~10 days) enables analysis of interannual and seasonal variability of the sea level. The T/P data represent the longest time-series of satellite altimetry measurements (September 1992 – August 2002 or 1 – 365 cycles) with the possibility of the data extension by J1 data along the same tracks (August 2002 – February 2009 or 1 – 259 cycles) and J2 (July 2008 – November 2009 or 1 – 51).

Satellite altimetry data processing methods and analysis as well as obtained results on the SSH variations were described in detail in the book by Lebedev and Kostianoy (2005). All necessary corrections from satellite altimetry data-base: microwave radiometer wet tropospheric, smoothed dual-frequency ionosphere and sea state bias are used in the data processing. Maximal tide height for the Caspian Sea is 2 cm in coastal zone so this correction isn't used in the data processing.

Regional MSS model of the Caspian Sea (GCRAS09 MSS) was calculated according to the following scheme. For satellite altimetry data processing dry tropospheric correction was calculated on atmospheric pressure from nearest weather stations located along the Caspian Sea costal line. From the T/P and J1/2 satellite altimetry data,

* Corresponding author. Geophysical Center, Russian Academy of Sciences, 3, Str. Molodezhnaya, Moscow, Russia.

the SSH synoptic and seasonal variations for all passes of each repeat cycle were eliminated. In last phase, the GCRAS09 MSS was constructed as a SSH function of latitude, longitude, and time with correction on climatic dynamic topography. For specified time interval SSH was interpolated on grid by radial basis function method.

Dynamic topography (DT) was constructed on the basis of the superposition of the SLA (calculated relative to the GSRAS09 MSS model) distribution over the climatic dynamic topography (or hydrodynamic level), which was calculated on the base of a three-dimensional baroclinic model.

3. RESULTS

The wind regime of the Caspian Sea is defined by three principal factors: regional atmospheric activity, topography of the coasts (orography) and local circulation induced by the thermal difference between the land and the sea. Comparison of wind speed data from meteorological stations and results of calculations of satellite altimetry data have shown that in-situ data and remote sensing measurements coincide within the limits of accuracy for satellite altimetry methods. The coefficient of correlation between these types of data was 0.819. In general wind speed is 1.5 times higher in winter than in summer with a maximum in the Middle Caspian. Seasonal variability of significant wave height shows that in general in the Middle Caspian wave heights are two times higher in winter than in summer and 1.5 times higher than in the Southern Caspian.

Investigation of the Caspian Sea level variation was based on the analysis of SSH variability in 7 crossover points (2 – the Northern Caspian, 2 – in the Middle Caspian and 3 – in the Southern Caspian). Integrated interannual variability of the Caspian Sea level is shown in Fig. 1 (black line). Comparison of SSH variations in 7 crossover points with data of 8 sea level gauges has shown that a maximal value of the correlation coefficient 0.967 was observed between the station in Baku and nearest crossover point. For the sea level time variability of the whole sea, which is traditionally calculated basing on the sea level gauges in Makhachkala, Baku, Fort Shevchenko and Krasnovodsk (nowadays Turkmenbashi), the correlation coefficient for all crossover points is higher than 0.94.

The process of Kara-Bogaz-Gol Bay refilling and its set in a climatic regime is well traced in the SA data of the T/P and J1/2. Fortunately, the start of the T/P mission successfully coincided with the beginning of the filling of the bay and the area of the bay is crossed by two tracks of the above-mentioned satellites. By the middle of 1996, the rapid filling of the bay with the Caspian Sea water had caused a rate of the bay level rise of about 168 cm/yr (Lebedev and Kostianoy, 2005, 2008). Then, the level rise stopped and its variations started to reflect seasonal changes well correlated with the seasonal level changes in the Caspian Sea. Thus, the rate of the level fall (until winter 2001/2002) in both basins was approximately 6 cm/yr. At present, the level of the bay oscillations is near an absolute mark of -27.5 m.

Analysis of seasonal DT shows existence of a gyre in the Middle Caspian, which changes its direction of rotation from a cyclonic one in winter months to an anticyclonic one in summer months. This transformation seems to be conditioned by seasonal variability of the Volga River dischage and wind conditions over the Caspian Sea. Dynamics of the Southern Caspian Sea have a pronounced vortical nature; wind variability is a cause of this phenomenon.

According to variation of the interannual Caspian Sea level change (Lebedev and Kostianoy, 2008; Kouraev *et al*., 2010) we determine five time periods: strong rise (1993–1995), strong drop (1995–1997), slow rise (2002–2006), slow drop (1997–2002 and 2006–2009). For investigation of spatial variability we constructed an annual MSS for each year from 1993 to 2008 with using the GCRAS09 MSS Model data and interpolation on regular grid by radial basis function method. Map of rate of the interannual Caspian Sea level change are calculated as difference between two annual MSS maps. For time period of strong sea level rise (1993–1995) mean value of the sea level change rate is 9.2 cm/yr. Maximum value (more than 12 cm/yr) was located in the Middle and Southern Caspian and correlated with depths. Near the Kara-Bogaz-Gol Bay rate of sea level rise of 8.1 cm/yr was less then the mean value. In next time period (1995–1997) of strong sea level drop a maximum value (more than 15 cm/yr) was observed in the Northern Caspian and minimum (less than 3 cm/yr) are located near southwestern coast of the Southern Caspian. Similar regime of slow sea level drop holded since 1997 till. Mean value of the sea level change rate was -4.8 cm/yr. In the time periods of slow drop (1997–2002) and slow rise (2002–2006) a rate of sea level change was well correlated with gravity anomaly field. Extreme variation of it is observed in the Middle and Southern Caspian near the Apsheron Swell.

REFERENCES

Cazenave, A., P. Bonnefond, K. Dominh, and P. Schaeffer (1997). “Caspian sea level from TOPEX/ POSEIDON altimetry: Level now falling”. Geophys. Res. Lett., vol. 24, no. 8, pp. 881-884, doi: 10.1029/97GL00809

Crétaux, J.-F., and C. Birkett (2006). “Lake studies from satellite radar altimetry”. C. R. Geosciences, vol. 338, no. 14-15, pp. 1098-1112, doi: 10.1016/j.crte.2006.08.002

Kosarev, A.N., and E.A. Yablonskaya (1994). “The Caspian Sea”, SPB Academic Publishing, The Hague, 259 pp.

Kostianoy, A.G., and A.N. Kosarev (Eds.) (2005). “The Caspian Sea Environment”. Hdb. Env. Chem., Vol. 5, Part P, Springer-Verlag, Berlin, Heidelberg, New York, 271 pp.

Kouraev, A.V., J.-F. Crétaux, S.A. Lebedev, A.G. Kostianoy, A.I. Ginzburg, N.A. Sheremet, R. Mamedov, E.A. Zakharova, L. Roblou1,, F. Lyard, S. Calmant, M. Berge-Nguyen (2010). “Satellite Altimetry Applications in the Caspian Sea”. In: Costal Altimetry. Eds: S. Vignudelli, A.G. Kostianoy, P. Cipollini, J. Benveniste, Springer, (in pr)

Lebedev, S.A., and A.G. Kostianoy (2005) “Satellite Altimetry of the Caspian Sea”. Sea, Moscow, 356 pp. (in Russian) (in Russian)

Lebedev, S.A., and A.G. Kostianoy (2008). “Integrated using of satellite altimetry in investigation of meteorological, hydrological and hydrodynamic regime of the Caspian Sea”. Terr. Atmos. Ocean. Sci., vol. 19, no. 1-2, pp. 71-82. doi: 0.3319/TAO.2008.19.1-2.71(SA).

Variability of Meridional Circulations in the Indo-Pacific Ocean: Zonal Structure and Inter-basin Linkages

T. Lee

Jet Propulsion Laboratory, California Institute of Technology, Pasadena, California, USA – Tong.Lee@jpl.nasa.gov

Abstract – The shallow meridional overturning circulations (MOCs) in the Pacific and Indian Oceans affect climate variability by regulating tropical heat content and air-sea interaction. Existing in-situ systems are inadequate to monitor these circulations. Scattterometer measurements of ocean surface wind stress and altimeter measurements of sea level anomaly are used to characterize the variability and structure of these circulations and to describe the underlying physics. Analysis of these satellite observations suggest that, on interannual-decadal time scales, (1) the western-boundary and interior flow of the Pacific MOC play opposite roles in controlling tropical Pacific heat content, and (2) the Pacific- and Indian-ocean MOCs play opposite roles in regulating tropical heat content. The atmospheric and oceanic processes that cause these anti-correlated variabilities are identified.

Keywords: ocean circulation, climate variability.

1. INTRODUCTION AND OBJECTIVES

The wind-driven, shallow meridional overturning circulations (MOCs) in the Pacific and Indian Oceans transport heat poleward by carrying warm surface water from the tropics to the subtropics and colder pycnocline water from the subtropics to the tropics. By regulating tropical upper-ocean heat content, these circulations affect ocean-atmosphere coupling in the tropics and thus low-frequency climate variability on interannual to decadal and longer time scales. There are difficulties in studying these MOCs using in-situ observations. In-situ observations of wind are far too sparse to characterize the forcing of the MOCs and to estimate the strength of the upper branch (meridional Ekman transport). In-situ observations have the potential capability to monitor the flow in the lower branch of the MOCs (pynocline flow). However, the lower branch of the Pacific MOC consists of an interior and western-boundary pathway (Lee & Fukumori 2003). Existing in-situ observations (e.g., from Argo and XBT) can capture the interior pathway of the lower branch (interior pycnocline flow), but they are too sparse near the boundaries to capture the variability of the western-boundary pycnocline flow.

There are limitations in using models to investigate the MOCs due to forcing field uncertainties and model deficiencies (e.g., resolution, physics). Moreover, modeling studies of the MOC are often based on the meridional transport stream function (MTSF), i.e., zonally integrated meridional transport above a given depth. The zonal integration masks out the relative variation of the interior and boundary flows in the lower branch. Moreover, a meaningful definition of the MOC requires volume conservation across a longitudinal section. Because of the large volume transport associated with the Indo-Pacific througflow (or Indonesian throughflow, ITF), MTSF cannot be defined for the Pacific and Indian Oceans separately. Therefore, modeling studies usually analyze the MTSF of the Indo-Pacific as a whole. This obscures the relative variation of the Pacific- and Indian-Ocean meridional circulations.

Due to the aforementioned obstacles, many aspects of the Indo-Pacific MOCs are not well understood until recent years when satellite observations (esp. scatterometers and altimeters) span over a decade. This paper highlights the efforts to use satellite scatterometer and altimeter measurements to address the following scientific questions related to Indo-Pacific MOCs: (1) How do the Pacific and Indian Ocean MOCs vary on interannual-decadal time scales? (2) What are the corresponding forcing mechanisms (e.g, local vs. remote forcing)? (3) Is there any linkage between the Pacific and Indian Ocean MOCs, and if so, what are the physical processes? (4) What is the zonal structure of the variability of meridional flows associated with the MOCs?

2. DATA AND METHOD

The data used for the investigation include (1) ocean surface wind stress measured by the ERS-1 and -2 scatterometers from 1992 to 2000 and QuikSCAT from 2000 to 2008 and (2) observations of sea level anomalies by the TOPEX/Poseidon and JASON-1 altimeters. Based on the Ekman relation, the zonal wind stress obtained from the scatterometer data are used to infer the variability of in the meridional Ekman transport (MOC upper branch). Based on the geostrophic relation, the difference of sea surface height (SSH) between the western and eastern boundary is used to infer the variability of the net meridional geostrophic flow in the pycnocline. The latter is possible because the SSH difference between the two boundaries reflects the zonal pressure gradient that drives the net meridional geostrophic flow in the pycnocline integrated across a latitude.

3. RESULTS

3.1 Zonal structure of the Pacific MOC

The most conspicuous feature of the zonal structure of the MOC variability in the Pacific Ocean is with regard to the western-boundary and interior pycnocline flows (Lee and Fukumori 2003, Lee and McPhaden 2008). For time mean, these flows re-enforce each other in regulating tropical heat content. On interannual-to-decadal time scales, however, they counteract each other with the interior flow being more dominant. Sea level anomaly from altimeters vividly illustrate these changes because the SSH difference across the low-latitude western-boundary currents (i.e., the Mindanao Current and New Guinea Coastal Undercurrent) are anti-correlated to SSH difference across the ocean's interior (i.e., from the eastern edge of a western boundary current to the eastern boundary). This behavior is the result of the oscillation of the tropical gyres in the western Pacific

caused by off-equatorial wind stress curl as clearly shown by scatterometer wind data. These variations of off-equatorial wind stress curl are associated with the movements of the Inter-tropical Convergence Zone and South Pacific Convergence Zone that are correlated with the oscillation of the Walker circulation.

3.2 Relation of the Pacific- and Indian-Ocean MOCs

Scatterometer and altimeter data show that the MOC in the Pacific (Indian) Ocean strengthened (weakened) in the 1990s, vice versa from 2000 to about 2006 (Lee 2004, Lee and McPhaden 2008) (Figures 1 and 2). On interannual-decadal time scales, the changes in the strength of the Pacific and Indian Ocean MOCs are anti-correlated. This is related to an atmospheric and an oceanic process.

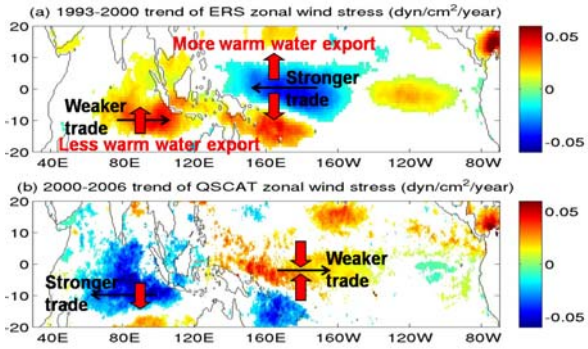

Figure 1. Linear trends of scatterometer-derived zonal wind stress during 1993-2000 (upper) and 2000-2006 (lower). The opposite patterns between the two periods indicate decadal variations that have changed tendency before and after 2000. The opposite trends in the Pacific and Indian Oceans suggest anti-correlated changes of trade winds that cause opposite anomalies of poleward Ekman transports.

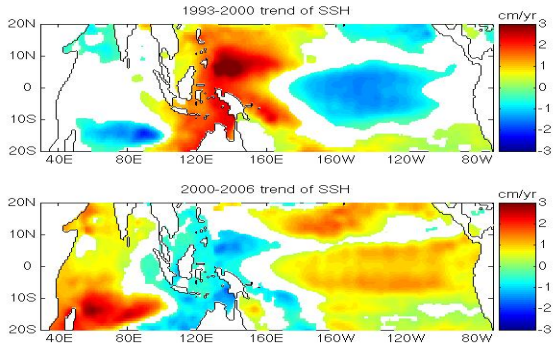

Figure 2. Linear trends of altimeter-derived SSH during 1993-2000 (upper) and 2000-2006 (lower), indicating opposite changes of zonal pressure gradient in the Pacific and Indian Oceans and thus opposite anomalies of equatorward geostrophic flow.

For the atmospheric processes, the oscillation of the Walker circulation leads to anti-correlated variability of the trade winds over both oceans and thus anti-correlated variations in poleward Ekman transports in the two oceans. For the oceanic processes, wind forcing associated with the Walker circulation modulates the pycnocline depth in the northwestern tropical Pacific, which transmits to the southeast Indian Ocean. Such modulation and wave transmission cause anti-correlated variations in the zonal pressure gradients that drive the equatorward pycnocline flow in the Pacific and Indian Oceans. Together, they play opposite roles in regulating the tropical heat content.

For the atmospheric processes, the oscillation of the Walker circulation leads to anti-correlated variability of the trade winds over both oceans and thus anti-correlated variations in poleward Ekman transports in the two oceans. For the oceanic processes, wind forcing associated with the Walker circulation modulates the pycnocline depth in the northwestern tropical Pacific, which transmits to the southeast Indian Ocean. Such modulation and wave transmission cause anti-correlated variations in the zonal pressure gradients that drive the equatorward pycnocline flow in the Pacific and Indian Oceans. Together, they play opposite roles in regulating the tropical heat content.

4. CONCLUSION

Satellite observations of ocean surface wind stress and sea level anomaly since the early 1990s have provided an unprecedented opportunity to study the variability, structure, and inter-basin linkages of the Pacific and Indian Ocean MOCs. For the Pacific MOC, the interior and western-boundary pathways play opposite role in controlling tropical Pacific heat content with the former being more dominant. The cause for this feature is the off-equatorial wind stress curl that spinup/spindown the tropical (horizontal) gyre in the western tropical Pacific. On interannual-decadal time scales, the Pacific- and Indian-Ocean MOCs play opposite roles in regulating tropical heat content because of the counteracting variation in their strengths. This characteristic is a result of an atmospheric process (oscillation of the Walker Circulation) and oceanic mechanism (coastal Kelvin waves that allow fast communication between the northwestern tropical Pacific and southeastern tropical Indian Ocean). Sustained and consistent measurements of wind stress and sea level are indispensible to the monitor of MOCs in the Pacific and Indian Oceans, to further understand the underlying physics on decadal time scales, and to evaluate their impact on decadal climate variability.

ACKNOWLEDGEMENTS

The research described in this paper was carried out in the Jet Propulsion Laboratory, California Institute of Technology, under a contract with the National Aeronautics and Space Administration (NASA). Copyright 2010 California Institute of Technology. The Government sponsorship acknowledged.

REFERENCES

Lee, T., and I. Fukumori (2003). "Interannual to decadal variation of tropical-subtropical exchange in the Pacific Ocean: boundary versus interior pycnocline transports". J. Clim., 16, 4022-4042.

Lee, T. (2004). Decadal weakening of the shallow overturning circulation in the South Indian Ocean. Geophys. Res. Lett., 31, L18305, doi:10.1029/2004GL020884.

Lee, T., and M.J. McPhaden (2008). Decadal phase change in large-scale sea level and winds in the Indo-Pacific region at the end of the 20th century. Geophys. Res. Lett., 35, L01605, doi:10.1029/2007GL032419.

Determination of Coral Depth with Multispectral Imagery

Cho-Teng Liu [a], Hsiu-Jui Chen [a] and Li-Guang Leu [b]

[a] Institute of Oceanography, National Taiwan University, Taipei, Taiwan – liuchoteng@gmail.com
[b] Department of Oceanography, Naval Academy, Kaohsiung, Taiwan

Abstract: In the coral reef zone, nautical chart displays no detail of bathymetry. Multispectral image of Formosat-2 satellite was used to derive depths d of coral reefs, because the reflectance ratio of blue to green band depends mostly on the water depth. The major error is from surface wave that is reduced by including NIR band. From this 3-band (B/G/NIR) method, one may estimate coral depths up to 30 m.

Keywords: Formosat, multispectral, coral depth, reflectance

1. INTRODUCTION

The shipboard echosounder is used for measuring water depth. For remote or shallow region, it is not accessible to ships. The density of depth data from echo sounders is limited by the distance d between cruise tracks for single beam echo sounders, and by the ratio of depth h to d (h/d) for multi-beam echo sounders. It is acceptable for navigation purpose or for regions of smoothly varying sea bottom, but it is far from real bathymetry of coral reefs, e.g. south of Taiwan (Fig. 1). It is 100 times more complicate than what the nautical chart shows (Fig. 1c). In regions of homogeneous clear water, remote sensing method may be applied on distribution of water depth in a fast and safe manner. Because the scattering of light by air or water molecules is proportional to 4th power of frequency of light, we see blue sky above us, and blue water in the ocean. The intensity of visible light at depth z, $L(z)$, is attenuated exponentially in sea water. $L(z)$ may be represented as (Stumpf et al., 2003):

$$L(z) = L(0)\, e^{-k_d z} \qquad (1)$$

$L(0)$ is the light intensity just below sea surface (z=0), k_d is the attenuation coefficient. This relation may be used to estimate water depth, but this single-band method requires many empirical coefficients, is difficult to use and its accuracy is susceptible to the change of bottom material. The maximal applicable depth is about 15 m.

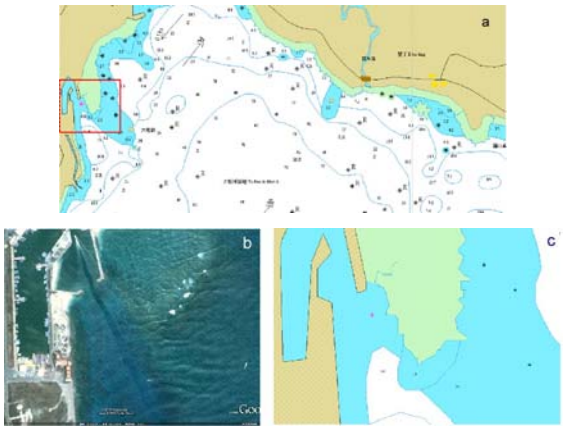

Fig. 1. (a) is a typical nautical chart, (b) is a image from Google Earth that shows abundance of knolls of coral that nautical chart (c) provides only three depth data.

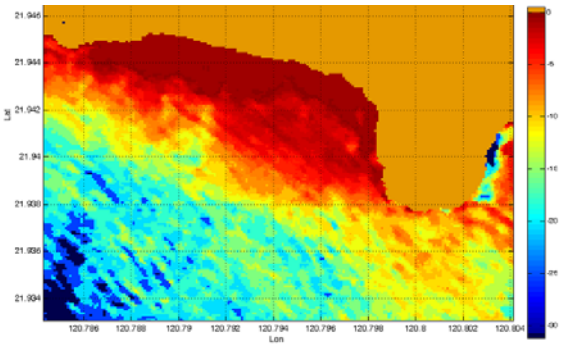

Fig. 2. Depth at southern tip of Taiwan, from single band method. Blue band was used for this single-band remote sensing of water depth. Brown color is land surface.

Leu (2004) applied a linear regression equation to derive the coral depths at southern tip of Taiwan. He found that three linear regression equations are needed for each of 0~10 m, 10~20 m and 20~30 m depths. Many observed data are required for regression analysis and the wave pattern in the estimated depths, like those in Fig. 2, can not be removed. Three-band method on remote sensing of water depth is proposed. The ratio of scattered blue light vs. green light is used to estimate the coral depth, the near IR (NIR) band is used to reduce swells' interference. This method eliminates the need of massive amount of in situ measured depth data for generating empirical equation, therefore, it has wider application with less constraints.

2. REGION OF STUDY AND DATA

The study region is off Kenting near southern coast of Taiwan in 21.9°~22°N, and 120.73°~120.8°E. Kuroshio branches into this region yearly around, and provides warm and clean sea water to coral reefs. The reef has a rugged bottom that discourages depth surveys. The available depth data is less than 1% of real depth changes. Level 1A Multi-spectral image of Formosat-2 at 10:09 local time of July 20, 2007 was used for this analysis. Radiative calibration and Geolocation correction were applied with ground control points. Total 606 depth data from multi-beam echosounder were compared with satellite-derived depth. Depth data range from 4m to 56 m, with horizontal distance 10 ~ 12 m. The in situ depth data were corrected for the tide, and the difference between the mean sea level and the mean lower low water level that was used in tidal analysis.

3. METHOD OF ANALYSIS

The remote sensing reflectance of the water just below sea surface (R_w^-) is defined (Stumpf et al., 2003):

$$R_{wi}^- = \pi\, L_{wi}^- / E_{di}^- \qquad (2)$$

R_{wi}^- is the reflectance of water body at wavelength λ_i, '-' means just below sea surface, L_{wi}^- is the upwelled radiance at λ_i band, and E_{di}^- is the downward solar irradiance at λ_i band. Atmospheric scattering includes Rayleigh

scattering (R_r) and aerosol scattering, where

$$R_r(\theta_d,\theta_v,\varphi) = \frac{\tau_R^{\lambda} P(\Theta)}{4\cos(\theta_d)\cos(\theta_v)} \quad (3)$$

θ_d is solar zenith angle, θ_v is satellite viewing angle, φ is the azimuth angle between the Sun and the satellite, τ_R^{λ}~0.235 for blue band□Θ is the scattering angle, and $P(\Theta)$ is the phase function, or the angular dependence of scattering coefficient. Fresnel reflectivity is about 2% for small incidence angle of skylight at sea surface. The incidence angle is the sum of θ_v and the tilt-away surface slope β. Near the coast, wave amplitude increases with shoaling effect, $\beta+\theta_v$ can be large to have increased Fresnel reflectivity on sky light at all bands of B/G/NIR. After subtracting the atmospheric scattering radiance, and radiance from surface reflectance and wave-induced reflectance, the radiance of B/G bands just below sea surface can be derived. The ratio of reflectance of B and G is used to estimate the water depth. The flow chart of data processing is shown in Fig. 3. The solar spectral irradiance reaching sea surface E_d^+ varies seasonally and it depends on the transmittance of the atmosphere and the incidence angle of sunlight at sea surface, $E_{di}^+ = E_{0i}\ T_{di}\ \cos(\theta_d)\ /r^2$, where E_{0i} is the annual mean solar irradiance at the top of atmosphere, '+' means above sea surface, r is the distance between the Sun and the Earth that varies seasonally, T_{di} is the transmittance of sunlight at λ_i band,θ_d is solar zenith angle that varies daily and seasonally.

$$L_s(IR) = L_c(IR) - L_\infty(IR) \quad (4)$$

L_∞ is the NIR radiance in the deep sea, and is nearly 2%, L_c is NIR radiance near the coast, and L_s is the swell-induced increase of NIR radiance. The increased reflectance can be computed with Eq.(2), same for B/G bands. The upward propagating radiance is composed of reflection of water body and of sea bottom:

$$\pi L_{wi}^- = E_{di}^- R_{\infty i}[1-e^{-2k_{di} z}] + E_{di}^- R_{bi} e^{-2k_{di} z} \quad (5)$$

where $R_{\infty i}$ is the reflectance at λ_i band from the water body in regions of optically deep, k_{di} is the attenuation coefficient at λ_i band, R_{bi} is the spectral reflectance at λ_i band from the sea bottom. Substitute Eq.(5) into Eq.(2), one can get the reflectance of water body at each pixel of the image:

$$R_{wi}^- = R_{\infty i}^- [1-e^{-2k_{di} z}] + R_{bi} e^{-2k_{di} z} \quad (6)$$

In deep zone ($k_{di}\, z >>1$), the reflection of sea bottom is too weak to be discernable from the noise of the data, $R_{wi}^- = R_{\infty i}^-$. Eq. (6) may be rewritten into Eq.(7) to derive water depth:

$$R_{wi}^- - R_{\infty I} = [R_{bi} - R_{\infty i}]\, e^{-2k_{di} z} \quad (7)$$

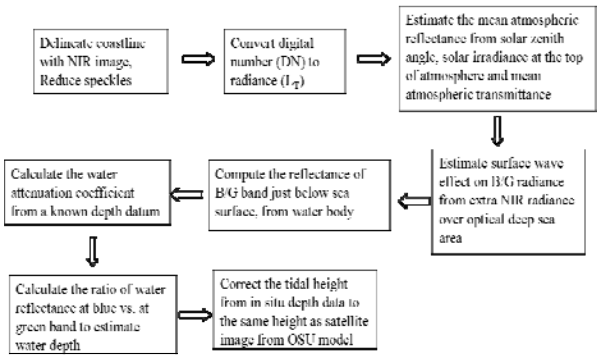

Fig. 3. Flow chart of data processing.

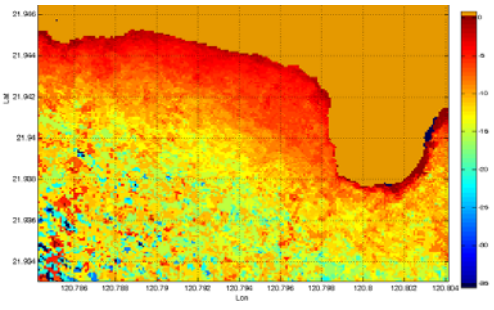

Fig. 4. Like Fig. 1, except depths are from 3-band method.

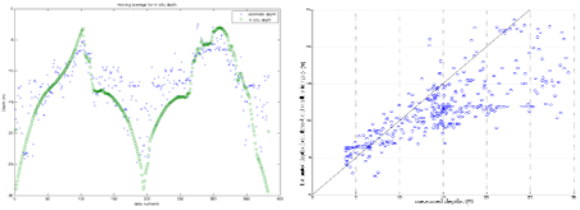

Fig. 5. Estimated coral depths (blue x) from 3-band satellite data against in situ water depths (green circle), (a) along track, (b) satellite-derived depth underestimates real depth.

The influence on underwater spectrum is more by water depth, than by type of bottom material (Lubin et al., 2001). Coral depth may be derived from Eq. (7):

$$z = \frac{1}{2(k_{di} - k_{dj})} \ln\left[\frac{(R_{wi} - R_{\infty i})}{(R_{bi} - R_{\infty i})}\frac{(R_{bj} - R_{\infty j})}{(R_{wj} - R_{\infty j})}\right] \quad (8)$$

i and j are for spectral bands λ_i *and* λ_j, namely B/G bands. From a few known depths in the satellite image, one may derive the attenuation coefficients for B/G bands.

4. RESULT AND DISCUSSION

The estimated coral depths of southern Taiwan are in Fig. 4. Isobaths are mostly parallel to the coast. The detectable water depth was up to 35 m. These depths were compared to 394 in situ measured depth in the range of 1-35 m, as shown in Fig. 5. In general, the estimated depth is shallower than the measured depth with correlation coefficient 0.768 for 0~30 m depth range, as shown in Fig. 5b. This is due to larger optical weight from shallower part of a pixel.

5. CONCLUSIONS

Remote sensing of coral depths gives far more details than nautical charts. Single band method requires many data for regression relation and it works to about 15 m. Two-band (B/G) method can see deeper but may be contaminated heavily by swells. Three bands (B/G/NIR) can reduce wave effect and the SD is ~15% of the mean depth, up to 35 m.

REFERENCES

Leu, L.G., 2004: Application of Quickbird image on water depth analysis around Kenting. J. of CSPRS, **9**, 23 – 42.

Lubin, D., W. Li, P. Dustan, C. Maxel and K. Stamnes, 2001: Spectral signatures of coral reefs: Features from space. *Remote Sens. Environ*. **75**, 127-137.

Stumpf, R. P., K. Holderied and M. Sinclair, 2003: Determination of water depth with high-resolution satellite imagery over variable bottom types. *Limnol. Oceanogr.*, **48** (1, part 2), 547-556

New Low Cost Technological Developments for Sea Monitoring: Satellite "Sea Truth" and Model Validation

M. Marcelli, V. Piermattei, A. Petri, A. Madonia, A. Pannocchi, U. Mainardi

[a] Laboratory of Experimental Oceanology and Marine Ecology of University of Tuscia Viterbo Italy – marcomarcell@unitus.it

Abstract - Operational forecasting is becoming an important tool for modern management and protection of the oceans and their living resources. It needs multidisciplinary input data, whose collection is hampered by two main factors: cost and technology. Satellites provide synoptic sea surface data, but their measurement validation still requires much sea-truth data as possible. Moreover marine "in situ" measures are expansive both for the platforms, ships and buoys, and for the measure instruments. In order to face these problems, initiatives (e.g. VOS) have been developed to use opportunity platforms and to promote the development of low-cost and user-friendly technologies. This work shows new cost-effective technological developments to provide a useful strategy for surface and sub-surface marine monitoring.

Keywords: sea-truth, low-cost technology, fluorimeter, model validation.

1. INTRODUCTION

According to WMO and IOC of UNESCO guidelines, the World Operational Oceanography, has promoted VOS development which uses platforms of opportunity as an alternative to research vessels, allowing more data to be acquired with high spatial and temporal coverage and with considerable costs reduction. Physical and biological processes of the marine ecosystem have a high spatial and temporal variability, whose study is possible only through high resolution and synoptic observations. Satellite remote sensing provides a unique synoptic view of phenomena such as chlorophyll concentration and sea surface temperature, but the measurement validation requires constant scrutiny and much sea-truth data as possible; for this reason the integration between field sampling and remote sensing technique should be improved also for the development of ecosystem and pollution forecasting models (NASA Goddard Earth Science Data Information Services Center). Therefore the oceans and coastal waters monitoring has to be cost-effective, modular, combining low cost "in situ" sensors with remote sensing and operational forecast. There is no way to quantify model performance without comparing the output to in situ data. When asked what is needed to improve model performance, all model developers coincide in requesting more data, ideally to get her with ancillary data such as nutrients and community structure (Carr et al., 2005). For this fundamental reason we have developed new low cost and user friendly technologies: T-FLAP (Temperature-Fluorescence-LAunchable Probe), Eco-BluBox and SAVE (Sliding Advanced Vehicle). T-FLAP (Marcelli *et al.*, 2007) is a low cost expendable probe developed for VOS in the MFSTEP project (Patent N.07425096.0) able to measure temperature and fluorescence of chl "a" along the water column. The autonomous Eco-BluBox device was developed to measure in-continuous temperature, conductivity and fluorescence of sea surface. SAVE is a system that slides along a towed electromechanical cable from upper to deeper waters providing continuous profiles of physical and optical measurements. Low cost and high automation features represent an important solution compared to what is currently. Instruments main objectives are self operating and opportunity ship availability to provide a great amount of data, suitable to calibrate satellite data (sea truth) and to be assimilated into numerical models.

2. TECHNOLOGICAL DEVELOPMENTS

Both T-FLAP and EcoBluBox measurement system is represented by a tube where the water flows in the inside: in the internal part of the tube are fixed the sensors which are in direct touch with water, while on the external part of the tube are placed the batteries and the electronics. Temperature Fluorescence and Conductivity signals are managed by a digital electronic system which can be improved and adapted to other several variables measure channels. SAVE platform is composed by a depressor, at fixed depth, towed by a surface unit and an instrumented vehicle, that slides along a cable from the surface to the bottom.

2.1. T-FLAP

This expendable probe (Figure 1) estimates Chlorophyll "a" fluorescence and water temperature until a depth of 350 m. It has a transmission system and a shape developed in order to allow its use from moving ships. The probe is able to detect the deep chlorophyll maximum (DCM), and to measure temperature through a high accuracy and a very low-cost glass bulb microsensor (0.01 °C).

Figure 1. T-Flap

2.2 Eco-BluBox

Eco-BluBox instrumental system, developed for Sailing VOS Project, is a low cost multiparametric improvement of T-FLAP technology. As seen in Figure 2, EcobluBox is formed by a portable unit containing a probe (measure unit) to measure sea-surface temperature, salinity and chlorophyll "a" fluorescence. It also contain a battery pack, a GPS interface, and a pump to drive sea-surface water into

the measure cell. Its autonomous functioning allows to adapt it on a large variety oceanographic measure platforms, while the GSM/GPRS communication system provides a quasi real-time and synoptic data acquisition. In addition to the standard T-FLAP sensors, Eco-BluBox is implemented with an *ad hoc* developed conductivity sensor. It consists of four platinum rings located at the end of the measure unit.

Figure 2. Eco-BluBox

2.3 Sliding Advanced Vehicle (SAVE)

SAVE is a new Sliding Advanced Vehicle, as seen in Figure 3. The aim of SAVE implementation is to resolve the scales of the marine processes. SAVE was designed to carry out detailed and rapid profiles, in order to have quasi-synoptic measures of physical and biological variables. The depressor was designed to work max 200m deep and between 2 and 8 knots speed. The depressor lodges a miniature pressure transducer, a biaxial inclinometer and a data acquisition board, in order to control the behavior during the navigation. The SAVE vehicle is constituted by an instrumented pressure cylinder; the guide system is located on the front side of the vehicle and is composed by pulleys connected to the cable.

Figure 3. Sliding Advanced Vehicle (SAVE)

3. RESULTS

Field tests and data analysis have confirmed the expected sensors accuracy and the user friendly operating protocols. Prototypes were tested in different oceanographic surveys: MedGOOS11 Southern Tyrrhenian Sea on November 2005 and ADR02 in Adriatic Sea on October 2008. In succession an example of the profiles shows a comparison between T-FLAP sensors and CTD profile. As seen in Figure 4, the first graph is an example that shows a comparison between fluorescence profiles, blue T-FLAP (converted in chlorophyll “a” with the calibration equation), green SCUFA by Turner Design . The second graph describes a comparison between temperature profiles, blue TFLAP (converted in temperature with the calibration equation), red SBE 911 probe. Eco-BluBox was tested in July 2008 in the Tyrrhenian Sea and on July 2009 from Alghero to Palma de Mallorca. As seen in Figure 5, trajectories are shown via sea surface temperature data.

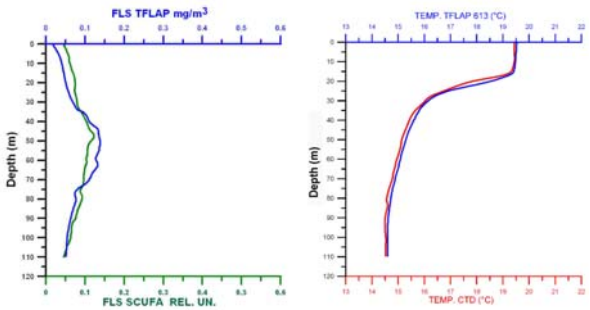

Figure 4. Comparison of T-FLAP and reference probes

3. CONCLUSIONS

These developments want to represent a contribution for an overall monitoring strategy to characterize high space and time variability phenomena. The low cost and user friendly features, together with a good sensors accuracy give these new instruments a key role in the future of operational oceanography. Developments presented in this work are charted in order to answer to the claim of cost effectiveness instruments able to face the problems of remote sensing sea truth, model validation and synopticity. Also, they aim to be the technological base for future satellite data calibration.

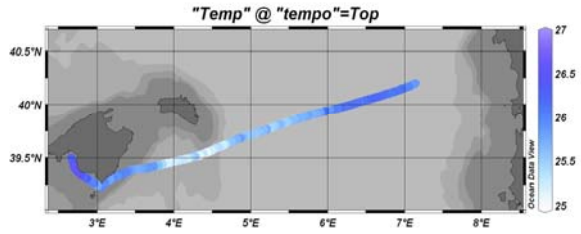

Figure 5. Eco-BluBox trajectories

ACKNOWLEDGEMENTS

Thanks are due to Prof.ssa N. Pinardi and to Ing. G. M. R. Manzella for their support to this work.

REFERENCES

M. Marcelli, A. Di Maio, D. Donis, U. Mainardi, and G. Manzella (2007). “Development of a new expendable probe for the study of the pelagic ecosystems from Voluntary Observing Ships”. Ocean Science, Vol. 3, no. 2, pp. 311-320.

Carr, M.-E., Friedrichs, M. A. M., Schmeltz, M., Ait´e, M. N.,Antoine, D., Arrigo, K. R., Asanuma, I., Aumont, O., Barber,R., Behrenfeld, M., Bidigare, R., Buitenhuis, E., Campbell, J.,Ciotti, A., Dierssen, H., Dowell, M., Dunne, J., Esaias, W.,Gentili, B., Groom, S., Hoepffner, N., Hishisaka, J., Kameda,T., LeQu´er´e, C., Lohrenz, S., Marra, J., M´elin, F., Moore, K.,Morel, A., Reddy, T., Ryan, J., Scardi, M., Smyth T., Turpie,K., Tilstone, G., Waters, K., and Yamanaka, Y.: A comparison of global estimates of marine primary production from ocean colour, Deep-Sea Res., Part II, 53, 741–770, 2005.

Ship Monitoring Service Based on Fusing EO SAR Images with Collaborative Polls

G. Margarit, A. Tabasco, C. Gómez Cid

GMV Aerospace, S.A.U. (SEOPS Business Unit), Barcelona, Spain – gmargarit@gmv.com

Abstract – This paper presents the Ship Monitoring Service (SIMONS) developed by GMV to tackle the problem of ship monitoring according to the requirements fixed by Spanish users. EO SAR images and collaborative polls (i.e. Automatic Identification System (AIS)) are merged together to provide advanced ship detection and categorization plus a set of added-value features, such as alarm triggering. A user-friendly web interface based on Open Geospatial Consortium (OGC) standards is adopted for data dissemination. This option permits the provision of most of the tools related to map data handling, but without restrictive software and hardware needs at user side. The paper describes the most important modules in SIMONS as well as some testing results with ENVISAT images.

Keywords: ship monitoring, SAR, AIS, OGC.

1. INTRODUCTION

In the last years, authorities have become aware about the necessity to enforce maritime law regulation. The increasing world population is putting intense pressure on ocean areas, over-consuming its resources and endangering a complex and fragile ecosystem. One main hot spot is overfishing as most of fishing grounds are currently close to their top sustainable production. In addition, the percentage of goods transported by sea is increasing and this puts the security of the balanced transportation corridors at risk.

The surveillance of ship activities is one important item in maritime regulation. Current vessel monitoring techniques include cooperative sensors, optical remote sensing, acoustic sensors or Inverse SAR (Inverse SAR) imagery. The lessons learnt in real scenarios have shown that none of these techniques, alone, is sufficiently effective. Main limitations are the high influence of the observation conditions and the lack of tracking autonomy and independence, especially for cooperative transponders.

For such purpose, EC has promoted a series of projects trying to provide insights about the future (technological) steps needed in ship monitoring. Among them, MARISS has been one of the last calls, which success has allowed the promotion of a scaling-up phase. There, the development of operational services that integrate cooperative polls (i.e. AIS) with layers of information derived from SAR image post-processing was the main concern. The experience has shown that SAR is a key information channel that provides 7/24 operation capability with independence from the targets to track. It also permits the development of some added-value products as coastline detection, ship detection and classification, alarm triggering and route propagation.

The result of all this effort has been the development of some operational monitoring services. Example is SIMONS, which is the solution conceived by GMV for Spanish users [Margarit 2009]. SIMONS is a service dealing mainly with SAR and adopting AIS as a supporting channel. The second version has been recently released and it uses state-of-the-art SAR-based techniques for land masking, ship detection and ship classification. It also includes key added-value features, such alarm triggering based on cross-checking AIS versus SAR information. Service interface is based on OGC web standards, which permit the provision of most of map utilities without heavy software and hardware demands at user side. The paper will present the most important details of the service, the key SAR processing steps and the dissemination web interface. Some tests performed with ENVISAT images that probe detection and classification performance are also described. The results show that, with medium resolution SAR images (30 m), ship detection has a false alarm ratio no larger than 5% with a positive classification ratio close to 60 %.

2. SIMONS SYSTEM OVERVIEW

The following figure presents SIMONS high-level scheme. Processing flow is from up to down. Four main stages are differentiated, namely: Input data Streams, Information Extraction, Value Addition and Product Generation.

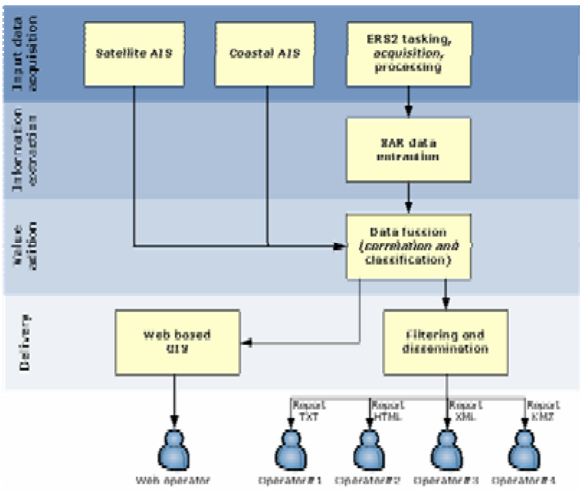

Figure 1. High level scheme of the SIMONS system

3. MAIN KERNEL PROCESSING MODULES

The main kernel processing modules are: land masking, ship detection, ship classification and AIS cross-check. Following, they are briefly described.

3.I Land Masking

Land masking is performed by applying a reflectivity gradient variance analysis plus morphological processing. Shape files support final result if detection confidence is low. This module is being improved with a new approach based on Wavelets and Geodesic Active Contours (GAC).

3.2 Ship detection

Ship detection is performed with the Wavelet Transform (WT) [Mallat 1998]. The idea is to properly combine the

different products among the scales to provide advanced morphological analysis that isolates particular features. This is the case of ships that present a marked coherent response in contrast to the noise-like incoherent behaviour of the sea. Advantages of this method are simplicity, no need of fine thresholding, more sensitivity to close targets and the possibility to compute a detection confidence parameter.

3.3 Ship Classification

Ship classification analyzes the RCS profile throughout the radar signature. Two main blocks are identified: Parameter Retrieval and Fuzzy Logic (FL) Processing [Tanaka 2007]. The first block aims to estimate the values of a parametric vector that characterizes the geometrical structure of ships, whereas the second one correlates this vector with a set of reference ones via FL. This approach also permits the calculation of a classification confidence parameter.

3.4 AIS-SAR Cross-Checking

This module groups the AIS polls acquired for the area covered by the SAR image in terms of the monitored ship to derive route tracks. In addition, it compensates error location due to the shifts caused by Doppler effects and the low number of polls that some tracks can have.

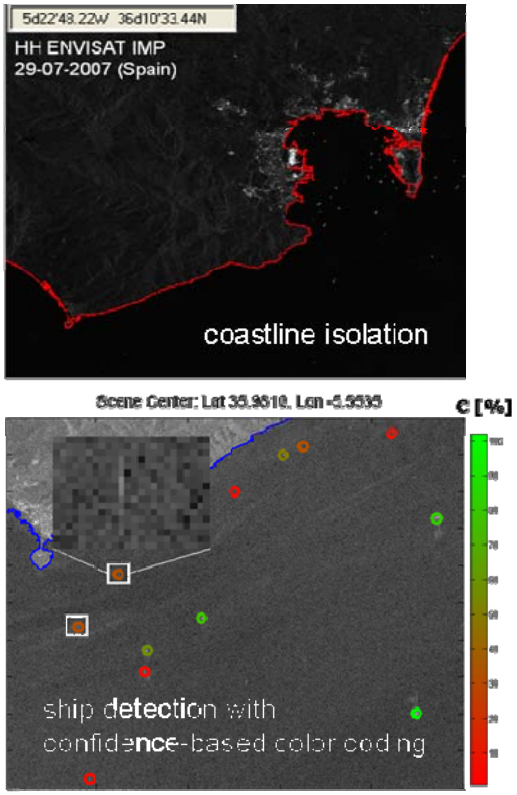

Figure 2. Example of automatic coastline isolation and ship detection applied in the Strait of Gibraltar (ENVISAT data).

4. SYSTEM INTERFACE

System interface is a web-based GeoPortal following the concept of Spatial Data Infrastructure (SDI). The result is a platform that integrates several state-of-the-art technologies and components, such as web services, geospatial and thematic databases, GIS clients, graphical utilities for cross-checking, dissemination and information. The service is modular and scalable in the sense that complexity and functionality can be increased according to new needs.

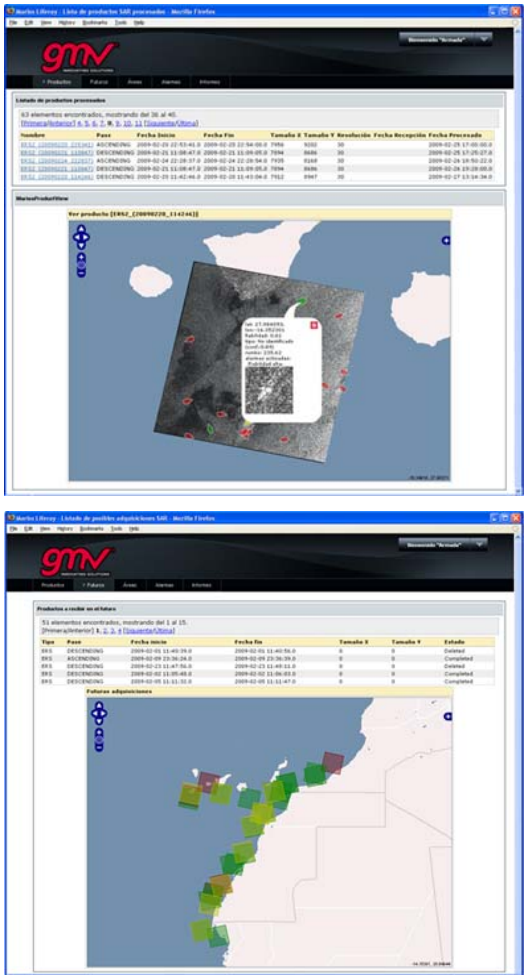

Figure 3. Web System interface snapshots based on SDI.

5. CONCLUSION

This paper has presented an operational ship monitoring approach that combines the information obtained from AIS polls and SAR image processing. A state-of-the-art web interface supports output presentation with alarm triggering, user profile definition and interactive ship info display. In addition, proper land masking, accurate ship detection and reliable ship classification is available for an algorithm that meets NRT requirements. The system is fully operational, reliable and unsupervised, and end-users have found it useful for supporting decision making in immigration and ship management activities.

ACKNOWLEDGEMENTS

The authors want to thank the support of Spanish users (Guardia Civil & Spanish Navy) in SIMONS development.

REFERENCES

[1] Margarit, G. et al, "Operational Ship Monitoring System based on Synthetic Aperture Radar Processing", Special Issue on Microwave Remote Sensing, Remote sensors, **2009,** *1*(3), 375-392; doi: 10.3390/rs1030375.

[2] Mallat, S.A. *Tour of Signal Processing*. Academic Press Inc.: Burlington, MA, USA, **1998**.

[3] Tanaka, K. *An Introduction to Fuzzy Logic for Practical Applications*. Rassel Inc.: New York, NY, USA, **2007**.

Influence of climate and environmental variability on phytoplankton dynamics in the spring reproductive area of *Engraulis anchoita* (Southwestern Atlantic Ocean)

M. Marrari [a], S. Signorini [a], C. McClain [a], M. Pájaro [b], M.D. Viñas [b,c], R. DiMauro [b,c], G. Cepeda [b,c,d]

[a] NASA Goddard Space Flight Center, Greenbelt, United States – marina@seawifs.gsfc.nasa.gov
[b] Instituto Nacional de Investigación y Desarrollo Pesquero, Mar del Plata, Argentina
[c] Consejo Nacional de Investigaciones Científicas y Técnicas, Mar del Plata, Argentina
[d] Centro Estudios Biodiversidad y Biotecnología, Fundación Investigaciones Biológicas Aplicadas, Mar del Plata, Argentina

Abstract –The main spring reproductive area of the Argentine anchovy, *Engraulis anchoita* includes a coastal thermal front established in the vicinity of the 50m isobath characterized by elevated spring phytoplankton abundances. We use a 12-year time series of SeaWiFS ocean color data to investigate chlorophyll dynamics in relation to climate and other environmental influences. During spring, chlorophyll concentrations were most influenced by the Southern Annular Mode (SAM) and sea surface temperature (SST), with negative phases of SAM and colder surface waters resulting in above-average chlorophyll *a* concentrations. In addition, interannual variability in chlorophyll *a* concentrations had a significant effect on zooplankton populations and reproductive success of *E. anchoita*. We discuss the mechanisms by which large scale climate phenomena may influence local populations in the Southwestern Atlantic Ocean.

Keywords: SeaWiFS, climate, Atlantic Ocean

1. INTRODUCTION

The Southwestern Atlantic Ocean (SWA), from coastal waters off Brazil to the southern areas of the Patagonian continental shelf is an area of complex circulation and dynamic processes, influenced by strong tidal cycles, the interaction of the Malvinas and Brazil currents, and several frontal systems characterized by elevated spring chlorophyll concentrations. Between 34 and 55°S, a variety of fronts can be identified (Acha et al., 2004), some of which are important reproductive grounds for fish of ecological and commercial importance.

On the continental shelf off Buenos Aires province, a thermal front, the Buenos Aires Coastal Front (BACF), is usually established in spring in the vicinity of the 50m isobath, separating mixed coastal waters from vertically stratified shelf waters (Fig. 1). This coastal front is an important reproductive area for *Engraulis anchoita*, which is the main pelagic fish in the area and the subject of a potentially significant fishery in the SWA. In this region, the continental shelf is influenced by the discharge of the Rio de la Plata, as well as the Negro and Colorado rivers, which supply a significant volume of freshwater to coastal areas. Previous studies have linked warm El Niño events to increased precipitation and abnormally high discharge of the Rio de la Plata, Negro, and Colorado rivers, with important ecosystem implications (Isla, 2008; Piola *et al.*, 2005; Scarpati *et al.*, 2001). The Southern Annular Mode (SAM), a zonally-symmetric atmospheric phenomenon characterized by a gradient in mean sea level pressure between 40 and 65°S, is the most important mode of variability in the Southern Hemisphere and has been associated to increased westerly winds in the Southern Ocean and a faster Antarctic Circumpolar Current (Lubedunski and Gruber 2005), which can have a strong impact on the biology of the region. However, its influence on the circulation and biology of the SWA, particularly the spring spawning area of *E. anchoita*, has not yet been investigated. Here, we examine variability in phytoplankton dynamics at the BACF in relation to climatic and other environmental influences, and we investigate the effects on abundance of zooplankton and larvae of *E. anchoita*.

2. METHODS, DATA SETS, AND RESULTS

2.1 Methods

The study area included continental shelf waters off the Buenos Aires province in the SWA (Fig. 1). Based on preliminary observations, a subregion including the most predictable location of the BACF was defined and chlorophyll *a* concentrations were obtained from SeaWIFS Level 2 data between September 1997 and December 2006 (2 km pixel^{-1}, 5-day composites, OC4v4 algorithm). A median chlorophyll *a* concentration was calculated at the subregion for each 5-day period and a time series was generated. In addition, a 12-year time series (1997-2009) of median chlorophyll *a* concentration was obtained from Level 3 data (9km pixel^{-1}, monthly composites). Monthly mean SST data from AVHRR Pathfinder also were obtained for the BACF. Time series of monthly ENSO (NOAA CPC) and SAM indices (http://www.atmos.colostate.edu/ao/Data/) were analyzed. Discharge volumes for the Rio de la Plata, Negro, and Colorado rivers were provided by Subsecretaría de Recursos Hídricos (Argentina).

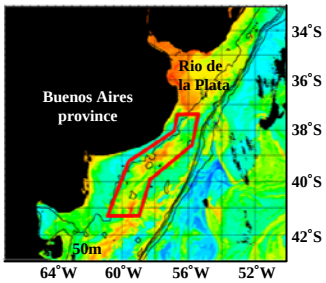

Figure 1. Example of distribution of chlorophyll *a* concentrations (mg m^{-3}) in October (1999) in the study area, and location of the Buenos Aires Coastal Front (red).

Zooplankton and ichthyoplankton net samples were collected over the continental shelf of the Buenos Aires province during 7 cruises in October of 1999, 2001, 2002, 2003, 2004, 2006, and 2008. PairoVET (200 µm) and Minibongo (67 and 200 µm) samples were obtained at multiple stations. Total copepods were counted and examined as a proxy for zooplankton abundance. In

addition, all eggs and larvae of *E. anchoita* were identified and enumerated.

2.2 Summary of results

Chlorophyll *a* concentrations at the BACF were highest during austral spring (October - November) and lowest in summer (February - March). The 10-year time series showed strong interannual variability, with several years characterized by higher than average chlorophyll *a* concentrations (1997, 2000, 2002, 2003) and others with only below-average values (1998, 2005). Maximum chlorophyll *a* concentrations occurred in October 2003, with a median value of 6.35 mg m^{-3}. Chlorophyll *a* concentrations were negatively correlated with SST at the BACF (r=-0.57, p=0.02) and SAM index with a 1-month lag (r=-0.26, p=0.01) (Fig. 2). In general, above-average chlorophyll *a* concentrations were associated with negative phases of SAM and colder surface waters. ENSO and freshwater discharge from the Rio de la Plata, Negro, and Colorado rivers had no significant influence on phytoplankton dynamics at the front.

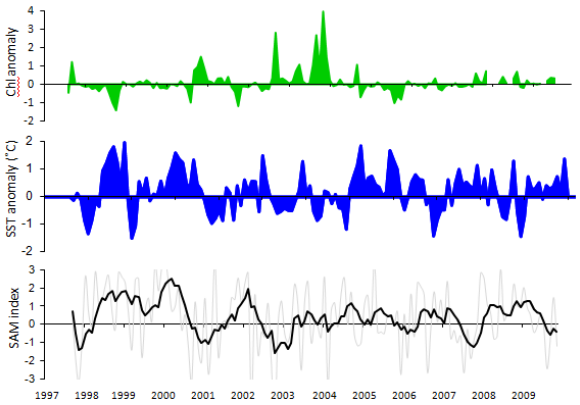

Figure 2. Time series of chlorophyll *a* concentration anomalies at the BACF, SST, and monthly SAM index.

Zooplankton aggregated at the front, with higher abundances at the BACF relative to other areas of the continental shelf. Annual mean copepod abundances were highest during years of above-average spring chlorophyll *a* concentrations (i.e. 2002 and 2003). In addition, densities of larvae of *E. anchoita* during October were negatively correlated with SST and SAM index in September, with years of negative phase of SAM and colder SST resulting in higher larval abundances (Fig. 3).

2.3 Discussion

SAM influenced variability in chlorophyll *a* concentrations at the BACF. During positive phases of SAM, westerly winds at ~55˚S strengthen, which leads to increased northward Ekman transport in the Polar Front Zone, north of 55˚S. On the other hand, the dominant easterlies at mid-latitudes result in southward Ekman transport in the Subtropical Zone, south of ~35˚S. The convergence of these two increase downwelling on the Patagonian shelf between 35-55˚S, resulting in warmer surface waters, stronger stratification, and reduced nutrient supply to the surface (Lobedunski and Gruber, 2005). We hypothesize that during negative phases of SAM, weaker westerlies lead to reduced downwelling in this area, resulting in colder SST and increased vertical mixing. The supply of colder nutrient-rich water to the surface would explain the above-average concentrations of chlorophyll *a* observed during negative phases of SAM.

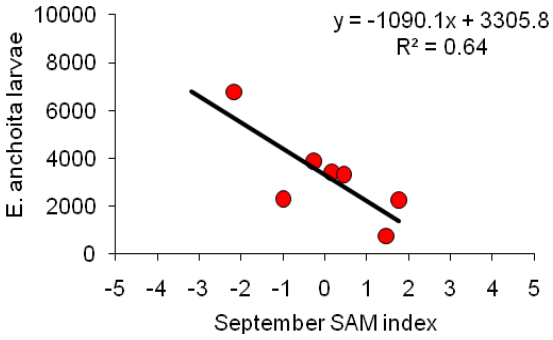

Figure 3. Abundance of larvae of *E. anchoita* (ind 10 m^{-2}) in October vs. September SAM index.

3. CONCLUSIONS

Chlorophyll *a* concentrations at the BACF between 1997 and 2009 showed strong seasonality, with maxima in spring when shelf waters stratify and nutrient and light conditions are favorable, and minima in late summer, when nutrients become depleted. SAM and SST influenced chlorophyll *a* dynamics, whereas ENSO and freshwater input had no significant effects. Periods of increased chlorophyll *a* concentrations were associated with abundant zooplankton, which represent an increased food supply for fish larvae. Thus, variability in large-scale climate phenomena can influence local populations through changes in nutrient supply to the surface.

ACKNOWLEDGEMENTS

We thank Drs Alberto Piola and Raul Guerrero for providing river discharge data, and John Wilding for helping with SeaWiFS data processing. This work was supported by NASA Postdoctoral Program to M.M. and Oak Ridge Associated Universities.

REFERENCES

Acha, E.M., Mianzan H.W., Guerrero, R.A., Favero, M. and J. Bava (2004). “Marine fronts at the continental shelves of austral South America. Physical and ecological processes”. Journal of Marine Systems, 44, 83-105.

Isla, F.I. (2008). “ENSO-dominated estuaries of Buenos Aires: the interannual transfer of water from western to eastern South America. Global and Planetary Change, 64, 69-75. Lubedunski, N.S. and N. Gruber (2005). “Impact of the Southern Annular Mode on Southern Ocean circulation and biology”. Geophysical Research Letters, 32, L11603.

Piola, A.R., Matano, R.P., Palma, E.D., Moller, O.O. and E.J.D. Campos (2005). “The influence of the Plata River discharge on the western South Atlantic shelf”. Geophysical Research Letters, 32, L01603, doi:10.1029/2004GL021638.

Scarpati, O.E., Spescha, L., Fioriti, M.J., and A.D. Capriolo (2001). “El Niño driven climate variability and drainage anomalies in Patagonian region, Argentina”. Cuadernos de Investigación Geográfica, 27, 179-191.

SAR Altimetry over Water Surfaces

C. Martin-Puig [a,*], O.B. Andersen [b], P.A.M. Berry [c], P. Cipollini [d], D. Cotton [e], C. Gommenginger [d], G. Ruffini [a], L. Stenseng [b], J. Benveniste [f], S. Dinardo [c]

[a] Starlab Barcelona S.L., Barcelona, Spain – cristina.martin@starlab.es
[b] DTU Space, National Space Institute, Copenaghen, Denmark
[c] De Montfort University, Leicester, UK
[d] National Oceanography Centre, Southampton, UK
[e] Satellite Oceanographic Consultants, Bramhall, UK
[f] European Space Agency, ESRIN, Frascati, Italy

Abstract – This poster aims to present an overview of the main results achieved by the ESA SAMOSA project. The poster will describe advanced processing techniques and retracking techniques to assess the performance of SAR altimetry over water surfaces.

Keywords: SAR altimeter, delay-doppler altimeter, CryoSat-2, Sentinel-3.

1. INTRODUCTION

The use of Synthetic Aperture Radar (SAR) techniques in conventional altimetry—i.e., Delay Doppler Altimetry (DDA)—was first introduced by R.K. Raney in 1998 [1]. This technique provides an improved solution for water surface observations due to two major innovations: the addition of along track processing for increased resolution, and multi-look processing for improved SNR. Cryosat-2 (scheduled for launch Feb. 2010) will be the first satellite to operate in SAR altimetry mode (a.k.a DDA mode). Although its main focus will be the cryosphere, this instrument will also be sporadically operative over water surfaces, thus provide an opportunity to test and refine the improved capabilities of DDA.

This poster will present an overview of the main results achieved by the ESA SAMOSA project. SAMOSA stands for "Development of SAR Altimetry Studies and Applications over Ocean, coastal zone and inland waters". For this study the SAMOSA consortium has developed new theoretical models and analyzed new processing techniques to assess the performance of DDA over water surfaces. These include the development of a new re-tracker.

The work presented here is of interest to the ESA's Sentinel-3 mission. This mission will be devoted to the provision of operational oceanographic services within Global Monitoring for the Environment and Security (GMES), and will include a DDA altimeter on board.

2. QUANTITATIVE COMPARISON OF LRM AND SAR(DDA) MODE OVER WATER SURFACES

Cryosat-2´s altimeter (SIRAL) has three operating modes: the Low Resolution Mode (LRM), the SAR mode and the inSAR mode. The first two are of interest for the quantitative comparison of conventional altimetry and SAR altimetry over water surfaces.

In LRM the altimeter performs as a conventional pulse limited altimeter (PRF of 1970 Hz); in SAR mode the pulses are transmitted in bursts (64 pulses per burst). In the last, correlation between echoes is desired [1], thus the PRF within a burst is higher than in LRM (PRF of 17.8 KHz). After transmission the altimeter waits for the returns, and transmits the next burst (burst repetition frequency of 85.7 Hz). The previous acquisition modes will provide different data products: level 1 or full bit rate data (FBR), level 1b or multi-looked waveform data, and level 2 for evaluation or geophysical products. The work presented under this section is only addressing L1b data from LRM and FBR data for SAR mode. In LRM the L1b data corresponds to echoes incoherently multi-looked on-board the satellite at a rate of ~ 20Hz, while in SAR mode FBR corresponds to individual complex echoes (I and Q), telemetered before the IFFT block [2]. Given that CryoSat-2 operational modes are exclusive, one task within SAMOSA aims to reduce SAR FBR data such that it emulates LRM FBR data allowing for the quantitative comparison of the measurement precision over identical sea state.

3. SAR ALTIMETER RETRACKER

The SAMOSA team has defined a waveform model, in the same spirit set by conventional altimeters [3, 4]. This waveform model is the basis of new re-tracking method for water surfaces that accounts for SAR altimeter observations. This poster will present the performance of this retracker over water surfaces.

To analyze the performance different studies were carried on a series of open ocean, coastal and in land water scenarios modeled by the CryoSat-2 Mission Performance Simulator (CRYMPS).

4. INLAND WATER

Complex and intricate echo shapes are returned from inland water surfaces, especially from rivers and wetlands. The EnviSat Individual Echoes have given a glimpse into the improvement in inland water measurements that could be obtained from the enhanced

* Corresponding author.

along-track sampling of the next generation of satellite radar altimeters. Realistic scenarios have therefore been prepared for the CRYMPS simulator for inland water targets, including lakes, river systems, wetland and estuarine components, and both SAR 20Hz and SAR FBR output waveforms have been analyzed and retracked, giving a valuable insight into the enhanced measurement capability over inland water and the coastal zone available with a higher PRF.

ACKNOWLEDGEMENTS

The authors of this paper would like to acknowledge Dr. Keith Raney (JHU/APL) for his animated discussions, comments, and creative suggestions. Furthermore, we would like to acknowledge the CRYMPS team for their support.

REFERENCES

[1] R.K.Raney, The Delay/Doppler Radar Altimeter, IEEE Trans. Georsci. Remote Sensing, vol. 36, pp. 1578–1588, Sep 1998.

[2] CryoSat Mission and Data Description, Doc No. CS-RP-ESA-SY-0059, 2007.

[3] Brown, G.S., The Average Impulse Response of a Rough Surface and Its Applications IEEE Trans. Antennas Propag., vol. AP-25, pp. 67-74, Jan.1977.

[4] Hayne, G.S. , Radar Altimeter Mean Return Waveform from Near-Normal-Incidence Ocean Surface Scattering IEEE Trans. Antennas Propag., vol. AP-28, pp. 687-692, Sep. 1980

A Preliminary In-Situ Investigation of the Living Sources of Optical Particulate Backscattering in the Open Ocean

V. Martinez-Vicente *, G.H. Tilstone, S. Sathyendranath, P.I. Miller, S.B. Groom

Plymouth Marine Laboratory, Plymouth , UK – vmv@pml.ac.uk

Abstract – This study explores the role of living organisms in producing the optical backscattering signal in the open ocean. Preliminary results from in-situ optical backscattering and phytoplankton counts using flow cytometry, reveal that a large part of the particulate backscattering (b_{bp}) signal variation can be explained by phytoplankton between 2 and 20 µm (nanoplankton). Further, the agreement between in-situ b_{bp} and re-constructed b_{bp} using only phytoplankton support this point. Although a significant part of the b_{bp} variability remains unexplained, these findings point to a larger than expected phytoplankton contribution to b_{bp}, which may affect the way primary production is computed from space.

Keywords: backscattering, phytoplankton, open ocean.

1. INTRODUCTION

The sources of marine optical particle backscattering (b_{bp}) need to be clarified (Stramski *et al.*, 2004) particularly if b_{bp} is to be used as a proxy for phytoplankton carbon in satellite algorithms of primary production (Behrenfeld *et al.*, 2005). Relationships between chlorophyll-a content (Chl-a) and b_{bp} can be found in the literature (Morel *et al.*, 2001; Huot *et al.*, 2008). According to scattering models (Stramski *et al.*, 2001), bacteria are the most efficient backscatterers of all the living organisms. However, the contribution of bacteria to b_{bp} is limited, leaving a portion of b_{bp} un-explained ('missing backscattering' (Stramski *et al.*, 2004)). It has been hypothesized that small non-living particles, that co-vary with phytoplankton (i.e. detritus), can be responsible for this 'missing backscattering'. The aim of this study is to relate the variation of b_{bp} to living organisms in the open ocean, using a dataset in which the range of variability in Chl-a is small, but variations in the abundance of variatious phytoplankton types and bacteria are high, such that their roles on the variation of b_{bp} can be discerned.

1.1 Backscattering contributors

Similarly to attenuation and scattering (Durand *et al.*, 1996), the contribution to b_{bp} from different organisms can be described by:

$$b_{bp} = \sum_{i=1}^{n} b_{bp,i} = \\ = \sum_{i=1}^{7} C_i \sigma_{bbpi} = \\ = C_{BACT}\sigma_{bbpBACT} + C_{PROC}\sigma_{bbpPROC} + C_{SYN}\sigma_{bbpSYN} \\ + C_{PICO}\sigma_{bbpPICO} + C_{NANO}\sigma_{bbpNANO} + C_{CRYP}\sigma_{bbpCRYP} + C_{COCCO}\sigma_{bbpCOCCO} \quad (1)$$

where C_i is the number concentration (in m^{-3}) for each type of plankton particle (i), detected by flow cytometry; bacteria - *BACT*, *Prochlorococcus spp.* – *PROC*, *Synecococcus spp.* – *SYN*, picoeukaryotes – *PICO*, nanoeukaryotes – *NANO* and coccolithophorids – *COCCO*. σ_{bbp} is the backscattering cross-section (in m^2) of a single particle of the ith component and is the result of the product of the geometric cross-section of the particle (S_i) by the backscattering efficiency factor (Q_{bbpi}, dimensionless). So that b_{bp} for a particle type i , can be written as (Chung *et al.*, 1998):

$$b_{bpi} = C_i \times [S_i \times Q_{bbpi}] \quad (2)$$

This approach has been applied to in-situ bio-optical and biological measurements.

2. METHODS

During summer 2007, a cruise took place at the Mid-Atlantic Ridge - MAR (ECOMAR cruise between 48 and 54°N: Fig. 1), and 46 coincident water samples at different depths were collected along with in-situ optical b_{bp} measurements. Cell abundances (C_i)were counted using flow cytometry distinguishing the groups in Eq.1. Microphytoplankton (larger than 20 µm) is not enumerated by this method. Particle backscattering was measured using a Wetlabs BB3 backscatter meter.

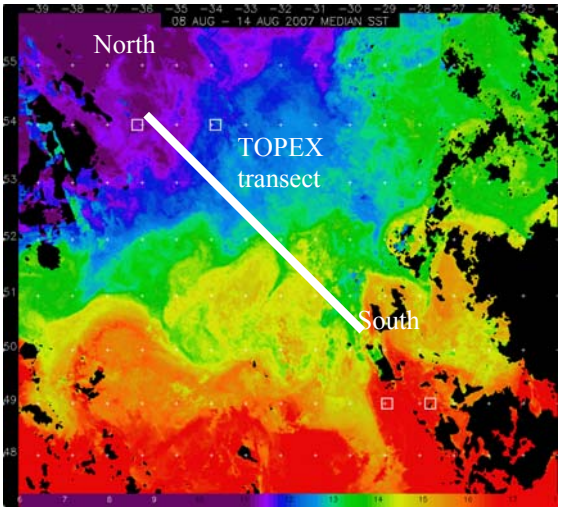

Fig. 1 Composite AVHRR sea surface temperature image (8 - 14 Aug 2007) during the ECOMAR cruise. Scale goes from 6 °C (purple) to 18 °C (red). The squares mark the position of the stations at both sides of the ridge. Samples were grouped in three areas: North, TOPEX and South.

* Corresponding author. Prospect Place, Plymouth PL1 3DH, UK, Tel: +44 (0)1752 633100 Fax: +44 (0)1752 633101.

3. RESULTS

Table A summarizes the regressions that best explain the variation of b_{bp} in the three areas studied. Using the measured abundances of each type of organism and by assuming values for S_i and a Q_{bbpi}, from two contrasting studies (Stramski *et al.*, 2001; Vaillancourt *et al.*, 2004), that proposed very different values for these parameters, particle backscattering can be computed ($b_{bp}(532)$ modelled, Fig. 2). Using Stramski *et al.* (2001) no significant relationship was observed between the measured values and the modelled values.

Table A. Linear regression estimates of the $\sigma_{bbp}(532)$ (mean±SE) for the plankton components (Eq.1). The coefficient units are m^{-2} part.$^{-1}$ and have to be multiplied by a 10^{-15} factor. The regression statistics are summarized by the coefficients of determination (R^2) and the F-ratio (NS-not significant, P>0.05; *, 0.001<P<0.05;**,P<0.001). CONSTANT is the intercept. An example of how the table should be read is: $b_{bp}(532)=0.30x10^{-15}+0.47x10^{-15}C_{pBACT}$, $R^2=0.91$, N=18.

Area	Parameter	Coefficient ± SE ($\times 10^{-15}$)	R^2	N
All data	CONSTANT	0.6 ± 0.1 **	70.2	46
	NANO	62 ± 65 **		
	CRYPTO	11143 ± 4475*		
South	CONSTANT BACT	0.3 ± 0.0** 0.5 ± 0.0**	91.2	18
TOPEX	CONSTANT PICO	0.9 ± 0.3* 208 ± 51*	61.2	11
North	CONSTANT NANO	1.1 ± 0.2** 608 ± 105**	67.0	17

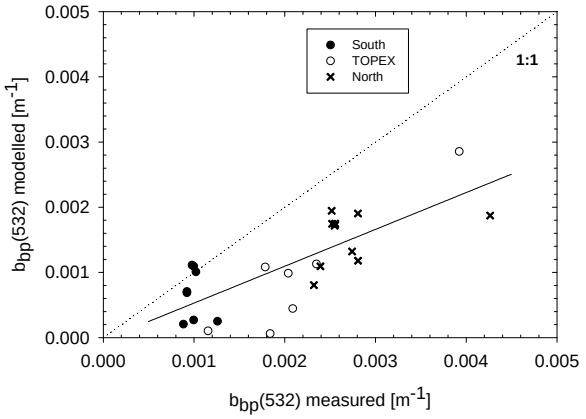

Fig. 3 Measured versus modelled particulate backscattering at 532 nm for each region at the Mid-Atlantic Ridge. Solid line represents the linear regression fit to the data. Dotted line is the 1-to-1 line. Modelled backscattering was calculated using Vaillancourt *et al.* (2004) parameters. Solid line is the regression fit to all data (N=26):
$b_{bp}(532)_{modelled}=0.57b_{bp}(532)_{measured}-3.8x10^{-5}$, $R^2=0.56$.

4. DISCUSSION AND CONCLUSIONS

A large part of the variability of in-situ $b_{bp}(532)$ has been found to be correlated to the phytoplankton abundance (nanoeukaryotes in particular). This contrasts with previous modelling, based on laboratory experiments (Stramski *et al.*, 2001), which found that the major living contributors to backscattering were bacteria. This could be explained by more complex models that take into account the layered structure of phytoplankton cells (Bernard *et al.*, 2009). The reconstructed backscatter using model parameters from the literature based on relatively high values of Q_i correlate well with the observations when no bacteria are considered. Note, however, that the slope of the relationship is 0.57, suggesting that the relationship does not account for over 40% of the signal. The sources of the unexplained variability and magnitude of the in-situ backscattering remain unknown.

ACKNOWLEDGEMENTS

We would like to thank the Master and crew of the RV James Cook. Funding is acknowledged from NERC project ECOMAR. Support from the NERC Field Spectroscopy Facility and from NERC NEODAAS is also acknowledged.

REFERENCES

Behrenfeld, M. J., Boss, E., Siegel, D. A. *et al.* (2005) Carbon-based ocean productivity and phytoplankton physiology from space. *Glob. Biogeochem. Cycle*, **19**, (GB1006, doi: 10.1029/2004GB002299)

Chung, S. P., Gardner, W. D., Landry, M. R. *et al.* (1998) Beam attenuation by microorganisms and detrital particles in the equatorial Pacific. *J. Geophys. Res.-Oceans*, **103**, (C6) 12669-12681.

Durand, M. D. and Olson, R. J. (1996) Contributions of phytoplankton light scattering and cell concentration changes to diel variations in beam attenuation in the equatorial Pacific from flow cytometric measurements of pico-, ultra- and nanoplankton. *Deep-Sea Res. Part II-Top. Stud. Oceanogr.*, **43**, (4-6) 891-906.

Huot, Y., Morel, A., Twardowski, M. S. *et al.* (2008) Particle optical backscattering along chlorophyll gradient in the upper layer of the eastern South Pacific Ocean. *Biogeosciences*, **5**, 495-507.

Morel, A. and Maritorena, S. (2001) Bio-optical properties of oceanic waters: A reappraisal. *J. Geophys. Res.-Oceans*, **106**, (C4) 7163-7180.

Stramski, D., Boss, E., Bogucki, D. *et al.* (2004) The role of seawater constituents in light backscattering in the ocean. *Progress in Oceanography*, **61**, (1) 27-56.

Stramski, D., Bricaud, A. and Morel, A. (2001) Modeling the inherent optical properties of the ocean based on the detailed composition of the planktonic community. *Applied Optics*, **40**, (18) 2929-2945.

Vaillancourt, R. D., Brown, C. W., Guillard, R. R. L. *et al.* (2004) Light backscattering properties of marine phytoplankton: relationships to cell size, chemical composition and taxonomy. *Journal of Plankton Research*, **26**, (2) 191-212.

Challenges to generating satellite-based diurnal SST fields for the Mediterranean Sea

S. Marullo [a,*], R. Santoleri [b], V. Banzon [c], R.H. Evans [d], M. Guarracino [a], K. Nittis [e]

[a] Agenzia Nazionale per le nuove tecnologie, l'energia e lo sviluppo economico sostenibile. Centro Ricerche Frascati, Frascati , Italy – salvatore.marullo@enea.it
[b] Istituto di Scienze dell'Atmosfera e del Clima, Consiglio Nazionale delle Ricerche, Rome, Italy – r.santoleri@isac.cnr.it
[c] National Climatic Data Center (NOAA-NESDIS) , Remote Sensing & Application Division, Asheville, NC, USA – Viva.Banzon@noaa.gov
[d] Rosenstiel School of Marine and Atmospheric Sciences, Miami (USA) - revans@rsmas.miami.edu
[e] Hellenic Centre for Marine Research - Institute of Oceanography, Athens, Greece.

Abstract – Providing SST fields that resolve the diurnal cycle can help produce more realistic simulations of Mediterranean processes. To meet this goal, an Optimal Interpolation schema recently proposed for the Tropical Atlantic by Marullo et al. (2010) was adapted. In this paper we discuss the proposed modifications and show preliminary results. While adjustments based on AMSR were required in the Atlantic, initial comparison with a limited number of Mediterranean buoys suggests that SEVIRI data are quite accurate for the area and an adjustment may not be needed.

Keywords: SST, diurnal cycle, SEVIRI, AMSR.

1. INTRODUCTION

Recent progress in the understanding of upper ocean processes, and the availability of more sophisticated numerical models, require a more precise estimate of sea surface temperature (SST) at all temporal and spatial scales, including the diurnal cycle (Bernie et al., 2007; 2008 among others). A well-resolved SST diurnal cycle can result in more realistic simulations. Recently Marullo et al. (2010; hereafter Ma2010) proposed a methodology to generate a Diurnal Optimally Interpolated SST (DOISST) product using SEVIRI data distributed by the Ocean and Sea Ice Satellite Application Facility (O&SI SAF, referred to herein as SAF for brevity; Météo-France, 2006). Ma2010 found that the input SAF data had a spatial bias when compared to buoy measurements, with the northern stations exhibiting a larger error than the southern stations (Fig. 1a). The spatial distribution of the bias was also found to vary seasonally, indicating that the SAF data required a non-static adjustment. An analogous satellite-buoy comparison using AMSR, a microwave (MW)-based polar-orbiting instrument, produced a flat bias pattern (Fig. 1b). Thus nighttime SST adjustment of the SAF data was introduced using AMSR as a reference field. The adjustment was performed daily due to the bias dependence on atmospheric factors that have short timescales. The AMSR-SAF bias is estimated during nighttime using two preliminary OI maps derived from AMSR night and SAF at 04:00 UTC respectively and applied to all the SAF uninterpolated data within the same 24 hour period before optimal interpolation. A comprehensive explanation of the observed seasonal bias and its latitudinal distribution was discussed in detail considering three environmental factors (wind, total columnar water vapor, and aerosols) that can cause problems with infrared(IR)-retrievals or IR-MW coupling. Details of this analysis can be found in Ma2010.

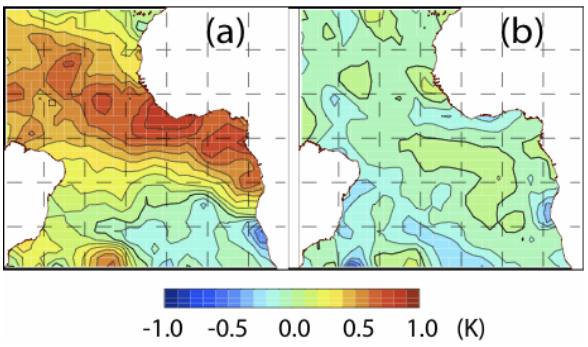

Figure 1. Contoured SST bias in situ (Coriolis) minus a) SAF and b)AMSR. (Modified from Ma2010)

In this paper we show preliminary results of the application of this OI schema to the Mediterranean. As already suggested by Ma2010, a number of modifications are needed. Away from the tropics, towards mid and high latitudes, different environmental conditions and scales are involved in the phenomena driving SST variability. The latitudinal extent of the Mediterranean is more limited than the Tropical Atlantic. But with a more northerly latitudinal extent, seasonal variations in daylength, have to be taken into account. Moreover, for small semi-enclosed seas like the Mediterranean Sea, the use of microwave data may be precluded by the presence of numerous small islands and an extensive coastline.

2. DATA

2.1 Satellite Data

This study uses a SAF regional dataset called the Low and Mid Latitudes (LML) dataset. It is available at 0.1º spatial resolution and covers the area between 60ºS and 60ºN, 100ºW and 45ºE. The SAF data for the Mediterranean are from the geostationary satellite MSG/SEVIRI. The SST fields are available at 3-hour intervals beginning at 0100 UTC. Although the IR instrument measures SST in the first few microns of the sea surface, the SAF retrieval algorithms are intended to produce subskin SSTs that generally differ from the skin by ~0.2K at night (Météo-France, 2006).

* Corresponding author. ENEA Centro Ricerche Frascati, Via Enrico Fermi 45, 00044 Frascati (Italy), Tel +390694005867.

Thus, SAF SSTs can be validated with *in situ* (e.g., buoy) measurements at night, but in the daytime the subskin temperature is decoupled from a buoy measurement by the magnitude of the diurnal warming.

2.2 In situ temperatures

For this initial comparison, 1 m depth water temperature data at 3 hours intervals has been obtained from the Poseidon E1-M3A mooring operating in the Cretan Sea since 2000 (Nittis 2007) as part of an integrated network of deep European observatories developed in the framework of EuroSITES (http://www.eurosites.info/).

3. APPLICATION OF THE OI SCHEMA TO THE MEDITERRANEAN SEA

3.1 Mediterranean DOISST

The use of MW data in the Mediterranean Sea is complicated by the presence of coastlines and many islands causing invalid MW retrievals. Thus, the first step was to validate SAF SSTs against in situ measurements to verify if a bias similar to the one found in the Tropical Atlantic was present. The preliminary results suggest that Mediterranean SEVIRI SST are not significantly biased. Comparison at the E1-M3A site for the year 2008 gives a mean difference between in situ and satellite data of -0.04±0.47 K. Until further buoy-SAF comparisons can be made, we chose to skip the bias adjustment procedure applied by Ma2010 in the tropical Atlantic and focus on the results of the applications of this simplified version the DOISST scheme to the Mediterranean Sea.

Although the bias over one year is small, over time the magnitude of the bias varies. Figure 2 indicates that, at this site, SEVIRI underestimates in situ SST during Summer by 0.2-0.4 K while, for the rest of the year it is confined between ±0.2 K with exception of April-May at 16:00 UTC where it reaches 0.5-0.6 K.

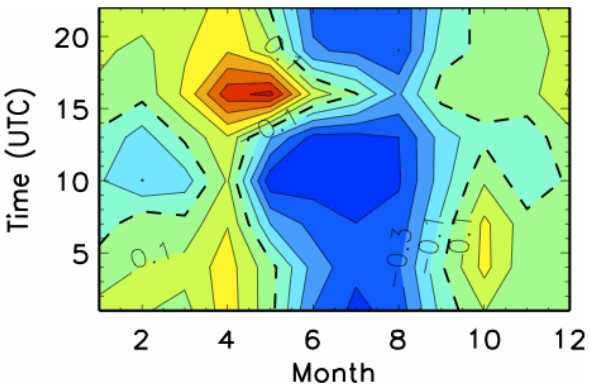

Figure 2. Contoured SST bias for year 2008 over the E1-M3A site as function of the month and time of the day. Contour interval is 0.1 K.

To compare the diurnal signal more easily in the two time series, we subtracted a 24-hour moving average. The average amplitude of the in situ SST anomalies ranges from 0.1-0.2 K in Winter to about 0.5 K in Summer, but may reach ~2.0 K on specific days. For DOISST anomalies, the amplitude is slightly higher but is consistent with the buoys in that both are concurrently high or low. The standard deviation of the buoy anomaly (0.2 K) is smaller than the DOISST anomaly (0.3 K), which is consistent with the expectation that the diurnal cycle is more damped at the 1-m depth of the buoy compared to the satellite penetration depth. The resulting SST anomalies are shown in Fig. 3 for August 2008. Note that there is no pronounced offset between buoy and satellite. However, comparison with other buoys is needed.

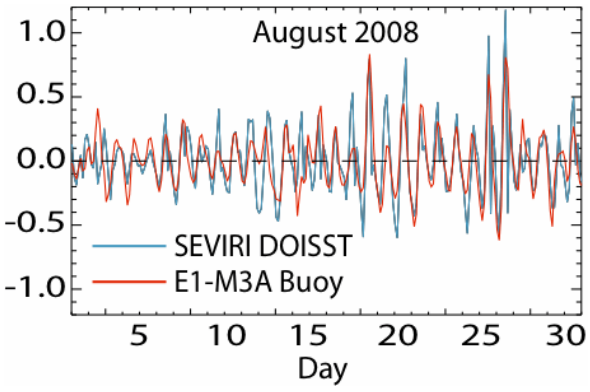

Figure 3. Comparison of DOISST and buoy SSTs diurnal anomalies at E1-M3A site (35.78 °N, 24.94 °E)

4. CONCLUSION

A simplified version of the Ma2010 DOISST schema is applied to the Mediterranean Sea and results are evaluated against a buoy in the Aegean Sea. Preliminary results are encouraging but buoy comparisons at more locations are needed. A Mediterranean DOISST product is clearly feasible but furthur improvements are needed.

ACKNOWLEDGEMENTS

SAF SST data were obtained from the EUMETSAT Ocean and Sea Ice Satellite Application Facility at Météo-France.

REFERENCES

Bernie, D.; E. Guilyardi, G. Madec, J. Slingo, S. Woolnough (2007). "Impact of resolving the diurnal cycle in an ocean-atmosphere GCM. Part 1: a diurnally forced OGCM", *Climate Dynamics*, *Volume 29*, Number 6, November 2007 , pp. 575-590.

Bernie, D.; E. Guilyardi, G. Madec, J. Slingo, S. Woolnough and j. Cole (2008). "Impact of resolving the diurnal cycle in an ocean-atmosphere GCM. Part 2: a diurnally coupled OGCM", *Climate Dynamics*, *Volume 31*, Numbers 7-8 / December, 2008, pp. 909-925.

Marullo S., R. Santoleri, V. Banzon, R. H. Evans, M. Guarracino (2010). " A diurnal-cycle resolving SST product for the tropical Atlantic", *Journal of Geophys. Res.*, in press.

Météo-France (2006), "Ocean & Sea Ice SAF: Atlantic Sea Surface Temperature Product manual", Version 1.6, http://www.osi-saf.org/

Nittis, K., Tziavos, C., Bozzano, R., Cardin, V., Thanos, I., Petihakis, G., Schiano, M.E. and Zanon, F., (2007). "The M3A multi-sensor buoy network of the Mediterranean Sea". Ocean Science, 3:229-243.

Inherent Optical Properties as derived from aircraft hyperspectral radiometric data in the Ligurian Sea in March 2009

E. Mauri [a,*], G. Pennucci [b], C. Trees [b], C. Pietrapertosa [c], F. Coren [a], M. Ampolo Rella [b]

[a] OGS, Istituto Nazionale di Oceanografia e Geofisica Sperimentale, Sgonico, Trieste, Italy – emauri@inogs.it
[b] NATO Undersea Research Centre, Viale San Bartolomeo 400, La Spezia, Italy
[c] CNR – Istituto di Metodologie per l'Analisi Ambientale (IMAA), 85050 Tito Scalo, Potenza, Italy

Abstract – Inherent Optical Properties (IOPs) of the water provide information in a variety of field including: penetration depth (bathymetry), phytoplankton ecology and naval applications. Knowledge of IOPs and their changes in time can be used to study oceanographic processes, such as river discharge, surface circulation patterns and sediment transports. Although field measurements have been made in the Ligurian, they are insufficient to analyse space-time variation, thus, rapid and accurate estimation of IOPs is important. In this study, three semi-analytical/quasi-analytical ocean colour models to retrieve the IOPs (phytoplankton, colour dissolved mater absorption and scattering of particles) were tested and tuned on the *in situ* data acquired during the BP09 campaign in March 2009. High resolution maps of phytoplankton absorption and colour dissolved mater absorption were produced for the area covered by the airplane track. The correlations between the total pigments or total chlorophyll and the best radiance ratios are also explored.

Keywords: hyperspectral, optical properties, atmospheric correction, Ligurian Sea.

1. INTRODUCTION

Airplane and satellite remote sensing is very useful for providing rapid information on environment properties over large areas. The maritime zone is a highly dynamic region where hydrodynamic and morphodynamic processes may change on a wide range of spatial and temporal scales. For those reasons, remote sensing of the coastal zone is very challenging and needs improvements.

The experiment BP09 (Battlespace Preparation 2009) addressed specific problems associated with remote sensing (RS) of denied areas, specifically to improve the quality of the optical properties derived from RS in marine coastal environments. The main objective of the experiment was to assist in the calibration and validation of large-scale ocean color sensors (MODIS, 1 km), medium scale sensors (MERIS, 300 m), and small scale sensors (GeoEye-1 and hyperspectral airplane over-flights, 1 and 2 m, respectively). During this trial, aerial and *in situ* sensors were used and integrated to provide combined measurements allowing the characterization of the nearshore zone both in spatial and spectral dimensions**.** In the present work we first focus on the atmospheric correction of the airplane-mounted Aisa EAGLE data and then on the testing of the semi/quasi analytical models. The ocean colour models are tuned on this specific area. The improved model is then applied on the airplane data to provide high resolution maps of the parameters. Since both the in-situ and Aisa EAGLE data are hyperspectral we also explore the correlations between the best radiance ratios and pigment concentration.

2. DATA AND METHODS

During the BP09 cruise organized from the 13th to the 26th of March 2009, HyperPRO, AC9+, HS2 data were collected in 68 stations. Concomitant water samples were collected to perform integrated sphere measurements. The 17th of March hyperspectral data were acquired by an airplane flying for about one hour (from 12:16 to 13:12 GMT time) over the two areas shown in Figure 1 (in front of Carrara and Viareggio). That day was particularly clear and also MODIS (12:52 GMT time) and MERIS (09:41 GMT time) data were also available. The semi and quasi-analytical ocean colour models tested are RP95 (Roesler and Perry,1995), GSM01 (Garver and Siegel, 1997, Maritorena, et al., 2002) and the QAA (ZhongPing Lee et al., 2002).

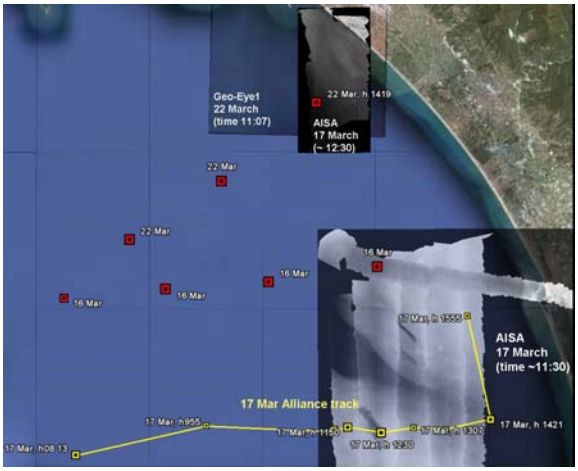

Figure 1. Ligurian Sea with the area covered by the airplane survey (2009-03-17, from 11:30 to 12:07 local time) (light grey), GeoEye-1 satellite coverage (2009-03-22, 11:07 local time) (upper part) and *in-situ* stations (red square and yellow track) sampled by NRV Alliance.

During the project several methodologies and algorithms[1,2,3,4] were developed and implemented. In this work, we would like to emphasize the airplane data that provided an innovative contribution to the development of optical information and assessments as well as coastal forecasting. Aircraft data were radiometrically and atmospherically corrected from the high-resolution satellite

* Corresponding Author. OGS, Borgo Grotta Gigante 42/c 34010 Sgonico (Italy).

acquisition and the *in situ* available coincident data. This georectification was performed using the aircraft metadata information and performing aircraft to satellite (GeoEye-1) image registration. After georectification, the TOA (Top Of the Atmosphere) radiances were atmospherically corrected to compare them with the other available radiances. Initially these corrections were performed using standard methodologies, in particular the Research System Incorporated (RSI) ENVI software package was used to perform dark subtraction and thermal infrared correction. Once the atmospheric contribution and noise were removed, the resultant imagery was compared with the *in situ* measurements. Therefore, since the results were not satisfying, we tested the Tafkaa algorithm [5] being a innovative methodology proposed by Marcos J. Montes and Bo-Cai Gao of the Naval Research Laboratory, Washington, D.C. This method is based on Atmospheric REMoval (ATREM) 4.0 and exploits as a scattering calculation the Second Simulation of the Satellite Signal in the Solar Spectrum (6S), but specular reflection of the air-water interface (sun glint, reflected sky and cloud light) is not taken into account. Knowing that, the resulting water reflectances were strongly contaminated by the surface reflectance and methodologies to estimate/remove these effects are definitely required. As a first approach, the "glint" contribution was removed from the data considering a constant offset at longer wavelengths and was subtracted on the overall water reflectance. An innovative correction scheme [6] that allows removal of surface-reflected sun glint and sky using *in situ* measurements (sky radiance, *in situ* absorption at 412 nm) is under development. After georectification, the atmospheric correction was performed using standard methodologies. In particular the Research System Incorporated (RSI) ENVI software package was used to perform dark subtraction, thermal infrared correction and to integrate the aerosol characterization information available from the *in situ* sensors (using FLAASH). Once the atmospheric contribution and noise were removed, the resultant imagery was converted from radiance values to reflectance and was compared with the *in situ* coincident available measurements (see stations in Figure 1). Three different semi/quasi-analytical models were used on the in-situ HyperPRO data to test their effectiveness. Once the models were tuned to obtain the best match with the in-situ data, the best model was applied to the airplane data to obtain maps of the output data.

3. PRELIMINARY RESULTS

Reflectances at 7 wavelengths were produced from MODIS and MERIS ocean color data. The comparison between these data and the *in situ* data were performed only for 4 days when the weather was perfectly clear. The result shows that MODIS grossly underestimates the *in situ* reflectances while MERIS overestimates them. This shift can be due to different reasons. We are comparing various ground resolution: MODIS has 1 km^2, MERIS 300 m^2 and the *in situ* data have an uncertainties in the position of about 10 m^2. Other reasons for the discrepancies can be inputted to the satellite navigating error (around 4-8 pixels) or to the optical variability near the coast or the uncertainties due to the atmospheric corrections. In the attempt to have a better knowledge we processed the aircraft data that provides better spatial and spectral accuracy: 2 m and 63 channels. From comparisons between the *in situ* and aircraft water leaving radiances it turned out that the land-based Tafkaa algorithm works better than the standard atmospheric correction and that the match is better for some wavelengths than others. In particular the water leaving radiances at wavelength below 500 nm are overestimated by the Tafkaa correction, while the results from standard atmospheric correction depart more from the *in situ* data. Although this comparison is not completely satisfying, the level of agreement between the two flight lines is encouraging considering the sizable differences in specular reflection. These preliminary results demonstrate that Tafkaa more successfully generates acceptable reflectance.

4. CONCLUSIONS

This study introduces an approach to analyze surf zone data from a distributed sensor system, emphasizing the role that an aircraft platform can provide. On the basis of the processing results, improved accuracy is being studied to minimize errors when fusing the *in situ* measurements. In particular, we found that the accuracy of the aircraft products surpassed the quality of those created by satellite systems and additionally can provide more accurate information in terms of spectral resolution.
Our goal is to implement the methodologies in [1,2,3 and 4] to determine high level products (such as optical parameters, visibility and bathymetry) and to generate high resolution aircraft maps similar to the satellites products but with better spatial and spectral resolution.

ACKNOWLEDGEMENTS

We would like to thanks Marcos Montes and Bo-Cai Gao (Naval Research Laboratory) for providing the Tafkaa 6s software and assistance in its utilization.

REFERENCES

[1] Garver and Siegel, (1997), Inherent optical property inversion of ocean color spectral and its biogeochemical interpretation. 1. Time series from the Sargasso Sea. Journal of Geophysical Research, vol.102, no C8 pp 18,607-18625.

[2] Roesler, C. S. and M. Perry, (1995). In situ phytoplankton absorption, fluorescence emission, and particulate backscattering spectra determined from reflectance. Journal of Geophysical Research, vol. 100, no C7,pp. 13,279-13,294.

[3] Maritorena, S., Siegel, D. A., & Peterson, A. (2002). Optimization of a semi-analytical ocean color model for global scale applications. Applied Optics, vol. 41, no 15, 2705– 2714.

[4] ZhongPing Lee, Kendall L. Carder, and Robert A. Arnone (2002). Deriving inherent optical properties from water color: a multiband quasi-analytical algorithm for optically deep waters Applied Optics, vol. 41, no. 27, 5755-5772.

[5] Montes, M., Gao, B., (2004). Tafkaa_6s: An atmospheric Correction Algorithm for the Land, Remote Sensing Division, Naval Research Laboratory, Washington, D.C. 20375.

[6] Gould, R.W. Jr., Arnone, R.A., Sydor, M., (2002). Testing a new remote sensing reflectance algorithm to estimate absorption and scattering in case 2 waters, Analytical Spectral, Spectral, 3039381645.

Advanced Low-spectral ALSAR Technology and Its Application for Charting Multi-Year Ice Parameters in the Central Arctic Ocean

V.V. Melentyev [a], V.I. Chernook [b], K.V. Melentyev [c], M.A. Shubina [d]

[a] Nansen International Environmental and Remote Sensing Center, St. Petersburg, Russia – vladimir.melentyev@niersc.spb.ru
[b] Research Institute of Fishery Fleet Designing (GYPRO Ryb Flot), St. Petersburg, Russia – chernook@grf.spb.ru
[c] St. Petersburg Branch of the State Academy of Customs, St. Petersburg, Russia – k.v.melentyev@mail.ru
[d] State Academy of Forestry Fleet Designing (LTA), St. Petersburg, Russia – nemsha@mail.ru

Abstract - Retrieving the parameters of MY ice in central Arctic and its sub-surface patterns was done with using advanced ALSAR technology. Thematic interpretation of airborne ALSAR survey allows reveal more numbers types of ice and fixes variability not only FY but also MY ice. ALSAR enlarge capability of satellite reconstruction heterogeneity of thick and solid ice (ice breccia) at second part of winter season. ALSAR were also applied for revealing origin of ice and history of ice formation as well detecting deformed zones with dividing rafted and ridged areas.

Keywords: MY ice, ALSAR technology, Arctic Ocean.

1. INTRODUCTION

Further advancement of satellite-airborne SAR technologies supposes designing multi - frequencies polarimetric instruments that make deeper sounding and increase number of revealing parameters. Important goal is application advanced low-spectral SAR (ALSAR) for charting polytypic water bodies situated in the Arctic and other geographical zones. ALSAR survey of coastal zones allows investigate arrangement of water masses and fix the frontal zones including sub-water charting off-shore river-bed with detecting continuation of river flux in open sea for study hydrology of shallow waters. Significant problem is using ALSAR for remote diagnosis of multi-year (MY) ice for navy and other economical activity in Polar Ocean.

2. INSTRUMENTS AND TOOLS

First SAR/ALSAR system in RF was installed in the beginning 1980-ties onboard research aircraft Il'ushin-18 "Pomor" well-equipped by following instruments - 3. 9 cm; 23. 0 cm; 68. 0 cm and 254. 0 cm (all devices allow the combination polarization: VV, HH, VH, HV). This multi-spectral complex was testified as a proto-type of radar that should be launched onboard Soviet space station "Almaz". Another ALSAR (MRLK) was equipped by another combination of channels - 0. 8 cm (VV, HH); 3. 0 cm (VV); 23. 0 cm (VV, HH, VH, HV) and 180. 0 cm (VV, HH, HV polarizations). It was testified for future installation onboard satellites "Okean" and "Resourse". Now we use two Russian flying laboratories - "Arktika" and "Nord" belonged to the Institute GYPRO Ryb Flot that disposes SAR and passive microwaves systems 4, 0 cm, 23, 0 cm.

3. OBJECTIVES AND TASKS

Experimental studies onboard flying laboratories represent initial stage of satellite scientific programs. There are many specific objectives and tasks but the main are instrumental charting of ecologically significant and hazardous ice phenomena as well supports of fish reconnaissance (mackerel fishing). Other priority of SAR/ALSAR survey is study the wavy sea and polytypical icy waters and charting wind speed parameters, frontal zones, currents, internal waves, water pollution, ice features of the inland water bodies (lakes, rivers and reservoirs).

4. APPLYING ALSAR FOR CHARTING MY ICE

Airborne ALSAR was used for ice reconnaissance in Arctic Ocen since 1992 in frame cooperation with the Murmansk Shipping Company (MSC). Convoy operations were provided along the Northern Sea Route from the Barents and White Sea at the west till the Chukchi and Bering Sea at the east. Several ALSAR surveys were fulfilled for support profit-making tourist routes to the North Pole when ALSAR data were successfully applied for optimal selection routing of the nuclear icebreakers. Fig. 1 a – d shows example of SAR/ALSAR survey northward Frants-Ioseph and Spitsbergen Archipelago, 120-150 km northwestward from Zemlya Aleksandra and I. Arthur. Airborne charting was fulfilled 15 May 1993. Coordinates the central point for each airborne track are – 83 42'N/46 52'E.

The second decade of May'93 at this part of Arctic could be characterized as continuation of the winter season when the melting processes doesn't start. As could be assessed from the analysis of ice conditions it was the mild season when the ice edge was shifted close to 79N. The ice edge is situated here at this time usually around 77N. According to ice charts of Norwegian Meteorological Institute (DNMI) at this part of Western Arctic is dominated here in May'93 only the single type of ice - multi-year (MY) ice. Ice massif adjoining southward to the Frants-Ioseph Archipelago and ice cover close to the Novaya Zemlya is designated in DNMI ice charts singularity-free as zone of dominance of first-year ice. The border between these two ice zones was marked as broken curve approximately directed along 80N. Airborne ALSAR (Fig. 1) established the falseness of these ice features at DNMI charts.

Fig. 1 shows that back-scattering of ice depends on roughness, deformation and solidity of ice (see special marks 1-5). Thickness of sounding layer varied with change of wavelength. As could be seen from Fig. 1, optimization of sounding is the problem and simple selection larger wavelengths not always follow the informative increase. Airborne ALSAR opens the possibility retrieve the type of ice, including dividing MY-FY ice border. It allows recognizing the outline and shapes of individual ice floes and fixing many other ices parameters. Millimeter and centimeter waves allow sounding of ice with resolution 10-12 m, and less. As could be seen from Fig. 1 a, b, there is radar contrast between MY and crystalline FY ice but there is heterogeneity's of signal within

the bounds of mentioned ice areas. Modification of radar signatures for thick FY ice at the different wavelengths is fixed at the lower part of Fig. 1 a - d. Change of the spectral features for MY ice are retrieved from the upper part of Fig. 1.

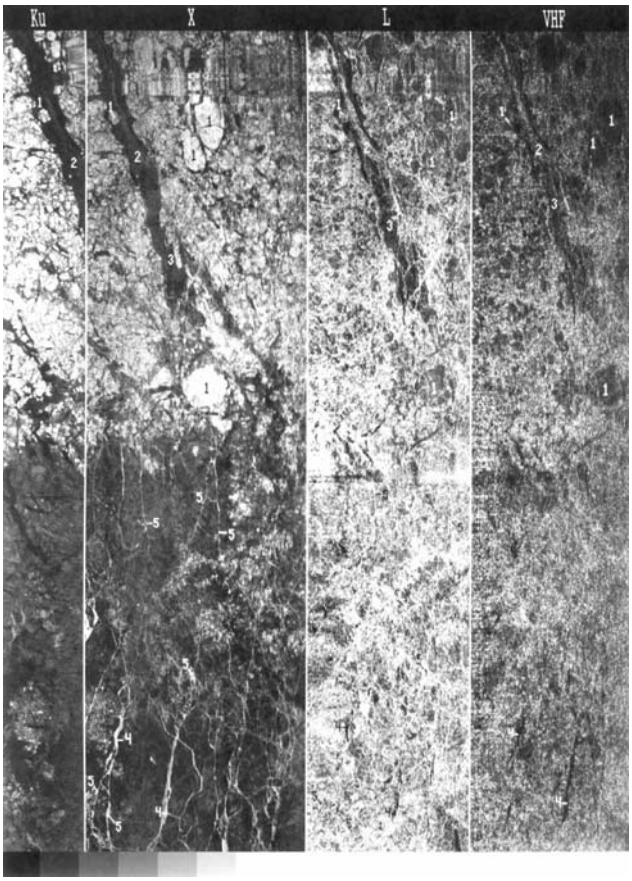

Figure 1 a - d. Multi-frequency airborne ALSAR survey, 15 May 1993: a) Ku-range, b) X-range, c) L-range, d) UHF.

ALSAR allows to fix that FY massif here was a level pack ice. Exactly these properties are responsible for a specific dark character of signatures of ice in millimeters and centimeters. Same types of FY ice are fixed also inside the MY ice zone as several vast dark zones elongated from NW to SE. According to our assumption these FY settings in are the results of shearing of MY ice and opening and following freezing of polynyas. Frozen fractures at the level FY ice and hummocks are identified by 3-cm radar as bright white lines in different parts of image. SAR-0, 8 fixed only separate heterogeneity of FY ice that locates near surface and couldn't distinguish sub-surface shearing of FY ice. Surface or volume scattering could be responsible for these effects. Deformations of crystalline ice settings inside MY ice are evident from low-spectral ALSAR data as broken bright lines inside vast dark area (marks 2 and 3, correspondingly). These features have had large spatial scale. But more important that these processes occurs inside more deep layers of the FY ice.

According to our conclusion, there fore only ALSAR systems could discover these subsurface phenomena. Shearing type of this heterogeneity inside refrozen polynyas is fixed by L-band and VHF radar as modification of signal texture. Comparative analysis of decimeter and meter images allows reconstruct the history of FY ice formation in fracture limits here. As known, ices grow from the bottom and most deformations occur with new and young ice. As result low-spectral data fix non-troughs, blind and other partial cracks inside FY ice massif. As we conclude effects of opening in ice were dominated here in studied area during the first stage of FY ice formation in 1992/93-winter season. Fig. 1 c shows that L-band radar couldn't be recommended for dividing FY-MY zones – both these areas at lower and upper part of image has the similar bright contrast.

But L-band "portrait" contains many other features. On our conclusion, these openings of MY ice happened at the time when FY ice at the lower part of Fig. 1 has thin or medium. At this time both FY-MY zones were consolidated and "existed" as united system – ice breccia. As result the openings that started at the north continued to the south part of image. Deformations of FY ice that happened half-year ago before our ALSAR survey are traced as white bright saw-toothed curve and L-channel fixes these heterogeneity (location, scale, orientation). ALSAR retrieval parameters are numerous and this is important for support of navigation and other specific marine and navy applications. Especially important that L-band is effective and informative for assessment of scale of penetration of pressures and decompresses inside FY ice – it could be fixed as brightening of signal. Dividing internal heterogeneity of ice in the Arctic and separation cracks from hummocks using ALSAR is the important results. Inter comparison C-band and low-spectral data (Fig. 1 b-d) allows assess arrangement "blind" cracks. This is important as well ALSAR fixation of the location and orientation of hummocks inside FY ice (marks 2-3 and 4–5, correspondingly): formation of partial cracks provides brightening of signal at all channels (marks 2-3). Hummocks and other rather shallow violations of external boundary of ice create the brightening in C-band, but L-band and VHF gives the dark signature (marks 4-5).

5. CONCLUSION

Comprehensive analysis airborne ALSAR survey shows advantages of multi-frequency radar observations, and low-spectral data in particular, because each channel supplemented self-descriptiveness each other. High transparency of snow and greater penetration into the ice before the beginning melting is the basis of low-spectral sub-surface sounding. For many applications applicable the possibility assesses using ALSAR heterogeneity of MY ice (marks 1). Giant floe was fixed at C-band as bright white zone and could be correlated as rough and deformed ice area. But low-spectral data (both L and VHF channels) fixes this floe as dark area. It allows relate this floe with level last year's fast ice zone trapped inside the pack ice. At least the establishing connection of ALSAR signatures with origin and solidity of ice, assessing type of water masses forming the concrete ice type is the important for oil/gas operations and optimal routing.

Ocean Front Maps: Towards a Generic Product for Satellite Oceanography

P.I. Miller *

Plymouth Marine Laboratory, Remote Sensing Group – pim@pml.ac.uk

Abstract – This paper explores novel techniques for visualising the location of thermal fronts – features of great importance to physical oceanography and fisheries. Three recent advances have enabled front maps to become a generic product for oceanography alongside sea-surface temperature (SST) and chlorophyll. First, a clustering algorithm has been developed to simplify satellite-derived front maps into continuous contours, allowing frontal systems to be tracked over long time-series, for instance in relation to basking shark sightings. Second, a 28-year time-series of satellite SST data has been analysed for frequently occurring fronts, enabling potential applications in the definition of biodiversity hotspots and marine protected areas. Finally, the technique has been applied to multiple EO data sources including infrared, colour, microwave, and model outputs.

Keywords: ocean fronts; continental shelf.

1. INTRODUCTION

The influence of oceanic fronts on biological productivity has long been studied (Pingree, 1977). Bakun (1996) identified fronts as important structures that could result in the 'triad' of enrichment, concentration and retention of nutrients. Many authors have investigated relationships between fronts and fish abundance, for instance swordfish (Podesta et al., 1993) and tuna and billfish (Worm et al., 2005). Fronts and eddies are now accepted to be key structures influencing the distribution of zooplankton, fish eggs and larvae (Bakun, 2006).

2. COMPOSITE FRONT MAPS

Fronts that extend to the sea surface may be observed by satellite if the water masses differ in temperature or colour. Remote sensing of fronts is promoted as a key tool in determining marine habitat hotspots (Palacios et al., 2006, Sydeman et al., 2006). Identifying fronts in satellite images manually is a tedious and subjective task, so several researchers have proposed image processing algorithms to do this semi-automatically, and have superimposed the locations of all fronts detected on a sequence of images to produce a single combined map (Podesta et al., 1993, Ullman and Cornillon, 1999). Miller (Miller, 2009) extended this methodology to visualise both dynamic and stable fronts, generating metrics to indicate their temperature gradient, persistence and proximity to other observations (allowing for some advection or tidal movement). This *composite front map* approach allows intuitive interpretation of mesoscale structures, and achieves a synoptic view without blurring dynamic features, an inherent problem with conventional time-averaging compositing methods. Note that the front detection does not use the simple image gradient, but a regional statistical approach based on histogram analysis and spatial homogeneity that is more specific to fronts. Priede and Miller (2009) applied these techniques to reveal a strong relationship between the track of a tagged basking shark and a thermal front. The shark followed a front for a whole day, keeping just to the warmer side. This provided additional support for Sims' (2005) argument that reverse diel vertical migration (DVM) with a dusk descent and dawn ascent is characteristic of basking sharks occupying inner-shelf areas near thermal fronts, tracking zooplankton displaying reverse DVM to avoid predation by chaetognaths.

3. SPAGHETTI TO SYNOPTIC FRONT CHART

These ocean front maps are beneficial to improve visualisation of features of interest, but are difficult to analyse quantitatively due to the clusters of observations of each front over time, and scattered unimportant lines. We have developed a new line clustering algorithm to simplify the 'spaghetti' maps to show just the main fronts (Miller, in preparation), coloured to indicate the warm and cold side, and the width indicates the strength of the front (Figure 1).

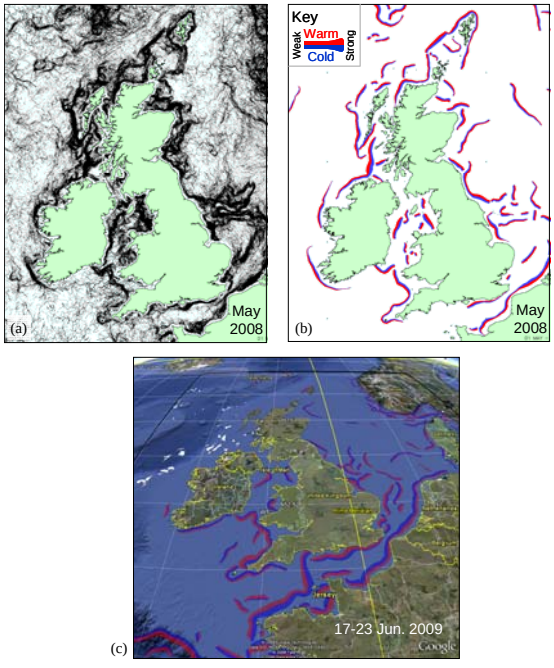

Figure 1. Synoptic front chart: (a) Monthly composite map, clusters of lines from 300 SST scenes; (b) simplified clustering algorithm, with warm/cold sides as red/blue and strength of front as line width; (c) GoogleEarth view.

* Corresponding author. PML, Prospect Place, Plymouth PL1 3DH, UK. Phone/Fax: +44 (0)1752 633485/633101.

This visualisation is analogous to the synoptic chart used for weather fronts, and has not been previously possible to automate for ocean fronts. The synoptic front chart can also be viewed as a layer in GoogleEarth, enabling easy comparison with other georeferenced datasets (Figure 1c). This form of quantitative front mapping should have many applications in basking shark and other fisheries management, and could be extended to any required region around the world.

4. TIME SERIES ANALYSIS OF FRONTS

Within the NERC Oceans 2025 programme we are also studying ocean fronts as one of a set of Earth Observation (EO) parameters that could assist in understanding the effects of climate change. The map in Figure 2 summarizes 30,000 satellite images acquired between 1999 and 2008, indicating the most frequent front locations around the UK.

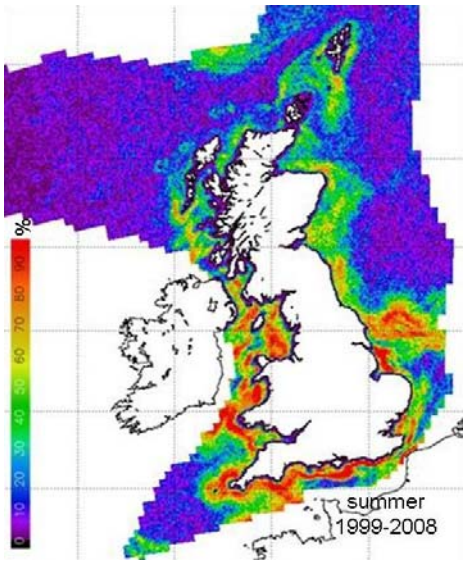

Figure 2. Frequent front analysis for UK shelf seas (summer, 1999-2008), estimated by the % of time for which a strong front was observed for each 1km grid cell, from 30,000 AVHRR passes; used for Marine Protected Areas.

This was calculated as the percentage of time for which a strong front was observed at each location. It is already known that the frequent front zones around the Isle of Man, Hebrides and SW Cornwall are associated with cetacean and basking shark sightings. We are using maps like these to study the temporal variability in physical processes, and identify any trends that could impact upon the ecosystem. With UK Defra we are exploring the application of this technique as a surrogate for identifying biodiversity hotspots (e.g. zooplankton, fish and sharks) and assist in the designation of potential Marine Protected Areas (MPAs).

5. CONCLUSION

We have developed novel tools for detecting and visualising ocean fronts from long time-series of satellite data. Initial results of the simplified synoptic front chart method and time-series analysis appear promising for many physical and biological studies. It is hoped that this comprehensive dataset of front locations will reveal new insights into the dynamic distribution of marine megafauna, and so increase the potential for marine protection strategies that vary seasonally or inter-annually. We are currently developing appropriate and generic front metrics based on the EO ocean front maps, in order to apply these to several case studies through statistical comparison with extensive datasets of megafauna sightings or tagged tracks. Apart from the aim of protecting marine biodiversity, it is hoped this research will also contribute to megafauna behavioural studies, fisheries management and ecosystem management. Further applications for these front visualisation tools include met-ocean, navy and ocean model validation. This presentation will preview recent progress on developing a global front map for multiple applications in operational and physical oceanography and fisheries management.

ACKNOWLEDGEMENTS

This research was funded under the NERC Oceans 2025 programme, Theme 6: Science for Sustainable Marine Resources, and the NERC ECOMAR Consortium.

REFERENCES

Bakun, A. (1996) Patterns in the ocean: ocean processes and marine population dynamics. University of California Sea Grant. San Diego, California.

Bakun, A. (2006) Fronts and eddies as key structures in the habitat of marine fish larvae: opportunity, adaptive response and competitive advantage. Scientia Marina, 70, 105-122.

Miller, P.I. (2009) Composite front maps for improved visibility of dynamic sea-surface features on cloudy SeaWiFS and AVHRR data. Journal of Marine Systems, 78(3), 327-336, doi:10.1016/j.jmarsys.2008.11.019.

Miller, P.I. (in preparation) A line clustering algorithm with application to simplifying ocean front maps derived from satellite data. Remote Sensing of Environment.

Palacios, D.M., Bograd, S.J., Foley, D.G., Schwing, F.B. (2006) Oceanographic characteristics of biological hot spots in the North Pacific: A remote sensing perspective. Deep Sea Research Part II: Topical Studies in Oceanography, 53(3-4), 250-269.

Pingree, R.D. (1977) Phytoplankton growth and tidal fronts around British-Isles. Transactions-American Geophysical Union, 58(9), 889-889.

Podesta, G.P., Browder, J.A., Hoey, J.J. (1993) Exploring the association between swordfish catch rates and thermal fronts on United-States longline grounds in the Western North-Atlantic. Cont Shelf Research, 13(2-3), 253-277.

Priede, I.G., Miller, P.I. (2009) A basking shark (Cetorhinus maximus) tracked by satellite together with simultaneous remote sensing II: New analysis reveals orientation to a thermal front. Fisheries Research, 95(2-3), 370-372.

Sims, D.W., Southall, E.J., Tarling, G.A., Metcalfe, J.D. (2005) Habitat-specific normal and reverse diel vertical migration in the plankton-feeding basking shark. Journal of Animal Ecology, 74(4), 755-761.

Sydeman, W.J., Brodeur, R.D., Grimes, C.B., Bychkov, A.S., McKinnell, S. (2006) Marine habitat "hotspots" and their use by migratory species and top predators in the North Pacific Ocean: Introduction. Deep Sea Research Part II: Topical Studies in Oceanography, 53(3-4), 247-249.

Ullman, D.S., Cornillon, P.C. (1999) Satellite-derived sea surface temperature fronts on the continental shelf off the northeast US coast. Journal of Geophysical Research-Oceans, 104(C10), 23459-23478.

Worm, B., Sandow, M., Oschlies, A., Lotze, H.K., Myers, R.A. (2005) Global patterns of predator diversity in the open oceans. Science, 309(5739), 1365-1369.

SAR Wind Measurements from Space: From Research to Operations

F. M. Monaldo [a,*], W. G. Pichel [b], D.R.Thompson [c]

[a] Johns Hopkins University Applied Physics Laboratory, Laurel, MD USA – frank.monaldo@jhuapl.edu
[b] National Oceanic Atmospheric Administration, Suitland, MD USA – william.g.pichel@noaa.gov
[c] Johns Hopkins University Applied Physics Laboratory, Laurel, MD USA – donald.r..thompson@jhuapl.edu

Abstract – For the last decade, NOAA and the Johns Hopkins University Applied Physics Laboratory (JHU/APL) have been routinely producing high-resolution (<1 km) wind field maps from spaceborne synthetic radar. Wind speed retrieval residuals are typically better than 2 m/s. With new generation of SAR systems are available this research system is being transitioned to operations. This paper describes the new system and how it exploits lessons learned from the research context.

Keywords: SAR, wind speed, radar.

1. INTRODUCTION

Active microwave measurement of winds from space relies on a fundamental relationship, the geophysical model function relating wind speed and direction to normalized radar cross section. This equation takes the general form of

$$\sigma^0 = U^\gamma (A + B\cos\phi + C\cos 2\phi) \qquad (1)$$

where σ^0 is radar cross section, U is wind speed, ϕ is the angle between the radar look direction and the wind direction. The parameters γ, A, B, C are parameters dependent upon radar frequency, polarization, and incident angle. Though the form of Eq. 1 may change slightly with different investigators, the equation characterizes the general features of the model function: (1) cross section increases with wind speed, (2) is a maximum when the radar is looking into the wind, (3) and is a minimum for cross winds. Much research over the past decade has focused on understanding this model function, its dependence on frequency and polarization, as well as its applicability in various wind speed regimes (Horstmann *et al.,* 2005; Monaldo *et al.*, 2003)

Perhaps the most salient characteristic of Eq. 1 is that given a wind speed and direction it is possible to compute a corresponding radar cross section. The inverse is not true. A specific cross section could correspond to a large number of wind speed and direction pairs. For conventional, 25-km resolution, scatterometers, this problem is addressed by measuring the same area of the ocean from different aspect angles and polarizations. The combination of multiple σ^0 measurements makes wind vector retrieval, with some ambiguities, possible. Considerations of continuity and assistance from weather models usually make unique wind vector retrievals possible.

With high-resolutions SARs, the approach has been to combine a known wind direction and a SAR-measured cross section with Eq. 1 to estimate the associated wind speed. The initializing wind direction can come either from models, from examining linear features in SAR images associated with the wind direction (Gerling, 1986), or some combination of the two. Both approaches have been shown to produce wind speed measurements that agree with buoy and scatterometer measurements to better than 2 m/s (Horstmann *et al*, 2000; Monaldo *et al.,* 2004).

2. ANSWRS

To exploit the SAR data from Radarsat-1 and now the new SAR systems (Envisat, ALOS PALSAR, Radarsat-2, and TerraSAR-X), NOAA and JHU/APL have developed the APL NOAA SAR Wind Retrieval System (ANSWRS) to routinely produce wind speed imagery that like shown in Figure 1. This system has run routinely for the last decade and the system is being transitioned to operations.

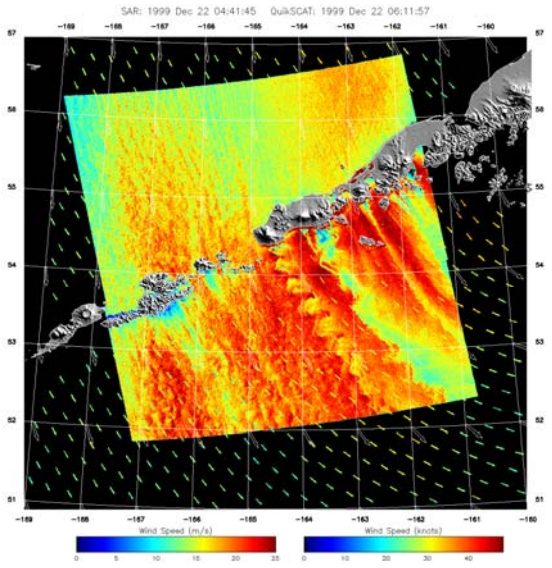

Figure. 1. Radarsat-1 wind speed retrieval image acquired 1999 Dec 22 04:41:45 UTC over the Aleutian Islands. Notice the von Karmon vortices in the wake of a volcanic mountain. The small arrows represent contemporaneous QuikSCAT scatterometer measurements.

* Frank Monaldo, Johns Hopkins University Applied Physics Laboratory, 11100 Johns Hopkins Road, Laurel MD USA, 20723–6099, Tel: 240–228–8648, Fax: 240–228–8648.

As a consequence of the fact that the system grew out of a research project, there was only a single-string route through the processing, making ANSWRS difficult to expand and intermediate products difficult to test and produce without significant code modification. We describe here the open architecture of a new generation system, ANSWRS 2.0, which minimizes the challenges of incorporating data from new satellites, potential improved algorithms, and new geophysical measurements. The new ANSWRS system incorporates a "backbone" approach relies on the creation of intermediate products that are all saved and shared on an Internet backbone. Such an approach is diagramed in Figure 2. The backbone could physically be a single disk drive or a complex set of cross-mounted drives, or even drives in the "cloud," depending upon the needs and capacities of any particular ANSWRS installation.

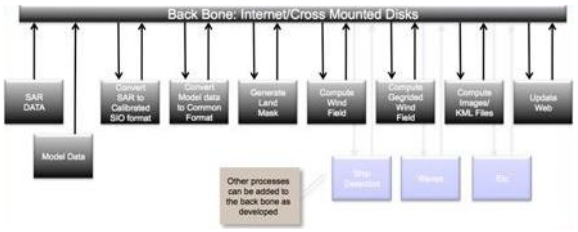

Figure 2. Processing flow in the backbone approach used by ANSWRS 2.0

This approach is currently being implemented by JHU/APL and NOAA. At this point, the front-end ingesters for currently flying SAR systems from which we have data (Radarsat-1/2, ALOS PALSAR, Envisat, TerraSAR-X, and ERS-2) are complete and being tested. As new SAR systems come on line, we need only add a new data "ingester," and all subsequent processing need not change. We plan to implement to wind processing module first.

All geophysical results are also stored on the backbone in a commonly defined format so that other geophysical measurements can be layered on top. For example, wind speed estimates would aid in the analysis of oil spill and in interpreting ship detection results.

All geophysical output files are to be stored in NetCDF format in one of two flavors: sampled at the same resolution and geometry as the original SAR data (level 2) and averaged and sampled onto a rectilinear longitude-latitude (level 3). We note that storage of information on a backbone also allows additional SAR geophysical measurements to be computed with a variety of tools written in a variety of languages. The first geophysical product produced will be the familiar wind speed images.

3. CONCLUSION

JHU/APL and NOAA are creating an operational version of ANSWRS to produced wind speed images. The new version is an outgrowth of lessons learned from the purely research version. The new software will allow easy incorporation of new SAR data and new geophysical algorithms.

REFERENCES

Gerling, T. W., (1986). "Structure of the surface wind field from the Seasat SAR". J. Geophys. Res., vol. 91, no. C2, pp. 2308–2320.

Horstmann. J, W. Kock, S. Lehner, and R. Tonboe, (2000). "wind retrieval over the ocean using synthetic aperture radar with C-band HH polarization". IEEE Trans. Geosci. Remote Sensing, vol. 38, no. 5, pp. 2122–2131.

Horstmann. J, H. C. Graber, W. Kock, and S. Iris, (2005). "Investigation of SAR wind field retrieval with respect to hurricane winds". Proc. IEEE Geoscience and Remote Sensing Symposium, Seoul Korea, vol. 6, pp. 4018–4021.

Monaldo, F. M., V. Kerbaol, P. Clemente-Colón, B. Furevik, J. Horstmann, J. Johannessen, X. Li, W. G. Pichel, T. Sikora, D. R. Thompson, and C. C Wackerman, (2003). "The SAR measurement of ocean surface winds". Second Workshop on Coastal and Marine Applications of SAR, Longyearbyen, Spitsbergen, Norway.

Monaldo, F.M., D.R. Thompson, W.G. Pichel, and P. Clemente-Colón, (2004). "A systematic comparison of QuikSCAT and SAR ocean surface wind speeds". IEEE Trans. Geosci. Remote Sensing, vol. 42, no. 2, pp. 283–291.

MODIS-reveals green dinoflagellate blooms in the English Channel and the Bay of Biscay: identification algorithms and spatio-temporal analyses of the phenomenon.

Eu. Morozov [a*] , O. Aniskina [a], D. Pozdnyakov [a], L. Pettersson [b]

[a] Nansen International Environmental and Remote Sensing Center, 14th Line 7, 199034, St. Petersburg, Russia – evgeny@niersc.spb.ru

[b] Nansen Environmental and Remote Sensing Center, Thormølhensgate 47, N-5006, Bergen, Norway – lasse.pettersson@nersc.no

Abstract – Two algorithms based on the neuron network and fuzzy c–mean logic techniques were developed for automated identification and delineation of blooms of *Lepidodinium chlorophorum* making use of MODIS-Aqua data. Training of the neural network algorithm and validation of performance efficiency of the both above algorithms were conducted employing in situ data from the waters of the Atlantic coastal zone of France. A spatio-temporal analysis (2002-2009) has been undertaken to study the extent and frequency trends of the phenomenon in the target waters. The developed algorithms are not area-specific and can be translated over other marine provinces.

Keywords: HAB, dinoflagellate blooms, *L.chlorophorum*, MODIS, English Channel, Bay of Biscay.

1. INTRODUCTION

*Prymnesiophytes, Raphidophytes, Cyanobacterium, Dinoflagellate*s, *Diatoms*, are typical phytoplankton groups responsible for harmful algae blooms (HABs) (Anderson, *et al.*, 1995) However until recently such a dinoflagellate species as *Lepidodinium chlorophorum* has not been mentioned in the literature as a harmful alga. Partly, this is because *Lepidodinium chlorophorum* was described for the first time in 1996, whereas more adequately it was characterized only in 2007 (Elbrächter, Schnepf, 1996). It was found that although *L. Chlorophorum* is not toxic, a massive growth of this species yields appreciable amounts of mucilage with an ensuing result of anoxia and extermination of mollusks. Thus, the area of *L. Chlorophorum* blooms should be considered as HABs, and their monitoring is important from the perspective of studying water dynamics and preserving marine resources.

2. METHODS, ALGORITHM DESCRIPTION, DATA USED

2.1 *L.chlorophorum*: Pigment composition and optical properties

It is conjectured that, evolutionary, *L.chlorophorum* stems up from the class *Prasinophytes* division Chlorophyta – primitive eukaryotic, marine green algae. Presumably, this genetic affinity caused the presence in their cells of green peridinin–containing plastids with the chlorophyll complex composed of chlorophyll–*a* (chl*a*) and chlorophyll-*b* (chl*b*) (Takishita *et al.*, 2008). The content of pigments in *L.chlorophorum* cells is such that the integral specific coefficient of absorption $a^*_{L,chl}$ is rather high [$3.32 \cdot 10^{-2}$ m^2mgchl-a^{-1}] as compared to some other marine algae, representative of phyla Dinophyta and Haptophyta (Claquin *et al.*, 2008). Information on the *spectral* values of $a^*_{L,chl}$ and specific backscattering coefficient $b^*_{b\,L,chl}$ is apparently absent in the available/reviewed literature.

2.2 Algorithms: methodology and realization

2.2.1. Neuron network emulation

The Stuttgart network simulator package (SNNS) has been exploited in our study (see ftp://ftp.informatik.uni-stuttgart.de/pub/SNNS/). The following architecture was employed: 6 neurons in the input layer (= number of the MODIS-Aqua spectral channels), 6 neurons in the hidden layer and one neuron in the output layer. Input data are underwater remote sensing reflectance [$R_{rsw}(\lambda)$] (Jerome et al., 1996) in the MODIS visible bands. Input values, $R_{rsw}(\lambda)$ in 6 channels are inverted by the network and the result is a number ranging from 0 to 1. 0 indicates the absence of *L. chlorophorum* blooming, 1 means that the pixel confidently belongs to *L. chlorophorum* blooming. Results in between 0 and 1 were considered as transition from not blooming to blooming area

2.2.2. Algorithm based on the fuzzy c-mean (FCM) technique

Fuzzy clusters are described by a matrix of fuzzy partitioning/fragmentation:

$$F = \lfloor \mu_{k\,i} \rfloor \quad , \quad \mu_{k\,i} \in [0\,,1], \quad k = 1\,,\ldots,M\,, i = 1\,,\ldots,c \qquad (1)$$

In which each k-line encompasses the degrees/weights of belonging of the object $(x_{k1}\,, x_{k2}\,, \cdots x_{kn})$ to clusters $A_1\,, A_2\,, \cdots, A_c$. Matrix F describes the degree of belonging to a cluster and, in the case of fuzzy partitioning, the degree of belonging of the given object to the cluster is assessed within the interval [0,1]. The conditions of fuzzy partitioning are formalized as follows:

* Corresponding author. 199034, St. Petersburg, Russia, Vasilievsky Island, 14th Line, 7, office 49, tel.: +7 (812) 324 51 03, fax: +7 (812) 324 51 02.

$$\sum_{i=1}^{c} \mu_{k\,i} = 1,\ k = 1, \ldots, M$$
$$0 < \sum_{k=1}^{M} \mu_{k\,i} < N,\ i = 1, \ldots, c \qquad (2)$$

Fuzzy partitioning permits to easily solve the problem related to objects located on the interface of two clusters: it is done through attributing to them the degree of belonging equal to 0.5. Fulfillment of fuzzy clusterization is based on non-linear optimization, which in our case is the Lagrangian method of non-determined factors/multiplies. The algorithm performance is effected through several sequential steps repeated iteratively (Shtobva, 2009).

2.3 Input *in situ* and satellite data

In situ measurements (identification of *L.chlorophorum* and number of cells) effected by IFREMER during 2001-2008 at two stations Ouest-Loscolo and Le-Croisic, located nearby the deltas of Rivers Vilain and Loire were employed. Only match-ups with MODIS overflights were used for NN algorithm development. As a result, a satellite data base was compiled of 6365 spectra of $R_{rsw}(\lambda)$, ~ 30 % of which belonged to *L.chlorophorum*.

Satellite data were subjected to a preliminary processing: $R_{rsw}(\lambda)$ spectra with a minimum (or a downward inflexion) in the third MODIS channel (488 nm) [due to chl-*b* and peridinin absorption in *L.chlorophorum*] were left for further analysis. The above criterion is not self-sufficient: the identification efficiency of the two algorithms resides in the analysis of the spectral signatures in *all* channels of MODIS, but this criterion proves to be very helpful.

3. RESULTS OF THE ALGORITHM APPLICATION TO MODIS-AQUA DATA

As Table shows, in all cases of high concentrations of *L.chlorophorum*, both algorithms unmistakenly identify the presence of this species. However, when the concentration is low or this species is marginal in the phytoplankton complex, the identification accuracy decreases due to suppression of *L.chlorophorum* spectral signatures in the resulting spectrum of $R_{rsw}(\lambda)$.

Though the two algorithms do not perform identically it can be seen from both the table and the figure that the results are very close.

Table. Efficiency of the NN and FCM algorithm identification of *L.chlorophorum* at one of the stations

Station	Date	Concentration of *L.chlorophorum* (cells/ml), determined in situ	Algorithm	
			NN	FCM
Ouest - Loscolo	09/09/2002	7200	0	0
	24/09/2002	380000	1	1
	07/06/2004	34000	1	1
	19/09/2005	400000	1	1
	03/10/2005	200000	1	1
	07/11/2006	66000	0	0
	29/05/2007	8600	0	0
	12/06/2007	160000	1	1
	24/07/2007	900000	1	1

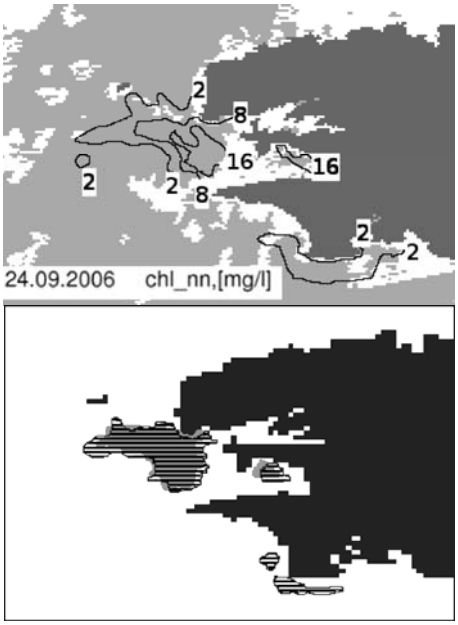

Figure 1. Chl*a* concentration –top panel; bottom panel-results obtained with the neural network (gray) and FCM (black dashed) algorithms in the area of intensive *L.chlorophorum* blooming in the Sea D'Iroise on 26.10.2006

Our retrospective analysis of MODIS-Aqua data over the time period 2002-2009 shows that there is a certain increase in both the *L. chlorophorum* blooming occurrence frequency and areal extent. However, the persistence of this tendency is liable to further substantiation through increasing the time series of satellite observations.

ACKNOWLEDGEMENTS

We extend our gratitude to our colleagues of IFREMER for ground-based data.

REFERENCES

Claquin P., Probert I., Lefebre S., Veron B. "Effects of temperature on photosynthetic parameters and TEP production in eight species of marine microalgae". Aquatic Microbial Ecology. 2008. V 5. P. 1-11, doi: 10.3354/ame01187.

Elbrächter M., Schnepf E. "Gymnodinium chlorophorum, a new,green bloom forming dinoflagellate (Gymnodiniales, Dinophyceae) with avestigial prasinophyte endosymbiont". Phycologia. 1996. V. 35. P. 381–393.

Hallegraeff G.M., Anderson D.M.and A.D. Cembella /Eds., "Manual on Harmful Marine Microalgae" IOC Manuals and Giudes, 1995. № **33**. Paris: UNESCO Publ., 430 p.

Jerome J., Bukata R., Miller J.,"Remote sensing Reflectance and its relationship to optical properties of natural water. Int. J. Rem. Sens., 1996. V.17. P. 43-52.

Shtobva S. D.2009. "Introduction into the theory of fuzzy ensambles and fuzzy logic". http://matlab.exponenta.ru/fuzzylogic/book1/12.php

Takishita K., Kawachi M., Noel M-H., Matsumoto T. "Origins of plastids and glyceraldehydes-3-phosphate dehydrogenase genes in the green-colored dinoflagellate *Lepidodinium chlorophorum*". Gene. 2008. V. 410. №. 1. P. 26-36.

Remote Sensing for Regional Earth System Prediction

R. Murtugudde

Earth System Science Interdisciplinary Center, Department of Atmospheric and Oceanic Science – University of Maryland, College Park, MD, USA – ragu@essic.umd.edu

Abstract – Regional Earth System Prediction (RESP) is the dynamic downscaling of global predictions and projections for day-to-day resource management for water, agriculture, human health, energy, and so on. Global models have made steady progress towards a comprehensive representation of the Earth System with an ever increasing spatial resolution. These models, especially under the auspices of IPCC are essential for global governance issues with their own observational needs as outlined under Group on Earth Observations (GEO). The concept is extended here to propose that sustainable management of the planet requires information at the street-level for most applications and the new technologies for in situ and space-based observations have to be driven to serve the needs of RESP to be able to effectively serve humanity.

Keywords: Earth System Prediction, Downscaling, Sustainability.

1. INTRODUCTION

No unique definition of the Earth System exists but the intuitive sense of natural-human systems interacting with each other serves us well (Schellnhuber 1999). The crucial role of sustained observations in constructing, improving, validating, and assessing the skill of Earth System models can hardly be overstated, especially as the urgency of avoiding the undesirable or unintended consequences of human actions becomes more evident. Observational needs for monitoring and predicting climate variability and change have been addressed before (Trenberth et al. 2002, Trenberth et al. 2006). Representation of human-natural system interactions in the present-day Earth System models rely on global and regional scale Earth System monitoring. The former is being co-coordinated under the Global Earth Observing System of Systems by GEO (http://www.earthobservations.org/geoss.shtml) with a vision of realizing a future wherein decisions and actions for the benefit of human kind are informed by coordinated, comprehensive and sustained Earth observations and information. The main objective here is to highlight the space-based observational needs for regional Earth System predictions and projections, where such predictions and projections are assumed *a priori* as the main decision-making tools for sustainable management of the Earth System (Murtugudde 2009, Murtugudde 2010a, and b). The observing systems of the future will have to consider the integral and interactive nature of the Earth System and drive new technologies for adaptive and smart systems where space and land-based platforms will interact with each other to optimize the web of sensors based on societal needs as noted by GEO, viz., disasters, health, energy, climate, water, weather, ecosystems, agriculture and biodiversity. National climate services will drive the synergy with global observations, research, and modeling with the link to the users occurring in the context of regional observations, research, and modeling (Miles et al. 2006).

2. SPACE-BASED PLATFORMS

A quantum leap in ocean observations has now been achieved with the Argo floats (http://www.argo.ucsd.edu/), which are now being instrumented for a number of other physical and biogeochemical measurements such as oxygen. It is easily conceivable that nascent technologies that allow direct sampling of genetic level information will soon be complemented by computational social-science approaches to establish adaptive optimization of webs of sensors for environmental monitoring outdoors and indoors for seamless model-data synthesis to generate routine RESP for sustainable management of the planet. Monitoring the human responses while learning-by-doing will require blending socio-economic data with environmental data to drive continuously validated, skillful RESP with uncertainties. Note that the time-scales of RESP will span the transition from weather to climate and climate change, as has eloquently been outlined for the global Earth System in Shapiro et al. (2010), and placed in the context of regional specificities in Murtugudde (2009). Space-based platforms need to be considered in this context to highlight their role and to visualize their uniqueness in providing the regional and global context that is often not achievable from land-based platforms.

2.1 Specific Example: Satellites for human health

No shopping list of essential observations can be exhaustive but a specific example of a practical application, viz., RESP for human health can be illuminating. The old paradigm of climate prediction for human health relies on finding correlations between climatic variables and disease incidences, outbreaks, or indicators that are precursors to an outbreak (Kelly-Hope and Thompson 2008). Climate change is already impacting not only the environmental conditions and microbial dynamics but also population growth and movement and thus the transmission dynamics of many diseases (Patz et al. 2004). The impacts of global change on humans mostly occur via local changes in weather, ecology, hydrology, etc. The observational system for human health must capture the linkages from climate change to human health to advance the process and predictive understanding of microhabitat selection by the relevant microbes, transmission dynamics, socioeconomics, and adaptation measures (Murtugudde 2009 and references therein). A space-based platform for human health must thus provide routine, accurate, and high-resolution data not only for climatic variables such as temperature, precipitation, humidity, land-cover, and vegetation but also track large-scale movements of harmful algal blooms, pests, humans, animals, and birds, including their responses to extreme events such as floods, droughts, fires, and earthquakes. Relevant epidemiological factors from space must then be combined with land-based observations and

models of environmental, genetic, chemical, and biological factors, microbial contamination processes, human behavior and exposure. This is an opportunity to drive technological innovation to support accurate, reliable, and timely RESP for air and water-borne, zoonotic and anthroponocic diseases by monitoring ever increasing details down to DNA and RNA, potentially on observing platforms such as Argo or have miniaturized probes that go from genetics and genomics to ecology to human health (DeLong 2009, Bowler et al. 2009). These technological innovations must drive creations of global digital libraries of air and water quality including pathogens and their genetic information and also instrumentation so that decision-makers on the ground carrying detectors such as hand-held bacterial counters or optimally distributed web of sensors that monitor environmental factors and pathogen levels can instantly validate the RESP via satellite links against the digital libraries (Stewart et al. 2008). Novel advances in computational social science that capture transmission dynamics by using human movement and behavior (Lazer et al. 2009), have to be merged with macro-scale human ecological observations from space and land-based platforms to provide effective decision-making tools for specific mitigation and adaptation measures and response training such that the evaluation of the impacts of policy and management decisions in modulating climate and regional weather changes, resource distributions, population movements and the associated cascades to human health must be a continuous feedback to the Earth System observation and prediction.

3. CONCLUDING THOUGHTS

Much has been said about the need for monitoring, predicting, and projecting climate variability and climate change. The concept of Earth System has been embraced by the IPCC to address global issues. Regional specificities of resources, populations, and the socio-economics dictate the information need for day-to-day management and RESP offers the best way forward by downscaling global climate and Earth System predictions and projections. The focus here has been to emphasize the human-natural system interactions in addition to the regional manifestations of global change and the demand for integrated observational systems to serve societal needs. Space-based observations are absolutely essential to provide the macroscopic view of the human-natural system interactions. Planned space missions for the coming years (e.g., NRC 2007) demonstrate the bias of natural scientists in planning and designing satellite missions. While the list is impressive for climate variability and climate change issues, most societal benefits are derived products such as droughts/floods, water resources, etc., and most of the applications for agro-economics, fisheries, health, and such, are not direct targets of the missions. It is evident that far more care is needed in designing observation systems, especially satellite missions for RESP. Interdisciplinary education must translate into a workforce that is able to diagnose the maladies of the Earth System and devise innovative approaches and technologies to cure what ails the Earth System.

ACKNOWLEDGEMENTS

NOAA supported the Chesapeake Bay Forecast System and partial NASA support is acknowledged. Input from Clarissa Anderson, Antonio Busalacchi, and Steve Halpern were crucial for developing this concept.

REFERENCES

Bowler, C., D. M. Karl, and R. R. Colwell, 2009: Microbial oceanography in a sea of opportunity. *Nature,* **459**, 207-212.

DeLong, E. F., 2009: The microbial ocean from genomes to biomes. *Nature,* **459**, 207-212.

Kelly-Hope, L., and M. C. Thompson, 2008. "Climate and infectious diseases". In **Seasonal Forecasts, Climatic Change, and Human Health**. M. C. Thompson et al. (Eds.), Springer Science+Business Media, 31-70.

Lazer, D., A. Pentland, L. Adamic, S. Aral, A-L Barabasi, D. Brewer, N. Christakis, N. Contractor, J. Fowler, M. Gutmann, T. Jebara, G. King, M. Macy, D. Roy, M. Van Alstyne, 2009: Computational Social Science**.** *Science*, **323**, 721-723.

Miles, E. L., A. K. Snover, L. C. Whitley Binder, E. S. Sarachik, P. W. Mote, and N. Mantua, 2006. "An approach to designing a national climate service". *Proc. Nat. Acad. Sci*., **103,** 19616-19623.

Murtugudde, R., 2009. "Regional Earth System prediction: A decision-making tool for sustainability?". *Curr. Op. Environ. Sust.*, **1,** 37-45.

Murtugudde, R., 2010a. "Observational needs for sustainable coastal prediction and management**".** In press**,** Management and Sustainable Development of Coastal Zone Environment, Ramanathan et al. (Eds.), Springer.

Murtugudde, R., 2010b. "Observational needs for regional Earth System Prediction". In press, *Proc. OceanObs09: Sustained Ocean Observations and Information for Society*. Hall, J., et al. (Eds.), ESA Publication WPP-306, 2010.

NRC 2007. "Earth Science and Applications from Space: National Imperatives for the Next Decade and Beyond". National Academy Press. 455pp.

Patz, J. A., P. Daszak, G. M. Tabor, A. A. Aquirre, M. Pearl, J. Epstein, N. D. Wolfe, A. M. Kilpatrick, J. Foufopoulos, D. Molyneux, D. J. Bradley, and Members of the working group on Land use change and disease emergence, 2004. "Unhealthy landscapes: Policy recommendations on land use change and infectious disease emergence". *Environ. Heal. Persp.*, **112,** 1092-1098.

Schellnhuber, H.J., 1999: 'Earth system' analysis and the second Copernican revolution. Nature, **402**, C19 – C23.

Shapiro, M., and co-authors, 2010. "An earth-system prediction initiative for the 21st century". In press, *Bull. Amer. Meterolog. Soc*.

Stewart, J. R., R. J. Gast, R. S. Fujioka, H. M. Solo-Gabriele, J. S. Meschke, L. A. Amaral-Zettler, E. del Castillo, M. F. Polz, T. K. Collier, M. S. Strom, C. S. Sinigalliano, P. DR Moeller, and A. F. Holland, 2008. "The coastal environment and human health: microbial indicators, pathogens, sentinels, and reservoirs". *Environ. Heal.*, **7(S2):S3,** 14pp.

Trenberth, K. E., T. R. Karl, and T. W. Spence, 2002. "The need for a systems approach to climate observations". *Bull. Amer. Meterolog.* Soc., **83**, 1558-1559.

Trenberth, K. E., B. Moore, T. R. Karl, and C. Nobre, 2006. "Monitoring and prediction of the Earth's climate: A future perspective". *J. Clim.*, **19,** 5001-5008.

Use of Fine Scale Satellite Imagery to Support Studies on the Distribution of the Small Octopus *Octopus tehuelchus* in a Marine Protected Area of Northern Patagonia

M. Narvarte [a,b,*], L.P. Storero [a,b], C. Schneider [c], R. González [a]

[a] Instituto de Biología Marina y Pesquera Almirante Storni, San Antonio Oeste, Río Negro, Argentina
[b] Consejo Nacional de Investigaciones Científicas y Técnicas (CONICET) Argentina – mnarvarte@gmail.com
[c] Asociación para la Conservación y el Estudio de la Naturaleza (ACEN), Córdoba, Argentina

Abstract - Satellite imagery was used to gain knowledge on spatial distribution, over a fine spatial scale, of the small Patagonian octopus and to relate it with environmental variables of significance (low tide line and extension of the rocky shore). Detailed spatial locations of octopus were recorded with differential GPS during coastal surveys performed during 2005-2007. Coastal line of the study area was redrawn from remote-sensed CBERS images. Distances from octopus locations to the near point of the low tide line were calculated. This allowed us to identify a seasonal pattern and evaluate the way in which this distance influences octopus distribution.

Keywords: octopus distribution, CBERS, Patagonia.

1. INTRODUCTION

Shellfish such as scallops, gastropods and octopuses are sedentary-low mobile animals that live in direct contact with the seabed (benthic species). Their limited mobility means that their growth, reproduction and survival depend on local environmental conditions. Octopuses have a complex lifecycle: they arrive to coastal waters to feed and reproduce; females deposit egg capsules in the rocky shore and they take care of them during the entire intracapsular development (around four months). Monitoring octopus distribution has been based on in situ data obtained with differential GPS following a very skilled fisherman in some specific sites along the intertidal coastal zone of San Matías Gulf. Larger-scale trends, however, could be determined using satellite-based observations to map the coastline and further relating abundance and distribution in relation to that well defined coastline. Geographic Information System (GIS) could help us improve the knowledge of coastal benthic resources and habitat uses.

This study has three fundamental goals: a) mapping the coastline in a marine protected area using different remote sensing spatial sources at a very fine scale; b) analyzing the spatial variability of octopus distribution; and c) relating octopus distribution to the derived coastal maps.

2. MATERIALS AND METHODS

2.1. Study site.

Islote Lobos (41°26'S/65°03´W) is constituted by six islands connected to land during low tide, characterized by rocky shores. It has been a traditional fishing ground until 1977 when it was erected as a protected area for the conservation of marine mammals and birds. Octopus abundance here is relatively high comparing with other sites of San Matías Gulf (Narvarte *et al.* 2006).

2.2. Collecting octopus distribution data.

Monthly samplings were performed during ebbing tides from 2005 to 2007. Adults of *O. tehuelchus* were caught by a skilled fisherman, following a transect (100 m long, 3 m width) and the location of each octopus was accurately recorded using a submetric precision GPS (Trimble©). Between 6 and 26 transects were monthly done. Distances from octopus locations to the near point of the low tide line were calculated using ArcGIS™ 9.3 (ESRI©), averaged per transect and seasonally grouped to assess octopus distribution along the intertidal zone.

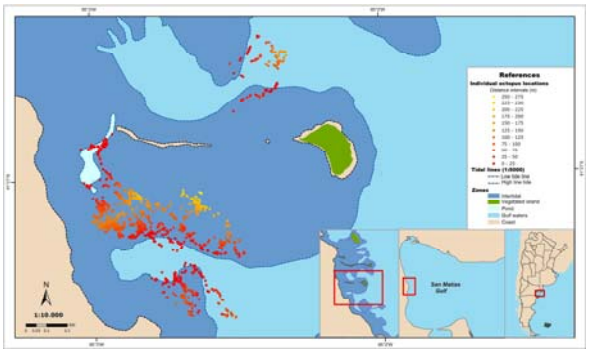

Figure 1. Study site, spatial location of octopuses and low/high tide lines derived from satellite images.

2.3. Remote sensed images and derived mapping.

For constructing coastal lines, the panchromatic image 168-D-146-5, Dec 23-2008 (CBERS 2B HRC; INPE, 2010), with 2.5 m spatial resolution, taken at low tide, was used. A selected fishing area was corrected using the geometric polynomial model to the WGS 84 reference system (datum WGS84, elipsoide WGS84), on the cartographic Transverse Mercator projection (zone 4). Conspicuous spatial attributes, identifiable in the satellite image, were recorded in the field with GPS and used as control points in the geometric correction of the scene. High and low tide lines were manually drawn using ArcGIS™ 9.3 (ESRI©), from visual interpretation on screen at scale 1:5000. For adjusting the lines on complex topographic sites, scenes from Google Earth™ of high spatial resolution (satellite QuickBird; 2010© DigitalGlobe), taken on Feb 22-2004, were used and geometrically co-registered with the panchromatic image.

* Corresponding author. Güemes 1030 (8520) San Antonio Oeste (RN), Argentina. Tel/Fax: +542934430764.

3. RESULTS

The root mean square error (RMSE) for the geometric correction of the panchromatic CBERS 2B image was 2.75, and for coregistration of QuickBird scenes was 1.58. Octopus density varied seasonally in relation to the distance from the low-tide line (Fig. 2). Octopuses were found widely extended along the intertidal zone, between the low-tide line to 200 m up to the coast, in spring–summer.

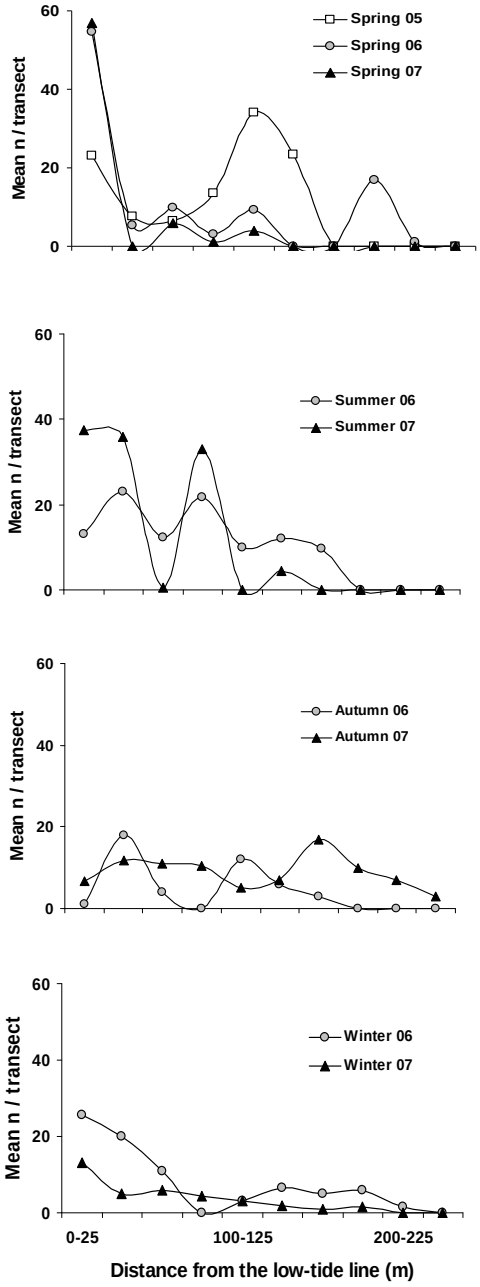

Figure 2. Seasonal variations of mean octopus numbers per transect in relation to the distance from low tide line.

A different distribution pattern was found during cold months: in autumn, the abundance decreased but octopuses were also widely extended along the intertidal zone, whereas in winter octopuses were caught only in the low intertidal zone close to the low-tide line, being practically absent 75-100 m away from the coastline.

4. DISCUSSION

Octopuses occupy almost the entire exposed intertidal zone but important variations were found among seasons, which may be attributed to life history traits: in summer octopuses present the highest growth rates (Storero *et al.* 2009), actively feeding on coastal organisms (mytilids and crustacean). Decreasing densities of octopus in autumn were confirmed by Ré (1989) and Iribarne (1990) who stated that females migrate to the nearby subtidal zones to take care of the offspring. Extreme environmental conditions in cold months (≈9ºC in tidal ponds) could explain the aggregation of octopuses near the low-tide line during this period.
Hydrodynamic features and the seasonal changes in the water masses control octopus migratory behavior to the coastal zone but the topography (better identified by satellite tools for mapping) also imposes limits for octopus distribution. According to this and in relation with the importance of conserving and monitoring the Marine Protected Areas, the satellite images are a unique tool for spatially integrate the twin objectives of conservation and sustainable management of fisheries.

5. CONCLUSIONS

Identification of high tide lines was optimum, since the high reflectance of sandy and rocky shores gave a well defined contrast comparing to sites of temporal humidity. The identification of low tide lines was improved by combining high resolution satellite images. Manual vectorization provided an accurate representation of line contours, higher than that obtained through classification algorithms. Visual interpreting of panchromatic images at fine grain spatial scale (1:5000) allowed us to achieve precise representations in complex topographic sites, with low investment effort. Satellite remote sensing for analyzing spatial resource distribution in coastal studies should be encouraged, since the development of advanced satellite sensors with high spatial resolution continue to progress.

ACKNOWLEDGEMENTS

We thank M. Ocampo R. and G. Williams for discussion. We are grateful for field activities to N. Dieu and M. Fidel. This work was supported by FONCYT of Argentina (PID 371), Ministry of Production of Río Negro and the National University of Comahue.

REFERENCES

Google Earth (2010). http://earth.google.es/index.html
INPE Brasil (2010). http://www.inpe.br/.
Iribarne, O. (1990). Ecology and harvest of the small Patagonian octopus *Octopus tehuelchus* (d´Orb). Ms. Sci. Thesis. Univ. Washington: 121pp.
Narvarte, M.A., R.A. González and M. Fernández (2006). Comparison of octopus abundance between an open access fishing ground and a marine protected area: evidence from a direct development species. Fisheries Research, vol. 79, pp. 112-119.
Ré M.E. (1989). Crecimiento y alimentación de *Octopus tehuelchus* en Puerto Lobos, Golfo San Matías. Doctoral Thesis, Universidad Nacional La Plata, Argentina, 262 p.
Storero, L., Ocampo-Reinaldo, M., González, R. and M. Narvarte (2009). Growth and life span of the small octopus *Octopus tehuelchus* in Patagonia: three decades of study. Marine Biology doi: 10.1007/s00227-009-1341-8.

Intrinsic Uncertainty in the Estimation of Suspended Mineral Concentrations from Reflectance Signals in Optically Complex Shelf Seas

C. Neil, A. Cunningham, D. McKee, I.C. Brown

University of Strathclyde, Rottenrow, Glasgow, G4 0NG – Claire.neil@strath.ac.uk

Abstract – This study investigates the intrinsic uncertainty introduced in estimations of mineral suspended solids (MSS) concentrations by the presence of other optically significant constituents (OSCs). Modelled reflectance spectra were generated using inherent optical properties representative of a coastal environment. Results showed that reflectance at 667 nm was the optimal wavelength for obtaining MSS concentrations from ocean colour data. However the sensitivity of modelled $R_{rs}667$ values to varying concentrations of other constituents highlighted an intrinsic uncertainty in the retrieval of MSS. Errors associated with this uncertainty varied with OSC values and were best indicated by explicitly stating the range of MSS concentrations that would be associated with a given R_{rs} signal.

Keywords: sediment, optically coplex waters, shelf seas.

1. INTRODUCTION

Mineral suspended sediments (MSS) play an important role in shelf sea ecosystems, limiting the penetration of light within the ocean and assisting with the transportation of pollutants throughout the water column. Accurate representation of MSS concentrations from satellite imagery is therefore crucial for understanding the biological and physical dynamics of optically complex shelf seas. Unfortunately the presence of MSS strongly degrades the efficiency of standard algorithms used to derive biological products from ocean colour data (Robinson, 2008).

Most algorithms for estimating MSS from ocean colour data have been developed using single band reflectances (Binding et al., 2003) or reflectance ratios (Doxaran et al., 2002). These techniques generate reasonable estimations of MSS in the regions for which they were developed, but since their performance is affected by the presence of optically significant constituents in the water their wider applicability cannot be assumed. This paper investigates the intrinsic uncertainty that arises from the presence of these other constituents. An alternative method of deriving concentrations of MSS from ocean colour data is presented which provides a range of possible concentrations for each reflectance signal and offers greater insight into the uncertainty associated with retrieving constituent concentrations from ocean colour data.

The colour of the ocean is determined by its inherent optical properties. In addition to water molecules, optically significant constituents that influence the light leaving the surface of a shelf sea are chlorophyll a (CHL, taken as a proxy for phytoplankton biomass), mineral suspended solids (MSS) and coloured dissolved organic matter (CDOM). Each of these components makes an individual contribution to the inherent optical properties (IOPs) of the medium. Remote sensing reflectance, R_{rs}, at a given wavelength, λ, just above the sea surface, is dependent on two IOPs, the bulk absorption, a, and backscattering, b_b, and can be expressed by the general form;

$$R_{rs}(\lambda) = \frac{(1-r_F)}{n^2}\left[\frac{f_{L\beta}}{Q}\right]\frac{b_b}{a} \quad (1)$$

where f is a variable function of the radiance distribution and volume scattering function, β, Q is the ratio of upwelling irradiance to radiance, r_F is the Fresnel reflectance and n is the refractive index of seawater. By expressing the IOPs as a product of the specific IOPs (SIOPs, denoted by superscript asterisk) and constituent concentrations, equation (1) can be expanded to include all possible optically significant constituents found in coastal areas;

$$R_{rs}(\lambda) \propto \frac{b_{b_w} + b^*_{b_{MSS}} MSS + b^*_{b_{CHL}} CHL}{a_w + a^*_{MSS} MSS + a^*_{CHL} CHL + a^*_{CDOM} CDOM} \quad (2)$$

where w indicates the contribution by water. Thus remote sensing signals are sensitive to MSS, CHL, and CDOM concentrations and their individual SIOP values.

2. ANALYSIS

To effectively model a coastal environment, SIOPs are required for each constituent. These were derived from *in-situ* AC-9 (absorption and scattering) and Hydroscat (backscattering) data measured on various Irish Sea research cruises (Brown, 2010). Reflectance signals were generated by supplying interpolated SIOPs and constituent concentrations to the HydroLight radiative transfer software package. Constituent concentrations were increased logarithmically, from 0.1 gm^{-3} to 10 gm^{-3} for MSS, 0.1 mg m^{-3} to 10 mg m^{-3} for CHL and 0.01 m^{-1} to 1 m^{-1} for CDOM. Calculations were performed for all possible constituent combinations in the visible wavebands of NASA Moderate Resolution Imaging Spectroradiometer (MODIS).

2.1 MSS only

The effects of adding MSS to pure seawater on the remote sensing reflectance signals are shown in Figure 1. Each line represents the relationship between R_{rs} at a given wavelength and concentration of MSS. Linearity of the relationship between R_{rs} at red wavelengths (667 nm, 678 nm) and concentrations of MSS can be attributed to the b_b/a ratio shown in equation (1). At red wavelengths, a is dominated by absorption due to water and b_b is determined predominantly by the MSS contribution (see Table. A). Consequently b_b increases significantly with increasing

concentrations of MSS, whereas *a* remains relatively unchanged.

Table A. Assumed Inherent Optical Property Contributions

λ	a^*_{MSS}	a_W	$b_b{}^*_{MSS}$	b_{bW}
477	0.0437	0.0121	0.0136	0.0017
532	0.0268	0.0438	0.0121	0.0011
650	0.0076	0.3400	0.0090	0.0005
676	0.0028	0.4585	0.0083	0.0004

In contrast, R_{rs} at shorter wavelengths tends to a constant value as MSS is increased. At low concentrations, MSS and water both contribute significantly to the b_b/a ratio in equation (1). At higher values, the water contribution becomes negligible and R_{rs} is increasingly determined by the MSS component: this has a constant b_b/a ratio irrespective of concentration. Consequently, the MSS vs. R_{rs} relationship is non-linear in the blue and green wavebands. The relationship is linear at 667 nm and 678 nm, but since the latter waveband is subject to the effects of chlorophyll fluorescence 667 nm is the waveband of choice for algorithm development.

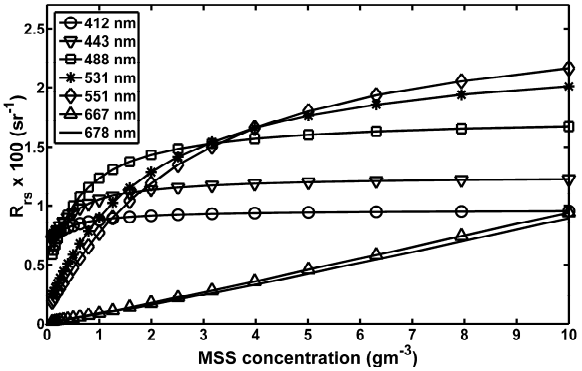

Figure 1. The effect of increasing MSS concentrations on R_{rs} at MODIS visible wavebands.

2.2 MSS plus other constituents

The effect on remote sensing reflectance at 667 nm, $R_{rs}667$, produced by adding constituents other than MSS to water is shown in Figure 2. The solid line represents remote sensing reflectance signals generated by only MSS and water.

Adding CDOM always reduces the magnitude of $R_{rs}667$, so that a general algorithm that relied on this reflectance would under estimate concentrations of MSS in areas where CDOM was present. The effect of adding CHL to water and MSS is more complex, since it can increase or decrease the R_{rs} signal depending on the concentration of MSS present. Varying the combinations of CHL and CDOM within the limits stated previously produced the range of $R_{rs}667$ shown in grey. For a single concentration of MSS, these are the possible R_{rs} signals that can be generated when other constituents are present. The upper and lower limits of this range, depicted by dashed lines on Figure 2, can be used to generate a potential range of MSS concentrations from the reflectance signal. These limits are expressed by equations (3) and (4),

$$MSS_{max} = 2.372x10^4 (R_{rs}667)^2 + 1186(R_{rs}667) - 0.004 \quad (3)$$

$$MSS_{min} = -4.879x10^4 (R_{rs}667)^2 + 1734(R_{rs}667) - 2.073 \quad (4)$$

where MSS_{max} and MSS_{min} are the maximum and minimum concentrations of MSS that can produce the R_{rs} signal when other constituents are present. For example, an $R_{rs}667$ signal of 0.006 sr^{-1} can have an MSS value between 6.57 and 7.97 gm^{-3}. Its actual value within this range is dependent on the concentrations of other constituents in the water.

By dealing with potential ranges of MSS, given by equations (3) and (4), more realistic estimations of MSS with associated uncertainties can be produced.

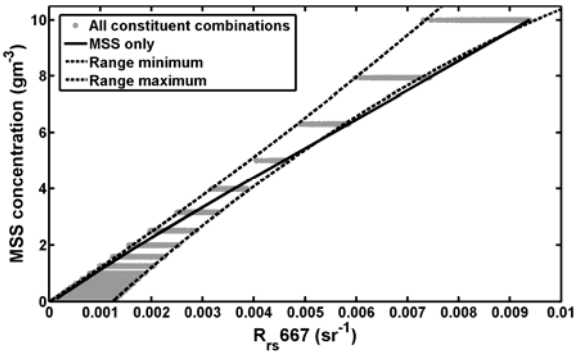

Figure 2. Effect of addition of CHL and CDOM on $R_{rs}667$.

3. CONCLUSIONS

Investigation of R_{rs} signals generated by adding MSS to pure seawater has suggested $R_{rs}667$ is the optimal wavelength for MSS estimation. Addition of other optically significant constituents affects the R_{rs} signal and introduces intrinsic uncertainties in the retrieval of MSS concentrations. The proposed method generates ranges of possible MSS values for a given R_{rs} signal, encompassing the uncertainty in the result. This provides a more realistic representation of MSS concentrations and the associated errors.

REFERENCES

Binding, C.E., Bowers, D.G., Mitchelson-Jacob, E.G., (2003), An algorithm for the retrieval of suspended sediment concentrations in the Irish Sea from SeaWiFS ocean colour satellite imagery. *International Journal of Remote Sensing*, vol 24, no 19, pp. 3791-3806.

Brown, I.C. (2010), The inversion of *in situ* inherent optical property measurements in shelf seas. PhD Thesis, University of Strathclyde, Glasgow.

Doxaran, D., Froidefond, J.M., Castaing, P., (2002), A reflectance band ratio used to estimate suspended matter concentrations in sediment-dominated coastal waters. *International Journal of Remote Sensing*, vol 23, no 23, pp. 5079-5085.

Robinson, I., (2008), Marine Board – European Science Foundation Position Paper 12, Remote Sensing of Shelf Sea Ecosystem - State of the Art and Perspectives.

Diurnal variability of suspended matter from the SEVIRI geostationary sensor and validation with high frequency in situ data

G. Neukermans [a,b]*, K. Ruddick [a]

[a] Management Unit of the North Sea Mathematical Models (MUMM), Royal Belgian Institute for Natural Sciences (RBINS), Brussels, Belgium – g.neukermans@mumm.ac.be, k.ruddick@mumm.ac.be
[b] Université Lille Nord de France, ULCO, Laboratoire d'Océanologie et Géoscience (LOG), CNRS, Wimereux, France

Abstract – Mapping Total Suspended Matter (TSM) from the SEVIRI sensor on board the METEOSAT geostationary weather satellite platform has recently been shown to be feasible for turbid waters (Neukermans *et al.*, 2009). The present study focuses on (i) the diurnal variability of TSM in turbid waters and possible correlations with hydrodynamical parameters and (ii) the validation of these SEVIRI TSM maps at very high temporal resolution with OBS data obtained from moored buoys in the Southern North Sea.

Keywords: geostationary, suspended matter, diurnal variability.

1. INTRODUCTION

The concentration of Total Suspended Matter (TSM) in shallow coastal waters is known to vary at time scales shorter than a day because of processes such as horizontal advection and/or vertical resuspension forced by tides or short wind events. This variability is often measured by in situ instrumentation and is represented in sediment transport models. However, optical remote sensors onboard polar-orbiting platforms, such as the AQUA and ENVISAT satellites, typically provide only one or two images of TSM per day. Since the real variability of TSM can be a factor of two or more (Eisma and Irion, 1988) it is clear that data from polar-orbiting sensors cannot represent conditions for a whole day and that any attempt to use such data to study longer term variability will be contaminated by aliasing.

Despite the increasing use of satellite-derived TSM data for environmental (Van den Berg, 1996; Lacroix *et al.*, 2007) or sediment transport (Vos *et al.*, 2000 ; Fettweis *et al.*, 2007) applications, this severe limitation of sampling frequency is only rarely addressed (Stumpf *et al.*, 1993). A significant increase in the temporal resolution of satellite-derived TSM data becomes possible from geostationary satellites (Neukermans *et al.*, 2009). For example, the SEVIRI sensor onboard MSG2 (longitude 0°E) provides data every 15 minutes for a disk covering most of Europe and Africa, while the Rapid Scan Service of the SEVIRI sensor onboard MSG1 (longitude 9.5°E) brings the temporal resolution down to 5 minutes for Europe. Although the SEVIRI sensor was not designed for mapping of TSM and has a detection limit that excludes many clear oceanic waters, it provides a basis for testing methods and assessing the potential of future geostationary ocean colour sensors such as GOCI (Kang *et al.*, 2004) - a taste of things to come.

A feasibility study for mapping TSM from the geostationary SEVIRI sensor (Neukermans *et al.*, 2009) has shown that TSM can be detected with sufficient accuracy in the turbid waters of the Southern North Sea. Furthermore, SEVIRI TSM maps showed good correlation to TSM maps from a conventional polar-orbiting ocean colour satellite (MODIS Aqua).

The present study investigates the diurnal variability of TSM in turbid waters in the Southern North Sea between January 2008 and June 2009 and possible correlations with hydrodynamical parameters such as tidal height and bottom stress. SEVIRI TSM maps are further validated with data obtained from a system of moored buoys in the Southern North Sea. Half-hourly OBS-derived TSM data from three CEFAS SmartBuoys, located in clear to turbid waters, provide an extensive validation dataset for SEVIRI TSM. This half-hourly validation was carried out for 1.5 years of SEVIRI TSM data (January 2008-June 2009).

2. MATERIALS AND METHODS

2.1 SEVIRI data processing

Atmospheric correction of SEVIRI solar imagery (VIS0.6 and VIS0.8) includes corrections for Rayleigh and aerosol scattering, absorption by atmospheric gases and atmospheric transmittances. The aerosol correction uses assumptions on the ratio of marine reflectances and aerosol reflectances in the red (VIS0.6) and near-infrared (VIS0.8) bands (for futher details, see Neukermans *et al.*, 2009). A single band TSM retrieval algorithm, calibrated by non-linear regression of seaborne measurements of TSM and marine reflectance was applied (Nechad *et al.*, 2010). The uncertainty on the derived TSM products, introduced by the uncertainties on these atmospheric correction assumptions is quantified.

3.2 Validation with autonomous platform data

Half hourly TSM data obtained from three CEFAS SmartBuoys, located in clear to turbid waters in the Southern North Sea (see Figure 1) were used for validation of SEVIRI TSM over a 1.5 year period (January 2008 until June 2009).

3. RESULTS AND DISCUSSION

3.1 Diurnal variability of TSM in turbid waters

Figure 2 shows the diurnal variability of TSM, captured by SEVIRI, on a cloudfree day (adapted from Neukermans *et al.*, 2009) for turbid water at the South East coast of Britain (51.67°N, 1.57°E). The estimated uncertainty on TSM ranges

* Corresponding author. Gulledelle 100, 1200 Brussels, Belgium. Tel.: +32(2)7732134, Fax: +32(2)7706972.

between 12 and 29%, while TSM concentration varies by a factor 2 over an 8h period.

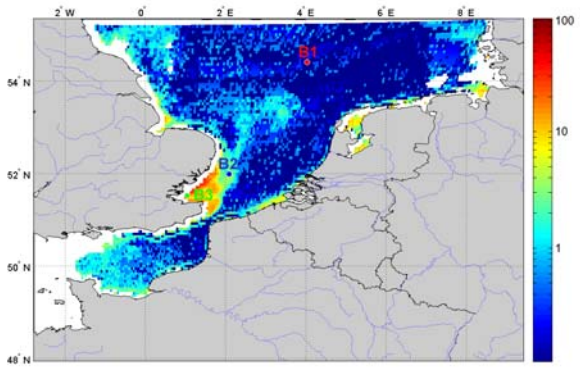

Figure 1. Location of CEFAS SmartBuoys (B1-B3) in the Southern North Sea superimposed on a TSM (mg/l) map from SEVIRI on June 29, 2006 at 12:00 UTC.

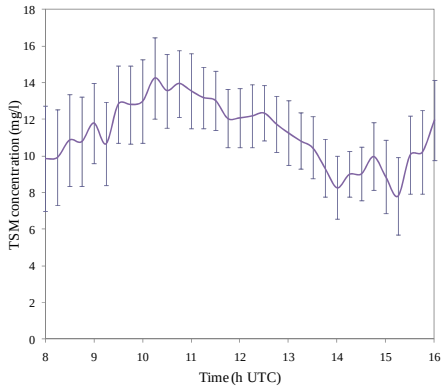

Figure 2. High frequency temporal variability for turbid water (51.67°N, 1.57°E) on a cloudfree day (June 29, 2006).

3.3 Validation with autonomous platform data

A preliminary analysis of half hourly TSM data obtained from CEFAS SmartBuoys B1-B3 against TSM from SEVIRI for a period of 35 days in June and July 2006 is shown in Figure 3.

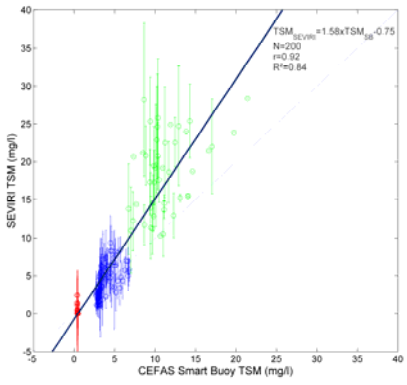

Figure 3. SEVIRI TSM *vs*. CEFAS TSM for SmartBuoys B1 (red), B2 (blue) and B3 (green) (locations in Figure 1).

4. CONCLUSION

Using the methodology developed by Neukermans *et al.* (2009), TSM data for the turbid waters of the Southern North Sea is derived from the geostationary SEVIRI sensor for a period of 1.5 years. This data is validated against high frequency *in situ* data from CEFAS SmartBuoys and is used to assess diurnal variability of TSM. While TSM is known to vary during the day in tidal waters, possibly by a factor of two or more, this cannot be resolved by the polar-orbiting sensors such as MODIS-AQUA and ENVISAT-MERIS. Use of the geostationary SEVIRI sensors allows this diurnal variability to be resolved and related to underlying hydrodynamic processes (advection and resuspension).

ACKNOWLEDGEMENTS

This research was supported by the BELCOLOUR-2 project, funded by the STEREO programme of the Belgian Science Policy Office under contract SR/00/104. Thanks to Nicholas Clerbeaux for providing SEVIRI data and kind help. CEFAS is thanked for providing OBS-TSM data from the SmartBuoys.

REFERENCES

Eisma, D., & Irion, G. (1988). Suspended matter and sediment transport. In *Pollution of the North Sea: an assessment* (pp. 20-35). Berlin: Springer-Verlag.

Fettweis, M., B. Nechad and D. Van den Eynde (2007). "An estimate of the suspended particulate matter (SPM) transport in the southern North Sea using SeaWiFS images, in situ measurements and numerical model results." Continental Shelf Research 27(10-11): 1568-1583.

Kang, G., S. Kang, S. Yong, J. KIm, Y. Chang and H. Youn (2004). Korea Geostationary Ocean Color Imager. IGARSS, IEEE.

Lacroix, G., K. Ruddick, Y. Park, N. Gypens and C. Lancelot (2007). "Validation of the 3D biogeochemical model MIRO&CO with field nutrient and phytoplankton data and MERIS-derived surface chlorophyll *a* images." Journal of Marine Systems 64(1-4): 66-88.

Nechad, B., K. Ruddick and Y. Park (2010). "Calibration and validation of a generic multisensor algorithm for mapping of total suspended matter in turbid waters" Remote Sensing of the Environment 114(2010): 854-866.

Neukermans, G., K. Ruddick, E. Bernard, D. Ramon, B. Nechad and P.-Y. Deschamps (2009). "Mapping total suspended matter from geostationary satellites: a feasibility study with SEVIRI in the Southern North Sea." Optics Express 17(16): 14029-14052.

Stumpf, R. P., G. Gelfenbaum and J. R. Pennock (1993). "Wind and tidal forcing of a buoyant plume, Mobile Bay, Alabama." Continental Shelf Research 13(11): 1281-1301.

van den Berg, A. J., S. M. Turner, F. C. van Duyl and P. Ruardij (1996). "Model structure and analysis of dimethylsulphide (DMS) production in the southern North Sea, considering phytoplankton dimethylsulphoniopropionate (DMSP) lyase and eutrophication effects." Marine Ecology Progress Series 145: 233-244.

Vos, R. J., P. G. J. t. Brummelhuis and H. Gerritsen (2000). "Integrated data-modelling approach for suspended sediment transport on a regional scale." Coastal Engineering 41(1-3): 177-200.

Proposal of an Absorption Method to Discriminate Phytoplankton Optical Groups in Natural Mixed Assemblages of the Mediterranean Sea

E. Organelli *, L. Lazzara, C. Nuccio, L. Massi

Dipartimento di Biologia Evoluzionistica "Leo Pardi", Università degli Studi di Firenze, Florence, Italy – emanuele.organelli@unifi.it; luigi.lazzara@unifi.it; caterina.nuccio@unifi.it; luca.massi@unifi.it

Abstract – Natural phytoplankton assemblages generally show high diversity in pigment composition, affecting their absorption responses. We propose an absorption method to discriminate, in natural mixed assemblages, the spectral signatures of seven phytoplankton groups with different marker pigments composition. Proposed routine is based on a pair-wise similarity computation, by means of *Spectral Angle Mapper* algorithm, between each natural spectrum and reference spectra of phytoplankton groups. Regressions between similarity indices and marker pigments concentrations show significant correlation coefficients, highlighting the power of this method and the possibility to optically determinate phytoplankton composition in mixed assemblages. The method represents an useful tool for the optical discrimination of phytoplankton groups.

Keywords: absorption, phytoplankton, optical groups.

1. INTRODUCTION

The knowledge of the different phytoplankton assemblages composition is an essential topic to improve the ocean biogeochemistry understanding. Even remote sensing copes with this problem through the definition of analytical methods to detect HAB events (Cullen *et al.*, 1997) or phytoplankton functional types (Aiken *et al.*, 2007). We propose here an absorption model and we evaluate its capability of determining spectral signatures of different phytoplankton optical groups, based on their pigment composition, in mixed assemblages of Mediterranean case 1 waters. We analyze also the relations with the pigments content of natural assemblages, in order to reconstruct their taxonomical composition.

2. METHODS

2.1 Bio-optical Analysis

The species used as references for different phytoplankton optical groups, mostly corresponding with algal classes, are listed in table A. All batch cultures were grown in a proper medium at 22 °C under L/D cycle of 12/12. All species were grown after acclimation at 150 µmol quanta m^{-2} s^{-1} in order to match with UML irradiance. Surface natural samples of phytoplankton were collected during several cruises across the Mediterranean Sea, organized in the framework of international strategies (EuroGOOS and MedGOOS) and carried out in autumn and early spring, between 2004 and 2008. Phytoplankton absorption spectra were measured by means of the quantitative filter-pad technique. Different aliquots of exponential phase cultures and natural samples were filtered on Whatman GF/F (Ø 25 mm). Total particulate measurements were carried out, from 400 nm to 700 nm, by Licor (LI1800UW) spectro-radiometer equipped with LI1800-12S integrating sphere according to the T-R method (Tassan and Ferrari, 2002), before and after pigment extraction in absolute methanol, in order to separate phytoplankton absorption from non algal particulate one. Concentrations of chlorophyll *a* + DV chl *a* (Chl *a*) and the marker pigments (MP) of phytoplankton groups (table A) were obtained by HPLC, according to Barlow *et al.* (1997).

Table A. Algal Classes, Cultured Species and Marker Pigment (MP) of Each Optical Group

Class	Species	Strain	MP
Bacillariophyceae	*Phaeodactylum tricornutum*	CCMP 632	Fuco
Dinophyceae	*Amphidinium carterae*	-	Perid
Prymnesiophyceae	*Emiliania huxleyi*	RRC 904	Hex-Fuco
Cryptophyceae	*Cryptomonas* sp.	-	Allo
Prasinophyceae	*Micromonas pusilla*	RCC 372	Pras
Cyanophyceae	*Synechococcus* sp.	RCC 322	Zea
Cyanophyceae	*Prochlorococcus marinus*	RCC 151	DV chl *a*

2.2 Spectral Similarity Analysis

Absorption spectrum of each cultured species was normalized by its spectral mean, and used as reference spectral signature of the specific algal group. *Spectral Angle Mapper* (SAM) technique (Sohn and Rebello, 2002), an algorithm recently used also in the inversion of semi-analytical spectral models (Maselli *et al.*, 2009), was applied to computed similarity between reference spectra and each natural absorption spectrum. A normalized-ratio transform (Millie *et al.*, 1997) and its fourth derivative were computed for each mean-normalized absorption spectrum. Hence, a similarity index (SI) between the fourth derivative of each reference spectrum and natural ones was calculated according to Millie *et al.* (1997):

$$SI = 1 - \frac{2 * \arccos\left[\frac{A_b \cdot A_c}{|A_b| \times |A_c|}\right]}{\pi} \quad (1)$$

where SI = similarity index
A_b, A_c = transformed mean-normalized spectra.

* Dipartimento di Biologia Evoluzionistica, via Micheli 1, 50121 Firenze, Italy; tel +39 0552757391, fax +39 055282358.

SI and logarithm of MP concentrations of each phytoplankton group were related.

3. RESULTS

3.1 Pigment Distribution in Natural Assemblages

Chl *a* in the Tyrrhenian and Eastern Mediterranean Sea was usually lower than 0.10 mg m^{-3} and increased until 0.53 mg m^{-3} in the Western Mediterranean Sea.

All assemblages were mainly characterized by the MP Zea and Hex-Fuco whose ratios, as the other pigments contributions, varied among sampling areas. In the oligotrophic Eastern Mediterranean Sea, Zea (on average 45% of the total marker pigments) dominated while Pras increased. In the Tyrrhenian assemblages Hex-Fuco (on average 35%) prevailed while in the Algerian Basin Dv chl *a* increased. In the Alboran Basin a very mixed composition occurred, in some assemblages Fuco dominated (up to 45 % to the total of MP) whilst in other ones Pras and Allo showed important increases.

3.2 Relationships between Similarity Indices and Marker Pigment Concentrations

Similarity indices obtained by a pair-wise analysis between the reference spectrum of a phytoplankton group and the spectra of natural assemblages were always lower than 0.5. Generally higher SI come out for Fuco, Pras and Perid, but Hex-fuco, Zea and DV chl *a* showed SI lower than 0.4.

All correlation coefficients (r) between SI and the logarithm of each MP (Fig. 1) had 1 % significance level. The best correlation coefficients (0.75 and 0.71) were found for Hex-fuco and Fuco. Among picoplanktonic marker pigments the best correlations were found for Pras (r = 0.68) and DV chl *a* (r = 0.61) whilst Zea, usually the most abundant pigment, showed very low SI (max 0.26) and a correlation coefficient of 0.58. Perid and Allo showed the lowest r, 0.52 and 0.55 respectively, in accordance with their small contributions to the pigment assemblages structures.

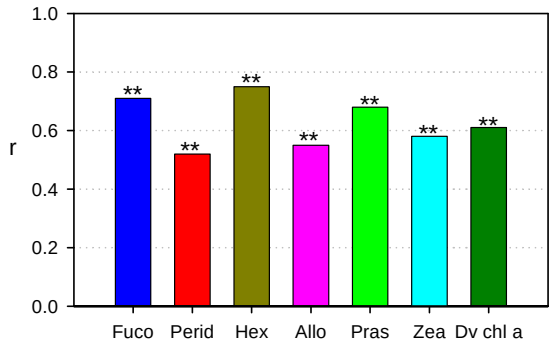

Figure 1. Correlation coefficients (r) of regressions between similarity indices and logarithm of MP concentrations. **= 1 % significance level.

4. DISCUSSION AND CONCLUSION

The method here described shows the capability to discriminate in natural assemblages all the spectral signatures of phytoplankton groups listed in table A. Usually optical discrimination concerned monospecific algal bloom (Cullen *et al.*, 1997), while the method proposed here allows to reconstruct marker pigments content of surface natural assemblages such as those of the Mediterranean Sea, that generally are characterized by oligotrophic conditions and highly diversified composition. A further analysis of marker pigments ratios could be tested to derive the taxonomical composition of phytoplankton assemblages.

This method has also showed encouraging results on nine wavelengths optical data (Organelli *et al.*, 2008). Hence, the possibility to retrieve phytoplankton absorption spectra from remote sensing reflectance (Lee and Carder, 2004) and the extension of this method to remote–sensed data, especially the hyper-spectral ones, could make real an optical reconstruction of the taxonomical composition of mixed natural assemblages.

ACKNOWLEDGEMENTS

We acknowledge dr. Chiara Melillo for her contribution.

REFERENCES

Aiken, J., J.R. Fishwick, S.J. Lavender, R. Barlow, G.F. Moore, H. Sessions, S. Bernard, J. Ras and N.J. Hardman-Mountford (2007). "Validation of MERIS reflectance and chlorophyll during BENCAL cruise October 2002: Preliminary validation of new products for phytoplankton functional types and photosynthetic parameters". International Journal of Remote Sensing, vol. 28, pp. 497-516.

Barlow, R.G., D.G. Cummings and S.W. Gibb (1997). "Improved resolution of mono- and divinyl chlorophylls *a* and *b* and zeaxanthin and lutein in phytoplankton extracts using reverse phase C-8 HPLC". Marine Ecology Progress Series, vol. 161, pp. 303-307.

Cullen, J.J., Á.M. Ciotti, R.F. Davis and M.R. Lewis (1997). "Optical detection and assessment of algal blooms". Limnology and Oceanography, vol. 42, no. 5, pp. 1223-1239.

Lee, Z. and K.L. Carder (2004). "Absorption spectrum of phytoplankton pigments derived from hyperspectral remote-sensing reflectance". Remote Sensing of Environment, vol. 89, pp. 361-368.

Maselli. F., L. Massi, M. Pieri and C. Santini (2009). "Spectral angle minimization for the retrieval of optically active seawater constituents from MODIS data". Photogrammetric Engineering and Remote Sensing, vol. 75, no. 5, pp. 595-605.

Millie, D.F., O.M. Schofield, G.J. Kirkpatrick, G. Johnsen, P.A. Tester and B.T. Vinyard (1997). "Detection of harmful algal blooms using photopigments and absorption signatures: A case study of the Florida red tide dinoflagellate, *Gymnodinium breve*". Limnology and Oceanography, vol. 42, no. 5, pp. 1240-1251.

Organelli, E., L. Massi, C. Nuccio, F. Fani and L. Lazzara (2008)."Phytoplankton spectral absorption and scattering for optical groups discrimination using complete and reduced spectral information". XIX Ocean Optics Conference (CD-ROM), Barga (Lu), Italy, pp. 11.

Sohn, Y. and N.S. Rebello (2002). "Supervised and Unsupervised Spectral Angle Classifiers". Photogrammetric Engineering and Remote Sensing, vol. 68, pp. 1271-1280.

Tassan, S. and G.M. Ferrari (2002). "A sensitivity analysis of the 'Transmittance-Reflectance' method for measuring light absorption by aquatic particles". Journal of Plankton Research, vol. 24, no. 8, pp. 757-774.

Optimizing the use of satellite winds to improve our view of air-sea fluxes

J. Patoux [a,*], R.C. Foster [b], R.A. Brown [c]

[a] Department of Atmospheric Sciences, University of Washington, Seattle, USA – jerome@atmos.washington.edu
[b] Applied Physics Laboratory, University of Washington, Seattle, USA – ralph@apl.washington.edu
[c] Department of Atmospheric Sciences, University of Washington, Seattle, USA – rabrown@atmos.washington.edu

Abstract – The impact of satellite wind measurements on our view of the surface pressure, wind, vorticity, and divergence fields, as well as air-sea fluxes, is discussed. A method is described to derive improved surface fields from satellite wind measurements. The derived surface wind field has improved spectral characteristics, which has implications for numerical weather prediction (NWP) model assimilation and the forcing of ocean circulation models. Cyclone statistics computed from satellite-enhanced surface pressure and vorticity fields reveal more and deeper cyclones than numerical weather prediction model analyses, along with stronger momentum fluxes into the ocean. This suggests that satellite wind information is under-utilized in NWP models and in the estimation of long-term, global-scale air-sea fluxes of momentum and heat.

Keywords: wind, cyclones, air-sea fluxes.

1. INTRODUCTION

Air-sea fluxes of momentum, sensible and latent heat are an important component of the climate system. Fluxes of momentum into the ocean determine the strength of Ekman pumping, upwelling, wave activity, and upper ocean mixing, while air-sea heat fluxes play an important role in the redistribution of heat between the tropics and the poles. Determining the exchanges of momentum, sensible and latent heat between the ocean and the overlying atmosphere is therefore crucial to understand the role played by the ocean in the global climate system on seasonal to interannual timescales. Air-sea fluxes are a function of the surface wind speed; satellite wind measurements should therefore improve our estimation of those fluxes. When satellite winds are assimilated into numerical weather prediction (NWP) models, the resulting air-sea fluxes should be improved. However, the information contained in satellite winds is considerably under-utilized by NWP models (Leslie and Buckley, 2006; Chelton et al., 2006). The satellite winds are either "thinned," or rejected due to quality control procedures that incorrectly reject good estimates of the wind. Data assimilation procedures generally have difficulty in making the best use of single-level wind data such as provided by satellite measurements. Moreover, NWP models misrepresent a certain percentage of the midlatitude cyclones; they either represent the intensity or structure of the pressure field incorrectly or miss the incipient cyclone altogether (Hilburn et al., 2003). In addition, the surface wind field is often underestimated in the high wind speed regime, in particular within midlatitude cyclones, where the surface wind speed is often higher than 20 m s^{-1} (Yuan, 2004). Finally, these limitations come in addition to uncertainties in the bulk parameterizations used to calculate the fluxes. We propose a method for incorporating satellite wind information into the analysis of sea-level pressure and several derived products: surface wind field, vorticity, divergence, and air-sea fluxes, as well as cyclone statistics. We show that the derived surface wind field has improved spectral characteristics, that more and deeper midlatitude cyclones are detected from satellite-enhanced surface pressure and vorticity fields, and that stronger momentum fluxes are computed as a result of the incorporation of satellite wind information.

2. METHODOLOGY AND RESULTS

2.1 Satellite-Derived Pressure Fields

Sea-level pressure (SLP) fields are derived from satellite wind measurements using the method described by Patoux et al. (2003). A swath of gradient wind vectors is calculated from the surface wind vectors using the University of Washington Planetary Boundary Layer (PBL) model (Brown, 1982). The gradient wind vectors are translated into pressure gradients using a gradient wind correction (Patoux and Brown, 2002) and a pressure field is fit to the swath of pressure gradients by least-squares minimization (Brown and Levy, 1986). Patoux et al. (2008) showed that such SLP fields estimated from QuikSCAT (QS) scatterometer measurements are in good agreement with buoy measurements and European Centre for Medium-Range Weather Forecasts (ECMWF) model analyses, and contain more spectral energy at the mesoscale than ECMWF analyses.

2.2 Improvement of the Satellite Winds

Through a reverse calculation, a new set of surface wind directions is calculated from the derived SLP fields and is used to produce a new surface wind dataset. Patoux et al. (2010) showed with QS measurements that the new surface winds are in better agreement with buoy measurements and ECMWF analyses than the original winds. Moreover, the energy spectrum of the new winds follows a power law down to a scale of about 50 km, in contrast with the flattening of the spectrum observed below ~500 km in the original QS winds (Fig. 1). However, while small-scale variability is filtered out, mesoscale information is retained, as can be seen by comparing the spectrum of the new winds with the spectrum of the ECMWF winds, which falls off rapidly at scales less than ~1000 km.

* Corresponding author. University of Washington, Department of Atmospheric Sciences, Box 351640, Seattle WA 98195-1640, USA, Ph: (206) 685-1736, Fax: (206) 543-0308

The methodology offers two advantages: (1) it improves the estimation of winds in rainy areas, where the measurement quality of instruments such as QS is degraded; and (2) the new winds can be corrected for stratification to yield an improved estimate of the surface vorticity and divergence (as opposed to neutral-equivalent vorticity and divergence).

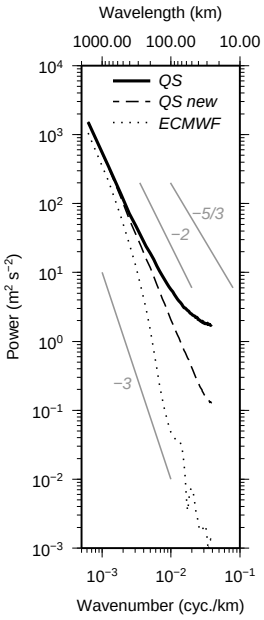

Figure 1. Comparison of surface wind energy spectra: QuikSCAT (bold), new surface winds obtained from the corresponding satellite-derived SLP field (dashed), and ECMWF (dotted).

2.3 Midlatitude cyclones and air-sea fluxes

Patoux et al. (2009) used the SLP fields derived from QS measurements to compute midlatitude cyclone statistics over the Southern Ocean. They incorporated the satellite-derived SLP fields into ECMWF analyses using a wavelet-based method and systematically detected and tracked midlatitude cyclones using the Melbourne University cyclone finding and tracking scheme (Simmonds and Murray, 1999; Simmonds et al., 1999). They detected 5-10% more cyclones than when using the original ECMWF analyses, especially incipient lows and short-lived mesoscale cyclones. They identified stronger storms and more spectral energy in the modified SLP fields. Furthermore, Yuan et al. (2009) showed that, when using this satellite-enhanced midlatitude cyclone database, 2-8% stronger fluxes of momentum into the ocean are observed, especially inside midlatitude cyclones. They also showed that short-lived mesoscale cyclones contribute a significant amount of the fluxes between the atmosphere and the Southern Ocean.

3. DISCUSSION AND CONCLUSION

These results suggest that the information contained in satellite wind measurements is under-utilized by NWP models for two reasons: (1) the small-scale noise apparent in the flattening of the satellite wind energy spectra at scales smaller than ~500 km negatively impacts the assimilation schemes; and (2) some of the wind measurements are rejected by the assimilation schemes due to thinning or quality control procedures that are not sufficiently well adapted to satellite measurements. We suggest that both issues can be addressed by first deriving a synoptic-scale SLP field from the satellite winds, as described above, and using that synoptic-scale information to correct the winds. The resulting wind field has reduced small-scale variability while retaining mesoscale information and resolution down to ~50 km, as shown by the power-law appearance of its energy spectrum. Such a wind field might have more of a positive impact when assimilated into NWP models. Such an improved spectral behavior also has important implications for the forcing of ocean models, where small-scale noise can create artificial curl and Ekman pumping. Our results also suggest that NWP models might be positively impacted by the assimilation of the satellite-derived SLP fields, in addition to the satellite winds. The cyclone tracking performed on satellite-enhanced SLP and vorticity fields suggests that some mesoscale activity is currently missing from the NWP analyses. These results suggest that an optimal way of assimilating satellite information would be to assimilate both the wind field and the derived SLP field in combination. This would ensure consistency of the surface fields while retaining a maximum of information. Moreover, the surface fluxes could be calculated as part of the pressure and wind retrieval, as $\sim u_*^2$, $\sim u_*\theta_*$, and $\sim u_* q_*$ for momentum, sensible, and latent heat fluxes respectively, where the velocity, temperature, and humidity scales u_*, θ_*, and q_* are calculated as PBL variables during the pressure and wind retrieval. Such a method might prove superior to calculating the fluxes from the winds *a posteriori*, as a by-product of the model output, using bulk coefficients.

ACKNOWLEDGEMENTS

We acknowledge NASA OVWST grant support under JPL subcontract 1285663.

REFERENCES

Brown, R.A. (1982). “On two-layer models and the similarity functions for the planetary boundary layer”. Bound. Layer Meteorol., **24**, 451–463.

Brown, R. A., and G. Levy (1986). “Ocean surface pressure fields from satellite sensed winds”. Mon. Wea. Rev., **114**, 2197–2206.

Patoux, J., and R.A. Brown (2002). “A gradient wind correction for surface pressure fields retrieved from scatterometer winds”. J. Appl. Meteorol., **41**, 133– 143.

Patoux, J., R.C. Foster, and R.A. Brown (2003). “Global pressure fields from scatterometer winds”. J. Appl. Meteorol., **42**, 813– 826.

Patoux, J., R.C. Foster, and R.A. Brown (2008). “An evaluation of scatterometer-derived oceanic surface pressure fields”. J. Appl. Meteorol. Climatol., **47**, 835–852.

Patoux, J., R.C. Foster and R.A. Brown (2010). “A method for including mesoscale and synoptic-scale information in scatterometer wind retrievals”. J. of Geophy. Res, accepted.

Patoux, J., X. Yuan and C. Li (2009). “Satellite-based midlatitude cyclone statistics over the Southern Ocean. Part I: Scatterometer-derived pressure fields and storm tracking”. J. of Geophys. Res., D04105, doi:10.1029/2008JD010873.

Yuan X., J. Patoux and C. Li (2009). “Satellite-based midlatitude cyclone statistics over the Southern Ocean. Part II: Tracks and surface fluxes”. J. of Geophys. Res., D04106, doi:10.1029/2008JD010874.

Space Based Surveillance: Advances Toward Oil Polluter Identification

M. Perkovic [a,*], H. Greidanus [b], G. Ferraro [b], O. Müllenhoff [c], S. Petelin [a], R. Harsch [a]

[a,*] University of Ljubljana, Faculty of Maritime Studies and Transport, Slovenia – marko.perkovic@fpp.uni-lj.si
stojan.petelin@fpp.uni-lj.si, rick.harsch@fpp.uni-lj.si
[b] Joint Research Centre, European Commission, Ispra , Italy – harm.greidanus@jrc.ec.europa.eu
gudo.ferraro@jrc.ec.europa.eu
[c] BMT Argoss, Milano, Italy – oliver.muellenhoff@ bmtargoss.com

Abstract – Marine oil spills pose a risk for European coastlines (ecological, socio-economic damage, etc). For this reason European coastal states have established surveillance systems to monitor the state of the seas, to deter illicit polluters and to support combating activities. The spaceborne SAR surveillance system provides added value to the problem of monitoring marine pollution from ship discharges. The paper focuses on the identification of illicit oil polluters through the integration of a vessel traffic service system together with a satellite surveillance system and the subsequent superimposition of meteorological and oceanographic conditions within oil spill application.

Keywords: pollution, oil spill, surveillance, backtracking.

1. INTRODUCTION

Illicit oil discharging, a common practice, represents the main source of marine pollution from ships, amplifying the demand for efficient detection and mapping of oil spills (Ferraro *et al.,* 2007). Key instruments for detecting and monitoring spills at sea are Synthetic Aperture Radar (SAR) systems, which are able to detect spills on the sea surface indirectly given the damping of Bragg waves. The oil film dampens these waves, the primary backscatter agents of the incident radar beam, appearing as dark patches on the SAR image. Bragg waves are induced by surface winds but are also modulated by other ocean surface features.

Diverse kinds of pollution can cause slicks detectable by SAR (e.g., vegetable oil, river runoff, drilling fluid from an oil rig, etc.) and the SAR sensor is currently not capable of distinguishing between the different pollutants. In practice it is very difficult to distinguish surface films from each other by merely analyzing the radar backscattering data (Müllenhoff *et al.,* 2008). Knowledge of environmental conditions as well as contextual information about slick position relative to surrounding objects (ships, maritime routes, rigs, wrecks and undersea pipelines) is in many cases essential for determining the probability of oil spills extant on SAR imagery (Ferraro *et al.,* 2010). Further, for successful backtracking of illicit polluters, when slicks are already weathered highly accurate metocean data are necessary to 'move' the slicks from their detected locations towards the origins of the spills and to identify the polluters.

To reduce or even eliminate illicit pollution at sea, in 2007 EMSA launched a European operational system for marine oil slick surveillance allowing detection of possible oil spills in all European waters. The system is CleanSeaNet (CSN), designed to support improvements such as greater consistency, efficiency and effectiveness of pollution monitoring efforts of Member States. Since CleanSeaNet's inception more than 2000 yearly SAR images have indicated almost 3000 slicks (per year). Some intensive validation was performed, confirming detections as oil. In a few cases illicit discharging was detected just as ships or other objects were pumping out oily water. But as yet there have been no cases in which a polluter was unassailably identified from analysis of weathered slicks.

Now EMSA will launch a new web based application allowing operators to run spill models that will move detected slicks against currents and winds towards potential polluters EMSA (2008).

2. BACKTRACKING MATERIALS AND METHODOLOGY

An ideal case - a freshly released slick or a ship attached to the slick - is rare. Usually the image shows a slick already weathered, and no ships or too many of them in the vicinity. If the slick is outside AIS range, polluter detection is virtually impossible. For precise backtracking, accurate metocean data and a view of the overall shipping situation in the area is required. Extensive local data must be available - contextual particulars of bathymetry, wrecks, piping and drilling activity, natural seeps, shore industry, metocean phenomena, fishing traffic, for truly accurate backtracking validation of metocean data is essential; and shipping data must be analyzed clearly and matched with port authorities' log books (Müllenhoff *et al.,* 2008, Ferraro *et al.,* 2010). Further complications are unknowns like the type of oil or mixture that was discharged, quantities and initial locations. Through this fog we must decide how long to backtrack the slick and roll back AIS archives. Oil type is an important factor, for the way an oil slick breaks up and dissipates depends largely on how persistent the oil is. Light products, non-persistent oils (e.g., kerosene), tend to evaporate and dissipate quickly and naturally and rarely need cleaning-up. Persistent oils, such as many crude oils, act more slowly and usually require clean-up. Physical properties such as density, viscosity and pour point all affect oil behavior. Dissipation also depends on weather conditions and whether the oil stays at sea or is washed ashore. Figure 1 illustrates the complete procedure for backtracking and identification.

* Corresponding author. Pot pomorscakov 4, 6320 Portoroz, Slovenia. Tel +386 41344569.

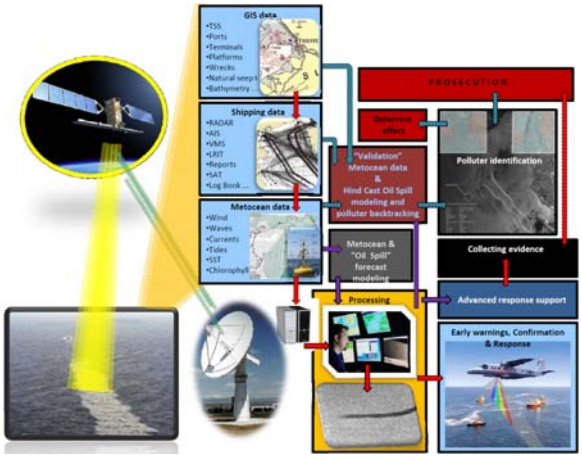

Figure 1. SAR processing and backtracking methodology.

3. RESULTS EXPLICATED BY CASE STUDY

During 2005/2006 the Faculty of Maritime Studies, along with EC JRC and other partners under the lead of REMPEC, was part of the AESOP (Aerial and Satellite surveillance of Operational Pollution in the Adriatic Sea) project, meant for validating the prospect of satellite radar control over illegal oil spills. The specific goal was identifying ships responsible for oil spills (Ferraro *et al.*, 2007). Following is one resultant case of pollution source identification by integration of satellite images, data on weather history conditions, AIS traffic archives and mathematic tools (PISCES) for hindcast oil spill simulations.

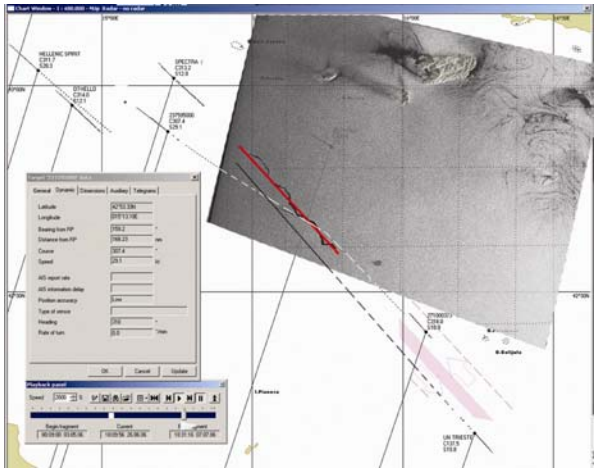

Figure 2. Hindcast simulation and polluter identification

The Figure 2 acquired by ERS2© on 26th June 2006 at 09:42 GMT, distinctly shows a dark feature, likely a partially weathered oil slick. To begin a search for the polluter, retrieving the AIS history database was necessary (The identification distance was almost 300 miles from the AIS antenna!). Given the dense traffic the direction of the ship responsible had to be determined. After geo-coordinating the SAR image and overlaying it on electronic charts it appeared the discharge began immediately after a north-bound vessel passed the traffic separation scheme; yet inspection of the shape indicated that the slick was much more weathered on the north side - that the ship was southbound. The next step was overlaying the currents field and wind conditions - evidently surface currents (more determinate than wind direction) moved almost perpendicular to the line of the slick. Even weak currents can rapidly disturb the slick shape, pushing it in a particular direction - north-east in this case, supporting the conclusion that the polluter was southbound. Further Metocean validation was performed, analyzing vessel drift using the average difference of ships' headings and courses through a sailing leg. Next, oil spill simulation in hindcast mode and retrieval of shipping archive data acquired by the AIS-based VTS system was required. Figure 2 shows the position of ships at the time the SAR image was acquired: 1032 LT. The suspect polluter, a cargo ship, "Un Trieste," was already at the end of the TSS. Sailing speed and course indicated that the illicit discharge started around 0725 LT – more than three hours before the SAR image was available. Because the slick was intensely disturbed in the middle toward the west direction, it was assumed that other ship crossed the slick, which was confirmed by AIS history – e.g., a fast passenger ship crossed at 29 kt. This disturbance provided further confirmation that the dark formation was indeed a slick.

4. CONCLUSION

This case clearly illustrates the importance of integrating several systems; yet another type of integration is necessary - between scientists and lawyers. In this case there was no possibility for prosecution as there was no sampling done. Clearly in the near future EU jurists must work with oil spill analysts to coordinate a system whereby space technology can lead to prosecution. At the same time 'space technologists' must work to develop finer remote sensor capability. Most important currently, however, is that this case demonstrates that important advances are being made toward eliminating operational pollution.

REFERENCES

Ferraro, G., Bernardini, A., David, M., Meyer-Roux, S., Muellenhoff, O., Perkovic, M., Tarchi, D., Topouzelis, K., (2007). "Towards an operational use of space imagery for oil pollution monitoring in the Mediterranean basin. Marine Pollution Bulletin". Volume 54, no. 4, pp. 403-422.

Müllenhoff, O., Bulgarelli, B., Ferraro, G., Perkovic, M. Topouzelis, K., Sammarini, V. (2008). "Geospatial modelling of metocean and environmental ancillary data for the oil spill probability assessment in SAR images". Proceedings of the SPIE, Volume 7110, pp. 71100R-71100R-10.

Ferraro, G. Baschek, B., de Montpellier, G., Njoten, O. Perkovic, M., and Vespe, M. (2010). "On the SAR derived alert in the detection of oil spills according to the analysis of the EGEMP". Marine Poll. Bull., vol. 60, no. 1, pp. 92-102.

EMSA (2008). EMSA's view on the further development of oil spill modelling, non paper. November 2008, Lisbon, http://cleanseanet.emsa.europa.eu.

Space-time SST variability in the upwelling zones of the N-W Black sea and near the Crimean peninsula in May-October 2005-2008

A. Polonsky [a], E. Mickailova [a], M. Muzyleva [b]

[a] Marine Hydrophysical Institute, Sevastopol, Ukraine – apol@alpha.mhi.iuf.net
[b] Sevastopol Branch of Moscow State University – marina-muz@mail.ru

Abstract – The characteristics of SST variability in the upwelling zones of the N-W part of the Black sea and near the Crimean peninsula in May-October 2005-2008 have been analyzed using satellite date and routine meteorological observations. A few different upwelling zones have been detected. The number of upwelling events varies in different zones from 1 to 3.5 events per year. In June 2005, the unique upwelling event occurred. It has being accompanied by persistent negative SST anomalies in all detected zones. The cause of such event has been analyzed using Japanese re-analysis and simulation results.

Keywords: SST, upwelling, Black Sea.

1. INTRODUCTION

The study of regional manifestations of upwelling is very importance because of theoretical and practical goals. In the Black sea, the most intense upwelling is observed in the coastal zone. However, there is strong space-time inhomogeneity of its manifestations in the SST. In this presentation which is the continuation of (Mickailova et al., 2009), more detailed analysis of the SST variability from May for October in N-W part of the Black sea and along the coast of the Crimea is carried out.

2. CHARACTERISTIC OF THE DATA SETS

The following data sets were used for description of upwelling in the N-W part of the Black sea and coastal zone of the Crimea:

1. Information of satellite SST images from NOAA–15/17 (1 by 1 km resolution) for May – October of 2005 – 2008. As upwelling events, the SST decreasing exceeding 5 ºC during 6 hours were considered (Lovenkova and Polonsky, 2005). Using the information from satellite images, the separate structural regions of coastal upwelling were detected. Criteria for their selection were the features of space-time structure of the SST anomalies of about 5 ºC and more.
2. Japanese reanalysis data sets (JRA) on wind parameters and the sea level pressure in May – October of 2005 – 2008 on 1,125° x 1,125° mesh.
3. Data of routine observations at 14 coastal hydrometeorological stations during 2005 - 2008
4. Results of numerical experiment using the primitive model (Ivanov et al., 1996).

3. RESULTS AND THEIR ANALYSIS.

3.1. General description of upwelling's areas

The analysis of satellite images showed that upwelling spreads very rarely along the all coast of the N-W part of the Black sea and the Crimea. More often the areas of SST decreasing refer to the separate areas of the coastal zones, which are characterized by the features of configuration of coastline and bottom relief. These features are favorable to upwelling development. In general, 7 areas of upwelling were detected. The picture 1 demonstrates the satellite images with the regions of negative SST anomalies, which correspond to the selected structural zones of upwelling. Note, the specific type of upwelling is detected in the area «G». It is related to the SST decreasing caused by evolution of the fields of density and temperature in the vicinity of Rim current meandering. Typical SST anomalies are up to 10 ^{0}C. In the period of 2005 – 2008, fifty upwelling events were detected. Interannual variability of upwelling events is represented in the Table 1.

Table 1 Recurrence of upwelling in seven structural areas

Area	2005	2006	2007	2008	Total in period 2005–2008
A	3	2	1	2	8
B	5	3	2	4	14
C	2	2	1	2	7
D	2	1	3	1	7
E	2	2	1	1	6
F	1	0	1	2	4
G	2	0	0	2	4
Total:	17	10	9	14	50

3.2. Analysis of intensive upwelling in 12–14.06.05

During analyzed period, upwelling in all selected areas was simultaneously observed twice, namely: 12 – 14.06.05 (the SST anomalies were 5 to 11^{0}C) and 6 – 7.08.2008 (the SST anomalies were 5 to 7^{0}C). We considered the first (more persistent and intense) case of upwelling in more detail. 12 hours before the appearance of horizontal SST inhomogeneous in the N-W part of the Black sea, south wind dominated there, while above the Crimea the south-east wind occurred. 6 h before SST decreasing, the wind changed the direction on the north-western one. Speed of wind in this period was 15 m/s. During two days wind field was persistent. The highest speed of wind (25 – 27 m/s) was registered 13.06.05 (in 3 o'clock). Then intensity of wind went down (to 17 – 19 m/s), however the direction remained the same. At 15 o'clock 14.05.06 the wind speed

was breakdown (to 10 – 11 m/s) and changed of its direction to southward. Such wind field evolution was caused by the unique weather situation. The cyclone above the N-W part of the Black sea and the Crimea was blocked by large anticyclone. Decrease of SST (from 24^0C to 17^0C) along all coast occurred 12.06.05 at 21 o'clock. Area of low SST was spreading in all structural zones at 9 o'clock 13.06.05. However, in the area «C» upwelling was developed only after two terms of observations (in 21 o'clock). 13.06.05, when SST in the coastal zone fell down to 13–15^0C, it was related to horizontal advection of cold waters in the upper mixed layer.

In all seven structural zones, upwelling attained the maximum development 14.06.05 (in 9 o'clock). According to satellite data, the zones of upwelling began gradually to narrow and 14.06.05 at 21 o'clock the SST anomalies already did not exceed 5^0C. For more detailed analysis of evolution of hydrotermodynamic fields during the described type of upwelling, the special numeral experiment in scope of three-dimensional high-resolved model was carried out. The evolution of upwelling was simulated under suddenly arisen homogeneous north-western wind (15 m/s). The anomalies of SST were $7,5^0$C, and the speeds of south-eastern currents generated by wind were 20 cm/s. Upwelling in the area «C» developed along the coast from island Dolgij to village Stereguchij.

Figure 1. Number of upwelling events in the seven zones (May-October of 2005 – 2008). Letters A,B,C,D,E,F.G point to the zone, while the number within each zone is the event number

During the next model day, cold water due to horizontal advection spread to southern part of the Kalamitskij bay. This conclusion is confirmed by the analysis of temporal variability of different terms of heat conservation equation for the upper mixed layer.

4. CONCLUSIONS

As a result of more detailed analysis of evolution of the SST anomalies in the N-W part of the Black sea and the coastal zone of the Crimea using the satellite data, routine observations and numeral simulation, the results of (Mickailova et al., 2009) were confirmed. In addition it was shown that the SST decreasing in the Karkynytskij bay was related to two physical mechanisms: wind upwelling, and horizontal advection of cold waters. Observed event of persistent upwelling (12–14.06.05) was selected especially by two reasons.

At first, the decreasing in a temperature was observed along all research coast. Secondly, the duration and intensity of this event were unique. It was result of seldom weather situation. The cyclone above the N-W part of the Black sea and the Crimea was blocked by large anticyclone. As a result, the homogeneous quasi-steady wind field (with speed up to 27 m/s) was formed.

ACKNOWLEDGEMENTS

We thank to Dr.S.Stanichny and Mr. D.Soloviev for satellite data and Mr.D.Basharin for the re-analysis product.

REFERENCES

Ivanov, V. et al. (1996). "Upwelling in the N-W Black sea in summer". Marine Hydrophysical Journal. No.4, 26-35. http://www.dvs.net.ua

Lovenkova, E. and A. Polonsky (2005). "Climate characteristics of upwelling near the Crimea coast and their variability". Russian Meteorology and Hydrology, No.5, 44-52.

Mickailova, E. et al. (2009). "Space-time variability of upwelling characteristics in the N-W Black sea and near the Crimean peninsula in 2005-2008". Systems of environmental control. Sevastopol.

Aerosol Remote Sensing Over Ocean in Glint Contaminated Regions Using AATSR and MERIS

R. Preusker *, J. Fischer

Freie Universität Berlin, Berlin, Germany – rene.preusker@fu-berlin.de, juergen.fischer@fu-berlin.de

Abstract – This document presents a method to quantify the sun glint of a wind roughed sea surface using measurements at 11µm, 12µm and 3.7µm as provided by AATSR. The sun glint is used in a subsequent step to estimate the aerosol optical thickness and the angstroem coefficient using co-registered measurements of MERIS at 0.78µm, 0.86µm and 0.89µm an AATSR at 0.86µm and 1.6µm.

Keywords: aerosols, sun glint, thermal emission.

1. INTRODUCTION

The Medium Resolution Imaging Spectrometer MERIS and the Advanced Along-Track Scanning Radiometer AATSR instruments, both onboard ESA's Environmental Satellite ENVISAT, provide similar spatial resolution and swath, but complementary information, encompassing different spectral domains and viewing geometries. Recent geophysical algorithms do not take advantage of a synergetic use of the measurements of both instruments, although the benefits in cloud and aerosol retrieval are obvious. This paper presents one example for a synergistic use of MERIS and AATSR imagery: The retrieval of aerosol optical thickness and Angstroem coefficient over the ocean, in particular in sun glint contaminated regions. Later we extend the focus on the potential of the estimation of aerosol absorption by means of its single scattering albedo.

2. MERIS AND AATSR IN SHORT

MERIS is an imaging spectrometer with 15 programmable spectral bands in the range 400nm – 1050nm. The operational band setting positions of the 15 bands are between 412.5nm and 900nm, including one narrow channel at 761.375nm in the O2 A-band absorption band, two bands to estimate the integrated water vapour content, and three bands to the retrieve aerosol properties. The MERIS swath covers 1150km across track. The original pixel size is 260m x 300m in nadir with a slight increase towards the edge of the swath. The full resolution data (FR) are spatially integrated (4x4 pixel) to the reduced resolution (RR) pixel with a 1040m x 1200m pixel size.

AATSR is a scanning radiometer with 7 spectral channels at visible, reflected infra-red and thermal infrared wavelengths with two ~500 km wide curved swaths, with 555 pixels across the nadir swath and 371 pixels across the forward swath. The nominal pixel size is 1km2 at the centre of the nadir swath and 1,5 km2 at the centre of the forward swath. This unique feature provides two views of the surface and improves the capacity for atmospheric correction and enables observations of the ocean surface under a tilt angle of ~46.9° in forward direction. The first 3 AATSR bands cover MERIS channels, however, the bandwidth of the AATSR channels is significantly larger.

3. THE ALGORITHM IN SHORT

The aerosol retrieval algorithm consists of three parts. The first part is the estimation of the ocean specular reflection at 3.7 micron, whereby an estimation of the thermally emitted part at 3.7 from the brightness temperatures at 11 and 12 micron is used. The thermal emitted radiance is subtracted from the top of atmosphere radiance and corrected for water vapour, resulting in the specular reflectance at 3.7 micron. The second part is the propagation of this reflectance a) to the MERIS channel wavelength (taken into account the wavelength dependence of the water refractive index) and b) to the corresponding MERIS observation geometry, which is necessary to account for the different scanning methods of MERIS (line scanner) and AATSR (conical scanner). The third part is the estimation of the aerosol optical properties (AOT at 550nm and Angstroem coefficient) utilizing the sea surface reflection as the lower boundary condition in a physical inversion.

3.1 Solar portion and specular reflection at 3.7µm

The top of atmosphere radiance at AATSR channel at 3.7µm top of atmosphere radiance consists of reflected and scattered solar radiation as well as emitted radiation from the atmosphere and the surface. For cloud free conditions the amount of molecular scattering is negligible ($\tau < 0.00005$), the amount of aerosol scattering is very small and, compared to the amount of reflected and emitted radiation, negligible as well. (Under special conditions, in particular for high aerosol loadings due to desert outbreaks or for undetected clouds, this may be different, but it is not considered here). Therefore we can assume the following equation:

$$L_{TOA} = L_{surf,E} + L_{atm,E} + L_{surf,S} \quad (1)$$

With $L_{TOA,E} = L_{surf,E} + L_{atm,E}$, the top of atmosphere radiance without any solar radiation, as it is observed e.g. during night, the sum can be further simplified and the equation can be rearranged to:

$$L_{surf,S} = L_{TOA} - L_{TOA,E} . \quad (2)$$

The estimation of $L_{TOA,E}$ is done by a linear regression of the measured brightness temperature at 11µm and 12µm (BT11 and BT12) to the brightness temperature at 3.7µm (BT3.7):

$$BT3.7 = a + b \bullet BT11 + c \bullet (BT11 - BT12) \quad (3)$$

*Weltraumwissenschaften, Carl-Heinrich-Becker-Weg 6-10; 12165 Berlin. Tel.: +49 30 83852375, Fax: +49 30 83856664.

The regression coefficients are: a = 4.91348 b = 0.978489 c = 1.37919. The coefficients have been found by analyzing cloud free sea surface night scenes. The intensive quantity BT3.7 is converted into the extensive radiance $L_{TOA,E}$. by a simple linear interpolation in an appropriate look up table $L_{TOA,E}$ = LUT [BT3.7]. Finally $L_{surf,S}$ is corrected for water vapor transmission $T_{3.7}$ and solar irradiation to obtain the bottom of atmosphere reflectance at 3.7µm:

$$\gamma_{3.7.}=L_{surf,S} / (E_0 T_{3.7}) \quad (4)$$

3.2 Geometrical / spectral conversion of glint at 3.7µm

The glint at MERIS wavelengths and MERIS viewing geometry is not equal to $\gamma_{3.7}$ because i) the refractive index of water is different at the visible and 3.7 micron and more important and more difficult to solve ii) the azimuth difference of the AATSR observation is different to the azimuth difference of the MERIS. The main quantity for this geometrical conversion is the **effective wind-speed** *ws*. It is assumed that there exists a unique relationship *CM* between the glint γ at a specific wavelength λ, the observation geometry (ϑ_{sun} , ϑ_{view} , φ_{diff}), the refractive index of sea water at that wavelength *n* and the wind-speed ws.

$$\gamma = CM\,(\vartheta_{sun} , \vartheta_{view} , \varphi_{diff} , n, ws) \quad (5)$$

But studies have shown, that this relation does not exist, at least not precisely. In particular the wind direction, existing (cross) swell and the history of the waves modulate the relationship and lead to different parameterizations of sea surface roughness. The task of the wind-speed *ws* is solely to act as a consistent parameter for the sea surface glint. Since *ws* is the only unknown in the upper simplified relationship, there could be an unique inverse solution:

$$ws = CM^{-1}\,(\vartheta_{sun} , \vartheta_{view} , \varphi_{diff} , n, \gamma) \quad (6)$$

Under the assumption that the unique inverse CM^{-1} exists, the geometrical conversion is straight forward and consists of the following two steps:

i) Calculation of the effective wind-speed

$$ws = CM^{-1}\,(\vartheta_{sun} , \vartheta_{view} , \varphi_{AATSR} , n_{3.7}, \gamma_{3.7}) \quad (7)$$

ii) Calculation of the glints γ_{MERIS}

$$\gamma_{MERIS} = CM\,(\vartheta_{sun} , \vartheta_{view} , \varphi_{MERIS} , n_{MERIS}, ws) \quad (8)$$

The forward operator *CM* is implemented and approximated by a look up table. The inverse operator CM^{-1} could not be approximated by an analytic function, because under some conditions or geometries it is not unique, but twofold (two effective wind-speeds can produce the same sun glints). Instead a simple and fast search algorithm was implemented, that gives the possible wind-speeds.

3.3 Estimation of aerosol properties

The estimation of the aerosol optical properties (AOT at 550nm and Angstroem coefficient α) is a physical inversion using the estimated sea surface reflection as the lower boundary condition. Eventually it is a simple LUT search where AOT and α are the search dimensions. The LUT was filled with radiative transfer calculations using the radiative transfere code MOMO (Fell and Fischer 2003). From theoretical investigations we know that for high and medium glint situations (see e.g Kaufmann et al 2003) the aerosol absorption is to some extend separable from aerosol optical thickness and aerosol asymmetry. We will search for a quantitative measure to identify such situations and apply an absorption retrieval (extension of the LUT search dimension to single scattering albedo) to these situations. However, this is not implemented yet (writing this abstract).

4. EXAMPLES

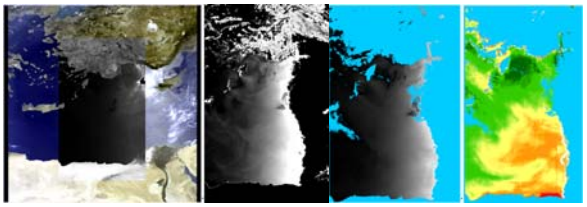

Figure 1: From left to right. 1.) True colour composite of a glint affected scene of the Mediterranean on the 13.Jun 2003 observed by MERIS and a black white overlay of AATSR 1.6µm nadir view. 2.) The same scene measured by AATSR 3.7µm. Due to the high reflectivity of the glint and some land surfaces this channel is partly saturated. 3.) The estimated sea surface glint at 0.89µm for the MERIS viewing geometry. 4.) The estimated aerosol optical thickness at 550nm (dark red = 0.4, dark green =0.1)

5. VALIDATION

In brief: open. The necessary validation of the retrieved aerosol properties is ongoing while writing this document. First comparisons with MERIS L2 standard products show a good agreement outside medium and high glint areas and more reasonable values for sun glint contaminated pixel.

ACKNOWLEDGEMENTS

This work was supported by ESA within the SYNERGY and GLINT projects.

REFERENCES

Cox, C. and W. H. Munk (1954a): Statistics of the sea surface derived from sun glitter. *J. Mar. Res.*, 13, 198–227.

Cracknell, A.P., (1993): A method for the correction of sea surface temperature derived from satellite thermal infrared data in an area of sunglint, Int. *J. Remote Sensing*, 14.

Ebuchi, N. and S. Kizu, (2002): Probability Distribution of Surface Wave Slope Derived Using Sun Glitter Images from Geostationary Meteorological Satellite and Surface Vector Winds from Scatterometers, *Journal of Oceanography*, Vol. 58, pp. 477 to 486.

Fell F, Fischer J, 2001: Numerical simulation of the light field in the atmosphere-ocean system using the matrix-operator method. *J QUANT SPECTROSC* RA 69 (3): 351-388 MAY 1 2001

Kaufman, Y, J.V. Martins, L.A. Remer, M.R. Schoeberl, and M.A. Yamasoe (2002: Satellite retrieval of aerosol absorption over the oceans using sunglint. *Geophysical research letters,* Vol. 29, No. 19, 1928, doi:10.1029/2002GL015403

17 Years of Altimeter Data Record for Climate and Ocean Studies

M.-I. Pujol [a,] *, G. Dibarboure [a], E. Bronner [b]

[a] Collecte Localisation Satellites, Space Oceanography Division, Ramonville Saint-Agne, France
[b] Centre National d'Etudes Spatiales, DCT/ME/OT, Toulouse, France

Abstract – An overview of the SSALTO/DUACS system is given: key features and processing used, last reprocessed products performances, upgrades scheduled for 2010/2011 …

Keywords: altimetry, AVISO, DUACS.

1. PROJECT OVERVIEW

1.1 Objectives

To provide operational applications with homogeneous and directly usable high quality altimeter data from all missions (Jason-1, Jason-2, T/P, ENVISAT, GFO, ERS1/2 and even GEOSAT). The system uses common processing facilities for global and regional applications. It ensures that upgrades are consistently applied on all products to better serve the altimetry user community.

1.2 Delayed Time (DT)

DUACS-DT products are composed of global data sets of along track and gridded Sea Level Anomaly, Absolute Dynamic Topography, and geostrophic currents, but also of regional-specific products (higher resolution, optimized parameters). DUACS recently reprocessed all past altimeter data. The data set is in the validation phase and will be delivered soon.

1.3 Near Real Time (NRT)

DUACS-NRT provides GODAE and climate forecasting centers with global Near Real Time altimeter data. The products are generated and distributed on a daily basis to reduce the NRT delay. The DUACS system also provides a long term monitoring of NRT data it has used. Quality Control reports are released twice per week.

1.4 Real Time (RT)

OGDR/FDGDR Jason-2, Jason-1 and Envisat data (lower quality but faster delivery) were integrated in the NRT system in order to improve the resilience and quality of the system. After an experimental phase in 2008/2009, this product is now entirely integrated to the DUACS system and should replace the NRT product in the coming months.

2. DT DATA SET ENTIRELY REPROCESSED

2.1 Main important changes

- Use of up-to-date standards (GDR-C or equivalent) [1]:
  - GDR-C products for Jason1/Jason2
  - GDR-C orbit for Envisat
  - GSFC orbits for Topex and GFO (except during maneuver periods)
  - GOT4v7 tide solution for all missions
  - New SSB solution from Labroue and Tran for Topex/Poseidon and GFO
- Bias from TP/Jason1 and Jason1/Jason2 were revised in order to correct geographical discrepancies affecting MSL observed with DUACS multi-mission MSLA. Use of the more accurate reference mission as soon as it is possible (Fig 1).
- Improved editing process, especially for the costal areas, for all missions.
- Reference Mean profile updated in order to take into account the new standards and to improve the quality near the coast. Extended temporal coverage offered by twin mission (TP/Jason and ERS/Envisat) was also exploited, but the product is still referenced to the 7-year [1993-1999] mean. [2]
- Optimization of the interpolation parameterization.
- Computation of SLA maps with a daily resolution
- Use of the new Mean Dynamic topography CNES-CLS-09 using the recent EIGEN-GRGS.RL02.MEAN-FIELD and improved processing method [2,3]

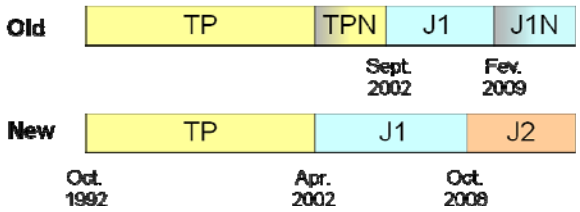

Figure 1. Reference mission used

2.1 Better products

First validation diagnostics show the improved quality of the reprocessed DUACS DT MSLA data set. The global reduction of the variance (Fig 2) traduces the impact of improved quality of the geophysical corrections, combined with improved orbits determination and changes of the reference missions. Data quality allows to better estimate the SLA in difficult areas such as the high latitudes. This was taken into account in order to optimize spatial coverage of MSLA product (Fig 3).

Impact on MSL trend:

The reprocessed data set don't significantly change the global MSL trend observation over the [1993,2009] period. However, local significant changes can be observed (Fig 4). They are in the range of MSL trend errors defined by Ablain et al. [4]. They are mainly connected to the improved orbit solutions and change in reference mission.

Impact on Coastal areas:

Improved corrections, improved editing process and more accurate mean profiles allow a better observation of coastal

* Corresponding author. mpujol@cls.fr

areas. Moreover, Absolute Dynamic Topography product constructed with MDT CNES-CLS-09 allows an improved restitution of major currents, also better defined near the coast.

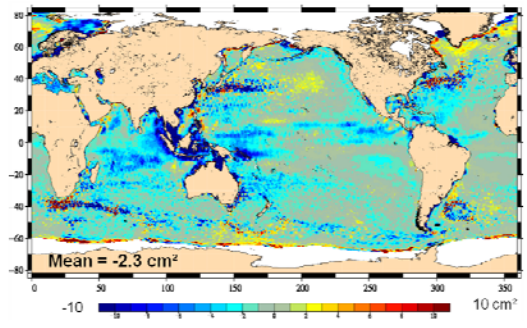

Figure 2. Variance reduction induced by the updated DT data set over the 16-year period [1993,2008] (« ref » version)

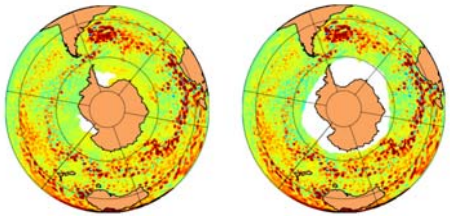

Figure 3. Example of MSLA maximal spatial coverage in the Antarctic.

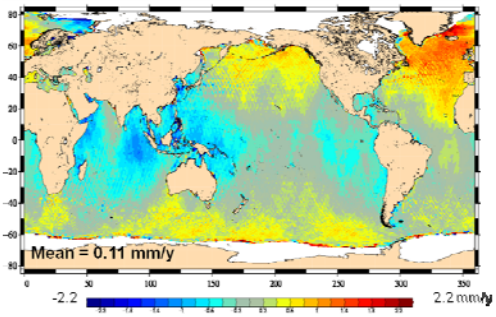

Figure 4. MSL trend differences between reprocessed and old DT data set (« ref » version)

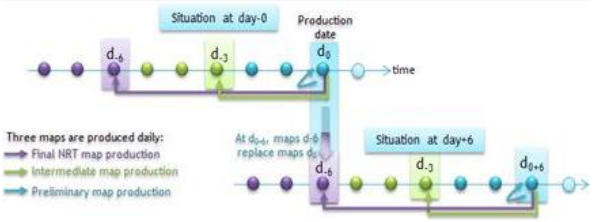

Figure 5. IGDR+OGDR-based (RT) production. Time window : 3 maps are produced every day. (d0, d-3 and d-6)

3. RT MAP DELIVERED WITHIN THE 0-DAY DELAY

Exploitation of real time OGDR/FDGDR data allows the DUACS system to produce multi-mission maps with 0-day and 3-day delay whereas historical NRT (IGDR-based) production have a 6-day delay (induced by historical trade-off in terms of timeliness vs quality)

Since July 2009 RT production is computing 3 maps every day:

- 0-day map = preliminary version of multi-mission map
- 3-day map = intermediate version
- 6-day map = final version

Time window process used is illustrated in Fig 5.

4. PROCESSING UPGRADES FOR 2010/2011

Continuous improvements on DUACS system are scheduled for 2010/2011, in the framework of MyOcean project :

- Improve the data latency with an “on the fly” RT (OGDR-based) data production
- Prepare the DUACS system to the future Envisat drifting orbit.
- Improve the accuracy and resilience of the system, taking advantage of ERS2 in reduced coverage, of the future missions (Cryosat2, AltiKa, HY2) and also past missions such as and Topex/Poseidon in its drifting orbit period and ERS1 with 3-day repetitivity.
- Implement, in its experimental phase, a new orbit reduction scheme (used for multi-mission cross-calibration), that is based on multiple reference missions rather than single reference mission, in order to minimize the impact of an anomaly on the reference mission.
- Develop new regional products for the Artic and Atlantic European shelves.
- Maintain the efforts for production and validation processing to deliver you the best quality products.

REFERENCES

[1] CalVal reports for the different altimeters: www.aviso.oceanobs.com/fr/calval/systematic-calval

[2] Faugère Y., M. Abalin, E. Bronner, N. Picot, Recent and coming improvements of the performance of open ocean altimetry products, Poster communication at OceanSciences symposium, 22-26 Feb. 2010, Portland

[3] Rio, M-H, P. Schaeffer, G. Moreaux, J-M Lemoine, E. Bronner (2009) : A new Mean Dynamic Topography computed over the global ocean from GRACE data, altimetry and in-situ measurements . Poster communication at OceanObs09 symposium, 21-25 September 2009, Venice.

[4] M. Ablain, P. Prandi, A. Cazenave, N.Picot, Error estimation of the global and regional mean sea level trends from altimetry data, Communication at OceanSciences symposium, 22-26 Feb. 2010, Portland

General Circulation of the Norwegian Sea with a Deeper Look into the Lofoten Basin From Space

R.P.Raj [a,b,*], J.E.Ø. Nilsen [a, c]

[a] Bjerknes Centre for Climate Research, Bergen ,Norway – roshin.raj@bjerknes.uib.no
[b] Geophysical Institute, University of Bergen, Bergen, Norway
[c] Nansen Environmental and Remote Sensing Center, Bergen, Norway – even@nersc.no

Abstract – The circulation pattern of the Atlantic waters in the Norwegian Sea which plays an important role in the Atlantic Meridional Overturning Circulation is studied. Importantly, it is analyzed that a strengthening of the baroclinic branch of Norwegian Atlantic current at the Voring Plateau results a larger eastward flow of Atlantic waters over the plateau and comparatively less waters flow along the Mohn Ridge. This increased eastward flow has large importance to the net heat loss and dense water formation in the Nordic Seas. Further, it is shown that the eddy kinetic energy of the Lofoten Basin, exhibits both seasonal and interannual variability.

Keywords: Atlantic current, meridional overturning circulation, mesoscale eddies, Norwegian Sea.

1. INTRODUCTION

The Norwegian Sea, comprised of Norwegian Basin (NB) and Lofoten Basin (LB), plays an important role in the Atlantic Meridional Overturning Circulation (AMOC). Lofoten Basin is the largest heat reservoir in the Nordic seas since it is occupied by Atlantic Water down to a depth of 800 m. The LB has large winter heat loss and is also the region of highest eddy activity in the Nordic seas and hence highly important in ocean - atmospheric interactions. The Atlantic waters (AW), entering the LB and the associated heat loss has large importance for the processes relevant for the AMOC. A new perspective of dense water formation in the Nordic Seas was made by Mauritzen (1996) proposing that the bulk of the transformation from North Atlantic waters to various intermediate and deep water types takes place along the direct advection path of AW, east of the Greenland and Iceland Seas, contradicting the traditional claim that the main dense water formation takes place in the Greenland and Iceland Seas. Later, Isachsen et al (2007) showed that the bulk of light to dense water transformation takes place in the deep NB and LB. Recently, Eldevik et al (2009) confirmed that Atlantic Water circulating in the Nordic Seas is the main source for property change in the overflow waters, which underlines the importance of dense water formation in the NS, since it is situated in the earliest part of the advective path of Atlantic waters poleward in the Nordic Seas.

2. DATA USED AND METHODS

High resolution weekly absolute geostrophic velocity maps ($1/3^o \times 1/3^o$) are computed from absolute dynamic topography obtained from merged JASON, TOPEX/, POSEIDON, ERS data using the conventional geostrophic relation;

$$u = -g/f\,(\partial h/\partial y) \text{ and } v = g/f\,(\partial h/\partial x), \quad (1)$$

where, u and v are east and north components of velocity, g is the acceleration due to gravity, f is the coriolis parameter, h is the sea surface height, while $\partial/\partial x$ and $\partial/\partial y$ are spatial derivatives in the respective ($1/3^o$) longitude and ($1/3^o$) latitude grids. Dynamic topography is the sum of sea level anomaly (SLA) and mean dynamic topography. Eddy Kinetic Energy (EKE) is calculated from geostrophic velocity anomalies u' and v'.

$$EKE = (u'^2 + v'^2)/2 \quad (2)$$

3. RESULTS AND DISCUSSION

The satellite derived weekly absolute geostrophic velocity maps during the past 14 years (1995-2009) were analyzed to study the circulation of the NS.

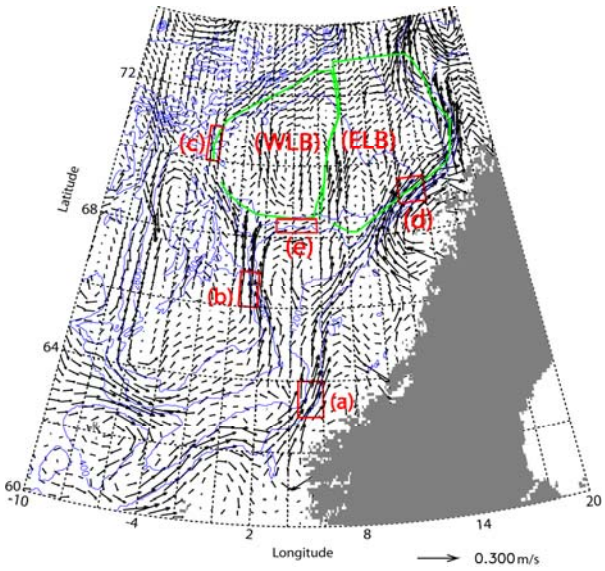

Figure1. Winter climatology (1993-2009) of absolute geostrophic velocity. (a) Svinoy, (b) Voring Jet, (c) Ext. west, (d) Ext east and (e) Voring North. The blue lines indicate bathymetry.

The figure clearly portrays the barotrophic (inner) and baroclinic (outer) branches of Norwegian Atlantic Current (NwAC) along with the cyclonic circulation of Atlantic

* Corresponding author. Allegaten 55, Bergen, Norway, 5007. Ph: +47 55582718, Fax: +47 55584330

waters inside the NB. The altimeter data shows that the NwAC in the Norwegian Sea is intensified at 3 major locations (shown as Svinoy, Voring Jet, Ext east in the figure). Further analysis displayed both seasonal and inter-annual variability in the velocity of the NwAC at all the selected 5 locations. Interestingly, a large increasing trend is depicted in the velocity of the ext west box during the past 14 years even though the trend is reversed at the Voring Jet and Voring North region (figure not shown).

Table-A shows the winter correlation (Dec-Mar) of inter-annual variability in velocities at 5 locations. The values in red are significant above 95 % confidence level.

	Ext East	Voring Jet	Voring North	Ext West	NAO
Svinoy	0.63	0.35	0.21	0	0.55
Ext East		0.43	0.34	-0.14	0.55
Voring Jet			0.39	-0.12	0.22
Voring North				-0.19	0.28
Ext West					0.12

From the table, it is obvious that the influence of North Atlantic Oscillation (NAO) is limited only to the inner branch of NwAC. The swift, narrow nature of the inner branch of NwAC during winter, explains the large correlation (0.63) between Svinoy and Ext east. The significant correlation (0.35) between the Svinoy and Voring Jet (western Voring Plateau) is likely to be due to the infiltration of AW from the inner branch of NwAC into the outer branch as indicated by the studies using drifters. The variability of Voring Jet and the Voring North is significantly correlated (0.39) due to the flow of outer branch of NwAC over the Voring Plateau. It is highly important to note the large correlation between the variability of Ext east velocity with both Voring Jet (0.43) and Voring North (0.34). This is also likely to be due to the eastward flow of baroclinic outer branch of NwAC over the Voring Plateau. From the above results, we hypothesize that the strengthening of outer branch of NwAC at the western Voring plateau (Voring Jet) results in an increased eastward flow over the Voring Plateau, which also links into the LB and a correspondingly decreased flow of the outer branch along the Mohn Ridge and vice versa. This hypothesis is able to explain the large increasing trend in velocities at Ext west during the past decade with the weakening of the outer branch of the NwAC at the western Voring Plateau (Voring Jet).

Composite analysis of high (figure 2) and low velocities at Voring Jet supports our hypothesis. Figure 2 shows the increased eastward flow of the outer branch of the NwAC over the Voring plateau and a decreased flow over the Mohn Ridge, when the flow over Voring Jet is strengthened. The increased input of AW into the LB is also displayed. The composite analysis of the low velocities (not shown), showed a reversing when compared to the composite of the high velocity and further confirms our hypothesis.

In the light of above discussions, we suggest that less amount of NwAC flowing eastward over the Voring plateau with less AW entering the LB and more of NwAC flowing northward via Mohn Ridge during the past decade is likely to have resulted in less heat loss and associated less dense water formation within this region influencing MOC.

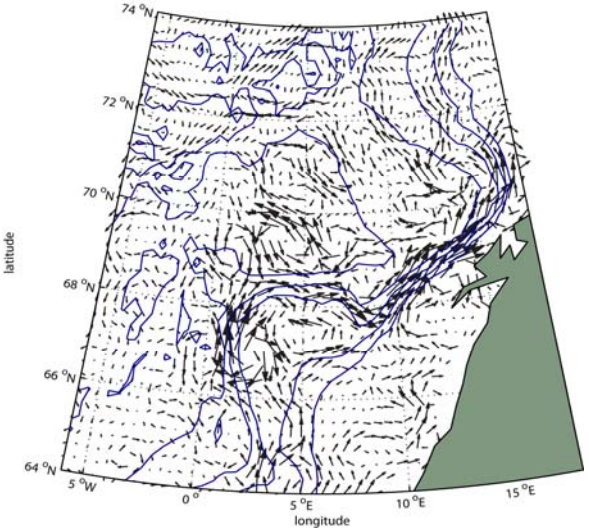

Figure2. The composite of absolute velocity anomalies at high Voring Jet velocities

The EKE of the eastern and western parts of the LB (ELB and WLB respectively from figure1) which is likely to influence the heat loss exhibits distinct seasonality. The analysis also showed that EKE of both the parts of the LB which is not found to be influenced by NAO shows an increasing trend during the past 14 years (figure not shown).

CONCLUSIONS

The study revealed the hotspots of intense currents in the NS. The proposed hypothesis of increased eastward flow of NwAC over the Voring Plateau and decreased flow over the Mohn Ridge as the velocity of the outer branch of NwAC at western Voring plateau strengthens is validated. The study proposes the possibility of a decrease in the heat loss and associated decrease in the dense water formation in the NS during the past decade. The effect of NAO is found to be limited to the inner branch of NwAC. Finally, the study showed an increase in the eddy activity of both the parts of the LB during the past decade.

ACKNOWLEDGEMENTS

This research was supported by the Norwegian Research Council through the project Polar Climate and Heat Transport (POCAHONTAS).

REFERENCES

Eldevik et al., (2009) “Observed sources and variability of Nordic seas overflow”. Nature Geoscience, DOI: 10.1038/ngeo518.

Isachsen, P. E.,C. Mauritzen and H.Svendsen (2007). “Dense water formation in the Nordic Seas diagnosed from sea surface buoyancy fluxes”. Deep-Sea Research-I, vol.54, pp. 22-41.

Mauritzen, C. (1996). “Production of dense overflow water feeding the North Atlantic across the Greenland-Scotland Ridge”. Deep Sea Res. I, vol. 43, pp. 769– 805.

Thermal fronts and their influence on the distribution of Dolphinfish (*Coryphaena hippurus*) in the Pacific coast of Colombia

J.J. Selvaraj, A.I. Guzman, A. Martinez

The National University of Colombia, Palmira Campus, Colombia – jjselvarajh@palmira.unal.edu.com, aiguzmana@palmira.unal.edu.com, adrimartinezarias@gmail.com

Abstract – Moderate Resolution Imaging Spectrometer (MODIS) Sea Surface temperature (SST) data were analyzed using Cayula-Cornillon edge detection algorithm to study spatio-temporal variation in the formation of thermal fronts along the Pacific coast of Colombia over the years 2003-2008. During the first semester of the year, two zones of persistent and intense fronts were observed, one near the coast in the Northern region and another far from the coast. Frontal regions were demarked as possible pelagic fish aggregation areas. An analysis of historic dolphinfish (*Coryphaena hippurus*) catch data from industrial fishing fleets (long liners) coincided with identified thermal fronts. There existed a negative correlation between catch per unit effort (CPUE) and distance to SST front.

Keywords: MODIS, thermal fronts, *Coryphaena hippurus*.

1. INTRODUCTION

The Pacific coast of Colombia is one of the areas with high level of ecological inter-connectivity, complex oceanographic features and diverse marine fisheries. One of the important pelagic fisheries resources along this coast is dolphinfish (*Coryphaena hippurus*), (Lasso and Zapata, 1999). Distribution and abundance of marine resources depends on oceanographic parameters, including Sea Surface Temperature (SST). SST obtained from satellite remote sensing technique has been widely used in defining abundance, distribution and availability of many pelagic fisheries resources. (Laurs *et al*., 1989; Miguel, 2000; Selvaraj *et al*., 2009). Studies by Olson *et al*., 1994, Brunet *et al*., 1992, Waluda *et al*., 2001; Wang *et al*., 2003 shows frontal and upwelling regions as areas with increased primary productivity leading to abundance of predatory pelagic fishes. The present study aims to identify formation of thermal fronts in the Pacific coast of Colombia and its influence on the availability of Coryphaena resources reported by the industrial long line fishing.

2. OBSERVATIONS

2.1 Methodology

Monthly level 3, 4 km resolution MODIS SST data were downloaded from NASA Ocean color website (http://oceancolor.gsfc.nasa.gov) for the years 2003-2008 for the pacific coast of Colombia (Fig. 1).

On monthly images we executed Cayula and Cornillon's single-image edge detection (SIED) algorithm (Cayula and Cornillon, 1992) which is readily available in Marine Geospatial Ecology Tools (MGET), an open-source collection of geoprocessing tools box for ArcGIS (Roberts *et al*., In review). SST data were downloaded in HDF format and they were converted to ArcGIS raster format. SIED algorithm was applied to create SST fronts for all months from 2003-2008. Spatial and temporal variations of thermal front distribution were then studied.

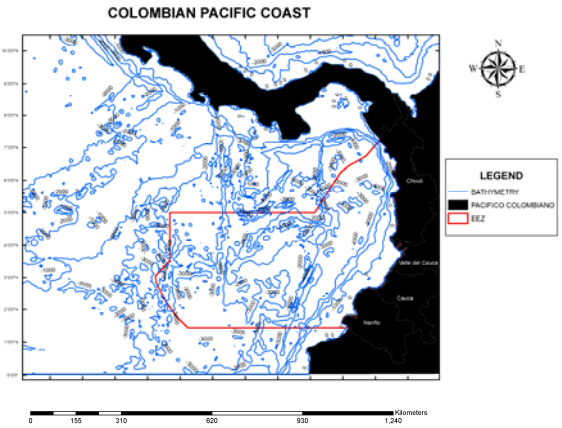

Figure 1. Study area- Pacific Coast of Colombia

On monthly SST images we executed Cayula and Cornillon's single-image edge detection (SIED) algorithm (Cayula and Cornillon, 1992) which is readily available in Marine Geospatial Ecology Tools (MGET), an open-source collection of geoprocessing tools box for ArcGIS (Roberts et al., In review). SST data were downloaded in HDF format and they were converted to ArcGIS raster format. SIED algorithm was applied to create SST fronts for all months from 2003-2008. Spatial and temporal variations of thermal front distribution were then studied.

To explore the relationship between *Coryphaena hippurus* distribution and SST fronts, fisheries catch data were collected from the logbooks of industrial long line fishing fleets for the year 2003-2008. The data included date, fishing location, number of individuals captured and number of hooks used. The index of relative abundance used was Catch for Unit Effort (CPUE) expressed in numbers (fish/1100 hooks). The fishing locations were mapped onto SST front maps using ArcGIS 9.3. The distance between the relative abundance CPUE and SST fronts were calculated.

2.2 Results and Discussions

Two zones of persistent and intense fronts were observed, one near the coast in the Northern region and another far from the coast. Both were observed in the first two trimesters (December-February and March-May). Studies from Belkin and Cornillon, 2003 showed that the Pacific coast of Colombia is a part of Pacific Central American Coastal Large Marine Ecosystem (LME), most of the fronts within this LME are generated by Coastal upwelling. Third trimester (June-August) and fourth trimester (September-November) exhibited very less persistent fronts near the

coast and along the southern coast when compared to other months. Some fronts off the pacific coast also originate from the quasi-regular burst of topographically generated wind blowing from the Caribbean across toward the Pacific Ocean. Other stable and predictable fronts were especially EGPF-East Gulf of Panama Front, WGPF-West Gulf of Panama front (Belkin *et al*., 2009). The WGPF extends far offshore till the Exclusive Economic Zone (EEZ) of Colombian Pacific. The spatial variability of fronts along the coast may also be associated with the mixing of tropical and temperate waters, one from the Californian current (north) and another is the Peruvian current from the south (Lasso and Zapata, 1999) and local precipitation patterns.
Mapping of long liner location and SST fronts showed that the industrial fisheries activities coincided with the frontal zone for exploiting dolphin fish (Fig. 2).

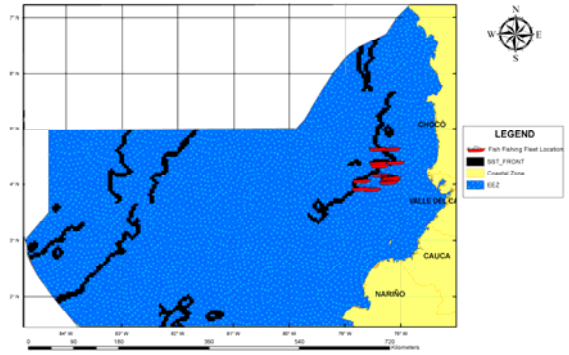

Figure 2. SST fronts and the Industrial dolphinfish fishing fleet locations in the month of February 2006

Our analysis in general identified a negative correlation (r = -0.72) between dolphinfish CPUE and the distance to SST fronts (Fig. 3). In some locations there did not exist a direct correlation suggesting influence of some other features like primary productivity and prey density on the distribution of dolphinfish.

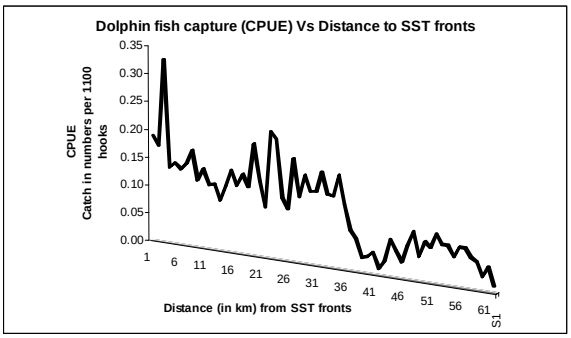

Figure 3. Relation between dolphinfish capture (CPUE) and Distance to SST fronts for the years 2003-2008

3. CONCLUSION

Persistent and intense SST fronts are present in the Colombian Pacific Coast. Some of these SST fronts could be dolphinfish aggregating zones. In addition to SST, other oceanographic factors such as wind and current may also determine distribution of fish resources in the study region. Daily and weekly SST fronts may provide additional insight into the distribution of dolphinfish, but this could not be carried out in this study due to cloud cover.

ACKNOWLEDGEMENTS

This work was supported by the project 036-2007T-6605-353-07 financed by the Colombian Ministry of Agriculture and Rural Development and co-financed by the office of Vice-Chancellor for research at the National University of Colombia.

REFERENCES

Belkin, I. M., Cornillon, P. C. and Sherman, K. (2009). “Fronts in Large Marine Ecosystems”. Progress in Oceanography, vol. 81, no.1-4, pp. 223- 236.

Brunet, C., J. M., Brylinski and S, Fronter. (1992). “Productivity, photosynthetic pigments and hydrology in the coastal front of the Eastern English Channel”. Journal of Plankton Research, vol. 14, pp. 1541–1552.

Cayula, J-F and P Cornillon. (1992). “Edge Detection Algorithm for SST Images”. Journal of Atmospheric and Oceanic Technology, vol. 9, pp. 67-80.

Lasso, J. and L. Zapata (1999). “Fisheries and biology of *Coryphaena hippurus* (Pisces: Coryphaenidae) in the Pacific coast of Colombia and Panama”. Scientia Marina, vol. 63, pp. 387- 399.

Laurs, R.M., P. C. Fiedler, D. R., Montgomery. (1989). “Albacore tuna catch distributions relative to environmental features observed from satellite”. Deep-Sea Research, vol. 31, no. 9, pp. 1085-1099.

Miguel P. Santos. (2000). “Fisheries oceanography using satellite and airborne remote sensing methods: a review”. Fisheries Research, vol. 49, pp. 1-20.

Olson, D. B, A.J. Mariano, C.J. Ashjian, G. Peng, R.W. Nero and G.P. Podestá. (1994). “Life on the edge: marine life and fronts”. Oceanography, vol. 7, pp. 52–60.

Roberts, J.J., B.D. Best, D.C. Dunn, E.A. Treml, and P.N. Halpin (in review) Marine Geospatial Ecology Tools: An integrated framework for ecological geoprocessing with ArcGIS, Python, R, MATLAB, and C++. Environmental Modelling & Software. http://mgel.env.duke.edu/tools

Selvaraj, J. J., Maya, R. and Angela, I. Guzman. (2009). “Application of Geographic Information System and Remote sensing in marine fisheries management and challenges for its development in Colombia”. Bulletin of Marine and Coastal Research, vol. 38, no. 1, pp. 105-120.

Waluda. C. M., P. G., Rodhouse, P.N., Trathan and G. J., Pierce. (2001). “Remotely sensed mesoscale oceanography and the distribution of Illex argentinus in the South Atlantic”. Fisheries Oceanography, vol. 10, pp. 207–216.

Wang, J., G. J. Pierce, P.R. Boyle, V. Denis, J. P. Robin and J. M. Bellido. (2003). “Spatial and temporal patterns of cuttlefish (*Sepia officinalis*) abundance and environmental influence—a case study using trawl fishery data in French Atlantic coastal, English Channel, and adjacent waters”. ICES Journal of Marine Sciences, vol. 60, pp. 1149–1158.

On the Identification of Marine Films using Optical Images

I.A. Sergievskaya, S.A. Ermakov

Institute of Applied Physics of Russian Academy of the Science, Nizhny Novgorod, i.sergia@hydro.appl.sci-nnov.ru

Abstract - A model of optical imaging (in particular, from satellites) of films on the sea surface is discussed. Different models of wind wave depression due to films with physical parameters typical for biogenic and for oil films are tested and corresponding variations of the surface radiance in areas covered by films are calculated. An impact of oil physical parameters (viscosity and elasticity) and oil film thickness on the short wind wave damping and correspondingly on the optical imaging of the film is investigated. Possibility of film characterization including estimates of oil film thickness from variations of the surface radiance in film patches is analyzed.

Keywords: optical imaging, marine films, oil

1. INTRODUCTION

Identification of marine films on the sea surface is an important problem in modern oceanography related to detection of pollutions (including oil pollution) and biologically productive areas in the ocean. Applications of optical methods for marine film detection have been extensively studied last decades. An optical method based on measuring the mean radiance from optical images (in particular, satellite images) can be efficient for identification and characterization of marine slicks.

2. ON MODELING OF OPTICAL IMAGING OF ROUGH SEA SURFACE

In general the sea surface radiance is determined by the sun and the sky radiance directly reflected from the sea surface and the volume sun radiance reflected from the water. The first two components strongly depend on the film on the sea surface. The reflected radiance depends on the reflection coefficient and on the surface slope variance, the latter can strongly depend on film thickness while the first does not when the film thickness is larger than tens of optical wavelengths.

The most important characteristic determining the variations of the surface radiance in areas covered by films is the variation of surface slope variance. The slope variance can be calculated as follows: $< q_{x,y}^2 > = \int_{-\infty}^{+\infty} k_{x,y}^2 F(\vec{k}) C(\vec{k}) d\vec{k}$, where $F(k)$ - wave height spectrum, $C(\vec{k})$ - the spectrum contrast equaled to the ratio between the spectrum on the contaminated and clean surface. We used wave height spectrum for fully developed waves [Elfouhaily et. al, 1997] and two different models to describe the wind wave damping [Ermakov et.al, 1984, Kudryavtsev et.al, 2005].

The model [Ermakov et.al, 1984] takes into account only free wind waves, and the model [Kudryavtsev et.al, 2005] describes also the bound short gravity-capillary waves, the intensity of which is determined by the intensity of longer surface waves.

3. WAVE DAMPING DUE TO MARINE FILMS

The biogenic marine films can be considered as thin films and the wave damping due to the films can be obtained using the model developed in [Levich, 1962]. The wave damping in this case depends on two physical parameters: surface tension and elasticity.

The typical values of the parameters are 40 mN/m and 20-25 mN/m [Ermakov et al., 2006]. Unlike biogenic quasi monomolecular films the oil films often have thicknesses of about 0,1 -1 mm. The wave damping due to oil films can be found in the frame of two liquid layers model. Field and laboratory experiments and theoretical analysis showed that the wave damping strongly depends on the volume oil viscosity, film thickness, interface elasticity, surface and interface tension [Jenkins A., 1997, Sergievskaya and Ermakov, 2008].

The analysis of the variation of surface slope variance has shown that there is a range of oil films thickness where the slope variations are strongly different for biogenic and oil films and the slope variation can be used to distinguish the material of the film. The limits of the range depend on the oil volume viscosity.

4. CONCLUSIONS

Biogenic and oil films can be distinguished when estimating how the surface slope variance changes in the zone covered by films.

ACKNOWLEDGEMENTS

The work was supported by the Russian Foundation of Basic Research (Projects 08-05-00634, 08-05-97011, 10-05-00101) and RAS (Program “Radiophysics”).

REFERENCES

T. Elfouhaily, B. Chapron, K. Katsaros, and D. Vandemark, (1997). “A unified directional spectrum for long and short wind-driven waves,” Journal of Geophysical Research, V.102, 781–96

Kudryavtsev V., Akimov D., Johannessen J., Chapron B. (2005), On radar imaging of current features: 1. Model and comparison with observations. JGR, V. 110, C07016, doi:10.1029.

Ermakov S.A., Pelinovsky E.N. (1984), Variation of the spectrum of wind ripple on coastal waters under the action of internal waves, Dyn. Atmos. Oceans, V.8, pp. 95-100.
Levich, V. G., Physicochemical Hydrodynamics, Prentice-Hall, Elmsford Park, N.J., 1962.

Ermakov S.A., and Kijashko S.V., (2006), Laboratory study of the damping of parametric ripples due to surfactant films, “Marine surface films” (ed. M.Gade, H. Huehnerfuss, G. Korenovski), Springer, pp.113-128.

Jenkins A., S. Jakobs (1997), “Wave damping by a thin layer of viscous fluid”, Phys. Fluids, 9(5), 1256-1264.

I.Sergievskaya, S.Ermakov, 2008), “On wave damping due to oil films”. Proc. US/EU/Baltic Symp., Tallinn, (CD), 6p.

Application of MODIS in the Determination of SST and Chlorophyll for a Model of Fishing Ground Prediction

D. Setyawan

Technique of Geodesy, Diponegoro University, Semarang, Indonesia – jurusan@geodesi.ft.undip.ac.id

Abstract – MODIS consist of 36 band spectral with band 1-19 and 26 in visible and near infrared, while the other in thermal. The calculation of sea surface temperature (SST) alighted by NOAA algorithm that is using two band of near infrared spectral [Pathfinde and Minet] 10.78 – 11.28 µ m and 11.77-12.27 µm), while to calculate of chlorophyll concentration alighted by algorithm of Seawifs satellite use comparison of band of visible spectral [Relly-21998] (0.438-0448 µm with 0.526-0.536 µm). Result of processing model using algorithm [Minnet, 2001] for the sea surface temperature and algorithm [Relly,1998] for the chlorophyll concentration assign spatial value which approach that obtained from satellite data of NOAA-AVHRR and also of SeaWifs.

Keywords: MODIS, SST, Chlorophyll, Fishing Ground.

1. INTRODUCTION

MODIS (Moderate Resolution Imaging Spectroradiometer) consists of 36 spectral bands, with band 1-19 and 26 in the visible and near infrared, and the others in the thermal infrared. With many band had by the data which include band of NOAA satellite, SeaWifs, Landsat, etc. Hence can be used to determine or measure parameter of sea surface till to atmosphere like measuring of sea surface temperature (SST) and chlorophyll concentration.

Determination model of fishing ground with MODIS data will use two parameter; sea surface temperature (SST) and chlorophyll concentration. The calculation of sea surface temperature (SST) alighted by NOAA algorithm that is using two band of near infrared spectral [Pathfinde and Minet] 10.78 – 11.28 µ m and 11.77-12.27 µm), while to calculate of chlorophyll concentration alighted by algorithm of Seawifs satellite use comparison of band of visible spectral [Relly-21998] (0.438-0448 µm with 0.526-0.536 µm). By joining two information (SST and chlorophyll concentration) expected potency of fish zone (fishing ground, FG) can be determined with larger accuration by using satellite of NOAA.

The information can be used by fisherman in activity of arrest of fish, so that arrest of fish will become more efficient and effective if fish horde area can be anticipated beforehand.

2. METHODS

2.1 MODIS Imagery Data

MODIS Data accepted or downloaded from internet kept in HDF format (Hierarchical Data Format) that is in format of level 1b. To facilitate its processing, data of MODIS converted to format of LAN beforehand. Then from format of LAN reconverted into ERS format, so that data of MODIS can be read in ER Mapper software.

2.2 Determination of Sea Surface Temperature.

Determination of sea surface temperature conducted with calculation of temperature brightness of water use equation of invers function of Planck (Black Body radiation) with earth ascription have temperature rates 3000 K.

$$Tb = \frac{C_2 v_i}{\ln(1 + C_1 v_i^{\,3} / N))} \quad (1)$$

where Tb = temperature brightness of water (in degree of Kelvin)
C_1, C_2 = constanta which is the each its value 1,1910659 x 10^{-5} $m^{-1}Wsr^{-1}$ cm^4 and 1,438833 cm K respectively.
v_i = central wave number for band 31 and band 32, 867,302 cm^{-1} and 831.95 cm^{-1} respectively.
N = obtained radiancy of R = R_Scale (SIR_Ofset) SI = Scale of Integer [1,32767 ; R_Scale 31 = 0.000840022, R_Scale 32 = 0.000729698
R_Ofset 31 = 1577.34, R_Ofset = 1658.22.

To calculate SST conducted only at cloudy free pixel.

1. If brightness temperature of band 32 (Tb32) smaller than 280° K hence the pixel is cloudy.
2. If difference between temperature brightness of band 31 (Tb31) and band 32 (Tb32) bigger than 2,5° K hence the pixel is cloudy.

Futhermore, calculation of SST at free pixels of cloud use equation of the following regressed.

$$SST = a + b(Tb_{31}, Tb_{32}) \quad (2)$$

where a,b = constanta that searched from equation of regression.

With input of parameter-parameter above hence calculated SST using algorithm.

$$SST = -0.024 + 3{,}129\ Tb31 - 2.52 Tb32 - .582 - 273$$

[P.Minet], SST in °C.

2.3 Determination of Chlorophyll Concentration.

Determination of chlorophyll distribution use characteristic sensor color ocean that is area of visible blue and green one. green light that bounced from sea surface (bringing information concerning chlorophyll concentration) detected by censor. More green light which accepted, more also chlorophyll. To see value of pixel spectral, processed with band combination (Relly, 1998).

$$R = (443)/(551) \quad (3)$$

where R = band combination

443 = visible blue
551 = visible green

If comparison between reflection (443)/(551) is low, hence content of chlorophyll is high, on the contrary when its high comparison, content of chlorophyll is low. After that conducted calculation of chlorophyll concentration using equation:

$$Klo = a + bLog\,[R(443)/(551\ )] \qquad (4)$$

where Klo = chlorophyll in mgm^{-3}
a,b = constanta obtained from equation of regressed.

By using band parameters 443 and 551 can be calculated chlorophyll concentration by algorithm:

$$Log(clr) = 0.283 - 2.753R + 1.457R^2 + 0.659R^3 - 1.403R^4$$

[Relly, 1998].

2.4 Result of SST.

From result of research by Suwargana, data processing of MODIS May 19 2002 for the water region territorial of sea of java was processed using algorithm [P.Minet, 2001], giving result good enough because indicating that sea surface temperature rates 28 - 32° C, but likely the algorithm require to modify, because needing the existence of field data to determine a constanta of equation of sea surface temperature for the water region territorial of Indonesia (Suwargana, 2002).

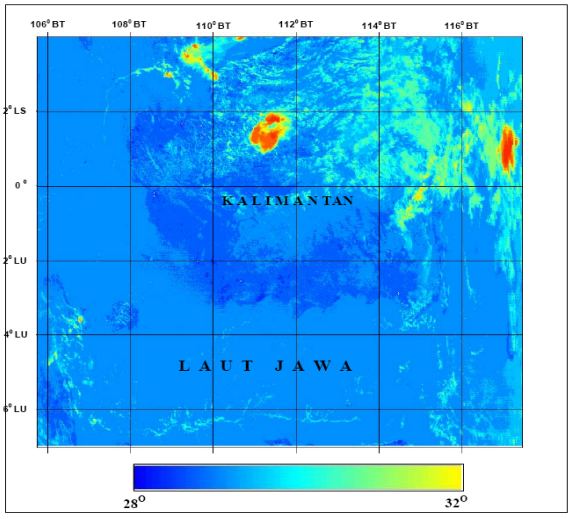

Figure 1. SST image of MODIS, band31 and band32, Mei 17 2002 at 10.26 am.
(Suwargana N, Arief M, Sidik H, 2008).

2.5 Result of Chlorophyll Concentration.

This research process by MODIS data May 19 2002 for the water region territorial of sea of java processed using algorithm [Relly, 1998]. Showing low chlorophyll rates 0,4672493 µg/l while the highest rates 1,537944 µg/l. But from the band combination obtained chlorophyll rates 0,45 µg/l - 1,18 µg/l (Suwargana, 2002).

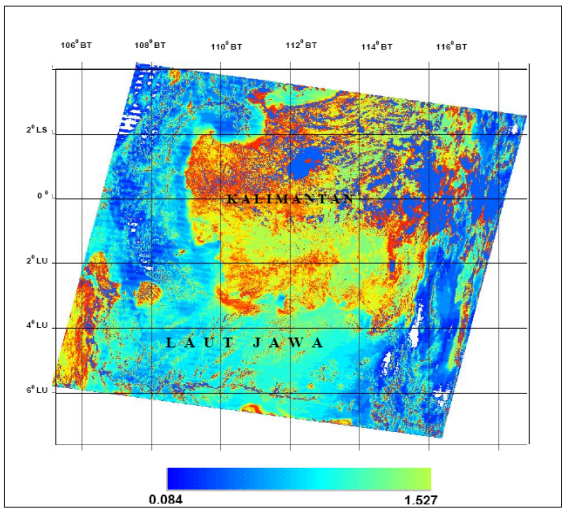

Figure 2. Chlorophyll image of MODIS, band 443 and band 551, May 17 2002.
(Suwargana N, Arief M, Sidik H, 2008).

3. CONCLUSION

Result of processing model using algorithm [Minnet, 2001] for the sea surface temperature and algorithm [Relly,1998] for the chlorophyll concentration assign spatial value which approach that obtained from satellite data of NOAA-AVHRR and also of SeaWifs, however the results still needed for development by furthermore validation, that aims to look for values of constanta for the algorithm used that wear for the region of territorial water of Indonesia (Suwargana, 2002).

ACKNOWLEDGEMENTS

I would like to thank to Mr. Kunarso and Mr. Suwargana which have shared science and journal concerning processing of MODIS image as model of fishing ground prediction so that this handing out can be finished.

My gratitude goes to Faculty of Fisheries and Marine Science, Diponegoro University, which have performed a training so that I earn more to comprehending of basic principle of method which used in this handing out.

REFERENCES

Kunarso (2007). "Excellence Study of Application Technological of Forecasting Tuna Fishing Ground in Upwelling Location which Image MODIS Daily". Faculty of Fisheries and Marine Science, Diponegoro University, Semarang, Indonesia.

N. Suwargana (2002). "Determination of Sea Surface Temperature and Chlorophyll Concentration for the Development Model Fishing Ground Prediction by Using Data of MODIS". National Institute of Aeronautics and Space of Indonesia, Jakarta, Indonesia.

Satellite Based Process Studies in the Baltic Sea

H. Siegel *, M. Gerth

Leibniz Institute for Baltic Sea Research, Warnemünde, Germany –
herbert.siegel@io-warnemuende.de, monika.gerth@io-warnemuende.de

Abstract – Satellite derived sea surface temperature and ocean colour products were used to study processes in the Baltic Sea in different temporal and spatial scales; long-term temperature development, upwelling, coastal discharge, and phytoplankton blooms. The yearly mean SST of the entire Baltic showed a linear trend of 1.41°C (1990-2008). The contribution of the different seasons to the yearly mean changed in the last years. The responsible processes also influence the development of phytoplankton in spring and summer. The blooms depend strongly on wind induced upwelling or mixing. Upwelling processes guide the Oder River discharge into the western Baltic Sea. Cold upwelled water partly covered this entire region which lowered the temperature trends for the open parts to 0.9 – 1.2 °C.

Keywords: ocean color, SST, cyanobacteria, Baltic Sea.

1. INTRODUCTION

The Baltic Sea is a semi-enclosed sea with limited water exchange with the ocean in the North Sea and the Danish Straits. High freshwater supply and limited evaporation result in a positive water balance with an outflow of low saline surface water. High saline and oxygen enriched surface water enters the Baltic Sea and generates permanent haline stratification. The warming phase in early spring stabilises the top layer by thermal stratification, starting condition for phytoplankton growth in the west. Wind mixing and upwelling processes transport nutrients into the top layer. After a stagnation period in late spring to early summer, nitrogen-fixating cyanobacteria develop in July and August depending on meteorological conditions. During calm conditions the cyanobacteria accumulate at the surface and are transported by large scale circulation. Strong wind-induced mixing during cloudy conditions may interrupt or terminate the bloom. This paper summarizes investigations of features and processes in the Baltic Sea based on satellite data in the visible and infrared spectral range.

2. AREA OF INVESTGATION AND DATA

The area of investigation is shown in Fig. 1 containing two maps the entire Baltic Sea with the large Basins and the western Baltic Sea with the German coast. The SST-maps of the period 1990-2008 were derived from data of the Advanced Very High Resolution Radiometer (AVHRR) of the NOAA- weather satellites. The German Federal Maritime and Hydrographic Agency Hamburg (BSH) operate a SeaSpace-HRPT (High Resolution Picture Transmission) receiving station and provide the data. The SST-data evaluation procedure is described by Siegel et al. (1994, 2008).

Figure 1: Maps of the areas of investigation: entire Baltic Sea and western Baltic Sea (after Siegel and Gerth, 2000a)

Ocean colour data of SeaWiFS, MODIS, and MERIS were used to investigate optically active water constituents and sensors of high spatial resolution like Landsat TM and ETM+ were implemented for local coastal studies to observe the detailed distribution features.

3. RESULTS AND DISCUSSION

In the period of recent global warming the sea surface temperature development of the entire Baltic Sea and particularly for the western parts was studied for the period 1990-2008 (Siegel *et al.*, 2009). In contrast to the global temperature development and that of the northern hemisphere the increase in the Baltic Sea continued until 2008 (Fig. 2). The linear trend of the yearly mean SST of the entire Baltic Sea for the last 19 years indicates an increase of app. 1.41 °C, (0.79 °C /decade) three to four times higher than for the northern hemisphere and for the globe. The trends depend strongly on seasons and regions.

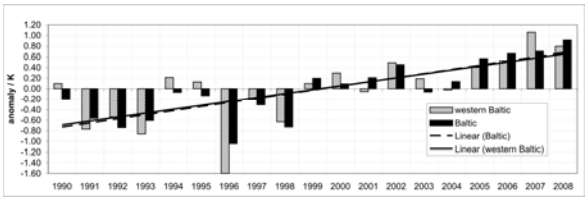

Fig. 2: Development of yearly means SST of the entire Baltic Sea 1990-2008 with anomalies and trend

*Corresponding author. Seestrasse 15, 18119 Rostock, phone +493815197190, fax +4938151974822.

In contrast to the period 1990-2005, the monthly trends became all positive because of the warm winters in the last 3 years (Siegel *et al.*, 2008). The summer and autumn months contribute mainly to the trend. Maximum values were derived for July and October. In contrast to the 1990 years, where August was the warmest month, the monthly mean temperatures of July and August are now in the same order of magnitude due to the lower August temperatures in the last years. The minimum trends occurred in March and lower values in February to May (Siegel et al. 2009). The spring bloom normally starts in the western Baltic Sea in March after thermal stratification, develops in the Arkona Sea and Bornholm Sea end of March to April, and in the central Gotland Sea in May as shown for the year 2000 by Siegel and Gerth (2008). The early increase of temperature and thermal stratification in the last winters led to enhanced phytoplankton concentration 2008 already in February in the western Baltic Sea. The cyanobacteria bloom started after the warm winters in June but due to strong wind situations and upwelling processes in the Gotlandsee in 2008 beginning of July. Because of changing meteorological conditions in August the maximum extent of cyanobacteria in 2008 was reached end of July (Fig. 3).

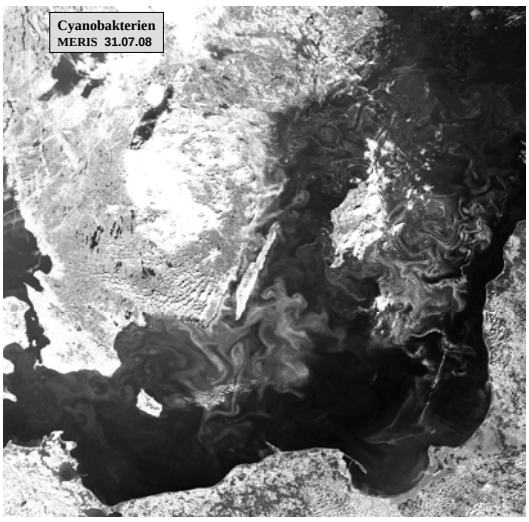

Fig. 3: Cyanobacteria distribution during maximum extent 2008 on 31 July 2008

The western Baltic Sea, the transition area between North and Baltic Seas, is strongly influenced by dynamical processes due to permanent outflow and local wind, supported by the alignment of the coast and topographic features and by the Oder River discharge. Dominating westerly and easterly winds (Siegel *et al.* 2005) induce upwelling processes (Fig. 4). During easterly winds (June 2008) upwelling processes develop along the southern coasts of Germany and Poland guide the Oder River discharge into the Arkona Sea and may influence the entire western Baltic Sea. During westerly winds (August 2005) upwelling processes along the coasts of Denmark and Sweden influence large parts of the western Baltic Sea. A third process influencing the SST patterns in the western Baltic Sea visible in the monthly mean SST of the entire Baltic Sea (Siegel *et al.*, 2008) is the early warming in spring and the earlier cooling in December both starting from the west. Because of the strong influence of these processes the trends for the western Baltic Sea differ partly significantly from that of the entire Baltic Sea. In the central parts of the western Baltic and in the Pomeranian Bight the SST increase is with 1.1-1.2 °C in the period 1990-2008 (entire Baltic Sea 1.41 °C) and lowest in the Bornholm Sea (0.9 °C). Regions which are mainly excluded from the dynamical processes such as Greifswald Bay and Kiel Bight slightly exceed the trend of the Baltic Sea with 1.44 and 1.42 °C, respectively.

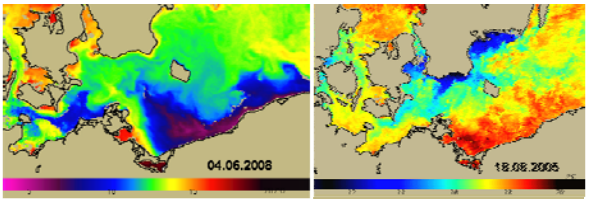

Fig. 4: SST patterns in the western Baltic Sea for easterly and westerly winds

4. CONCLUSION

Satellite data of SST and ocean color are continuously used to investigate the seasonal and inter-annual development of temperature and phytoplankton for the yearly assessment of the entire Baltic Sea. Mild winters in the last years led to early phytoplankton development in spring. Wind mixing terminated the bloom of Cyanobacteria beginning of August 2008. In the dynamically high variable western Baltic Sea the trends of yearly mean SST are reduced to 0.9-1.2°C compared to entire Baltic (1.41°C) for the period 1990-2008.

ACKNOWLEDGEMENTS

Ocean color satellite data were received from MODIS-Rapid Response System and ESA. The SST data were provided by the BSH Hamburg.

REFERENCES

Siegel, H., Gerth, M., 2008. Optical remote sensing applications in the enclosed Baltic Sea. In: Remote Sensing of European Seas. Ed. By Barale and Gade, Chapt. 7, Springer, 91-102.

Siegel H., Gerth M. & Tschersich G. 2006. Sea surface temperature development of the Baltic Sea in the period 1990-2004. Oceanologia 48, suppl., 119-131

Siegel, H., Gerth, M., Tschersich, G., 2008. Satellite-derived Sea Surface Temperature for the period 1990-2005. In: State and Evolution of the Baltic Sea, 1952 – 2005, Ed. By R. Feistel, G. Nausch, N. Wasmund, Wiley, 241-265.

Siegel, H., Gerth, M., Tschersich, G., 2009. Sea Surface Temperature trends in the western Baltic Sea since 1990. Boreal Environment Research, submitted

Siegel, H., Gerth M., Rudloff R. & Tschersich G. 1994. Dynamic features in the western Baltic Sea investigated using NOAA-AVHRR data. Deutsche hydrographische Zeitschrift 46, 191-209

Siegel H., Seifert T., Schernewski G., Gerth M., Ohde T., Reissmann J. & Podsetchine V. 2005. Discharge and transport processes along the German Baltic Sea Coast. Ocean Dynamics 55, 47-66

Wasmund, N., H. Siegel, 2008. Phytoplankton. In: State and Evolution of the Baltic Sea, 1952 – 2005, A Detailed 50-Year Survey of Meteorology and Climate, Physics, Chemistry, Biology, and Marine Environment. Ed. By R. Feistel, G. Nausch, N. Wasmund, Wiley 2008, 441-481

The Carbon Sink Variability in the NW Sub-Polar North Atlantic: an Integrated Approach Using Satellite Ocean Color Data and Numerical Models

S. Signorini [a,*], A. Olsen [b], C.R. McClain [c], S. Häkkinen [c], A.M. Omar [b]

[a] SAIC and NASA Goddard Space Flight Center, Maryland , USA – sergio.signorini@nasa.gov
[b] Bjerknes Center for Climate Research, Bergen, Norway – are.olsen@gfi.uib.no, abdirahman.omar@bjerknes.uib.no
[c] NASA Goddard Space Flight Center, Maryland, USA – [c] charles.r.mcclain@nasa.gov, [d] sirpa.m.hakkinen@nasa.gov

Abstract – We use an ecosystem/biogeochemical model, that includes multiple phytoplankton functional groups and carbon cycle dynamics, to investigate physical-biological interactions in Icelandic waters. Satellite and in situ data were used to validate the model. The seasonality of the coccolithophore and "other phytoplankton" (diatoms and flagellates) blooms compare well with satellite ocean color products. The effect of biological changes on the seasonal variability of the surface ocean pCO_2 exceeds the temperature effect by ~70%. The surface ocean pCO_2 growth during 1981-2008 was 2.8±0.3 µatm yr^{-1}, faster than the atmospheric growth of 1.6±0.1 µatm yr^{-1}. The recent ocean is becoming more neutral by a reduction in the sea-air pCO_2 difference of ~1.1 µatm yr^{-1}.

Keywords: carbon cycle, bio-geo-chemistry, CO_2 uptake.

1. INTRODUCTION

The waters surrounding Iceland are characterized by the cold Polar Water of the East Greenland Current and Arctic Water of the East Icelandic Current from the north, and the warm North Atlantic Water of the Irminger Current from the south . These waters converge and form the Polar Front (PF), which varies slightly in location seasonally and is identified by strong gradients of surface temperature (SST) and salinity (SSS). Sea ice is present throughout the year along the east coast of Greenland, with the ice edge extending farthest offshore in winter-spring, and retreating in the fall. Ice melt in summer-fall freshens (32-34 psu) the surface waters north of the PF. South of the PF waters are saltier (~35 psu) and warmer (8 to 12°C) as a result of Atlantic Water intrusions. During winter and spring, MLDs average 100 to 500 meters south of the PF. In summer, the vertical stratification is significant with MLDs less than 20 meters. North of the PF the MLDs are shallow (<40m) throughout the year due to the southward advection of fresher Polar and Arctic waters, and ice melting in summer-autumn. These large seasonal changes in stratification play an important role in the euphotic zone nutrient renewal and on the onset and duration of the phytoplankton spring bloom. Variability in the timing and intensity of primary production in general, and of the spring bloom in particular, affects the population dynamics of higher trophic levels, such as the commercially important Atlanto-Scandian herring. Figure 1 shows the satellite-derived primary production and calcite rates for June 1998, during one of the most intense coccolithophore blooms recorded by ocean color satellites. Seasonal and interannual changes in phytoplankton production are strictly linked to atmospheric CO_2 uptake and surface ocean pCO_2 variability, and therefore a major component of the carbon cycle. We use a coupled biogeochemical-physical model, which includes multiple phytoplankton functional groups and carbon cycle dynamics, in conjunction with field observations and satellite ocean color products, to study the carbon sink variability in the northwest sub-polar North Atlantic.

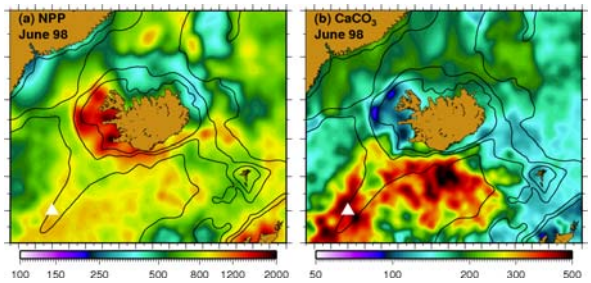

Figure 1. Satellite-derived net primary production (a) and calcification rate (b) for June 1998 (units are mg C m^{-2} d^{-1}). The white triangle indicates the position of the 1D ecosystem/carbon model simulations.

2. METHODS, DATA SETS AND RESULTS

2.1 Biogeochemical Model

The biogeochemical model is an upgraded version of the Signorini and McClain (2003) model, which includes additional conservation equations for diatoms, coccolithophores, calcite ($CaCO_3$), silicate (SiO_2) and alkalinity. The ecosystem model is coupled to a mixed layer model which provides physical forcing (light, temperature, salinity, eddy diffusivity) to the biological components. A 3D circulation model (Sirpa Häkkinen personal communication) provided hydrographic data for bottom forcing. Long-term trends of inorganic carbon were obtained from CARINA station data for bottom boundary conditions (http://cdiac.ornl.gov/ftp/oceans/CARINA/). Model simulations were performed from 1981 to 2008.

2.2 Satellite Data and Field Observations

Model results are validated using satellite derived products from SeaWiFS, MODISA, and AVHRR Pathfinder. These include Chl-a, calcite ($CaCO_3$) and SST. Additional products (PAR and K_{490}) are used as inputs for primary production and calcification rate models (Behrenfeld and Falkowski, 1997; Balch *et al*., 2007). Modeled surface ocean pCO_2 seasonal variability was verified using 2005 field measurements (Olsen *et al*., 2008). Atmospheric pCO_2 originated from GLOBALVIEW-CO_2 (ftp.cmdl.noaa.gov).

* Corresponding Author. NASA GSFC, Greenbelt, MD 20771; tel +1 301-286-9891.

2.3 Summary of Results

Figure 2a shows the seasonal cycles of satellite and model Chl based on monthly averages for the period of 2003-2008. This seasonal plot combines MODIS-derived Chl and the model seasonal Chl. The broadband backscatter from coccolithophore blooms (*Emiliania Huxleyi* blooms are intense in this region as shown in Figure 1) affect the Chl retrievals. However, the ocean color Chl algorithm has a flag for coccolithophore presence which excludes most of their influence on the Chl retrievals. Nevertheless, there is a good agreement between the Chl seasonal cycles from the model and satellite. It is clear that the onset of the bloom seen by the satellite starts earlier with a more gradual rise when compared to the model. This may be due to advection of Chl from the south by the Irminger Current transporting biogenic materials from lower latitudes where the onset of the spring bloom occurs earlier in the season, a feature not captured by the 1D dynamics.

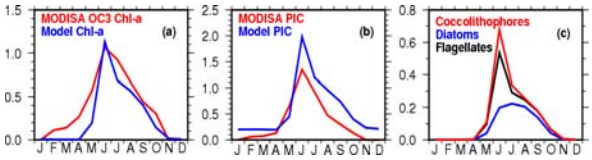

Figure 2. Model vs. satellite Chl-a (a, mg m^{-3}) and PIC (b, mmol C m^{-3}), and phytoplankton groups (mmol N m^{-3}).

There is good agreement between the seasonal cycle of calcite (PIC) from MODIS and the model, as shown in Figure 2b, with the model PIC showing higher values, with a more pronounced difference during the peak of the coccolithophore bloom in June. A low bias in the retrieval of satellite calcite due to elevated subpolar cloudy conditions may explain, at least in part, the observed difference. The phasing and peak of the coccolithophore, diatoms, and flagellates blooms are well represented in the model. The seasonal variability of the three major phytoplankton groups is shown in Figure 2c in units of mmolN m^{-3}. Flagellates and coccolithophores bloom from May to September with a distinct peak in June (0.5 to 0.7 mmolN m^{-3}), while the diatom bloom has a much broader seasonal cycle with peak values of ~0.2 mmolN m^{-3}.

The baseline simulation was performed with all components of the biogeochemical model turned on. The results were used to estimate the physical forcing and biological response in the study region, and consequences on the CO_2 uptake variability. The biological effect on the surface ocean pCO_2 seasonal cycle far exceeds the effect of temperature changes, in agreement with observations (Olsen et al., 2008). The observed seasonal ranges of pCO_2 due to biological and temperature effects are 114.2 µatm and 67.5 µatm, respectively. The equivalent values for the modeled seasonal ranges are 124.0 µatm and 72.0 µatm. Another model run was made with the biological uptake turned off. Figure 3 compares the 2005 measured and model simulated seasonal pCO_2 cycles with and without biological uptake. The atmospheric pCO_2 is also shown as a reference. A significant difference is noticeable between the two simulations. Without the biological uptake, the ocean would become oversaturated during the warmer period (May-September) and the net annual sea-air ΔpCO_2 would be reversed (from -20 to + 9 µatm). The biological drawdown results from an annual new production of 49 g C m^{-2} yr^{-1}, which is in agreement with published estimates. The long-term (1981-2008) surface ocean pCO_2 (not shown) trends upward at 2.8 µatm yr^{-1}, faster than the observed atmospheric pCO_2 growth (1.6 µatm yr^{-1}). This is a result of not only local temperature and biological effects, but also advection of warm, carbon rich Atlantic Water from the south. There is evidence that warm subtropical waters have recently increased their penetration toward the Nordic Seas (Häkkinen and Rhines, 2009).

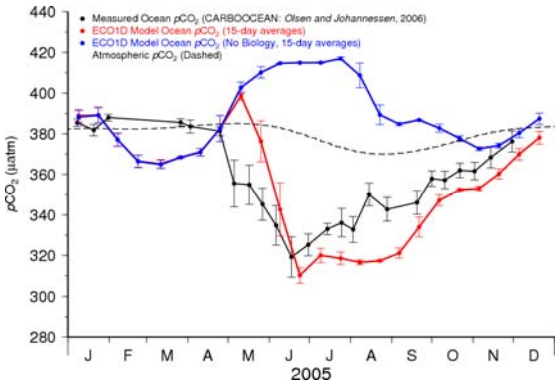

Figure 3. Seasonal cycle of measured and modeled pCO_2 with and without biological uptake.

4. CONCLUSIONS

The surface ocean pCO_2 trend in the NW sub-polar North Atlantic (SPNA) during the past three decades (1981-2008) has increased at a pace faster than the atmospheric pCO_2 growth. This is due to the combined effects of local uptake/release of CO_2 via temperature and biological effects, and the northward advection of Atlantic water rich in DIC. The biological uptake plays a significant role in the CO_2 drawdown during the growth season (May-September) and has maintained the SPNA waters undersaturated. However, more recently, the surface SPNA has become more saturated in response to a complex interaction between primary production, vertical mixing, anthropogenic CO_2, and horizontal transport.

ACKNOWLEDGEMENTS

This work was supported by the NASA Ocean Biology and Biogeochemistry Program.

REFERENCES

Balch, W., *et al*. (2007). "Prediction of pelagic calcification rates using satellite measurements". DSR-II, *54*, 478-495.

Behrenfeld, M. J. and P. G. Falkowski (1997). "Photosynthetic rates derived from satellite-based chlorophyll concentration". *Limnology and Oceanography*, *42*, 1-20.

Olsen, A. et al. (2008). "Sea-surface CO_2 fugacity in the subpolar North Atlantic". *Biogeosciences, 5*, 535-547.

Häkkinen, S. and P. B. Rhines (2009). "Shifting surface currents in the northern North Atlantic Ocean". *Journal of Geophysical Research*, *114*, C04005, doi:10.1029/ 2008JC004883.

Signorini, S. R. and C. R. McClain (2003). "Further Studies on Oceanic Biogeochemistry and Carbon Cycling". NASA/TM-2003-212245, 51 pp., NASA GSFC, Greenbelt.

Inter-Annual Variability of Chl-a Along the Western Coast of Africa

R.P. Singh [a], W. Mehdi [b], A. Chauhan [b]

[a]Department of Physic, Computational Science and Engineering, Schmid College of Science, Chapman University, One university Drive, Orange, CA 92866, USA – rsingh@chapman.edu
[b]Research and Technology Development Center, Sharda University, Greater Noida, India

Abstract – The western coast of Africa is very dynamic: land-ocean-atmosphere coupling is found to be very strong. As a result, both spatial and temporal distribution of chlorophyll-a (Chl-a) display strong annual and inter-annual variability. In the present case, we show a detailed analysis of ocean color (Chl-a), sea surface temperature (SST) and atmospheric parameters during 2002-2008. Chl-a and SST are found to be influenced by changes in atmospheric aerosols due to dust storms transporting Shahra dust.

Keywords: ocean color, dust event, Chl-a, SST, Africa.

1. INTRODUCTION

Dust events are common at many places of the world. Transport of dust is observed to travel longer distances, sometime dusts are found to be transported from one continent to other continents and during transport, the dusts deposits on the land, land cover, snow and ocean surfaces. The dust transport influences the ecology of the countries due to the dust.

In recent decade, remote sensing data is used widely in monitoring the ecology of coastal regions (Sarmient et al., 1988; Singh et al. 2006, 2007, 2008; Dasgupta et al., 2009). The spatial and temporal variability of chlorophyll concentrations have been widely studied in the Arabian Sea and Bay of Bengal using satellite ocean color data (Dasgupta et al., 2009). Satellite data is also used to study the changes in ocean color parameters after the cyclones, hurricanes and tsunami (Singh et al., 2007). Recent studies (Singh et al., 2008) show influence of dust in enhancing chlorophyll concentration of the Arabian Sea.

McTainsh and Strong (2007) have studied ecological affect associated with the Australian dust events. Singh et al. (2008) have found dust transported from the Arabia Peninsula over the Indo-Gangetic plains affecting Arabian ocean and atmosphere. Even dusts are found to influence meteorological parameters (Singh et al., 2009). Sahara dust is common which affect the western coast of Africa. Ramos et al. (2009) have shown influence of dust storm in ocean blooming in the north-west of south Africa. In the present paper, we have used multi sensor data to study the changes along the western coast of Africa at number of locations and the spatial and temporal variability of chlorophyll-a is shown for the period 2002-2008.

2. STUDY AREA AND SATELLITE DATA

We have taken 10 locations at a regular interval along west coast of Arica (Figure 1), Locations are selected at regular interval along the west coast of Africa. These locations lie in the region 5 N to 32.2 N and 8.4 W to 17.2 W. The chlorophyll-a data with temporal resolution of 8 days and spatial resolution of 9 km is obtained from SeaWiFS ftp://oceans.gsfc.nasa.gov/SeaWiFS/Mapped/Monthly/CHLO/), the aerosols optical depth at wavelength 869 nm is taken from MODIS-Aqua Monthly Global 9-km Products http://reason.gsfc.nasa.gov/OPS/Giovanni/ocean.aqua.shtml.

The monthly sea surface temperature (day and night) (SST) data is taken from Physical Oceanography DAAC site htp://podaac.jpl.nasa.gov/pub/sea_surface_temperature/reynolds/oisst/data/oimonth_v2.

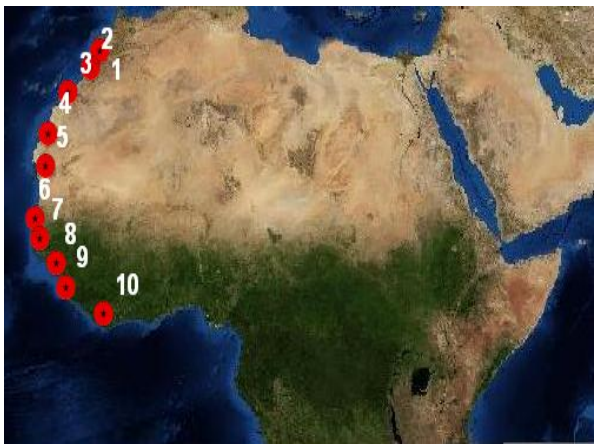

Figure 1 showing locations of detailed analysis of atmospheric and ocean color parameters.

3. RESULTS AND DISCUSSION

The aerosol optical depth (AOD) at 869nm values is showing higher anomalies throughout the region of studies. Northern most locations of study show smaller values of AOD which gradual increases as locations shifts towards equator. Higher values of AOD are observed during November to February each year. In general, whenever the dust storms are prevalent, higher aerosol optical depth is found (Figure 2a). The dust storms in the atmosphere reduces sun radiations incident on the ocean surface leading to decrease in the SST. A clear reduction or increase in SST is observed associated with dust storm.

Chl-a and its correlation with day and night SST is shown for location #10. Higher Chl –a is observed (Figure 2b) when the SST is minima due to dust storms, when AOD is found to be higher. The detailed analysis of Chl-a , AOD and SST, we have found that the Chl-a is maximum at locations #5 and #6. SST continuously found to increase from location #1 to #10 due to close proximity to the

equator. From Figures 2a, b it is clearly seen that Chl-a enhanced anomalously when the SST is found to be low.

Change in concentration of Chl-a plays a significant role in account of the effect of photosynthesis on ocean-atmosphere carbon exchange. Availability of fish and other sea life/food depends on nutrients, photo-synthetically active radiations etc. Chlorophyll concentration increases initially as one moves from north to south along the coast of south Africa which is likely due to the general decrease of SST and also due to intense dust storms during the dust season. Overall the pattern is not clearly visible unless dust and non-dust events are clearly monitored and data is available for the comparison.

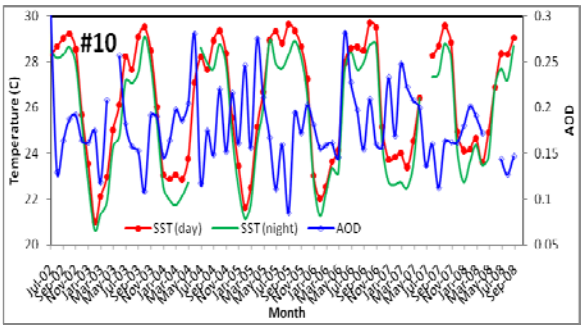

Figure 2a shows variation of AOD and SST at location #10 (given in Figure 1), higher values of AOD is seen during dust season (May – July), SST shows higher values when AOD is generally higher, although not a systematic pattern of SST and AOD is observed during 2002- 2008.

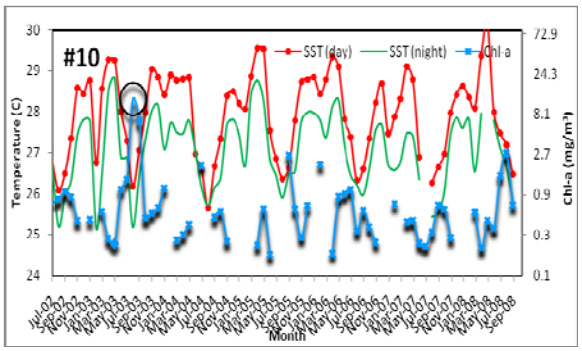

Figure 2b. showing monthly variations of day (SST – day) and night (SST – night) and Chl – a over location #10.

Table 1 provides information about correlation of day and night SST and aerosol optical depth and Chl –a for locations #1 to #10. For location #6, higher inverse correspondence is observed, showing dust events decrease the SST that leads to increase in Chl-a concentrations.

Table 1. Correlation of day and night time SST with Chl-a and Chl-a and AOD for different locations 1 – 10 (Lo#).

Lo #	Lat.	Lon.	SST(d) & chl	SST(n) & Chl	Chla & AOD
1	31.2	8.9	0.29	0.28	0.22
2	29.5	10.1	0.22	0.19	0.39
3	27	12.9	0.24	0.05	0.15
4	23	15.5	0.31	0.21	-0.01
5	19.7	15.9	0.48	0.43	0.33
6	14.5	17.2	-0.57	-0.61	0.39
7	12.5	16.6	-0.59	-0.59	0.15
8	10.1	14.5	-0.30	-0.22	0.43
9	7.7	13.3	0.18	0.15	0.20
10	5	8.4	-0.34	-0.35	-0.06

ACKNOWLEDGMENTS

One of the authors (WM) is grateful to the Director, Research and Technology Development Center, Sharda University, Greater Noida for the financial support. The authors are grateful to NASA Giovanni team for data support.

REFERENCES

Dasgupta, S., R. P. Singh, R.P, and M. Kafatos, (2009), Comparison of global chlorophyll concentrations using MODIS data, Advances in Space Research, vol. 43, pp. 1090-1100.

McTainsh, G. and C. Strong, (2007), The role of aeolian dust in ecosystems, Geomorphology, vol. 89, pp. 39-54.

Micha J.A., C.A. Rijkenberg, et al., (2008), Changes in iron speciation following a Saharan dust event in the tropical North Atlantic Ocean, Marine Chemistry, vol. 110, 1-2, pp. 56-67.

Ramos, A. G., Cuevas, E., et al., (2009), Saharan dust-induced chlorophyll blooms in the northwest African upwelling, Remote Sensing of Inland, Coastal, and Oceanic Waters. Edited by Frouin, Robert J.; Andrefouet, Serge; Kawamura, Hiroshi; Lynch, Mervyn J.; Pan, Delu; Platt, Trevor. Proceedings of the SPIE, vol. 7150, pp. 715011-715011-13.

Singh, R.P., S. Dey, S. Bhoi, D. Sun, G. Cervone, and M. Kafatos, (2006). Anomalous increase of chlorophyll concentrations associated with earthquakes. Advances in Space Research, vol. 37, pp. 671-680.

Singh, R.P., G. Cervone, M. Kafatos, A.K. Prasad, A.K. Sahoo, D. Sun, D. Tang, and R. Yang, 2007, Multi-sensor studies of the Sumatra earthquake and tsunami of 26 December 2004, International J. Remote Sensing, 28, pp. 2885-2896.

Singh, R. P., A. K. Prasad, V. K. Kayetha, and M. Kafatos, (2008), Enhancement of oceanic parameters associated with dust storms using satellite data, J. Geophys. Res., 113, C11008, doi:10.1029/2008JC004815.

Stegmann, P.M., (2000), Ocean-color satellites and the phytoplankton-dust connection, Elsevier Oceanography Series, vol. 63, pp. 207-223.

Maritime Aerosol Network as a Component of AERONET – Relevance to Ocean Color Remote Sensing

A. Smirnov [a,b], B. Holben [b], A. Macke [c], Y. Courcoux [d], P. Croot [e], S. Sakerin [f], T. Smyth [g], G. Zibordi [h], T. Zielinski [i], M. Harvey [j], J. Goes [k], N. Nelson [l], P. Quinn [m], V.Radionov [n], S. Triquet [o], J. Sciare [p], C. Duarte [q], K. Voss [r], K.Krishna Moorthy [s], N. Nalli [t], E. Joseph [u], G. Milinevsky [v], S. Gulev [w], D. Covert [x], I. Slutsker [a,b], N. O'Neill [y], D. Giles [a,b], T. Eck [z,b]

[a] Sigma Space Corporation, Lanham, Maryland, USA – Alexander.Smirnov-1@nasa.gov
[b] Goddard Space Flight Center, Greenbelt, Maryland, USA – Brent.N.Holben@nasa.gov
[c] Leibniz Institute for Tropospheric Research, Leipzig, Germany – macke@tropos.de
[d] Universite de la Reunion, Saint Denis de la Reunion, France – yann.courcoux@univ-reunion.fr
[e] Leibniz Institute of Marine Sciences at Kiel University, Kiel, Germany – pcroot@ifm-geomar.de
[f] Institute of Atmospheric Optics, Russian Academy of Sciences, Siberian Branch, Tomsk, Russia – sms@iao.ru
[g] Plymouth Marine Laboratory, Plymouth, UK – tjsm@pml.ac.uk
[h] European Commission - Joint Research Center, Ispra, Italy – giuseppe.zibordi@jrc.ec.europa.eu
[i] Institute of Oceanology, Polish Academy of Sciences, Sopot, Poland – tymon@iopan.gda.pl
[j] National Institute of Water and Atmospheric Research, Wellington, New Zealand – m.harvey@niwa.co.nz
[k] Bigelow Laboratory for Ocean Sciences, West Boothbay Harbor, Maine, USA – jgoes@bigelow.org
[l] University of California at Santa Barbara, Santa Barbara, California, USA – norm@icess.ic.ucsb.edu
[m] Pacific Marine Environmental Laboratory, Seattle, Washington, USA – Patricia.K.Quinn@noaa.gov
[n] Arctic and Antarctic Research Institute, Saint Petersburg, Russia – vradion@aari.ru
[o] Universite de Paris 7 et Universite de Paris 12, Creteil, France – sylvain.triquet@lisa.univ-paris12.fr
[p] Laboratoire des Sciences du Climat et de l'Environnement, Gif-sur-Yvette, France – jean.sciare@lsce.ipsl.fr
[q] Mediterranean Institute for Advanced Studies, Mallorca, Spain – carlosduarte@imedea.uib-csic.es
[r] University of Miami, Coral Gables, Florida, USA – voss@physics.miami.edu
[s] Vikram Sarabhai Space Center, Trivandrum, India – krishnamoorthy_k@vssc.gov.in
[t] National Environmental Satellite, Data, and Information Services, Camp Springs, Maryland, USA – Nick.Nalli@noaa.gov
[u] Department of Physics and Astronomy, Howard University, Washington, DC, USA – ejoseph@howard.edu
[v] Taras Shevchenko National University of Kyiv, Kyiv, Ukraine – genmilinevsky@gmail.com
[w] P.P.Shirshov Institute of Oceanology, Russian Academy of Sciences, Moscow, Russia – gul@sail.msk.ru
[x] Department of Atmospheric Sciences, University of Washington, Seattle, Washington, USA – dcovert@u.washington.edu
[y] Universite de Sherbrooke, Sherbrooke, Quebec, Canada – Norman.T.ONeill@USherbrooke.ca
[z] University of Maryland - Baltimore County, Baltimore, Maryland, USA – Thomas.F.Eck@nasa.gov

Abstract – The paper presents the current status of the Maritime Aerosol Network (MAN) as a component of AERONET. The MAN started collecting aerosol optical data in various regions of the World Ocean in November 2006 and has completed over 70 cruises, with many cruises ongoing and planned. The aerosol optical depth data collection will provide the international scientific community with the much needed data for the satellite retrieval validation, atmospheric correction and other applications. A public domain web-based archive is essential in the fundamental scientific aspect of aerosol optical studies over the oceans.

Keywords: optical depth, maritime aerosol, AERONET.

1. INTRODUCTION

Atmospheric aerosol optical depth studies over the oceans were sparse and not systematic till the middle of the nineties (Smirnov et al. 2002). Aerosol Robotic Network established standardization in the instrumentation and data processing (Holben et al. 1998; Holben et al. 2001). Island-based data acquisition enriched significantly our knowledge on aerosol optical properties over the oceans (Holben et al. 2001; Eck et al. 2001; Smirnov et al. 2002; Smirnov et al. 2003). The establishment of the Maritime Aerosol Network as a component of AERONET, affiliated with the AERONET calibration and data processing, complements island-based AERONET measurements, spatially extending data collection to the areas where no islands exist (Smirnov et al. 2009). After two pilot projects were conducted (in 2004 and in the winter of 2005-2006) the regular measurements started in November 2006. Since then data acquisition continued accumulating now over 1600 days of measurements (see Table A). Data archive provides data for satellite retrieval validation, atmospheric correction, global aerosol transport model simulations, and radiative forcing computations.

Table A. MAN Activity Summary

	N
Completed cruises	76
Measurement days	1612
Measurement series	9838
Ongoing cruises	3
Planned cruises	11

2. MARITIME AEROSOL NETWORK STATUS

Maritime Aerosol Network deploys hand held sunphotometer Microtops II with 5 spectral channels and utilizes the calibration and data processing traceable to AERONET. Measurement areas included various parts of the World Ocean. MAN products include aerosol optical depth, Angstrom parameter, columnar water vapor and aerosol optical depth at 500 nm partitioned into fine and

coarse components according to O'Neill et al. (2001). All products have three data quality levels: Level 1.0 (unscreened), Level 1.5 (cloud-screened), and Level 2.0 (cloud-screened and quality assured). Figures 1-4 show MAN global coverage: cruise tracks and daily averages of various parameters.

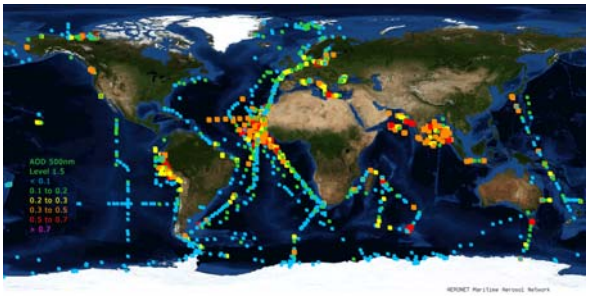

Figure 1. Maritime Aerosol Network global coverage: cruise tracks and daily averages of aerosol optical depth (Level 1.5) are shown.

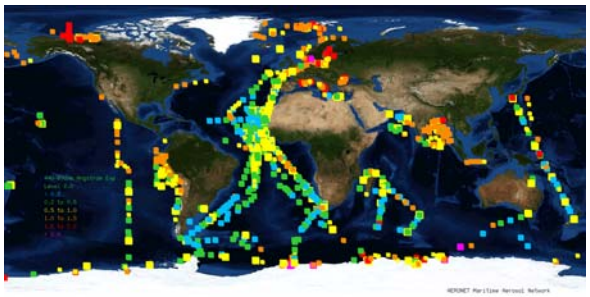

Figure 2. Maritime Aerosol Network global coverage: cruise tracks and daily averages of the Angstrom parameter (Level 2.0) are shown.

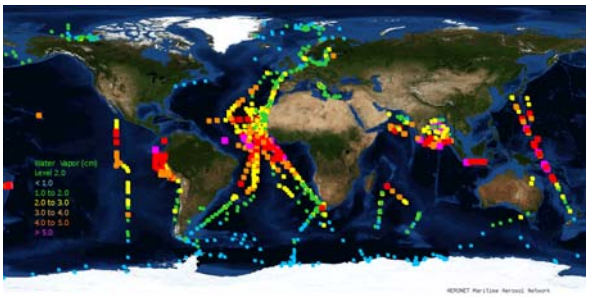

Figure 3. Maritime Aerosol Network global coverage: cruise tracks and daily averages of the columnar water vapor content (Level 2.0) are shown.

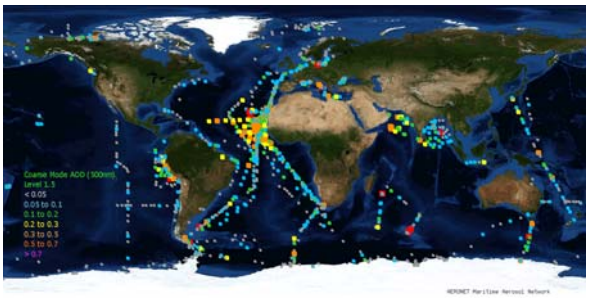

Figure 4. Maritime Aerosol Network global coverage: cruise tracks and daily averages of aerosol optical depth (coarse fraction) (Level 1.5) are shown.

We would like to emphasize that some areas (e.g. in the South Ocean, in the "roaring forties" and even in the Bering Sea) previously have no coverage at all. Aerosol optical depths at the high latitudes were smaller than satellite data suggest they should be. Measurements in the Pacific Ocean quite surprisingly showed a variety of optical conditions especially in the region off the West Coast of South America.

A public domain web-based archive dedicated to the MAN activity can be found at the AERONET webpage: http://aeronet.gsfc.nasa.gov/new_web/maritime_aerosol_network.html.

3. CONCLUSION

Many areas of the World Ocean still have little or no coverage. Our international, multi-institutional collaborative effort will significantly enhance our knowledge on the global aerosol distribution over the oceans. We foresee a continuation of this effort on various ships of opportunity.

ACKNOWLEDGEMENTS

We would like to thank Dr. Hal Maring (NASA Headquarters) for his support of AERONET. We also wish to extend our thanks to scientists and technicians who participated in data collection and/or provided logistical support.

REFERENCES

Eck, T.F. et al. (2001). "Column integrated aerosol optical properties over the Maldives during the NE monsoon for 1998-2000". J. Geophys. Res., 106, 28,555-28,566.

Holben, B.N. et al. (1998). "AERONET - A federated instrument network and data archive for aerosol characterization". Rem. Sens. Env., 66, 1-16.

Holben, B.N. et al. (2001). "An emerging ground-based aerosol climatology: Aerosol optical depth from AERONET". J. Geophys. Res., 106, 12,067-12,097.

O'Neill, N.T. et al. (2001) "Bimodal size distribution influences on the variation of Angstrom derivatives in spectral and optical depth space". J. Geophys. Res., 106, 9787-9806.

Smirnov, A. et al. (2009). "Maritime Aerosol Network as a component of Aerosol Robotic Network". J. Geophys. Res., 114, D06204, doi:10.1029/2008JD011257.

Smirnov, A. et al. (2003). "Effect of wind speed on columnar aerosol optical properties at Midway Island". J. Geophys. Res., 108(D24), doi: 10.1029/ 2003JD003879.

Smirnov, A. et al. (2002). "Optical properties of atmospheric aerosol in maritime environments". J.Atm.Sci., 59, 501-523.

Microwave radiometric system for remote sensing of the oceans from ISS

M.T. Smirnov [a,*], Yu.G. Tishchenko [a], V.S. Ablyazov [b], A.A. Khaldin [b], A.V. Kuzmin [c], M.N. Pospelov [c]

[a] Institute of Radioengineering and Electronics, RAS, Moscow reg., Russia – smirnov@ire.rssi.ru
[b] Special Design Bureau IRE, RAS, Moscow reg., Russia – ahaldin@sdb.ire.rssi.ru
[c] Space Research Institute, RAS, Moscow, Russia – alexey.kuzmin@asp.iki.rssi.ru

Abstract – New microwave radiometric system which will operate on International Space Station (ISS) aimed on sea salinity and its state measurements is under development. This system will consists of two parts: L-band radiometer complex measuring sea salinity and multichannel microwave radiometers for sea surface wave state retrieval. The main ideas of the space experiments were tested in the field experiments on marine platform

Keywords: microwave, salinity, waves, ISS.

1. INTRODUCTION

Last time interest to sea surface salinity measurements from space is very high. For this purpose may be used microwave radiometers in prospective (optimal) L-band region of spectrum. One of the most powerful L-band instrument which was launched at the end of year 2009 is SMOS (Barré *et al.*, 2008). It contains very complicated interferometric imaging radiometer with synthetic aperture antenna. In Russia under development is much simpler microwave radiometer (Armand *et al.*, 2007). Key features and state of its creation are described in this paper. One of the most important parameter which must be taken into account for precise sea salinity retrieval is sea surface roughness. In order to have information about sea surface wave state the second instrument is proposed. It is multichannel polarimetric radiometers with 3 beams pointed in 3 different elevation angles. An idea of radiometric measurements usage for surface wave spectrum retrieval was proposed by IKI researchers, first in (Irisov *et al.*, 1987), where it was suggested to apply multifrequency radiometry. Another approach was proposed in (Trokhimovski, 2000), where angular radiometric measurements were realized.

The scientific program for this instrumentation includes the following main goals:

- sea salinity measurements in open ocean,
- soil moisture retrieval over the territories in regional and global scales,
- study of the geothermal activity regions,
- investigation of energy-exchange in the ocean-land-atmosphere system (in combination with the data of other sensors).

The main ideas of the space experiments were tested in the field experiments on marine platform. It was analyzed some aspects of measurements in L-band and experimentally test the sea surface curvature spectrum retrieval algorithm from angular radiometric measurements.

2. SPACE MICROWAVE RADIOMETRIC SYSTEM

Space microwave radiometric complex on ISS will consists of two parts: L-band radiometric system measuring sea salinity and multichannel microwave radiometers for sea surface wave state retrieval. Microwave instruments will be installed on the module of Russian segment of International Space Station (RS ISS). L-band radiometric system is scheduled for launch by the end of year 2010. Full radiometric complex will be accomplished by microwave radiometric system "Wind" later. L-band radiometric complex is a set of radiometers with 8 beams antenna. Fields of view will be pointed across the satellite orbit symmetrically to nadir direction. Central beams will have spatial resolution about 50 km. General specification of the instrument is presented in table A.

Table A. L-band radiometric complex

Main frequency, MHz	1410
Bandwidth, MHz	20
Radiometric sensitivity, K	0.2-0.3
Polarization	linear
Number of beams	8
FOW, km	50
Swath width, km	400
Antenna size, mm	1200x1920

Due to relatively large size of the antenna and requirements to deliver instrument in compact state through the manhole it has folding elements and will be deployed manually by cosmonauts. Microwave radiometric complex "Wind" is a set of polarimetric radiometers with 3 beams pointed at 3 different elevation angles and measuring thermal emission at 2 frequencies. General specification of this instrument is presented in table B. The geometry of observation is presented in fig. 1. The same region of Earth will be observed sequentially due to satellite motion.

Table B. Microwave radiometric complex "Wind"

Main frequencies, GHz	13.3, 36.5
Radiometric sensitivity, K	0.08
Polarization	3 Stokes param.s
Number of beams	3
Incidance angles, deg. from nadir	0, 30, 60
FOW (nadir), km	50

* Corresponding Author. Vvedenskogo sq. 1, Fryazino, Moscow region, 141190, Russia, tel. +7 495 702 95 88 , fax +7 495 702 95 72.

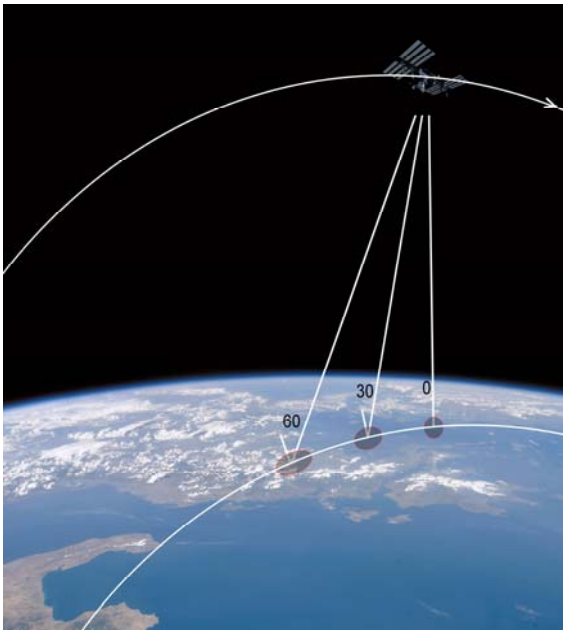

Figure 1. Geometry of Earth observation by microwave radiometric complex "Wind".

Polarimetric measurements will allow retrieving wind speed and wind direction. Data from 3 different angles, 2 frequencies and 3 polarization will provide information about surface wave spectrum parameters.

3. GROUND BASED EXPERIMENTS

Ground base experiments with microwave instruments were held in June 2005, August 2007 and October 2009 in Black Sea on the off-shore marine platform near to Katsiveli, Crimea, Ukraine (Pospelov *et al.*, 2008). List of radiometers used during the experiments included: L-band radiometer (V- or H-polarization); S-band radiometer (V-pol.); K-band polarimeter (3 Stokes parameters); Ka-band polarimeter (3 Stokes parameters); W-band radiometer (V- and H-pol.); IR-radiometer (8-12 mm). Corresponding wavelength ranged from 21 cm down to 8 mm. All radiometers (except L-band) were mounted on the scanning platform which allowed to measure angular distribution of thermal radiance of sea and atmosphere.

During this experiment data on radio interference, natural variations of sea brightness temperatures and angular dependences of the sea surface emission in L-band were obtained. Among the different measurements it was registered daily variations of the brightness temperatures and simultaneous measurements of a wind speed.

An algorithm of the spectrum parameters retrieval from angular radiometric measurements reduces an inverse problem to the direct one, i.e. the brightness contrast produced by the waves with any particular (randomly defined) parameters of spectrum is computed, and then the combination of the spectrum parameters is chosen that ensures the best fit of the computed contrasts to the measured experimentally.

An example of the sea surface curvature spectrum retrieved from angular radiometric measurements in Ka-band is presented in fig. 2.

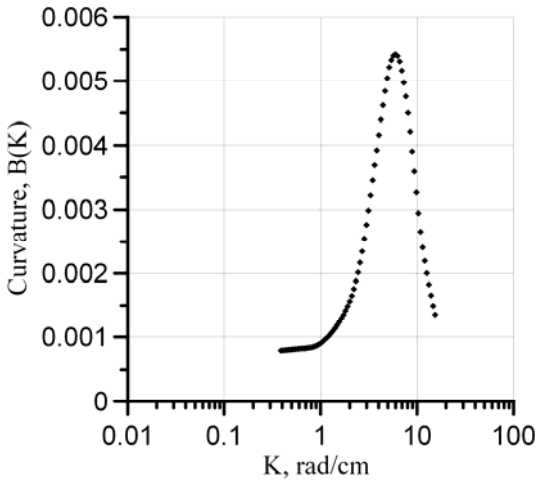

Figure 2. Curvature spectrum retrieved from Ka-band radiometric data (wind speed 4.2 m/s)

4. CONCLUSION

Combination of L-band and multifrequancy multiangle microwave measurements from ISS may allow reliable retrieving ocean salinity. Ground based measurements with analogous instruments and independent contact data from marine platform should be used for validation purposes.

ACKNOWLEDGEMENTS

This work was supported in part by grants RFBR 08-05-00890-a, 09-02-00780-a.

REFERENCES

Hubert M. J. P. Barré, Berthyl Duesmann, and Yann H. Kerr (2008). "SMOS: The Mission and the System," IEEE Transactions on Geoscience and Remote Sensing, Vol. 46, No. 3, pp. 587-593

N.A. Armand, M.T. Smirnov, and Yu.G. Tishchenko (2007). "Hardware for scientific and applied studies in Earth resource remote sensing and in environment monitoring from the International Space Station Russian segment", Cosmonautics and rocket engineering, No. 4 (49), pp. 91-94 (in Russian)

M. Pospelov, Y. Goryachkin et al. (2008). "Air-sea interaction monitoring by remote and contact easurements: the results of the CAPMOS'05 and CAPMOS'07 experiments on an oceanographic platform in the Black Sea" 10th Specialist Meeting on Microwave Radiometry and Remote Sensing of the Environment (MicroRad 2008), p. 191-192

Irisov, V.G., Y.G. Trokhimovski, and V.S. Etkin, Radiothermal spectroscopy of the ocean surface (1987). Sov. Phys. Docl., 32, No.11, 914-915, [Translated from Russian: Doklady Akad. Nauk SSSR, 297, 587-589]

Trokhimovski, Y.G. (2000). Gravity-capillary wave curvature spectrum and mean-square slope retrieved from microwave radiometric measurements (Coastal Ocean Probing Experiment), J. Atmosph. and Oceanic Techn., 17, No. 9, p. 1259-1270

Determining the Response of the Tropical Pacific to Global Warming

B.J. Soden [a,*], G.A. Vecchi [b], A.C. Clement [c]

[a] Rosenstiel School for Marine and Atmospheric Science, Miami, FL USA – bsoden@rsmas.miami.edu
[b] NOAA/Geophysical Fluid Dynamics Laboratory, Princeton, NJ USA – gabriel.a.vecchi@noaa.gov
[c] Rosenstiel School for Marine and Atmospheric Science, Miami, FL USA – aclement@rsmas.miami.edu

Abstract – This study highlights the contrasting records of sea surface temperature trends over the tropical Pacific, underscores the importance of this difference to the understanding of the physical climate processes in this region and of projections for the future, and discusses the role of satellite observations in reconciling this discrepancy.

Keywords: climate change, tropical Pacific, ENSO.

1. INTRODUCTION

There is a long-standing debate in the climate community as to how the tropical Pacific will respond to increased greenhouse gases: Will the structure of the *time-mean* changes in the ocean surface temperature more closely resemble an El Niño or a La Niña? This distinction is of profound significance because conditions in the tropical Pacific affect a range of weather phenomena including tropical cyclone activity, global patterns of drought and flood, agricultural productivity, and oceanic biological activity.

2. COUPLED MODEL PROJECTIONS

There is substantial modeling and observational literature advocating both sides of the debate, and these opposing points of view remain to be reconciled (Vecchi and Soden, 2007). Consider Figure 1 which shows the response of coupled models of varying complexity to a warming climate and observational estimates of the long-term trend in Pacific SST. The upper panel shows an adaptation of the results of Clement et al (1996) of the response of the Cane-Zebiak model to an imposed surface warming of 2K, normalized by the imposed surface forcing of 2K. The second and third panels show the average response of SST to CO_2 doubling from thirteen models for which both fully-coupled GCM and mixed-layer ocean GCM data were available from the IPCC-AR4 model database, normalized by the SST change averaged 30°S-30°N, 0-360° (Vecchi and Soden, 2007).

3. OBSERVATIONAL RECORDS

Historical reconstructions of SST trends over the past century are currently unable to resolve this dispute; The fourth and fifth panels of Figure 1 show the observed 1880-2005 SST trends from the reconstructions of Rayner, *et al,* (2003) and Smith and Reynolds (2004), respectively, normalized by the corresponding SST trend averaged 30°S-30°N, 0-360°. One reconstruction – HadISST [Rayner et al. 2003] – shows a 'La Niña-like' pattern, with an increase in the zonal SST gradient. However, the NOAA extended reconstruction of SST (ERSST) [Smith and Reynolds 2004] exhibits an 'El Niño-like' pattern, and is consistent with recent analyses of sea level pressure data indicating a weakening of the Walker circulation.

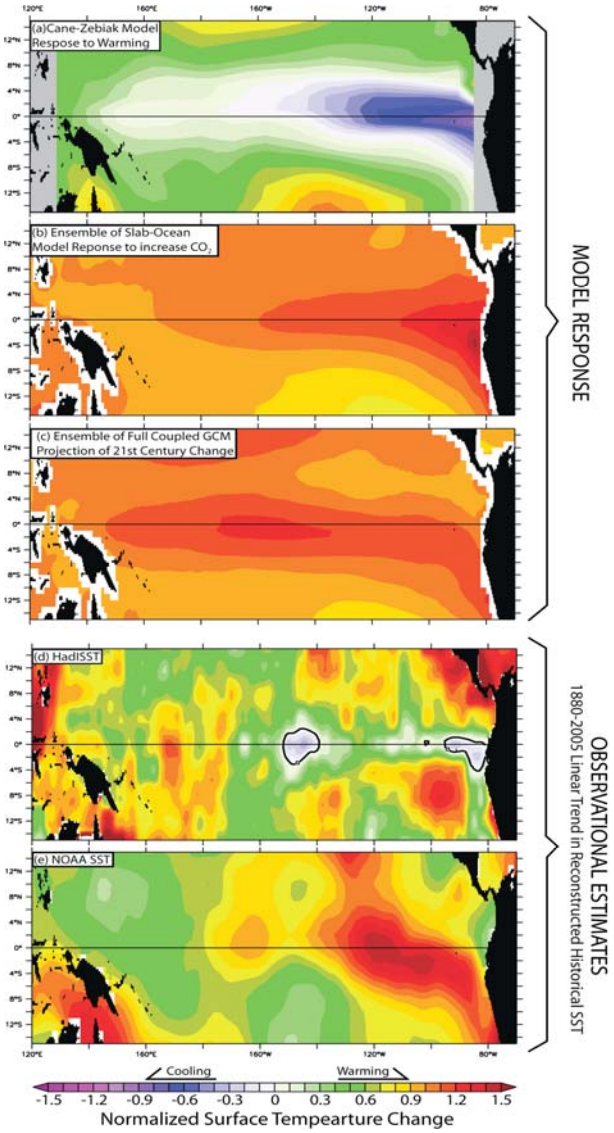

Figure 1. Observed SST trends for the 20th Century and model projected patterns of warming due to increased greenhouse gases.

* Corresponding author. RSMAS/MPO, University of Miami, Miami, FL 33149 USA. Tel 305-421-4202, Fax 305-421-4696

Closer inspection of the contrasting SST reconstructions indicates that the differing behavior between the products arises primarily during two periods around the 1930s and 1980s. These periods are roughly coincident with, respectively, the period of greatest change in "bucket-to-intake" corrections of SST measurements (a correction that differs between the products) and the beginning of satellite infrared SST retrievals (satellite data is used in HadISST, but not in ERSST). We propose that a focused effort be placed towards identifying the specific sources of this discrepancy and the appropriate corrections.

4. CONCLUSION

Theory, models and observations present diverging views of the Pacific response to global warming. It may be possible to reconcile the different theoretical frameworks for understanding the Pacific response to increased CO2 within state-of-the-art coupled GCMs. However, the test of how these mechanisms operate in reality is in the hands of the observationalists, and the consequences for our understanding of the climate not only in the tropical Pacific, but in all the regions affected by ENSO, are great.

REFERENCES

Clement, A.C., R. Seager, M.A. Cane, and S.E. Zebiak, (1996), An ocean dynamical thermostat.. *J. Climate*, 9, 2190-2196.

Rayner, N.A., *et al.*, (2003), Global analyses of sea surface temperature, sea ice, and night marine air temperature since the late nineteenth century. *J. Geophys. Res.*, 108(D14) 4407, doi:10.1029/2002JD002670.

Smith, T.M., and R.W. Reynolds, (2004). Improved extended reconstruction of SST (1854–1997). *J. Climate*, 17, 2466-2477.

Vecchi, G.A. and B.J. Soden, 2007: Global warming and the weakening of the tropical circulation. *J. Climate*, 20, 4316-4340.

Ballast Water Risk Index

K. Stelzer *, C. Brockmann

Brockmann Consult, Geesthacht, Germany – kerstin.stelzer@brockmann-consult.de,
carsten.brockmann@brockmann-consult.de

Abstract – This abstract describes a model approach developed for the assessment of the risk for ballast water exchange in the North Sea and Baltic Sea. Different input data sources have been combined in such a way that the recommendations of the Ballastwater Convention are properly taken into account. Ground based data and remote sensing data are combined in this approach.

Keywords: ballast water, ocean colour, MERIS, BEAM.

1. INTRODUCTION

The intrusion of invasive species into oceanic waters and especially coastal waters is among the four highest risks for our marine environment. The International Maritime Organisation has drafted the "International Convention for the Control and Management of Ships' Ballast Water and Sediments", an international convention to prevent the potentially devastating effects of the spread of harmful aquatic organisms carried by ships' ballast water. In the transition period until management options according to regulation D2 of the Ballast Water Convention are available, in cases where for exceptional reasons the under normal circumstances required management procedures fail and where no areas exist that meet the Ballast Water Exchange criteria according to the BWM Convention, the Convention opens the possibility to arrange suitable management options which may include designation of Ballast Water Exchange Zones. The ESA Innovator II Project Ballast Water has been initiated to test the possibilities of spaceborne remote sensing techniques for the subject of Ballast water. The goal is to develop a risk assessment for ballast water exchange in the North Sea and Baltic Sea by including information derived from satellite remote sensing data and ground based information. The project started in January 2009 and will be completed in summer 2010.

2. METHODS

Two products are developed within the project:

(1) A Risk Index that provides a map indicating the risk for the environment if Ballast Water is exchanged at a certain location. The map is daily updated taking up-to-date current data and long term mean water quality parameters into account

(2) An average Risk Index providing information about regions with trends to high or low risk index as well as stable and variable regions.

2.1 Input Data

Components or parameters included in the Risk Index Model are, for example, the distance to coast, distance to protected areas, the current field or the distribution of water quality parameters such as chlorophyll concentration, concentration of total suspended matter or water transparency. The current field is provided from the current prediction model running operationally at the BSH, while water quality parameters are derived from optical satellite data specially designed for the retrieval of ocean colour parameters. Data of the MERIS sensor have been processed with to Level2 products using the Case2Regional processor implemented in the BEAM Software. Level 3 long year averages (2006-2009) of 10 and 30 days are used to describe the situation for a respective date.

2.1 Model Approach

The Risk Index RI at a specific date and position (t0,x0,y0) consists of different components that can be regarded as Indices themselves (Fig. 1). All components are combined in a model to retrieve the non-static Risk Indices.

$RI_{(t,x,y)}$ is composed of the so called Law Index (RI_{Law}) and an Ecological Index (RI_{Eco}). The Ecological Risk Index itself depends on the assessment of the ecological situation of the exchange location as well as for the location where the ballast water may be drifted after a certain time. It depends on ship type and also on the location of Ballast Water uptake. Hence it is calculated individually and is using earth observation and daily current model data as input.

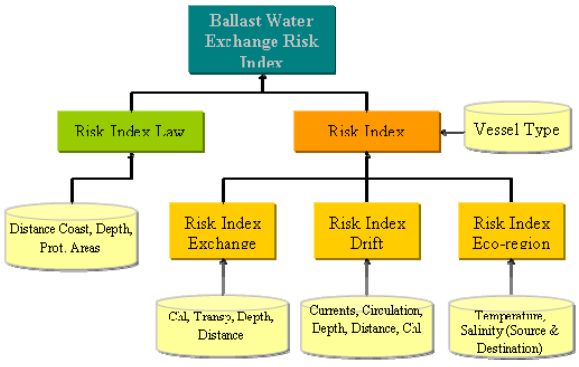

Figure 1. Risk Index Model and input products

All components integrated in the different indices are transformed to values between 0 and 1 and are combined using a weighted sum function. Further, the risk index for ballast water exchange depends on the amount of ballast water to be exchanged and the source of the ballast water.

* Corresponding author. Max-Planck-Str. 2, +49(0)4152-889307 & +49(0)4152-889333

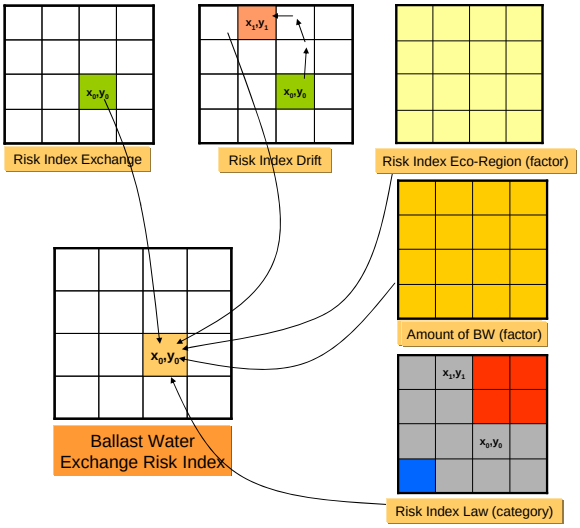

Figure 2. Model approach for the definition of the risk index on a certain position.

3. RESULTS

The final products of the project are daily risk index maps (Fig. 3) showing the risk for ballast water exchange. This depends on the ecological situation, the drift situation and the distance to coast as well as to protected areas. Each risk index depends on the source of the ballast water to be exchange. The products have been calculated for 2006 as demonstration year.

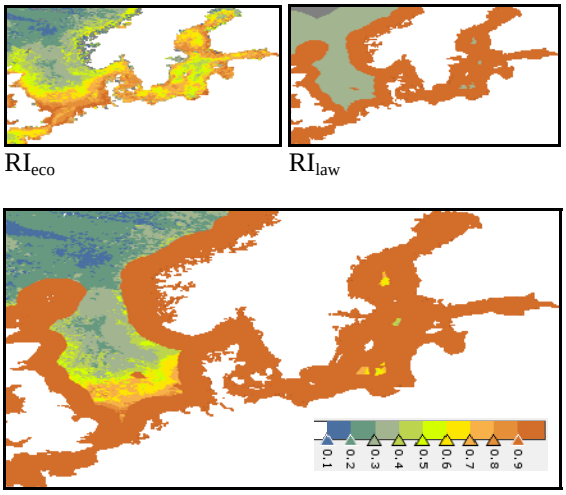

Figure 3. Combination of Risk Indices for the North Sea and Baltic Sea

Besides the flexible, ship depending risk index, an average risk index has been produced, providing information about the mean seasonal situation for risks of ballast water exchange.

4. CONCLUSION

The Risk Index provides a tool for the assessment of the current situation in the North and Baltic Sea for ballast water exchange. After the conception of the Risk Index and implementation as a prototype, the implementation of a processing chain is now planned. Trial products shall be delivered for the testing to BSH. The project will be completed in summer 2010.

ACKNOWLEDGEMENTS

The BallastWater project is funded by the European Space Agency under the DUE Innovator II programme. We would like to thank the Federal Maritime and Hydrographic Agency (BSH, Germany) for its important support for product definition, data provision and critical review.

Assimilating Space-Borne Observations in a Global Ocean Variational Assimilation System

A. Storto [a,*], S. Dobricic [a], S. Masina [a,b], P. Di Pietro [b]

[a] Centro Euro-Mediterraneo per i Cambiamenti Climatici, Bologna , Italy – andrea.storto@cmcc.it, srdjan.dobricic@cmcc.it
[b] Istituto Nazionale di Geofisica e Vulcanologia, Bologna, Italy – masina@bo.ingv.it, dipietro@bo.ingv.it

Abstract – A global ocean three-dimensional variational data assimilation system was developed with the aim of assimilating along-track altimetric observations along with *in-situ* data for studies of inter-annual ocean variability. We have computed a new global mean dynamic topography from the model long-term mean sea-surface height, adjusted by means of assimilation output statistics. Sea-level anomaly data are proved to significantly improve the subsurface temperature and salinity fields, as well as the near-surface circulation, especially in the tropical region. Finally, we present preliminary results on the impact of assimilating sea-surface temperature observations derived from space-borne microwave instruments.

Keywords: 3D-Var, reanalysis, SLA, SST.

1. INTRODUCTION

Accurate analysis of subsurface ocean fields for low-frequency ocean variability studies requires the optimal combination of *in-situ* and satellite observations with a prior knowledge of the ocean state given by an ocean model. Sea-level anomaly (SLA) observations were proved to be very beneficial not only for monitoring spatial variations of sea-level height at both regional and global scale, but also to adjust column-integrated temperature and salinity fields within ocean data assimilation systems. Nevertheless, the successful assimilation of altimetric data requires i) a good definition of the mean dynamic topography (MDT), since the data are provided as anomalies from the time-averaged sea-level height referenced to the Earth Geoid; ii) the consistency between the scales measured by altimetric satellites and those resolved by the ocean model; iii) a good definition of the SLA observational error, which may account for the uncertainty of the observation operator and mean dynamic topography, further to the instrumental accuracy and the representativeness error. We have treated in details these three issues and implemented a scheme for assimilating altimetric and in-situ data in the CMCC global three-dimensional variational data assimilation system, called OceanVar, which superseded the former reduced-rank Optimal Interpolation scheme (Bellucci *et al.*, 2008) in order to allow for contemporaneous assimilation of a huge amount of observations.

2. THE DATA ASSIMILATION SYSTEM

The data assimilation system is the global implementation of OceanVar (Dobricic and Pinardi, 2008), which is a three-dimensional variational assimilation system with a First Guess at Appropriate Time (FGAT) algorithm, i.e. computation of initial observation departures and linearization of observation operators are performed using the background field closer to observation. The analyzed fields are temperature and salinity in the native ocean model three-dimensional grid. Background-error covariances are modeled as a sequence of linear operators, which account separately for horizontal correlations, through a four-iteration application of a first-order recursive filter and for vertical covariances by means of ten-mode seasonal bivariate empirical orthogonal functions (EOFs) of temperature and salinity at full model resolution. The ocean model used is the OPA model in its configuration 8.2 (Madec *et al.*, 1998) at 2 degrees of resolution, although the resolution increases up to 0.5 degrees in correspondence of the Equator. *In-situ* data are supplied by the U.K. MetOffice Hadley Center EN3 observational dataset, and consist of subsurface measurements of temperature and salinity from bathythermographs, buoys, ship reports and Argo floats.

3. ASSIMILATION OF SLA

3.1 Data

Sea-level anomaly data were provided by AVISO after usual geophysical removals and multi-satellite cross-calibration for reducing residual orbital error and large-scale biases (Le Traon and Ogor, 1998). The data used here refer to the period from October 1992 to January 2006, where all SLA from Topex/Poseidon, ERS-1 and -2, Geosat Follow-On, Jason-1 and Envisat were assimilated. An along-track one-dimensional Lanczos filter was applied to the SLA data to filter out the signal at scales not resolved by the model.

3.2 Observation operator

Sea-level anomalies initial departures from model-equivalent values are computed from the OPA model sea-surface height, to which the mean dynamic topography is subtracted. The observation operator used in the minimization derives from the geostrophic relation, whereas the sea-level anomaly innovation (i.e. the observation minus first guess) is proportional to the column-integrated density increment from a "level of no-motion" (where horizontal velocities are assumed to vanish) upwards. The density increment is therefore spread along the water-column according to the bivariate definition of the background-error vertical covariances.

3.3 Mean Dynamic Topography

The mean dynamic topography was firstly computed from the long-term mean SSH from reanalyses produced by assimilating *in-situ* observations only. According to

* Corresponding author. Viale Aldo Moro 44, I-40127 Bologna, Italy. Tel +39513782605, Fax +39513782655.

Dobricic (2005), assimilation output statistics (i.e. observation minus first guess data) may be exploited to correct the mean dynamic topography if one assumes that the mean dynamic topography bias dominates the observation minus first guess bias. We have subsequently corrected the mean dynamic topography obtained from SSH fields. The resulting MDT (called MDTOI) shares very similar features with other gravimetry-derived MDTs.

3.4 Characterization of SLA observational error

Sea-level anomaly error variance for use in 3D-Var was decomposed in several error variance contributions: i) instrumental error variance, assumed constant and spatially homogeneous and set to 2 to 3 cm depending on the platform; ii) mean dynamic topography error variance, assumed to be spatially-varying and proportional to the SSH anomaly variance; iii) observation operator error variance, assumed to depend on the latitude only, as the accuracy of the observation operator relies on the degree of geostrophy. It was computed from the differences between the SSH increments prognosed by the ocean model and those diagnosed by means of the observation operator; iv) representativeness error variance, computed from the differences between the gridpoint averaged SLA and the raw SLA data.

3. SELECTED RESULTS

We have found that assimilating sea-level anomaly observations improves the sea-surface height fields, verified against both mapped SLA data and non-coastal tide-gauge stations, especially in the Indian and Pacific Oceans, while a smaller impact was found in the Atlantic. This is a non-trivial result as sea-surface height is not analysed but adjusted via the ocean model. With respect to TAO, PIRATA and RAMA array verification (see the upper-ocean temperature RMSE in the Tropical Pacific in Fig. 1), temperature and salinity skill scores are benefited by the SLA observations. For salinity RMSE, the use of a gravimetry-based MDT (RIOMDT) instead of our MDT increases the RMSE even with respect to the control experiment with in-situ data assimilation only. Near-surface ocean circulation, verified against the OSCAR dataset, is proved to benefit from the SLA assimilation, especially in the North-Atlantic region.

4. ASSIMILATION OF SST

As an additional spaceborne dataset, sea surface temperature derived from microwave instruments (TMI and AMSR-E) were assimilated and their preliminary impact assessed for the period 2002-2006 (provided by Remote Sensing Systems). We tested several combinations of data sources: i) optimally interpolated (OI) foundation SST (TMI+AMSR-E) with corrected diurnal overwarming (Gentemann *et al.*, 2003); ii) raw SST data from TMI and AMSR-E; iii) raw SST data from TMI and AMSR-E with corrected diurnal overwarming. It turned out, from preliminary results, that OI SST led to most consistent positive scores, also in terms of near-surface salinity adjustments.

5. CONCLUSIONS AND PERSPECTIVES

We have developed a global ocean 3D-Var data assimilation system able to successfully assimilate altimetric data together with all the in-situ observations. We found improvements to sea-surface height and temperature and salinity subsurface fields, verified against in-situ data. Furthermore, the assimilation of sea-surface temperature data derived from space-borne microwave instruments was proved to improve near-surface temperature and salinity fields. Both the results are very promising for forthcoming increase of resolution in our reanalysis system.

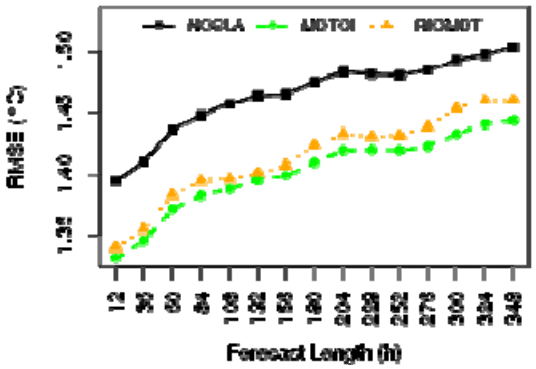

Figure 1. Root mean square error of three different experiments verified against the TAO array (Tropical Pacific) as a function of forecast length, for the period 1993-2005.

ACKNOWLEDGEMENTS

This work has been partly supported by the INGV study program "Programma Internazionale di Studi Avanzati sull'Ambiente e sul Clima", funded by the "Fondazione Cassa di Risparmio di Bologna" and partly by the European Commission-funded project MyOcean. The authors want to thank the AVISO team for the support in the use of SLA data, Dr. Simon Good (U.K. Met Office) for the support in the use of the EN3 dataset, the TAO Project Office of NOAA/PMEL for letting the authors use the TAO/RAMA/PIRATA dataset. Microwave OI SST data are produced by Remote Sensing Systems and sponsored by National Oceanographic Partnership Program (NOPP), the NASA Earth Science Physical Oceanography Program, and the NASA MEaSUREs DISCOVER Project.

REFERENCES

Bellucci, A., S. Masina, P. Di Pietro and A. Navarra (2008). "Using temperature-salinity relations in a global implementation of a multivariate data assimilation scheme". Monthly Weather Review, vol. 135, pp. 3785-3807.

Dobricic, S. (2005). "New mean dynamic topography of the Mediterranean calculated from assimilation system diagnostics". Geophysical Research Letters, vol. 32, L11606.

Dobricic, S. and N. Pinardi (2008). "An oceanographic three-dimensional assimilation scheme". Ocean Modelling, vol. 22, pp. 89-105.

Gentemann, C., C.J. Donlon, A. Stuart-Menteth and F.J. Wentz (2003). "Diurnal signals in satellite sea surface temperature measurements". Geophysical Research Letters, vol. 30, 1140-1143.

Le Traon, P.-Y. and F. Ogor (1998). "ERS 1/2 orbit improvement using Topex/Poseidon: the 2 cm challenge". Journal of Atmospheric and Oceanic Technology, vol. 9, pp. 687-698.

Madec, G., P. Delecluse, M. Imbard and C. Lévy (1998). "OPA 8.2 ocean general circulation model reference manual". Note No 11, Institut Pierre-Simon Laplace, 91 pp.

Testing the MODIS SST retrieval algorithm using M-AERI measurement and LBLRTM

M. Szczodrak*, P.J. Minnett

Rosenstiel School of Marine and Atmospheric Science, University of Miami, Miami, USA – goshka@rsmas.miami.edu, pminnett@rsmas.miami.edu

Abstract – Infrared spectra measured by the M-AERI, are used with an atmospheric radiative transfer model, LBLRTM, driven with ship-based radiosonde profiles, to create 'synthetic' MODIS brightness temperatures to which the standard SST retrieval algorithm is applied to calculate MODIS SST. These MODIS 'retrievals' are evaluated by comparison to the SST derived from M-AERI.

Keywords: MODIS, SST, M-AERI, LBLRTM.

1. INTRODUCTION

The algorithm used to retrieve SST from MODIS radiance measurements is based on statistical relationship between MODIS brightness temperatures and SST measured by surface instruments. The MODIS SST formula has the form:

$$SST = a_1 + a_2 T_{31} + a_3 (T_{31}-T_{32}) T_{rey} + a_4 (T_{31}-T_{32}) \sec(\theta) + \delta \quad (1)$$

where T_{31}, T_{32} are brightness temperatures in MODIS channels 31 and 32, T_{rey} is Reynolds SST, θ is the satellite viewing angle, δ Is a skin effect correction, and a_1 to a_4 are the coefficients obtained from analysis of match-ups with buoy measurements. The coefficients are derived separately for each month of the year for several latitude bands to capture the variability of atmospheric conditions between the sea level and the satellite. The accuracy of this approach is typically better than 0.4K but, as with any statistical approach, a question arises how good are these statistically based retrievals if they are applied to conditions that depart from the distribution represented by the retrieval coefficients. Intrusions of Saharan air layer (SAL) over the eastern Atlantic Ocean represent such a departure from average atmospheric conditions and the accuracy of SST retrieval under the SAL needs to be examined. Thus, one needs to focus on the relationship between atmospheric profiles of temperature and humidity and the difference between MODIS and surface measured SST.

2. APPROACH

Simultaneous measurements of atmospheric profiles, MODIS-retrieved SST, and surface measured SST are rare. The University of Miami Remote Sensing Group has conducted a number of research cruises during which radiosondes were launched at sea and SST was measured radiometrically from ships by the Marine-Atmosphere Emitted Radiance Interferometer (M-AERI; Minnett *et al*., 2001). Much of the radiosonde data coincide with AQUA or TERRA overpasses but can only be used in this study if no clouds are present. For example, during the 2006 cruise on the NOAA ship *Ronald H. Brown* in the eastern Topical Atlantic, which lasted 6 weeks and had 4 radiosonde launches per day, only 2 best quality MODIS SST retrievals were matched even though throughout the cruise M-AERI skin SST measurements were taken every 15 min. The dataset can be expanded if 'synthetic' MODIS SST retrievals can be generated to match the M-AERI measurements. Thus, LBLRTM (Clough, *et al.*, 1995) was employed using the atmospheric profiles measured by radiosondes and skin SST measured by M-AERI, to compute the IR radiance spectra at satellite level. Only clear sky conditions were considered. MODIS spectral response functions were then applied to the generated spectra to obtain MODIS channel 31 and 32 radiances and these in turn were converted to brightness temperatures T_{31} and $T_{32.}$ The MODIS SST algorithm (Eq. 1) was then used to compute MODIS SST. This synthetic MODIS SST can be compared to skin SST measured radiometrically by the M-AERI. Radiosonde measurements provide atmospheric profiles of temperature and water vapor; profiles of other atmospheric species used in the LBLRTM calculations were taken from standard atmospheric models corresponding to the location of the measurements. Aerosol is another factor that affects the radiative transfer in the atmosphere but is not accounted for in the LBLRTM. Neglecting such factors can introduce errors to the synthetic MODIS SST. To eliminate such cases a downwelling IR spectra were also calculated by the LBLRTM and compared with the spectra measured M-AERI. Only cases with good agreement of the downwelling spectra represent good synthetic MODIS SST.

3. TEST CASES

Figure 1 shows radiosonde profile taken on 10 July 2006 over the Atlantic Ocean. These data were used to generate both upwelling and downwelling IR spectra using LBLRTM. The downwelling spectrum is shown in Figure 2 together with the spectrum measured by M-AERI at the time of the radiosonde launch. The agreement between measured and calculated spectra is very good, with mean difference of -0.18K across the spectral range. The difference between the SST measured by M-AERI (300.18K) and the synthetic MODIS SST (300.13K) is in this case 0.05K. The MODIS retrieved SST is 299.77K. Figure 3 shows radiosonde from 6 July 2006 1510 UTC and Figure 4 show both measured and calculated spectra of downwelling IR radiation.

* Corresponding Author. 4600 Rickenbacker Causeway, Miami, FL 33149-1098, USA; tel +1 305 421 4996.

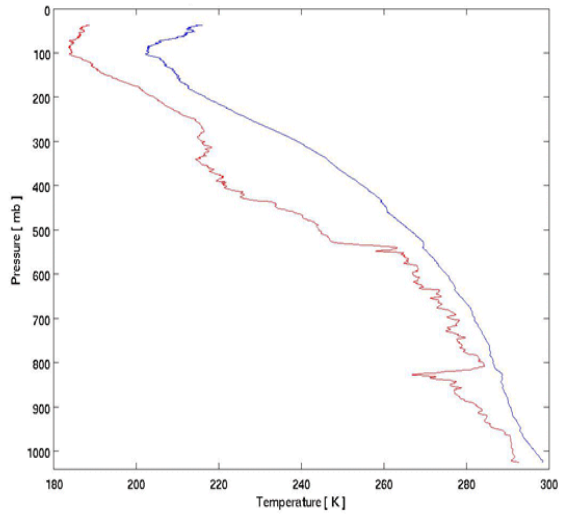

Figure 1. Atmospheric profiles taken on 10 July 2006 by radiosonde launched at 1729 UTC.

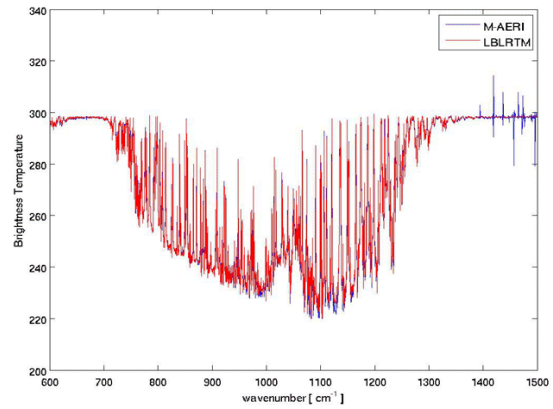

Figure2. Spectra of brightness temperature measured by M-AERI on 10 July 2006, 1729 UTC (blue) and modeled by LBLRTM for the atmospheric profile shown in Figure 1.

In the 6 July case the agreement if the downwelling spectra is poor and the measured and synthetic SST difference is 0.74K. A possible cause of the poor agreement is presence of aerosol that are not accounted for in the LBLRTM. On board Microtops measurements indicated aerosol optical depth near 0.8 on 6 July 2006 near 1500UTC whereas in previous case of 10 July the aerosol optical depths were around 0.1.

4. CONCLUSION

MODIS SST can be simulated with LBLRTM with atmospheric profiles measured by radiosondes. This synthetic MODIS can be used to test the sensitivity of the SST algorithm to atmospheric profiles of temperature and water vapor. In certain situations, e.g. aerosol laden atmospheres, the synthetic MODIS SST can be subject to significant errors and not representative of the actual MODIS SST measurement. However, M-AERI spectral measurements help detect such cases and eliminate them from comparisons. The discrepancies allow the influence of aerosols on the SST retrievals to be studied.

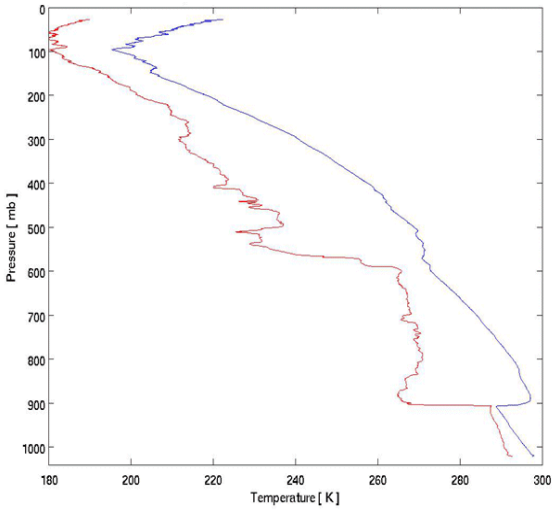

Figure 3. Atmospheric profiles taken on 6 July 2006 by radiosonde launched at 1510 UTC.

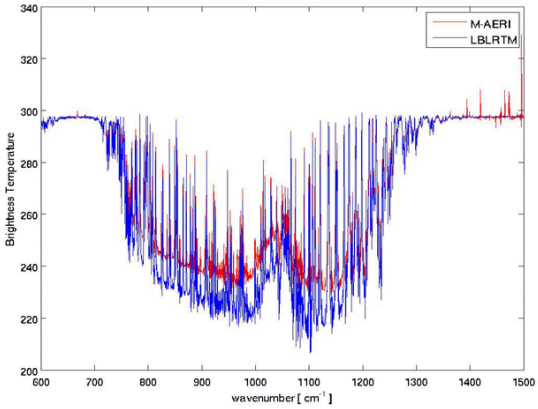

Figure4. Spectra of brightness temperature measured by M-AERI on 6 July 2006, 1510 UTC (blue) and modeled by LBLRTM for the atmospheric profile shown in Figure 3.

ACKNOWLEDGEMENTS

This work is funded by the NASA Physical Oceanography Program, Dr Eric Lindstrom, though grants NNX07AF83G and NNX08AE58G.

REFERENCES

Clough, S.A. and M.J. Iacono, 1995: Line-by-line calculations of atmospheric fluxes and cooling rates II: Application to carbon dioxide, ozone, methane, nitrous oxide, and the halocarbons. Journal of Geophysical Research, 100, 16,519-16,535.

Minnett, P. J., R. O. Knuteson, F. A. Best, B. J. Osborne, J. A. Hanafin, and O. B. Brown, 2001: The Marine-Atmospheric Emitted Radiance Interferometer (M-AERI), a high-accuracy, sea-going infrared spectroradiometer. Journal of Atmospheric and Oceanic Technology, 18, 994-1013.

Inversion of Temperature Profiles from Satellite Data in the Tropical Atlantic

Y. Tanguy *, S. Thiria, J. Brajard, S. Arnault

[a] LOCEAN / IPSL, Université Pierre et Marie Curie, Paris, France –
ytlod@locean-ipsl.upmc.fr, thiria@locean-ipsl.upmc.fr, jbrlod@locean-ipsl.upmc.fr, sa@locean-ipsl.upmc.fr

Abstract – This study deals with the problem of temperature profile inversion in the tropical and sub-tropical Atlantic. The aim is to benefit from the surface global satellite coverage to determine the vertical oceanic temperature profile using neuronal approach. Different temperature profiles available along the opportunity ship line AX-11, crossing the Atlantic basin are used to learn a self-organizing map (SOM). From this map we can next determine an approximation of the temperature structure knowing the sea surface temperature and the altimetric sea surface height.

Keywords: temperature inversion, SOM, altimetry.

1. INTRODUCTION

With the appearance of the satellites and their use in oceanography since the second part of the XXth century, numerous data of the ocean surface parameters are now available. Spatial and temporal coverage of the satellites is better than all the measurements obtained with other in situ techniques.

Simultaneously, the number of in-situ measurements has increased thanks to autonomous means such as expendable bathythermographs (XBTs) from ship opportunity, or Argo floats. But the resolution of these measurements remains less than the satellite one. In consequence, any method determining the internal structure of the ocean from surface satellite information will be useful especially for long term variability study.

First investigations have been lead using multiple linear regression method (Guinehut *et al*., 2004). More recently, neuronal approaches have been used but merely referring to ocean biogeochemistry rather than ocean thermodynamics (Niang *et al*., 2006). In our study, we investigate how such neuronal techniques can be applied to altimetry in order to get information on the oceanic thermal structure T.

2. DATA AND PROCESSING

The ARAMIS (Altimétrie sur un Rail Atlantique et Mesures In Situ) project has provided a long term survey for the thermohaline structures of the tropical Atlantic between 2002 and 2008. The AX11 World Ocean Circulation Experiment XBT merchant ship line from Europe to South America, was selected for the project (Fig. 1). The ARAMIS XBT processing is given in Tanguy *et al.* (2010).

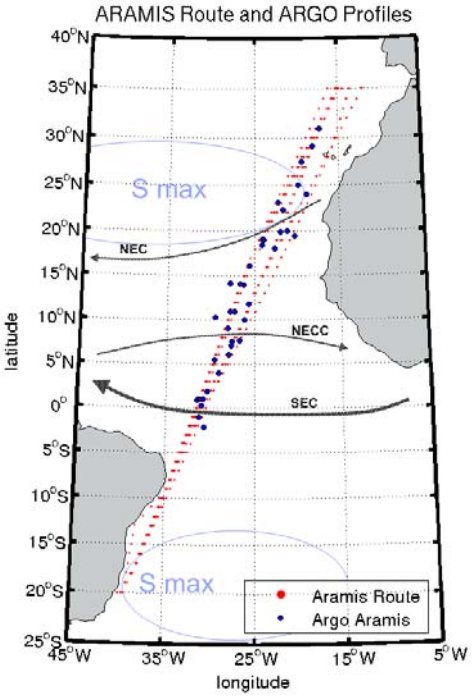

Figure 1 ARAMIS route, deployment of Argo floats and main surface currents in the region

The Coriolis data center (http://www.coriolis.eu.org/) in Brest provided all the complementary T profiles from 2002 to 2009 in a 2° longitude distance of the mean ARAMIS route. About 6 300 profiles have been retained for this study. We also used the Ssalto-Duacs 1/3°x1/3° gridded absolute dynamic topography (ADT) from the AVISO center in Toulouse (http://www.aviso.oceanobs.com/). The sea surface temperature (SST) is obtained from the Remote Sensing System site http://www.remss.com . It consists in an 1/4°x1/4° optimally interpolated product of microwave radiometers (TMI and AMSRE).

3. USE OF SELF ORGANISED MAP

3.1 Self Organizing Map presentation

The Self Organizing Map (SOM), also called self organizing feature map or Kohonen map, is one type of neuronal network. A SOM consists in components called nodes or neurons, arranged in a regular spacing in a rectangular or hexagonal grid. The map represents in a low-dimensional view a high-dimensional dataset (the input).

* Corresponding author. LOCEAN, UMR CNRS/IRD/UPMC/MNHN, 4 place Jussieu, Case 100, Tour 45-55 5ème étage, 75252 Paris cedex 05, France. Tel +33 (0)1 44 27 70 71, Fax +33 (0)1 44 27 71 59.

Each node is associated with a vector which represents a typical aspect of the dataset.

3.2 Results

To build the map, we use latitude, ADT, SST and T profile (1m resolution between 5 and 650m) informations. The obtained structure is a 14x7map.

The T profiles of the different nodes (not shown) reveal a repartition with marked thermocline on the top of the map and quasi barotropic structures on the bottom of the map. From the left to the right, we observe a decrease of the isothermal layer depth.

Figure 2 gives as example the repartition of latitude on the map, which is in good agreement with the previous remarks. Effectively, the top of this SOM corresponds to equatorial profiles where it is known that a two-layer system, thus a well-defined thermocline, prevails. The bottom is associated with the most northern laltitudes where the T is more homogeneous in the upper layers. The southern tropical profiles are on the left and the northern ones on the right, which can be explained by the non exactly north-south direction of the ARAMIS route.

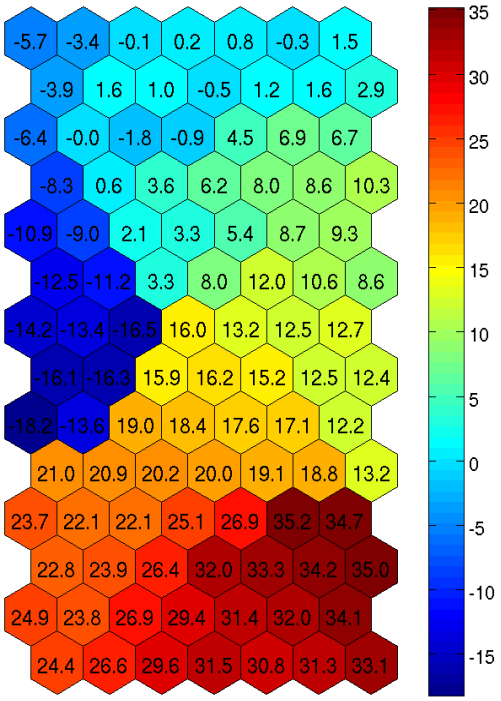

Figure 2. Repartition of latitude in the SOM.

Knowing latitude, ADT and SST, it is possible then to determine a probable corresponding node, and in consequence, a T profile. Figure 3 gives an example of "inversed" (red) compared to the "true" profile (blue). In this case, the surface data informations are enough to determine a realistic T structure.

4. CONCLUSION

The SOM method gives a good representation of the oceanic thermal structure in the tropical Atlantic and highlights the dynamic processes occurring in the region. First results on the inversion problem are encouraging. Next step will be to use this method to get a representation of the variability of T along the ARAMIS route during the "altimetry" years, thus to benefit from the accuracy and length of the TOPEX/Poséïdon/Jason1&2 series to capture the interannual variability of thermal structures in the tropical Atlantic Ocean.

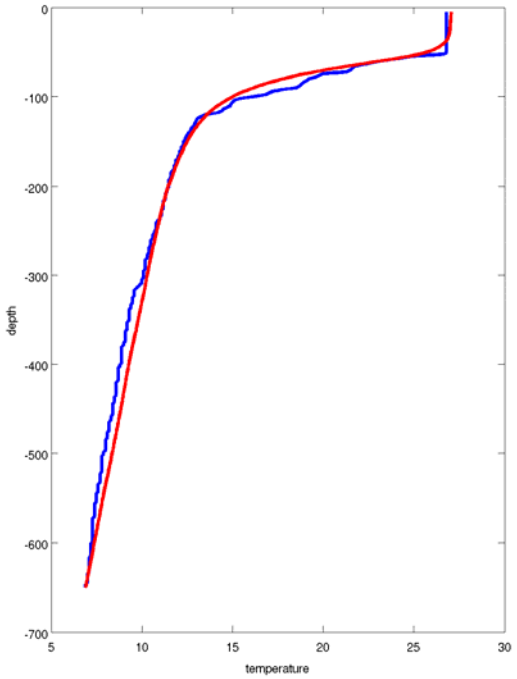

Figure 3. Example of inversed profile (red) compared to the true profile (blue) along the ARAMIS route.

ACKNOWLEDGEMENTS

The ARAMIS project is funded by the French CNES (Centre National d'Etudes Spatiales) and IRD (Institut de Recherche pour le Développement) organizations.
Support for this research was provided for Y. Tanguy by the Ministère de l'Education Nationale, de l'Enseignement Supérieur et de la Recherche; for S. Thiria by the Université Versailles-Saint Quentin; for J. Brajard by the Université Pierre et Marie Curie; for S. Arnault by IRD.

REFERENCES

Guinehut, S., P.Y. Le Traon, G. Larnicol and S. Phillips (2004), "Combining Argo and remote-sensing data to estimate the ocean three-dimensional temperature fiels – a first approach based on simulated observation", Journal of Marines systems, 46 (1-4), 85-98.

Niang A., F. Badran, C. Moulin, M. Crepon and S. Thiria (2006), "Decoding aerosol typology and optical thickness over the Mediterranean from SeaWifs images using neural methodology", Remote Sensing of Environment, 100(0): 82-94.

Tanguy, Y., S. Arnault and P. Lattes (2010). "Isothermal, mixed, and barrier layers in the subtropical and tropical Atlantic Ocean during the ARAMIS experiment". Deep-Sea Research I (2010), doi:10.1016/j.dsr.2009.12.012.

A new methodology for marine plankton communities complex investigations

Yu. Tokarev, V. Melnikov

The Kovalevsky Institute of Biology of the Southern Seas (IBSS), Sevastopol, Ukraine – y.tokarev@gmail.com

Abstract – The new methodology of the neritic zone plankton communities complex investigations was worked out and tested in the Black Sea. Simultaneous study of the species and small-scale (meters – hundreds of meters) plankton spatial structure together with the operational estimation of its functional state is the base of it. These purposes can be achieved owing to use of the new hydrobiophysical and plankton equipment complexes: "Salpa-M" and cassette planktometer MTCP. "Salpa-M" complex is intended for studying the organisms bioluminescent emission intensity in regime of the vertical sounding or horizontal towing. Interface and original software provides possibility to use channels of observing the underwater photosynthetic active radiation, chlorophyll "a" fluorescence, temperature, electroconductivity (of calculated salinity) and turbidity together with bioluminescence. Melnikov – Temnykh Cassette Planktometer is towed in step with "Salpa-M" complex by a metal rope, collecting discrete samples at the given horizon and taking layers of plankton accumulations with 5 minutes interval. Materials, demonstrating advantages of the new methodology, such as combinations of the horizontal towing and vertical sounding together with marine plankton communities structuredness and functioning investigations are showed.

Keywords: bioluminescence, plankton, spatial structure, functional state.

1. INTRODUCTION

It became obvious under comparison of scales of hydrophysical and biological processes in the ocean and existing methods of their investigation, that evident methodological problems exist in the biological oceanography in the range minutes - days (Tokarev, 2006). That is why, particularly, the small-scale (meters - hundreds of meters; minutes – days) plankton changeability, which is the fundamental base of the processes, occurring in the pelagic system, is not practically investigated.

Methods of the plankton communities functional state operative estimation are still less developed. Indication of environment physical-chemical parameters only is not enough for the direct prediction of the ecosystem possible response to the pollutants activity. That is why new, biophysical methods of marine environment biomonitoring, which provide estimation of chorological structure and investigated cenosis physiological state, are being used now for these purposes.

The discovered connection between organisms bioluminescence and their bioenergetics gives opportunity to evaluate functional state of plankton. Besides, bioluminescence can serve as a marker of spatial structure of plankton communities (Tokarev, 2006). Obtaining of the plankton community structural-functional characteristics and marine environment ecological state under combination of complex hydrological, hydrobiological and biophysical measurements in regime of multiple vertical soundings, while the vessel drifting, and in regime of the measuring complexes towing, is the main idea of the new methodology.

2. RESULTS AND DISCUSSION

Ship equipment complex includes the hydrobiophysical device "Salpa-M" (1), cassette planktometer (2), bathometers cassette (3), satellite navigation system (4) and multiple-frequency echo sounder (5) (fig.1).

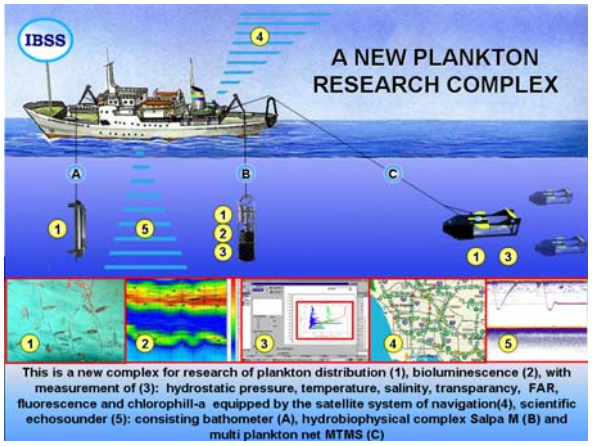

Fig.1 Ship equipment complex of IBSS of NAS of Ukraine for realization of the new plankton communities investigation methodology.

Complex "Salpa-M" is meant for studying the bioluminescence emission intensity in the upper productive water layer (0 – 200 m) in regime of the multiple vertical sounding with the velocity up to 1,2 $m \cdot s^{-1}$ and horizontal towing with the velocity up to 7 $km \cdot h^{-1}$ (fig.2). The complex size is 97x20

Fig.2 General view of the small-sized towed (left) while sounding "Salpa-M" complex.

cm with the weight of about 15 kg. The equipment complex "Salpa-M" allows to conduct uninterrupted measurements of the water environment temperature, its electroconductivity, hydrostatical pressure, turbidity, photosynthetic active radiation, chlorophyll "a" fluorescence as well as biolumi-

nescence at the horizon of the devise location (Tokarev *et.al.*, 2009).

The new plankton collector, called the Melnikov – Temnykh Cassette Planktometer (MTCP) have been worked out for studying the structure and size of the zooplankton "patches", peculiarities of its thin distribution in the hydrological and hydrochemical gradients layers, variability of the spatial structure under impact of Langmuir circulation, inner waves and other (Melnikov and Temnykh, 2009). MTCP has the sucking hole of 500 cm^2 and 10 filtering cones, made of sieve with the cell of 115 micron, the length of the device is 150 cm, the weight of it is 25 kg (fig.3).

MTCP is being towed by the metal rope with the velocity of 1,5 – 2 meters per second and permit to collect 10 samples for one catch. The device can collect the samples at any given horizon in the upper productive layer, move along the sinusoid and catch thin the vertical layers with the interval of 5 m. MTCP is equipped with the depth sensor, stream sensor, which gives data to the microcomputer.

Fig.3 MTCP cassette planktometer.

In situ working out of the complex methodic for estimation of the biological, biophysical and hydrophysical parameters of the water environment in the coastal region of Sevastopol was conducted after complex debugging and their measuring canals adjustment. The unique data about character and causes of marine zooplankton and biophysical fields "patches" distribution appearance were obtained. Materials on changing some biophysical and hydrophysical characteristics in the neritic Sevastopol zone with the help of "Salpa-M" complex in sounding regime are shown in fig.4.

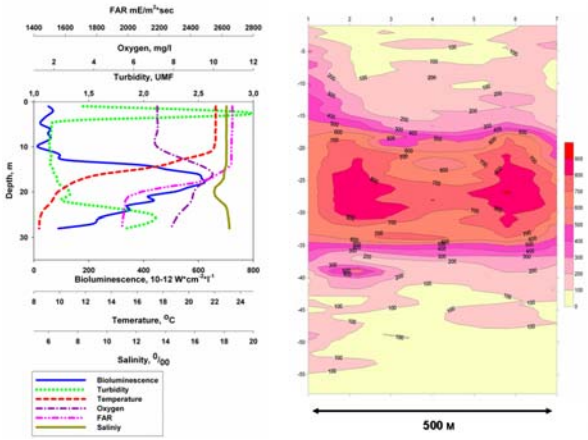

Figure 4. Example of representing the hydrological, hydrooptical and biophysical data, obtained in the Sevastopol neritic zone with the help of "Salpa-M" complex sounding.

Example of using this complex in the towing regime and character of obtaining information is in the fig.5. Request frequency of the measuring channels corresponds to 5 Hz, which allows to do the full measurements cycle in each 0,4 meters of the travel under the optimal velocity of 3,5 knots. The biological samples collection with the help of MTCP was being made simultaneously with the towing. All biophysical parameters were determined at the moment of the sample taking.

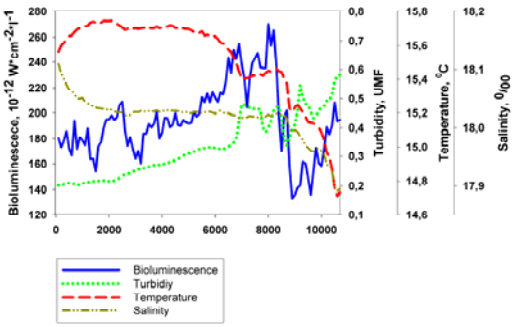

Fig.5 Graphs of the bioluminescence, turbidity, temperature and salinity change, drew according to the averaged indices under "Salpa-M" towing in the coastal waters of Sevastopol.

CONCLUSSIONS

The new methodology of the coastal ecosystems plankton communities ecological state investigation on the base of "Salpa-M" and MTCP equipment complexes and methodic of their simultaneous towing was developed and used for the first time.

The complex monitoring of the Sevastopol coastal waters is being conducted on the base of this methodic. The plankton community parameters spatial-temporal changeability on the background of Black Sea hydrological fields variability was studied. The databases for storage and analysis of the collected information were created. The unique data about character and causes of zooplankton and biophysical fields spatial distribution and materials about horizontal and vertical zooplankton "patchiness" parameters at the Sevastopol coastal waters in the different months of 2009 were obtained.

REFERENCES

Tokarev Yu.N. (2006) Basin of hydrobionts biophysical ecology. ECOSI – Hydrophysics, Sevastopol: 342 pp. (In Russian).

Tokarev Yu.N. V.I. Vasilenko, V.F. Juk. (2009) "The new hydrobiophysical complex for estimate of the coastal zone ecosystems". In: The modern methods and device of the oceanology investigations / Proceedings of the XI International Scientific-Technical Conference. Part 3. 25 – 27 November 2009, Moscow: pp. C. 23-27. (in Russian).

Melnikov V.V., A.V. Temnykh. (2009) "The cassette planktonometer". In: The modern methods and device of the oceanology investigations / Proceedings of the XI International Scientific-Technical Conference. Part 3. 25 – 27 November 2009, Moscow: pp. C. 27-31. (in Russian).

Parameter Estimation for Peaky Altimetric Waveforms

J.-Y. Tourneret [a,*], J. Severini [a], C. Mailhes [a], P. Thibaut [b]

[a] University of Toulouse, ENSEEIHT-IRIT, Toulouse, France – { jyt,jerome.severini,corinne.mailhes }@enseeiht.fr
[b] Collecte Localisation Satellite (CLS), Ramonville Saint-Agne, France – pierre.thibaut@cls.fr

Abstract – A simple parametric model was recently introduced to model peaky altimetric waveforms. This model assumes that the received altimetric waveform is the sum of a Brown echo and Gaussian peaks. This paper derives the maximum likelihood estimator for the parameters of this Brown + peak model. Simulation results conducted on synthetic and real altimetric waveforms allow one to appreciate the performance of the proposed estimator.

Keywords: altimetry, maximum likelihood, Brown model.

1. NTRODUCTION

The contamination of ocean echoes by land returns or by the summation of backscattered signals coming from separate reflective surfaces considerably damages availability and quality of altimeter waveforms. A great effort is devoted to process these waveforms in order to move the altimetric measurements closer to the coast. In the frame of the CNES/ PISTACH project aiming at improving coastal altimeter products, waveforms are classified according to their geometrical shapes (Thibaut and Poisson, 2008). The goal of this classification is to isolate echoes having similar geometrical characteristics in order to estimate the corresponding altimeter parameters thanks to dedicated retracking algorithms. In this paper, we study an innovative retracking algorithm based on maximum likelihood estimation for waveforms corrupted by the presence of peaks on their trailing edge. The proposed algorithm is based on a mathematical model recently introduced by Gómez-Enri et al. (2009).

2. PROBLEM FORMULATION

A simplified formulation of Brown's model assumes that the received altimeter waveform (after removing the thermal noise that can be estimated from the first data samples) is parameterized by three parameters P_u, τ and σ_c via the following equation

$$x_k = \frac{P_u}{2}\left[1+erf\left(\frac{kT_s-\tau-\alpha\sigma_c^2}{\sqrt{2}\sigma_c}\right)\right]\exp\left[-\alpha\left(kT_s-\tau-\frac{\alpha\sigma_c^2}{2}\right)\right] \quad (1)$$

where $x_k=x(kT_s)$ is the kth data sample of the received altimetric signal, T_s is the sampling period, $erf(t)=\left(2/\sqrt{\pi}\right)\int_0^t e^{-z^2}dz$ stands for the Gaussian error function and α is a known parameter depending on the satellite. The parameters P_u and τ appearing in (1) are referred to as amplitude and epoch whereas the third parameter σ_c is related to the significant wave height *SWH* as follows:

$$\sigma_c^2 = \sigma_p^2 + \left(\frac{SWH}{2c}\right)^2$$

where c denotes the light speed and σ_p^2 is a known parameter depending on the altimeter point target response. The Brown model has been derived for modeling altimeter echoes associated to oceanic surfaces. However, this model is not appropriate to altimetric waveforms backscattered from non-oceanic surfaces such as ice and land or from coastal areas (Gómez-Enri et al. 2009, Thibaut and Poisson, 2008). Indeed, over such surfaces, altimetric echoes can show some peaks in their trailing edge due to backscattering returns from non water areas. A simple mathematical model for altimetric waveforms corrupted by peaks was recently introduced in Gómez-Enri et al. (2009). This model assumes that an altimetric waveform denoted as $\tilde{x}_k$ can be represented as the superposition of a Brown echo x_k and a sum of Gaussian peaks p_k

$$\tilde{x}_k = x_k + p_k$$

where x_k has been defined in (1),

$$p_k = \sum_{i=1}^{q} A_i \exp\left[-\frac{(kT_s-t_i)^2}{2\sigma_i^2}\right] \quad (2)$$

and q is the number of peaks. Any peak defined in (2) is parameterized by an amplitude A_i, a location parameter t_i and a width related to the variance σ_i^2 with $i=1,\ldots,q$. As a consequence, the unknown parameters for the q peaks are gathered in $\mathbf{A} = (A_1,\ldots,A_q)$, $\mathbf{t} = (t_1,\ldots,t_q)$ and $\boldsymbol{\sigma}^2 = (\sigma_1^2,\ldots,\sigma_q^2)$. A particular attention will be devoted to the case of a single peak (i.e., $q = 1$) in this summary. However, the case of multiple peaks will be addressed in the final paper. Note that the migration of peaks along the trailing edge as in Gómez-Enri et al. (2009) is not considered here. Altimeter data are corrupted by multiplicative speckle noise. In order to reduce the influence of this noise affecting each individual echo, a sequence of L consecutive echoes are averaged on-board. Assuming pulse-to-pulse statistical independence (Walsh, 1982), the resulting speckle noise denoted as n_k is distributed according to a gamma distribution whose shape and scale parameters equal the number of looks L (i.e., the number of incoherent summations of consecutive echoes). When using the Brown + peak model defined previously, an observed altimetric waveform can be expressed as

$$\tilde{y}_k = \tilde{x}_k n_k, \quad k = 1,\ldots,N. \quad (3)$$

The problem addressed in this paper is the joint estimation of the Brown model parameter vector $\boldsymbol{\theta}_B = (P_u, \tau, \sigma_c)^T$ and the peak parameter vector $\boldsymbol{\theta}_p = (\mathbf{A}, \mathbf{t}, \boldsymbol{\sigma}^2)^T$ using the data samples $\tilde{\mathbf{y}} = (\tilde{y}_1,\ldots,\tilde{y}_N)^T$. We propose to extend the

* Corresponding Author. 2 rue Camichel, BP 7122, 31071 Toulouse cedex 7, France; tel: 0561588477, fax: 0561588306.

maximum likelihood (ML) estimation strategy initially derived by Dumont (1985) for estimating the parameters of the Brown model to the Brown + peak model defined by Gómez-Enri et al. (2009).

3. MAXIMUM LIKELIHOOD ESTIMATION

Since the proposed estimation strategy strongly relies on the ML estimator (MLE) derived in Dumont (1985), this section first recalls briefly some principles of this estimator. The extension to the Brown + peak model is then investigated.

3.1 Maximum Likelihood for Brown's Model

The MLE of $\boldsymbol{\theta}_B$ is classically obtained by differentiating the log-likelihood of the observed data with respect to the unknown parameters P_u, τ and σ_c Kay (1993). Due to the absence of closed-form expressions for the MLE of $\boldsymbol{\theta}_B$, iterative algorithms searching for local maxima of the log-likelihood have been proposed by Dumont (1985). More precisely, the following recursion referred to as the quasi-Newton recursion is currently used for estimating the parameters of the Brown model

$$\boldsymbol{\theta}_B(n+1) = \boldsymbol{\theta}_B(n) - \mu_n \left(\mathbf{B}\mathbf{B}^T\right)^{-1}\mathbf{B}\mathbf{D} \qquad (8)$$

where $\mathbf{B}$ is a 3xN matrix whose elements are $B_{ik} = \frac{1}{x_k}\frac{\partial x_k}{\partial \theta_{B,i}}$ and $\mathbf{D}$ is an N x 1 vector whose elements are $D_k = 1-(y_k / x_k)$ with i = 1,…,3 and k = 1,…,N. This recursion has been implemented in all the current retracking algorithms used in Jason/Envisat ground processing chains.

3.2 Maximum Likelihood Estimation for Brown + Peak Model

We will show in the full paper that the MLE of $\boldsymbol{\theta} = \left(\boldsymbol{\theta}_B^T, \boldsymbol{\theta}_p^T\right)^T$ can be determined by using the following quasi-Newton recursion

$$\boldsymbol{\theta}(n+1) = \boldsymbol{\theta}(n) - \mu_n \begin{pmatrix} \tilde{\mathbf{B}}\tilde{\mathbf{B}}^T & \tilde{\mathbf{B}}\tilde{\mathbf{P}}^T \\ \tilde{\mathbf{P}}\tilde{\mathbf{B}}^T & \tilde{\mathbf{P}}\tilde{\mathbf{P}}^T \end{pmatrix}^{-1} \begin{pmatrix} \tilde{\mathbf{B}} \\ \tilde{\mathbf{P}} \end{pmatrix} \mathbf{D}$$

where $\tilde{\mathbf{B}}$ is a 3xN matrix whose elements are $\tilde{B}_{ik} = \frac{1}{\tilde{x}_k}\frac{\partial x_k}{\partial \theta_{B,i}}$ with i = 1,…,3, k = 1,…,N and $\tilde{\mathbf{P}}$ is a ($3q$)xN matrix whose elements are $\tilde{P}_{ik} = \frac{1}{\tilde{x}_k}\frac{\partial p_k}{\partial \theta_{p,i}}$ with i = 1,…,3q and k = 1,…,N.

4. SIMULATION RESULTS

Many simulations have been conducted to validate the proposed MLE for the Brown + peak model. The first example considers the sum of a Brown waveform with parameters P_u=*60*, τ=32 and *SWH*=2 (σ_p^2 has been adjusted to its nominal value used for Jason-2 satellite) and a Gaussian peak defined by $\boldsymbol{\theta}_p = (A_1, t_1, \sigma_1^2) = (90,60,25)$. The resulting synthetic signal has been contaminated by a multiplicative speckle noise with *L=100* looks. The proposed quasi-Newton recursion (referred to as PEAK-MLE) has been tested on the resulting echo and has been compared with the usual MLE which ignores the presence of the Gaussian peak. The results depicted in Fig. 1 (top) show that the proposed PEAK-MLE allows one to estimate the parameters of the Brown model as well as the peak parameters, while the classical MLE obviously fails to correctly estimate θ_B. The second example considers a real Jason-2 waveform collected close to Mariana island, between the Philippines and Hawaii. As shown in Fig. 1 (bottom), the proposed estimator allows one to capture the joint characteristics of the Brown waveform and the Gaussian peak for this echo.

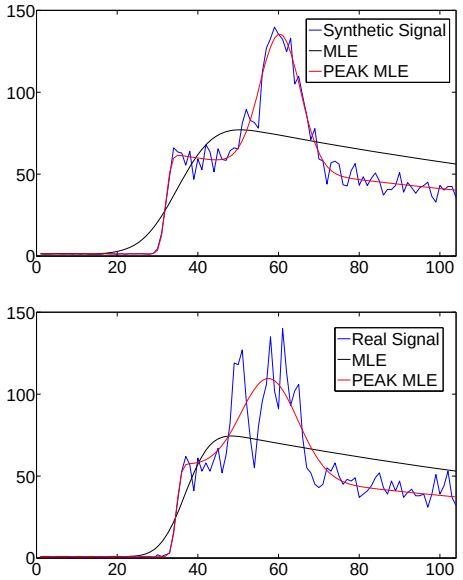

Figure 1. Synthetic Brown + peak signal and its estimations using MLE and PEAK-MLE (top); real JASON-2 waveform and its estimations using MLE and PEAK-MLE (bottom).

5. CONCLUSION

We studied an estimation strategy based on the maximum likelihood principle for a Brown + peak model. The model is appropriate for altimetric signals resulting from the summation of a Brown echo and Gaussian peaks. Next, we shall study the performance of the proposed estimator in terms of mean square error for a database of peaky altimetric signals. This database has been obtained from a classifier studied within the PISTACH project (Thibaut and Poisson, 2008). The generalization of the proposed algorithm to multiple Gaussian peaks and to other shapes of peaks is currently under investigation.

REFERENCES

Dumont, J.P. (1985). *Estimation optimale des paramètres altimétriques des signaux radar Poséidon*. PhD thesis, Institut National Polytechnique (INP), Toulouse, France.

Gómez-Enri, J., S. Vignudelli, G.D. Quartly, C.P. Gommenginger, P. Cipollini, P.G. Challenor and J. Benveniste (2009). Modeling ENVISAT RA-2 waveforms in the coastal zone: case-study of calm water contamination. *3rd Coastal Altimetry Workshop*, Frascati (I).

Kay S.M. (993). *Fundamentals of Statistical Signal Processing: Estimation Theory*. Prentice Hall, Englewood Cliffs (NJ).

P. Thibaut, P. and J.C. Poisson (2008). Waveform Processing in PISTACH project. *2nd Coastal Altimetry Workshop*, Pisa (I).

E.J. Walsh, E.J. (1982). Pulse-to-pulse correlation in satellite radar altimeters. *Radio Science*, 17(4):786-800.

Adaptive re-tracking of Jason-1 altimeter data for coastal zone of the Gorky reservoir

Yu. Troitskaya [a] , G. Rybushkina [a,]*, I. Soustova [a], S.A. Lebedev [b], L. Filina [c], A. Panyutin [c]

[a] Institute of Applied Physics RAS, Nizhny Novgorod, Russia – ryb@appl.sci-nnov.ru
[b] Geophysical Center of RAS, Moscow, Russia – s.lebedev@gcras.ru
[c] Hydrometeorology and Environmental Monitoring Center in Nizhny Novgorod, Russia

Abstract – The problem of coastal altimetry is investigated on the base of the Gorky reservoir of the Volga River. A method of adaptive re-tracking taking into account geographical features of the Gorky reservoir is proposed. A step-by step procedure for complex coastal areas is discussed.

Keywords: coastal, altimetry, re-tracking, inland waters.

1. INTRODUCTION

Altimetry data processing developed for the open ocean may be inapplicable for the case of coastal and inland waters. The problems of inland water data processing are very similar to those arising in the coastal zone of the ocean from contamination of the received signal by reflection from the land. This effect is very strong in the Gorky reservoir with the maximal width of 14 km with steep 10-20 m banks. Under these conditions few telemetric impulses fit the validity criteria, which causes a severe loss of data. As a result the Gorky reservoir is not included in the data bases by LEGOS and U.S. Department of Agriculture's Foreign Agricultural Service. This talk is about the experience of retrieving water level in the Gorky reservoir by an adaptive re-tracking algorithm, which dramatically increases the number of data involved in monitoring. General principles of the considered local re-tracking algorithm may be useful for coastal altimetry.

2. GDR DATA WATER LEVEL RESULTS

According to NASA/CNES data (see fig. 1) the water area of the Gorky Reservoir and the Volga River is intersected by 2 tracks (55-th and 142-nd) of altimeter satellites T/P and Jason-1,2 and some tracks of altimeter satellites ERS-1, ERS-2, ENVISAT, GEOSAT, and GFO. We used data for the 142-nd track of Jason-1 (before maneuver), which intersects the Gorky Reservoir in its northern part (figure 1) with the track length within the reservoir being about 15 km. There is a possibility to compare altimetry data of this track with the measurements from the ground station Yur'evets (a small town on the right bank of the Gorky reservoir). At the first stage, Geophysical Data Records (GDR) of Jason-1 (J1) satellite were processed. All altimetry data available along track 20Hz Jason-1 were used and all the required corrections were calculated. The wet and "dry" troposphere correction was calculated by meteorological data (atmospheric pressure and air humidity) from the nearest weather station. DORIS ionosphere correction was used for correcting altimetry measurements of reservoir surface height.

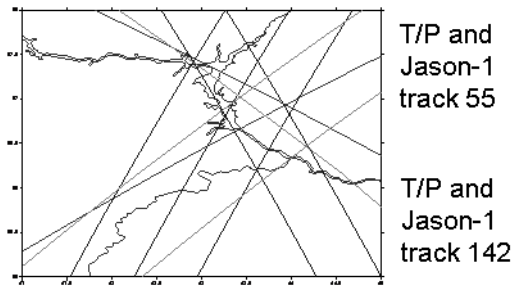

Figure 1. T/P, Jason-1, ERS-1/2, GEOSAT and GFO-1 tracks over the Gorky reservoir water area.

An analogous procedure was used earlier for determining the hydrological regime of large rivers in South America, Africa and Siberia (see, e.g., Campos et al., 2001; Birkett et al., 2002; Kouraev et al., 2004), as well as for assessing water level in the lower reaches of the Volga river (Lebedev and Kostianoy, 2005). Comparison with data of hydro gauging stations verified efficiency of this procedure for large inland water areas. The results of data processing following the described procedure were used to plot water levels in the Gorky Reservoir with a resolution of 10 days for the period from 2002 to 2007 (green squares in figure 2). The results of calculations were compared with the measurement data obtained at the hydro gauging stations of the State observation network. This comparison clearly shows the shortcomings of the ocean re-tracking algorithm in application to the Gorky reservoir, namely a severe loss of data and substantial errors.

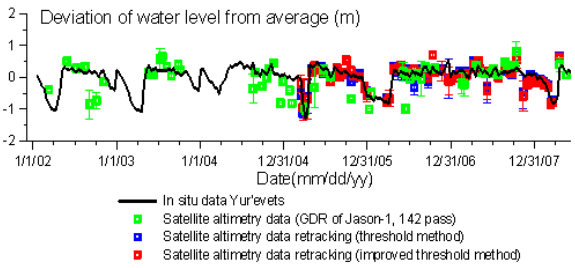

Figure 2. Water level dynamics in the Gorky reservoir.

3. ADAPTIVE RE-TRACKING SGDR RESULTS

Significant scatter of satellite data may evidently be explained by the shortcomings of direct extension of the algorithms of water level calculation developed for large water basins (seas and oceans) to medium area basins in

* Corresponding author. 46 Ulyanov str., 603950, N.Novgorod, Russia, tel.: (+7)8314160670, fax: (+7)8314362792 .

which the spot of altimeter pulse dispersion substantially falls to the share of land. Consequently, we analyzed the wave forms of the reflected pulses received by altimeter antenna. The needed data were taken from the SGDR data base of Jason-1 satellite. Special software was developed for analysis of the shape of an averaged reflected pulse for high spatial resolution points with the averaging interval of 0.05 s. The software enables tracing changes in pulse shape as the averaging point is moving along the satellite track. Examples of varying wave forms for the point moving in the area marked by the white circle in the map are presented in figure 3. The wave forms shown in the lower figure on the left, represent the received reflected power as a function of time (the number of altimeter gate is laid off along the horizontal axis, 1 gate corresponds to the time interval dtg=3.125 ns; and the power of the reflected signal is laid off along the vertical axis). Analysis of these wave forms suggests that the scatter in the water level data may be caused by drawbacks of the standard algorithm of computations in which the 32-nd gate of the plots is regarded to be the arrival time of reflected signal. However, one can see from the plot presented above that the reflected signal may also arrive both before and after the mentioned gate, whereas the error of 1 gate leads to the error in water level measurements of $dtg*c_{light}/2$. This means that special algorithms must be developed for medium size basins that would take into consideration all needed geographic features of the basin.

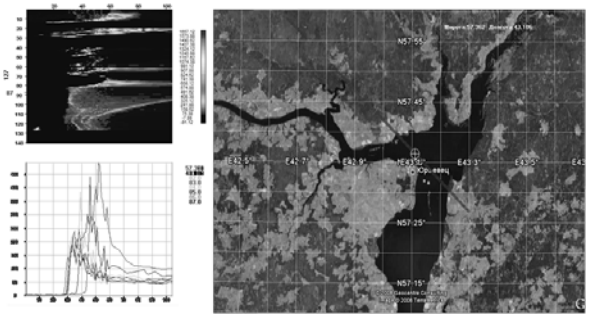

Figure 3. Copy of the software monitor with examples of reflected wave forms from SGDR data base of Jason-1.

Towards this end, we considered a geographic model of the Gorky reservoir area surrounding the 142-nd satellite track (left part of figure 4) and calculated reflected wave forms for this model (right part of the figure 4.) The calculations were done using the theoretical model proposed in the work by Brown (1977) for the case of nadir antenna radiation (downright). Based on the pattern of calculated wave forms we set the validity criteria for wave forms in this local algorithm: we restricted our consideration to the longitudes ranging from 43,14 E to 43.22 E, and omitted deviations of water level from the average value exceeding ±2m. For the valid wave forms we used the following local re-tracking algorithms appropriate for the Gorky reservoir for track 142 including 2 steps. At the first step we estimated a tracking point determined by a definite threshold. The second step is refinement of the estimates: 4 points in the neighbourhood of the threshold are fitted by the error function, taking into account the analytical results. The results of re-tracking wave forms from SGDR are shown by red squares in figure 2. One can see that the number of valid points increased significantly compared with ocean-1 processing. We investigated correlation of altimetry data and the ground station measurements. The ocean-1 re-tracking algorithm used in GDR gives the correlation coefficient of 0.33 with the ground data, while local re-tracking algorithm provides 0.8 correlation coefficient.

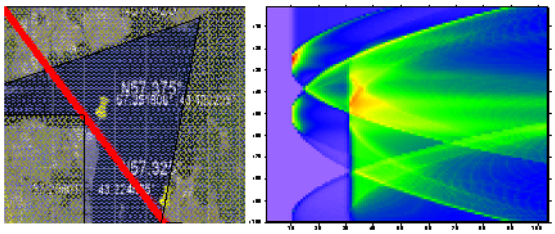

Figure 4. Model of the Gorky reservoir area near 142-nd track of Jason-1- left and wave form diagram -right.

A similar procedure can be applied for constructing local adaptive re-tracking algorithms for retrieving water level for complex area (land, coastal zone, inland waters, etc) from satellite altimetry. The surface is divided into fractions with constant parameters. For example, a coastal zone can be represented as 3 strips (sea, land, intermediate area with different SWH). Contributions from the fractions are calculated and summed analytically, then based on wave form modelling validity criteria are imposed, and step-by-step improving re-tracking is done.

4. CONCLUSION

The local adaptive re-tracking algorithm enables retrieving water level even in the case of a very complex reflecting surface. Application of the algorithm increases significantly the number of valid data and improves dramatically accuracy of the water level retrieving from the altimetry data. General principles of the adaptive re-tracking algorithm based on calculations of the wave form taking into account statistical inhomogeneity of the reflecting surface adjusted to a certain geographic region allow constructing a step-by-step strategy for improving water-level estimations for complex areas (land, coastal zone, inland waters, etc) .

ACKNOWLEDGEMENTS

The authors thank Galina Balandina for help in numerical calculations. The work was done with financial support from the Russian Foundation for Basic Research (project No. 08-05-97016-r_povolzhye_a).

REFERENCES

Birkett C.M., et al (2002) “Surface water dynamics in the Amazon Basin: Application of satellite radar altimetry,” J. Geophys. Res., vol. 107. no. D20, pp. 8059.

Brown, G. (1977) “The average impulse response of a rough surface and its applications,” Antennas and Propagation, IEEE Trans., vol.25, 1, pp. 67 – 74.

Campos I.O., et al (2001) “Temporal variations of river basin waters from Topex/Poseidon satellite altimetry. Application to the Amazon basin,” Earth and Planetary Sciences, vol. 333, no. 10, pp. 633-643.

Kouraev A.V., et al (2004) “Ob’ river discharge from TOPEX/Poseidon satellite altimetry (1992-2002),” Remote Sensing of Environment, vol. 93, pp. 238-245.

Lebedev S.A., Kostianoy A.G. (2005) “Satellite Altimetry of the Caspian Sea,” “MORE” Publ., Intern. Inst. of the Ocean, Moscow, 366pp. [in Russian].

Decennial Variability of Global Seawifs-Derived Marine Particles Backscattering Coefficient and Spectral Dependency.

V. Vantrepotte [a] *, H. Loisel [a], F. Mélin [b], L. Duforêt [a] and D. Dessailly [a]

[a] LOG, CNRS-UMR 8187, Wimereux, France – Vincent.Vantrepotte@univ-littoral.fr
[b] European Commission - Joint Research Centre, IES, Global Environment Monitoring Unit TP272, Ispra 21027, Italy

Abstract – This work illustrates the temporal variability detected in a SeaWiFS-derived 10-year time series of marine particles backscattering coefficient at 490 nm, $b_{bp}(490)$, an indicator of the particulate organic carbon concentration, and backscattering spectral dependency γ, a qualitative indicator of the relative proportion of smaller- and larger-sized particles. The importance of seasonality in the $b_{bp}(490)$ and γ signals was assessed using the Census X-11 time series decomposition method. In addition, the presence of significant monotonic changes in the data was estimated using non-parametric Kendall statistics. Variations in $b_{bp}(490)$ and γ temporal patterns are discussed and compared to those observed for the chlorophyll data, emphasizing variations in the composition and controlling factors of the particulate matter pool.

Keywords: backscattering, particulate matter, size distribution, SeaWiFS, time series, Census X-11.

1. INTRODUCTION

The suspended particulate matter pool in the open ocean is comprises phytoplankton, heterotrophic organisms, viruses and organic detritus, the relative proportion and size distribution of which are susceptible to vary widely in space and time, with biogeochemical conditions and physical forcing (Loisel *et al.*, 2002; Loisel *et al.*, 2006). Knowledge on the particulate matter space-time dynamics in the global ocean, and in particular knowledge of particle size distribution (PSD), conditioning particle physical transport and bio-geo-chemical interactions, is still very scarce, but represents a fundamental information for understanding marine ecology and bio-geo-chemistry. Particles backscattering coefficient at 490 nm ($b_{bp}(490)$) retrieved from satellite observation (IOCCG 2006) may be used to characterize the spatio-temporal variability of particulate organic carbon (POC) in the absence of mineral particles (Loisel *et al.*, 2002) providing relevant information on the biogeochemical status of surface waters. Moreover, recent studies have shown the potential of using satellite derived backscattering coefficient spectral slope (γ) for estimating qualitatively the relative proportion between small-sized and larger particles in the surface of the ocean (Loisel *et al.*, 2006; Kostadinov et al, 2009). The present study aims to characterize, using appropriate statistical techniques, the temporal variability of both γ and $b_{bp}(490)$ at global scale from the 10-year time series of monthly SeaWiFS data. Specifically, variations in the importance of seasonality as well as in the presence of significant decennial trends are presented and compared to the patterns detected for the phytoplankton chlorophyll *a* (chl*a*) concentration.

2. MATERIAL AND METHODS

2.1 Ocean color data

The satellite products are the monthly backscattering coefficient of particles at 490 nm ($b_{bp}(490)$) (Loisel and Stramski, 2000) and the spectral slope of particles backscattering spectrum (γ, see Loisel *et al.*, 2006 for the detailed method) in the upper layer of the ocean derived from the SeaWiFS sensor (reprocessing 2009.1). The latter products are mapped on 5'-resolution cylindrical equidistant grids (9.26 km at the equator) for the period October 1997 to November 2007 (10 years).

2.2 Statistical analyses

The analysis of the time series of b_{bp} and γ had to consider the spatial variability in the temporal coverage of the ocean color data. A pre-treatment was applied to b_{bp} and γ data in order to eliminate gaps in the series. This led essentially to the consideration of shortened time series (of variable period, p; see the detailed method in Vantrepotte and Mélin, 2009, 2010). A time series X(t) (here the monthly series of γ and $b_{bp}(490)$) can be decomposed as X(t) = S(t)+T(t)+I(t), where S, T and I represent, respectively, the seasonal, the trend-cycle, and the irregular (or residual) component. In practice, this decomposition has been performed by using the Census X-11 method which is based on an iterative bandpass filter algorithm that explicitly allows the consideration of inter-annual variations in the seasonal cycle shape (Pezzuli *et al.*, 2005; Vantrepotte and Mélin, 2009). The relative part of variance of the initial series associated with the component S(t) has then been estimated on a grid-point basis in order to indentify the main spatial patterns of temporal variability. In addition, the presence of significant monotonic change in the data over the period investigated has been assessed using the seasonal Kendall test applied on X(t). The amplitude of the observed changes (in $\%.yr^{-1}$) has been quantified using the Sen's slope estimator.

3. RESULTS AND DISCUSSION

Figures 1a and 1b present the spatial distribution of the relative contribution of the X-11 seasonal component S(t) (%) to the variance of $b_{bp}(490)$ and γ signals, respectively. The same parameter computed for SeaWiFS-derived chl*a* over the same period of time is recalled for completeness from Vantrepotte & Mélin (2009) in Figure 1c. Observed spatial patterns differ between chl*a*, γ and $b_{bp}(490)$. The high S(t) contributions detected in two subtropical bands for chl*a* data (Vantrepotte & Mélin, 2009; Yoder *et al.*, 2003) are only partially retrieved for γ, while high contributions of S(t) for $b_{bp}(490)$ (> 50%) are mostly found for latitudes higher than 45° in both hemispheres (Loisel *et al.*, 2002).

* Corresponding Author. 32 av. Foch, 62930 Wimereux, France; tel +33-321996414, fax +33-321996401.

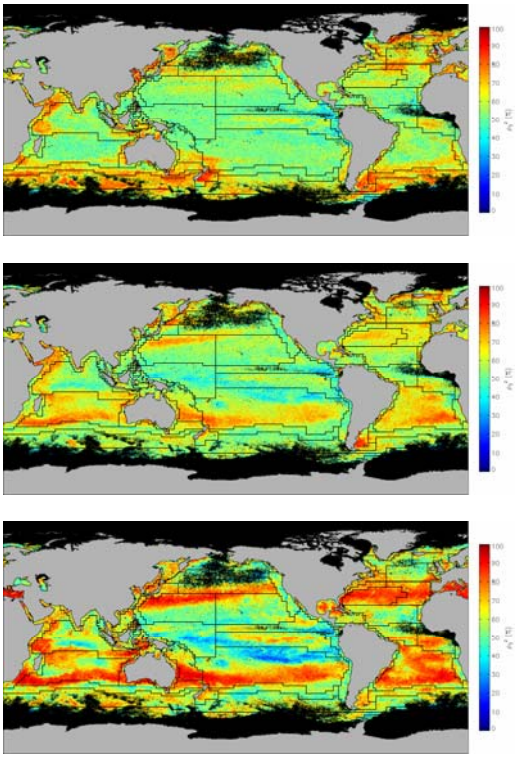

Figure 1. Relative contribution of S(t) (%) to the variance of (upper panel) $b_{bp}(490)$, (middle panel) γ and (lower panel) chl*a* detected from SeaWiFS 10-year monthly time series.

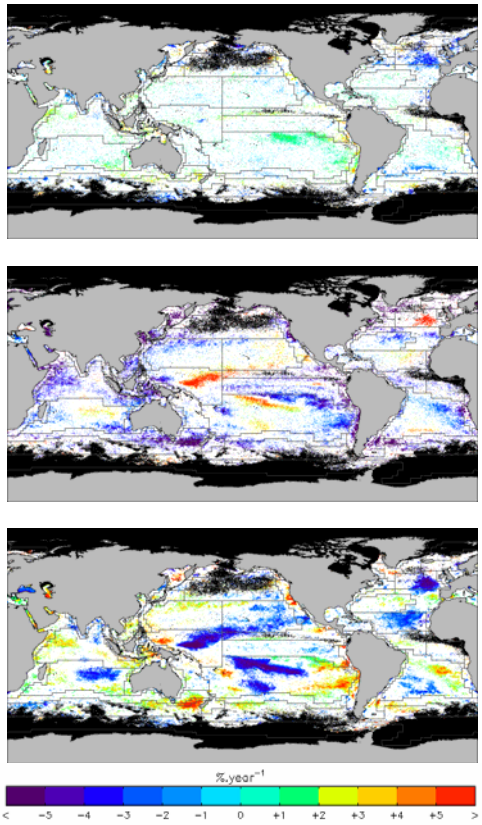

Figure 2. Significant monotonic trends ($p<0.05$) in (upper panel) $b_{bp}(490)$, (middle panel) γ and (lower panel) chl*a* (see Vantrepotte & Mélin, 2009) over the 10 years of SeaWiFS data (in % yr^{-1}).

The S(t) contributions for chl*a* are generally greater than those found for γ and $b_{bp}(490)$ (Vantrepotte & Mélin, 2009). This might be related to stronger sub-annual variations and/or to the occurrence of seasonal fluctuations of lower amplitude for the 2 latter parameters. Differences between the temporal evolution of γ, $b_{bp}(490)$ and of chl*a* are also evident when examining distribution and amplitude of the significant monotonic trends, which can be detected over the 10 years of SeaWiFS data (Figure 2a, 2b and 2c). For $b_{bp}(490)$, significant changes of small amplitude are visible in two regions: the north Atlantic and the tropical southern Pacific. Interestingly, other regions where a significant and strong change in chl*a* has been emphasized (Vantrepotte & Mélin, 2009, Figure 2c) are not associated with a significant change in $b_{bp}(490)$. Conversely, significant decennial evolution in γ are found in larger regions of the ocean and are generally of great amplitude (<-5 or > +5 %.yr^{-1}). Globally, an inverse relationship is observed between the trends in γ and chl*a* even though this feature is not systematic. This tends to indicate that a diminution of the phytoplankton biomass is accompanied by a decrease of the mean particle size as already noted by Loisel *et al.* (2006).

4. CONCLUSION

Our results demonstrate the time variability heterogeneities of γ, $b_{bp}(490)$ and chl*a* in terms of seasonal fluctuations and decadal trends. These can be related to variations in particulate matter assemblages, phytoplankton communities (Loisel et al, 2006) and changes in environmental forcing.

ACKNOWLEDGEMENTS

The authors thank Ocean Biology Processing Group of NASA, for the SeaWiFS data, and *Agence Nationale de la Recherche*, for financial support of the GLOBPHY project.

REFERENCES

IOCCG Report 5 (2006). "Remote Sensing of Inherent Optical Properties: Fundamentals, Tests of Algorithms, and Applications". Ed. by ZhongPing Lee, pp. 126.

Kostadinov, T. S., D. A. Siegel and S. Maritorena (2009). "Retrieval of the particle size distribution from satellite ocean color observations", Journal Geophysical Research, 114, C09015, doi:10.1029/2009JC005303.

Loisel, H., and D. Stramski (2000). "Estimation of the inherent optical properties of natural waters from irradiance attenuation coefficient and reflectance in the presence of Raman scattering", Applied Optics, vol 39, pp 3001–3011.

Loisel, H., J.-M. Nicolas, P.-Y. Deschamps, and R. Frouin (2002). "Seasonal and inter-annual variability of particulate organic matter in the global ocean", Geophysical. Research Letter, vol 29, no. 24, 2196, doi:10.1029/2002GL015948.

Loisel, H., J.-M. Nicolas, A. Sciandra, D. Stramski, and A. Poteau (2006). "Spectral dependency of optical backscattering by marine particles from satellite remote sensing of the global ocean", Journal of Geophysical Research, vol 111, C09024, doi:10.1029/2005JC003367.

Pezzulli, S., D.B. Stephenson, and A. Hannachi (2005). "The variability of seasonality". Journal of Climate, vol 18, pp 71-88.

Vantrepotte V. and Mélin F. (2009). "Temporal variability of 10-year global SeaWiFS time-series of phytoplankton chlorophyll a concentration ". ICES Journal of Marine Science, vol. 66, no. 7, pp1547-1556.

Vantrepotte V. and Mélin F. (2010). "Temporal variability in SeaWiFS derived apparent optical properties in European seas". Continental Shelf Research, 30,311-334.

Extended Abstracts in Two-Column Format for "Oceans from Space" Venice 2010

R. Venegas *, T. Strub, R. Letelier, C.O. Davis, N.B. Tufillaro

Oregon State University, Corvallis, OR, USA – rvenegas@coas.oregonstate.edu, tstrub@coas.oregonstate.edu, letelier@coas.oregonstate.edu, cdavis@coas.oregonstate.edu, nbt@coas.oregonstate.edu

Abstract – We introduce an automated Frontal Retrieval of Oceanic dyNamic Topography (FRONT) algorithm for identifying and estimating the persistence of sea surface features. This algorithm is applied to data from different satellites sensors over a range of spatial and temporal scales. The FRONT algorithm improves the visualization and quantification of bio-physical dynamic oceanic processes. Frontal features were extracted from Sea surface temperature (SST), Chlorophyll pigment concentration (CHL), and water column turbidity (K490) fields from MODIS Aqua data and CHL fields from MERIS full resolution data. Dynamic feature maps were then created through the combination of frontal feature location, strength and persistence over several days. SST, CHL and K490 dynamic feature maps were compared with multi mission AVISO/Altimeter Sea Level Anomaly (SLA) fields to assess the influence of eddies and meso-scale circulation on these surface features.

Keywords: FRONT, MODIS, MERIS, altimetry.

1. INTRODUCTION

For the last few decades remotely sensed data from satellites have been an important component in evaluating both physical and biological processes of the upper oceans. The ability to construct nearly instantaneous two-dimensional maps of multiple parameters has made it possible to recognize and monitor from space a variety of oceanic fronts and other features. In general, fronts that extend to the sea surface may be observed by satellite sensors if neighboring water masses differ enough in temperature or color, separated by a sharp boundary. Fronts evolve on time scales of days to weeks primarily as a result of differential horizontal and vertical advection (Roden and Paskausky, 1978), often accompanied by biological processes. Most studies of fronts have been conducted with sea surface temperature (SST) fields. The strongest thermal fronts are characterized by convergent or divergent flow at the surface (Bowman, 1978), which are directly linked with biologically productive regions (Castelao et al, 2006). The relationship between SST and sea surface pigment concentration (CHL) has been studied principally in coastal areas (e.g. Belkin and O'Reilly, 2009), where wind-driven upwelling and baroclinic instabilities in coastal currents cause vertical motion that raises colder and more nutrient rich water into the sunlit euphotic zone. The consistency between SST and CHL is mostly determined by the relative strength of physical processes compared to the biogeochemical processes and predation, which also control the phytoplankton distribution. Most satellite studies have used semi-automatic or automatic methods to specify frontal locations. Methods include the gradient method (e.g. Belkin and O'Reilly, 2009), use of histograms (e.g. Cayula and Cornillon, 1996) and other related approaches. The majority of these studies provide individual or overlapping frontal maps, while a few studies have merged the concepts of compositing and feature detection. By comparison, Miller (2009) has taken an additional step of combining frontal locations (determined using the single-image edge detection [SIED] algorithm) with further information from the fields (gradient strength, proximity and persistence) to visualize dynamic physical and biological oceanic processes such fronts, eddies and blooms. In this study we follow the approach suggested by Miller (2009) to combine automated detection of frontal locations with other information about the fields to identify dynamic features. We refer to this as an automated Frontal Retrieval of Oceanic dyNamic Topography (FRONT) algorithm. By applying the technique to multiple satellite sensors and parameters, we examine the ability of the methodology to identify dynamic features on different spatial and temporal scales. Maps of these features are overlayed on altimeter sea level anomaly fields to relate the bio-physical processes to mesoscale circulation.

2. FRONT PROCESSING

The FRONT algorithm is shown conceptually in Figure 1. It begins with a hierarchical mean-shift segmentation algorithm (Paris and Durand, 2007), which is based on non-parametric clustering analysis methods used in computer vision and image processing. The sea surface feature composite approach combines the location, strength and persistence of all features observed over several days into a single map (Miller, 2009). The FRONT algorithm achieves synoptic views of the oceanic surface patterns without blurring dynamic features, which is an inherent problem with conventional time-averaging composite methods. The parameters used in this study include SST, CHL and water column turbidity (K490) from MODIS Aqua, and CHL fields from MERIS. Comparisons are shown between maps of features derived from these fields and multi-mission AVISO/Altimetry sea level anomaly (SLA) maps.

3. EXAMPLE RESULTS

The FRONT algorithm detects and extracts sea surface features from multiple satellite-derived parameters on different spatial and temporal scales. In Figure 2 the spatial and temporal patterns from MODIS Aqua CHL, SST and K490 are compared. Sequential maps of dynamic features such as these can be used in planning oceanographic cruises, mooring locations and gliders paths, identification of hot spots for open ocean fisheries studies and top trophic species, as well as for planning marine protected areas.

* Corresponding Author. 104 COAS Admin. Building, Corvallis, OR, 97331, USA; tel (541)737-5707, fax (541) 737-2064

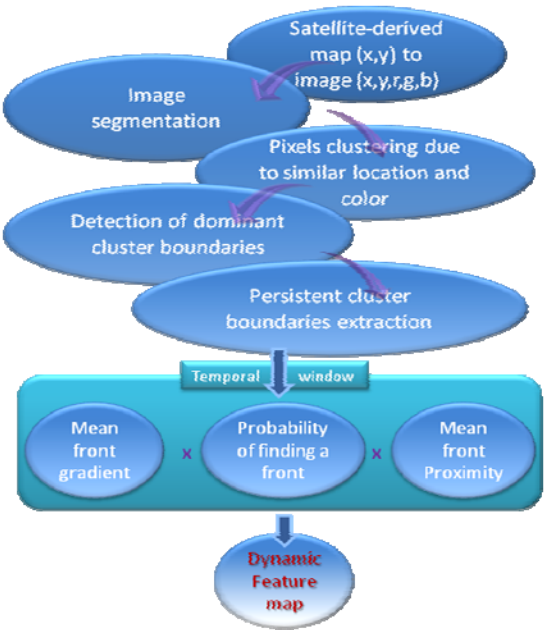

Figure 1. FRONT data processing diagram.

ACKNOWLEDGEMENTS

We would like to acknowledge the support for this study from the NOAA-NSF GLOBEC Program, the NASA Ocean Surface Topography Science Team and NOAA/NESDIS' Cooperative Institute for Oceanographic Satellite Studies.

REFERENCES

Belkin, I.M., O'Reilly, J.E., 2009. An algorithm for oceanic front detection in chlorophyll and sea surface temperature satellite imagery. Journal of Marine Systems. 78 (3), 319–326.

Bowman, M. J. (1978). Oceanic fronts in coastal processes, in Oceanic Fronts in Coastal Processes, edited by M. Bowman and W. Esias, pp. 2-5, Springer, New York.

Cayula, J.-F., Cornillon, P., 1996. Cloud detection from a sequence of SST images. Remote Sensing of Environment 55 (1), 80–88.

Castellao, R. M., T. P. Mavor, J.. A. Barth and L. C. Breaker (2006). Sea surface temperature fronts in the California Current System from geostationary satellite observations. J. of Geophysical Research, vol. 111, C09026.

Paris S. and F. Durand. (2007). A topological Approach to Hierarchical Segmentation using Mean-shift. Proceedings of the IEEE conference on Computer Vision and Pattern Recognition (CVPR'07).

Miller, P.I. (2009). Composite front maps for improved visibility of dynamic sea-surface features on cloudy SeaWiFS and AVHRR data. Journal of Marine Systems. 78, 327-336.

Roden, G. I., and D. F. Paskausky (1978). Estimation of rates of frontogenesis and frontolysis in the North Pacific ocean using satellite and surface meteorological data from January 1977, J. Geophys. Res., 83, 4545-4550.

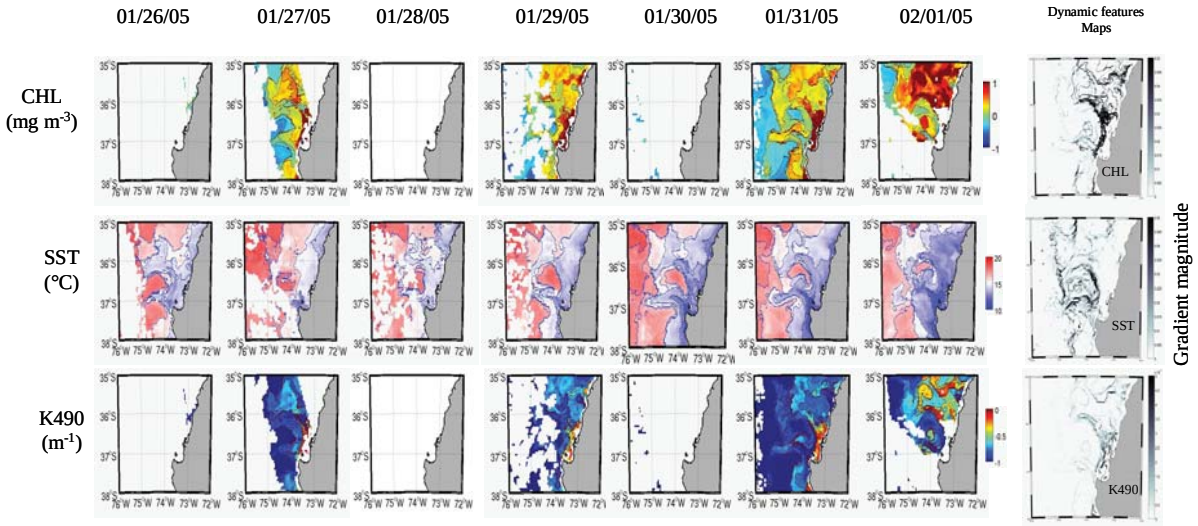

Figure 2. Individual frontal maps, from January 26 – February 1, 2005, are displayed for Sea surface temperature (SST), Phytoplankton pigment concentration (CHL), and water column turbidity (K490) along the south-central coast of Chile. The corresponding maps of dynamic features obtained for each parameter from the 7 daily fields are shown on the right.

The Use of Ocean Colour Data in Global Biogeochemical Model Assessment

M. Vichi [a,b,*], S. Masina [a,b]

[a] Centro Euro-Mediterraneo per i Cambiamenti Climatici, Bologna , Italy – vichi@bo.ingv.it
[b] Istituto Nazionale di Geofisica e Vulcanologia, Bologna, Italy

Abstract – Global Ocean Biogeochemistry General Circulation Models (OBGCM) simulates biogeochemical processes at global and large scales as driven by advection and mixing oceanic processes. Ocean colour data and derived products are an essential resource for OBGCM skill assessment and have been used in this work to validate the results of a comprehensive global biogeochemical model (PELAGOS).

Keywords: biogeochemical model, ocean colour, validation

1. INTRODUCTION

Ocean biogeochemical general circulation models combine the physical processes resolved by GCM with biogeochemical models that simulates the biomass production of lower trophic levels with the aim to describe the founding components of the ocean carbon cycle. The assessment of model skill is a necessary prerequisite before using OBGCMs for building projections of changes in the carbon cycle under future climate scenarios. One of the most comprehensive OBGCM has been thoroughly validated against biogeochemical data from the period 1980-2001 (Vichi and Masina, 2009). Following considerations in Friedrichs et al. (2009), Vichi and Masina further demonstrated that satellite-derived primary production models show similar skills as fully-prognostic OBGCMS when compared with independent observations from the equatorial Pacific. Therefore global estimates of primary production from ocean color data have still limited use for model validation in certain regions. Model validation issues in ocean biogeochemistry are similar to the one in social sciences. Given the substantial assumptions in model construction and model-data equivalence, goodness-of-fit (GOF) tests based on null hypotheses that model fits data are expectably false, especially when the sample is large as in the case of global coverage data as ocean colour. However, the methodology underlying these tests turns out to be extremely useful to separate the sources of error when making comparisons. In this work we present methods that evidence the importance of an adequate comparison between ocean colour chlorophyll data and model output for the purpose of validation and model improvement, with an emphasis on the grid choice used for comparison. The global ocean biogeochemical model used in this study is PELAGOS (PELAgic biogeochemistry for Global Ocean Simulations, Vichi et al., 2007a,b), which is a coupling between the OPA (Océan PArallélisé) general circulation model (Madec et al., 1999) and the global ocean version of the Biogeochemical Flux Model (BFM, http://bfm.cmcc.it). The model grid is irregular with mesh size varying from 0.5 at the equator to 2 degrees.

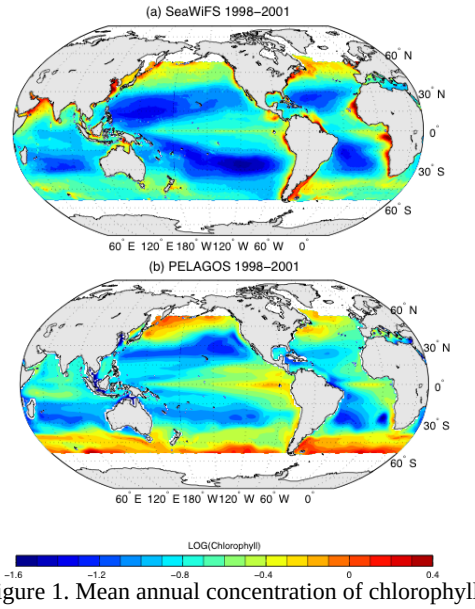

Figure 1. Mean annual concentration of chlorophyll (logarithmic scale) from (a) SeaWiFS and (b) PELAGOS.

The biogeochemical model is a multiple nutrient, multiple plankton functional group model described in terms of biomass of carbon and major macro and micronutrients. The ratios of the biogeochemical components in the living and non-living chemical functional groups vary dynamically, including the chlorophyll:carbon ratio in phytoplankton. The model is fully detailed in Vichi et al. (2007a,b) and the inter-annual simulation forced by the ECMWF ReAnalysis (ERA40, 1958-2001) used in this work is described in Vichi and Masina (2009). Here we focus on the period of the simulation covered by Sea-viewing Wide Field-of-view Sensor (SeaWiFS) data (1998-2001).

2. COMPARISON WITH OCEAN COLOUR

2.1 Mean chlorophyll

Face validity is the visual comparison of model and observations, usually done by means of climatological means; it is a first necessary step, yet its interpretation is purely subjective and strongly based on the choice of colours, axes intervals or contour levels. Model chlorophyll data shown in Fig. 1 in logarithmic units were computed by averaging over the dynamically-computed euphotic zone. Model and data are compared on regular grids varying from 0.25 to 4 degrees and on the original grids, using binning for ocean colour and “nearest neighbour” interpolation for model data. With respect to the climatological results presented in Vichi et al. (2007b) chlorophyll distribution is much improved.

* Corresponding Author. Viale A. Moro 44, 40127 Bologna, Italy.

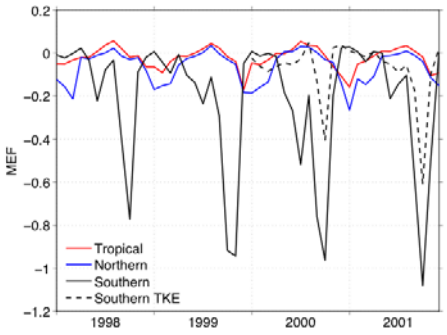

Figure 2. Temporal variation of MEF in ocean regions

Apart from the lack of coastal maxima, the largest biases are in the Southern Ocean and in the Indian Ocean, with an overestimation in the former and underestimation in the latter. To move beyond face validity, pattern correlation can be evaluated objectively by means of the Spearman rank correlation coefficient, which quantifies the relationship between highs and lows. The resulting value from data in Fig. 1 is ρ=0.69, which is highly significant according to a comparison with an empirical Monte Carlo distribution of ρ values.

Another useful measure is the Modelling Efficiency (Nash and Sutcliffe, 1970) that computes the ratio between model error and data variability (spatial in this case):

$$MEF = 1 - \frac{\sum_{n=1}^{N}(O_n - P_n)^2}{\sum_{n=1}^{N}(O_n - \overline{O})^2} \quad (1)$$

where O_n, P_n = observation and prediction pairs, N is the total number of model or observation data and the bar indicates the mean. GOF is achieved when MEF tends to 1, whereas values close to 0 indicate that the model is as good a predictor as the mean of observations. MEF can be used to assess the temporal evolution of model error and can be also separated into sub-regions as shown in Fig. 2 modified from Vichi and Masina (2009). The picture shows that the largest error is found in the Southern Ocean especially during the Austral spring. The dashed lines indicate the reduction of model error when deeper mixed layers are artificially induced by increasing the total kinetic energy in the first 300 m of the ocean (Vichi and Masina, 2009). It may also be argued that the binning of SeaWiFS data onto a coarser grid generates a significant loss of information. For instance, the large spatial variability of ocean colour data linked to ocean mesoscale may contribute to the lack of fit of the model, which is by construction able to resolve only larger scale ocean dynamics. A method to estimate independently from model data the variability of observations can be derived from the lack-of-fit (LOF) tests in the analysis of variance with replicate observations (e.g. Smith and Rose, 1995). In our context, it is assumed that the multiple observations are the number of pixels K_n found in a given regular bin of variable size. The average over this bin is equivalent to the observation mean used in eq. (1) and shown in Fig. 1. Using the same notation as above, it may be shown that

$$SSD = \sum_{n=1}^{N}\sum_{k=1}^{K_n}\left(O_{nk} - \overline{O}_n\right)^2 + \sum_{n=1}^{N} K_n\left(\overline{O}_n - P_n\right)^2 \quad (2)$$

where SSD is the sum-of-square-distance between each observation and the two terms represent the data variance (pure error, SSPE) and the model lack-of-fit (SSLOF), respectively. We are interested in the mean SSD that is obtained by adjusting for proper degrees of freedom MSPE=SSPE/(K-N) and MSLOF=SSLOF/N. In Table 1, we present the results of the mean terms in eq. (2) as a function of the regular grid used for the comparison. MSPE is much smaller than MSLOF indicating that the mean error is dominated by model LOF. However this value decreases with the grid size and it is smaller when the native grids are used (MSPE cannot be computed in those cases because interpolation is used and not binning).

Table 1.

Grid (°)	N	K	MSPE	MSLOF
4	1387	798912	0.0039	60.1
2	6145	884880	0.0023	15.3
1	25680	924480	0.0012	3.79
0.5	105391	945716	0.0006	0.98
0.25	422833	950669	0.0004	0.25
data (1/6)	953270			0.11
model (0.5-2)	10554			0.12

3. CONCLUSION

Model validation depends principally on the objectives and operational assumptions of the model. Vichi and Masina (2009) demonstrated that PELAGOS can provide objectively valid estimates of carbon transformation rates in selected regions despite the limited skill in reproducing ocean colour data at the global scale. However, the usage of ocean colour data is essential to improve model discrepancies in poorly simulated regions such as the Southern Ocean. It is also shown that the variability of ocean colour observations is a second order term in GOF analysis. The GOF analysis against high-resolution ocean data reduces the LOF when the data are interpolated on either the model or data native grids.

ACKNOWLEDGEMENTS

This work was funded by Centro Euro-Mediterraneo per i Cambiamenti Climatici (CMCC). Use of SeaWiFS data according to the Research Data Use Terms & Agreements.

REFERENCES

Friedrichs et al. (2009), Assessing the uncertainties of model estimates of primary productivity in the tropical pacific ocean, J. Mar. Sys., 76(1-2), 113–133

Madec, G., P. Delecluse, M. Imbard, and C. Levy (1999), OPA8.1 ocean general circulation model reference manual, Notes du pole de modelisation, IPSL, France,

Nash, J., and J. Sutcliffe (1970), River flow forecasting through conceptual models, Part 1 — a discussion of principles, Journal of Hydrology, 10, 282–290.

Smith, E. P., and K. A. Rose (1995), Model goodness-of-fit analysis using regression and related techniques,
Ecol. Model., 77 (1), 49–64.

Vichi, M., S. Masina, and A. Navarra (2007b), A generalized model of pelagic biogeochemistry for the global ocean ecosystem. Part II: numerical simulations, J. Mar. Sys., 64, 110–134.

Vichi, M., N. Pinardi, and S. Masina (2007a), A generalized model of pelagic biogeochemistry for the global ocean ecosystem. Part I: theory, J. Mar. Sys., 64, 89–109.

Vichi, M. and Masina, S. (2009) Skill assessment of the PELAGOS global ocean biogeochemistry model over the period 1980–2000, Biogeosciences, 6, 3511-3562.

Interannual-Decadal Variability of Cyclonic Activity over the Mediterranean and Black Sea Regions

E.N. Voskresenskaya*, V.N. Maslova, T.M. Bayankina

Marine Hydrophysical Institution, Sevastopol, Ukraine – elena_voskr@mail.ru

Abstract – The aim of this paper is to analyze the interannual and decadal variability of the parameters of cyclones over the Mediterranean and Black Sea regions associated with the North Atlantic Oscillation (NAO), El-Nino – Southern Oscillation (ENSO) and Pacific Decadal Oscillation (PDO). Daily NCEP / NCAR reanalysis data sets in 1948 – 2006 and satellite information from EUMETSAT in 1996 – 2009 were used. It was shown that the joint influence of the NAO and ENSO is responsible for more than 50% of the cyclonic variability in the studied regions. The climatic shift in the variability of the parameters of cyclones associated with the PDO phase change in the middle of the 1970s was detected.

Keywords: Mediterranean cyclones, NAO, ENSO, PDO.

1. INTRODUCTION

Black Sea - Mediterranean region is one of principal regions regarding to policy making on sustainable development of surrounding countries. Due to favourable climate conditions these region is known as rich agriculture, fishery and recreational zones with high density of population. There are some of the best resorts all over the world. At the same time, human activity and human health are vulnerable to climate changes and variability. One of the principal indicators of climate change and variability in the region is cyclonic activity associated with large scale processes in the ocean-atmosphere system.

Parameters of cyclonic variability in the Black Sea region associated with North Atlantic Oscillation were analysed by Bardin *et al.* (2007). NCEP reanalyses data sets in 1950 – 1998 permited to receive some statistical sygnificant characteristics of the NAO influece on the frequency of cyclones (Bardin *et al.*, 2007). At the same time, Southern Oscillation (SO) is an important global interannual climatic signal too. Its manifestations in some hydrometeorological fields of the Atlantic-European region including Black Sea were analyzed for instance by Cullen *et al.* (2002) and Polonsky *et al.* (2003a). Joint NAO and ENSO influence on some parameters of European / Black Sea environment was studied in particular by Compo *et al.* (2001) and Polonsky *et al.* (2003b). However, cyclonic activity in the Black Sea - Mediterranean region associated with ENSO and PDO was not studied yet for now.

The aim of the paper is to study the interannual-decadal variability of the cyclonic activity in the Mediterranean and Black sea regions associated with joint NAO, ENSO and PDO influence using improved NCEP / NCAR re-analyses data sets for the period 1948 – 2006 and satellite data sets.

2. DATA AND METHODOLOGY

On the basis of daily NCEP / NCAR reanalyses data sets on the 1000 mb geopotential high on the 2.5º x 2.5º greed square in 1948 – 2006 the cyclones were selected for the Black Sea region and eastern and western Mediterranean, as shown in Figure 1.

Figure 1. The boundaries of the studied regions.

The following procedure was used to select cyclones in the studied regions and to calculate the main characteristics of cyclones – frequency, depth, area and intensity for each month, season and year. This procedure was described in detail by Bardin *et al.* (2007). The technique includes the following equations:

$$f_h = \int x \in S_i \, f(x) ds, \tag{1}$$

$$l_h = \int x \in S_i l(x) ds, \tag{2}$$

where f_h, l_h = coordinates of cyclonic centre
S_i = area of a figure limited by the first isobar contour (see Figure 2).

Depth (D) at the even greed square is

$$D = |h - Z(S_0)|, \tag{3}$$

where $Z(S_0)$ – the last exclusive contour
S_0 = area of the figure limited by the last isobar contour
h = the nearest to the minimum depth point greed junction.

Area (A) limited by the last exclusive contour, volume (V) and intensity (I) are accordingly:

$$A = \int x \in S_0 ds, \tag{4}$$

$$V = \int x S_0 (Z(x) - Z(S_0)) ds, \tag{5}$$

$$I = \frac{V}{A}. \tag{6}$$

* Corresponding Author. Kapitanskaya St. 2, Sevastopol, 99011, Ukraine.

To select cyclones on the basis of Meteosat 2 – 8 satellite data sets from EUMETSAT on cloudiness in visible and IR range in winter season of 1983-2009 the special software package was created (Voskresenskaya *et al*., 2007).

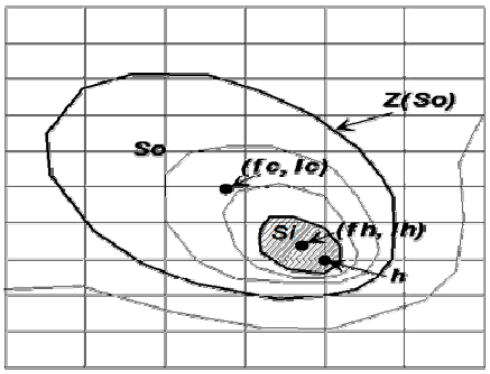

Figure 2. Isobar contour chart, f_h, l_h – coordinates of the cyclone centre (minimum depth point); f_c, l_c – coordinates of the geometrical cyclone centre.

To analyze influence of the large-scale processes in the ocean-atmosphere system on interannual-decadal variability of the parameters of cyclones the NAO, SO (Southern Oscillation) and PDO indices were used.

3. RESULTS AND DISCUSSION

The comparison between parameters of cyclones selected from NCEP / NCAR and associated ones detected using satellite data sets for three studied regions showed good agreement. The correlation coefficients between them reach 0.86, it is due to the fact that the NCEP / NCAR reanalysis after 1979 is based mostly on satellite data.

Analysis of the variability of the parameters of cyclones showed that the maximum magnitudes of interannual-decadal cyclonic activity are in winter-spring season, the minimum ones are in summer months. Polynomial trends of the calculated parameters of cyclones reveal, apart from interannual variability, quasiperiodical decadal fluctuations of the analyzed time series. The linear trends similar with lower frequency variations are typical for their variability.

Spectrum analysis revealed quasi-biennial variability inherent to the all studied regions. Spectral maximum on 4.3 – 4.8 years occur frequently too. Time scales of 7 – 8 years are allocated some rarely. Hence, this result supports the statement that cyclonic variability over the studied regions is characterized by the same time scales as NAO and ENSO.

The correlation analysis of monthly cyclonic characteristics with the NAO and SO indices was done. Maximum correlation coefficients of the winter-spring cyclonic parameters with NAO-index exceed 0.6, while with SO-index reaches 0.49 with time lags of 4–6 months. Thus we can conclude that the joint influence of NAO and ENSO is responsible for more than 50% of cyclonic variability in winter and spring in the Mediterranean-Black Sea region.

Finally, the composite analysis of the characteristics of cyclones in 1948 – 1976 and 1977 – 2006 associated with the periods of negative and positive PDO phases demonstrates the climatic shift in the middle of the 1970s. In Figure 3, the example of differences between the mean values of cyclonic frequency is seen.

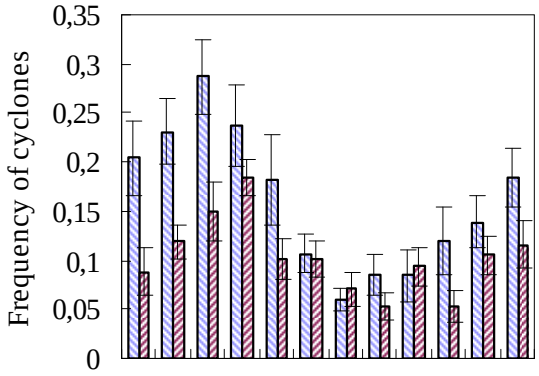

Figure 3. Composites of the frequency of the Black Sea cyclones in negative (left column) and positive PDO phases (right column). Error range corresponds to 80% of statistical significance.

4. CONCLUSIONS

It is shown that typical scales of cyclonic variability over the studied regions are 2, 4.3–4.8 and 7–8 years, this confirms that this variability is characterized by the same time scales as NAO and SO. The joint influence of the NAO and ENSO is responsible for more than 50% of the cyclonic variability in the studied regions. The climatic shift in the variability of the parameters of cyclones associated with the PDO phase change in the middle of the 1970s was detected.

REFERENCES

1. Bardin, M.Yu., A.B. Polonsky and E.N. Voskresenskaya (2007). "Statistical characteristics of cyclones and anticyclones over the Black Sea in the second half of the 20th century". Physical Oceanography, vol. 17, no. 6, pp.348-359.

2. Voskresenskaya E., T. Bayankina (2007). "Mediterranean cyclones and weather-climate anomalies in the Black Sea region". Systems of the environmental monitoring, ECOSI-Hydrophysics, pp. 319-323.

3. Compo, G.P., P.D. Sardeshmukh, C. Penland (2001). "Changes of subseasonal variability associated with an El Nino". Journal of Climate **14** (16), pp. 3356-3374.

4. Cullen, H.M., A. Kaplan, Ph.A. Arkin, P.B. Demenocal (2002). "Impact of the North Atlantic Oscillation on Middle Eastern climate and streamflow". Climatic Change **55**, pp.315-338.

5. Polonsky, A., E. Voskresenskaya (2003a). "ENSO-induced climate variability over the Europe". Studia Geograficzne, Wroclaw, **75** (2532), pp. 87-97.

6. Polonsky, A., E.Voskresenskaya, D. Basharin (2003b). "Coupled ocean-atmosphere system and its impacts on European climate". In book: Climate in transition, ed. by L.C. Nkemdirim, Washington, DC Minuteman Press, pp.15–27.

Significant Wave Height of Typhoon Induced Ocean Waves from Multi-Satellite Altimetry Data

J.Yang [a,b], X. Chen [a], R. Zhang [a], J. Wang [a], W. Huang [a,b]

[a] State Key Laboratory of Satellite Ocean Environment Dynamics, Second Institute of Oceanography, State Oceanic Administration, Hangzhou, China
[b] Department of Ocean Science and Engineering, Zhejiang University, Hangzhou, China

Abstract –The significant wave height (SWH) data from GFO, TOPEX/Poseidon, Jason-1 and Envisat are merged to analyze the temporal and spatial features of ocean waves in case of typhoon Rananim passing by. The relationship between SWH and wind speed of typhoon Rananim are also studied by using QuikSCAT data. Case studies show good results.

Keywords: significant wave height, altimetry, typhoon.

1. INTRODUCTION

The merged data from multiple remote sensors is often used to increase the temporal and spatial resolution of data coverage. Since the launch of TOPEX/Poseidon in 1992, data from at least two satellite altimeters are available in a given period. This paper presents the feasibility of temporal and spatial features analysis of typhoon Rananim induced ocean waves from multi-satellite altimetry data.

2. METHODOLOGY

As we have studied before, there is little difference between the merged results for different fusion methods in case the altimeter data are not sparse (Yang, et al. 2008). In this paper, we use the successive correction method. This method is one of the most popular interpolation methods. It starts with a first-guess field (F_{ij}), which it then corrects by adding in weighted averages of the observed data (C_{ij}). It can be formulated as (Cressman, 1959)

$$G_{ij} = F_{ij} + C_{ij} \tag{1}$$

where G_{ij} the interpolation result at the center of grid cell (i, j) , and

$$C_{ij} = \sum_{s=1}^{n} Q_s W_s / \sum_{s=1}^{n} W_s \tag{2}$$

where n the number of observation points in the grid cell with radius R , Q_s the difference between mean and first-guess value of the s th point, W_s the weight, and

$$W_s = \exp(-4r^2 / R^2) \quad r \le R \tag{3}$$

3. DATA

GFO, TOPEX/Poseidon, Jason-1 and Envisat altimetry SWH data used in this study are from NOAA, NASA and ESA (Figure.1). These satellites have revisit periods of 17, 10, 10 and 35 days respectively. Corrections are made to ensure the consistency of SWH data from different altimeters (Queffeulou, 2003).

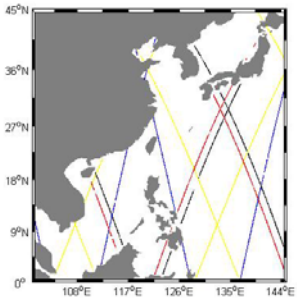

Figure.1. Tracks of altimeters on 8 Aug. 2004

4. SOME RESULTS

It is shown that the merged data could reveal the moving path of Rananim very well (Figure.2).

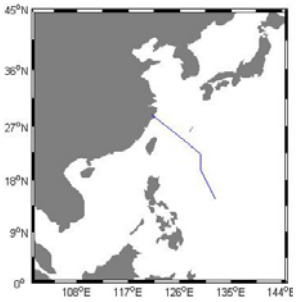

Figure.2. Path of typhoon Rananim

As Rananim evolved from a tropical storm into a powerful typhoon, the wave height became higher and higher. The daily average wave height increased from 5.5m to 8.5m and the maximal wave height increased from 6m to 10m. The spatial distributions of wave height are asymmetrical to the center of typhoon. The range/radius of wind speed above 15 m/s agree with that of wave height above 3m (Figure.3a-i)

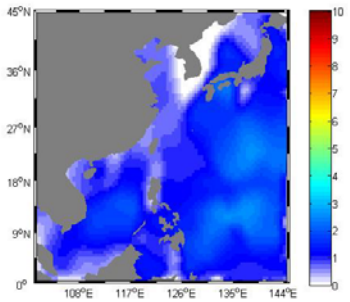

(a) 5 Aug.

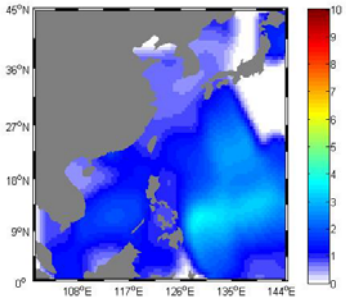

(b) 6 Aug.

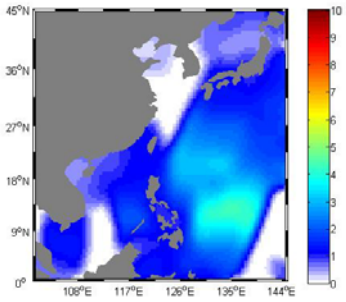

(c) 7 Aug.

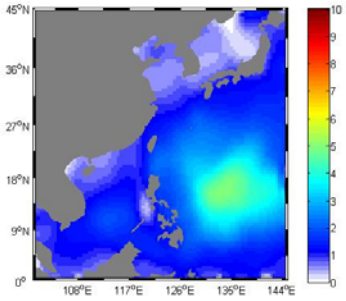

(d) 8 Aug.

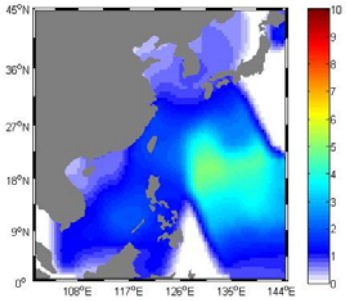

(e) 9 Aug.

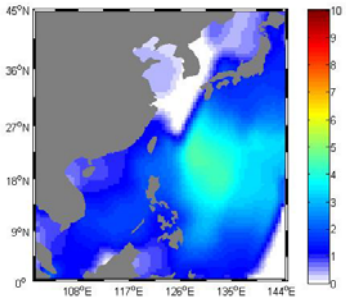

(f) 10 Aug.

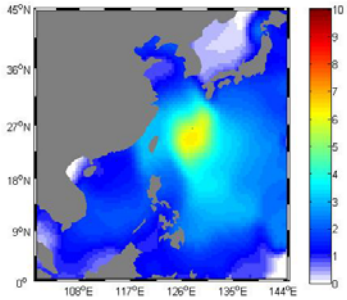

(g) 11 Aug.

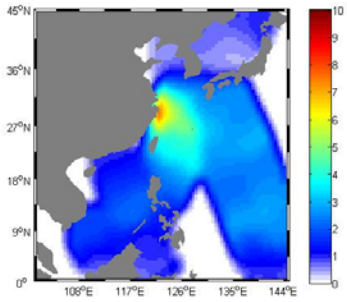

(h) 12 Aug.

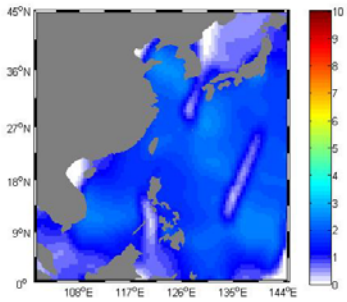

(i) 13 Aug.

Figure.3. Maps of SWH from 5-13 Aug. 2004

REFERENCES

Cressman, G. P. (1959). "An operational objective analysis system", *Monthly weather review*, vol87, pp. 367-374.

Queffeulou, P. (2003), "Long term quality status of wave height and wind speed measurements from satellite altimeters", *Proceedings of the ISOPE conference*, Honolulu, Hawaii, USA.

Queffeulou, P. (2003) "Validation of ENVISAT RA-2 and JASON-1 altimeter wind and wave measurements", *International Geoscience and Remote Sensing Symposium*, Toulouse, France, pp. 2987-2989.

Yang, J. et al. (2008). "Data fusion of significant wave height from multiple satellite altimeters", *Proceedings of SPIE*, v7154

AERONET-OC: a standardized network for satellite ocean color validation

G.Zibordi [a], B.Holben [b], F.Mélin [a], D.D'Alimonte [c], J.-F.Berthon [a], I.Slutsker [d], D.Giles [d]

[a] Institute for Environment and Sustainability, Joint Research Centre, European Commission, Ispra, Italy
[b] Goddard Space Flight Centre, NASA, Greenbelt, MD 20771, USA
[c] Centro de Inteligência Artificial, Universitade Nova de Lisboa, Caparica, Portugal
[d] Sigma Space Corporation, Goddard Space Flight Center, Greenbelt, MD 20771, USA

Abstract – The Ocean Color component of the Aerosol Robotic Network (AERONET-OC) was established to support satellite ocean color validation activities in coastal waters through standardized measurements of atmospheric and marine optical quantities. Specifically, AERONET-OC provides *in situ* spectral values of the normalized water-leaving radiance, L_{WN}, and aerosol optical thickness, τ_a, through autonomous radiometers operated on fixed platforms in coastal waters. This work summarizes the network elements and data applications.

Keywords: ocean color, radiometry, validation.

1. INTRODUCTION

Satellite ocean color has very strict accuracy requirements imposed by the relatively small contribution to top-of-atmosphere signal of the so called water-leaving radiance L_w (5-10% at the best) that carries information on the optically significant materials suspended and dissolved in seawater. Because of this, major satellite ocean color programs actively support the collection of *in situ* data to assess the accuracy of derived remote sensing products. Ideal i*n situ* data for the validation of satellite derived primary products should be: *i.* traceable to reference standards and with defined uncertainties; *ii*. globally distributed to represent the wide range of geophysical conditions that remote sensing sensors are expected to observe; *iii.* continuous to ideally embrace successive space missions; *iv*. cross-site consistent to exhibit comparable uncertainties at the various measurement sites for similar measurement conditions; and finally *v.* accessible to any calibration and validation program through a suitable data policy.

Aiming at supporting the former requirements, the Ocean Color (OC) component of the Aerosol Robotic Network (AERONET) generates *in situ* L_w from continuous *standardized measurements performed at different sites with identical measuring systems and protocols, calibrated using a single reference source and method, and processed with the same code* (Zibordi *et al*. 2009b).

2. AERONET-OC

AERONET-OC is a component of AERONET (Holben *et al.* 1998), a federated instrument network and data archive, managed by the Goddard Space Flight Center (GSFC) of the U.S. National Aeronautics and Space Administration (NASA) and specifically conceived to support aerosol investigations (Holben *et al.* 2001). Similar to AERONET, AERONET-OC relies on NASA's commitment for field instrument calibration, data processing and archiving. These basic activities are complemented by world wide spread contributions of individuals and institutions aiming at establishing and maintaining CE-318 modified sun-photometers at coastal sites of interest. These modified sun-photometers, called SeaWiFS Photometer Revision for Incident Surface Measurements (SeaPRISM), have the capability of performing autonomous above–water radiometric measurements in addition to usual AERONET atmospheric measurements.

Key features of AERONET-OC are: *i.* near-real time data collection, processing and archiving; *ii.* use of standardized instruments, calibration and data processing; *iii.* open access to measurements and products through a specified data policy. The primary data product of AERONET-OC is L_{WN} at wavelengths suitable for satellite ocean color applications. Additional product is the aerosol optical thickness, τ_a, complemented by phase function, particle size distribution and single scattering albedo of aerosols, all having potential importance to assess the performance of the atmospheric correction process applied to satellite data.

The quality assurance of L_{WN} (see Zibordi et al. 2009b) includes checking for: *i.* cloud contamination; *ii.* high variance of multiple sea- and sky-radiance measurements utilized for computing L_{WN}; *iii*. elevated differences between pre- and post-calibrations of SeaPRISM radiometers; and *iv*. spectral inconsistency of L_{WN} data. Estimated uncertainties of *in situ* L_{WN} data are 4-5% in the blue-green spectral regions and ~8% in the red for moderately turbid waters (Zibordi et al. 2009b).

Taking advantage of available and accessible offshore grounded structures, AERONET-OC sites are mostly located in coastal regions. Figure 1 displays a map of current, planned and potential AERONET-OC sites.

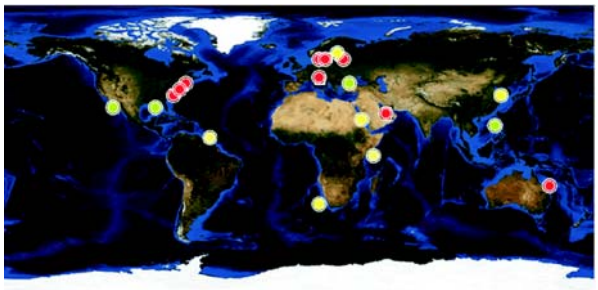

Figure 1. Map of AERONET-OC sites. Filled red circles indicate active sites while green and yellow circles indicate planned and potential new sites.

3. APPLICATIONS

The validation of ocean color radiometric products is the most direct application of AERONET-OC data. However, additional regional applications are the vicarious calibration of satellite data, and the minimization of cross-mission uncertainties and biases.

The vicarious calibration of satellite ocean color data aims at minimizing uncertainties affecting both the absolute

calibration of the space sensor and the atmospheric correction process. The need for generating global satellites ocean color products requires that vicarious calibrations are performed at sites (e.g., deep oligotrophic regions) representative of the majority of oceanic waters. However, AERONET-OC sites satisfying basic requirements of spatial homogeneity, distance from the coast to minimize adjacency effects in remote sensing data and water depth to avoid bottom perturbations, can also be considered vicarious calibration targets for regional applications as demonstrated with time-series from the Adriatic and Baltic Sea sites (Mélin and Zibordi, 2010).

Different space sensors, calibration schemes and atmospheric corrections codes, are the source of diverse uncertainties in remote sensing primary products (Zibordi et al. 2006), which might lead to unpredictable differences in high level products like chlorophyll-a concentration commonly used as a proxy for phytoplankton biomass (Mélin et al. 2007). Thus, the assessment of primary satellite derived radiometric products is a pre-requisite for the use of remote sensing data in climate change studies. By relying on AERONET-OC data, example of such an assessment is proposed for L_{WN} data derived with the SeaWiFS Data Analysis System (SeaDAS) software package version 5.2 (Fu et al. 1998) using data from the Moderate Resolution Imaging Spectroradiometer (MODIS) onboard the Aqua platform.

AERONET-OC data also have application in the minimization of errors introduced in satellite derived L_{WN} by the atmospheric correction process regardless of the applied vicarious calibration (D'Alimonte et al. 2008, Zibordi et al. 2009a). This regional application, which relies on the use of match-ups of satellite and *in situ* data to statistically model systematic errors in remote sensing products, is absolutely relevant in view of the merging of primary radiometric products from independent space missions.

4. CONCLUDING REMARKS

This overview highlights the relevance of AERONET-OC data to complement measurements performed with oceanographic ships and optical moorings, for the validation of ocean color primary radiometric products. Additionally, in agreement with accuracy requirements for the Global Earth Observation System of Systems (GEOSS), AERONET-OC strengthens the capability to trace uncertainties in products from different remote sensing systems through time-series of highly consistent *in situ* data from coastal sites exhibiting different marine optical properties. Finally, the demonstrated applicability of AERONET-OC data to determine regional vicarious adjustments factors for satellite sensors calibration coefficients, and additionally to minimize systematic errors induced by the atmospheric correction process, opens to the possibility to generate regional high level remote sensing products of unprecedented accuracy.

ACKNOWLEDGEMENTS

The authors also wish to thank the whole AERONET team for the continuous effort in supporting AERONET-OC, the NASA Ocean Biology Processing Group for granting access to the MODIS and SeaWiFS data, and the ESA Cal/Val Program for the support provided for the Adriatic Sea AERONET-OC site.

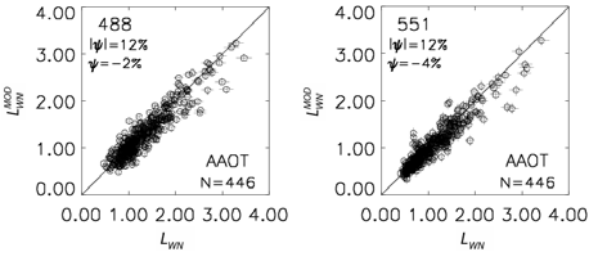

Figure 2. Scatter plots of normalized water leaving radiances obtained at the northern Adriatic Sea AERONET-OC site from MODIS top-of-atmosphere radiances (L_{WN}^{MOD}) and *in–situ* radiometric measurements (L_{WN}) at 488 and 551 nm. Symbols $|\psi|$ and ψ indicate uncertainties and biases expressed through the average of absolute differences and the average of differences, respectively. *N* indicates the number of match-ups (after Zibordi and Voss, 2010).

REFERENCES

D'Alimonte, D., Zibordi, G., and Mélin, F. (2008). "A statistical method for generating cross-mission consistent normalized water-leaving radiances". IEEE Transactions on Geoscience and Remote Sensing, Vol. 46, pp. 4075–4093.

Fu, G., Baith, K., and McClain, C. 1998. The SeaWiFS Data Analysis System. In proceedings of the 4th Pacific Ocean Remote Sensing Conference, Qingdao, China, July 1998, pp. 73–79.

Holben, B.N., Tanré, D., Smirnov, A., Eck, T.F., Slutsker, I., Abuhassan, N., Newcomb, W.W., Schafer, J., Chatenet, B., Lavenue, F., Kaufman, Y.J., Vande, Castle, J., Setzer A., Markham, B., Clark, D., Frouin, R., Halthore, R., Karnieli, A., O'Neill, N.T., Pietras, C., Pinker, R.T., Voss, K., and Zibordi G. (2001). "An emerging ground-based aerosol climatology: Aerosol Optical Depth from AERONET". Journal of Geophysical Research, Vol. 106, pp. 12067–12097.

Mélin, F., and Zibordi, G. (2010). "Vicarious Calibration of Satellite Ocean Color Sensors at Coastal Sites". Applied Optics, Vol. 49 (in press).

Mélin, F., Zibordi, G. and Berthon J.-F. (2007). "Assessment of satellite ocean color products at a costal site". Remote Sensing of Environemnt, 110, 192–205.

Zibordi, G., Berthon, J.-F., Mélin, F., D'Alimonte, D., and Kaitala, S. (2009a). "Validation of satellite ocean color primary products at optically complex coastal sites: northern Adriatic Sea, northern Baltic Proper and Gulf of Finland". Remote Sensing of Environment, Vol. 113, pp. 2574–2591.

Zibordi, G., Holben, B., Slutsker, I., Giles, D., D'Alimonte, D., Mélin, F., Berthon, J.-F., Vandemark, D., Feng, H., Schuster, G., Fabbri, B. E., Kaitala, and S., Seppälä, J. (2009b). "AERONET-OC: a network for the validation of Ocean Color primary radiometric products". Journal of Atmospheric and Oceanic Technology, Vol. 26, pp. 1634–1651.

Zibordi, G., Mélin, F., and Berthon, J.-F. (2006). "Comparison of SeaWiFS, MODIS and MERIS radiometric products at a coastal site". Geophysical Research Letters, Vol. 33, L06617, doi:10.1029/2006GL25778.

Zibordi, G. and Voss, K. J. (2010). "Field Radiometry and Ocean Color Remote Sensing". In *Oceanography from Space, revisited.* Barale V., Gower J.F.R. and Alberotanza L. Ed.s, Springer, Dordrecht, pp. 307–334.

Subject Index

Author Index

European Commission

EUR 24324 EN – Joint Research Centre – Institute for Environment and Sustainability
Title: Proceedings, “Oceans from Space” Venice 2010
Extended Abstracts of the Contributions presented at the “Oceans form Space” Symposium
Scuola Grande di San Giovanni Evangelista, Venice (Italy), 26-30 April 2010
Authors: V. Barale, J.F.R. Gower, L. Alberotanza, ed.s
Luxembourg: Publications Office of the European Union
2010 – 266 pp. – 21.0 x 29.7 cm
EUR – Scientific and Technical Research series – ISSN 1018-5593
ISBN 978-92-79-15577-2
DOI 10.2788/8394

Abstract

The Extended Abstracts of the poster presentations delivered at the 4th “Oceans from Space” Symposium – held in Venice, Italy, on 26-30 April 2010 – address every facet of space sciences and technologies applied to marine and maritime issues. Missions, satellites, sensors, passive and active techniques, calibration and validation schemes, algorithms and models are covered. Applications range from the study of physical dynamical processes to that of biological and ecological status, from local to global scales. The results already achieved, or soon to come, demonstrate the potential of oceanographic remote sensing to explore the dynamical and bio-geo-chemical features of the World’s Oceans.

How to obtain EU publications

Our priced publications are available from EU Bookshop (http://bookshop.europa.eu), where you can place an order with the sales agent of your choice.

The Publications Office has a worldwide network of sales agents. You can obtain their contact details by sending a fax to (352) 29 29-42758.

The mission of the JRC is to provide customer-driven scientific and technical support for the conception, development, implementation and monitoring of EU policies. As a service of the European Commission, the JRC functions as a reference centre of science and technology for the Union. Close to the policy-making process, it serves the common interest of the Member States, while being independent of special interests, whether private or national.

JRC
EUROPEAN COMMISSION

LB-NA-24324-EN-C

ISBN 978-92-79-15577-2

Publications Office